DEVELOPMENT OF BUTYRYLCHOLINESTERASE LIGANDS FOR THE IMAGING OF NEUROLOGICAL DISORDERS

by

Ian Roderic Macdonald

Submitted in partial fulfilment of the requirements
for the degree of Doctor of Philosophy

at

Dalhousie University
Halifax, Nova Scotia
June 2013

DALHOUSIE UNIVERSITY

DEPARTMENT OF MEDICAL NEUROSCIENCE

The undersigned hereby certify that they have read and recommend to the Faculty of Graduate Studies for acceptance a thesis entitled "Development of Butyrylcholinesterase Ligands for the Imaging of Neurological Disorders" by Ian Roderic Macdonald in partial fulfilment of the requirements for the degree of Doctor of Philosophy.

Dated: June 12, 2013

External Examiner: _____

Research Supervisor: _____

Examining Committee: _____

_____

_____

Departmental Representative: _____

DALHOUSIE UNIVERSITY

DATE: June 12, 2013

AUTHOR: Ian Roderic Macdonald

TITLE: Development of Butyrylcholinesterase Ligands for the Imaging of Neurological Disorders

DEPARTMENT OR SCHOOL: Department of Medical Neuroscience

DEGREE: PhD CONVOCATION: October YEAR: 2013

_____

Signature of Author

To my Parents, Andrew, Lindsay and Elizabeth

Even now the world is full of enigmas, of hidden properties, of unknown forces. Consequently, science, far from being exhausted, invites everybody with inexhaustible veins of ore. Since, fortunately, we live in the dawn of man's knowledge of nature; since we are still surrounded with a dark cloud which is rent by human curiosity only here and there; and if, anyhow, scientific discovery is due no more to genius than to chance, then we can all be inventors. To do so, it is enough to play obstinately and persistently on one and the same number in this lottery. It is entirely a question of patience and perseverance.

Santiago Ramón y Cajal
1852 – 1934

TABLE OF CONTENTS

LIST OF TABLES

LIST OF FIGURES

ABSTRACT

Butyrylcholinesterase (BuChE) is a serine hydrolase enzyme that, along with acetylcholinesterase (AChE), catalyzes the hydrolysis of acetylcholine. These enzymes are associated with the pathology of neurologic disorders such as Alzheimer's disease (AD) and multiple sclerosis (MS). In particular, AChE and BuChE accumulate in β-amyloid (Aβ) plaques and tau neurofibrillary tangles in the AD brain. Thus, imaging cholinesterase activity associated with plaques and tangles in the brain has the potential to provide definitive diagnosis of AD during life. This would be advantageous since, at present, confirmation of AD relies on detecting pathology through post-mortem examination of the brain. In a similar respect, BuChE is associated with the characteristic lesions in MS brain and thus, is a promising target for diagnosis and monitoring of pathology in this disease. It is hypothesized that cholinesterase-binding radiopharmaceuticals can be used in SPECT or PET imaging to visualize these enzymes associated with AD and MS pathology in the living brain.

Several classes of cholinesterase ligands were synthesized and exhibited potent binding and specificity towards AChE and BuChE using enzyme kinetic analysis. These compounds were rapidly radiolabelled with ^{123}I and purified. Radiolabelled molecules accumulated *in vitro* in areas known to contain cholinesterase activity in transgenic AD mice and post-mortem human AD brain tissues, using autoradiography. Furthermore, cholinesterase activity associated with Aβ plaques was visualized in human and transgenic mouse AD brain tissues.

An enzyme kinetic approach was employed to determine critical residues in the BuChE active site gorge for ligand binding. In particular, residues pertaining to the peripheral site of the enzyme were identified and found to be involved in the binding of various ligands. These results are crucial for optimizing the enzyme binding properties of cholinesterase imaging agents. Finally, PET imaging of a transgenic mouse model of AD was performed as a vanguard for pre-clinical evaluation of cholinesterase imaging agents. PET imaging identified similar characteristics between this AD mouse model and the human condition. This is a promising approach for evaluation of cholinesterase imaging agents.

Radioligands specific for cholinesterases have the potential to provide a non-invasive means for early diagnosis of neurological diseases using brain scanning.

LIST OF ABBREVIATIONS USED

5XFAD	B6SJL-Tg(APPSwFlLon,PSEN1*M146L*L286V)6799Vas/Mmjax
αCTF	α-carboxy terminal fragment
βCTF	β-carboxy terminal fragment
A-site	acylation site
Aβ	β-amyloid
ACh	acetylcholine
AChE	acetylcholinesterase
$AChE_H$	'Hydrophobic' AChE
$AChE_R$	'Readthrough' AChE
$AChE_T$	'Tailed' AChE
AD	Alzheimer's disease
AICD	APP intracellular domain
ALS/PDC	amyotrophic later sclerosis/parkinsonism-dementia complex of Guam
[^{11}C]-AMP	*N*-[^{11}C]methylpiperidyl acetate
APH-1	anterior pharynx-defective-1
ApoE	apolipoprotein-E
APP	amyloid precursor protein
AV	anteroventral
BACE1	β-site APP cleaving enzyme 1
BACE2	β-site APP cleaving enzyme 2
BBB	blood-brain barrier
BF	basal forebrain
BOLD	blood-oxygenation-level-dependent
BuChE	butyrylcholinesterase
$BuChE_T$	'Tailed'BuChE
BuLi	butyl lithium
BP	boiling point
BW	bandwidth
BW 284 C 51	1,5-bis (4-allyl dimethylammonium phenyl) pentan-3-one dibromide
CAA	cerebral amyloid angiopathy
CBD	cortical-basal degeneration
ChAT	choline acetyl transferase
CIS	clinically isolated syndrome
CLINDE	^{123}I-6-chloro-2-(4′iodophenyl)-3-(N,N-diethyl)-imidazo[1,2-a]pyridine-3-acetamide
ColQ	collagen Q
CNS	central nervous system
CT	computed tomography
DAB	3,3'-diaminobenzidine
DEPT	distortionless enhancement by polarization transfer
DMSO	dimethyl sulfoxide

DP	dementia pugilistica
DTI	diffusion-tensor imaging
DTNB	5, 5'-dithio-bis(2-nitrobenzoic acid)
EAE	experimental autoimmune encephalomyelitis
FA	fractional anisotropy
FAD	familial AD
FDA	Food and Drug Administration
FDDNP	2-(1-(6-((2-[^{18}F] fluoroethyl) (methyl) amino)-2-naphthyl)ethylidene) malononitrile
FDG	2-deoxy-2-(^{18}F)fluoro-D-glucose
[^{18}F]-FEtP4A	*N*-[^{18}F]fluoroethylpiperidin-4-yl acetate
Florbetapir	(E)-4-(2-(6-(2-(2-(2-[^{18}F]fluoroethoxy)ethoxy)ethoxy)pyridine-3-yl)vinyl)-*N*-methylbenzenamine
fMRI	functional MRI
FOV	field of view
FTD	frontotemporal dementia
FT-IR	fourier transform-infrared spectroscopy
GABA	γ-aminobutyric acid
GPI	glycophosphatidylinositol
HMPAO	99^{m}Tc-hexamethylpropyleneamine oxime
HPLC	high-performance liquid chromatography
Iba-1	ionized calcium binding adaptor molecule 1
IL-17	interleukin-17
IL-23	interleukin-23
IMPY	[$^{123/125}$I]-2-(4'-dimethylaminophenyl)-6-iodoimidazo[1,2-a]pyridine
k_a	second-order deactivation constant
K_{app}	apparent Michaelis constant
k_E	second order hydrolysis rate constant
K_I	inhibition constant
K_m	affinity constant
KO	knock-out
LRP-1	LDL receptor-related protein-1
M_1-M_5	muscarinic receptors$_{1-5}$
mAChR	muscarinic acetylcholine receptor
MAPT	microtubule associated protein tau
MCI	mild cognitive impairment
MD	mean diffusivity
MHC	major histocompatibility complex
MIP	maximum intensity projection
MLEM	maximum-likelihood expectation maximization
MMFF	Merck molecular force field
MP	melting point
[^{11}C]-MP4B	1-^{11}C-Methyl-4-piperidinyl n-butyrate
MRI	magnetic resonance imaging
MS	multiple sclerosis
nAChR	nicotinic acetylcholine receptor

NAWM	normal-appearing white matter
NCS	*N*-chlorosuccinimide
NFT	neurofibrillary tangle
NMR	nuclear magnetic resonance
NO	nitric oxide
Normal, Aβ+	cognitively normal with Aβ plaques
Normal, Aβ-	cognitively normal without Aβ plaques
NP	neuritic plaque
OCT	optical coherence tomography
P-site	peripheral site
PB	phosphate buffer
PEN-2	presenilin enhancer-2
PET	positron emission tomography
PHF	paired helical fragment
PIB	*N*-methyl-[^{11}C]-2-(4'-methylaminophenyl)-6-hydroxybenzothiazole
PIP	phenyl 4-(iodo)phenylcarbamate
^{123}I-PIP	phenyl 4-([^{123}I]iodo)phenylcarbamate
PK11195	^{11}C-1-(2-chlorophenyl)-*N*-methyl-*N*-(1-methyl-propyl)-3-isoquinoline carboxamide
PLP	proteolipid protein
[^{11}C]-PMP	*N*-[^{11}C]methylpiperidyl propionate
PPMS	primary progressive MS
PRiMA	proline rich membrane anchors
PS1	presenilin1
PS2	presenilin2
PSP	progressive supranuclear palsy
ROI	region of interest
RRMS	relapsing remitting MS
SF	straight filament
SPECT	single photon emission computed tomography
SPMS	secondary progressive MS
SUV	standardized uptake value
$t_{1/2}$	half-life
T_E	echo time
T_R	repetition time
TBS	tris buffered saline
Th17	T-helper 17 cells
THF	tetrahydrofuran
TNFα	tumour necrosis factor α
V_{max}	maximum velocity
WT	wild-type

ACKNOWLEDGEMENTS

For Dr. Sultan Darvesh. His passion is irreproachable and enthusiasm unbridled. This without question has left an imprint. He is an exceptional mentor and benevolent individual. I am grateful for his tutelage which has had such profound resonance.

I have had the immense honour of working with Professor Earl Martin. He is a generous mentor and a formidable scientist. His fervor and passion for the lifelong pursuit of the unknown has made an immeasurable impression.

Dr. Ian Pottie has been an ambitious influence. He is an astute mentor that has consistently laid the challenge to strive for excellence. I am grateful to have had such exceptional guidance.

Andrew Reid has occupied a central role for this work. He has given without question his time and efforts to ensure the success of research efforts. He has been a colleague and friend for whom I hold the upmost respect and appreciation.

For my graduate committee, Dr. Donald Weaver, Dr. Bill Baldridge and Dr. Steven Burrell. I thank them for the years of guidance and most of all reassurance that the voyage was, at least, in the right direction.

Many past and present members of the Darvesh lab have made a lasting impression. In particular, Courtney Jollymore, Meghan Cash, Andrea LeBlanc and Jillian Soh. They have been shining examples of dedication and industry. The warmth they bring is without question.

I have had the good fortune to work with many who toiled in the chemistry labs of MSVU. Their enthusiasm and perseverance is a perpetual reminder of the excitement of scientific endeavour and elation of discovery.

For the fellow students that were allied by the Department of Anatomy & Neurobiology / Medical Neuroscience. I found great solace in celebrating with such a commendable group the scattered highs and copious lows that accompany the plight of a graduate student.

Concerning Eric Joy, Jake Yorke, Frank MacDonald, Amy Morris, Heather Cosh and Jenn Jackson. How fortuitous that such exceptional individuals would be found together. In spite of miles and sometimes oceans, I continue to marvel at the tenacity of this Team. I consider my membership of the highest value.

For my family and friends. They have been a source of unwavering and unconditional support. This has been an origin of strength and an unsinkable buoy.

For Elizabeth. Your love and support has been boundless. This is the cornerstone in which all else rests.

CHAPTER 1 INTRODUCTION

1.1 PREFACE

Neurological diseases, in particular Alzheimer's disease (AD) and multiple sclerosis (MS), are a central focus of this thesis. Described in this Chapter are the clinical characteristics and pathogenesis of these diseases. A particular emphasis is placed on neuroimaging approaches for the diagnosis of AD and MS. The cholinergic system is briefly reviewed with a focus on the two acetylcholine-regulating enzymes, acetylcholinesterase (AChE) and butyrylcholinesterase (BuChE). The role of these enzymes in AD and MS is described and evidence presented for their potential as disease diagnostic targets. Finally, the literature pertaining to AChE and BuChE imaging agents is reviewed to provide insight into strengths and weaknesses of these compounds. The goal of this thesis was to develop cholinesterase imaging agents for the visualization of neurological disease pathology.

1.2 ALZHEIMER'S DISEASE

1.2.1 HISTORICAL VIEW

The recognition of dementia has its roots in the very depths of our past. Ancient Egyptians in 2000 BC were aware that age could be accompanied by memory disorder (Signoret and Hauw, 2001). Later, Hippocrates (460-370 BC) and Galen (129-216 AD) even considered the irreversible disruption of higher cognitive function to be due to cerebral impairment resulting from disease in other organs of the body (Boller and Forbes, 1998). As the field of medicine evolved, the descriptions of anatomy and pathogenesis of dementia began to emerge. Philippe Pinel, viewed as one of the founders

of modern psychiatry, provided one of the first complete descriptions of dementia and is considered, by some, to be the first to use this term in 1797 (Torack, 1983).

The description of Alzheimer's disease (AD), in modern times, had its beginnings in 1901 with the admittance and examination of Auguste D by Alois Alzheimer at the municipal mental asylum in Frankfurt, Germany. Auguste D, a 51 year old woman, suffered from paranoia, delusions, hallucinations and impaired memory for five years before her death in 1906 (Maurer et al., 1997). The brain of Auguste D was examined in detail by Alzheimer and the histopathological changes were presented for the first time in 1906 at the 37th Meeting of Southwest German Psychiatrists (Alzheimer, 1906). These findings were subsequently published one year later (Alzheimer, 1907). Alzheimer had written "in the centre of an otherwise almost normal cell there stands out one or several fibrils due to their characteristic thickness and peculiar impregnability. Numerous small miliary foci are found in the superior layers. They are determined by the storage of a peculiar substance in the cerebral cortex. All in all we have to face a peculiar disease process". These early observations provided the foundation for modern AD research. The eponym AD was bestowed by Emil Kraepelin (Kraepelin, 1910) in recognition of the pioneering studies by Alzheimer. Clinical and pathological characteristics defined by Alzheimer remain a focus in efforts towards definitive diagnosis and treatment of AD.

1.2.2 Clinical Description

AD is a progressive neurodegenerative disorder and is the most common form of dementia in the elderly. Currently, dementia has a prevalence of 0.02% in ages 30-39 years and 10.8% in ages 80-90 years (Burns et al., 2002). The estimated lifetime risk of

AD is nearly one in five for women and one in ten for men, however; this discrepancy is attributed to the longer life expectancy of women (Seshadri et al., 2006). In the United States, the number of new cases of AD is expected to more than double to 959,000 by the year 2050 (Hebert et al., 2001). Also, in Canada 480,000 suffered from dementia in 2010 and this number is projected to rise to 1,100,000 by 2038, in just one generation (Smetanin et al., 2009). The associated Canadian economic burden for AD is projected to increase from 15 billion to 150 billion dollars over this same period (Smetanin et al., 2009). With current standards for the treatment and management of AD, this disease is poised to dominate health care expenditure around the world and may prove to be a crippling burden to economies dealing with aging populations (World Health Organization and Alzheimer's Disease International, 2012).

Recently, the clinical criteria for the diagnosis of AD has been revised and updated (McKhann et al., 2011) from the original which was established almost 30 years previously (McKhann et al., 1984). The first aspect is the determination of dementia which is defined by criteria such as interference of function at work or usual activities, a decline from previous levels of function and performance, symptoms that are not explained by delirium or psychiatric disorders and that cognitive impairment is present. This cognitive impairment must involve two or more of memory, reasoning and judgment, visuospatial abilities, language function or behavioural changes. An important distinction is made between dementia and mild cognitive impairment (MCI) (Albert et al., 2011). MCI patients demonstrate objective evidence of cognitive impairment however activities of daily living are not interfered. Despite advances to standardize this distinction, it remains highly influenced by the subjectivity of the clinician.

Assessment of AD in the dementia population has been divided into three categories, probable AD dementia, possible AD dementia and dementia unlikely due to AD (McKhann et al., 2011). Probable AD dementia must demonstrate insidious onset, worsening of cognition, amnestic presentation and non-amnestic presentation (deficits in language, visuospatial or executive functions). However, an extensive list of confounders exists that include temporally related history of stroke, severe white matter loss, other active neurological or non-neurological disorders, certain medications and other dementias. A formidable challenge is the differential diagnosis among dementias and thus, disorders such as dementia with Lewy bodies, behavioural variant frontotemporal dementia and primary progressive aphasia can all manifest similar to that of AD. Possible AD dementia demonstrates the core clinical manifestations of AD; however, it may manifest with an atypical course (e.g. sudden onset) or be etiologically mixed with one or more of the above listed confounders being present. Dementia unlikely due to AD can be considered in the context of three scenarios. First, if the clinical criteria established above for AD is not present; second, regardless of fulfilling the clinical AD criteria, if there is sufficient evidence of an alternative diagnosis that does not normally overlap with AD; third, a lack of characteristic AD pathology at autopsy, such as Aβ and tau deposits and neuronal injury, suggests an alternative from AD.

1.3 Pathogenesis of Alzheimer's Disease

The pathogenesis of AD remains unknown; however, histopathological studies have identified several pathologic structures associated with the disease. Neuritic plaques (NP), neurofibrillary tangles (NFT) and cerebral amyloid angiopathy (CAA) are

hallmarks of the disease and post-mortem visualization is required for definitive diagnosis.

1.3.1 Neuritic Plaques

The putative predominant route for the pathogenesis of AD currently centers on the 'amyloid cascade hypothesis' (Selkoe, 1991; Hardy and Higgins, 1992). This hypothesis maintains that β-amyloid (Aβ) protein aggregation, from monomer to plaque, and its deposition in the brain triggers all events and features characteristic of the disease. The Aβ peptide was first sequenced from AD and Down's syndrome tissue (Glenner and Wong, 1984a, b) and subsequently was recognized as the primary component of AD plaques (Masters et al., 1985; Selkoe et al., 1986). Aβ is a protein that may contain up to 43 amino acid residues generated by cleavage of the amyloid precursor protein (APP) mapped to human chromosome 21 (Goldgaber et al., 1987; Kang et al., 1987; Robakis et al., 1987; Tanzi et al., 1987). APP is a transmembrane protein containing a single membrane-spanning domain with a large extracellular (N-terminal) and a small cytoplasmic (C-terminal) domain (Kang et al., 1987). APP_{695} is expressed in neuronal populations and lacks the Kunitz-type serine protease inhibitor motif, unlike the ubiquitously expressed isoforms APP_{751} and APP_{770} (Kitaguchi et al., 1988; Ponte et al., 1988; Tanzi et al., 1988). APP is thought to function in neurite outgrowth, cell adhesion, synaptic functions and induction of apoptosis (Koo, 2002). Related to neuronal migration, APP knockout mice exhibit early lethality with a high incidence of cortical dysplasia (Herms et al., 2004). In addition, the cytosolic domain of APP is involved in a myriad of cell signaling (Van Gassen et al., 2000) which, when disrupted, results in

phenotypes such as cellular misorganization (Howell et al., 1997). APP is transported in axons via fast anterograde axonal transport (Koo et al., 1990) and may function in the packaging of other components in this transport system (Kamal et al., 2000) including its own proteolytic processing enzymes (Kamal et al., 2001). The APP gene location corresponds to the site of autosomal dominant mutations associated with hereditary cerebral hemorrhage (Levy et al., 1990) and with familial AD (St George-Hyslop et al., 1987; Goate et al., 1991; Hendriks et al., 1992; Mullan et al., 1992). These familial AD mutations primarily cluster at cleavage sites of APP that render various fragments and are found to increase the production of Aβ (Citron et al., 1992; Cai et al., 1993; Suzuki et al., 1994). In contrast, one APP mutation has been identified to have a protective effect against AD and is characterized by low levels of Aβ fragments (Jonsson et al., 2012). In addition to AD conditions, Aβ is also produced from APP by cells during normal metabolism (Haass et al., 1992) and thus, is not specific for the disease.

APP undergoes cleavage by a series of enzymes termed secretases which produce varied fragments with distinct functions. The intracellular location of APP determines which of two competing proteolytic pathways are active and thus, which fragments are produced. α-secretase is a zinc metalloprotease (Roberts et al., 1994) that cleaves APP primarily at the plasma membrane (Sisodia, 1992) to produce a large, soluble N-terminal fragment (Weidemann et al., 1989) and a small C-terminal fragment (Selkoe et al., 1988). This cleavage site is within the Aβ sequence and thus, precludes the production of this protein fragment (Esch et al., 1990). The liberated soluble N-terminal fragment, sAPPα (C83), has been generally regarded as protective for the central nervous system due to its roles in facilitating neuronal plasticity and survival as well as suppression of

neuroexcitotoxicity (Furukawa et al., 1996), among other functions (Mattson, 1997). In addition, the phenotype of APP deficient mice can be rescued by expression of sAPPα (Ring et al., 2007); thus, many of the physiological functions of APP may be mediated through this N-terminal fragment. The α-carboxy terminal fragment (αCTF) can further be cleaved by another secretase, γ-secretase, to yield two fragments, P3 (P83) and the APP intracellular domain (AICD) (Haass et al., 1992; Haass et al., 1993; De Strooper et al., 1998). The normal function of P3 and its potential role in AD has remained elusive. In contrast, AICD is involved in modulating transcription of various proteins, including its parent molecule, APP (Cao and Sudhof, 2001; Kimberly et al., 2001; Baek et al., 2002; Kim et al., 2003; Cao and Sudhof, 2004; von Rotz et al., 2004; Pardossi-Piquard et al., 2005; Liu et al., 2007; Zhang et al., 2007b). Cleavage by γ-secretase occurs in the transmembrane domain of APP, a previously uncharacterized site of activity, which has led to a particular focus on the function of this enzyme. The activity of γ-secretase is associated with a high molecular weight complex consisting of presenilin, either presenilin1 (PS1) or presenilin2 (PS2), nicastrin, anterior pharynx-defective-1 (APH-1) and presenilin enhancer-2 (PEN-2) (Kimberly et al., 2003; Takasugi et al., 2003). Presenilins in this complex undergo cleavage into N- and C-terminal fragments that form catalytically functional heterodimers (Thinakaran et al., 1996; Edbauer et al., 2003). Recognition of a cleavage site by γ-secretase is not completely determined by the substrate primary sequence but rather may depend on interactions and position within the membrane (Murphy et al., 1999). Thus, γ-secretase cleavage can produce fragments of similar but varying residue lengths from the same protein precursor. In addition to APP, γ-secretase has catalytic activity towards other proteins, such as Notch, which is involved

in cell fate decisions (Song et al., 1999). Therefore, γ-secretase may modulate a variety of biological functions in addition to its role in APP processing.

A competing pathway to that described above for APP processing involves cleavage by both β- and γ-secretase and produces Aβ as one of the byproducts. The major β-secretase for cleavage of APP is β-site APP cleaving enzyme 1 (BACE1) (Sinha et al., 1999; Vassar et al., 1999; Yan et al., 1999). BACE1 is found in various cellular locations including early Golgi, late Golgi/early endosomes and endosomes as well as the cell surface (Vassar et al., 1999; Huse et al., 2000; Walter et al., 2001). BACE1 can recognize two competing cleavage sites on APP, eventually giving rise to full length or 11 amino acid truncated forms of Aβ (Vassar et al., 1999; Farzan et al., 2000; Huse et al., 2002). Similar to α-secretase, β-secretase cleavage of APP first produces a soluble fragment, βAPPs (C99), and a C-terminal fragment, β-carboxy terminal fragment (βCTF). Overexpression of βCTF has led to cytotoxicity and neurodegeneration (Yankner et al., 1989; Oster-Granite et al., 1996). Subsequent cleavage of βCTF by γ-secretase produces the Aβ fragment as well as the AICD fragment (Sisodia, 1992), which is also produced in the α-secretase processing pathway. A second member of the β-secretase family, β-site APP cleaving enzyme 2 (BACE2), displays similar cleaving properties; however, its low concentration in the brain compared the BACE1 has limited its consideration as a major factor in Aβ production *in vivo* (Bennett et al., 2000). Nonetheless, due to its activity on APP processing BACE2 may still contribute to the pathogenesis of AD. In addition to APP, BACE1 has a multitude of other substrates, such as voltage gated sodium channels and neuroregulins (Vassar et al., 2009), suggesting that this enzyme may have a role in various physiological processes.

Mutations in presenilin genes, PS1 (Sherrington et al., 1995) and PS2 (Levy-Lahad et al., 1995; Rogaev et al., 1995), are found in familial AD. These mutations alter the APP cleavage products, in particular resulting in elevation of Aβ42 relative to Aβ40 levels (Scheuner et al., 1996; Citron et al., 1997). Aβ42 is thought to be more prone to aggregate and to be more toxic than Aβ40 (Jarrett et al., 1993); however, both of these species of Aβ are the most commonly found variants in AD plaques. Aβ40 is abundantly produced in both healthy and AD brain while another 20 species of Aβ can be produced at lower levels (De Strooper, 2010; Benilova et al., 2012). Early in AD progression, diffuse plaques contain predominantly Aβ42 however mature, dense plaques also contain Aβ40 (Iwatsubo et al., 1994). The pathway from Aβ monomer to plaque deposition proceeds through various intermediate species that may have biological activities that contribute to the pathogenesis of AD. In this respect, neither a universal mechanism for the route of aggregation nor a clear identification of the toxic Aβ species in AD has been established. This in part may be attributed to the large variety of Aβ species and their complex interactions, differing techniques of isolation and lack of rigorous Aβ species characterization (Benilova et al., 2012). Residues 18-42 of Aβ form a β-strand-turn-β-strand motif containing two β-sheets formed by residues 18-26 and 31-42 (Luhrs et al., 2005). This portion of Aβ42 is capable of unidirectional aggregation with other identical fragments. Aβ, in particular Aβ42, is found to readily aggregate into dimers, trimers and oligomers under physiological conditions (Podlisny et al., 1995; Walsh et al., 2000; Shankar et al., 2008). Adding to the complexity of Aβ aggregation has been the identification of atypical oligomers. For example, spherical oligomers have been isolated from the brains of AD patients and found to correlate with disease severity (Noguchi et

al., 2009; Matsumura et al., 2011). Furthermore, these spherical Aβ species appear to be distinct from the fibrillogenesis pathway leading to plaque deposition and thus, may be a novel effector of Aβ toxicity (Matsumura et al., 2011). Protofibrils occur as intermediates in Aβ fibrillization and are typically up to 200 nm in length and 10 nm in width with a large degree of β-sheet and random coil structure (Harper et al., 1997; Walsh et al., 1997; Walsh et al., 1999; O'Nuallain et al., 2010). Protofibrils also mark the first point in the Aβ aggregation process to which the dyes Congo Red and Thioflavin-T bind (Walsh et al., 1999). Continued fibrillization of Aβ leads to the characteristic macroscopic plaques indicative of AD. Although Aβ has a tendency for aggregation, it may exist in a dynamic equilibrium between its various states (Walsh et al., 1999) however, a rigorous proof for this concept has not yet been fully realized (Benilova et al., 2012).

The toxic effects of Aβ species have been demonstrated to effect many different systems (Cavallucci et al., 2012). For example, Aβ may form an ion channel pore, in particular for calcium, which could disrupt normal functions in neurons (Arispe et al., 1993; Mirzabekov et al., 1994; Kim and Weaver, 2000; Lin et al., 2001). Aβ also interacts with various neurotransmitter systems, such as the cholinergic system. For example, nicotinic acetylcholine receptors (nAChR) associate with Aβ plaques (Wevers et al., 1999) and Aβ can inhibit acetylcholine (ACh) release and calcium influx due to interactions with nAChRs in the cortex and hippocampus (Wang et al., 2000). In addition, glutamatergic system dysfunction (Cavallucci et al., 2012) and mitochondrial dysfunction (Reddy et al., 2010), have been extensively studied in AD and appear to be influenced by Aβ species. Despite an intense focus on the effects of specific Aβ species,

a single aggregated form has not yet been identified as the major contributor to AD. It is possible that neural cell death in AD may result from the nucleation and polymerization process itself rather than the effects of a particular Aβ aggregate (Wogulis et al., 2005). Although certain species of Aβ may influence processes such as synaptic function, these subtle changes do not lead to overt and widespread cellular death. Thus, it may be insufficient to attribute neuronal cell death in AD solely to oligomer or fibrillar Aβ.

Extracellular deposition of Aβ within the AD brain follows a defined anatomical pattern segregated into 5 stages (Thal et al., 2002). Aβ deposition begins in the neocortical regions such as the frontal, parietal, temporal and occipital cortices in Stage 1. Stage 2 is defined by extension of deposition into the entorhinal, hippocampal and insular regions. Involvement of subcortical structures such as the caudate nucleus, putamen, claustrum, basal forebrain, thalamus and hypothalamus are the hallmarks of progression to Stage 3. Stage 4 demonstrates deposition in brainstem structures such as the colliculi, substantia nigra, red nucleus, central gray of the midbrain and the inferior olivary nucleus. Continued extension of Aβ deposition into brainstem structures such as the pontine nuclei and the locus coeruleus as well as the cerebellum marks progression to Stage 5. Interestingly, some parallels can be drawn between the route of Aβ progression and neuroanatomical connectivity (Thal et al., 2002). For example, the hypothalamic nuclei, involved in Stage 3, obtain input from the amygdala and hippocampus, involved in Stage 2. Despite such parallels, the mechanism(s) behind regional susceptibility to Aβ deposition in the AD brain remain to be elucidated.

A significant caveat to the 'amyloid cascade hypothesis' is that some elderly individuals, perhaps as high as 30%, without cognitive decline have widespread

deposition of Aβ pathology in the brain (Snowdon, 1997; Riley et al., 2002; Snowdon, 2003; Mortimer, 2012). This suggests that Aβ aggregation and deposition is necessary but not sufficient to cause AD. It is unclear whether these individuals would eventually develop clinical symptoms of AD and thus, represent a prodromal or pre-clinical AD state. Thus, factors such as cognitive reserve, in which brain function continues at normal levels despite mounting insults (Lo and Jagust, 2013), may delay the effects of AD pathology. On the other hand, a crucial disease component may be lacking in these individuals that, when combined with NP deposition, leads to AD. Thus, despite having rampant Aβ pathology typical of AD, these individuals would not be expected to experience cognitive decline. Until this issue is resolved, the 'amyloid cascade hypothesis' occupies a precarious position as the apogee of AD.

1.3.2 Neurofibrillary tangles

Much like NPs, Alzheimer also described NFTs however, the main component of tangles, microtubule associated protein tau (MAPT), was not discovered until 1975 (Weingarten et al., 1975). Within the CNS, tau is found predominantly in the axons of neurons and to a lesser extent cell bodies and dendrites (Binder et al., 1985; Papasozomenos and Binder, 1987). The main function of tau in neurons is to associate with tubulin, spectin and actin filaments (Griffith and Pollard, 1982; Selden and Pollard, 1983; Carlier et al., 1984; Correas et al., 1990; Henriquez et al., 1995) to stabilize microtubules (Matus, 1994) and facilitate their interaction with cytoskeletal components such as neurofilament (Leterrier et al., 1982; Aamodt and Williams, 1984; Miyata et al., 1986). Tau can also mediate interactions with organelles, such as mitochondria (Rendon

et al., 1990), the plasma membrane (Brandt et al., 1995) and other proteins such as PS1 (Takashima et al., 1998). Microtubules bestow cellular structure as well as form transport networks which mediate the movement of micronutrients, neurotransmitters, and organelles along the axons. Tau dysfunction has been linked to neurodegenerative disorders, most notably frontotemporal dementia (FTD) and Parkinsonism, through identification of mutations in its gene on chromosome 17 (Hutton et al., 1998; Poorkaj et al., 1998; Spillantini et al., 1998). The human tau gene contains 16 exons (Andreadis et al., 1992; Andreadis et al., 1995) and thus, is subject to complex splicing patterns. Human brain specific exons 2, 3 and 10 are alternatively spliced (Andreadis et al., 1992) and give rise to 6 isoforms ranging from 352-441 amino acid residues (Goedert et al., 1989b; Goedert et al., 1989a; Himmler et al., 1989). These isoforms generally differ by the presence of either three (3R) or four (4R) microtubule binding domain repeats in the C-terminal and by the presence or absence of two inserts at the N-terminal (Goedert et al., 1989b; Goedert et al., 1989a; Himmler et al., 1989; Kosik et al., 1989a). Exon 10 encodes for one of the C-terminal repeats so that the presence of this exon produces 4R while its absence yields 3R tau. Some evidence exists for the differential distribution of tau isoforms in neuronal subpopulations (Goedert et al., 1989b), suggesting that each isoform may possess a unique biochemical function. This notion is further reinforced by the varied isoform expression during development (Kosik et al., 1989b; Goedert and Jakes, 1990). Tau can undergo a wide variety of post translational modifications including phosphorylation, glycosylation, ubiquitination, glycation, polyamination, nitration and proteolysis (Gong et al., 2005). Of the 79 potential Ser and Thr phosphorylation sites of the longest tau isoform, at least 30 have been identified as sites

of actual phosphorylation (Hasegawa et al., 1992; Morishima-Kawashima et al., 1995; Lovestone and Reynolds, 1997; Paudel and Li, 1999), with most lying outside of the microtubule binding domain repeats. There are over a dozen kinases able to phosphorylate tau and almost all major phosphatases can dephosphorylate tau (Buee et al., 2000; Lau et al., 2002; Avila et al., 2004). However, the *in vivo* phosphorylation dynamics of tau, including the identity of involved kinases and phosphatases in normal and diseased brain, is not fully elucidated.

Aggregation of tau protein, much like Aβ, is central to the putative pathogenesis of AD. An initial process involves the redistribution of tau to the cytoplasm followed by aggregation and can be mediated by hyperphosphorylation (Noble et al., 2003) and mutations (Hasegawa et al., 1998; Hong et al., 1998). Phosphorylation levels of tau from AD brain are 3-4 folds higher than normal tissues (Ksiezak-Reding et al., 1992; Kenessey and Yen, 1993; Kopke et al., 1993); however, the particular extent and sites of tau phosphorylation responsible for toxicity or aggregation have not been defined. The mechanism(s) by which hyperphosphorylated or mutant cytoplasmic tau form aggregates is also poorly understood, but may involve co-factors, such as sulphated aminoglycans, RNA or metals (Goedert et al., 1996; Kampers et al., 1996; Gamblin et al., 2000), or additional post-translational modifications. Aggregation of tau leads to paired helical fragments (PHFs) and straight filaments (SFs), the major components of NFTs (Grundke-Iqbal et al., 1986a; Ihara et al., 1986; Kosik et al., 1986; Wischik et al., 1988; Iqbal et al., 1989; Lee et al., 1991). In AD, all six isoforms of tau are found localized within NFTs, (Grundke-Iqbal et al., 1986a; Grundke-Iqbal et al., 1986b; Goedert et al., 1989b; Goedert et al., 1992), a characteristic that can distinguish between AD and some other

tauopathies. Like AD, Down syndrome, post-encephalitic Parkinsonism, amyotrophic later sclerosis/parkinsonism-dementia complex of Guam (ALS/PDC), dementia pugilistica (DP), and some forms of FTDP-17 all contain aggregations of the 6 tau isoforms. In contrast, cortical-basal degeneration (CBD), progressive supranuclear palsy (PSP) and other forms of FTDP-17 contain only 4R isoforms while Pick's disease contains only 3R isoforms (Buee et al., 2000). Ultimately, contribution of tau to neurotoxicity in AD brain may be a result of a gain of function, such as aberrant protein interactions, loss of function, such as microtubule stabilizing function, and/or its aggregation into PHFs and SFs.

Much like for Aβ, the chronology of the anatomical distribution of tau in the AD brain has been extensively mapped (Braak and Braak, 1991; 1995). This chronological evaluation of NFT pathology identifies six stages of pathological deposition. Stages I-II exhibits severe transentorhinal pathology and usually does not present with any cognitive symptoms. Stages III-IV is the engagement of both the entorhinal and transentorhinal regions with severe NFT formation as well as involvement of the hippocampus. The most severe deposition of NFT, stages V-VI, demonstrates profound pathology in almost all subdivisions of the cerebral cortex and correlates strongly with clinical symptoms of AD. In advance of NFT formation, neurons in the transentorhinal region abruptly begin to demonstrate progressive cytoskeletal changes that ultimately result in the characteristic tangle pathological structure (Braak et al., 1994). Interestingly, the progression and distribution of NFTs may occur in advance of widespread Aβ plaque deposition.

1.3.3 Cerebral Amyloid Angiopathy

Deposition of Aβ has long been described in leptomeningeal and cortical vessels (Benedek and McGovern, 1949; Margolis, 1959; Neumann, 1960; Schwartz et al., 1965) but was first attributed to a specific pathological process due to its involvement in intracerebral hemorrhagic stroke (Okazaki et al., 1979; Vinters, 1987). This CAA is now recognized to be associated with cognitive decline (Neuropathology Group Medical Research Council Cognitive Function and Aging Study, 2001; Pfeifer et al., 2002) and intracerebral infarcts (Kimberly et al., 2009; Prabhakaran et al., 2010; Gregoire et al., 2011). CAA has been estimated to occur in 10-50% of the general healthy elderly population (Auriel and Greenberg, 2012); however, Aβ deposited in CAA is similar to that found in the plaques of AD. Interestingly, a high level of plasma Aβ does not produce CAA in a transgenic model of AD (Fukuchi et al., 1996). In contrast, inoculation of Aβ in an APP overexpressing mouse can give rise to CAA in addition to the usual cerebral amyloidosis (Eisele et al., 2010). The likely source of Aβ accumulation in CAA is from neuronal origins and may involve a clearance or drainage process from cellular populations (Herzig et al., 2006). Several lines of evidence indicate that Aβ40 is the predominant species in CAA (Joachim et al., 1988; Prelli et al., 1988; Miller et al., 1993; Castano et al., 1996; Van Dorpe et al., 2000; Winkler et al., 2001; Fryer et al., 2003; Miao et al., 2005) and that increasing the brain Aβ40/Aβ42 ratio (Herzig et al., 2004) or the Aβ42/Aβ40 (Van Dorpe et al., 2000; Fryer et al., 2003) ratio can facilitate either vascular or parenchymal Aβ deposition, respectively.

Unlike distributions of NPs and NFTs, CAA accumulation has an erratic pattern in the human brain; however, some relationships have emerged. Vascular Aβ is

prominent in neocortical and, in some cases, hippocampal regions of the brain (Vinters and Gilbert, 1983; Masuda et al., 1988; Pfeifer et al., 2002) however, deep structures such as the basal ganglia typically remain unaffected (Mandybur, 1986). Interestingly, the most prevalent and severe CAA pathology is present in the occipital lobe (Pfeifer et al., 2002) which is typically not involved in the clinical symptoms associated with AD. The vulnerability of the occipital lobe for CAA and its potential contribution to AD remains unknown.

1.3.4 Brain Clearance of B-Amyloid and Other Proteins

The mutations associated with familial AD are generally related to Aβ production through modulation of APP or the secretase enzymes, leading to elevated Aβ protein levels and subsequent aggregation. However, a considerable emphasis has been placed on the elucidation of Aβ clearance mechanisms from the brain, as this may represent another prominent pathogenic process leading to the hallmark structures of AD. Three mechanisms for Aβ, and other protein, clearance from the brain have been proposed.

Drainage of Aβ with interstitial fluid has been found to occur along perivascular spaces leading to the cervical lymph nodes (Cserr et al., 1992; Weller et al., 1998; Weller et al., 2000; Preston et al., 2003; Nicoll et al., 2004). Two consequences may arise related to protein drainage in AD brain. Firstly, an altered or impaired mechanism may promote CAA genesis, especially in arteries and, secondly, the delivery of AD proteinacious species to the lymph nodes may serve as a promoter for neuroinflammation leading to exacerbation of pathological effects. Another method of protein clearance from the brain is by direct transport across the blood-brain barrier (BBB) to the blood

(Ghersi-Egea et al., 1996; Ji et al., 2001). This clearance is mediated by LDL receptor-related protein-1 (LRP-1) which may become modified or impaired with aging or in AD brain (Shibata et al., 2000). In addition to clearance either directly to the blood or to the lymph node, proteins such as Aβ are also degraded in the brain by proteolytic cleavage. Many peptidases, the majority being metalloproteases, have been shown to degrade Aβ. These include neprilysin, insulin degrading enzyme, angiotensin-converting enzyme, endothelin-converting enzyme, matrix metalloproteinases, plasmin and cathepsin (De Strooper, 2010). Impaired activity of these proteases may lead to increased Aβ levels in the brain, thereby facilitating aggregation. However, genetic linkage to AD remains sparse for these enzymes and furthermore, their upregulation is detected in some cases of sporadic AD (Miners et al., 2009; Palmer et al., 2009). Increased expression of Aβ degrading enzymes may be a late stage event in AD pathogenesis and may represent a response to elevated Aβ levels in the brain. Nonetheless, altered levels of these enzymes may have a prominent role in the progression and spread of pathogenesis in the AD brain.

The Aβ clearance mechanisms described above all involve the removal of Aβ and other proteins from the brain and if impaired, may lead to aggregation as is typical in AD. Thus, in addition to the overproduction of Aβ, in particular documented with familial AD mutations, clearance of Aβ may represent another crucial and central pathway towards the pathogenesis of AD.

1.3.5 Apolipoprotein-E as a Risk Factor for Alzheimer's Disease

Apolipoprotein-E (ApoE), a well-known lipid transport protein, is a genetic risk factor associated with sporadic AD. ApoE alleles are localized to chromosome 19, and

can express 3 potential polymorphisms, ε2, ε3 and ε4, in the brain. ApoE ε4 is associated with increased risk of sporadic AD (Corder et al., 1993; Saunders et al., 1993; Strittmatter et al., 1993) while the ε2 isoform offers a protective effect (Corder et al., 1994). In the brain, apoE is produced mainly by astrocytes (Pitas et al., 1987; Grehan et al., 2001) although under some conditions neurons can contribute to expression (Xu et al., 1996; Xu et al., 1999). ApoE is a key regulator of lipid metabolism involved in their distribution within and between neural tissues. In contrast to the periphery, different apoE isoforms do not influence cholesterol or lipid metabolism in the brain (Verghese et al., 2011). Thus, detrimental or protective effects for AD due to apoE isoforms may act through alternate pathways independent of lipid regulation.

The mechanism by which apoE isoforms contribute to AD pathogenesis is still not clear. However, apoE can be found localized to NPs, NFTs and vascular amyloid (Namba et al., 1991). In an isoform-specific manner, apoE is capable of regulating the clearance of Aβ from the brain *in vivo* (Castellano et al., 2011) and can stabilize putative toxic oligomeric Aβ species *in vitro* (Cerf et al., 2011). Thus, expression of apoE ε4 may promote aggregation of Aβ in the AD brain, thereby increasing disease severity and lowering the age of onset (Corder et al., 1993; Craft et al., 1998). In contrast, apoE ε2 may inhibit these processes, thus leading to a protective effect and delaying the age of onset of AD in these individuals (Corder et al., 1993; West et al., 1994; Craft et al., 1998). Although strong links exist between apoE isoforms and Aβ aggregation pathways, the full contribution of this protein to AD remains to be determined.

1.4 Multiple Sclerosis

1.4.1 Historical View and Clinical Description

Modern clinical and pathological descriptions of a variety of neurological disorders emerged from the Salpêtrière hospital in Paris towards the end of the 19th century. This focal and influential work principally flowed from the efforts of Jean Martin Charcot (1823-1893), a neurologist and anatomical pathologist. Charcot first described MS in a series of lectures that included both clinical and pathological findings (Charcot, 1877). This first patient of Charcot's, in whom he described clinical symptoms of MS, was rumoured to be his housemaid (Poser and Brinar, 2004). Charcot's work emphasized demyelination in the brain that has since become a hallmark of the disease. Since that time, both the clinical diagnosis and pathogenesis of MS have been an area of intense interest.

Clinical criteria for MS are centered around the demonstration of dissemination of characteristic brain lesions in both time and space and the exclusion of other diagnoses (Polman et al., 2011). It was not until 1954 that the first authoritative diagnostic criteria was established for MS, also known in Britain as disseminated sclerosis (Allison and Millar, 1954). Proposed in these criteria were that clinical symptoms would vary with time, in particular demonstrating a relapsing-remitting quality, and furthermore, suggested that pathology may adhere to a similar course. The modern landmark criteria for MS was established in 1965 and clearly identified that, by means of history and physical, multiple and separate lesions in the central nervous system must be indicated by signs of neurological dysfunction (Schumacker et al., 1965). This criteria gold standard heralded the beginning of epidemiological studies and large organized clinical trials to

evaluate therapeutics for MS. Revisions to MS diagnostic criteria continued for several decades until an international panel proposed updated guidelines for diagnosis that included the use of brain magnetic resonance imaging (MRI) techniques along with traditional clinical history and physical (McDonald et al., 2001). Furthermore, these guidelines described the commonly recognized courses of MS. Subsequently, these criteria have been updated in 2005 (Polman et al., 2005) and 2010 (Polman et al., 2011) in particular focusing on advances in MRI imaging in MS patients.

Patients with MS may present with clinically isolated syndrome (CIS) which is consistent with either a monofocal or multifocal central nervous system (CNS) inflammatory disease usually involving the optic nerve, brainstem/cerebellum, spinal cord or cerebral hemispheres (Polman et al., 2011). These symptoms commonly include sensory disturbances, unilateral optic neuritis, diplopia, trunk and limb parathesias, limb weakness, clumsiness, gait ataxia, and neurogenic bladder and bowel symptoms (Noseworthy et al., 2000). An attack due to MS is characterized by either patient-reported or objective signs of acute inflammatory demyelinating event in the CNS with duration of 24 hours. Multiple episodes are necessary for diagnosis and at least one must be corroborated with clinical findings, such as neurological exam, visual evoked potentials or MRI evidence of brain lesions. The most common course of the disease, relapsing remitting MS (RRMS), features an attack followed by a period of recovery before onset of another attack. This course typically continues until the remission period is no longer evident and the course becomes secondary progressive MS (SPMS). An insidious course from the initial clinical presentation without evidence of distinct remissions is primary progressive MS (PPMS). Other, typically rare, courses of MS have

been defined such as benign MS, which is characterized by more than 20 years without symptoms (Noseworthy et al., 2000). However, it remains to be fully explored whether a variant, such as benign MS, is indeed a full remission of MS pathogenesis or whether the initial symptoms, originally attributed to MS, were due to an alternative and distinct cerebral pathological event.

Estimates of global and regional prevalence and incidence of MS demonstrates wide variability in reporting methods and a lack of standardization (Evans et al., 2013). Thus, rigorous and repeated estimates have not been described for many regions in the world. However, in Canada, prevalence estimates range from 50-300 per 100,000 with approximately a 3:1 female to male ratio. Prevalence of MS increases throughout young adulthood and reaches a maximum for both sexes around 30-35 years (Allison and Millar, 1954; Alter et al., 1962; Goldberg, 1974). Epidemiology studies on MS have described a distinct geographical pattern for prevalence that may be attributed either to genetic and/or environmental factors. The risk of disease is greatest in areas furthest from the equator, such as North America and Europe (Alter et al., 1960; Goldberg, 1974). Interestingly, residency in an area until the age of approximately 15 years imbues that regions risk factor for MS, regardless of migration patterns, later in life (Alter and Okihiro, 1971). In particular, vitamin D derived from sunlight and regional diets are two theories behind this geographical distribution (Goldberg, 1974).

1.4.2 Pathogenesis

MS in considered both a neuroinflammatory and neurodegenerative disease as both processes play a prominent role in the pathogenesis. However, a causative event for

the initiation of MS remains to be elucidated. The inflammatory component of MS is hypothesized to occur when the integrity of the BBB is disrupted allowing leukocytes from the periphery to enter the brain. These leukocytes can then target an antigen thereby, triggering a cascade of events leading to demyelination (Raine, 1994). An association between MS and major histocompatibility complex (MHC) genes (Compston et al., 1976; Terasaki et al., 1976) has reinforced the important contribution that immune function has towards the disease. Autoreactive lymphocytes, such as CD4+ T-cells, in MS, are resistant to apoptosis, due to overexpression of β-arrestin 1 (Shi et al., 2007) and thus, may promote an aberrant immune response in the MS brain. In addition, CD8+ T-cells in the MS brain cluster around the lateral ventricles as well as areas of white matter such as the corpus callosum, optic nerves, brainstem and throughout the spinal cord. MS inflammation is thought to be driven by interleukin-23 (IL-23) stimulation of a class of CD4+ cells termed T-helper 17 cells (Th17) which secrete interleukin-17 (IL-17) (Langrish et al., 2005). The result of this stimulation is increased penetration of Th17 cells across the BBB. Accumulation of T- and B-lymphocytes and macrophages in brain tissue results in concentrated cytokine signaling that further amplifies the immune response and recruits naïve microglia to the lesion site. Lethal signals are delivered to oligodendrocytes through tumour necrosis factor α (TNFα) and phagocytosis of myelin is mediated through the presence of complement (Zajicek et al., 1992). Demyelinating lesions expand in all directions and exhibit decreasing inflammation in their interior. In addition, diffuse microglial activation occurs in the normal-appearing white matter (NAWM) (Kutzelnigg et al., 2005). A molecular showdown may occur in the NAWM between anti-inflammatory genes of oligodendrocytes and pro-inflammatory signaling of

microglia (Zeis et al., 2008). A resulting edge towards pro-inflammation may modulate the progression and subsequent enlargement of MS lesions in the brain. Upon phagocytic removal of myelin debris, remyelination can occur in some lesions due to the recruitment of oligodendrocytic precursors (Scolding et al., 1998; Williams et al., 2007; Chandran et al., 2008). It is estimated that 20% of MS patients have extensive lesion remyelination (Patrikios et al., 2006). However, the functional recovery of a lesion area after remyelination has not been established. As well, the cause of prolonged demyelination in the majority of lesions, whether due to a constitutive demyelinating process or disruption in oligodendrocyte recruitment, has not been fully elucidated.

Characterization of lesions is not unified within the MS research community and various schemes exist for their classification (van der Valk and De Groot, 2000). Most of these schemes rely on the extent of neuroinflammation for their classification and one of the most widely adopted is that proposed by Bo and Trapp (Bo et al., 1994a). This classification scheme divides all MS lesions into three categories, active, chronic active and chronic inactive, based upon cellularity. An active lesion possesses a hypercellular environment while a chronic active lesion displays a hypocellular center and a hypercellular rim. This division attempts to recognize the putative spread of pathology, in which the neuroinflammatory response and demyelination progresses radially from the center of a lesion. Finally, a chronic inactive lesion is hypocellular indicating that the neuroinflammatory and demyelinating events have largely already occurred and have subsided in this particular region. The Bo and Trapp lesion classification scheme also contains an element of chronology as active lesions are thought to eventually proceed to

chronic active and finally chronic inactive states. However, the *in vivo* duration of such a progression remains unknown.

Research on the pathogenesis of MS has long been focused on the neuroinflammatory events of the disease; however, interest in the neurodegenerative component has emerged and details for its contribution to MS continue to be elucidated. Despite this renewed focus, description of axonal pathology has its roots in early MS research (Kornek and Lassmann, 1999). In particular, axonal transection and loss has been well documented (Ferguson et al., 1997; Trapp et al., 1998; Ganter et al., 1999; Lovas et al., 2000; Bjartmar et al., 2001) as has progressive brain atrophy (Rudick et al., 1999b; Simon et al., 1999; Miller et al., 2002). Correlations exist between the degree of inflammation in a particular lesion and the number of transected axons. Thus, demyelinating neuroinflammation may drive the neurodegenerative aspect of MS early in the disease (Ferguson et al., 1997; Trapp et al., 1998). Furthermore, demyelination may expose the axon to detrimental substances, in particular from the neuroinflammatory environment of the MS lesions mediated by both CD4+ and CD8+ T-cells (Babbe et al., 2000). Cytokines, proteolytic enzymes, free radicals and oxidative products from immune cells (Hohlfeld, 1997) may all contribute to the transection of axons. In addition, elevated levels of nitric oxide (NO) in MS (Bo et al., 1994b; Liu et al., 2001) can lead to axonal death (Smith and Lassmann, 2002) through various pathways, including inhibition of mitochondrial respiration (Brown and Borutaite, 2002). Another potential mechanism contributing to neurodegeneration in MS is glutamate excitotoxicity, a common mechanism attributed to other neurodegenerative processes. Elevated glutamate levels are present in MS lesions and NAWM (Srinivasan et al., 2005) and

altered glutamate metabolism has been associated with myelin degradation and cellular toxicity (Li and Stys, 2000; Tekkok and Goldberg, 2001; Micu et al., 2006). The typical disease course of RRMS proceeding to a progressive state may reflect pathogenesis driven by neuroinflammation transitioning to neurodegeneration. Interestingly, neuroinflammation largely subsides once the progressive course has been established (Rudick et al., 1999a). However, it cannot be ruled out that these two processes may proceed independently of one another and that neurodegeneration, due to its potential involvement through all stages of disease, may represent the principal pathological process contributing to MS.

1.5 Imaging in Neurological Disorders

1.5.1 Overview of Imaging Modalities

Several imaging modalities exist for the visualization of the CNS such as structural imaging using MRI and metabolic and molecular imaging using approaches such as functional MRI (fMRI), positron emission tomography (PET) and single photon emission computed tomography (SPECT). MRI has the capability to detect structural changes in brain volume and thus, can measure atrophy characteristic of dementias. However, the non-specific aspect of this modality has limited its applicability in differentiating between certain dementias, especially when atypical patterns of atrophy may present in any given disorder. Imaging using blood-oxygenation-level-dependent (BOLD) contrast with MRI (fMRI), 2-deoxy-2-(^{18}F)fluoro-D-glucose (FDG) with PET or 99^{m}Tc-hexamethylpropyleneamine oxime (HMPAO) with SPECT can provide regional measures of neural function which may be characteristic of a particular disease. Different

CNS disorders have distinct patterns of progression thus, repeated analysis of brain regions demonstrating altered function over time may be indicative of the ongoing disease process. However, this approach suffers the same caveat as structural MRI, as these changes can be non-specific and may be attributed to a multitude of different disorders with a wide variance of pathogenesis. Molecular imaging with PET or SPECT can target specific proteins related to a given disease and, thus, may be the most effective for the definitive visualization of a specific disorder. A critical aspect of this approach is the determination of an appropriate target that is unique for the disorder of interest.

1.5.2 Alzheimer's Disease

Early and definitive diagnosis of AD is crucial for the timely clinical management of the disease and will have tremendous applicability for the evaluation of potential disease modifying therapies. At present, providing a differential diagnosis of AD versus other dementia conditions is clinically challenging. Therefore, brain imaging presents an opportunity for a significant advance in the early diagnosis and management of AD patients as well as knowledge of the pathological course of this disorder.

Structural MRI in AD usually demonstrates atrophy in the entorhinal cortex and hippocampus (Scheltens et al., 1992; Jack et al., 1997; Jack et al., 2002), two areas of early NFT pathology. Although cross-sectional measurement is of limited utility, longitudinal assessment of the rate of hippocampal atrophy can potentially distinguish AD from cognitively normal controls (Barnes et al., 2009). Semi-automated methods for assessment of hippocampal size has improved bias introduced by visual assessment alone and, furthermore, provides a means for standardization across different centers (Pruessner

et al., 2000). However, hippocampal and other cerebral atrophies are not specific for AD and can also be observed in cohorts of healthy controls (Dubois et al., 2007; Ikram et al., 2010; Staff et al., 2010). Thus, MRI structural imaging is limited by its non-specificity; however, continued improvements, such as longitudinal automated analysis of particular regions associated with AD, for example cortical thickness (Querbes et al., 2009), may improve the utility of such an approach for the diagnosis of AD.

Neural activity, assessed by measuring brain blood flow dynamics with fMRI, may prove to be a powerful tool for the detection of AD throughout the disease process. In this context, populations considered at risk, due to the presence of apoE ε4, demonstrate greater activity in the hippocampus (Bookheimer et al., 2000; Bondi et al., 2005; Filippini et al., 2009). Such increased activation may be due to neural compensation mechanisms that elevate activity in impaired regions in order to continue normal function. On the other hand, this elevated activity may be an epiphenomenon associated with apoE ε4 expression, and thus, could be unrelated to the pathogenesis of AD. Furthermore, conflicting fMRI studies have reported altered activation of brain regions in at risk populations for AD which complicate robust associations of fMRI activity to disease pathogenesis (Machulda et al., 2003; Trivedi et al., 2006; Borghesani et al., 2008). Additional undetermined risk factors for AD, experimental paradigms, analysis methods and subject populations may contribute to the disparity of these studies for AD. In addition to regional alterations in neural activity, fMRI can detect variances in connectivity of neuronal networks in the brain which may be indicative of AD (Li and Wahlund, 2011). In particular, the default mode network (Raichle et al., 2001), a brain network that is suspended during task or goal directed behavior, demonstrates alterations

in AD compared to cognitively healthy controls (Greicius et al., 2004; Sorg et al., 2007; Wang et al., 2007). Alterations in brain connectivity, in particular resting state networks, may be disease specific and thus, could offer the opportunity for definitive diagnosis. However, much remains to be validated for this approach, such as determination of longitudinal changes in connectivity, specific resting state systems involved as well as application in a clinical setting.

In AD, the characteristic HMPAO perfusion (Holman et al., 1992; Jagust et al., 2001; Matsuda, 2007) and FDG metabolism patterns (Choo et al., 2007; Samuraki et al., 2007; Langbaum et al., 2009), as visualized with SPECT or PET imaging, respectively, demonstrate a bilateral decrease to the posterior cingulate and parietotemporal lobes with some frontal cortex involvement. Unfortunately, for diagnostic purposes, atypical patterns may exist. For example, early in the disease there may be significant asymmetry in the brain (Herholz, 2003). Nuclear imaging is relatively accurate in distinguishing AD from other forms of dementia; however, there are common diagnostic confounders which limit the specificity of this approach to 70-90%, (Devous, 2002). While brain perfusion and metabolism imaging with SPECT and PET, respectively, is widely available, the lack of sensitivity and specificity in the early AD stages (Herholz, 2003) demands that more accurate diagnostic imaging approaches be developed.

In addition to the described structural and functional imaging, several potential disease-specific approaches have emerged for the neuroimaging of AD. At the forefront of this field is development of PET or SPECT imaging of Aβ and tau deposits in the brain. Development of Aβ imaging agents have centered on derivatives of conjugated dyes such as Congo Red and Chrysamine G, which are known to bind to β-sheet

aggregated structures. In addition, Thioflavin-T and –S have been employed for the visualization of Aβ aggregation due to its ability to bind these structures in a manner similar to the conjugated dyes. Although these compounds possess great utility for *in vitro* and *ex vivo* studies, their *in vivo* potential is mired by poor penetrance of the BBB. Thus, derivatives of these molecules, in particular thioflavin-T (Klunk et al., 2001; Mathis et al., 2002), have been developed that show greater ability to cross the BBB. Interestingly, numerous distinct binding sites on Aβ have been identified, in particular for the styrylbenzene and thioflavin frameworks. However, common functional groups among these molecules involve either a methylamino or dimethylamino group along with a conjugated ring system. Based on these principles, small molecules can be tailored to bind to Aβ aggregates for use as *in vivo* SPECT or PET imaging agents (Figure 1.1).

Imidazo[1,2-α]pyridine derivatives, based on the benzothiazole ring system of thioflavin, are promising molecules for use as Aβ imaging agents. In this respect, incorporation of an *N,N*-dimethylaminophenyl group in the benzothiazole system has provided the Aβ SPECT imaging agent, [$^{123/125}$I]-2-(4'-dimethylaminophenyl)-6-iodoimidazo[1,2-a]pyridine (IMPY) (Zhuang et al., 2003). This imaging agent has been used in preclinical animal studies (Kung et al., 2004) and for assessing therapeutic efficacy in clinical trials (Greenberg et al., 2013). IMPY is the leading Aβ aggregation imaging agent that utilizes SPECT. The thioflavin-T derivative *N*-methyl-[^{11}C]-2-(4'-methylaminophenyl)-6-hydroxybenzothiazole (PIB) (Mathis et al., 2003) is the most studied Aβ imaging agent for PET analysis and has ushered in a novel field dedicated to the diagnosis of AD using brain imaging. Many studies have validated the use of this ligand for visualizing NPs in human and transgenic rodent brain (Bacskai et al., 2003;

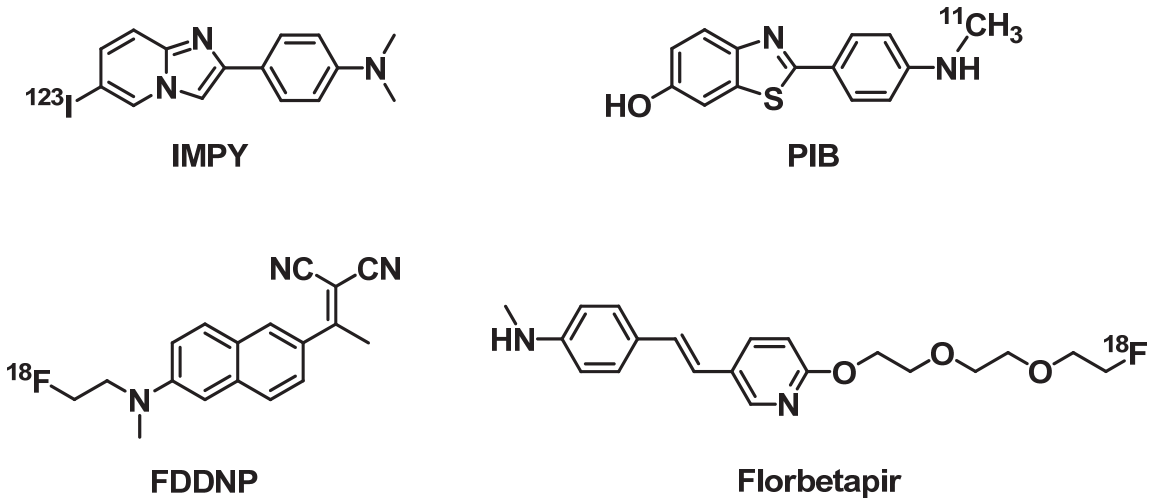

Figure 1.1. Structures of β-amyloid imaging agents.

Klunk et al., 2004; Klunk et al., 2005; Mintun et al., 2006; Driscoll et al., 2012; Niedowicz et al., 2012). PIB imaging has revealed that the rate of Aβ accumulation in the brain may be independent of cognitive decline associated with progression of AD (Engler et al., 2006; Mintun et al., 2006). In particular, Aβ plaque burden may reach a plateau despite ongoing cognitive changes (Engler et al., 2006; Villain et al., 2012; Villemagne et al., 2013). This represents persuasive *in vivo* evidence that Aβ plaque load does not correlate with dementia severity, thus limiting the ability of such imaging for the diagnosis, prognosis and treatment monitoring of AD. Furthermore, PIB-detected Aβ burden is present in many atypical presentations of dementia which does not relate to the clinical phenotype (Wolk et al., 2012b). It is unclear whether these atypical disorders will progress to the typical AD phenotype or whether they are distinct entities that share the phenomenon of Aβ pathology. Despite the disconnection between Aβ plaque pathology and cognition in AD, in normal elderly, cognitive status does relate to Aβ burden (Snitz et al., 2013). Due to the observed plateau of Aβ deposition, it may be that only in a very early disease state, before clinical presentation, does Aβ burden reflect cognitive status.

A practical caveat has hampered widespread adoption of PIB for AD brain imaging. The short half-life ($t_{1/2}$) of ^{11}C (~20 min) has limited the use of this imaging agent to highly specialized centers that have a capacity to produce ^{11}C, incorporate and immediately utilize radiolabelled PIB. Thus, distribution and adoption of PIB imaging is restricted. On the other hand, imaging agents labeled with ^{18}F ($t_{1/2}$ = ~110 min) allow for distribution to multiple centers and thus, have great applicability for clinical use. One agent to have emerged for Aβ imaging is the naphthol derivative, 2-(1-(6-((2-[^{18}F]-

fluoroethyl) (methyl) amino)-2-naphthyl)ethylidene) malononitrile (FDDNP) (Agdeppa et al., 2001). Unlike IMPY and PIB, FDDNP binds to both Aβ plaques and NFTs (Agdeppa et al., 2001; Shoghi-Jadid et al., 2002) and thus, may possess a greater capacity to diagnose AD and monitor pathological changes. However, comparison with PIB demonstrates that FDDNP may not be as sensitive to accumulation of pathology potentially due to non-specific binding (Tolboom et al., 2009b). In addition,, FDDNP may suffer from similar drawbacks as PIB for the definitive diagnosis of AD. This is mainly a lack of correlation between uptake and cognitive changes (Ossenkoppele et al., 2012). In contrast, specific focus on episodic memory has established correlation with FDDNP accumulation in the brain (Tolboom et al., 2009a). The longitudinal dynamics of AD cognitive decline relative to FDDNP uptake require further elucidation before the applicability of this agent for diagnosis can be determined. For example, the rate of NP and NFT deposition needs to be compared to cognitive decline throughout all stages of AD. In addition, visualization of NFT pathology applies to numerous neurodegenerative disorders, such as chronic traumatic encephalopathy (Small et al., 2013), that are distinct from AD. Thus, although NFT pathology is an integral process in AD pathogenesis, visualization of these structures may be confounding toward AD diagnosis due to non-specificity.

Developed from the styrene scaffold (Zhang et al., 2005; Zhang et al., 2007a), (E)-4-(2-(6-(2-(2-(2-[^{18}F]fluoroethoxy)ethoxy)ethoxy)pyridine-3-yl)vinyl)-N-methylbenzenamine (Florbetapir) is another fluorine radiolabelled imaging agent that binds to Aβ aggregations (Choi et al., 2009). This imaging agent has been validated for the visualization of Aβ plaque neuropathology with minimal non-specific binding and

favourable safety, kinetic and metabolic profiles (Lister-James et al., 2011; Clark et al., 2012). Comparisons between PIB and Florbetapir have determined that the two agents display similar properties for the detection of aggregated Aβ *in vivo* (Wolk et al., 2012a; Landau et al., 2013). Florbetapir is the sole Aβ imaging agent to gain approval from the Food and Drug Administration (FDA), United States, for use in routine clinical settings to assess brain amyloidosis (Yang et al., 2012). Progression of Aβ brain imaging into the clinical setting has demanded that strict guidelines be considered for the applicability and conclusions drawn from such an approach (Johnson et al., 2013a; b). However, the diagnostic, prognostic and treatment monitoring capability of Aβ imaging in the clinical setting remains unresolved. Due to limitations of targeting Aβ deposition, such as its presence in cognitively normal individuals and lack of correlation with severity of cognitive impairment, definitive diagnosis of AD may be unattainable with such an approach. Nevertheless, the development of Aβ brain imaging has set the stage for the search for imaging agents that target AD-specific pathology for the definitive diagnosis of this disease.

1.5.3 Multiple Sclerosis

Brain imaging in MS, in particular MRI, has been established as a powerful approach for visualizing the characteristic lesion pathology. In this respect, the recent guidelines for diagnosis contain a considerable emphasis on the use of structural MRI to detect MS lesions disseminated in time and space (Polman et al., 2011). However, many advances in MS imaging are emerging that range from novel techniques, such as

diffusion-tensor imaging (DTI), to optimized analysis with structural imaging, such as detection of gray matter lesions.

Imaging of MS brain with MRI detects lesions frequently located asymmetrically in the juxtacortical white matter, periventricular white matter and corpus callosum (Ormerod et al., 1987) as well as the spinal cord (Bot and Barkhof, 2009). In particular, spinal cord lesions, visualized as T2-hypointensities, are characterized by their cervical level, span of no more than two vertebral segments and occupation of half the cross sectional area of the cord. The presence of spinal cord lesions in CIS populations predicts progression to definitive MS (Patrucco et al., 2012) and may discriminate disability levels (Oh et al., 2013). MRI techniques have improved to provide accurate visualization of grey matter abnormalities. In this respect, MS pathology in grey matter may yield valuable insights into the pathogenesis of the disease as well as afford an approach for diagnosis and treatment monitoring. The development of grey matter pathology may result from the presence of white matter lesions (Muhlau et al., 2013). Both focal and diffuse grey matter damage have been chronicled in the MS brain (Geurts and Barkhof, 2008) and may be indicative of a more progressive disease course (Kutzelnigg et al., 2005; Calabrese et al., 2013). Furthermore, cortical lesions are found to occur early in MS and increase in size and number with disease progression (Calabrese et al., 2010). Cortical lesions have been correlated with cognitive impairment (Calabrese et al., 2009) but detection of these lesions suffers from poor sensitivity (Seewann et al., 2012). The use of higher field magnets, such as 7T, offers capabilities to improve lesion visualization using MRI techniques and may be especially beneficial for the visualization and characterization of cortical grey matter (Filippi et al., 2013).

Breakdown of the BBB is a putative early event in the formation of MS lesions and may represent a valuable target for diagnostic imaging of this disease. Intravenous administration of a gadolinium-containing MRI contrast agent provides a common assessment of BBB integrity. In this respect, breakdown of this barrier allows the contrast agent to accumulate in brain tissue and is readily visualized with T1 weighted MRI (Grossman et al., 1986; Hawkins et al., 1990; Kermode et al., 1990; Tas et al., 1995). BBB breakdown is an acute phenomenon which resolves even though lesion activity continues. Therefore, contrast-enhanced MRI is one validated method to determine chronology of lesions and is a strategy for the diagnosis of MS (Polman et al., 2011).

Imaging with fMRI in the MS brain has indicated that brain plasticity and compensation occurs throughout the disease process as evidenced by increased activation and recruitment of alternate areas to perform tasks (Cader et al., 2006; Levin et al., 2006; Mainero et al., 2006; Loitfelder et al., 2011). This phenomenon seems to occur regardless of the neural system affected, whether motor or cognitive. In addition, resting state networks, such as the default mode network, exhibit distinct alterations in the MS brain (Rocca et al., 2012). This may be one strategy employed by the CNS to limit the functional consequences of MS pathology in the brain. Reorganization of brain networks and compensation may also be, at least partially, a cause of the poor correlation between clinical symptoms and lesion burden (Barkhof, 2002). Exhaustion of these abilities, especially late in disease course, may be associated with pronounced clinical progression leading to severe disability (Rocca et al., 2005).

DTI is a MRI method to assess molecule movements in space and can provide measurements of mean diffusivity (MD) and fractional anisotropy (FA) within the brain.

In particular, the myelinated axon is an organized structure that restricts movement of molecules, such as water, to a longitudinal direction. Therefore, breakdown of the myelin structure would increase movement in all other directions. Diffusion abnormalities measured with DTI in the MS brain can be detected before lesions can be visualized with conventional MRI (Wahl et al., 2011). In this respect, DTI may have applicability for prediction of disease onset and progression in both RRMS and PPMS. In RRMS, alterations in MD precede, by several months, breakdown of the BBB and subsequent lesion formation (Liu et al., 2012) providing an approach to predict relapse. For cortical imaging, DTI can visualize changes to normal appearing grey matter which may predict advancement to the progressive stage of MS (Bozzali et al., 2002).

Optic neuritis is one of the most common (17-19%) presenting conditions associated with MS (Sorensen et al., 1999) and will occur at some point during the disease in a high number of patients (55-60%) (Cantore, 1996). Optic neuritis leads to reduction of the retinal nerve fiber layer thickness (Sergott et al., 2007), suggestive of ongoing axonal injury and disease progression in the brain. This phenomenon can be visualized using optical coherence tomography (OCT) (Huang et al., 1991; Drexler et al., 2001; Chen et al., 2005). An advantage of this analysis is that it is a rapid, non-invasive, high resolution method for detection of changes in retinal nerve fiber layer microstructure. However, heterogeneity in the MS population may limit the use of this approach for clinical diagnosis and disease monitoring (Serbecic et al., 2010). In addition, OCT is thought to reflect general axonal degeneration in the brain and, thus, alterations can be found in the retinal nerve fiber layer in a variety of other disorders such as AD and Parkinson's disease (Greenberg and Frohman, 2010).

Relative to the wealth of MRI techniques for MS, approaches to visualize pathology associated with the disease by SPECT and PET imaging remain few. SPECT perfusion has documented lesions (Pozzilli et al., 1987) and has demonstrated correlations with some symptoms of MS such as verbal fluency and memory (Pozzilli et al., 1991). However, SPECT perfusion was found not to be sufficiently sensitive for reliably detecting MS pathology (Lycke et al., 1993; Assadi et al., 2010). This is further complicated since lesions in SPMS are found in areas demonstrating low perfusion while those in RRMS are found in areas of higher perfusion (Holland et al., 2011). Thus, lesions in high perfusion areas may have a greater capacity for remyelination and functional recovery which is characteristic of RRMS. Accumulation of lesions in low perfusion areas may be one mechanism that contributes to a progressive disease course. This is an interesting avenue for MS perfusion imaging however, robust further investigation is required. Metabolic PET imaging can visualize areas of neuroinflammation in the spinal cord of a MS animal model (Buck et al., 2012); however, this approach may also suffer from limited sensitivity (Bolcaen et al., 2012).

Molecular imaging of peripheral benzodiazepine receptors (translocator protein 18kDA), which are upregulated on macrophages and activated microglia, is a promising approach to specifically determine the extent of neuroinflammation. SPECT ligands, such as ^{123}I-6-chloro-2-(4′iodophenyl)-3-(N,N-diethyl)-imidazo[1,2-a]pyridine-3-acetamide (CLINDE, Figure 1.2), have been developed that visualize this target in a mouse model of experimental autoimmune encephalomyelitis (EAE) (Mattner et al., 2005). Also a PET agent for these receptors, ^{11}C-1-(2-chlorophenyl)-*N*-methyl-*N*-(1-methyl-propyl)-3-isoquinoline carboxamide (PK11195, Figure 1.2), has visualized MS

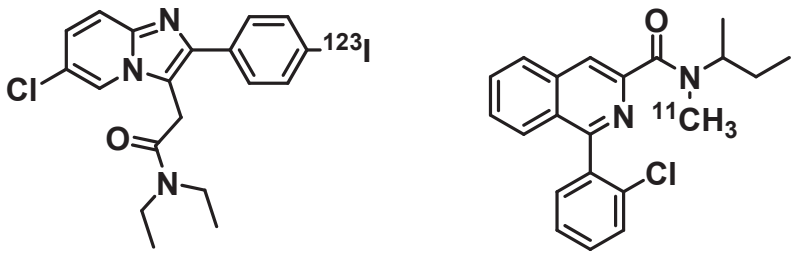

Figure 1.2. Structures of peripheral benzodiazepine receptor (translocator protein 18kDA) imaging agents.

lesions (Banati et al., 2000) as well as alterations in normal appearing white matter (Debruyne et al., 2003) and grey matter (Banati et al., 2000; Politis et al., 2012). Other SPECT/PET ligands have been developed for visualization of this translocator protein (Chauveau et al., 2008; Fookes et al., 2008), in efforts to overcome shortcomings of PK11195 such as the short half-life of ^{11}C and high non-specific binding.

Imaging agents towards several other targets have been developed which may show efficacy for the visualization of MS pathology. Associated with MS pathology are matrix metalloproteinases which have been visualized with SPECT and PET molecular imaging (Wagner et al., 2006). White matter integrity has been visualized with SPECT (Briard et al., 2011) and PET imaging (Wang et al., 2009) and may be promising for clinical application. Also, BBB permeability can be assessed using PET and SPECT agents which may offer some advantage over Gd-enhanced MR imaging (Iannotti, 1992). In addition, some imaging agents developed for Aβ imaging, such as PIB, can also detect myelin changes (Stankoff et al., 2011). This ability may be due to non-specific uptake of PIB in this structure and thus, is independent of Aβ binding properties. Some major drawbacks of these imaging agents are that their targets are also involved in the pathology of various other disorders of the CNS and thus, are not specific for MS.

1.6 Cholinergic System

1.6.1 Overview

The cholinergic system has an integral role in the functioning of the CNS, PNS and the immune system. Several components such as the neurotransmitter ACh, its

receptors and hydrolyzing enzymes, acetylcholinesterase (AChE) and butyrylcholinesterase (BuChE) have varied but distinct roles in both health and disease.

1.6.2 Neuronal Cholinergic System

Neurons which release the neurotransmitter ACh (Loewi, 1921; Dale et al., 1936) are considered cholinergic. In the CNS, these consist of projection neurons located in the forebrain and upper brainstem, such as the pontine reticular formation, and interneurons in the caudate-putamen, nucleus accumbens, hippocampus, cerebral cortex, hypothalamus and spinal cord. Motor neurons in the spinal cord as well as parasympathetic and preganglionic sympathetic neurons are also cholinergic (Martinez-Murillo and Rodrigo, 1995). The basal forebrain (BF) is considered one of the centers of cholinergic activity in the brain, and in addition to ACh, this area contains many other neurotransmitters such as γ-aminobutyric acid (GABA) (Fisher et al., 1988; Gritti et al., 1993), glutamate (Jones and Muhlethaler, 1998), and neuropeptides (Walker et al., 1989). One of the major projections of the BF is to the cerebral cortex (Woolf et al., 1983; Saper, 1984; Luiten et al., 1987; Gritti et al., 1997) which indicates widespread influence for brain function. The hippocampus is another target of BF projections (Detari et al., 1999) along with indirect cortical connections via the thalamus (Bickford et al., 1994; Asanuma, 1997). Therefore, cholinergic signaling is important for functions such as memory. Subcortical structures such as the olfactory bulb, amygdala, posterior hypothalamus, and interpeduncular nucleus (Semba and Fibiger, 1989) also receive input from the BF. In addition, a discrete population of cells sends projections from the BF to the brainstem (Semba et al., 1989). BF afferents originate in diverse regions including limbic,

diencephalic and brainstem structures (Semba and Fibiger, 1989; Zaborszky et al., 1991). Most of the ascending input is considered as part of an arousal and attention system. The BF is therefore intricately connected with widespread efferents and afferents and, thus, the cholinergic system governs a complex system of neural transmission that contributes to multiple brain functions.

Generally, the cholinergic system consists of the acetylcholine synthesizing enzyme, choline acetyl transferase (ChAT, EC 2.3.1.6), two classes of acetylcholine receptors, nicotinic (nAChR) and muscarinic (mAChR) receptors and two acetylcholine hydrolyzing enzymes, AChE and BuChE. ChAT synthesizes ACh (Nachmansohn and Machado, 1943) from choline and acetyl-CoA (Malthe-Sorenssen, 1976; Kim et al., 2006) and the expression of ChAT is a requirement for a neuron to be considered cholinergic. In this respect, ChAT is the most reliable marker for the visualization of cholinergic structures in the brain (Kimura et al., 1980). In contrast, neurons containing cholinergic system components, such as nAChRs or mAChRs, but without ChAT activity are considered cholinoceptive (Eckenstein and Sofroniew, 1983). A variant of ChAT is present in peripheral tissues and thus, traditional immunohistochemical methods for visualization of this enzyme only detects its presence in the CNS (Bellier and Kimura, 2011). Therefore, the extent of ACh synthesis and subsequent functions in various tissues, in particular outside of the nervous system, remains to be fully elucidated.

ACh signaling is mediated through two distinct receptor types, nAChR and mAChR, which are structurally unrelated. nAChR belong to the family of receptor-gated ion channels (ionotropic) and mAChR to the G protein-coupled receptors family (metabotropic) (Hosey, 1992). Five genetically defined muscarinic receptors have been

identified (M_1-M_5) (Caulfield and Birdsall, 1998) that have various expressions and functions. M_1, M_3 and M_5 are usually coupled to $G\alpha_{q/11}$ protein thereby, activating phospholipase C while M_2 and M_4 are typically coupled to $G\alpha_{i/o}$ protein thereby, producing inhibitory effects on cAMP synthesis (Eglen, 2006). In particular, M_1 and M_2 are expressed in the brain (Oki et al., 2005) and are involved in learning and memory (Terry and Buccafusco, 2003). Thus, alteration of expression levels or functions of these receptors may contribute to cognitive impairment. nAChRs are pentameric hetero- or homooligomers consisting of various combinations of six α and three β subunits. These receptors are responsible for regulating neurotransmitter release, cell excitability and modulation of circuits involved in such physiological functions as sleep, pain and cognition (Wevers, 2011). Multiple methods of detection have been used to define distribution of nAChRs in the brain; however, these are generally subunit non-specific and a reliable distribution remains unclear. Nevertheless, nAChRs are implicated in many CNS functions and undergo alterations in response to insult or disease.

The brain cholinergic system is involved in cognition and cortical plasticity (Arendt and Bigl, 1986; Schliebs et al., 1996; Bigl and Schliebs, 1998) along with other functions in controlling cerebral blood flow (Biesold et al., 1989; Barbelivien et al., 1999; Sato et al., 2004), cortical activity (Detari et al., 1999; Lucas-Meunier et al., 2003) and sleep-wake cycles (Lee et al., 2005). Modulation of central cholinergic function impacts cognition such as learning and memory in humans (Drachman and Leavitt, 1974; Drachman, 1977; Molchan et al., 1992). Correlation of clinical dementia ratings and disruptions of cortical cholinergic markers such as levels of ACh, AChR binding and ChAT indicate that a decline in cholinergic function is associated with cognitive defects

(Sims et al., 1980; Bowen et al., 1981; Bierer et al., 1995; Davis et al., 1999; Gsell et al., 2004). This has led to the implication of the cholinergic system in memory dysfunction in AD (Davies and Maloney, 1976; Perry et al., 1977; Bartus et al., 1982; Coyle et al., 1983; Bartus, 2000), in particular through the degeneration of the basal forebrain cholinergic cells (Whitehouse et al., 1982; Arendt et al., 1983; Arendt et al., 1985; Mesulam, 1986; Schliebs and Arendt, 2006).

1.6.3 Non-Neuronal Cholinergic systems

Aspects of a cholinergic function distinct from the central and peripheral nervous systems emerged 50 years ago (Whittaker, 1963). The non-neuronal cholinergic system appears to be involved in the regulation of basal functions in nearly all mammalian cells (Wessler et al., 1998, 1999). This has led to the proposal that ACh is a 'universal cytotransmitter' (Grando, 1997; Grando and Horton, 1997).

Immune cells are capable of synthesizing, storing, releasing and breaking down ACh (Kawashima and Fujii, 2004; Kawashima et al., 2012; Verbout and Jacoby, 2012). Lymphocytes (Fujii et al., 1996; Kawashima et al., 1998; Tayebati et al., 2002), monocytes (Hecker et al., 2006; Neumann et al., 2007), macrophages (Wessler and Kirkpatrick, 2001), neutrophils (Hagforsen et al., 2000), dendritic cells (Kawashima et al., 2007), mast cells (Nechushtan et al., 1996; Wessler et al., 2003) and eosinophiles (Hagforsen et al., 2000; Durcan et al., 2006) all express aspects of cholinergic machinery. Furthermore, the mechanism of release of ACh is probably distinct from the neuronal mechanism (Kawashima et al., 2012). In immune cells, ACh release occurs through active transport directly upon synthesis and may be mediated by the organic cation

transporter family (Wessler et al., 2001). Thus, the cholinergic system seems to have an integral and complex role in the regulation of the immune system throughout the body.

The cholinergic system has also been implicated in development, predominantly due to its presence in embryonic stem cells (Landgraf et al., 2010). Very early in development non-neuronal cells express cholinergic system components (Paraoanu et al., 2007). In an evolutionary sense, ACh is broadly distributed throughout living organisms (Horiuchi et al., 2003) such as bacteria (Stephenson and Rowatt, 1947) and plants (Smallman and Maneckjee, 1981). These observations also suggest a general non-neural function for the cholinergic system. In particular, a proliferative effect on many different types of cells may be a principal role of ACh (Wessler et al., 1999). It is not clear if functions of the cholinergic system are transient and varying throughout life or if early roles, such as stem cell proliferation, and later roles, such as nervous system function, involve distinctly different ACh signaling systems.

1.7 Acetylcholinesterase and Butyrylcholinesterase

1.7.1 Distribution, Properties and Functions

Isolations from horse serum first identified an enzyme that could hydrolyze ACh (Stedman and Easson, 1932). This discovery validated previous predictions made by Otto Loewi and others (Loewi and Navratil, 1926) that ACh was hydrolyzed in an enzymatic process. It was subsequently recognized that the hydrolysis of ACh is governed by two enzymes (Alles and Hawes, 1940), 'True Cholinesterase', acting specifically on esters of choline, and 'Pseudo Cholinesterase' that, in addition to ACh, hydrolyzes a variety of non-choline esters (Mendel and Rudney, 1943). The two

enzymes, ‘True Cholinesterase’ and ‘Pseudo-Cholinesterase’ are now recognized as AChE (EC 3.1.1.7) and BuChE (EC 3.1.1.8), respectively.

The first histochemical method for the visualization of cholinesterases was developed by Gomori (Gomori, 1948); however, it was not until the method of Koelle (Koelle, 1954) that visualization of cholinesterase activity became robustly explored. This method involved the application of choline thioesters which, upon hydrolysis by cholinesterases, would form a precipitate with copper in the staining solution. This cuprous thiocholine precipitate demonstrated the location of cholinesterase activity. Based on their respective hydrolysis rates, acetylthiocholine and butyrylthiocholine were used for the visualization of AChE and BuChE, respectively. However, this Koelle product of cuprous thiocholine is colourless and thus, must be subjected to additional steps for proper visualization. The method of Karnovsky and Roots (Karnovsky and Roots, 1964) improved on these principles. This method involved incubation of tissue with acetylthiocholine or butyrylthiocholine along with potassium ferricyanide, cupric sulfate and citrate. The putative mechanism involves the hydrolyzed thiocholine reduction of ferricyanide to ferrocyanide which combines with copper(II) to produce insoluble and coloured cupric ferrocyanide (Hatchett’s Brown). Citrate is thought to prevent formation of cuprous thiocholine, the Koelle product, in the solution. Subsequent contrast enhancement of the Hatchett’s Brown precipitate is achieved with 3,3'-diaminobenzidine (DAB) in the presence of hydrogen peroxide (Mesulam and Asuncion Moran, 1987). Cobalt chloride can be applied to increase the reactivity of the DAB enhancement (Adams, 1977). Based on these advances, a modified Karnovsky-Roots method has shown robust visualization of both AChE and BuChE in brain tissue

(Darvesh et al., 1998). Although the exact structure of Hatchett's Brown has not been resolved with X-ray crystallography, the chemical composition (Tewari et al., 1982) and a possible structure has been proposed (Darvesh et al., 2010a).

The histochemically-detected distributions of AChE and BuChE activities demonstrate both overlapping and distinct patterns in the CNS. AChE is found in all cortical areas in both fibers and neurons, especially in layers 3 and 5 (Mesulam et al., 1987; Geula and Mesulam, 1989). More specifically, AChE activity is found in limbic areas (Mesulam et al., 1987), such as the hippocampus (Friede, 1967), the cerebellar cortex, brainstem nuclei, such as the hypoglossus, and the dorsal and ventral spinal cord (Friede, 1967). BuChE distribution in the brain was initially mapped for several different species, including human (Silver, 1974). Very little activity for this enzyme is found in the neocortex except for occasionally in larger pyramidal neurons (Okinaka et al., 1961; Friede, 1967). AChE and BuChE activity has been extensively described in the hippocampal formation and amygdala (Darvesh et al., 1998) as well as in the thalamus (Darvesh and Hopkins, 2003). In particular, these regions contain some nuclei that express only AChE or only BuChE and some nuclei that express both cholinesterases. This suggests that cholinergic signaling may be unique in each nucleus, based on the expression levels of AChE and BuChE, and may give rise to distinct properties or functions. Brainstem nuclei, such as the dorsal motor nucleus of the vagus nerve and the hypoglossal nucleus possess very high BuChE activity (Friede, 1967; Tago et al., 1992). In contrast to AChE, BuChE activity is high in the white matter (Foldes et al., 1962; Friede, 1967) and is found in association with myelin (State et al., 1977) and oligodendrocytes (Friede, 1967). However, not all myelinated areas demonstrate glial

BuChE as exemplified by the pyramidal tracts (Friede, 1967). Thus, some oligodendroglia may be devoid of BuChE activity potentially giving rise to distinct populations based on the presence of this enzyme. Moderate BuChE activity is also found in blood vessels signifying expression in endothelial cells. (Friede, 1967; Tago et al., 1992). Peripherally, AChE and BuChE are expressed at the neuromuscular junction (Feng et al., 1999; Krejci et al., 1999). AChE is found in circulating blood associated with erythrocytes (Dutta-Choudhury and Rosenberry, 1984). Interestingly, BuChE is present in almost every tissue except for erythrocytes and is also expressed in the serum (Lockridge et al., 1987). Knock-out (KO) transgenic animals for AChE and BuChE have further contributed to understanding of the roles of these two enzymes. BuChE-KO animals do not have an overt phenotype except for marked susceptibility to cholinesterase inhibition which signifies a scavenger role for BuChE (Li et al., 2006; Li et al., 2008a; Duysen et al., 2009). In addition, the BuChE-KO model had reinforced the historical view that BuChE may play only an accessory role to AChE. On the other hand, AChE-KO mice are viable, albeit with some extreme phenotypes (Xie et al., 2000). BuChE expression was not altered in these animals however, this enzyme activity compensated for AChE function (Li et al., 2000; Mesulam et al., 2002). These studies solidified the notion that both AChE and BuChE have roles in cholinergic neurotransmission and that their functions are not completely redundant.

AChE is encoded by a single gene on human chromosome 7 that spans ~5 kb and has six exons (Li et al., 1991; Getman et al., 1992). Alternative splicing of exons 5 and 6 leads to three different AChE isoforms that contain the same catalytic domain but differ in the C-terminal (Massoulie et al., 1993; Massoulie et al., 1998; Massoulie, 2002).

'Readthrough' AChE ($AChE_R$) results from a lack of splicing downstream of the catalytic domain exons which produces a soluble and monomeric enzyme that does not have features for attachment to other molecules. $AChE_R$ is found in embryonic tissues but is not typically expressed in the adult brain (Legay et al., 1993). 'Hydrophobic' AChE ($AChE_H$), possessing exon 5, exists as a glycophosphatidylinositol (GPI)-anchored dimer and is mainly expressed in hematopoietic cells (Legay et al., 1993; Li et al., 1993). 'Tailed' AChE ($AChE_T$), possessing exon 6, is present in a variety monomers, dimer, tetramers and oligomers. These oligomers can be associated with Collagen Q (ColQ), at the neuromuscular junction (Krejci et al., 1997), or proline rich membrane anchors (PRiMA), at plasma membranes in brain and muscle (Perrier et al., 2002). Oligomerization and anchoring of AChE does not affect catalytic activity; therefore, the function of ColQ and PRiMA anchors is for the proper positioning of the enzyme. For example, fast and slow muscles in the rat demonstrate different compositions and distributions of ColQ anchored AChE (Krejci et al., 1999) which may contribute to the respective synaptic properties of these muscles. Nucleotide polymorphisms are rare for AChE and have not been associated with alterations of protein properties. This may reflect an absolute requirement for AChE function (Soreq and Seidman, 2001).

In contrast to the complex splicing pattern of AChE, BuChE expression on chromosome 3 (Sparkes et al., 1984; Yang et al., 1984; Gnatt et al., 1990) only affords the 'Tailed' BuChE ($BuChE_T$) form. The genomic region for BuChE spans ~70 kb and has four exons (Arpagaus et al., 1990). The considerable genomic size difference between AChE (5 kb) and BuChE (70 kb) is attributed to intron lengths. Much like $AChE_T$, $BuChE_T$ can oligomerize as well as associate with ColQ and PRiMA anchors

(Massoulie, 2002). However, in contrast to AChE, many mutations of BuChE have been described (Arpagaus et al., 1990; La Du et al., 1990; Darvesh et al., 2003a). Several prominent BuChE variants arise from point mutations that alter the function of this enzyme. Atypical BuChE is characterized by a point mutation that changes Asp70 to Gly that imbues resistance to dibucaine inhibition (McGuire et al., 1989). This atypical variant is commonly (~90%) found in association with the BuChE K-variant, possessing an Ala539 to Thr mutation (Bartels et al., 1992). The BuChE K-variant demonstrates a ~30% reduction in activity compared to wild-type enzyme (Rubinstein et al., 1978). A heterogeneous group of mutations can lead to <10% of normal BuChE activity and are termed silent phenotypes (Primo-Parmo et al., 1996). These mutations produce a virtually catalytically inactive protein, lower expression levels or, as a result of an improper stop codon, produce a truncated form. Historically, silent BuChE variants have been identified in individuals due to their marked sensitivity to muscle relaxants, such as succinylcholine, which are normally scavenged by this enzyme (Liddell et al., 1962).

AChE and BuChE are serine hydrolases and are closely related in primary sequence (51-54% homology) (Chatonnet and Lockridge, 1989), structure and function. Both enzymes are glycoproteins (Lockridge et al., 1987; Millard and Broomfield, 1992) that catalyze the hydrolysis of esters of choline (Silver, 1974). The X-ray crystal structure of AChE was obtained after isolation of the enzyme from the *Torpedo californica* electric organ (Sussman et al., 1991). The X-ray structures of human AChE (Kryger et al., 2000) and BuChE (Nicolet et al., 2003) were subsequently elucidated after much difficulty in part due to technical challenges such as glycosylation of the enzymes (Nachon et al., 2002). AChE and BuChE have a central β-sheet surrounded by α-helices

(Millard and Broomfield, 1992) and, in this respect, belong to the α/β fold protein superfamily (Ollis et al., 1992; Soreq and Seidman, 2001). Human AChE and BuChE catalytic subunits have critical residues for function that were determined first through site directed mutagenesis (Harel et al., 1992; Neville et al., 1992; Radic et al., 1993; Vellom et al., 1993; Barak et al., 1994; Masson et al., 1996; Saxena et al., 1997, 1999). The catalytic triad of human AChE (Shafferman et al., 1992) and BuChE (Lockridge et al., 1987) consists of serine 203/198, histidine 447/438, and glutamic acid 334/325, respectively, at the bottom of a 20 Å active site gorge. These residues are the site of hydrolysis for substrates, such as ACh (Figure 1.3), as well as aromatic amides (Darvesh et al., 2006). The active site gorges of AChE (Sussman et al., 1991) and BuChE (Nicolet et al., 2003) are lined by 14 and 6 aromatic amino acid residues, respectively, that may facilitate guidance of substrate entry and exit of the gorge (Sussman et al., 1991). Despite the fact that substrates must traverse the active site gorge, the cholinesterases, in particular AChE, are among the catalytically fastest enzymes known (Quinn, 1987). In addition to the catalytic triad, other residues are involved in the alignment of substrates and thus, are critical for hydrolytic efficiency. In AChE and BuChE tryptophan 86/82 comprises the site where the cationic quaternary nitrogen of ACh forms a π-cation bond. The oxy-anion hole, formed by residues glycine 118/116, glycine 119/117 and alanine 201/199, stabilizes the carbonyl oxygen of ACh thus, positions this substrate's carbonyl carbon in proximity to the serine of the catalytic triad to facilitate hydrolysis. A pocket accommodates the acyl CH_3 portion of ACh, phe295 and phe297 in AChE (Vellom et al., 1993) while smaller val288 and leu286 in BuChE (Nicolet et al., 2003) provide steric differences in this region between AChE and BuChE that account for substrate selectivity

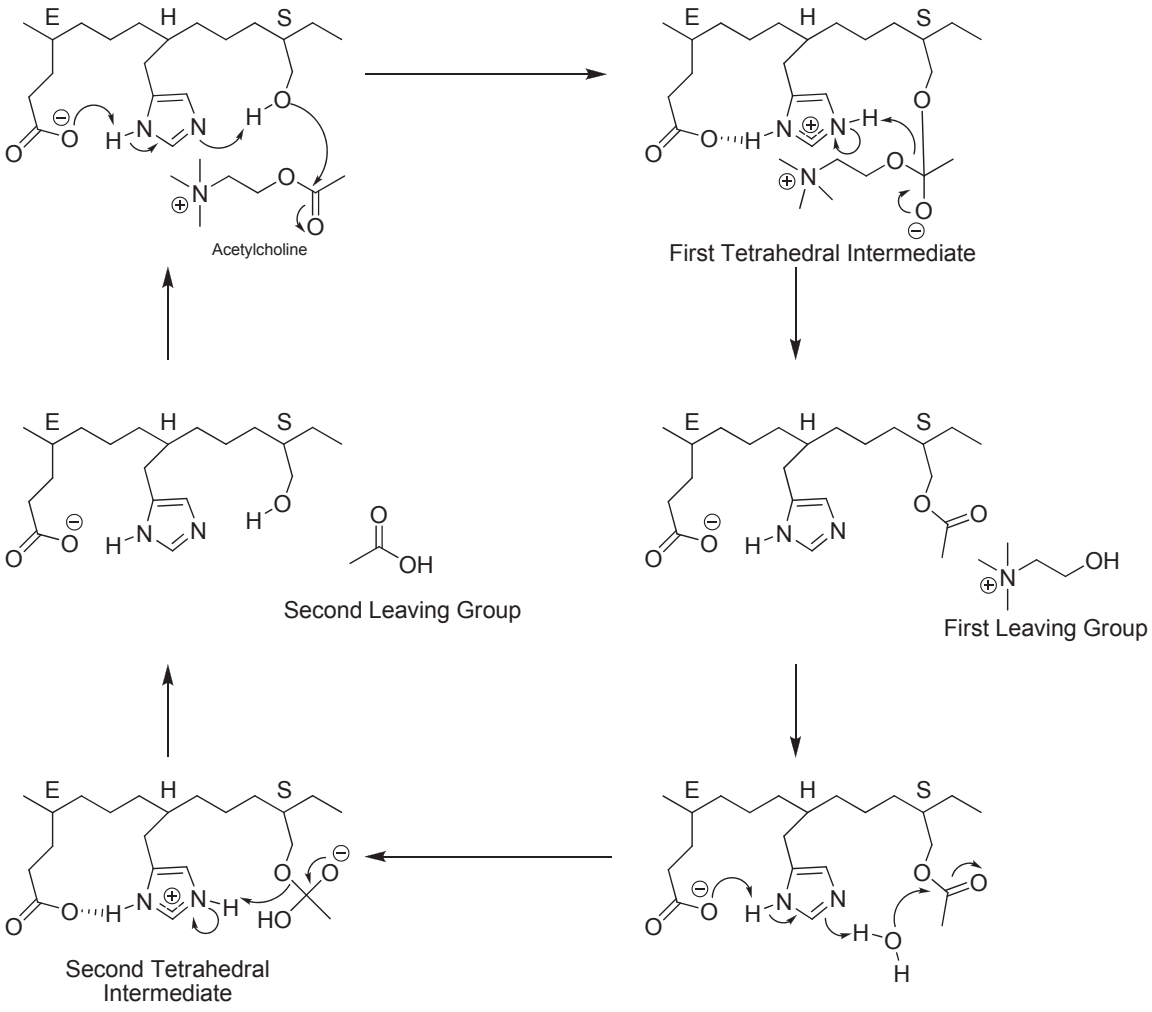

Figure 1.3. Mechanism of cholinesterase catalyzed hydrolysis of acetylcholine. E: glutamate, H: histidine, S: serine.

divergence between the two enzymes. Furthermore, the active site gorge volumes for AChE and BuChE are approximately 300 $Å^3$ and 500 $Å^3$, respectively. This allows BuChE to accommodate a much wider array of substrates and other molecules compared to AChE.

In addition to the active site region of the cholinesterases, a peripheral site (P-site) has been identified on each enzyme by its interaction with substrate and inhibitor molecules. Influenced by the P-site ionic interactions with cationic ACh at high substrate concentrations, AChE undergoes inhibition (Nachmansohn and Wilson, 1951; Mallender et al., 2000) which is thought to occur by steric blockade of product release from the active site due to interactions at the P-site (Szegletes et al., 1998). In contrast, under these conditions, BuChE undergoes activation, perhaps due to a conformational change or stabilization of the catalytic tetrahedral intermediate mediated by interaction at the P-site (Masson et al., 1996). Thus, the P-sites of both AChE and BuChE appear to play a critical role in the function of these enzymes. The P-site of AChE has been extensively defined both in structure and function (Taylor and Lappi, 1975; Sussman et al., 1991; Radic et al., 1993; Barak et al., 1994; Harel et al., 1996; Szegletes et al., 1998; Mallender et al., 2000; Harel et al., 2008; Auletta et al., 2010). Asp74 is the 'peripheral anionic site' and is joined by trp286, tyr72 and tyr124 in constituting the P-site. This site binds substrates destined for the active site, such as ACh (Bourne et al., 2006), as well as inhibitors such as Thioflavin-T (Harel et al., 2008; Auletta et al., 2010) which do not reach the bottom of the gorge. BuChE also contains a 'peripheral anionic site' involving asp70, and most likely proximal P-site residues yet to be clearly defined. Expansion of our understanding of the P-sites for AChE and BuChE will further the delineation of the

functions of these enzymes *in vivo* and aid in the design and development of specific ligands.

Although the catalytic function of AChE and BuChE has been a major research focus, other roles for these enzymes have emerged. Both cholinesterases are implicated in development, such as maturation of the nervous system (Kostovic and Goldman-Rakic, 1983; Dubovy and Haninec, 1990; Layer, 1990, 1991; Boopathy and Layer, 2004; Bytyqi et al., 2004; Paraoanu et al., 2006; Paraoanu and Layer, 2008; Vogel-Hopker et al., 2012). Furthermore, cell adhesion molecules, also members of the α/β fold superfamily, share high structural similarities with both cholinesterases (Tsigelny et al., 2000; Koehnke et al., 2008; Leone et al., 2010; Falugi and Aluigi, 2012; Halliday and Greenfield, 2012). Thus, there is a possibility that AChE and BuChE may function in this regard. In addition, BuChE has been found to modulate the activity of other proteins such as trypsin due to protein-protein interactions (Darvesh et al., 2001). The extent that cholinesterases may interact and influence other proteins has not been adequately explored.

1.7.2 Roles in Alzheimer's Disease

Almost 50 years ago it was first discovered that cholinesterases are associated with pathological hallmarks in AD brain (Friede, 1965; Perry et al., 1980). It was subsequently determined that NPs, NFTs and CAA contain both AChE and BuChE (Mesulam and Asuncion Moran, 1987; Carson et al., 1991; Moran et al., 1993; Gomez-Ramos et al., 1994). It is noteworthy that the optimum pH for Karnovsky-Roots staining of NP- and NFT-associated cholinesterase was 6.8 compared to pH 8.0 used for typical neuronal and glial cholinesterase visualization (Geula and Mesulam, 1989). In addition,

higher concentrations of inhibitors were necessary to attenuate staining of cholinesterases that were associated with AD pathology. Furthermore, AChE and BuChE associated with AD structures may have unique susceptibility to inhibition by compounds, such as bacitracin, compared to neural cholinesterases (Wright et al., 1993a). Despite these differences, cholinesterases isolated from AD tissue were found to be identical in function as those from cognitively normal adults (Darvesh et al., 2010a). This suggests that the microenvironment of the NP and NFT may alter the biochemical function of AChE and BuChE through a currently unknown mechanism. In addition, molecular forms and glycosylation of AChE and BuChE differ in AD from cognitively normal brain. In particular, the levels of monomeric enzyme increase while the tetrameric form levels decrease. These alterations in molecular forms are comparable to expression patterns during development (Atack et al., 1986; Arendt et al., 1992). In addition, these molecular forms were differentially glycosylated (Saez-Valero et al., 1999). Splice variations of AChE are also altered in AD and are characterized by a reduction in $AChE_R$ (Darreh-Shori et al., 2004). A relatively high brain abundance of $AChE_R$ is neuroprotective in transgenic mice; however, in contrast, relative increases in other forms of AChE can lead to intensified neurodeterioration (Sternfeld et al., 2000). The source of AChE and BuChE associated with AD pathology may be glial cells since cholinesterases in astrocytes and microglia demonstrate many of the same properties as the NP and NFT-associated enzymes (Wright et al., 1993b). For example, expression of NP-BuChE in the neocortex, an area normally devoid of this enzyme, may be due to glial recruitment associated with the pathological structure.

Generally, in areas implicated in AD, such as the hippocampus, levels of AChE decrease while BuChE levels either increase (Perry et al., 1978) or remain the same (Atack et al., 1987; Darvesh et al., 2010a). Association of BuChE with AD pathological structures, especially in areas such as the cortex that normally express low levels of this enzyme, may contribute to its overall expression stability or increase. In contrast, reduction in AChE is attributed to the loss of cholinergic neurons which express high levels of this enzyme. This loss possibly outweighs the increase of AChE due to its association with AD structures.

To date, symptomatic treatment for AD has been achieved by targeting cholinesterase catalytic activity with inhibitors (Birks, 2006). The only other drug used for AD, memantine, is thought to show efficacy due to modulation of the glutamatergic system (Danysz and Parsons, 2012). Cholinesterase inhibitors used clinically are donepezil, rivastigmine and galantamine (Cummings, 2000; Giacobini, 2000). The hypothesis behind efficacy of cholinesterase inhibitors is that their action is capable of increasing ACh levels in the brain (Giacobini, 2000; Greig et al., 2005). Such treatment is expected to return ACh towards normal levels and, therefore, offer relief from adverse cognitive and behavioural symptoms associated with AD. Although these inhibitors are used for treatment of AD, they have not been found to have conclusive effects on duration and progression of the illness (Giacobini, 2003) and thus, are viewed solely as symptomatic interventions. This suggests that AChE and BuChE involvement in AD pathology may be distinct from their usual catalytic activity that is targeted by cholinesterase inhibitors. In this respect, AChE and BuChE have been directly implicated in the aggregation of Aβ. AChE promotes aggregation at its P-site (Inestrosa

et al., 1996) while, in contrast, the BuChE C-terminal region has an attenuating effect (Diamant et al., 2006). What contribution these effects may have *in vivo* on Aβ aggregation kinetics and cellular toxicity is unknown. Although the role of cholinesterases in AD pathology is not fully defined, it has been suggested that the presence of these enzymes, in particular BuChE, may result in a NP maturation process culminating in neuronal toxicity (Guillozet et al., 1997). This is supported by observations in an AD animal model in which BuChE is associated with a sub-population of NPs that were independently detected through thioflavin-S staining. This suggests that the presence of BuChE may delineate only mature NPs (Darvesh et al., 2012b). However, the chronology of cholinesterase incorporation into AD pathology and the role of these enzymes in this disease requires additional investigation.

Further evidence for cholinesterase involvement in AD is demonstrated by genetic risk factors for this disorder. As described above, individuals expressing apoE ε4 are at greater risk for the development of AD. In addition, expression of the K-variant of BuChE also results in greater risk of the disease (Lehmann et al., 1997; Lehmann et al., 2000; Lehmann et al., 2001; Holmes et al., 2005; Ghebremedhin et al., 2007; Podoly et al., 2009; Darreh-Shori et al., 2011b; Darreh-Shori et al., 2011a). Recently, BuChE was associated with Aβ pathology burden as visualized by florbetapir PET imaging (Ramanan et al., 2013). However, not all studies are in agreement that BuChE K-variant associates with AD (Bertram et al., 2007). In line with the hypothesis of BuChE being involved in maturation of AD pathology, the BuChE K-variant is associated with progression from MCI to AD (Lane et al., 2008). Genetic studies have implicated BuChE in AD, just as

histochemical visualization before it. However, elucidation of the role of this enzyme in AD still remains in infancy.

1.7.3 Roles in Multiple Sclerosis

The cholinergic system may play an integral role in the pathogenesis of MS. In particular, the presence of ACh produces an anti-inflammatory state (Wang et al., 2003; Wang et al., 2004) and thus, depletion of this signaling agent may facilitate neuroinflammation (Nizri et al., 2006). Cholinergic anti-inflammatory effects, mediated by α7 nAChR signalling, downregulate cytokine production by macrophages and suppress lymphocyte proliferation (Nizri et al., 2006). Administration of a cholinesterase inhibitor, rivastigmine, to a mouse model of MS alleviated, at least in part, the neuroinflammatory response (Nizri et al., 2008). A study of human MS brain lesions found that BuChE activity associated with myelin is lost as demyelination progresses (Darvesh et al., 2010b). Furthermore, inflammatory cells expressed high levels of BuChE but only in active and chronic active lesions. AChE expression was not altered in these lesions. Increased concentration of BuChE, associated with neuroinflammatory cells, in an actively demyelinating lesion, may lead to a localized decrease in ACh. Thus, cholinesterase enzyme activity in MS may serve to drive the progression of the neuroinflammatory response through modulation of the cholinergic system. Alternatively, cholinesterases, in particular BuChE, are capable of hydrolyzing compounds other than ACh. Several proteins, such as myelin basic protein, proteolipid protein (PLP) and myelin oligodendrocyte glycoprotein are associated with the myelin sheath and may have roles in structural stability. Fatty acid thioester analogues of PLP

can be hydrolyzed by BuChE *in vitro* (Pottie et al., 2011). Thus, aberrant expression of BuChE, perhaps linked to neuroinflammation, can potentially facilitate decompaction of the myelin sheath leading to epitope spreading and thus, facilitating lesion pathogenesis in MS. Furthermore, the progressive stages of MS are characterized by neurodegeneration through unknown mechanisms. Because of their putative involvement in other neurodegenerative disorders, such as AD, it is conceivable that the cholinesterases may have some yet undefined role in SPMS and PPMS.

1.8 Imaging of Cholinesterases

Cholinesterase imaging with PET first relied on the radiolabelling of organic phosphate compounds, such as sarin, known to be irreversible cholinesterase inhibitors (Prenant and Crouzel, 1990). However, the potential toxicity associated with organophosphate irreversible inhibitors is not favourable for the development of imaging agents. Subsequently, several agents have emerged that are either non-specific for the cholinesterases, specific for AChE or specific for BuChE (Figure 1.4). ^{11}C radiolabelled physostigmine (Bonnot-Lours et al., 1993; Planas et al., 1994), a potent pseudo-irreversible inhibitor of both AChE and BuChE (Darvesh et al., 2003b) demonstrated uptake indicative of known regions of AChE activity in the rodent brain, such as accumulation in the AChE-rich striatum. However, the striatum to cortex accumulation in humans (2:1) (Pappata et al., 1996) was lower than expected for AChE imaging (Finkelstein et al., 1988) and, furthermore, this agent demonstrated complex *in vivo* kinetics (Blomqvist et al., 2001). These factors have contributed to lack of further use for this imaging agent. Donepezil, a reversible cholinesterase inhibitor used to treat AD, has

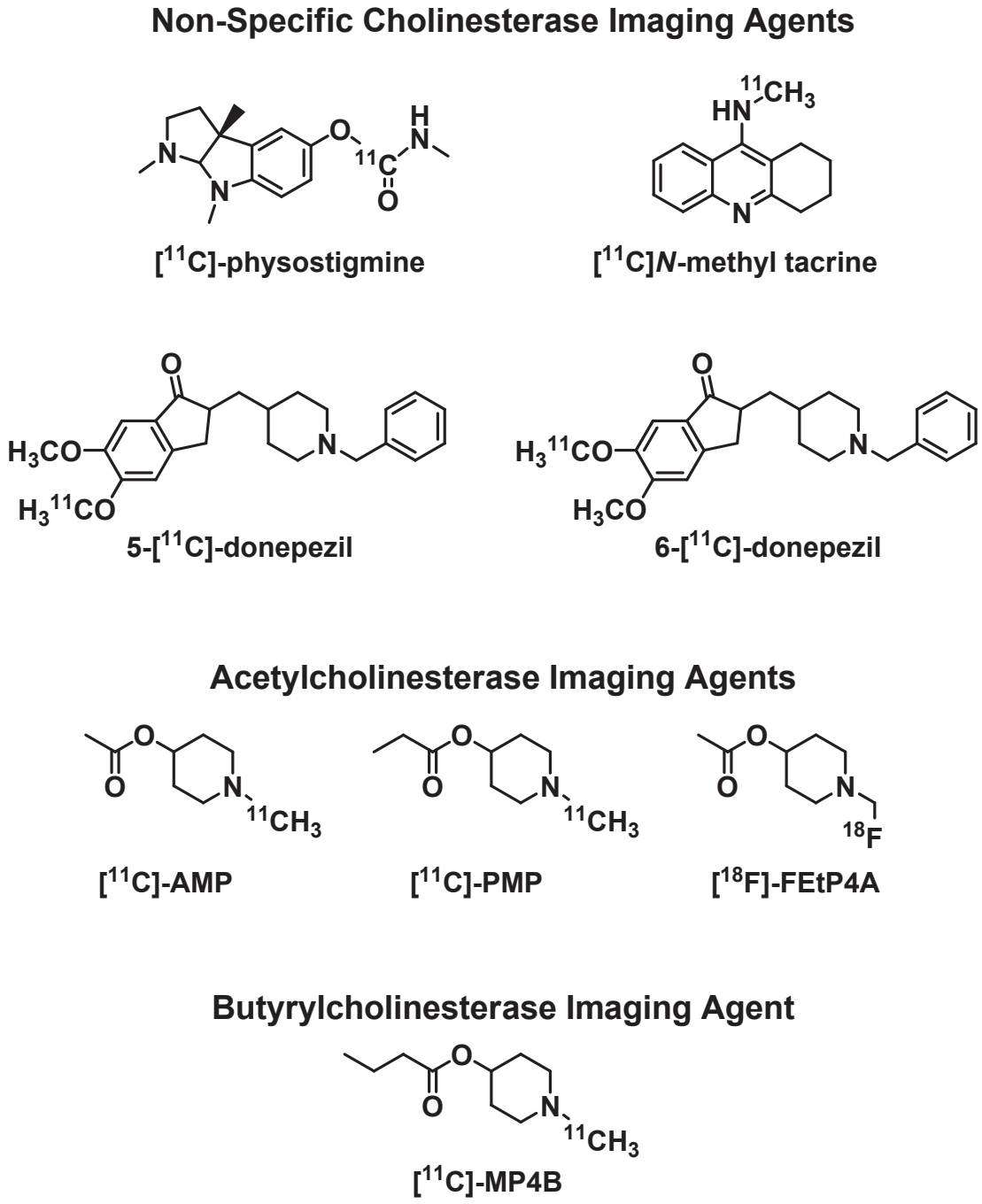

Figure 1.4. Structures of cholinesterase imaging agents.

also been radiolabelled and assessed for imaging the brain (Okamura et al., 2008; Hiraoka et al., 2009; Kasuya et al., 2012). These studies have been valuable for assessing the *in vivo* binding and AChE inhibition in response to donepezil administration. Interestingly, the position of the radiolabelled carbon of donepezil drastically alters its ability as an AChE imaging agent, potentially due to *in vivo* metabolism. [5-^{11}C-methoxy]donepezil effectively binds AChE (Funaki et al., 2003) while [6-^{11}C-methoxy]donepezil demonstrates no *in vivo* labeling of the enzyme (De Vos et al., 2000). ^{18}F radiolabelled donepezil analogues have also emerged and demonstrate similar binding characteristics as the ^{11}C labeled agents (Lee et al., 2000). Another potent reversible cholinesterase inhibitor, tacrine, has been methylated with ^{11}C and used for imaging; however, its distribution was non-specific and did not reflect AChE levels in the brain (Tavitian et al., 1993; Traykov et al., 1999). Radiolabelling of the common pseudo-irreversible cholinesterase inhibitor, rivastigmine, has to date been unsuccessful for imaging. However, further analogues are being developed based on this molecular scaffold (Wang et al., 2008). The failure of radiolabelled known cholinesterase inhibitors to accurately recapitulate the distribution of AChE has led to the synthesis and development of novel compounds specifically for this purpose. A series of *N*-benzyl piperidine derivatives containing a tricycle are potent and selective reversible AChE inhibitors (Villalobos et al., 1995) and have been radiolabelled with ^{11}C (Bencherif et al., 2002; Musachio et al., 2002) and ^{18}F (Lee et al., 2004; Ryu et al., 2005; Kim et al., 2011). These compounds have been used for AChE imaging and show promise for visualization of this enzyme activity *in vivo*.

In addition to cholinesterase inhibitors, as described above, enzyme substrates have also been explored as imaging agents for AChE. A hypothesis proposes that substrate imaging agents will diffuse into the brain where they will be metabolized by AChE producing a hydrophilic metabolite that accumulates at the site of enzyme activity. This concept has been referred to as the 'Metabolic Trapping Principle' (Irie et al., 1994; Kikuchi et al., 2007). Several *N*-[^{14}C]methylpiperidyl ester derivatives were synthesized, based on their structural similarities to ACh, as potential AChE imaging agents (Figure 1.4) (Irie et al., 1994). These molecules, based on rodent brain tissue homogenate kinetics, were deemed specific for AChE and accumulated in AChE-rich areas, such as the striatum, in the rodent brain. These results were further extended to the non-human primate where brain AChE visualization was also observed (Namba et al., 1994). In attempts to afford greater AChE selectivity with the *N*-methyl piperidyl scaffold, benzoate esters were synthesized, radiolabelled and evaluated as AChE imaging agents. However, *in vitro* kinetics were not performed and these molecules were not found to be hydrolyzed by AChE *in vivo* (Bormans et al., 1996). Based on these studies, less bulky substrates such as *N*-[^{11}C]methylpiperidyl acetate ([^{11}C]-AMP) and *N*-[^{11}C]methylpiperidyl propionate ([^{11}C]-PMP) emerged as leading AChE imaging agents. These compounds both demonstrated favourable kinetics in non-human primate however, [^{11}C]-PMP, due to its lower AChE hydrolysis rate, was considered the better agent (Kilbourn et al., 1996). Parallel rodent work also identified AMP and PMP as leading compounds for AChE imaging (Irie et al., 1996). Humans have lower levels of cortical AChE compared to mice thus, despite different hydrolysis rates, both AMP and PMP were considered suitable for human studies. [^{11}C]-AMP has high hydrolytic specificity

and thus, was the first of the *N*-methylpiperdyl ester imaging agents to advance to human studies. Administration of [^{11}C]-AMP in AD patients demonstrated distinct patterns of reduced AChE uptake in areas, such as the parietotemporal cortex, when compared to cognitively normal controls (Iyo et al., 1997; Shinotoh et al., 2000). However, the AD patients of this study also demonstrated reductions in cerebral blood flow in areas with reduced [^{11}C]-AMP accumulation. Follow up studies demonstrated that in cognitively healthy adults, the levels of AChE remain constant in the cerebral cortex with aging even though some decreases in cerebral blood flow occur (Namba et al., 1998; Namba et al., 1999). AChE imaging with [^{11}C]-AMP and [^{11}C]-PMP has been applied to determine the extent of AChE activity in AD patients under a cholinesterase inhibitor treatment regime (Kuhl et al., 2000; Kaasinen et al., 2002; Bohnen et al., 2005). Detection of AChE alterations in MCI and early AD populations show focal reduction in some areas, such as the hippocampus and temporal cortex, (Rinne et al., 2003; Herholz, 2008; Haense et al., 2012; Marcone et al., 2012) and may be a promising approach for AD diagnosis. AChE activity has been visualized in many conditions in addition to AD such as MS. Interestingly, in MS, there were no differences between patients with cognitive impairment and healthy controls (Virta et al., 2011).

Efforts to develop an ^{18}F labeled AChE imaging agent have produced several potential compounds based on the *N*-substituted piperidyl ester scaffold. A derivative of AMP, *N*-[^{18}F]fluoroethylpiperidin-4-yl acetate ([^{18}F]-FEtP4A), demonstrates favourable kinetics towards AChE (Zhang et al., 2002). However, its reduced specificity and low hydrolysis rate compared to PMP and AMP has limited its applicability. Further optimization has afforded similar fluorinated ligands (Shao et al., 2003; Kikuchi et al.,

2005) that are promising ^{18}F radiolabelled AChE imaging agents comparable to [^{11}C]-PMP and [^{11}C]-AMP (Shao et al., 2005; Kikuchi et al., 2010).

The majority of AChE imaging agents have been developed for PET; however, SPECT agents have recently been developed (Mejri et al., 2010) and have shown promise for the *in vivo* imaging of this enzyme activity (Mejri et al., 2013). However, some tracers that have shown efficacy as PET ligands, labeled with ^{11}C or ^{18}F, are unsuitable when a SPECT radioisotope, such as ^{123}I, is incorporated instead (Lee et al., 2007).

BuChE imaging has been a more limited focus of study. In addition to the non-specific cholinesterase inhibitor imaging agents, such as tacrine, that have been evaluated, as described above, specific BuChE imaging agents are under development. *N*-methyl piperidyl derivatives, similar to those developed for AChE, have been the only imaging agents developed specifically for BuChE (Kikuchi, 2001; Snyder et al., 2001; Kikuchi et al., 2004). The lead BuChE imaging agent from these studies, 1-^{11}C-Methyl-4-piperidinyl n-butyrate ([^{11}C]-MP4B, Figure 1.4), demonstrated an acceptable safety profile (Virta et al., 2008). Human brain imaging with [^{11}C]-MP4B demonstrated partial recapitulation of known BuChE activity; however, areas such as the AChE-rich striatum demonstrated unexpectedly high uptake of radioactivity (Roivainen et al., 2004). Furthermore, [^{11}C]-MP4B imaging of AD patients demonstrated a decrease in brain binding when compared to cognitively normal controls (Kuhl et al., 2006). This result is in contrast to the known BuChE activity in the AD brain. Interestingly, this decrease in [^{11}C]-MP4B binding was similar to the decrease observed with the AChE agent, [^{11}C]-PMP, in the same AD patients. Thus, these *in vivo* human studies suggest that [^{11}C]-MP4B is unable to accurately visualize BuChE activity in the living brain.

1.9 Relevance and Chapter Overviews

This Chapter described characteristics of AD and MS, from clinical symptoms to molecular pathogenesis. In addition, neuroimaging methods for diagnosis were described however, as argued, significant drawbacks exist for these current approaches. The cholinergic system was described, in particular the distribution, function and structure of AChE and BuChE. Evidence for the association of these enzymes with the hallmark pathology of AD and MS was presented. Furthermore, the potential for targeting cholinesterases as a definitive diagnostic target was discussed. Current AChE and BuChE imaging agents have failed to visualize these enzymes associated with AD and MS pathology. AChE and, in particular, BuChE imaging agents have the potential to provide definitive diagnosis of AD and MS as well as treatment monitoring of these diseases.

Chapter 2 describes the synthesis and evaluation of a class of ester compounds, modeled after the structure of acetylcholine, as BuChE imaging agents. Chapter 3 details the synthesis and application of thioester compounds as a strategy towards the evaluation and optimization of cholinesterase imaging agents. Chapter 4 describes the synthesis and evaluation of a carbamate compound as a cholinesterase imaging agent. The capability of this compound for the definitive diagnosis of AD is presented. Chapter 5 chronicles a kinetic approach to mapping the cholinesterase active site, in particular that of BuChE. Identification of critical enzyme amino acid residues that mediate ligand binding is presented. This approach will be beneficial for the continued development and optimization of cholinesterase imaging agents. Chapter 6 describes the relationship between glucose metabolism, assessed with neuroimaging, and pathology in an AD

mouse model. Similar neuroimaging studies in this model will be critical for providing robust preclinical evaluation of developed imaging agents for their ability to visualize cholinesterase activity associated with disease pathological structures. Finally, Chapter 7 provides general discussions and conclusions based on the complete works presented in this thesis.

CHAPTER 2 ESTER DERIVATIVES AS IMAGING AGENTS

2.1 PREFACE

As an initial venture into the development of cholinesterase imaging agents, several molecules, based on the structure of acetylcholine, were investigated. In this Chapter, the synthesis, enzyme kinetics, radiolabelling and evaluation of these molecules as specific-butyrylcholinesterase imaging agents are detailed. The content of this Chapter describes work done as part of this thesis that has been published as Macdonald *et al.*, Mol Imaging Biol, 2011, 13(6):1250-61.

2.2 INTRODUCTION

Currently, a definitive diagnosis of Alzheimer's disease (AD) requires the detection of dementia and demonstration of characteristic AD pathology, amyloid plaques and neurofibrillary tangles, at autopsy (Hyman and Trojanowski, 1997; Blennow et al., 2006). Accurate diagnosis of AD in patients during life is imperative to initiate early treatment and to monitor treatment effects.

In AD brains, there is widespread cell loss and, in particular, loss of cholinergic neurons (Davies and Maloney, 1976), leading to a decrease in the enzyme choline acetyltransferase and its product, the neurotransmitter, acetylcholine. This loss is responsible, in part, for the characteristic cholinergic dysfunction in AD (Bartus et al., 1982; Coyle et al., 1983). An enzyme regulating acetylcholine, acetylcholinesterase (AChE, EC 3.1.1.7), also shows significant loss in AD brains (Perry et al., 1978). However, activity of the related enzyme, butyrylcholinesterase (BuChE, EC 3.1.1.8), also

able to catalyze acetylcholine hydrolysis, has been observed to increase in AD (Perry et al., 1978).

In the healthy brain, AChE is found in neurons and neuropil (Mesulam and Geula, 1991) while BuChE is found in white matter, glia and specific populations of neurons (Friede, 1967; Darvesh et al., 1998; Darvesh and Hopkins, 2003; Darvesh et al., 2003a). In AD brain tissue, AChE and BuChE are also associated with amyloid plaques, predominantly located in the cerebral cortex (Friede, 1965; Geula and Mesulam, 1989; Mesulam and Geula, 1994; Geula and Mesulam, 1995; Guillozet et al., 1997; Darvesh et al., 2010a). This association should allow molecular imaging of AD pathology during life using cholinesterase-specific radiolabelled compounds. However, in normal and AD cerebral cortex, the distribution of BuChE (Figure 2.1a and d), AChE (Figure 2.1b and e) and β-amyloid (Figure 2.1c and f) indicates that compounds specific for BuChE, rather than AChE, would be more suitable for imaging AD pathology. BuChE and β-amyloid levels are both low in normal cerebral cortex (Figure 2.1a and c) and high in AD cerebral cortex (Figure 2.1d and f). However, AChE levels are comparably high in both normal (Figure 2.1b) and AD (Figure 2.1e) cerebral cortex and would make it difficult to distinguish normal from AD with AChE neuroimaging. BuChE activity associated with AD pathology, in areas of the brain where this enzyme is not normally prominent, suggests that visualizing BuChE activity by neuroimaging could be valuable in detection of AD pathology in the living brain. This could facilitate early diagnosis of AD during life.

Synthesis and evaluation of BuChE-specific radiolabelled imaging agents, derived from *N*-methylpyrrolidinol and *N*-methylpiperidinol have been previously reported

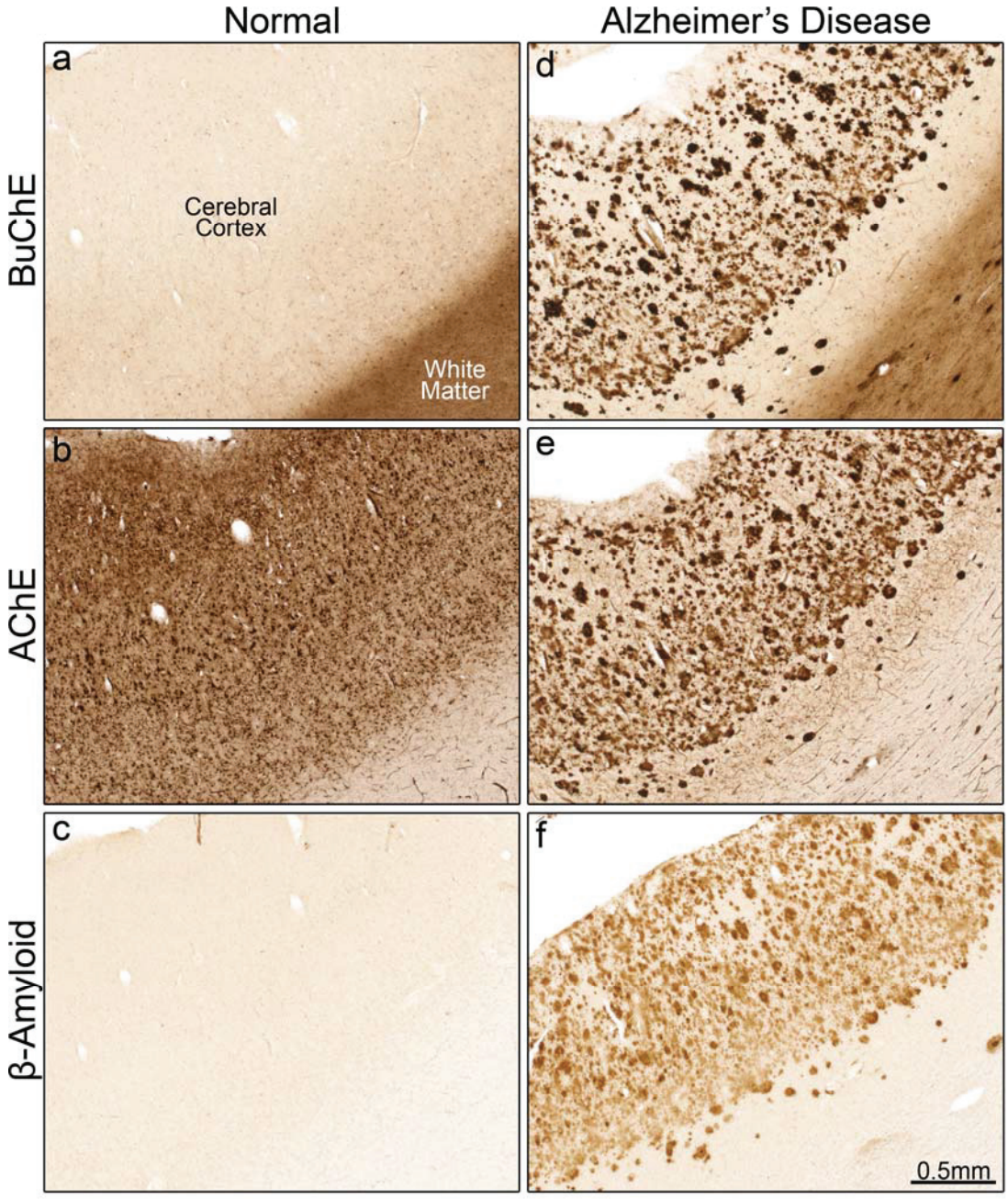

Figure 2.1. Photomicrographs of butyrylcholinesterase (BuChE), acetylcholinesterase (AChE) and β-amyloid staining in normal (a, b, c) and Alzheimer's disease (AD) (d, e, f) cerebral cortex. Note similar plaque staining with BuChE (d), AChE (e) and β-amyloid (f) in AD. These structures are absent in normal brain (a, b, c). In normal brain there is a low level of BuChE (a) in the cortex and no β-amyloid plaques (c) while there is relatively intense AChE staining (b). These differences make BuChE a suitable target over AChE for imaging AD pathology. BuChE and AChE histochemistry was done as described previously (Darvesh et al., 2010a). β-amyloid was stained using a standard immunohistochemical technique.

(Kikuchi, 2001; Snyder et al., 2001; Kikuchi et al., 2004). One such molecule, predicted to be BuChE-specific, 1-^{11}C-methyl-4-piperidinyl n-butyrate (^{11}C-MP4B), was developed for PET imaging. Biodistribution studies with ^{11}C-MP4B, performed in the human brain (Roivainen et al., 2004) and other organs (Virta et al., 2008), indicated high initial brain uptake but with a rapid clearance over 30 minutes (Roivainen et al., 2004). Most significant, labelling did not correlate (Kuhl et al., 2006) with the known histochemical localization of BuChE in normal (Friede, 1967; Darvesh et al., 1998; Darvesh and Hopkins, 2003; Darvesh et al., 2003a) or in AD brains (Friede, 1965; Geula and Mesulam, 1989; Mesulam and Geula, 1994; Geula and Mesulam, 1995; Guillozet et al., 1997; Darvesh et al., 2010a). A possible reason for this lack of correlation is that in ^{11}C-MP4B, the radioisotope is located on the part of the substrate that is the initial leaving group in the mechanism of BuChE catalysis.

In an effort to prevent early loss of radiolabel from the BuChE-substrate complex, we incorporated a radioactive marker on the acyl moiety of the ester, the last component of the substrate to dissociate from the enzyme following hydrolysis. To develop BuChE-specific imaging agents that would have the potential to remain bound longer, 4-iodobenzoate derivatives of *N*-methylpyrrolidinol and *N*-methylpiperidinol were prepared and evaluated. The rationale for synthesizing these compounds was that the size of the iodobenzoate moiety should render such esters more susceptible to hydrolysis by BuChE over AChE. Also, the iodo group on the acyl portion of the molecule should be amendable to subsequent exchange with ^{123}I. Lastly, previous studies have shown that chemical structures that contain *N*-methylpyrrolidinol or *N*-methylpiperidinol moiety readily enter the brain (Kikuchi et al., 2004; Roivainen et al., 2004; Kuhl et al., 2006).

To evaluate whether these radiolabelled compounds could be used for imaging BuChE activity in the brain, a normal rat model system was used in the present study to examine whole body biodistribution while brain autoradiograms were used to compare radiolabel distribution to the known histochemical distribution of BuChE in the rat brain (Darvesh et al., 1992; Tago et al., 1992).

2.3 Materials and Methods

2.3.1 Materials

Butyl lithium, 1-methylpiperidin-4-ol, (S)-1-methylpyrrolidin-3-ol, (R)-1-methylpyrrolidin-3-ol, 4-iodobenzoyl chloride, hexabutylditin, tetrakis(triphenylphosphine)palladium and purified recombinant human acetylcholinesterase (AChE) were obtained from Sigma-Aldrich. Purified human plasma butyrylcholinesterase (BuChE) was a gift from Dr. Oksana Lockridge. $Na^{123}I$ was obtained from MDS Nordion in 0.1 N NaOH. Synthetic reactions were performed under an argon atmosphere (99.999% purity, Air Liquide). Male wistar rats were purchased from Charles River Laboratories (Canada) and aged until 3-6 months old.

2.3.2 Chemical Analysis of Synthetic Compounds

Melting points (MP) were determined using a Fisher-Johns Melting Point Apparatus. Infrared spectra were recorded as Nujol mulls or as neat liquids between sodium chloride plates on a Nicolet Avatar 330 fourier transform-infrared spectroscopy (FT-IR) spectrometer. Peak positions were reproducible within 1-2 cm^{-1}. Nuclear magnetic resonance (NMR) spectra were recorded at the Nuclear Magnetic Resonance

Research Resource (NMR-3), Dalhousie University, on a Bruker AVANCE 500, operating at 500.1 MHz for ^{1}H and 125.8 MHz for ^{13}C. Chemical shifts are reported in ppm relative to Me_4Si in $CDCl_3$ or dimethyl sulfoxide (DMSO). For Proton NMR experiments, the coupling constants are reported in Hz and the multiplicities are apparent. For Carbon NMR data, the number of attached protons for each signal, as determined by a Distortionless Enhancement by Polarization Transfer (DEPT) experiment, are given in parentheses. Low resolution mass spectra were obtained using an Agilent 6890 N GC with an Agilent 6890 N Electron Impact Mass Spectrometer (Waldbronn, Germany) operating at 70 eV. High resolution mass spectra were obtained with accurate mass positive-ion electrospray ionization measurements recorded at the Mass Spectrometry Laboratory at Dalhousie University using a Bruker Daltonics microTOF with a flow rate of 2 μL/min, spray voltage of 4500 V and tray temperature of 180 ºC or were recorded on a CEC 21-110B spectrometer using electron ionization at 70 volts and an appropriate source temperature with samples being introduced by means of a heatable port probe. Mass measurements were within 3 ppm of the calculated value. Purity of all compounds was determined using an Agilent Technologies 1200 series high-performance liquid chromatography (HPLC) system with a reverse phase 18C column and methanol as the mobile phase.

2.3.3 Synthesis of Non-Radioactive Piperidinol and Pyrrolidinol Iodobenzoate Derivatives

The non-radioactive 4-iodobenzoate esters of *N*-methylpiperidinol (**1**) and (S) and (R) *N*-methylpyrrolidinol (**2** and **3**, respectively) were synthesized according to the reaction scheme depicted in Figure 2.2a.

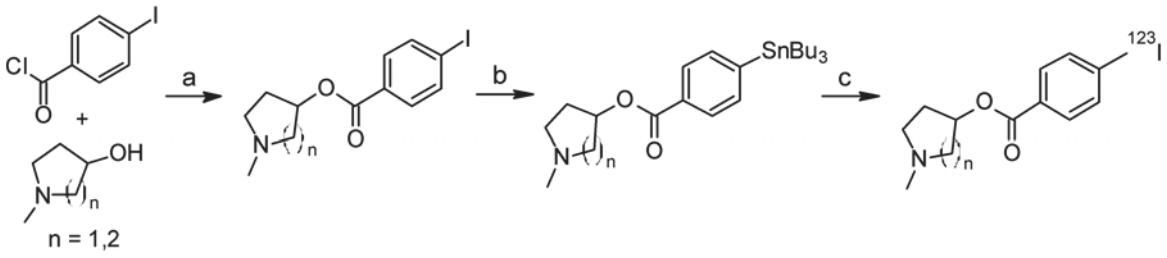

Figure 2.2. Synthetic reaction scheme for the non-radioactive esters, tributyltin intermediates and ^{123}I labelled esters, respectively. For the *N*-methylpyrrolidinols (n = 1), compounds were enantiomerically pure. (a) BuLi, THF. (b) Sn_2Bu_6, $Pd(PPh_3)_4$, THF. (c) $Na^{123}I$, NCS, MeOH.

For synthesis of 1-methylpiperidin-4-yl 4-iodobenzoate (**1**), under an argon atmosphere, 1-methylpiperidin-4-ol (0.3837 g, 3.331 mmol) was dissolved in tetrahydrofuran (THF) (20 mL). To this solution was added butyl lithium (BuLi) (2.10 mL, 3.36 mmol) at -78 ºC followed by a solution of 4-iodobenzoyl chloride (0.8002 g, 3.003 mmol) in THF (10 mL) and the mixture was stirred at room temperature for 16 hours. The reaction was quenched with water (20 mL) and extracted with ethyl acetate (3 × 20 mL). The combined organic layers were washed with brine (2 × 20 mL) and dried over Na_2SO_4. The solvent was removed *in vacuo* to produce a white solid. The product was purified by silica gel chromatography (30:70 MeOH/CH_2Cl_2) to give a white powder (0.5561 g, 54%). Analytical data: MP: 128-130 ºC (Lit MP = 130 ºC (Singh et al., 1997)). IR (Nujol): 1711, 1585, 1283, 1268, 1118, 754 cm^{-1}. ^{1}H-NMR ($CDCl_3$): δ 1.84-1.91 (m, 2H), 2.01-2.08 (m, 2H), 2.31-2.39 (m, 5H), 2.67-2.73 (m, 2H), 5.02-5.08 (m, 1H), 7.75 (d, *J*=8.5 Hz, 2H), 7.81 (d, *J*=8.5 Hz, 2H). ^{13}C-NMR ($CDCl_3$): δ 31, 46, 53, 70, 100, 130, 131, 138, 166. EI-MS m/z: 55, 70, 82, 97, 114, 203, 231, 345 (M^+). HRMS (EI): M^+ found 345.0233, calcd for $C_{13}H_{16}NO_2I$ =345.0226.

For synthesis of (S)-1-methylpyrrolidin-3-yl 4-iodobenzoate (**2**), under an argon atmosphere, (S)-1-methylpyrrolidin-3-ol (0.257 mL, 2.52 mmol) was dissolved in THF (10 mL). To this solution was added BuLi (1.60 mL, 2.56 mmol) at -78 ºC followed by a solution of 4-iodobenzoyl chloride (0.5870 g, 2.203 mmol) in THF (10 mL). The solution was refluxed for 3 hours and the reaction was quenched with water (15 mL). The aqueous layer was extracted with ethyl acetate (2 × 10 mL), washed with brine (2 × 15 mL) and dried over $MgSO_4$. The solvent was removed *in vacuo* and the product was recrystallized from hexanes to yield yellow crystals (0.3053 g, 41%). Analytical data:

$MP_{(hexanes)}$: 69-70 ºC. IR (Nujol) 1723, 1586, 1268, 1235, 1115, 754 cm^{-1}. ^{1}H-NMR ($CDCl_3$): δ 1.99-2.03 (m, 1H), 2.37-2.42 (m, 5H), 2.77-2.81 (m, 1H), 2.83 (d, *J*=2.6 Hz, 1H), 2.85-2.88 (m, 1H), 5.40-5.43 (m, 1H), 7.75 (dt, *J*=2.0, 8.7 Hz, 2H), 7.79 (dt, *J*=2.0, 8.7, 2H). ^{13}C-NMR ($CDCl_3$): δ 33 (3), 42 (1), 55 (1), 62 (2), 76 (2), 101 (0), 130 (0), 131 (1), 138 (1), 166 (0). EI-MS m/z: 42, 58, 74, 83, 104, 203, 231 (M^+ - 101, C_7H_4IO). HRMS (ESI): M^+H^+ found 332.0142; calcd for $C_{12}H_{14}NO_2I$ = 332.0147.

For synthesis of (R)-1-methylpyrrolidin-3-yl 4-iodobenzoate (**3**), under an argon atmosphere, (R)-1-methylpyrrolidin-3-ol (0.260 mL, 2.37 mmol) was dissolved in THF (10 mL). To this solution was added BuLi (1.60 mL, 2.56 mmol) at -78 ºC followed by a solution of 4-iodobenzoyl chloride (0.5932 g, 2.226 mmol) in THF (10 mL). The solution was refluxed for 3 hours and the reaction was quenched with water (15 mL). The aqueous layer was extracted with ethyl acetate (2 × 10 mL), washed with brine (2 × 15 mL) and dried over $MgSO_4$. The solvent was removed *in vacuo* and the product was recrystallized from hexanes to yield light yellow crystals (0.3696 g, 51%). Analytical data: $MP_{(hexanes)}$: 69-70 ºC. IR (Nujol): 1724, 1586, 1268, 1235, 1115, 754 cm^{-1}. ^{1}H-NMR ($CDCl_3$): δ 2.00-2.03 (m, 1H), 2.37-2.42 (m, 5H), 2.77-2.81 (m, 1H), 2.83 (d, *J*=2.6 Hz, 1H), 2.84-2.88 (m, 1H), 5.31-5.43 (m, 1H), 7.76 (dt, *J*=1.9, 8.5 Hz, 2H), 7.80 (dt, *J*=1.7, 8.6 Hz, 2H). ^{13}C-NMR ($CDCl_3$): δ 33 (2), 42 (3), 55 (2), 62 (2), 76 (1), 101 (0), 130 (0), 131 (1), 138 (1), 166 (0). EI-MS m/z: 42, 58, 74, 83, 104, 203, 231 (M^+ - 101, C_7H_4IO). HRMS (ESI): M^+H^+ found 332.0142; calcd for $C_{12}H_{14}NO_2I$ = 332.0147.

2.3.4 Synthesis of Tributyltin Intermediates

The synthesis of tributyltin intermediates was carried out as depicted in Figure 2.2b.

For synthesis of 1-methylpiperidin-4-yl 4-(tributylstannyl)benzoate intermediate, under argon atmosphere, 1-methylpiperidin-4-yl 4-iodobenzoate (**1**) (0.1660 g, 0.4810 mmol) was dissolved in degassed toluene (40 mL). Hexabutylditin (0.60 mL, 1.198 mmol) was added, followed by a solution containing tetrakis(triphenylphosphine)palladium (0.0303 g, 0.0262 mmol), also dissolved in degassed toluene (15 mL). The resulting solution was refluxed for 20 hours and the solvent removed *in vacuo*. The product was purified by silica gel column chromatography (15:1 toluene/triethylamine) to yield a viscous yellow liquid (0.1795 g, 71%). Analytical data: IR (Neat): 1717, 1590, 1275, 1104, 752 cm^{-1}. ^{1}H-NMR ($CDCl_3$): δ 0.88 (t, *J*=7.3 Hz, 9H), 1.08 (p, *J*=6.3 Hz, 6H), 1.36 (sext, *J*=7.4 Hz, 6H), 1.57 (p, *J*=7.6 Hz, 6H), 1.89-1.94 (m, 2H), 2.03-2.08 (m, 2H), 2.36 (s, 3H), 2.37-2.39 (m, 2H), 2.69-2.72 (m, 2H), 5.09-5.10 (m, 1H), 7.59 (d, *J*=8.1 Hz, 2H), 8.00 (d, *J*=8.1 Hz, 2H). ^{13}C-NMR ($CDCl_3$): δ 10 (2), 13 (3), 27 (2), 29 (2), 31 (2), 46 (3), 53 (2), 70 (1), 128 (1), 130 (0), 136 (1), 149 (0), 166 (0). EI-MS m/z: 41, 55, 82, 96, 170, 198, 241, 340, 396, 452 (M^+ - 57, $C_{21}H_{34}NO_2Sn$). HRMS (ESI): M^+H^+ found 510.2389; calcd for $C_{25}H_{44}NO_2Sn$ = 510.2394.

For synthesis of (S)-1-methylpyrrolidin-3-yl 4-(tributylstannyl) benzoate intermediate, under argon atmosphere, (S)-1-methylpyrrolidin-3-yl 4-iodobenzoate (**2**) (0.1001 g, 0.3022 mmol) was dissolved in degassed toluene (30 mL) and hexabutylditin (0.355 mL, 0.709 mmol) was added. Tetrakis(triphenylphosphine)palladium (0.0107 g,

0.0092 mmol) also dissolved in toluene (15 mL) was added. The resulting solution was refluxed for 20 hours and the solvent removed *in vacuo*. The resulting crude product was purified by silica gel column chromatography (11:8:1, hexanes/ethyl acetate/triethylamine) to yield a viscous yellow liquid (0.1157 g, 78%). Analytical data: IR (Neat): 1717, 1591, 1275, 1105, 752 cm^{-1}. ^{1}H-NMR (DMSO): δ 0.85 (t, *J*=7.5 Hz, 9H), 1.08 (p, *J*=7.6, 8.2 Hz, 6H), 1.28 (sext, *J*=7.4 Hz, 6H), 1.51 (p, *J*=7.3 Hz, 6H), 1.83-1.86 (m, 1H), 2.26 (s, 3H), 2.28-2.31 (m, 2H), 2.63-2.66 (m, 1H), 2.69-2.72 (m, 2H), 5.25-5.27 (m, 1H), 7.56 (d, *J*=7.9 Hz, 2H), 7.82 (d, *J*=7.9 Hz, 2H). ^{13}C-NMR (DMSO): δ 9 (2), 13 (3), 27 (2), 28 (2), 32 (2), 42 (3), 54 (2), 62 (2), 75 (1), 128 (1), 129 (0), 136 (1), 149 (0), 166 (0). EI-MS m/z: 42, 58, 83, 105, 196, 241, 326, 382, 438 (M^+ - 57, $C_{20}H_{32}NO_2Sn$). HRMS (ESI): M^+H^+ found 496.2232; calcd for $C_{24}H_{42}NO_2Sn$ = 496.2238.

For synthesis of (R)-1-methylpyrrolidin-3-yl 4-(tributylstannyl) benzoate intermediate, under argon atmosphere, (R)-1-methylpyrrolidin-3-yl 4-iodobenzoate (**3**) (0.1010 g, 0.3050 mmol) was dissolved in degassed toluene (30 mL) and hexabutylditin (0.355 mL, 0.709 mmol) was added. Tetrakis(triphenylphosphine)palladium (0.0105 g, 0.0091 mmol) dissolved in toluene (15 mL) was added. The resulting solution was refluxed for 20 hours and the solvent removed *in vacuo*. The resulting crude product was purified by silica gel column chromatography (11:8:1, hexanes/ethyl acetate/triethylamine) to yield a viscous yellow liquid (0.1150 g, 78%). Analytical data: IR (Neat): 1717, 1591, 1275, 1104, 752 cm^{-1}. ^{1}H-NMR ($CDCl_3$): δ 0.94 (t, *J*=7.4 Hz, 9H), 1.13 (p, *J*=7.9, 8.2 Hz, 6H), 1.37 (sext, *J*=7.3 Hz, 6H), 1.57, (p, *J*=7.9, 8.2 Hz, 6H), 2.08-2.13 (m, 1H), 2.43-2.47 (m, 2H), 2.52 (s, 3H), 2.90-2.93 (m, 2H), 5.45-5.48 (m,

1H), 7.54 (d, *J*=8 Hz, 2H), 7.96 (d, *J*=8 Hz, 2H). ^{13}C-NMR ($CDCl_3$): δ 10 (2), 14 (3), 28 (2), 29 (2), 31 (2), 43 (3), 56 (2), 63 (2), 75 (1), 129 (1), 133 (0), 137 (1), 150 (0), 167 (0). EI-MS m/z: 42, 58, 83, 105, 196, 241, 326, 382, 438 (M^+ - 57, $C_{20}H_{32}NO_2Sn$). HRMS (ESI): M^+H^+ found 496.2232; calcd for $C_{24}H_{42}NO_2Sn$ = 496.2238.

2.3.5 *In Vitro* Evaluation of Nonradioactive Iodobenzoates as Cholinesterase Ligands

The specificity, affinity and rate of hydrolysis of each synthetic compound was determined spectrophotometrically, making use of differences in the aryl chromophores of substrates and products. Briefly, 15 µL of AChE (9 units) or BuChE (9 units) dissolved in 0.1% $gelatin_{(aq)}$, containing 0.01% sodium azide, and 1.44 mL of 0.1 M phosphate buffer (pH 8.0) were placed in a quartz cuvette of 1 cm path length. The reaction was commenced with the addition of 50 µL of 5 mM substrate (**1**, **2** or **3**) in 50% $acetonitrile_{(aq)}$. The absorbance was scanned from 200-300 nm every 2 min for a total of 30 min using a Ultrospec 2100 pro UV/Visible Spectrophotometer (Biochrom) with Swift II software (Amersham). The wavelength corresponding to the maximum absorbance change for each compound during hydrolysis was used for the subsequent determination of affinity constant (K_m) and maximum velocity (V_{max}), using Lineweaver-Burk double reciprocal plots. This was accomplished by measuring the change in absorbance per min (ΔA/min), using a fixed amount of enzyme (2.7 units) and varying amounts of compounds **1**-**3** (1.67×10^{-5}-1.67×10^{-4} M), using a Spectronic 1001 (Milton Roy). The plot of 1/v against 1/s gave K_m as the negative reciprocal of the intercept on the 1/s-axis and V_{max} as the reciprocal of the 1/v-axis intercept. As defined previously, 0.1 unit is the amount of cholinesterase that gives a ΔA/min of 1.0 in the presence of 1.6×10^{-4} M

substrate (acetylthiocholine for AChE, butyrylthiocholine for BuChE) (Darvesh et al., 2001).

2.3.6 Computation of Preferred Conformations and Log P values

Computational chemistry studies, to determine the most stable geometries of compounds **1-3**, were carried out at the molecular mechanics level of theory using the Merck Molecular Force Field (MMFF), employing Spartan '06 (Wavefunction, 2006). Log P values were calculated to assess the ability of the compound to cross the blood–brain barrier by diffusion. The values were obtained using ALOGPS v 2.0 system method that compares the structure of the molecule with a large database of known molecular partition coefficients (Tetko et al., 2001).

2.3.7 Radiosynthesis and Purification of ^{123}I labelled Iodobenzoates

Substrates labelled with ^{123}I were prepared from tributyltin intermediates according to the general scheme shown in Figure 2.2c. To a solution (8 μL) of $Na^{123}I$ (68.45 MBq) in 0.1 M $NaOH_{(aq)}$ (8.0×10^{-4} mol) was added NaI (3 μL, 5.5×10^{-9} mol) and 0.1 M HCl (16 μL, 1.6×10^{-3} mol) to neutralize the hydroxide. The tributyltin intermediate (50 μL, 4.0×10^{-7} mol) was added to this solution, followed by *N*-chlorosuccinimide (NCS, 28 μL, 8.4×10^{-8} mol), both of which were dissolved in methanol. The reaction proceeded for 15 min at room temperature; then 0.1 M $NaHCO_3$ (24 μL, 2.4×10^{-3} mol) was added to quench the reaction. Purification was accomplished by HPLC, using a Waters system with a ZORBAX Eclipse XDB-C18, 4.6 x 250 mm, 5μm column (Agilent Technologies) and 2.0 mL/min of 80% $methanol_{(aq)}$ eluent.

Fractions were collected every 20 sec for 20 min with a RediFrac fraction collector (Amershan Biosciences). Retention times were determined using the corresponding cold iodobenzoate as a non-radioactive standard. Collected fractions that contained purified product were combined and the solvent removed under a stream of N_2 gas. The product was redissolved either with methanol, to assess the radiochemical yield and purity, or in 20% ethanol$_{(aq)}$, for animal administration.

2.3.8 Animal Studies

Animals were cared for according to the guidelines set by the Canadian Council on Animal Care. Formal approval to conduct the experiments was obtained from the Dalhousie University Committee on Laboratory Animals.

2.3.9 Biodistribution Studies of Radiolabelled Iodobenzoates

Whole body dynamic scintigraphic imaging of male wistar rats (~500 g) were obtained. The animals were anaesthetized using a constant stream of isoflurane gas and the tail vein was cannulated. The animals were positioned on the head of a gamma camera (Millennium MG; GE Healthcare) equipped with a low-energy high-resolution parallel-hole collimator. Immediately following injection of the radiolabelled compound (~37 MBq), counts were acquired by the gamma camera in dynamic frame mode (energy window centered on the 159 keV photopeak of ^{123}I; 128 × 128 pixels frame matrix; 180 × 5 s, and 45 × 60 s frames, for a total of 60 min). At the end of the 1 hour imaging period, the animals were sacrificed with sodium pentobarbital. Regions of interest (ROI) representing the head (ROI_1), heart (ROI_2) and bladder (ROI_3) were manually defined on

the whole body image using the gamma camera's workstation image edit tools (Xeleris version 2.1220; GE Healthcare). Background- and radioactive decay-corrected ROI time activity curves were calculated and plotted, using the same tools, showing the percentage fraction of the injected dose as a function of time in the organ. The whole-body counting rate from minute 1 to minute 5 was used to estimate the total injected activity.

2.3.10 Brain Autoradiography

Animals were prepared as described for the biodistribution studies, except that the body temperature was maintained on a circulating water heating pad at set at 40 ºC for the duration of the experiment. The radiolabelled ligand was administered (~37 MBq) and after 30 min the animals were sacrificed by an injection of sodium pentobarbital (0.3 mL). The animals were immediately perfused transcardially with 200 mL of isotonic saline followed by 500 mL of 4% paraformaldehyde in 0.1 M phosphate buffer, pH 7.4. The brains were quickly removed and immediately frozen using dry ice. The brains were sectioned in 100 µm thick coronal slices on a SM2000R Leica microtome with a freezing stage and BFS-30TC controller (Physitemp) and immediately mounted on glass slides. The slides were then placed under a phosphor imaging screen (Molecular Dynamics). After 36 hr, the screen was visualized using a Typhoon 9410 Phosphorimager (GE Healthcare) to produce the autoradiogram. A color gradient was placed on autoradiograms in Adobe Photoshop 7 to highlight areas with radioactivity. Three animals underwent this procedure for each of the three radiolabelled compounds.

2.3.11 Butyrylcholinesterase Histochemistry

A modified Karnovsky-Roots method was used for examination of butyrylcholinesterase activity in brain sections, as described previously (Darvesh et al., 2010a). Briefly, 40 μm brain sections were rinsed in 0.1 M maleate buffer (pH 7.4) for 30 min and reacted for 3 hr at 37 ºC in an incubation medium containing 0.5 mM sodium citrate, 0.47 mM cupric sulfate, 0.05 mM potassium ferricyanide, 0.8 mM butyrylthiocholine iodide and 0.01 mM 1,5-bis (4-allyl dimethylammonium phenyl) pentan-3-one dibromide (BW 284 C 51) in 0.1 M maleate buffer (pH 8.0) for BuChE staining. Sections were rinsed with gentle agitation for 30 min in distilled water and placed in 0.1% cobalt II chloride in water for 10 min. After a further rinse in distilled water, sections were placed in a solution of 1.39 mM 3,3'-diaminobenzidine tetrahydrochloride (DAB) in 0.1M phosphate buffer (pH 7.4). After 5 min, a solution of 0.3% hydrogen peroxide in distilled water was added at a ratio of 20:1 (DAB solution : hydrogen peroxide solution) and the reaction was carried out for approximately 4 min. Sections were then washed in 0.1 M acetate buffer, pH 3.3, mounted on slides, coverslipped and examined with brightfield microscopy.

Sections were photographed on a Zeiss Axioplan 2 motorized microscope with a Zeiss Axiocam HRc digital camera and AxioVision 4.6 software. Image levels were adjusted in Adobe Photoshop 7 so the background from different images matched.

2.4 Results

Three non-radiolabelled iodobenzoate esters were synthesized and tested *in vitro* for their ability to bind to, and be hydrolyzed by, BuChE and AChE. Lack of AChE

hydrolysis for each compound confirmed specificity for BuChE. All three BuChE-specific substrates studied were then radiolabelled and evaluated *in vivo* and *ex vivo* using whole body dynamic scintigraphic imaging and brain autoradiography, respectively.

2.4.1 Synthesis of Non-Radioactive Iodobenzoate Derivatives

1-methylpiperidin-4-yl 4-iodobenzoate (**1**), (S)-1-methylpyrrolidin-3-yl 4-iodobenzoate (**2**) and (R)-1-methylpyrrolidin-3-yl 4-iodobenzoate (**3**) (Table 2.1), were synthesized (Figure 2.2a) in moderate (41-54%) yields and were found to be ≥97% pure by HPLC analysis. Chemical analysis of each was consistent with its structure. All three derivatives synthesized had similar calculated log P values (Table 2.1), comparable to compounds known to cross blood-brain barrier (Darvesh et al., 2003b).

2.4.2 *In Vitro* Evaluation of Non-radioactive Iodobenzoates as Cholinesterase Ligands

The three purified and characterized compounds (**1**-**3**) were evaluated *in vitro* as substrates for human AChE and BuChE, making use of the natural chromophores of the aromatic moiety of each ester. Repetitive scan analyses detected changes in absorbance profile to indicate hydrolytic catalysis by the enzyme. Each compound was found to be hydrolyzed by BuChE but not AChE.

The affinity constant (K_m) and maximum velocity (V_{max}) for each compound (**1**-**3**) hydrolyzed by BuChE under the same condition were obtained from Lineweaver-Burk plots and are summarized in Table 2.1. The kinetic parameters (K_m and V_{max}) for compounds **1** and **2** are similar to one another but distinctly different from those obtained for the (R) *N*-methylpyrrolidinol derivative (**3**). A comparison of the most stable

Table 2.1. Enzyme kinetic and log P values for synthesized iodobenzoate esters **1-3**

Compound	Structure	BuChE K_m (µM)	V_{max} (µM min^{-1})	Log P
1	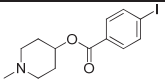	26 ± 2	8.4 ± 0.4	3.16
2	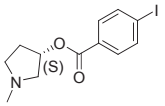	16 ± 4	6.1 ± 0.5	3.05
3	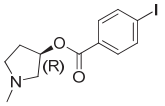	50 ± 2	33.2 ± 2.7	3.05

conformations of the three esters (Figure 2.3) indicated, as with the kinetic parameters, that the overall preferred conformations of **1** and **2** are similar to one another but distinct from the conformation of compound **3**. These differences in molecular geometries may be largely responsible for the differences in affinities and rates of hydrolysis of compounds **1** and **2** compared to **3**.

2.4.3 Synthesis of Tributyltin Intermediates

In order to incorporate ^{123}I into iodobenzoate esters, a stable intermediate had to be developed with a functionality readily replaced by ^{123}I. Thus, compounds **1**-**3** were converted to their corresponding tributyltin intermediates (Figure 2.2b) in high (73-78%) yields. These tributyltin intermediates were found to be stable over several months when stored without solvent, in the dark, at 4 ºC. However, the ester linkage underwent transesterification in methanol and hydrolysis in water, over several days, when diluted in either solvent. Therefore, fresh solutions of tributyltin intermediates were prepared for each radiolabel incorporation reaction described below.

2.4.4 Radiosynthesis and Purification of ^{123}I labelled Iodobenzoates

Incorporation of ^{123}I into the benzoate esters was achieved in a rapid, one step reaction (Figure 2.2c), under mild conditions (15 min, ambient temperature). Na^{123}I was obtained commercially in 0.1 N NaOH, in the minimal volume available. The presence of NaOH in the reaction mixture rapidly hydrolyzed the ester of the tributyltin intermediate and led to lower yields. To circumvent this, the NaOH was first neutralized with a slight excess of 0.1 M HCl. Slightly acidic conditions allowed the reaction to

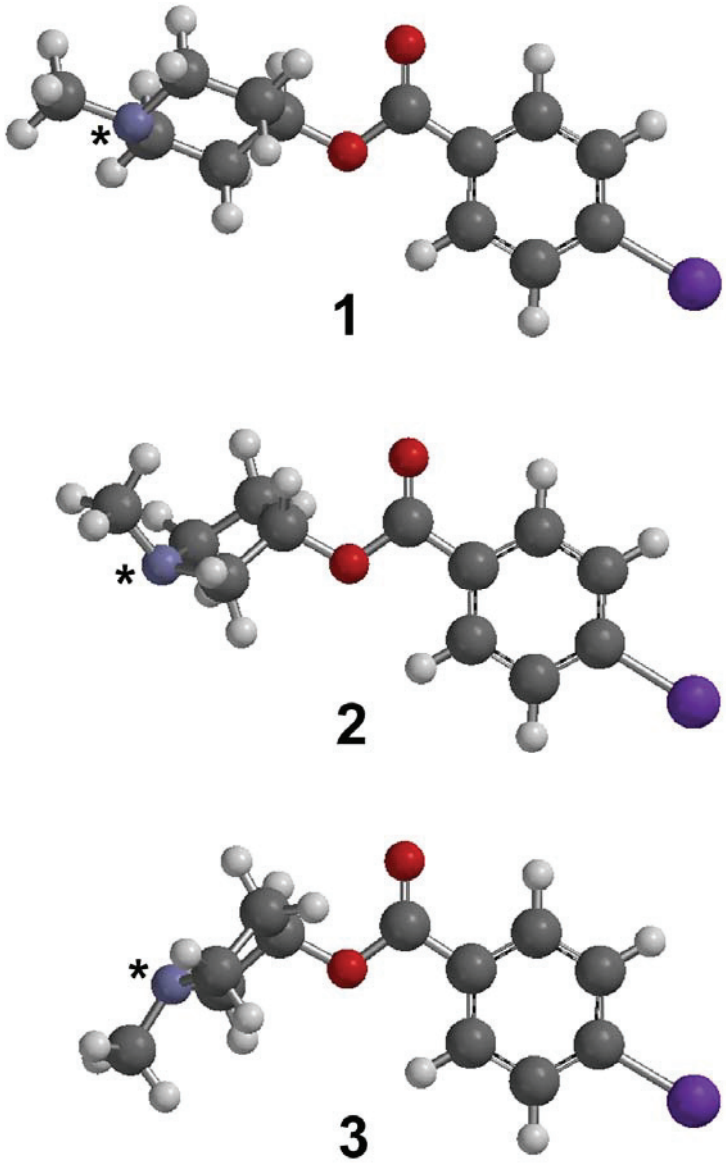

Figure 2.3. Preferred conformations of compounds **1-3.** Note similarity in geometry between compounds **1** and **2** with respect to the position of nitrogen (*) containing alcohol moiety.

proceed rapidly without ester hydrolysis. *N*-chlorosuccinimide (NCS) was used to form N-^{123}I-iodosuccinimide *in situ*. Since the amount of ^{123}I is limiting in the reaction, non-radioactive NaI was added to the radioactive Na^{123}I population in order to generate a greater amount of product. Purification of the radiolabelled ligand from the reaction mixture was achieved using HPLC with a reverse phase column and 80% methanol$_{(aq)}$ as eluent (Figure 2.4). Fractions were collected and those containing radiolabelled compound, as predetermined by elution profiles using non-radioactive esters (Figure 2.4), were combined and the solvent removed, using a stream of nitrogen gas and gentle heating. The product was redissolved into 20% ethanol$_{(aq)}$. Synthesis and purification of radiolabelled compounds was performed within one hour, with 63-92% radiochemical yield and 90-96% purity.

2.4.5 Biodistribution Studies

The dynamic biodistribution of radiolabelled ligands in the rat were monitored over one hour (Figure 2.5). Biodistribution was similar for the three agents. Regions of interest (ROI) were head (ROI$_1$), heart (ROI$_2$) and bladder (ROI$_3$). As can be seen in the plot in Figure 2.5, there was rapid clearance of radioactivity from the blood pool, as indicated by the heart ROI, via the kidneys, as indicated by the bladder ROI. There was also a rapid increase in the radioactivity in the head region (ROI$_1$) that remained relatively constant throughout the duration of scanning. Within ROI$_1$, a number of structures, including the brain and salivary glands, may accumulate the radioligands. Since the resolution of scanning did not define regional accumulation of radioactivity

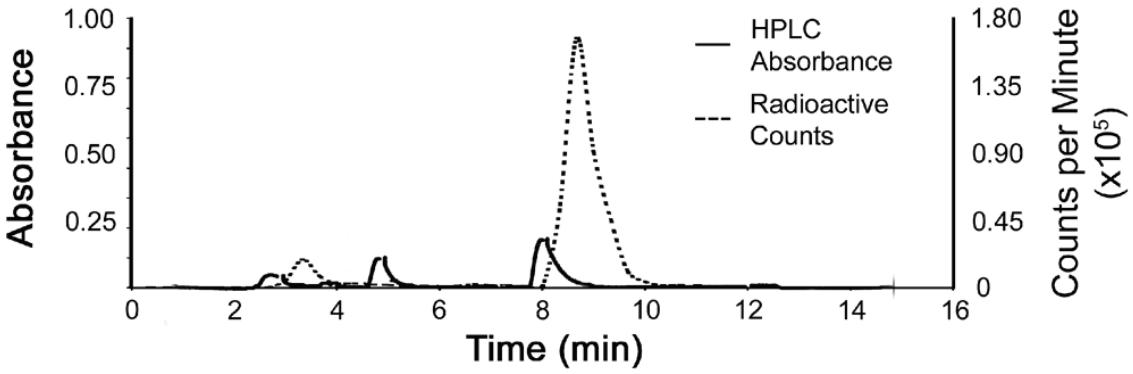

Figure 2.4. Absorbance traces and radioactive counts demonstrating the separation of radiolabelled compound **1** from the reaction mixture using HPLC. The desired radioactive product **1** has retention time between 8 and 10 min. The lag in the peaks of the retention times between the absorbance and radioactivity is a consequence of difference in the delivery system to the two different detectors.

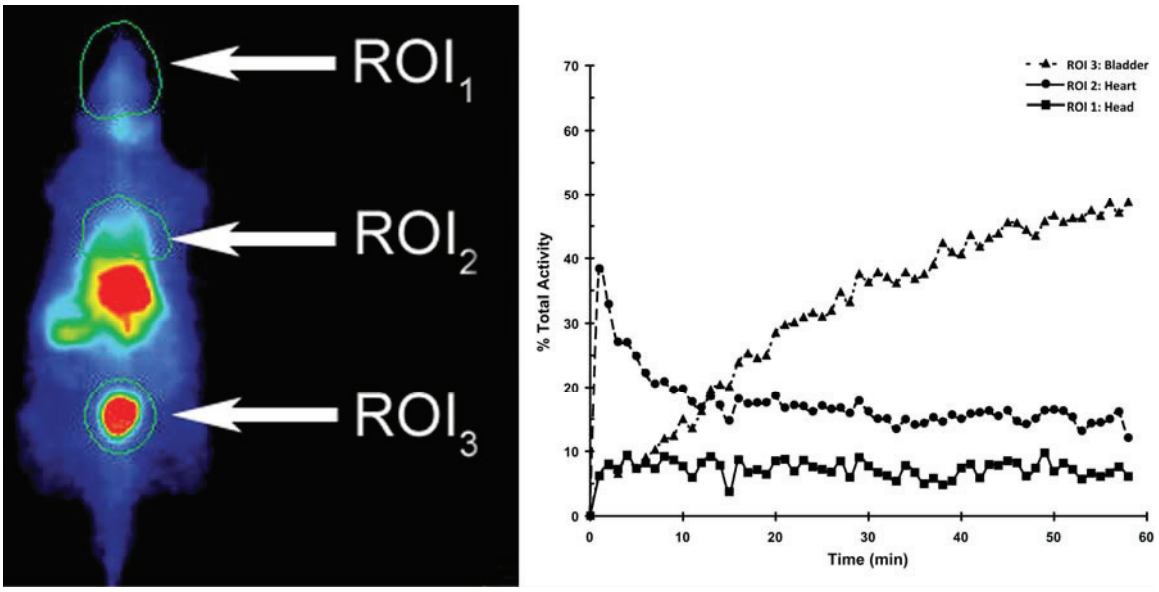

Figure 2.5. An example of the biodistribution of compound **1** in the rat. Composite images from 60 min of scanning indicates that compounds **1-3** accumulate (image on the left) in the head (ROI_1), heart (ROI_2) and bladder (ROI_3). Activity levels (Plots on the right) were measured in these regions for the duration of imaging.

within the brain itself, autoradiography was performed to provide details of brain distribution.

2.4.6 Comparison of Brain Autoradiography and Butyrylcholinesterase Histochemistry

Autoradiography of brain sections, after injecting any of the radiolabelled iodobenzoates into the normal rat model, revealed that each entered the brain and had a regional distribution, with areas of high and low accumulation, which corresponded to specific neuroanatomical structures (Table 2.2).

Experimental conditions required to produce brain autoradiograms led to the loss of BuChE enzymatic activity. As a result, the same tissue could not be used for direct comparative BuChE histochemical staining but could be stained with thionin, to visualize cell bodies, for correlation between accumulation of radioactivity and neuroanatomy. These were compared with similar sections from other rat brain tissues, stained for BuChE activity. Figures 2.6 and 2.7 provide representative levels for comparison of neuroanatomy, autoradiograms and BuChE distribution.

Throughout the central nervous system, most areas with low radioactivity corresponded to areas of known low BuChE activity (e.g., cerebral cortex and the caudate-putamen) (Figure 2.6). A number of areas with accumulation of radioactivity corresponded to areas with BuChE activity, as demonstrated by histochemical staining. These areas included certain thalamic nuclei (e.g., habenula) (Figure 2.6), pontine nuclei (e.g., laterodorsal, ventral and pontine tegmentum) (Figure 2.7), as well as certain nuclei in the medulla oblongata (e.g., hypoglossal and dorsal motor nucleus of the vagus) (Figure 2.7). However, there were also areas known to have BuChE activity by

Table 2.2. Distribution of BuChE and radioactivity accumulation in the rat brain

Area	BuChE activity	Radioactivity
Caudate putamen	-	-
Cerebral cortex	+	+
Hippocampus	+	++
Hypothalamus	+	++
Islands of Calleja	++++	-
Septal region	++	++
Thalamus		
Anterior nuclear group	++++	-
Anterior pretectal nucleus	+++	++
Geniculate nuclear group	+	-
Habenula	++	++
Lateral nuclear group	+++	-
Medial, midline, ventral and posterior nuclear groups	++	-
Zona incerta	++	++
Midbrain		
Inferior colliculus	+	+
Interpeduncular nucleus	+++	-
Occulomotor nucleus	-	++++
Periaqueductal gray	++	++
Red nucleus	++	++++
Superior colliculus	++	++
Pons		
Facial nucleus	++	++++
Lateral dorsal tegmental nucleus	+++	++
Locus coeruleus	++	++
Motor Trigeminal nucleus	-	++++
Pedunculopontine tegmental nucleus	+++	++
Pontine nuclei	+	+
Ventral tegmental nucleus	+++	++
Medulla oblongata		
Dorsal motor nucleus of the vagus	++++	++++
Hypoglossal nucleus	++++	++++
Medullary tegmentum	+	++
Spinal trigeminal nuclei	+	+
Vestibular nuclei	++	+++

Area	BuChE activity	Radioactivity
Cerebellum		
Cerebellar cortex	++	+
Cerebellar nuclei	+	++
White Matter		
Anterior commissure	++	-
Corpus callosum	++	-
External capsule	+	-
Fimbria	+	-
Internal capsule	+	-
Pyramidal tract	+	-

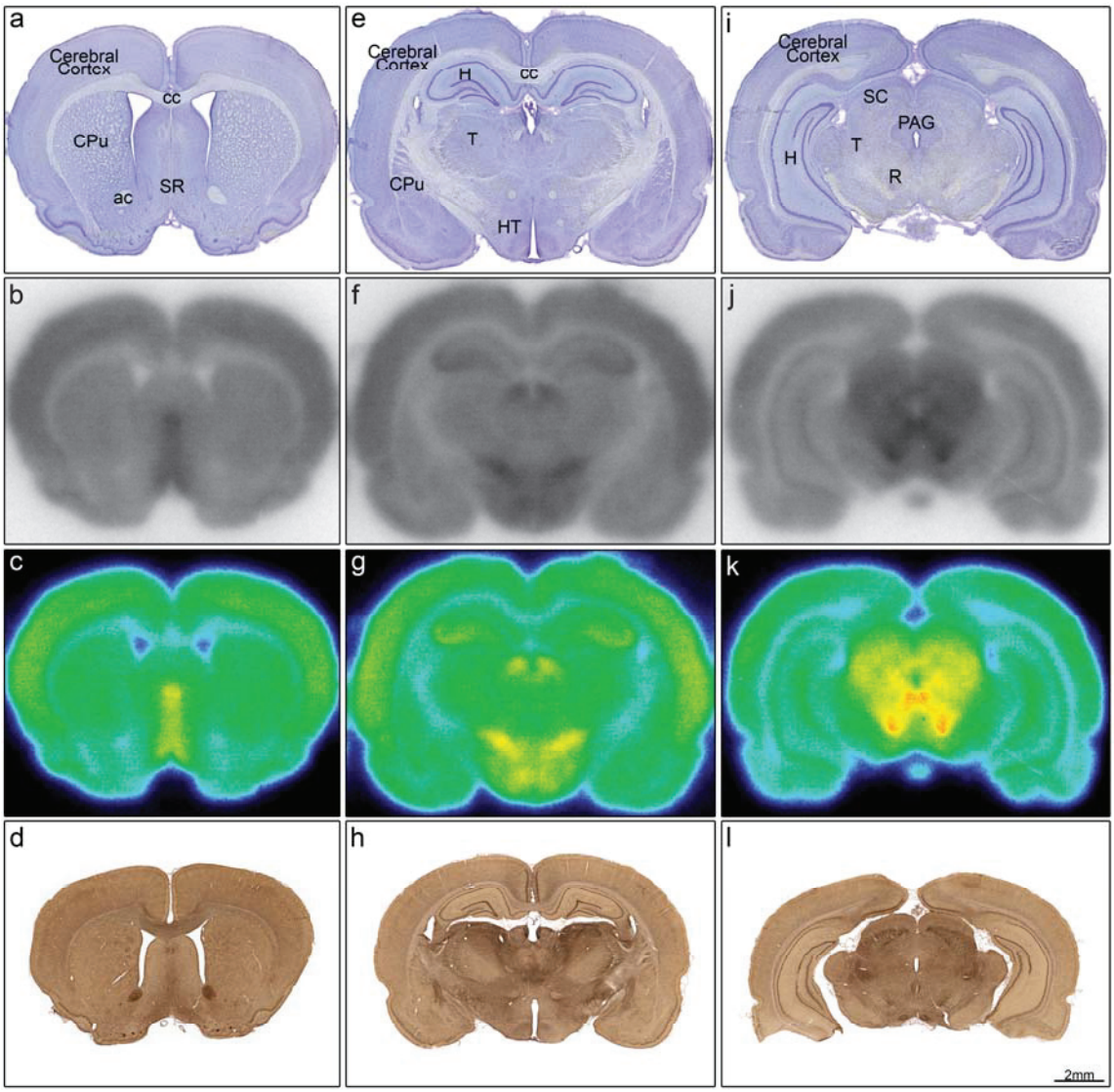

Figure 2.6. Comparison of neuroanatomy (a, e, i), radioactivity distribution (b, f, j) and corresponding gradient maps (c, g, k), as well as butyrylcholinesterase histochemistry (d, h, l) in the rostral aspect of the rat brain. ac: anterior commissure, cc: corpus callosum, CPu: caudate putamen, H: hippocampus, HT: hypothalamus, MTg: midbrain tegmentum, PAG: periaqueductal grey, R: red nucleus, SC: superior colliculus, SR: septal region, T: thalamus.

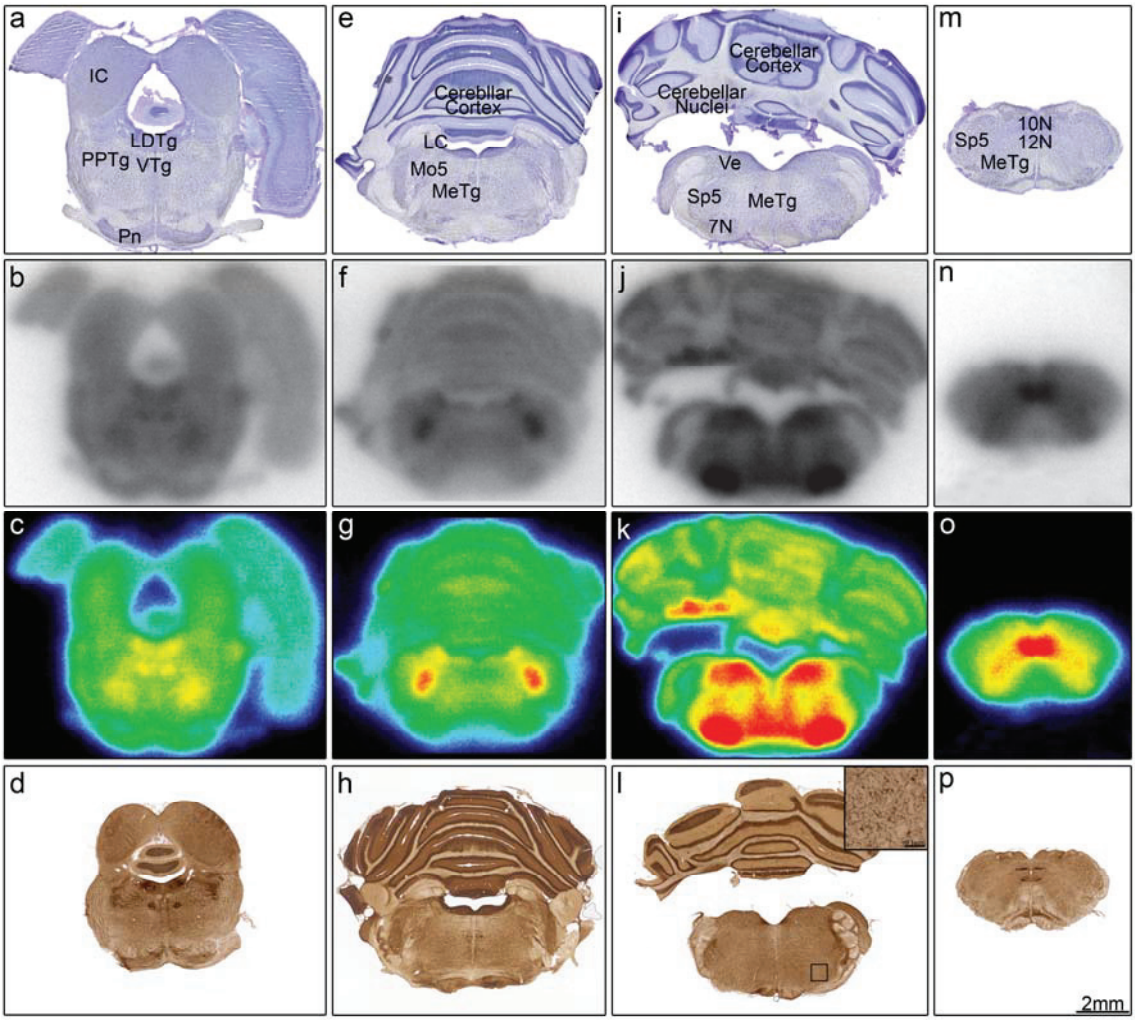

Figure 2.7. Comparison of neuroanatomy (a, e, i, m), radioactivity distribution (b, f, j, n) and corresponding gradient maps (c, g, k, o), as well as butyrylcholinesterase histochemistry (d, h, l, p) in the caudal aspect of the rat brain. 7N: facial nucleus, 10N: dorsal motor nucleus of the vagus, 12N: hypoglossal, IC: inferior colliculus, LC: locus coeruleus, LDTg: lateral dorsal tegmental nucleus, MeTg: medullary tegmentum, Mo5: motor trigeminal nucleus, PPTg: pedunculopontine tegmental nucleus, Sp5: spinal trigeminal nucleus, VTg: ventral tegmental nucleus, Ve: vestibular nuclei.

histochemical observation that did not appear to accumulate radioactivity. These structures included fiber tracts (e.g., the anterior commissure) and the anterior group of the thalamus (Figure 2.6). Conversely, a few areas, such as the motor trigeminal nucleus (Figure 2.7), without BuChE activity in histochemical analysis, demonstrated uptake of radioactivity.

2.5 Discussions

BuChE activity associated with AD neuropathological structures (Friede, 1965; Geula and Mesulam, 1989; Mesulam and Geula, 1994; Geula and Mesulam, 1995; Guillozet et al., 1997; Darvesh et al., 2010a), especially in regions of the brain with normally low BuChE activity, makes this enzyme a suitable potential target for molecular neuroimaging in AD. Previous attempts to image this enzyme have met limited success in that the radioimaging results (Kikuchi et al., 2004; Roivainen et al., 2004; Kuhl et al., 2006) did not correspond to the known histochemical distribution of this enzyme in normal (Friede, 1967; Darvesh et al., 1998; Darvesh and Hopkins, 2003; Darvesh et al., 2003a) or in AD brains (Friede, 1965; Geula and Mesulam, 1989; Mesulam and Geula, 1994; Geula and Mesulam, 1995; Guillozet et al., 1997; Darvesh et al., 2010a).

Of the three compounds synthesized and examined here, only 1-methylpiperidin-4-yl 4-iodobenzoate (**1**) had been previously synthesized and studied for potential dopamine transporter affinity (Singh et al., 1997), as an analgesic (Cheng et al., 1982) or an anticonvulsant (Waters et al., 1986). However, this compound did not display any of these properties (Cheng et al., 1982; Waters et al., 1986; Singh et al., 1997). Its potential as a cholinesterase substrate and/or imaging agent was not previously reported.

The structure of the molecules synthesized and evaluated here provide some advantages as BuChE imaging agents. Based on differences in the known crystal structures of BuChE (Nicolet et al., 2003) and AChE (Sussman et al., 1993), the estimated mean volume of the BuChE gorge (502 $Å^3$) is larger than that of AChE (302 $Å^3$) (Saxena et al., 1997) and the BuChE acyl pocket (L286 and V288) is able to accommodate larger acyl moieties, such as the iodobenzoyl group. The three iodobenzoate derivatives (compounds **1**-**3**) possess a bulky aromatic ring providing selectivity towards BuChE over AChE. As a result, all three iodobenzoate esters are selective for BuChE over AChE. Their affinities for BuChE (Table 2.1) are comparable to the extensively studied substrate for the enzyme, butyrylthiocholine (30.9 μM) (Darvesh et al., 2003b).

Although the three compounds were specific for BuChE, compounds **1** and **2** had better affinity for this enzyme relative to compound **3**. In order to understand this difference in affinity, and to facilitate future refinement of these lead compounds, computational studies were undertaken. These determinations revealed that the most stable conformations for compounds **1** and **2**, particularly in relation to the *N*-methyl ring system were similar (Figure 2.3). Specifically, the methyl group on the nitrogen of the ring in **1** and **2** point in the same direction, while in **3** this same methyl group points in the opposite direction. Binding of compounds to the active site gorge of BuChE is facilitated by interaction of the nitrogen with W82 of the enzyme active site gorge (Nicolet et al., 2003). These studies indicate that compounds with conformations similar to **1** and **2**, with respect to the nitrogen, would be desirable to improve binding to BuChE for imaging since they have higher affinity and are hydrolyzed more slowly that

compound **3**. This would imply a longer time period for the radiolabel to be part of the acylated BuChE complex.

For radiosynthesis, the replacement of non-radioactive iodine with ^{123}I for imaging was found to occur efficiently through a stable tributyltin intermediate (Figure 2.2c). This most likely occurred through a free radical mechanism that permitted rapid synthesis. In addition, efficient purification permitted subsequent timely administration into experimental animals. For the present study, to allow recovery of the small quantities of the radiolabelled material in sufficient quantity, albeit at the expense of the desired higher specific radioactivity, non-radioactive iodide was added to favour higher product yield. Incorporation of ^{123}I in compounds **1**-**3** occurred in 15 min at ambient temperature and was rapidly purified using HPLC (see Figure 2.4 for compound **1** as an example). Total time required for synthesis, purification, and preparation for injection was approximately one hour, an acceptable time when labelling with ^{123}I.

The ^{123}I labelled compounds showed initial high uptake in the heart ROI, undoubtedly reflecting the initial blood pool (Figure 2.5). The blood pool activity diminished rapidly with time. Such quick disappearance was expected since these esters are susceptible to hydrolysis by BuChE in the blood. This was accompanied by a rapid increase in the bladder (ROI_3), indicating the kidneys were the primary route of excretion (Figure 2.5). There was some activity in the neck centrally (Figure 2.5) which could include the thyroid gland. This will require further investigations as these compounds are developed further.

Importantly, for the present study, a smaller but significant amount of uptake was also detected in the head region (Figure 2.5). *In vivo* scanning resolution was insufficient to

definitively establish the distribution within the head to determine whether it included the brain. The rapid clearance from the blood pool indicates the relatively constant uptake in the head was not simply related to blood perfusion. A metabolic trapping principle (Kikuchi et al., 2007) of compounds metabolized by enzymes within the brain supported the accumulation observed. Also, it is possible that the limited uptake in the head region, and specifically in the brain, was due to metabolism of the radioligand in the blood.

To determine whether the ^{123}I labelled iodobenzoate esters actually accumulated in the brain, and in regions of known BuChE activity, detailed autoradiography of brain sections was carried out and compared to BuChE and thionin staining. Data in Table 2.2 and in Figure 2.6 and 2.7, confirm a high degree of overlap between radiolabel accumulation and BuChE activity. Importantly, in a region of normally low BuChE activity, such as the cerebral cortex, little uptake of ^{123}I was seen (Figure 2.6). However, certain discrepancies were also observed. For example, the motor trigeminal nucleus, that has low BuChE activity in histochemical analyses, displayed high radioactivity accumulation (Figure 2.7). This discrepancy may be due to a number of factors, that could include binding of these iodobenzoate esters to other enzymes and receptors unique to such regions. Conversely, some areas, such as the anterior commissure and the corpus callosum, that exhibit high histochemical BuChE activity (Table 2.2), little ^{123}I accumulation was observed in the autoradiograms (Figure 2.6). However, in white matter regions, where BuChE activity is high in histochemical analysis, low accumulation of radioactivity may be due to relatively less blood flow to these structures (Vaucher et al., 1995). These issues will require further investigations. Nonetheless, observations presented herein, in general, hold promise that these ^{123}I iodobenzoate

esters, or other more refined but comparable derivatives, will be able to detect elevated BuChE activity in the cortex, where this enzyme is associated with the neuropathological structures of AD.

2.6 Conclusions

A total of 3 potential imaging agents have been synthesized and enzyme kinetic studies have indicated that these compounds have high BuChE affinity and are specific for that enzyme over AChE. Synthetic tributyltin derivatives provided a suitable intermediate for incorporation of ^{123}I. Biodistribution in the rat revealed that the injected radiolabelled compounds are retained in the head region and autoradiography provided a localized distribution of radioactivity in the brain. Despite some differences between the autoradiograms and histochemical visualization, many areas that are known to contain BuChE corresponded to areas of radioactivity accumulation. Importantly, the region of the brain where BuChE accumulates in association with AD neuropathology, the cerebral cortex, did not exhibit accumulation of iodobenzoate radiolabel in the normal rat brain examined here. Therefore, these reported ^{123}I iodobenzoate esters show promise in guiding the development of future BuChE imaging agents that can detect AD pathology *in vivo*, thus permitting early diagnosis of this disease.

CHAPTER 3 THIOESTERS AND THEIR USE

3.1 PREFACE

Rapid and efficient screening of ester compounds, such as those described in Chapter 2, is required for continued development and optimization of ester imaging agents for cholinesterases. In this respect, this Chapter describes a kinetic method for determining the binding properties of a wide range of ester compounds for acetylcholinesterase (AChE) and butyrylcholinesterase (BuChE). Furthermore, a histochemical method is presented to screen potential imaging agents in tissues of interest without introduction of a radioisotope. Several compounds were evaluated using these methods including literature-described AChE and BuChE imaging agents as well as compounds comparable to those in Chapter 2. The content of this Chapter describes work done as part of this thesis that has been published as Macdonald *et al.*, J Enzyme Inhib Med Chem, 2013, 28(3):447-55.

3.2 INTRODUCTION

In earlier attempts to realize cholinesterase imaging, several ^{11}C-radiolabelled alkyl esters of *N*-methylpiperidinol were synthesized as acetylcholinesterase (AChE)-specific imaging agents. Two such compounds, 4-(N-[^{11}C] methyl)piperidinyl acetate ([^{11}C]-AMP) and 4-(N-[^{11}C] methyl) piperidinyl propionate ([^{11}C]-PMP), were examined (Irie et al., 1994; Irie et al., 1996; Kilbourn et al., 1996; Kilbourn et al., 1998; Snyder et al., 1998) and provided some reproduction of the known brain distributions of AChE (Irie et al., 1996; Kilbourn et al., 1996). Specific butyrylcholinesterase (BuChE) visualization was also attempted with 4-(N-[^{11}C] methyl) piperidinyl *n*-butyrate ([^{11}C]-MP4B) (Snyder

et al., 2001) but was unsuccessful (Kuhl et al., 2006). Alternate types of BuChE imaging ligands, derived from *N*-methylpiperidinol and *N*-methyl pyrrolidinol, were subsequently synthesized and tested in a normal rat model system (Macdonald et al., 2011). Using autoradiographic analysis these para-[^{123}I]-iodobenzoate esters were found to have entered the brain and their distribution recapitulated, for the most part, the known distribution of BuChE therein. Based on these observations, *N*-methylpiperidinyl compounds remain promising agents for the imaging of cholinesterases in the living brain.

In vivo testing of the *N*-methylpiperidinyl cholinesterase imaging agents, [^{11}C]-AMP, [^{11}C]-PMP and [^{11}C]-MP4B, has been extensive. However, methodology for determination of their specificity and direct measurement of their actual affinity constants for AChE and BuChE has been difficult due to the lack of a suitable chromophore that would allow the use of sensitive spectrophotometric methods. Tracking hydrolysis by radiolabelling reactants and products (Kikuchi, 2001) or by employing the chromophore of *m*-nitrophenol to tag reactants in a spectrophotometric approach (Snyder et al., 2001) have both proved cumbersome for screening of compounds as potential imaging agents. Thus, a rapid *in vitro* evaluation method would be beneficial for the continued development of imaging agents derived from *N*-methylpiperidinol.

The Ellman spectrophotometric method (Ellman et al., 1961), or variations thereof, (Pottie et al., 2011) remains the most rapid, reliable and sensitive means to measure AChE or BuChE activity. The principle on which this assay is based is that, thioesters, such as acetylthiocholine and butyrylthiocholine, are kinetically analogous to their corresponding esters with respect to cholinesterase catalysis. A kinetic analysis

(Masson et al., 2007) comparing benzoylcholine and benzoylthiocholine supports this notion. In addition to their use in Ellman cholinesterase assays, thioesters are employed for *in vitro* histochemical detection of cholinesterase activity in tissues. One of the commonly used histochemical techniques for detection of AChE and BuChE is the Karnovsky-Roots method (Karnovsky and Roots, 1964). In this procedure, hydrolysis of acetylthiocholine and butyrylthiocholine generates a thiolate anion that leads to a precipitate in the area of enzyme activity. This precipitation facilitates detection of enzyme distribution under the microscope. Thus, in theory, any thioester susceptible to cholinesterase hydrolysis could be characterized using Ellman enzyme kinetics and should enable histochemical visualization of areas containing enzyme activity in brain tissue using the Karnovsky-Roots method.

Herein this Chapter is described the synthesis, enzyme kinetics and histochemical evaluation, as cholinesterase substrates, of alkyl and aryl thioesters of *N*-methyl-4-piperidinethiol as an indirect means to evaluate potential cholinesterase imaging agents, such as the corresponding *N*-methyl-4-piperidinol esters.

3.3 Materials And Methods

3.3.1 Materials

Butyl lithium, triethylamine, sodium borohydride, *N*-methylpiperidin-4-ol, *N*-methyl-4-piperidone, 4-iodobenzoyl chloride, 4-fluorobenzoyl chloride, 4-cyanobenzoyl chloride, acetyl chloride, propionyl chloride, butyryl chloride and purified recombinant human acetylcholinesterase were purchased from Sigma-Aldrich. Hydrogen sulfide was

purchased from Air Liquide. Purified human plasma butyrylcholinesterase was a gift from Dr. Oksana Lockridge (University of Nebraska Medical Center).

3.3.2 Characterization of Synthesized Products

Melting points were determined using a Fisher-Johns Melting Point Apparatus. Infrared spectra were recorded as Nujol mulls or as neat liquids between sodium chloride plates on a Nicolet Avatar 330 FT- IR spectrometer. Peak positions were reproducible within 1–2 cm^{-1}. Nuclear magnetic resonance spectra were recorded at the Nuclear Magnetic Resonance Research Resource (NMR-3), Dalhousie University (Halifax, Nova Scotia, Canada), on a Bruker AVANCE 500, operating at 500.1 MHz for ^{1}H and 125.8 MHz for ^{13}C. Chemical shifts are reported in parts per million relative to Me_4Si in $CDCl_3$. For proton NMR experiments, the coupling constants are reported in hertz and the multiplicities are apparent. For carbon NMR data, the number of attached protons for each signal, as determined by a DEPT experiment, are given in parentheses. Low-resolution mass spectra were obtained using an Agilent 6890N GC with an Agilent 6890N Electron Impact MS (Waldbronn, Germany) operating at 70 eV. High-resolution mass spectra were obtained with accurate mass positive-ion electrospray ionization measurements recorded at the Mass Spectrometry Laboratory at Dalhousie University using a Bruker Daltonics microTOF with a flow rate of 2 μL/min, spray voltage of 4500 V and tray temperature of 180 °C or were recorded on a CEC 21-110B spectrometer using electron ionization at 70 V and an appropriate source temperature with samples being introduced by means of a heatable port probe. Mass measurements were within 14 ppm of the calculated value. Purity of all compounds was determined using an Agilent

Technologies 1200 series HPLC system with a reverse phase C18 column and methanol as the mobile phase.

3.3.3 Brain Tissues

Brain tissues used in this study were provided by the Maritime Brain Tissue Bank, (Halifax, Nova Scotia, Canada), following approval from the Capital Health Ethics Board, from the brain of a 90 year old female, removed within 20 hours of death. The brain was immersion fixed in 10% formalin in 0.1 M phosphate buffer (pH 7.4) for approximately 94 h and cut in 1-2 cm slabs. These slabs were cryoprotected by immersion in increasing concentrations of sucrose, ranging from 10% to 40% in 0.1 M phosphate buffer (pH 7.4). The brain tissue was in each concentration of sucrose solution for approximately 48 h and was stored in 40% buffered sucrose (pH 7.4) with 0.6% sodium azide until used.

3.3.4 Synthesis of Compounds

Synthesis of *N*-methylpiperidin-4-yl 4-cyanobenzoate (**1**)

Under an argon atmosphere, *N*-methylpiperidin-4-ol (0.92 g, 8.00 mmol) was dissolved in THF (15 mL). To this solution was added 1.6 M butyl lithium in hexanes (5.00 mL, 8.00 mmol) at –78 °C followed by a solution of 4-cyanobenzoyl chloride (1.21 g, 7.30 mmol) in THF (20 mL) and the mixture was stirred at –78 ºC for 16 h. Water (20 mL) was added to the reaction mixture and extracted with ethyl acetate (3 × 20 mL). The combined organic layers were dried over Na_2SO_4. The solvent was removed *in vacuo* to produce a yellow solid. The product was purified by silica gel chromatography (1:9

MeOH/CH_2Cl_2) to give a white solid (1.06 g, 59%). The solid was recrystallized from hexanes to afford white crystals. Analytical data: $MP_{(hexanes)}$: 119-120 ˚C. IR (Nujol): 2228, 1718, 1278, 1122, 1030 cm^{-1}. ^1H NMR ($CDCl_3$): δ 1.92-2.03 (m, 2H), 2.10-2.18 (m, 2H), 2.44-2.56 (m, 2H), 2.42 (s, 3H), 2.72-2.87 (m, 2H), 5.08-5.19 (m, 1H), 7.77-7.79 (m, 2H), 8.15- 8.17 (m, 2H). ^{13}C NMR ($CDCl_3$): δ 30.9 (2), 46.2 (3), 52.9 (2), 71.4 (1), 116.4 (0), 118.0 (0), 130.1 (1), 132.2 (1), 134.5 (0), 164.3 (0). EI-MS m/z: 244 (M^+, 44%), 130 (22%), 114 (20%), 102 (29%, 98 (80%), 97 (100%), 96 (80%), 82 (32%), 70 (14%), 57 (10%), 55 (29%). HRMS (EI): M^+ found 244.1216, calcd for $C_{14}H_{16}N_2O_2^+$ = 244.1206.

Synthesis of *N*-methylpiperidin-4-yl 4-fluorobenzoate (**2**)

Under an argon atmosphere, *N*-methylpiperidin-4-ol (0.94 g, 8.16 mmol) was dissolved in THF (15 mL). To this solution was added 1.6 M butyl lithium in hexanes (5.00 mL, 8.00 mmol) at −78 °C followed by a 4-fluorobenzoyl chloride (0.88 g, 7.30 mmol) and the mixture was stirred at –78 ºC for 16 h. Water (20 mL) was added to the reaction mixture and extracted with ethyl acetate (3 × 20 mL). The combined organic layers were dried over Na_2SO_4. The solvent was removed *in vacuo* to produce a yellow solid. The product was purified by silica gel chromatography (1:9 MeOH/CH_2Cl_2) to give a pale yellow solid (0.72 g, 42%). The solid was recrystallized from hexanes to afford white crystals. Analytical data: $MP_{(hexanes)}$: 48-49 ˚C. IR (Nujol): 1726, 1274, 1114, 852 cm^{-1}. ^1H NMR ($CDCl_3$): δ 1.83-1.88 (m, 2H), 2.00-2.05 (m, 2H), 2.32 (s, 3H), 2.33-2.40 (m, 2H), 2.63-2.77 (m, 2H), 4.96-5.10 (m, 1H), 7.08-7.13 (m, 2H), 8.04-8.08 (m, 2H). ^{13}C NMR ($CDCl_3$): δ 30.9 (2), 46.2 (3), 52.9 (2), 70.3 (1), 115.4 (J_{CF}=22 Hz, 1)

126.9 (0), 132.0 (J_{CF}= 10 Hz, 1), 164.7 (J_{CF}=254 Hz, 0), 166.7 (0). EI-MS m/z: 237 (MH^+, 30%), 123 (30%), 114 (15%), 98 (53%), 97 (100%), 96 (82%), 95 (31%), 82 (35%), 75 (12%), 70 (14%), 55 (28%). HRMS (EI): M^+ found 237.1173, calcd for $C_{13}H_{16}FNO_2^+$ = 237.1160.

Synthesis of *N*-methylpiperidin-4-yl 4-iodobenzoate (**3**)

Synthesized according to a previously described procedure (Macdonald et al., 2011) and the analytical data was consistent and purity greater than 98%. Analytical data: MP: 128–130 °C (Lit MP: 130 °C (Singh et al., 1997)). IR (Nujol): 1711, 1585, 1283, 1268, 1118, and 754 cm^{-1}. ^1H NMR ($CDCl_3$): δ 1.84–1.91 (m, 2H), 2.01–2.08 (m, 2H), 2.31–2.39 (m, 5H), 2.67–2.73 (m, 2H), 5.02–5.08 (m, 1H), 7.75 (d, *J*=8.5 Hz, 2H), 7.81 (d, *J*=8.5 Hz, 2H). ^{13}C NMR ($CDCl_3$): δ 31 (2), 46 (3), 53 (2), 70 (1), 100 (1), 130, 131, 138, and 166. EI-MS m/z: 345(M^+, 16%), 231 (12%), 203 (9%), 114 (11%), 97 (100%), 82 (22%), 70 (7%), 55 (14%). HRMS (EI): M^+ found 345.0233, calcd for $C_{13}H_{16}NO_2I$ = 345.0226.

Synthesis of *N*-methyl-4-piperidinethiol

N-Methyl-4-piperidone (52.92 g, 469.7 mmol) was dissolved in isopropanol (200 mL). Hydrogen sulfide was bubbled through the solution using a glass frit at 0 °C resulting in the precipitation of white solid, which was collected by suction filtration after 1 h. The filtrate was again treated with hydrogen sulfide for an additional 30 min and all further white solid was collected by suction filtration for a total of 80.47 g. Sodium borohydride (16.62g, 439.3 mmol) was suspended in isopropanol (150 mL) followed by

the slow addition of the white solid at 0˚C. The reaction mixture was returned to room temperature and stirred under an argon atmosphere for 16 h. Excess solvent was removed under reduced pressure to produce a white paste which was partitioned between 150 mL of both water and ether. The aqueous layer was extracted with ether (4 x 50 mL) and the combined organic layers washed with brine (2 x 30 mL) and dried over anhydrous Na_2SO_4. The solvent was removed *in vacuo* to yield a colourless liquid which was distilled (BP: 168-172 °C, lit. BP: 62 °C at 0.8mm (Barrera and Lyle, 1962); to yield the product as a clear colourless oil (21.22 g, 34%). IR (Neat): 3338, 2944, 1278, 1132 cm^{-1}. ^1H NMR ($CDCl_3$): δ 1.55 (d, *J*=7.0, 1H), 1.64-1.71 (m, 2H), 1.99-2.04 (m, 4H), 2.26 (s, 3H), 2.67-2.80 (m, 3H). ^{13}C NMR ($CDCl_3$): δ 35.5 (1), 36.9 (2), 46.1 (3), 55.2 (2). EI-MS m/z: 131 (M^+ 32%), 98 (100%), 96 (12%), 70 (18%), 55 (27%). HRMS (ESI): MH^+ found 132.0841, calcd for $C_6H_{14}NS^+$ = 132.0841.

Synthesis of (*N*-methylpiperidin-4-yl) 4-cyanobenzenecarbothioate (**4**)

Under an argon atmosphere, triethylamine (0.53 mL, 3.80 mmol) was added to dichloromethane (20 mL), followed by *N*-methyl-4-piperidinethiol (0.45 mL, 3.80 mmol) and 4-cyanobenzoyl chloride (0.629 g, 3.80 mmol). The reaction mixture was stirred for 24 h at room temperature. The reaction was extracted with saturated $NaHCO_3$ (3 x 20 mL) and the organic layer dried over Na_2SO_4. The solvent was removed *in vacuo* to yield a light yellow solid which was recrystallized from hexanes to afford pale yellow crystals (0.24 g, 24%). Analytical data: $MP_{(hexanes)}$: 152-153 ºC. IR (Nujol): 2229, 1655, 1208, 860 cm^{-1}. ^1H NMR ($CDCl_3$): δ 1.82-1.89 (m, 2H), 2.10-2.15 (m, 2H), 2.25-2.33 (m, 2H), 2.35 (s, 3H), 2.74-2.85 (m, 2H), 3.72-3.82 (m, 1H), 7.74-7.76 (m, 2H), 8.02-

8.04 (m, 2H). ^{13}C NMR ($CDCl_3$): δ 32.1 (2), 40.4 (1), 46.3 (3), 55.1 (2), 116.5 (0), 117.8 (0), 127.6 (1), 132.4 (1), 140.3 (0), 190.2 (0). EI-MS m/z: 260 (M^+, 4%), 130 (54%), 102 (20%), 98 (100%), 97 (81%), 96 (30%), 70 (15%), 55 (22%), 44 (10%), 42 (18%). HRMS (ESI): MH^+ found 261.1056, calcd for $C_{14}H_{17}N_2OS^+$ = 261.1056.

Synthesis of (*N*-methylpiperidin-4-yl) 4-fluorobenzenecarbothioate (**5**)

Under an argon atmosphere, triethylamine (0.53 mL, 3.80 mmol) was added to dichloromethane (20 mL), followed by *N*-methyl-4-piperidinethiol (0.45 mL, 3.80 mmol) and 4-fluorobenzoyl chloride (0.18 mL, 3.80 mmol). The reaction mixture was stirred for 4 days at reflux temperature. The reaction was extracted with saturated $NaHCO_3$ (3 x 20 mL) and the organic layer dried over Na_2SO_4. The solvent was removed *in vacuo* to yield a light yellow solid which was purified by silica gel chromatography (7% MeOH in CH_2Cl_2) and recrystallized from hexanes to afford pale yellow crystals (0.11 g, 28%). Analytical data: $MP_{(hexanes)}$: 66-68 ºC. IR (Nujol): 1655, 1225, 1202, 1155, 916, 843 cm^{-1}. ^{1}H NMR ($CDCl_3$): δ 1.88-1.95 (m, 2H), 2.11-2.20 (m, 2H), 2.41 (s, 3H), 2.81- 2.94 (m, 2H), 3.69-3.81 (m, 1H), 7.10-7.15 (m, 2H), 7.95-7.99 (m, 2H). ^{13}C NMR ($CDCl_3$): δ 32.5 (2), 40.2 (1), 46.6 (3), 55.5 (2), 116.2 (J_{CF}=22 Hz, 1), 130.2 (J_{CF}=9 Hz, 1), 134.0 (0), 166.4 (J_{CF}=255 Hz, 0), 190.4 (0). EI-MS m/z: 253 (M^+, 3%), 130 (39%), 123 (24%), 98 (82%), 97 (100%), 96 (36%), 95 (24%), 82 (10%), 75 (10%), 70 (17%), 55 (21%), 42 (17%). HRMS (ESI): MH^+ found 254.1009, calcd for $C_{13}H_{17}FNOS^+$ = 254.1009.

Synthesis of (*N*-methylpiperidin-4-yl) 4-iodobenzenecarbothioate (**6**)

Under an argon atmosphere, triethylamine (0.53 mL, 3.80 mmol) was added to dichloromethane (20 mL), followed by *N*-methyl-4-piperidinethiol (0.45 mL, 3.80 mmol) and 4-iodobenzoyl chloride (1.01 g, 3.80 mmol). The reaction mixture was stirred for 24 h at reflux temperature. The reaction was extracted with saturated $NaHCO_3$ (3 x 20 mL) and the organic layer dried over Na_2SO_4. The solvent was removed *in vacuo* to yield a light yellow solid which was recrystallized from hexanes to afford pale yellow crystals (0.41 g, 30%). Analytical data: $MP_{(hexanes)}$: 136-137 ºC. IR (Nujol): 1650, 1208, 824 cm^{-1}. ^1H NMR ($CDCl_3$): δ 1.80-1.87 (m, 2H), 2.09-2.14 (m, 2H), 2.25-2.32 (m, 2H), 2.34 (s, 3H), 2.74-2.83 (m, 2H), 3.67-3.78 (m, 1H), 7.64-7.67 (m, 2H), 7.79-7.82 (m, 2H). ^{13}C NMR ($CDCl_3$): δ 31.9 (2), 39.6 (1), 46.0 (3), 54.9 (2), 100.8 (0), 128.2 (1), 136.2 (0), 137.6 (1), 190.6 (0). EI-MS m/z: 361 (M^+, 1%), 230 (12%), 130 (30%), 98 (60%), 97 (100%), 96 (22%), 76 (14%), 70 (10%), 55 (12%), 42 (10%). HRMS (ESI): MH^+ found 362.0070, calcd for $C_{13}H_{17}INOS^+$ = 362.0070.

Synthesis of (*N*-methylpiperidin-4-yl) ethanethioate (**7**)

N-Methylpiperidine-4-thiol (0.5 mL, 4.2 mmol) was dissolved in dry CH_2Cl_2 (5 mL) under an argon atmosphere. To this was added acetyl chloride (0.90 mL, 13 mmol) and the reaction refluxed for 1.5 h. The solvent was removed *in vacuo* and the resulting oil dissolved in saturated $NaHCO_3$ (20 mL). This solution was extracted with CH_2Cl_2 (4 x 20 mL), dried over Na_2SO_4 and the solvent removed *in vacuo* to produce a clear colourless oil. This oil was purified by silica gel column chromatography (1:19 MeOH/CH_2Cl_2) to produce a clear colourless viscous liquid (0.69 g, 96%). Analytical

Data: IR (Neat): 2941, 1686, 1448, 1219, 915 cm^{-1}. ^{1}H NMR ($CDCl_3$): δ 1.58-1.65 (m, 2H), 1.88-1.92 (m, 2H), 2.08-2.18 (m, 2H), 2.21 (s, 3H), 2.24 (s, 3H), 2.59- 2.70 (m, 2H), 3.33-3.48 (m, 1H). ^{13}C NMR ($CDCl_3$): δ 30.6 (3), 31.8 (2), 39.3 (1), 46.0 (3), 54.9 (2), 195.2 (0). EI-MS m/z: 173(M^+, 17%), 130 (52%), 98 (100%), 97 (30%), 96 (33%), 70 (26%), 55 (45%). HRMS (ESI): MH^+ found 174.0947, calcd for $C_8H_{16}NOS^+$ = 174.0947.

Synthesis of (*N*-methylpiperidin-4-yl) propanethioate (**8**)

N-Methylpiperidine-4-thiol (0.5 mL, 4.2 mmol) was dissolved in dry CH_2Cl_2 (5 mL) under an argon atmosphere. To this was added propionyl chloride (0.94 mL, 11 mmol) and the reaction refluxed for 2 h. The solvent was removed *in vacuo* and the resulting oil dissolved in saturated $NaHCO_3$ (20 mL). This solution was extracted with CH_2Cl_2 (4 x 20 mL), dried over Na_2SO_4 and the solvent removed *in vacuo* to produce a clear colourless viscous liquid. This oil was purified by silica gel column chromatography (1:19 MeOH/ CH_2Cl_2) to produce a clear colourless viscous liquid (0.45 g, 57%). Analytical data: IR (Neat): 2939, 2782, 1689, 1463, 1129, 937 cm^{-1}. ^{1}H NMR ($CDCl_3$): δ 1.19 (t, *J*=7.5, 3H), 1.65-1.72 (m, 2H), 1.95-1.98 (m, 2H), 2.13-2.25 (m, 2H), 2.28 (s, 3H), 2.55 (q, *J*=7.5, 2H), 2.63-2.83 (m, 2H), 3.41-3.54 (m, 1H). ^{13}C NMR ($CDCl_3$): δ 9.6 (3), 32.1 (2), 37.5 (2), 39.1 (1), 46.2 (3), 55.1 (2), 199.8 (0). EI-MS m/z: 187 (M^+, 17%), 130 (61%), 98 (100%), 97 (27%), 96 (28%), 70 (17%), 55 (20%). HRMS (ESI): MH^+ found 188.1104, calcd for $C_9H_{18}NOS^+$= 188.1104.

Synthesis (*N*-methylpiperidin-4-yl) butanethioate (**9**)

N-Methylpiperidine-4-thiol (0.5 mL, 4.2 mmol) was dissolved in dry CH_2Cl_2 (5 mL) under an argon atmosphere. To this was added butyryl chloride (1.3 mL, 13 mmol) and the reaction refluxed for 1.5 h. The solvent was removed *in vacuo* and the resulting oil dissolved in saturated $NaHCO_3$ (20 mL). This solution was extracted with CH_2Cl_2 (4 x 20 mL), dried over Na_2SO_4 and the solvent removed *in vacuo* to produce a clear colourless viscous liquid. This oil was purified by silica gel column chromatography (1:19 MeOH/ CH_2Cl_2) to produce a clear colourless oil (0.56 g, 67%). Analytical data: IR (Neat): 2938, 2782, 1686, 1447, 1129, 994 cm^{-1}. ^1H NMR ($CDCl_3$): δ 0.95 (t, *J*=7.3, 3H), 1.62-1.71 (m, 4H), 1.89-2.01 (m, 2H), 2.08-2.22 (m, 2H), 2.25 (s, 3H), 2.49 (t, *J*=7.3, 2H), 2.59-2.81 (m, 2H), 3.38-3.53 (m, 1H). ^{13}C NMR ($CDCl_3$): δ 13.3 (3), 19.0 (2), 32.1 (2), 39.1 (1), 45.9 (2), 46.20 (3), 55.1 (2), 198.9 (0). EI-MS m/z: 201 (M^+, 16%), 130 (65%), 98 (100%), 97 (28%), 96 (26%), 70 (17%), 55 (20%). HRMS (ESI): MH^+ found 202.1260, calcd for $C_{10}H_{20}NOS^+$ = 202.1260.

3.3.5 Enzyme Kinetics

Measurement of Aryl Ester Hydrolysis

Cholinesterase specificity and maximum absorbance change during hydrolysis for each benzoyl ester was determined spectrophotometrically, making use of differences in the aryl chromophores of substrates and products determined through repetitive absorbance scans. Briefly, 15 µL of AChE (2.5 U) or BuChE (5.4 U) dissolved in 0.1% $gelatin_{(aq)}$, containing 0.01% sodium azide, and 1.44 mL of 0.1 M phosphate buffer (pH 7.4) were placed in a quartz cuvette of 1 cm path length. The reaction was commenced

with the addition of 50 μL of 5 mM ester in 50% acetonitrile$_{(aq)}$. The absorbance was scanned from 200–300 nm every 2 min for a total of 30 min using a Ultrospec 2100 pro UV/Visible Spectrophotometer (Biochrom) with Swift II software (Amersham). The wavelength corresponding to the maximum absorbance change during hydrolysis (235 nm for compounds **1**-**3**) was used for the subsequent determination of BuChE affinity constants (K_m values) using Lineweaver-Burk double reciprocal plots.

Determination of affinity constants (K_m) and maximum velocity values (V_{max}) was accomplished by measuring change in absorbance per min (ΔA/ min) at 235 nm, using a fixed amount of enzyme AChE (8.3 U) or BuChE (5.9 U) and varying amounts of compounds (1.67×10^{-4} – 1.67×10^{-5} M), using a Spectronic 1001 (Milton Roy) UV-visible spectrophotometer. The plot of 1/v against 1/s gave K_m as the negative reciprocal of the intercept on the 1/s-axis and gave V_{max} as the reciprocal of the intercept of the 1/v-axis. As defined previously (Darvesh et al., 2001), 0.1 U is the amount of cholinesterase that gives a ΔA/min of 1.0 in the presence of 1.6×10^{-4} M substrate (acetylthiocholine for AChE, butyrylthiocholine for BuChE).

Measurement of Thioester Hydrolysis

The kinetics of both alkyl and aryl thioester hydrolysis by AChE or BuChE was determined using a modification (Pottie et al., 2011) of the method described by Ellman *et al.* (Ellman et al., 1961). Briefly, 1.40 mL of buffered 5, 5'-dithio-bis(2-nitrobenzoic acid) (DTNB) solution (pH 7.4) and 0.05 mL of AChE (8.3 U) or BuChE (5.9 U), in 0.1% aqueous gelatin, were mixed in a quartz cuvette of 1 cm path-length and zeroed at 412 nm. The reaction was initiated by the addition of thioester in a 50% aqueous

acetonitrile solution to give a final substrate concentration from 1.7 x 10^{-4} to 3.3 x 10^{-6} M. The reactions were performed at 23 ˚C. The rate of change of absorbance (ΔA/min), reflecting the rate of hydrolysis of the thioester, was recorded every 5 sec for 1 min, using a Milton-Roy 1201 UV–vis spectrophotometer. The molar extinction coefficient for the Ellman product, 5-thio-2-nitrobenzoic acid, used to convert the change in absorbance at λ = 412 nm to moles of product was 14,150 M^{-1} cm^{-1}. These experiments were performed at least in triplicate and the values averaged.

3.3.6 Structural Analysis

Computational chemistry studies, to determine the most stable geometries of compounds, were carried out at the molecular mechanics level of theory using the Merck Molecular Force Field (MMFF), employing Spartan '06 (Wavefunction, 2006).

3.3.7 Cholinesterase Histochemistry with Thioester Substrates

Brain tissue containing the thalamus was cut on a Leica SM2000R microtome with a Physitemp freezing stage in 50 μm thick coronal sections. Sections were stored in 40% sucrose in 0.1 M phosphate buffer (pH 7.4) at -20˚C until used. A modified (Darvesh et al., 1998) Karnovsky-Roots method was employed for AChE and BuChE staining. Substrates used to provide staining were synthesized thioesters and the standards, butyrylthiocholine and acetylthiocholine in the absence of cholinesterase inhibitors. Briefly, tissue sections were rinsed in 0.1 M maleate buffer (pH 7.4) for 30 min and then placed in 0.1 M maleate buffer, pH 7.4, containing 0.15% hydrogen peroxide for 30 min to quench endogenous peroxidase activity. Following a second rinse

in 0.1 M maleate buffer, pH 7.4, for 30 min, sections were incubated for 1 h (acetylthiocholine, [*N*-methylpiperidin-4-yl] ethanethioate) (**7**) or 18 h (butyrylthiocholine, [*N*-methylpiperidin-4-yl] butanethioate (**9**) and [*N*-methylpiperidin-4-yl] 4-cyanobenzenecarbothioate) (**4**) in a medium containing 0.5 mM sodium citrate, 0.47 mM cupric sulfate, 0.05 mM potassium ferricyanide and thioester substrate in 0.1 M maleate buffer (pH 7.4). Substrate concentrations were 4 mM for acetylthiocholine, butyrylthiocholine, (*N*-methylpiperidin-4-yl) ethanethioate, (*N*-methylpiperidin-4-yl) butanethioate and 0.5 mM for the less soluble (*N*-methylpiperidin-4-yl) 4-cyanobenzenecarbothioate. Sections were then rinsed for 30 min in distilled water and placed in 0.1% cobalt (II) chloride in water for 10 min. After a further rinse in distilled water, sections were placed in a 3, 3'-diaminobenzidine tetrahydrochloride (DAB) solution consisting of 1.39 mM in 0.1M phosphate buffer (pH 7.4). After 5 min, a solution of 0.15% hydrogen peroxide in distilled water was added at a ratio of 10:1 (DAB solution : hydrogen peroxide solution) and the reaction was carried out for approximately 2 min. Sections were then washed in 0.01 M acetate buffer, pH 3.3, mounted on slides, coverslipped and examined with brightfield microscopy.

Sections were photographed with an AxioCam HRc camera on a Zeiss Axioplan II microscope. The photographic plates were assembled using Adobe Photoshop 7.0. The images were color balanced, contrast enhanced and brightness adjusted to match the background from different images.

3.4 Results and Discussions

3.4.1 Organic Synthesis

To synthesize *N*-methyl-4-piperidinethiol, *N*-methyl-4-piperidone was mixed with hydrogen sulfide and the resulting reaction produced a dithiol. This intermediate was then reduced with sodium borohydride (Figure 3.1), in a reaction adapted from an earlier procedure (Meanwell et al., 1993). Thioesters were subsequently generated by esterification of this thiol with an acid chloride (Figure 3.1). Benzoate esters were also synthesized, as previously described (Macdonald et al., 2011), (Figure 3.1, Table 3.1, **1-3**) in order to directly compare cholinesterase kinetic parameters for aryl thioesters and esters. Two classes of thioesters were synthesized, those from aryl acid chlorides (Table 3.1, **4-6**), analogous to the benzoate esters, and those from alkyl acid chlorides (Table 3.1, **7-9**), analogous to previously developed alkyl ester imaging agents (Irie et al., 1994; Snyder et al., 2001).

3.4.2 Kinetic Analysis

Thioester analogues of aryl esters such as benzoylcholine have been found (Masson et al., 2007) to be kinetically comparable to their ester counterparts for cholinesterase hydrolysis. Therefore, thioesters can provide a rapid, indirect enzyme kinetic screening method for analysis of potential ester imaging agents. All aryl and alkyl thioesters, producing a thiol product, upon hydrolysis, are amenable to kinetic analysis as cholinesterase substrates via an Ellman assay. Furthermore, since all aryl esters showed distinct UV spectral differences between reactant and product (Figure 3.2),

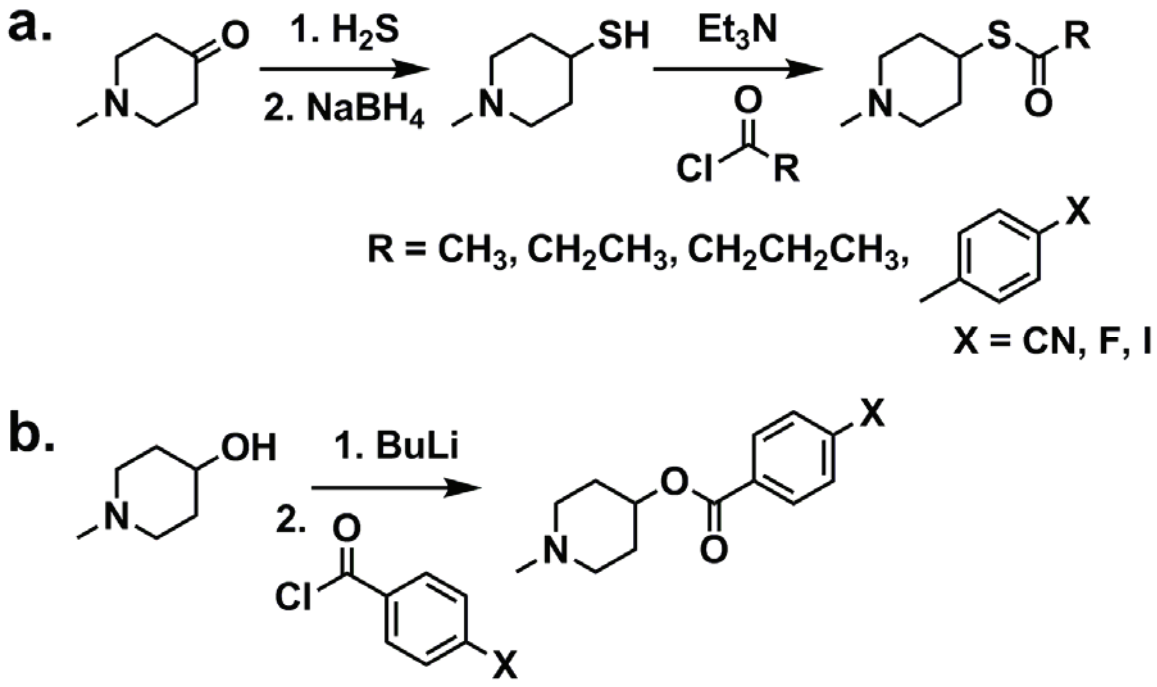

Figure 3.1. Reaction scheme for the synthesis of (**a**) alkyl and aryl thioesters and (**b**) aryl esters.

Table 3.1. Affinity constants (K_m) and maximum velocity values (V_{max}) for *N*-methylpiperidinyl alkyl thioesters, *N*-methylpiperidinyl aryl esters and corresponding thioesters with butyrylcholinesterase (BuChE) and acetylcholinesterase (AChE). None of the aryl compounds (**1-6**) were hydrolyzed by AChE under the conditions used (X).

	Structure	AChE		BuChE	
		K_m (μM)	V_{max} (μM min^{-1})	K_m (μM)	V_{max} (μM min^{-1})
1	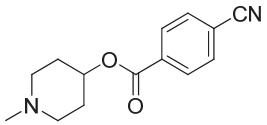	X	X	438 ± 75	45.0 ± 6.6
2	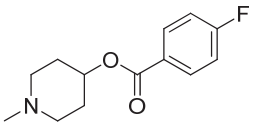	X	X	284 ± 28	24.7 ± 2.0
3	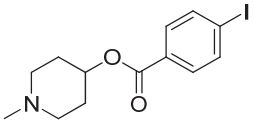	X	X	123 ± 42	21.0 ± 5.1
4	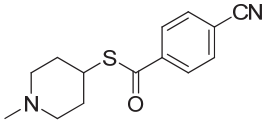	X	X	167 ± 17	30.7 ± 2.4
5	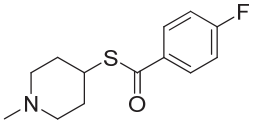	X	X	173 ± 13	27.6 ± 1.7
6	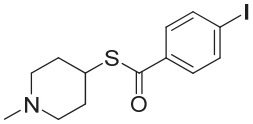	X	X	11 ± 1	9.7 ± 0.3
7	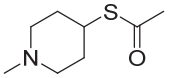	751 ± 26	18.3 ± 0.2	684 ± 54	16.7 ± 1.3
8	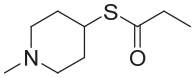	1108 ± 106	21.4 ± 2.2	302 ± 2	20.7 ± 0.1
9	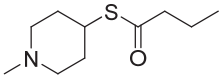	X	X	129 ± 12	7.0 ± 0.3

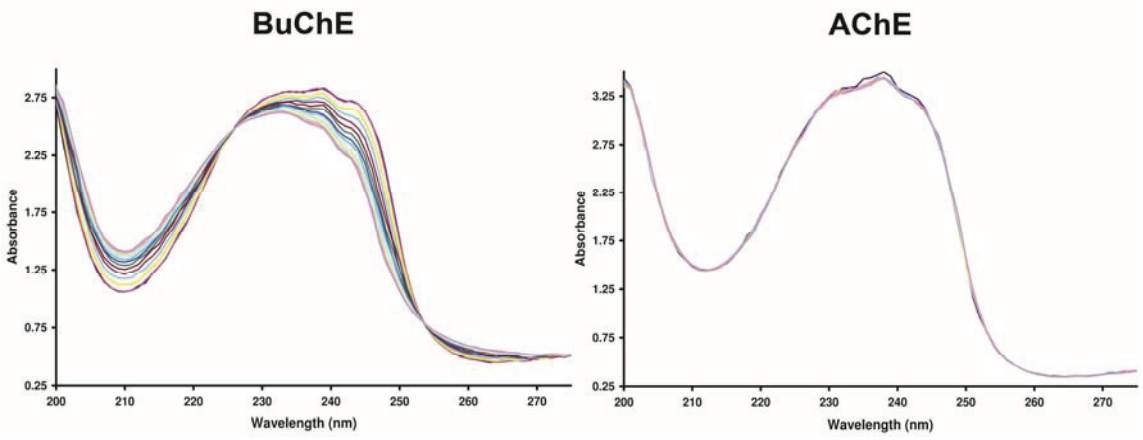

Figure 3.2. Repetitive absorbance scans for *N*-methylpiperidin-4-yl 4- cyanobenzoate in the presence of butyrylcholinesterase (BuChE) or acetylcholinesterase (AChE). Note change in absorbance over time when the compound was incubated with BuChE (left) reflecting hydrolysis of the compound by this enzyme. No change in absorbance with AChE (right) indicates no hydrolysis by this enzyme. The absorbance was measured every 2 min for 30 min.

they could be analyzed for comparison with thioester kinetic parameters by an alternate method employing changes in absorbance. Esters and thioesters of substituted benzoic acids gave comparable affinity constants and maximum velocity values (Table 3.1), in agreement with the earlier observation comparing benzoylcholine and benzoylthiocholine analogues (Masson et al., 2007). In general, the thioester derivatives had a slightly greater affinity towards BuChE than did the esters. In addition, none of the aryl thioesters, as observed earlier for aryl esters (Macdonald et al., 2011), were susceptible to hydrolysis by AChE (Figure 3.2).

Although it was not possible to directly obtain affinity constants for the esters of *N*-methylpiperidinol derived from acetic acid, propionic acid and butyric acid, it is reasonable to expect, from comparable studies with aryl derivatives (Table 3.1;(Masson et al., 2007)), these values to be similar to those for the comparable thioesters (Table 3.1). This is supported by the observation that for AChE, like the analogous thiocholine esters, the acetyl ester of *N*-methyl-4-piperidinethiol (**7**, Table 3.1) had the greatest affinity, followed by the propionyl ester (**8**), while the butyryl derivative (**9**) was not hydrolyzed by AChE under these conditions. In addition, BuChE affinity increased with longer substrate side chains, consistent with the known preference of this enzyme for longer acyl chains (Darvesh et al., 2006; Pottie et al., 2011). The observation that the thioester analogue of MP4B is BuChE-specific is also in keeping with the earlier report (Kikuchi, 2001) that the ester is only hydrolyzed by BuChE. Of note is that the affinities of the acetyl (**7**) and propionyl (**8**) thioesters for BuChE are greater than for AChE. Even though the corresponding radiolabelled esters, [^{11}C]-AMP and [^{11}C]-PMP, have been developed as AChE imaging agents, these kinetic results suggest that BuChE is also

capable of efficiently hydrolyzing these compounds and thus, both AChE and BuChE may be detected in molecular imaging studies with these agents, rendering them to be non-specific.

3.4.3 Structural Analysis

The preferred geometries of the synthetic thioesters and their ester counterparts were computed at the molecular mechanics level in order to further explore any subtle differences observed in the cholinesterase kinetic affinities. In general, the preferred conformations for each oxygen and sulfur analogous pair were comparable (Figure 3.3). However, slight differences in molecular shape, because of the presence of the bulkier and electronically distinct sulfur atom, most likely contributed to observed differences in relative affinity constants for BuChE (Table 3.1) in each analogous pair. The structural similarity further suggests that thioesters are acceptable kinetic surrogates for corresponding ester imaging agents.

3.4.4 Histochemical Evaluation of *N*-Methyl Piperidinyl Thioesters

Distribution of an imaging agent within the living brain is dependent upon a number of factors. These include cerebral blood flow, penetration of the blood-brain barrier, interaction with the target molecules and fate of the metabolites. Thus, determining the *in vitro* distribution of the imaging agent in brain tissues would be valuable before advancing to *in vivo* radioimaging studies. The cholinesterases are commonly stained in brain tissues using thioesters such as butyrylthiocholine or acetylthiocholine (Karnovsky and Roots, 1964; Darvesh and Hopkins, 2003). In order to

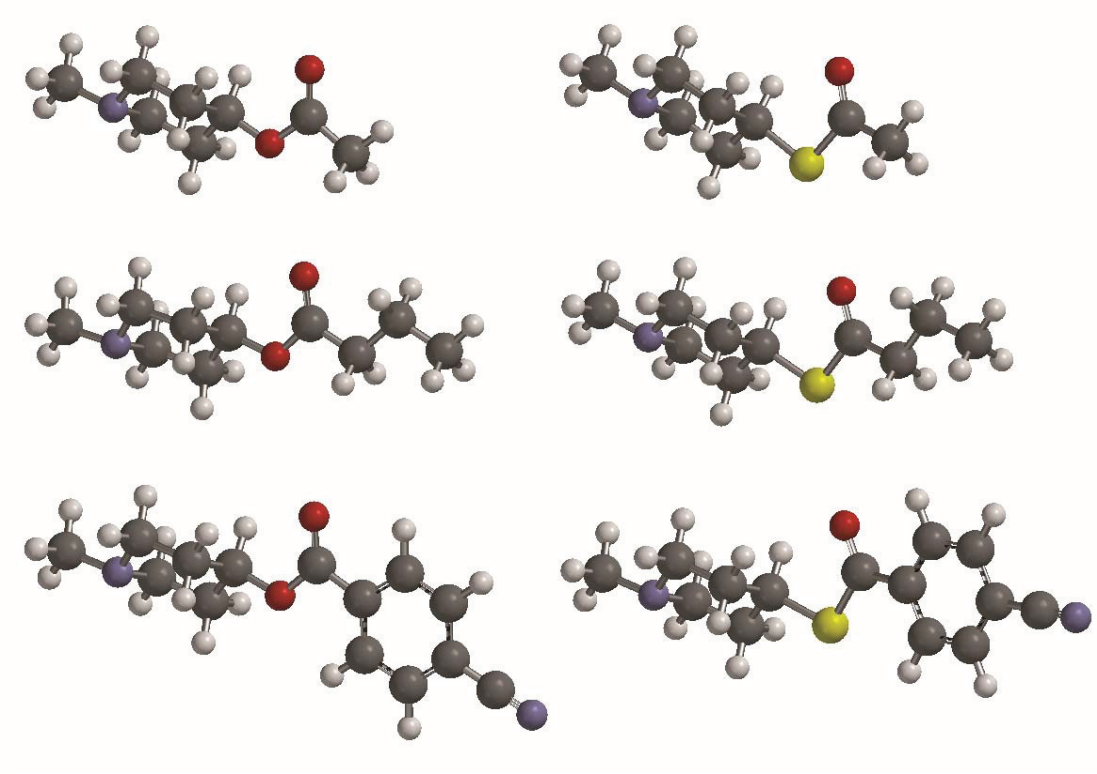

Figure 3.3. Preferred geometries of select *N*-methylpiperidinyl esters (left) and the corresponding thioesters (right).Note similarity in geometry between ester and thioester pairs. Top row: acetyl *N*-methylpiperidinyl derivatives. Middle row: butyryl *N*-methylpiperidinyl derivatives. Bottom row: cyano benzoate *N*-methylpiperidinyl derivatives.

explore cholinesterase specificity and to determine their potential to detect the distribution of cholinesterases in the brain, several of the thioesters prepared in this study were tested as histochemical substrates and compared with choline thioesters for staining human thalamus brain tissue (Figure 3.4). This region of the brain was chosen because it has been precisely mapped for cholinesterase activity and certain nuclei, such as the anteroventral (AV) nucleus (Figure 3.4A), exhibit distinct patterns of AChE and BuChE activity (Darvesh and Hopkins, 2003). In the AV nucleus of the thalamus, AChE activity is found only in the neuropil while BuChE activity is observed only in neurons. As can be seen in Figure 3.4, acetylthiocholine (Figure 3.4B) and *N*-methylpiperidinyl acetylthioester (**7**; Table 3.1; Figure 3.4C) show comparable neuropil staining typical of AChE activity in this nucleus. That is, both the choline and *N*-methylpiperidinethiol acetyl thioester substrates provided histochemical staining consistent with the previously described distribution of AChE in this region of the brain (Darvesh and Hopkins, 2003). This observation is also in agreement with the *in vitro* enzyme kinetic results indicating that AChE is capable of efficiently hydrolyzing the *N*-methylpiperidinyl acetylthioester (Table 3.1). *N*-methylpiperidinyl acetylthioester (**7**) is hydrolyzed by both AChE and BuChE (Table 3.1), similar to acetylthiocholine (Darvesh et al., 2003b), using Ellman method. However, the Modified Karnovsky-Roots method for histochemical staining requires shorter (1 h) incubation for staining AChE and longer (18 hr) for BuChE. Based on this difference in the incubation time, staining in Figure 3.4C is predominantly for AChE. Similarly, to evaluate specific histochemical visualization of BuChE activity in the human thalamus, comparative staining with butyrylthiocholine, *N*-methylpiperidinyl butyrylthioester (**9**; Table 3.1) and cyanobenzoate thioester (**4**; Table 3.1) was carried out

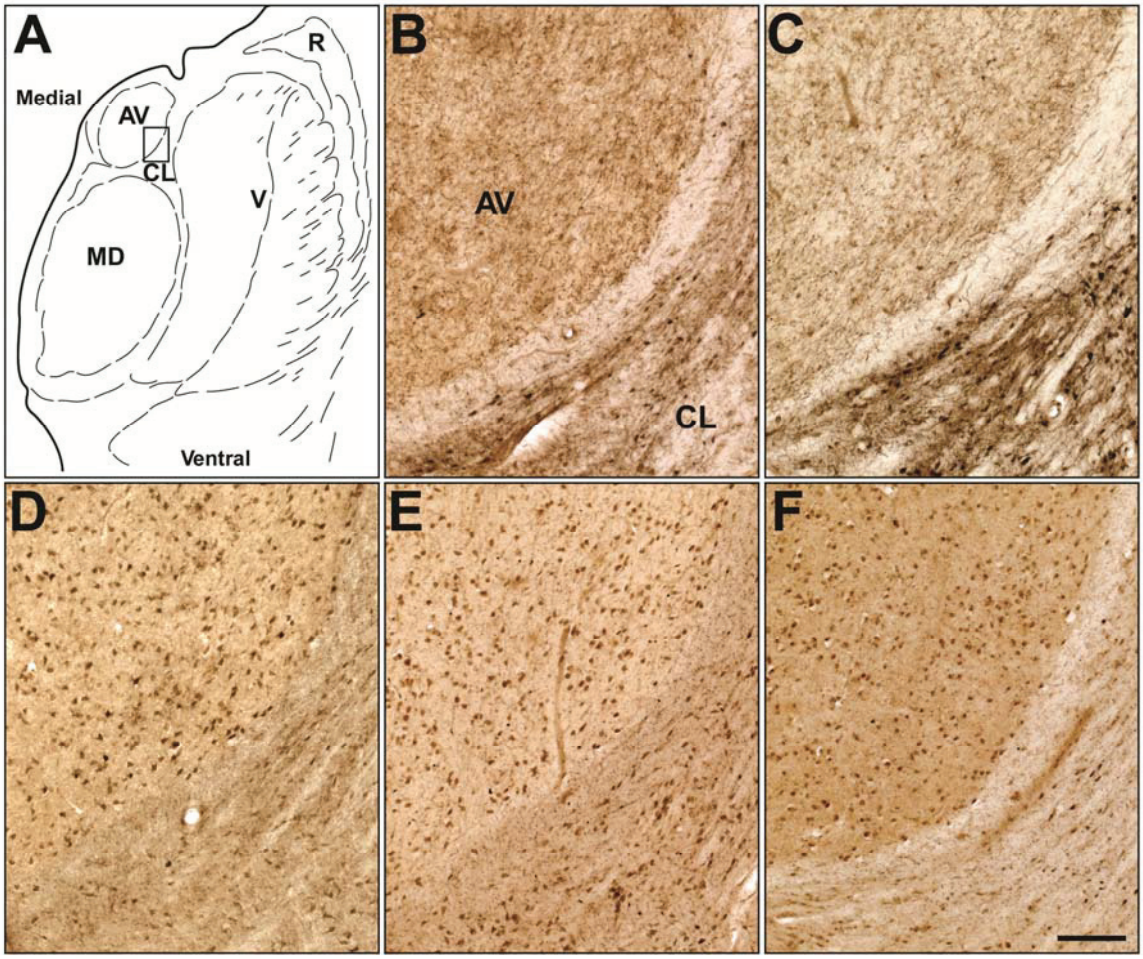

Figure 3.4. Histochemical staining of human brain tissue at the level of the thalamus in a coronal plane. **A.** Parcellation of the thalamus in the region used to compare histochemical staining by various cholinesterase substrates; **B.** Acetylthiocholine. **C.** (*N*-methylpiperidin-4-yl) ethanethioate. Note that both of these substrates produced a similar pattern of staining recapitulating the known distribution of acetylcholinesterase in this region. **D.** Butyrylthiocholine. **E.** (*N*-methylpiperidin-4-yl) butanethioate. **F.** (*N*-methylpiperidin-4-yl) 4-cyanobenzenecarbothioate. Note that these substrates produced a similar pattern of distribution that reflected the known distribution of butyrylcholinesterase in this region. AV: anteroventral nucleus, CL: central lateral nucleus, MD: mediodorsal, R: reticular nucleus, V: Ventral nuclei. Scale bar = 200 μm.

(Figure 3.4D, E, F). BuChE staining using butyrylthiocholine as substrate (Figure 3.4D) was comparable to that obtained with the butyryl (Figure 3.4E) and 4-cyanobenzoyl (Figure 3.4F) derivatives of *N*-methylpiperidinethiol. Furthermore, the BuChE staining profiles (Figure 3.4D, E, F) were distinct from those for AChE observed with the acetyl thioesters (Figure 3.4B and C) in the same region of the brain. High (> 1 mM) thioester concentrations are typically required in the staining medium to achieve adequate visualization of cholinesterase activity. Because of this, solubility limitations prohibited use of the iodo- and fluorobenzoate thioesters in similar histochemical analysis to that provided by the cyanobenzoate derivative (Figure 3.4F). However, successful histochemical recapitulation of enzyme activity with an aryl thioester provides a critical proof-of-principle that analogous radiolabelled compounds are potential imaging agents to be highly sensitive detectors of cholinesterase activity in brain tissue.

3.5 Conclusions

This study indicates that *N*-methylpiperidinyl thioesters are effective surrogate substrates for the evaluation and development of corresponding ester compounds as AChE and BuChE imaging agents. These thioester analogues have comparable affinities towards AChE and BuChE to their ester counterparts. These similarities permit screening of corresponding ester substrates as potential radioligands for specific detection of AChE or BuChE activity. These thioester compounds can also be employed for histochemical detection of enzyme activity in brain tissue which could then be used for comparison with the *in vivo* images generated by the analogous radiolabelled molecules. Development of compounds, screened in this manner, could facilitate discovery of

suitable molecular imaging agents for the detection of AChE and BuChE in the living brain for application to neurological disorders involving the cholinergic system, such as AD.

CHAPTER 4 CARBAMATE DERIVATIVES AS IMAGING AGENTS

4.1 PREFACE

Chapters 2 and 3 described the development of ester and thioester compounds as potential cholinesterase imaging agents. A significant drawback to these molecules is that they are rapidly hydrolyzed by AChE and BuChE and thus, may be subject to diffusion away from *in vivo* sites of enzyme activity. This may limit the utility of ester derivatives as imaging agents for cholinesterases. In contrast, cholinesterase hydrolysis of compounds containing a carbamate functional group is much slower than esters. Therefore, imaging agents possessing carbamate functionality have great promise for visualizing cholinesterases. This Chapter presents the synthesis, kinetic analysis, radiolabelling and *in vitro* tissue evaluation of a carbamate compound as a potential cholinesterase imaging agent. The content of this Chapter describes work done as part of this thesis and has been the subject of US Provisional Patent Application No. 61/697,114.

4.2 INTRODUCTION

Alzheimer's disease (AD) is a neurodegenerative disorder and is the most common cause of dementia in older adults (Blennow et al., 2006). The prevalence of AD is predicted to dramatically rise over the next few decades with concomitant increases in social and economic burdens related to the disease (World Health Organization and Alzheimer's Disease International, 2012). Efforts towards the development of disease-modifying interventions for AD are hampered by the lack of an early and definitive diagnosis. Currently, diagnosis of AD must be confirmed by post-mortem brain visualization of β-amyloid (Aβ) plaques and tau neurofibrillary tangles, two hallmarks of

the disease (Hyman and Trojanowski, 1997). Brain imaging methods have emerged for the visualization of Aβ plaques in the living human brain to aid in the diagnosis of AD. This approach has involved the development of imaging agents, such as 2-(4'-dimethylaminophenyl)-6-[^{123}I]iodo-imidazo[1,2-a]pyridine (IMPY) (Kung et al., 2004), [*N*-Methyl-[^{11}C]2-(4'-methylaminophenyl)-6-hydroxybenzothiazole (PIB) (Klunk et al., 2004) and (*E*)-4-(2-(6-(2-(2-(2-([^{18}F]-fluoroethoxy)ethoxy)ethoxy)pyridin-3-yl)vinyl)-*N*-methyl benzenamine (Florbetapir) (Clark et al., 2012) that bind to Aβ plaques *in vivo* and are visualized using single photon emission computed tomography (SPECT) or positron emission computed tomography (PET). However, a significant number of cognitively normal adults have Aβ plaque pathology without exhibiting clinical evidence of AD (Mortimer, 2012). This limits the utility of Aβ plaque imaging for the pre-mortem definitive diagnosis of AD since it has the potential to identify false positives.

Changes in the cholinergic system have long been associated with AD (Davies and Maloney, 1976; Bartus et al., 1982; Coyle et al., 1983), in particular there is loss of acetylcholine containing neurons in the basal forebrain and other regions. Two enzymes, acetylcholinesterase (AChE) and butyrylcholinesterase (BuChE), hydrolyze acetylcholine and thus, co-regulate cholinergic neurotransmission in the brain (Darvesh et al., 2003a). These enzymes also associate with Aβ plaques in AD (Geula and Mesulam, 1989; Moran et al., 1993; Gomez-Ramos et al., 1994; Geula and Mesulam, 1995; Darvesh et al., 2010a). The nature of this association remains unknown but may be related to plaque formation and maturation (Guillozet et al., 1997). This notion is supported by the fact that these enzymes, in particular BuChE, associate with a subpopulation of plaque pathology (Darvesh et al., 2012b). Therefore, AChE and BuChE may be specific

markers for Aβ plaques indicative of AD. Imaging of cholinesterases in the brain, because of their association with Aβ pathology, may provide an early and definitive diagnosis of AD (Darvesh, 2013).

Imaging agents targeting AChE (Irie et al., 1994; Irie et al., 1996; Kilbourn et al., 1996; Snyder et al., 1998) and BuChE (Kikuchi, 2001; Snyder et al., 2001; Kikuchi et al., 2004; Macdonald et al., 2011) have been developed for human brain imaging of AD pathology (Figure 4.1). However, visualization of these enzymes associated with AD plaques has not been realized using these compounds. A significant drawback to such imaging agents is that, being cholinesterase ester substrates, they are rapidly metabolized by these enzymes. Thus, the ability to image cholinesterase activity with these agents relies on the 'metabolic trapping principle' (Irie et al., 1994; Kikuchi et al., 2007) in which a radiolabelled hydrophilic product of enzyme catalysis gets trapped within the brain following ester hydrolysis. In contrast, compounds containing a carbamate functional group, which are also cholinesterase substrates, are able to form a long-lived intermediate with these enzymes ('enzymatic trapping'), potentially leading to a prolonged association. A radiolabelled imaging agent containing carbamate functionality is expected to have a longer binding duration to cholinesterases compared to ester substrates, thus improving visualization of cholinesterase activity associated with structures such as Aβ plaques.

Herein, are detailed the synthesis, radiolabelling and evaluation of phenyl 4-([^{123}I]iodo)phenylcarbamate (^{123}I-PIP) that exhibits affinity towards cholinesterases. It is demonstrated that this compound is able to visualize cholinesterases associated with Aβ plaques in human AD brain tissues using autoradiography. In addition, this

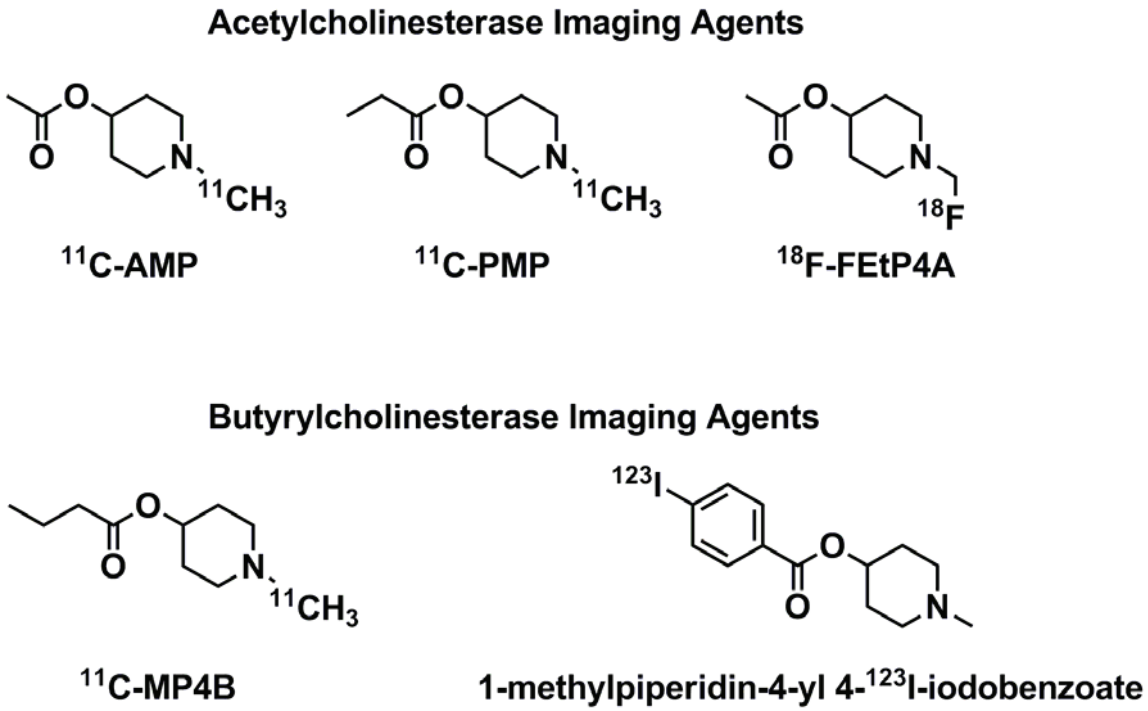

Figure 4.1. PET and SPECT ester-type brain imaging agents for acetylcholinesterase and butyrylcholinesterase. *N*-[^{11}C]methylpiperidyl acetate, ^{11}C-AMP; *N*-[^{11}C]methylpiperidyl propionate, ^{11}C-PMP; *N*-[^{18}F]fluoroethylpiperidin-4-yl acetate, ^{18}F-FEtP4A; 1-^{11}C-Methyl-4-piperidinyl n-butyrate, ^{11}C-MP4B.

molecule is compared with the Aβ plaque imaging agent, ^{123}I-IMPY, for the ability to distinguish Aβ plaques in AD brain tissues from those in cognitively normal brain.

4.3 Materials and Methods

4.3.1 Synthesis Materials

Phenol, 4-iodophenylisocyanate, hexabutylditin, 2-amino-5-pyridine, tetrakis(triphenylphosphine)palladium, sodium bicarbonate, triisopropylsilyl triflate, triethylamine and purified recombinant human acetylcholinesterase were obtained from Sigma Aldrich (St. Louis, USA). 2-Bromo-1-(4-dimethylaminophenyl)ethanone was obtained from Santa Cruz Biotechnology (Santa Cruz, USA). Purified human plasma butyrylcholinesterase was a gift from Dr. Oksana Lockridge (University of Nebraska Medical Center). Na^{123}I was obtained from MDS Nordion (Vancouver, CAN) in 0.1 N NaOH. Synthetic reactions were performed under an argon atmosphere (99.999% purity, Air Liquide).

4.3.2 Compound Characterization

Melting points were determined using a Fisher-Johns melting point apparatus. Infrared spectra were recorded as Nujol mulls or as neat liquids between sodium chloride plates on a Nicolet Avatar 330 FT- IR spectrometer. Peak positions were reproducible within 1–2 cm^{-1}. Nuclear magnetic resonance spectra were recorded at the Nuclear Magnetic Resonance Research Resource (NMR-3), Dalhousie University, on a Bruker AVANCE 500, operating at 500.1 MHz for ^{1}H and 125.8 MHz for ^{13}C. Chemical shifts are reported in parts per million relative to Me_4Si in $CDCl_3$ or DMSO. For ^{1}H NMR

experiments, the coupling constants are reported in Hertz and the multiplicities are apparent. For ^{13}C NMR data, the number of attached protons for each signal, as determined by a DEPT experiment, are given in parentheses. Low-resolution mass spectra were obtained using an Agilent 6890N GC with an Agilent 6890N Electron Impact MS (Waldbronn, Germany) operating at 70 eV. High-resolution mass spectra were obtained with accurate mass positive-ion electrospray ionization measurements recorded at the Mass Spectrometry Laboratory at Dalhousie University using a Bruker Daltonics microTOF with a flow rate of 2 μL/min, spray voltage of 4500 V and tray temperature of 180 °C or were recorded on a CEC 21-110B spectrometer using electron ionization at 70 V and an appropriate source temperature with samples being introduced by means of a heatable port probe. Mass measurements were within 3 ppm of the calculated value. Purity of all compounds was determined using an Agilent Technologies 1200 series HPLC system with a reverse phase C18 column and methanol as the mobile phase.

4.3.3 Synthesis and Radiolabelling

Synthesis of Phenyl 4-(iodo)phenylcarbamate (**1**, PIP)

Phenol (1.021 g, 10.85 mmol) was dissolved in dry toluene (2 mL) under argon atmosphere and 4-iododiphenylisocyanate (2.658 g, 10.85 mmol), dissolved in dry toluene (13 mL), was added to the solution. The reaction was refluxed for 5 h, hot gravity filtered and the resulting white crystals collected (1.983 g, 54%). Analytical Data. $MP_{(toluene)}$: 159-161 ºC. IR (Nujol): 3316, 1734, 1709, 1590, 1534, 1232 cm^{-1}. ^1H NMR ($CDCl_3$): δ 6.95 (s, 1H), 7.19 (d, J = 7.3 Hz, 2H), 7.24-7.28 (m, 3H), 7.41 (t, J =

7.3 Hz, 2H), 7.65 (d, J = 8.6 Hz, 2H). ^{13}C NMR ($CDCl_3$): δ 87.0, 120.6, 121.6, 125.9, 129.5, 137.2, 138.1, 150.4, 151.4. EI-MS m/z: 90 (21), 118 (11), 217 (2), 245 (100). HRMS (ESI): MNa^+ found 361.9648, calcd for $C_{13}H_{10}INNaO_2^+$ = 361.9648.

Synthesis of Phenyl 4-(tributylstannyl)phenylcarbamate (**2**)

Phenyl 4-(iodo)phenylcarbamate (**1**, 0.200 g, 0.59 mmol) was suspended in dry CH_2Cl_2 (10 mL) under argon atmosphere. To this was added triethylamine (0.180 mL, 1.3 mmol) followed by triisopropyl triflate (0.32 mL, 1.2 mmol). This solution was then added to tetrakistriphenylphosphate palladium (0.026 g, 0.023 mmol) and to this was added hexabutylditin (0.60 mL, 1.2 mmol). The reaction was refluxed for 16 h and purified by silica gel flash chromatography (1:9 ethyl acetate/hexanes) to yield a white solid (0.147 g, 50%). Analytical Data. $MP_{(hexanes)}$: 53-55 ºC. IR (Nujol): 3331, 2852, 1719 cm^{-1}. ^{1}H NMR ($CDCl_3$): δ 0.95 (t, J = 7.3 Hz, 9H), 1.09-1.12 (m, 6H), 1.37 (sex, J = 7.4 Hz, 6H), 1.55-1.60 (m, 6H), 6.90 (s, 1H), 7.19-7.25 (m, 3H), 7.39-7.44 (m, 6H). ^{13}C NMR ($CDCl_3$): δ 9.6, 13.7, 27.4, 29.1, 118.3, 118.4, 121.6, 125.7, 129.4, 136.7, 137.2, 150.6, 151.5. EI-MS m/z: 352 (100%), 296 (60%), 238 (98%), 162 (9%), 119 (9%). HRMS (ESI): MNa^+ found 526.1738, calcd for $C_{25}H_{37}NNaO_2Sn^+$ = 526.1738.

Synthesis of Phenyl 4-([^{123}I]iodo)phenylcarbamate (**3**, ^{123}I-PIP)

To a solution (9 μL) of $Na^{123}I$ (64.42 MBq) in 0.1 M $NaOH_{(aq)}$ ($9.0x10^{-7}$ mol) was added 0.1 M HCl (18 μL, $1.8x10^{-6}$ mol) to neutralize the hydroxide. Phenyl 4-(tributylstannyl)phenylcarbamate (**2**, 50 μL, $4.0x10^{-7}$ mol) was added to the solution followed by *N*-chlorosuccinimide (NCS, 28 μL, $8.4x10^{-8}$ mol), both of which were

dissolved in MeOH. The reaction proceeded for 15 min at room temperature; then 0.1 M $NaHCO_3$ (27 μL, $2.7x10^{-3}$ mol) was added to quench the reaction. Purification was accomplished by HPLC, using an Agilent system with a Zorbax Eclipse XDB-C18, 4.6x150 mm, 5 μm column (Agilent Technologies), and 1.0 mL/min of 80% $MeOH_{(aq)}$ eluent. Fractions were collected every 20 sec for 15 min with a RediFrac fraction collector (Amershan Biosciences). Retention times were determined using the corresponding cold PIP (**1**) as a non-radioactive standard. Collected fractions that contained purified product were combined, acidified with 0.1 M HCl and the solvent removed under a stream of N_2 gas with heating to yield the desired radiolabelled compound as a residue (radiochemical yield 87%, radiochemical purity >96%). The residue was dissolved in 0.1 M maleate buffer pH 7.4 for incubation with tissue.

Synthesis of 2-(4'-Dimethylaminophenyl)-6-iodoimidazol[1,2-a]pyridine (IMPY, **4**)

IMPY was synthesized according to a previously published procedure (Zhuang et al., 2003). Briefly, 2-Bromo-1-(4-dimethylaminophenyl)ethanone (0.484 g, 2 mmol) and 2-amino-5-pyridine (0.440 g, 2 mmol) were dissolved in ethanol (25 mL) under argon atmosphere. The solution refluxed for 2 h before returning to room temperature. $NaHCO_3$ (0.250 mg, 3 mmol) was added and the reaction refluxed. After 4 h the mostly clear yellow solution was returned to room temperature and a yellow precipitate formed. The precipitate was collected and recrystallized from ethanol to produce yellow crystals (0.088 mg, 12%). Analytical Data was consistent with the literature (Zhuang et al., 2003). $MP_{(ethanol)}$: 234-236 ºC. IR (Nujol): 1613, 1504, 1368, 794 cm^{-1}. ^1H NMR ($CDCl_3$): δ 3.02 (s, 6H), 6.79 (d, J = 8.9 Hz, 2H), 7.30 (dd, J = 9.5, 1.5 Hz, 1H), 7.40 (d, J = 9.6 Hz,

1H), 7.69 (s, 1H), 7.82 (d, J = 9.2 Hz, 2H), 8.35 (dd, J = 0.9, 0.6 Hz, 1H). ^{13}C NMR ($CDCl_3$): δ: 40 (3), 74 (0), 106 (1), 112 (1), 118 (1), 121 (0), 127 (1), 130 (1), 132 (1), 144 (0), 147 (0), 151 (0). EI-MS m/z: 363 (100), 347 (7), 235 (5), 220 (9), 181 (9). HRMS (ESI): MH^+ found 364.0314, calcd for $C_{15}H_{15}IN_3^+$ = 364.0305.

Synthesis of 2-(4'-Dimethylaminophenyl)-6-tributylstannylimidazol[1,2-a]pyridine (**5**)

To tetrakistriphenylphosphate palladium (0.020 g, 0.017 mmol) was added 2-(4'-dimethylaminophenyl)-6-iodoimidazol[1,2-a]pyridine (**4**, 0.201 g, 0.55 mmol) suspended in toluene (25 mL) followed by hexabutylditin (0.84 mL, 1.7 mmol) under argon atmosphere. The reaction was refluxed for 40 h and purified using silica gel column chromatography (1-5% MeOH/CH_2Cl_2) to yield a brown oil (0.193 g, 66%). Analytical Data. IR (Neat): 2955, 2925, 2870, 2851, 1614, 1505, 1338, 798 cm^{-1}. ^{1}H NMR ($CDCl_3$): δ 0.96 (t, J = 7.4 Hz, 9H), 1.08-1.23 (m, 6H), 1.40 (sext, J = 7.3 Hz, 6H), 1.53-1.68 (m, 6H), 3.04 (s, 6H), 6.80 (d, J = 8.9 Hz, 2H), 7.12 (dd, J = 9.4, 0.9 Hz, 1H), 7.57 (d, J = 8.6 Hz, 1H), 7.72 (s, 1H), 7.85 (d, J = 8.8 Hz, 2H), 8.35 (t, J = 0.9, 1H). ^{13}C NMR ($CDCl_3$): δ: 10 (2), 14 (3), 27 (2), 29 (2), 41 (3), 106 (1), 112 (1), 117 (1), 121 (0), 122 (0), 127 (1), 130 (1), 131 (1), 146 (0), 146 (0), 150 (0). EI-MS m/z: 361 (24), 269 (100), 213 (24), 177 (25), 155 (19). HRMS (ESI): MH^+ found 528.2386, calcd for $C_{27}H_{42}N_3Sn^+$ = 528.2395.

Synthesis of 2-(4'-Dimethylaminophenyl)-6-[^{123}I]iodoimidazol[1,2-a]pyridine (**6**, ^{123}I-IMPY)

To a solution (1 μL) of $Na^{123}I$ (2.90 MBq) in 0.1 M $NaOH_{(aq)}$ ($1.0x10^{-7}$ mol) was added 1 M HCl (50 μL, $5.0x10^{-5}$ mol), 2-(4'-Dimethylaminophenyl)-6-tributylstannylimidazol[1,2-a]pyridine (**5**) dissolved in MeOH (50 μL, $3.8x10^{-7}$ mol) and 3% $H_2O_{2\,(aq)}$ (50 μL, $4.41x10^{-4}$ mol). After 15 min at room temperature, 1 M NaOH (100 μL, $1x10^{-4}$ mol) was added. Purification was accomplished by HPLC, using an Agilent system with a Zorbax Eclipse XDB-C18, 4.6x150 mm, 5 μm column (Agilent Technologies), and 1.0 mL/min of 80% $MeOH_{(aq)}$ eluent. Fractions were collected every 20 sec for 15 min with a RediFrac fraction collector (Amershan Biosciences). Retention times were determined using the corresponding cold IMPY (**4**) as a non-radioactive standard. Collected fractions that contained purified product were combined and the solvent removed under a stream of N_2 gas with gentle heating to yield the desired radiolabelled compound as a residue (radiochemical yield 71%, radiochemical purity >99%). Radiochemical purity was comparable to literature (Zhuang et al., 2003). The residue was dissolved in 0.1% bovine serum albumin in maleate buffer pH 7.4 for incubation with tissue.

4.3.4 Esterase Activity Assay

The ability of the compounds to inhibit cholinesterases was evaluated by using a modification (Darvesh et al., 2001) of Ellman's spectrophotometric method (Ellman et al., 1961) using human recombinant AChE and acetylthiocholine as the substrate, or human serum BuChE with butyrylthiocholine as the substrate. The esterase activity of AChE

and BuChE was determined by adding 0.05 mL of 4.8 mM substrate (acetylthiocholine for AChE or butyrylthiocholine for BuChE, in 50% $CH_3CN_{(aq)}$) to 1.40 mL of buffered 5, 5'-dithio-bis(2-nitrobenzoic acid) (DTNB) solution (pH 8.0) and 0.05 mL of enzyme (~0.04 U), to initiate the reaction. Assays were carried out at 23 °C over a 1 min period, taking readings every 5 s, after initial 5 s delay using a Milton-Roy 1201 UV-visible spectrophotometer (Milton- Roy, Ivyland, PA), set at λ: 412 nm. 0.1 U is the amount of cholinesterase that gives a ΔA/min of 1.0 under the conditions described. To test for enzyme deactivation over time, loss of enzyme activity was monitored. Briefly, 1.35 mL of buffered DTNB solution (pH 8.0), 0.05 mL of enzyme (~0.04 U of BuChE or AChE in 0.1% aqueous gelatin containing 0.01% sodium azide) and 0.05 mL of 1 mM PIP (**1**) dissolved in 50% $CH_3CN_{(aq)}$ in a stoppered cuvette of 1 cm path length. After mixing and bringing the absorbance to zero, 0.05 mL of 4.8 mM aqueous acetyl- or butyrylthiocholine substrate solution was added to the cuvette after incubation of the enzyme with PIP (**1**) and buffered DTNB for periods of up to 10 min. A zero- time sample was also obtained by adding enzyme last to initiate reaction and the second-order rate constants for enzyme deactivation (k_a values) were determined as previously described (Darvesh et al., 2003b). The k_a value was calculated by plotting the extent of inhibition, given by $\ln (e_0/e_t)/[I]$, against time, where e_0 is the enzymatic activity at time zero (without preincubation of enzyme and inhibitor), e_t is the enzymatic activity at time t min of preincubation, and [I] is the molar concentration of inhibitor. The slope of this plot gave the second-order rate constant. Experiments were done at least in triplicate and the values averaged.

4.3.5 *In Vitro* Autoradiography with Mouse and Human Tissues

4 Male B6SJL wild-type (WT) mice and 4 male 5XFAD (B6SJL-Tg(APPSwFlLon,PSEN1*M146L*L286V)6799Vas/Mmjax) mice were obtained from Jackson Laboratory (Bar Harbor, ME). Animals were cared for according to the guidelines set by the Canadian Council on Animal Care. Formal approval to conduct the experiments was obtained from the Dalhousie University Committee on Laboratory Animals. Mice were sacrificed by somnitol injection, perfused transcardially with saline (25 mL, 0.9% NaCl, 0.1% $NaNO_3$) followed by fixative (50 mL, 4% formalin). Brains were removed, post-fixed for 1 hour, frozen with dry ice and cut in 40 μm serial sections on a SM2000R Leica microtome with a freezing stage and BFS-30TC controller (Physitemp). Human brain tissues from 4 normal and 4 AD cases used in this study were provided by the Maritime Brain Tissue Bank, (Dalhousie University, Department of Medical Neuroscience, Halifax, Nova Scotia, Canada), following approval from the Capital Health Ethics Board. After removal, brains were immersion fixed in 10% formalin in 0.1 M phosphate buffer (pH 7.4) and cut in 1–2 cm coronal slabs. These slabs were cryoprotected by immersion in increasing concentrations of sucrose, ranging from 10% to 40% in 0.1 M phosphate buffer (pH 7.4). Brain tissue was in each concentration of sucrose solution for approximately 48 h and stored in 40% 0.1 M phosphate buffered sucrose (pH 7.4) with 0.6% sodium azide until used. Blocks of tissue from the orbitofrontal cortex, an area of high Aβ plaque accumulation in AD, were cut on a on a Leica SM2000R microtome with Physitemp freezing stage and BFS-30TC controller in 50 μm sections. Sections were stored in 40% sucrose in 0.1 M phosphate buffer (pH 7.4) at −20˚C until used. Prior to use, sections were thawed and rinsed in

0.1M maleate buffer pH 7.4. To each human tissue section in 900 µL of 0.1M maleate buffer pH 7.4 was added 100 µL of maleate buffer pH 7.4 containing ^{123}I-PIP (**3**, 1.1 MBq) and the tissue incubated for 3 h with gentle agitation. The tissue was then rinsed twice for 1 min in distilled water, mounted, dried on a slide warmer and exposed to a high resolution phosphorimaging screen (GE Healthcare). The screen was scanned with a typhoon 9400 imager (GE Healthcare) to produce the autoradiogram. Images were saved in ImageQuant and contrast was adjusted with Adobe Photoshop CS5.

Sections to be incubated with ^{123}I-IMPY (**6**) were first thawed, washed in maleate buffer pH 7.4, mounted and dried. The sections were rehydrated in maleate buffer pH 7.4 for 3 min and incubated in 35 mL maleate buffer pH 7.4 with 560 µL of 0.1% bovine serum albumin in maleate buffer pH 7.4 containing ^{123}I-IMPY (**6**, 1.7 MBq/per section). The tissue was incubated for 1 h with gentle agitation and subsequently rinsed for 2 min in saturated Li_2CO_3 in 50% $EtOH_{(aq)}$, 2 min in 50% $EtOH_{(aq)}$, and 30 sec in distilled water. The sections were dried, exposed to the phosphorimaging screen and images generated as described above.

4.3.6 Butyrylcholinesterase Histochemistry

A modified Karnovsky-Roots method was used for examination of BuChE activity in brain sections, as described previously (Darvesh et al., 2012b). Briefly, 50 µm brain sections, adjacent to those used for *in vitro* autoradiography, were rinsed in 0.1 M maleate buffer (pH 7.4) for 30 min. Tissue was incubated in 0.15% H_2O_2 in 0.1 M maleate buffer pH 7.4 to quench endogenous peroxidase activity. Tissue was reacted for 2.5 h at room temperature in an incubation medium containing 0.5 mM sodium citrate,

0.47 mM cupric sulfate, 0.05 mM potassium ferricyanide, 0.8 mM butyrylthiocholine iodide and 0.01 mM 1,5-bis (4-allyl dimethylammonium phenyl) pentan-3-one dibromide (BW 284 C 51) in 0.1 M maleate buffer (pH 6.8). Sections were rinsed with gentle agitation for 30 min in distilled water and placed in 0.1% cobalt II chloride in water for 10 min. After a further rinse in distilled water, sections were placed in a solution of 1.39 mM 3,3'-diaminobenzidine tetrahydrochloride (DAB) in 0.1M phosphate buffer (pH 7.4). After 5 min, a solution of 0.3% hydrogen peroxide in distilled water was added at a ratio of 20:1 (DAB solution : hydrogen peroxide solution) and the reaction was carried out for approximately 4 min. Sections were then washed in 0.1 M acetate buffer, pH 3.3, mounted on slides and coverslipped.

4.3.7 B-Amyloid Immunohistochemistry of Human Tissue

Adjacent sections to those used for *in vitro* autoradiography were rinsed for 30 min in 0.1 M phosphate buffer (pH 7.4), 5 min in 0.05 M phosphate buffer (pH 7.4) and 15 min in distilled water. Sections were treated with 90% formic acid with gentle agitation for 2 min for Aβ antigen retrieval (Kitamoto et al., 1987). Sections were rinsed 5 times in dH_2O for 1 minute each and 2 times in phosphate buffer for 15 minutes. Sections were placed in 0.3% H_2O_2 in PB for 30 minutes to quench endogenous peroxidase activity and rinsed again for 30 minutes in PB. Sections were then incubated in PB containing 0.1% Triton X-100, normal goat serum (1:100), and a polyclonal rabbit anti Aβ antibody (1:400; 71-5800, Invitrogen, Camarillo, CA), specific for the 4- to 5-kDa amyloid peptide (Jankowsky et al., 2007) for approximately 16 h at room temperature. After rinsing, sections were incubated in PB with 0.1% Triton X-100,

biotinylated goat anti-rabbit secondary antibody (1:500), and normal goat serum (1:1000) for 1 h. After another rinse, sections were placed in PB with 0.1% Triton X-100 and Vectastain Elite ABC kit (1:182; PK- 6100, Vector Laboratories, Burlingame, CA), according to the manufacturer's instructions for 1 h. Sections were rinsed and developed in a solution of PB containing 1.39 mmol/L DAB. After 5 min, 50 μL of 0.3% H_2O_2 in dH_2O was added per ml of DAB solution, and the sections were incubated for 2-3 min. The reaction was stopped by rinsing the sections in 0.01 M acetate buffer (pH 3.3).

4.3.8 Thioflavin-S Staining

Sections were mounted onto glass slides, air-dried, rehydrated in dH_2O, dehydrated in a series of ethanol washes, cleared in xylene, and rinsed in 50% ethanol. Sections were then incubated for 20 h in a solution of 0.05% thioflavin-S in 50% ethanol, rinsed in 80% ethanol and dH_2O, and coverslipped with a glycerol/gelatin mounting medium.

Sections were analyzed and photographed on a Zeiss Axioplan 2 motorized microscope with a Zeiss Axiocam HRc digital camera and AxioVision 4.6 software. Image levels were adjusted in Adobe Photoshop CS5 so the background from different images matched.

4.4 Results

4.4.1 Synthesis and Radiolabelling

Phenyl 4-iodophenylcarbamate (PIP, **1**) was synthesized from phenol and 4-iodophenylisocyanate as shown in Figure 4.2. Radiolabelling proceeded by necessary

protection of the carbamate functionality with a triisopropylsilyl group and subsequent generation of a tributyltin intermediate followed by introduction of ^{123}I. Synthesis of IMPY (**4**) followed a previously published procedure (Zhuang et al., 2003) according to Figure 4.3. The corresponding tributyl tin intermediate was generated and ^{123}I introduced. ^{123}I-PIP (**3**) and ^{123}I-IMPY (**6**) were both purified by HPLC and recovered in high yield and purity (Figure 4.4).

4.4.2 Cholinesterase Kinetics

PIP (**1**) demonstrated inhibition of both AChE and BuChE that was time dependent, as determined with second-order deactivation constants (k_a values). Deactivation by PIP was more rapid towards AChE (k_a: 1.56±0.18 x10^4 M^{-1} min^{-1}) compared to BuChE (k_a: 3.47±0.82 x10^2 M^{-1} min^{-1}, Figure 4.5).

4.4.3 Mouse Tissue Autoradiography

The distribution of ^{123}I-PIP and ^{123}I-IMPY was determined *in vitro* in WT and 5XFAD mouse brain sections (Figure 4.6). These same sections were subsequently stained with thioflavin-S to visualize Aβ aggregations. Both ^{123}I-PIP and ^{123}I-IMPY were found to accumulate in areas of high Aβ plaque burden as assessed with thioflavin-S staining. In addition, ^{123}I-PIP accumulated in the white matter in both the WT and 5XFAD tissues, a region of high BuChE activity. Some accumulation of ^{123}I-IMPY was also observed in the white matter of the 5XFAD animals.

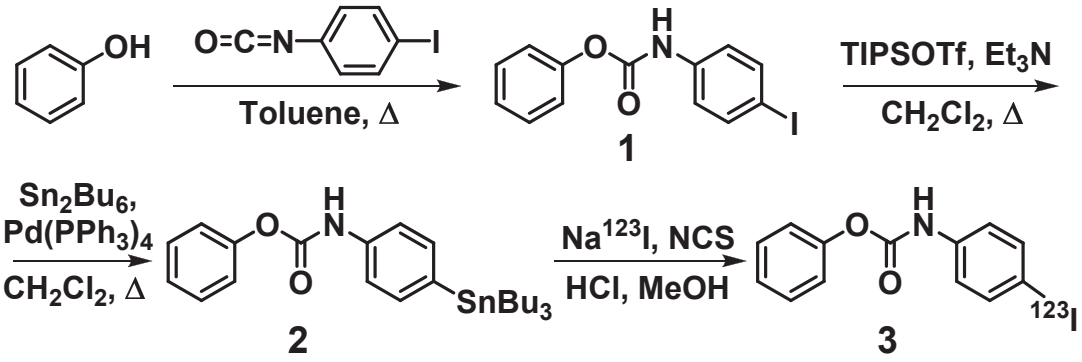

Figure 4.2. Synthesis of phenyl 4-(iodo)phenylcarbamate (**1, PIP**), corresponding tributyltin precursor (**2**) and ^{123}I radiolabelled product (**3, ^{123}I-PIP**). TIPSOTf: Triisopropylsilyl trifluoromethanesulfonate. Et_3N: Triethylamine. Sn_2Bu_6: Hexabutylditin. $Pd(PPh_3)_4$: Tetrakis(triphenylphosphine)palladium(0). NCS: *N*-Chlorosuccinimide.

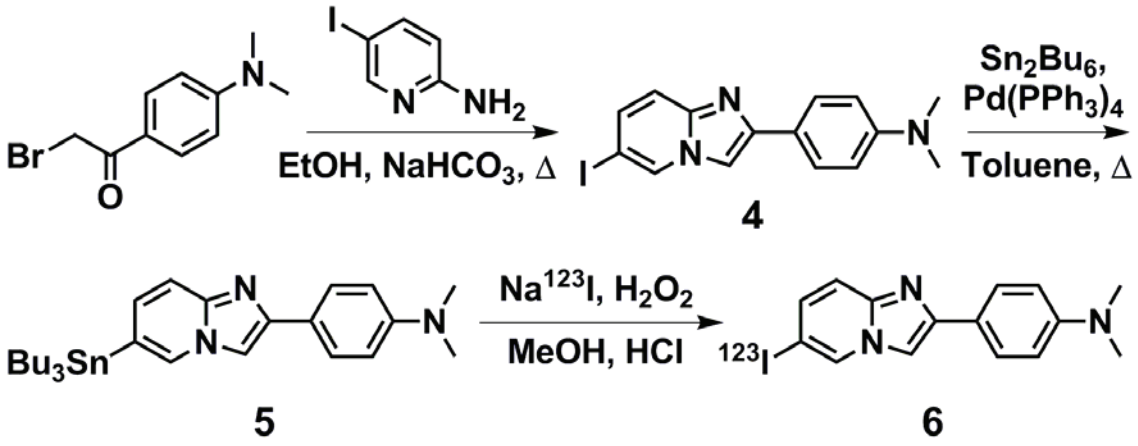

Figure 4.3. Synthesis of 2-(4'-dimethylaminophenyl)-6-iodoimidazol[1,2-a]pyridine (**4**, **IMPY**), corresponding tributyltin precursor (**5**) and ^{123}I labelled product (**6, ^{123}I-IMPY**). Sn_2Bu_6: Hexabutylditin. $Pd(PPh_3)_4$: Tetrakis(triphenylphosphine)palladium(0).

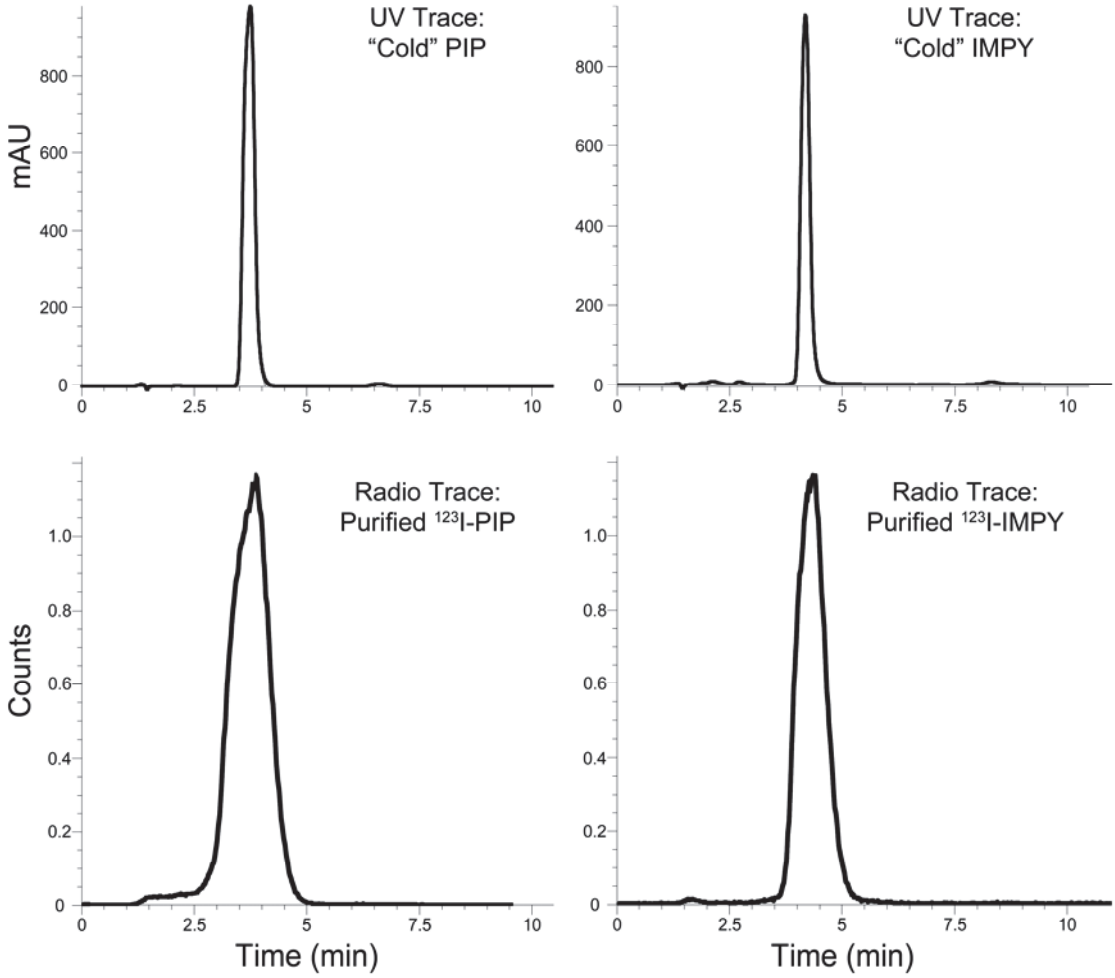

Figure 4.4. HPLC trace of unlabelled ("cold") PIP (**1**) and IMPY (**4**, top) and corresponding radiotrace of purified ^{123}I-PIP (**3**) and ^{123}I-IMPY (**6**, bottom).

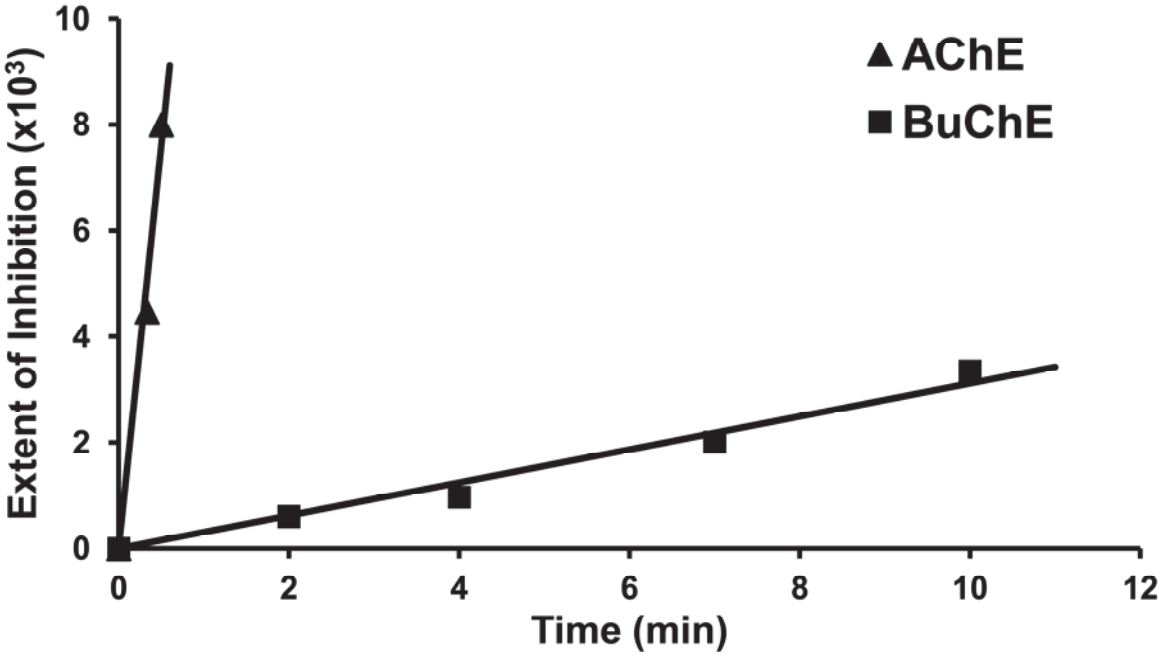

Figure 4.5. Plots to determine second-order rate constants (k_a values) of PIP (**1**) with AChE and BuChE. The slopes of these plots yield k_a values.

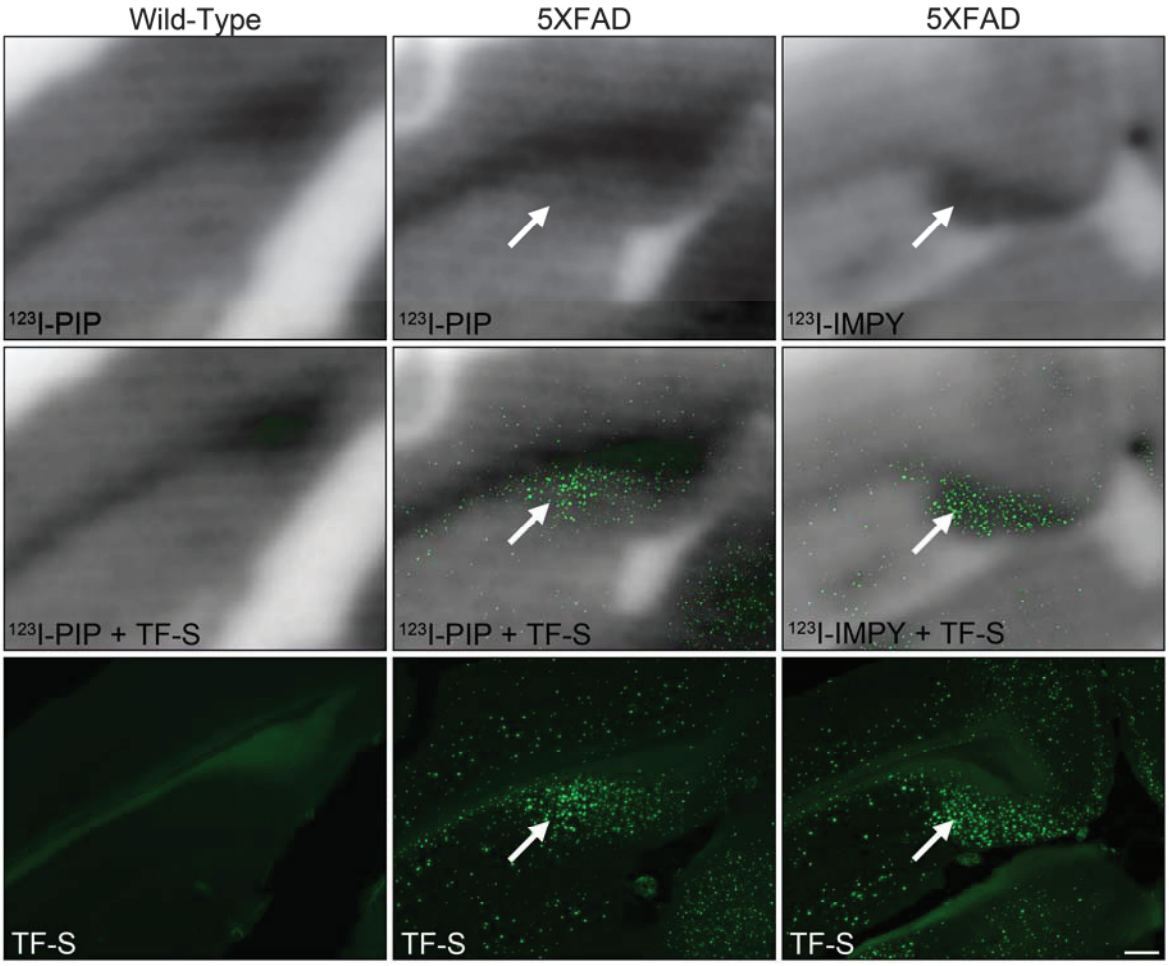

Figure 4.6. *In Vitro* mouse brain autoradiography of the subiculum with ^{123}I-PIP (**3**) and ^{123}I-IMPY (**6**) in wild-type and 5XFAD animals. Each section was stained with thioflavin-S (TF-S) to visualize Aβ plaque deposits. In the 5XFAD animals, ^{123}I-PIP (**3**) and ^{123}I-IMPY (**6**) accumulated in areas of dense TF-S positive Aβ plaques (arrows). Scale bar: 250 μm.

4.4.4 HUMAN TISSUE AUTORADIOGRAPHY

Brains from human cases were divided into three distinct classifications, AD, cognitively normal with Aβ plaques (Normal, Aβ+) and cognitively normal without Aβ plaques (Normal, Aβ-), based on clinical and pathological evidence (Figures 4.7-4.9). The distribution of ^{123}I-IMPY in these tissues demonstrated accumulation in the cerebral cortex of AD and normal with Aβ cases (Figure 4.7). No accumulation was found in this region in the normal without Aβ cases. White matter uptake and retention of ^{123}I-IMPY was apparent in all three cases. Similarly, ^{123}I-PIP also afforded accumulation of radiolabel in the cerebral cortex of AD cases (Figure 4.7). However, in cognitively normal brains with and without Aβ plaques this region was devoid of ^{123}I-PIP radiolabel accumulation. In addition, white matter of all three cases demonstrated considerable uptake and retention of ^{123}I-PIP.

Adjacent cortical tissue sections were compared from all brain cases for the histochemical visualization of Aβ, thioflavin-S and cholinesterase activity relative to ^{123}I-IMPY (Figure 4.8) and ^{123}I-PIP (Figure 4.9) accumulation. In AD brain, ^{123}I-IMPY and ^{123}I-PIP accumulation aligned with areas of thioflavin-S positive Aβ plaques that also exhibited cholinesterase activity, respectively (Figures 4.8 and 4.9). In contrast, sections from normal brain without Aβ did not demonstrate any cortical accumulation of ^{123}I-IMPY or ^{123}I-PIP and was devoid of thioflavin-S positive Aβ plaques and cholinesterase activity. Normal brains with Aβ plaques demonstrated thioflavin-S staining of these

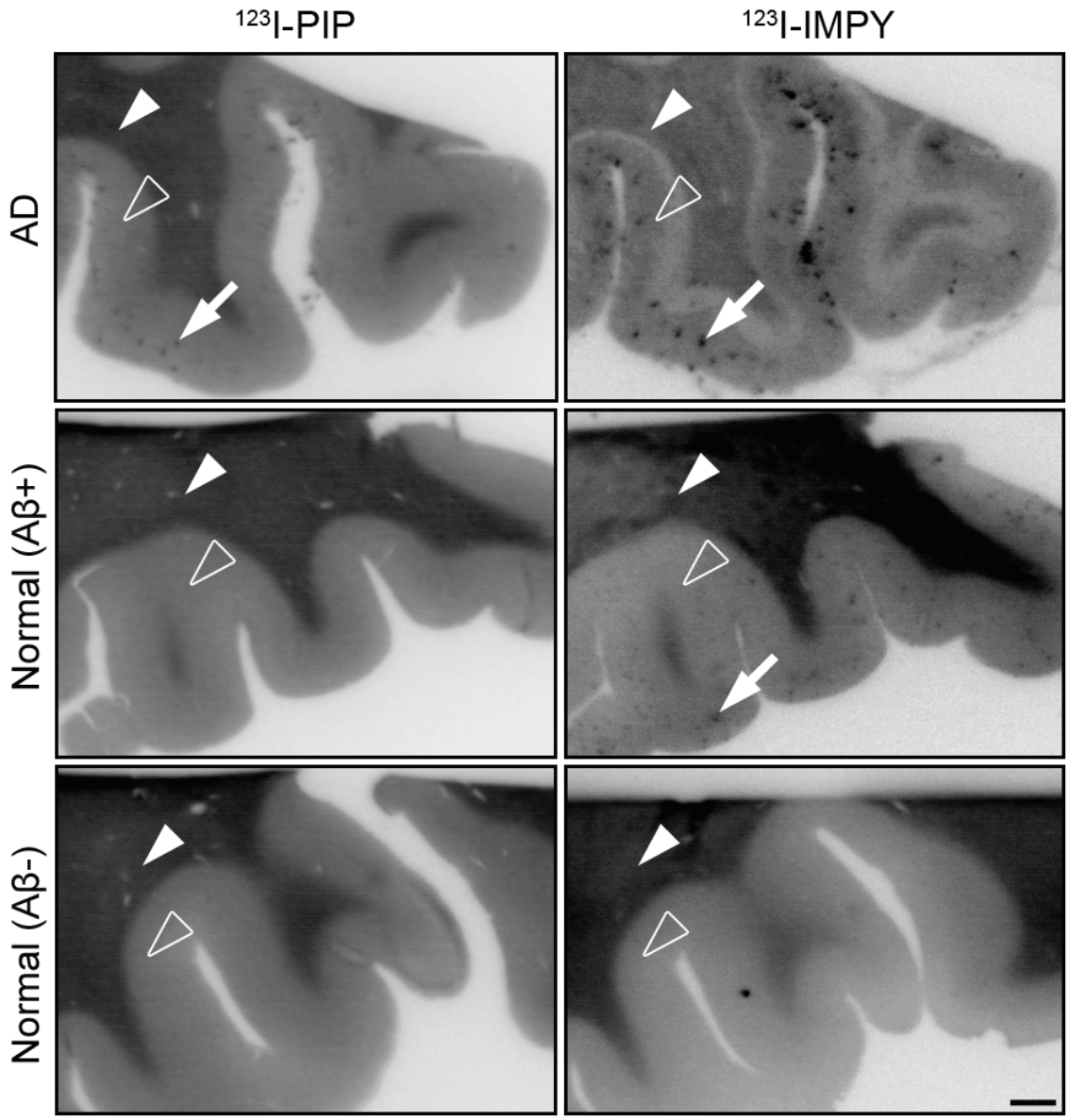

Figure 4.7. *In Vitro* human brain autoradiography with ^{123}I-PIP (**3**) and ^{123}I-IMPY (**6**). Both imaging agents visualized Aβ plaques in the orbitofrontal cortex of AD brain tissues. Aβ plaques in cognitively normal brains (Normal, Aβ+) were visualized with ^{123}I-IMPY (**6**) but were not labelled with ^{123}I-PIP (**3**). The cortex of cognitively normal brain without Aβ plaques (Normal, Aβ-) did not show accumulation of either ^{123}I-PIP (**3**) or ^{123}I-IMPY (**6**). ^{123}I-PIP (**3**) demonstrates selectivity for the detection of Aβ plaques in AD brain and not those in cognitively normal brain. Arrowhead: white matter; open arrowhead: cortex; arrow: Aβ plaque. Scale bar: 1 mm.

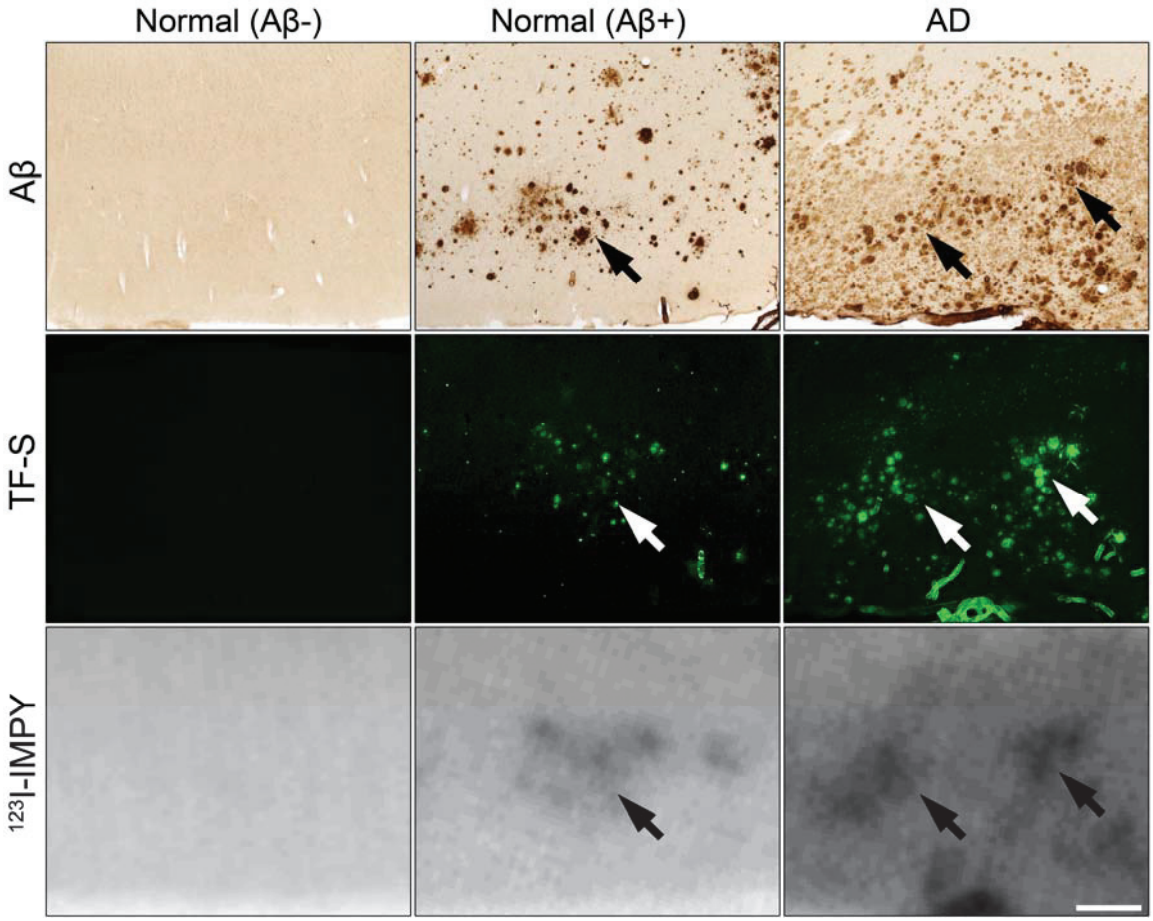

Figure 4.8. Orbitofrontal cortex of human brain tissues with immunohistochemical staining for β-amyloid (Aβ), histochemical staining with thioflavin-S (TF-S) and autoradiography with ^{123}I-IMPY (**6**). Accumulation of ^{123}I-IMPY (**6**) in the cortex corresponded to TF-S positive Aβ deposits in both Alzheimer's disease (AD) and cognitively normal brains with plaques (Normal, Aβ+). Cognitively normal brains devoid of Aβ plaques (Normal, Aβ-) did not show cortical accumulation of ^{123}I-IMPY (**6**). Imaging of Aβ deposition with ^{123}I-IMPY is not able to distinguish AD from cognitively normal brains with plaques. Scale bar: 500 μm.

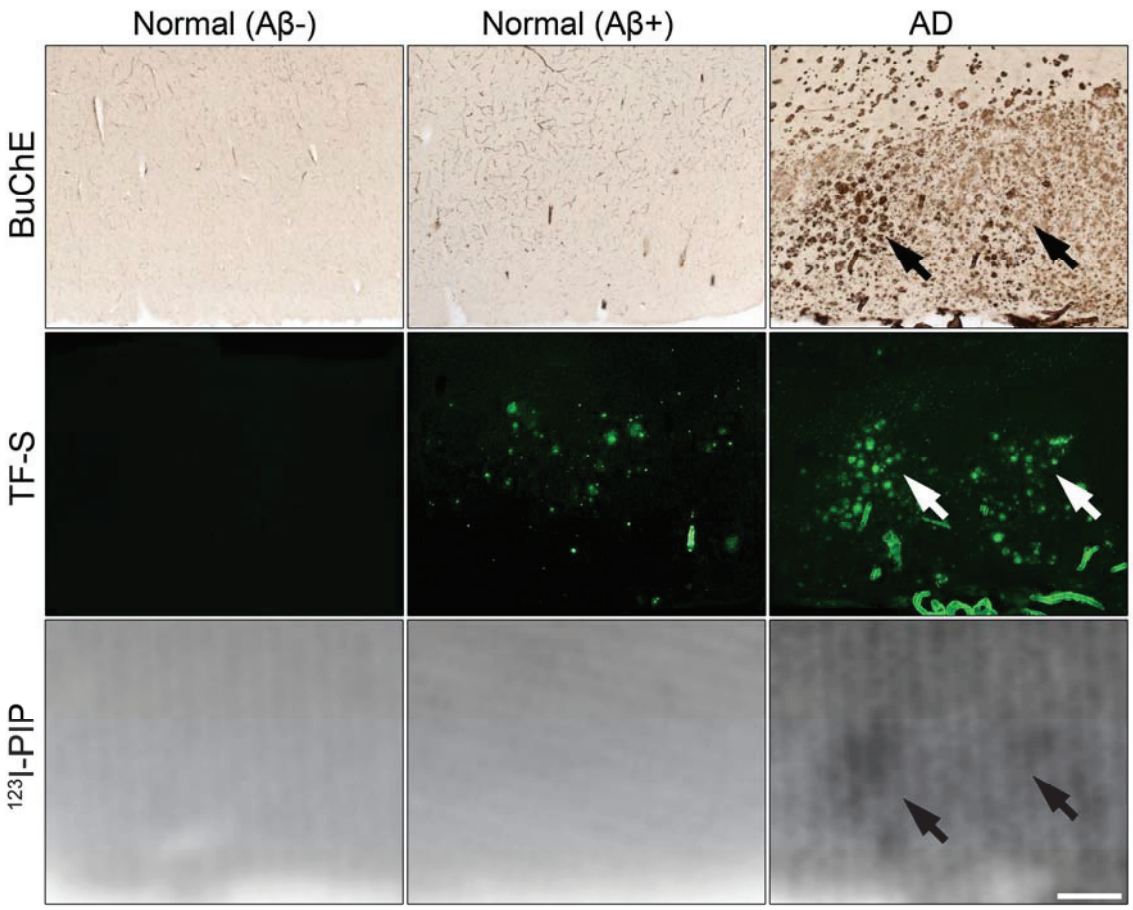

Figure 4.9. Orbitofrontal cortex of human brain tissues with histochemical staining for butyrylcholinesterase (BuChE) and thioflavin-S (TF-S) as well as autoradiography with ^{123}I-PIP (**3**). Accumulation of ^{123}I-PIP (**3**) in the cortex corresponded to BuChE and TF-S positive Aβ deposits in Alzheimer's disease (AD) brain (arrows). Cognitively normal brains with plaques (Normal, Aβ+) were positive for TF-S however, BuChE activity was not associated with these structures and ^{123}I-PIP (**3**) did not accumulate in the cortex. Cognitively normal brains (Normal, Aβ-) were devoid of Aβ plaques and ^{123}I-PIP (**3**) accumulation. Imaging of cholinesterase-associated Aβ deposition with ^{123}I-PIP (**3**) is able to distinguish AD from cognitively normal brains with plaques. Scale bar: 500 μm.

structures which aligned with ^{123}I-IMPY accumulation (Figure 4.8). However, the plaques in these cases did not contain histochemically-detected cholinesterase activity and, furthermore, ^{123}I-PIP did not show accumulation in these cortices (Figure 4.9).

4.5 Discussion

4.5.1 Synthesis and Radiolabelling

PIP (**1**) synthesis was achieved in a one-step reaction (Figure 4.2). ^{123}I-PIP (**3**) radiolabelling involved protection of PIP (**1**) with a triisopropylsilyl group followed by conversion to a tributyltin intermediate by reaction with hexabutylditin in the presence of a palladium catalyst. In contrast to comparable ester tributyltin intermediate synthesis (Macdonald et al., 2011), attempts at conversion to the tributyltin intermediate without silyl protection were unsuccessful. This suggests that the unprotected carbamate functional group interacts with either hexabutylditin or the palladium catalyst, thereby interfering with stannylation of the iodophenyl moiety of PIP (**1**). The silyl protecting group on the carbamate was found to be readily removed after stannylation during the work up process. Triisopropylsilyl protection has been reported to occur on the nitrogen of carbamates and normally requires concentrated acid for removal (Roby and Voyer, 1997). The easier removed silyl protecting group of PIP (**1**) reported here may be due to steric effects of the neighbouring phenyl rings. After stannylation, subsequent incorporation of ^{123}I occurred readily at room temperature in the presence of NCS. An acidic medium was required after HPLC purification during solvent removal using N_2 gas; otherwise a breakdown of the desired radiolabelled product occurred.

Conversion of IMPY (**4**) to the tributyltin intermediate (Figure 4.3) was achieved using a similar procedure to that employed for PIP (**1**) and previous ester molecules (Macdonald et al., 2011). However, subsequent attempts to incorporate ^{123}I using NCS as a free radical initiator, were unsuccessful. The use of hydrogen peroxide to initiate the reaction, as previously described for ^{123}I-IMPY (**6**) synthesis (Zhuang et al., 2003), yielded the desired radiolabelled product (Figure 4.4).

4.5.2 Cholinesterase Kinetics

PIP (**1**) inhibited both AChE and BuChE and, similar to most other carbamate cholinesterase inhibitors (Darvesh et al., 2003b; Darvesh et al., 2008), produced a time dependent deactivation of the enzymes (Figure 4.5), suggesting the formation of a carbamoylated enzyme intermediate. Although the rate of deactivation by PIP (**1**) is greater for AChE than BuChE, both of these rates are much slower than other known inhibitors of cholinesterases such as physostigmine and rivastigmine (Darvesh et al., 2003b). The majority of previously tested cholinesterase imaging agents act as ester substrates (Figure 4.1) and are hydrolyzed rapidly by AChE and BuChE. Such rapid hydrolysis is expected to be detrimental for *in vivo* imaging this enzyme activity as it would permit diffusion of the product containing the radiolabel away from the target enzyme. In contrast, the time dependent deactivation of these enzymes by PIP (**1**) indicates that the time radioactivity is bound with the enzyme through this compound is significantly longer compared with ester substrates. This longer lived association of radioactive PIP (**1**) components with cholinesterases is expected to afford optimal visualization of this enzyme activity.

4.5.3 Mouse Tissue Autoradiography

Similar to what is found in human AD, cholinesterase enzymes are associated with Aβ plaques in transgenic mouse models of AD (Darvesh et al., 2012b). The 5XFAD mouse used in this study is an aggressive model of brain amyloidosis characterized by robust Aβ plaque deposition beginning early in life (Oakley et al., 2006). Thus, this is a promising preclinical model for assessing the binding capability of cholinesterase imaging agents to AD plaque pathology. *In vitro* incubation resulted in ^{123}I-PIP (**3**) accumulation in areas that also exhibited high thioflavin-S positive plaque density (Figure 4.6). This distribution was similar, but not identical, to the accumulation observed with ^{123}I-IMPY (**6**). BuChE activity is known to be high in the brain white matter and it is evident that ^{123}I-PIP (**3**) is concentrated in this region of the mouse brain (Figure 4.6). This suggests that ^{123}I-PIP (**3**) is capable of visualizing cholinesterases associated with plaque pathology in the 5XFAD mouse model.

4.5.4 Human Tissue Autoradiography

This study utilized post-mortem brain tissue from three specific clinical and pathological classifications, AD, cognitively normal with Aβ plaques and cognitively normal without Aβ plaques (Figure 4.7). The presence of Aβ plaques is a pathological hallmark of AD but can also be found in the brains of some cognitively normal individuals (Snowdon, 2003; Mortimer, 2012). Cholinesterases associate with AD plaque pathology and have been suggested to contribute to maturation of these structures (Guillozet et al., 1997) promoting neurotoxicity. To further explore this notion, we have identified cognitively normal brains with robust Aβ deposition that are devoid of

associated cholinesterase activity. This is in stark contrast to AD cases in which plaque pathology demonstrated high cholinesterase activity (Figure 4.9). Autoradiography using these tissues demonstrated that ^{123}I-IMPY (**6**) detects, without discrimination, thioflavin-S positive deposits of Aβ in both AD and plaque-containing cognitively normal brains (Figures 4.7 and 4.8). In contrast, ^{123}I-PIP (**3**) only accumulated in regions of thioflavin-S positive Aβ plaques in AD brain and not cognitively normal brains with Aβ plaques (Figures 4.7 and 4.9). Furthermore, it was determined that these focal ^{123}I-PIP (**3**) accumulations correspond to areas of high cholinesterase activity associated with Aβ plaque pathology (Figure 4.9). Thus, ^{123}I-PIP (**3**) was capable of distinguishing AD brain pathology from cognitively normal brain containing Aβ plaques based upon the presence or absence of cholinesterase activity.

4.6 Conclusions

The cholinesterases, AChE and BuChE, are associated with Aβ plaques in the AD brain and are therefore, potential definitive imaging targets for the diagnosis of this disease. We have described the synthesis and radiolabelling of the cholinesterase ligand, phenyl 4-[^{123}I]iodophenylcarbamate (^{123}I-PIP), which binds to both enzymes. This radioimaging agent visualized cholinesterases associated with Aβ plaques in rodent and human AD brain tissues. ^{123}I-PIP is able to visualize Aβ plaques in AD brain due to the association of these structures with cholinesterases in this disease. In contrast, this imaging agent does not detect Aβ plaques in cognitively normal brain tissue where plaque-associated cholinesterase activity is minimal. This represents a critical step

towards the visualization of cholinesterases-associated with Aβ pathology for the definitive diagnosis of AD during life.

CHAPTER 5 CHOLINESTERASE ACTIVE SITES – KINETIC AND STRUCTURAL CONSIDERATIONS

5.1 PREFACE

The preceding Chapters 2-4 described the synthesis and evaluation as well as approaches for optimization of imaging agents for acetylcholinesterase (AChE) and butyrylcholinesterase (BuChE). Previous studies have identified amino acid residues in the AChE active site that are critical for substrate and inhibitor binding through enzyme kinetic and x-ray crystallographic analyses. In contrast, comparable details of the active site gorge of BuChE, especially pertaining to the peripheral binding site of this enzyme, have been hampered by a lack of x-ray crystallographic studies. This Chapter describes a kinetic approach which identifies residues in the BuChE active site gorge that participate in inhibitor binding. Designing compounds that target these residues will be crucial for the continued development and refinement of imaging agents for BuChE. The content of this Chapter describes work done as part of this thesis that has been published as Macdonald *et al.*, Biochemistry, 2012, 51(36):7046-53.

5.2 INTRODUCTION

Acetylcholinesterase (AChE, EC 3.1.1.7) and butyrylcholinesterase (BuChE, EC 3.1.1.8) are serine hydrolase enzymes that catalyze the hydrolysis of acetylcholine (Silver, 1974). X-ray crystallography analysis of these cholinesterases (Sussman et al., 1991; Nicolet et al., 2003) have established that catalysis involves a triad of amino acid residues, serine, histidine and glutamate, located near the bottom of a 20 Å deep gorge (Figure 5.1). This region of the gorge has been denoted the acylation site (A-site) in AChE. (Szegletes et al., 1998; Johnson et al., 2003). The efficiency of this A-site in the

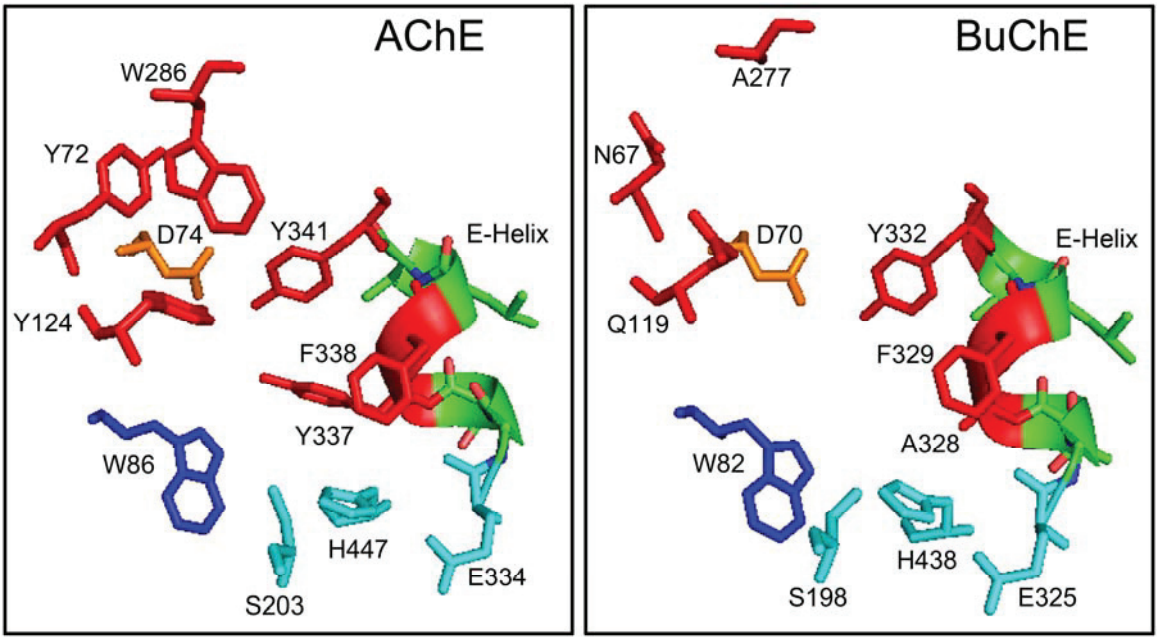

Figure 5.1. Active site gorge with homologous residues shown for acetylcholinesterase (AChE) and butyrylcholinesterase (BuChE). The crystal structures of human AChE (PDB ID: 1B41) (Kryger et al., 2000) and BuChE (PDB ID: 1POI) (Nicolet et al., 2003) were obtained from the Protein Data Bank (Berman et al., 2000) and PyMol (DeLano, 2002) was employed to delete all amino acids save for those selected residues found in the active site.

catalytic process has been shown to be influenced by events occurring at amino acid residues some distance away in the gorge. For example, a tryptophan residue (W86 in AChE, W82 in BuChE) near the A-site is known to facilitate catalysis by forming π-cation interactions with substrates helping align these molecules with the catalytic serine. This tryptophan residue is linked through a polypeptide segment (Ω loop) with an anionic aspartate residue (D74 in AChE; D70 in BuChE) that is one of the components of a peripheral site (P-site) that interacts with cationic substrates. At high substrate levels, the activity of AChE is decreased (Nachmansohn and Wilson, 1951; Mallender et al., 2000) while that of BuChE is increased (Masson et al., 1996). This phenomenon of substrate inhibition of AChE is thought to occur through steric block of product release that results from the binding of a substrate molecule to the P-site (Szegletes et al., 1998). Substrate activation of BuChE may be mediated by the binding of a second substrate molecule to a P-site that triggers a conformational change extending to the region near the catalytic triad in the active site (Masson et al., 1996). In addition, this catalytic enhancement may be facilitated by stabilization of the tetrahedral intermediate (Tormos et al., 2005). Such substrate activation has also been observed for certain substrates with AChE (Johnson et al., 2003). Mutation of the P-site aspartate residue, D74 in AChE and D70 in BuChE, to an uncharged glycine residue largely eliminates substrate inhibition in AChE and substrate activation of BuChE (Masson et al., 1996; Mallender et al., 2000). In addition to this anionic aspartate residue, other amino acid residues, especially those with aryl side chains in AChE, have been found to contribute to catalysis through interactions at the gorge periphery.

The P-site of AChE has been well mapped using mutant studies (Radic et al., 1993; Barak et al., 1994) as well as by X-ray crystallography of the enzyme bound to inhibitors that interact with various components of this site (Sussman et al., 1991; Harel et al., 1996; Harel et al., 2008). The inhibitors propidium and thioflavin T bind to the P-site of AChE while edrophonium binds to W86 and Y337, thus, interfering with access to the A-site. X-ray crystallography studies corroborate a kinetic approach that determined binding site competition between these inhibitors, thereby helping to define details of the AChE P-site (Auletta et al., 2010).

Studies with a series of *N*-10-carbonyl derivatives of phenothiazine (Darvesh et al., 2005; Darvesh et al., 2007; Darvesh et al., 2008; Darvesh et al., 2010c) as well as *N*-10-alkyl phenothiazines such as ethopropazine (Sinko et al., 2011) also indicate the relevance of aryl residues close to the mouth of the active site gorge of BuChE that are contiguous with the catalytic triad glutamate through the E-helix (Darvesh et al., 2008). This helix (E325-Y332) includes tyrosine and phenylalanine residues (F329, Y332 in BuChE) whose side chains project into the active site gorge. The residue Y332 has been implicated in the binding of substrates and inhibitors to BuChE suggesting that this amino acid residue is part of the P-site of this enzyme (Masson et al., 1997; Nachon et al., 1998; Masson et al., 1999b). Inhibitors binding to this region may function by blocking substrate access to the active site and/or by altering hydrolytic efficiency through a conformational change that extends to the catalytic triad.

The P-site of BuChE has not been explored to the extent of the comparable AChE site. Although mutant studies have provided valuable insights (Saxena et al., 1997), lack of X-ray crystallographic data has hampered definition of BuChE P-site details. Since

inhibitor binding site competition analysis and mutant studies were successful in mapping AChE P-site components, a similar approach was made to probe the BuChE P-site. To that end, studies were undertaken using wild-type and mutant BuChE species and the enzyme inhibitors thioflavin T, propidium, edrophonium and two synthetic phenothiazine derivatives.

5.3 Materials and Methods

5.3.1 Materials

Thioflavin T (**1**), propidium iodide (**2**), edrophonium chloride (**3**), and purified recombinant human AChE (~1500, units as determined by the supplier) were purchased from Sigma Aldrich (St. Louis, USA). AChE concentration was calculated using the assumption of 450 units/nmol (4.8 ΔA_{412}/[min × nM])) (De Ferrari et al., 2001). *N*-[2-(*N'*,*N'*–diisopropylamino)ethyl]-10H-phenothiazine-10-carboxamide (**4**) and anthracen-9-yl(10H-phenothiazine-10-yl) methanone (**5**) were synthesized as described previously (Darvesh et al., 2007; Darvesh et al., 2010c). Purified human plasma wild-type BuChE and its mutants D70G, A328Y, F329A and Y332A were a gift from Dr. Oksana Lockridge (University of Nebraska Medical Center, USA). BuChE concentration was calculated using the assumption of 62.5 Unit/nmol (0.94 ΔA_{412}/[min × nM]) (Darvesh et al., 2006). As defined previously, 0.1 Unit is the amount of BuChE that gives a ΔA/min of 1.0 in the presence of 1.6×10^{-4} M butyrylthiocholine in a 1.5 ml assay (Darvesh et al., 2001).

5.3.2 Inhibition Constant Determination

Inhibition constants of inhibitors for AChE or BuChE were determined using a modification of a described method (Auletta et al., 2010). Briefly, varying amounts of inhibitor (in 50 μL of 50% $CH_3CN_{(aq)}$) was added to 1.60 mL of buffer (0.09 M phosphate buffer, pH 8.0), 5, 5′-dithio-bis(2-nitrobenzoic acid) (0.32 mM), and either acetylthiocholine (5 μM, for AChE) or butyrylthiocholine (5 μM, for BuChE) in a quartz cuvette of 1 cm path length, and the mixture was zeroed at 412 nm. The reaction was initiated by the addition of 50 μL of AChE (to 1 nM) or BuChE (to 1 nM), in 0.1% aqueous gelatin. Assays were conducted at 23 ºC. The rate of change of absorbance (ΔA/min), reflecting the rate of hydrolysis of the substrate, was recorded every 2 sec for 1 min, using an Ultraspec 2100 pro UV-visible spectrophotometer (Fisher Scientific) equipped with Swift II application software. The molar extinction coefficient for the Ellman product, 5-thio-2-nitrobenzoic acid, used to convert the change in absorbance at λ = 412 nm to moles of product, was 14150 M^{-1} cm^{-1}. The second order hydrolysis rate constant (k_E) was determined at low initial substrate concentration ($[S]_0$) (i.e., $[S]_0 \leq \sim 0.2$ K_{app} (Eastman et al., 1995), where K_{app} is the apparent Michaelis constant) according to Eq. (5.1) (Auletta et al., 2010), where [S] is the concentration of substrate remaining at time (t) in the presence of the enzyme ($[E]_{tot}$). Alternatively, k_E can be determined according to Eq. (5.2) where A_{412} is absorbance, $k_{obs} = k_E[E]_{tot}$, and where $\Delta A_{412} = A_{412(final)} - A_{412(t=0)}$. Values of k_E calculated using Eq. (5.1) or Eq. (5.2) were comparable. The ratio of k_E without and with inhibitor, described by Eq. (5.3) (Auletta et al., 2010), was plotted against inhibitor concentration, and the data were fitted to solve for the inhibition constant (K_I) as well as for the ratio of the relative acylation rate constant to the

relative affinity of the ligands in the ternary complex (α). All experiments were performed at least in triplicate and the values averaged. Data fitting by nonlinear regression was conducted with Excel Solver program and errors calculated using the Solver Statistics Macro (Billo, 2011).

$$[S] = [S]_0 e^{-k_E [E]_{tot} t} \tag{5.1}$$

$$A_{412} = A_{412\,final} - \Delta A_{412}\, e^{-k_{obs} t} \tag{5.2}$$

$$\frac{k_{E[I]=0}}{k_{E+I}} = \frac{1 + ([I]/K_I)}{1 + (\alpha[I]/K_I)} \tag{5.3}$$

5.3.3 Inhibitor Competition Determination

When a single inhibitor binds to cholinesterase the rate of substrate hydrolysis is reduced. If a second inhibitor targets the same site as the first, competition between the two inhibitors will ensue and this will result in a further alteration in substrate hydrolysis rate. Determining the change in the rate of substrate hydrolysis in the presence of two inhibitors provides information as to whether these are interacting with the same or different enzyme binding sites (Billo, 2011). Based on this principle, assays were conducted as described above in the presence of a fixed concentration of one inhibitor [I1], here being one of propidium iodide (**2**), edrophonium chloride (**3**), *N*-[2-(*N'*,*N'*–diisopropylamino)ethyl]-10H-phenothiazine-10-carboxamide (**4**) or anthracen-9-yl(10H-phenothiazine-10-yl) methanone (**5**), and varying concentrations of a second inhibitor [I2], namely thioflavin T (**1**). The ratio of k_E in the presence of a fixed concentration of inhibitor, [I1], and varying concentrations of another inhibitor, [I2], to k_E in the presence

of only I1 was plotted against [I2] and fitted to Eq. (5.4) with Excel Solver as described above. In this equation, K_1 and K_2 are the known equilibrium dissociation constants for the inhibitors I1 and I2 with enzyme, respectively, having been determined as K_I values with Eq. (5.3) as detailed above. K_{12} is the fitted equilibrium dissociation constant for I1 with the binary complex of enzyme and I2. The ratio $[I1]/K_{12}$ reflects whether the two inhibitors are interacting with the same or different enzyme binding sites. Thus, as this ratio approaches zero, it signifies that the inhibitors are in competition for a common binding site on the enzyme. By setting this ratio to zero, a theoretical dataset representing complete competition between the inhibitors was generated with Eq. (5.4). The curve for this theoretical dataset along with that for the fitted dataset was graphed using GraphPad Prism (California, USA). A numeric value for such competition was calculated as the ratio of K_{12}/K_1 where a value of ~ 1 indicates no binding competition and values >> 1 indicate competition between the inhibitors.

$$\frac{k_{E+I2}}{k_{E[I2]=0}} = \frac{K_2(1+([I1]/K_1))}{K_2(1+([I1]/K_1))+[I2](1+([I1]/K_{12}))} \qquad (5.4)$$

5.3.4 Butyrylcholinesterase Mutant Inhibition Studies

Inhibitor potency towards wild type BuChE and towards each of the BuChE mutants, D70G, A328Y, F329A and Y332A, was determined. The esterase activity was determined by a modification (Darvesh et al., 2003b) of the Ellman (Ellman et al., 1961) spectrophotometric method. Briefly, one of the inhibitors (compounds **1-5**) or blank (in 50 µL of 50% $CH_3CN_{(aq)}$) was added to 1.35 mL of buffer (0.09 M phosphate buffer, pH 8.0), 5, 5′-dithio-bis(2-nitrobenzoic acid) (0.32 mM), and BuChE (~0.035 units) in 0.1%

aqueous gelatin in a stoppered cuvette of 1 cm path length. The mixture was zeroed at 412 nm, and the reaction was initiated by the addition of 50 μL of butyrylthiocholine in an aqueous solution at a final concentration of 1.6×10^{-4} M. The reactions were performed at 23 ºC. The rate of change of absorbance (ΔA/min), reflecting the rate of hydrolysis of butyrylthiocholine, was recorded every 5 s for 1 min, using a Milton-Roy 1201 UV–vis spectrophotometer (Milton-Roy, Ivyland, PA) set at $\lambda = 412$ nm. The amount of activity with and without inhibitor was determined for wild type BuChE and the BuChE mutants.

5.4 Results and Discussion

In AChE, in addition to the anionic residue D74, there are several amino acid residues that constitute the P-site (Sussman et al., 1991; Radic et al., 1993; Barak et al., 1994; Harel et al., 1996; Harel et al., 2008). Of the substrate and inhibitor binding sites at the BuChE active site gorge, D70 has previously been determined to be part of the P-site (Masson et al., 1996). The present work was undertaken to determine whether, in addition to D70, BuChE has other amino acid residues that constitute this site. Determining the P-site of BuChE will facilitate elucidation of the role of these components in the functioning of the enzyme and aid in development of inhibitors that might have therapeutic value. To that end, several compounds (**1-5**) (Figure 5.2) were evaluated using both inhibitor competition and BuChE mutant studies to identify amino acid residues that may contribute to P-site function in BuChE.

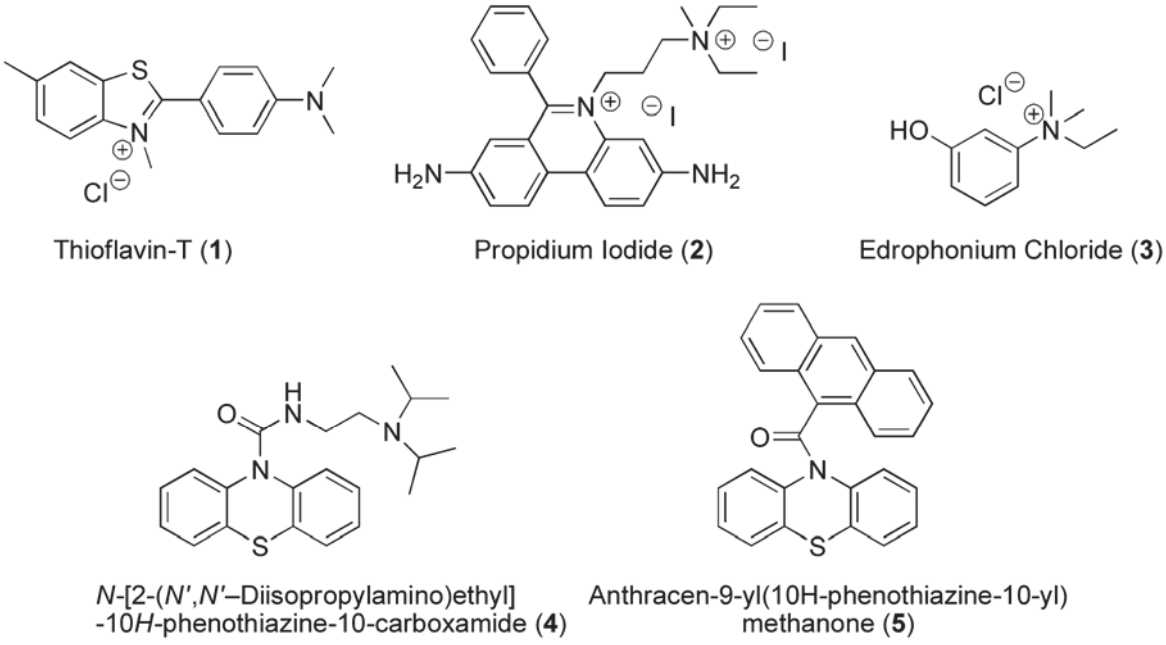

Figure 5.2. Structures of cholinesterase inhibitors used.

5.4.1 Inhibition Constants

The inhibition constants (K_I values) for the cholinesterase inhibitors used in this study are summarized in Table 5.1. Plots of the ratio of second order hydrolysis rates ($k_{E[I]=0}/k_{E+I}$, Eq. [5.3]) demonstrated a linear relationship with increasing inhibitor concentrations, indicating that the constant α in Eq. (5.3) assumed a value close to zero as observed previously for rapidly hydrolyzed substrates (Auletta et al., 2010) such as acetylthiocholine and butyrylthiocholine. Examples of such plots for thioflavin T (**1**) and propidium (**2**) are presented in Figure 5.3. Edrophonium (**3**) and the phenothiazine urea (**4**) and amide (**5**) also showed similar linear relationships. Thioflavin T (**1**), the known AChE P-site inhibitor (Auletta et al., 2010), was observed to also inhibit BuChE with comparable potency (Table 5.1). This fluorescent inhibitor probe has been shown in earlier kinetic and X-ray crystallographic studies to bind to the P-site of the AChE active site gorge (De Ferrari et al., 2001; Harel et al., 2008).

Another fluorescent inhibitor probe, propidium (**2**), also interacts with the AChE P-site (Taylor and Lappi, 1975), but it is thought to be able to enter the larger active site gorge of BuChE and bind closer to the catalytic triad (Masson et al., 1996; Saxena et al., 1997). In the present study, propidium (**2**) inhibited BuChE with about five fold higher potency than for AChE (Table 5.1). Edrophonium (**3**), which interacts with the catalytic site of AChE (Taylor and Lappi, 1975), was about 200 fold weaker as an inhibitor of BuChE (Table 5.1), consistent with results described previously (Saxena et al., 1997).

As observed earlier (Darvesh et al., 2010c), the phenothiazine urea derivative (**4**) was 80 fold more potent as an inhibitor of BuChE relative to AChE (Table 5.1). Similarly, the phenothiazine amide derivative (**5**) (Darvesh et al., 2007) was a robust

Table 5.1. Inhibition constants (K_I) for AChE and BuChE; binding site competition ratios (K_{12}/K_1) for AChE and BuChE for each inhibitor in the presence of thioflavin T. A K_{12}/K_1 ratio of ~ 1 indicates no competition at binding sites (NC) whereas values >> 1 denotes competition at the same binding site (C).

	Compound	AChE		BuChE	
		K_I (μM)	**K_{12}/K_1**	**K_I (μM)**	**K_{12}/K_1**
1	Thioflavin T	4.99 ± 0.13	-	3.62 ± 0.18	-
2	Propidium	9.73 ± 0.04	93 (C)	2.03 ± 0.30	1.1 (NC)
3	Edrophonium	1.01 ± 0.10	1.5 (NC)	198 ± 1	1.6 (NC)
4	*N*-[2-(*N*′,*N*′–Diisopropylamino)ethyl]-10H-phenothiazine-10-carboxamide	1.64 ± 0.10	70 (C)	0.021 ± 0.004	72 (C)
5	Anthracen-9-yl(10*H*-phenothiazine-10-yl) methanone	No Inhibition	-	0.016 ± 0.006	1.1 (NC)

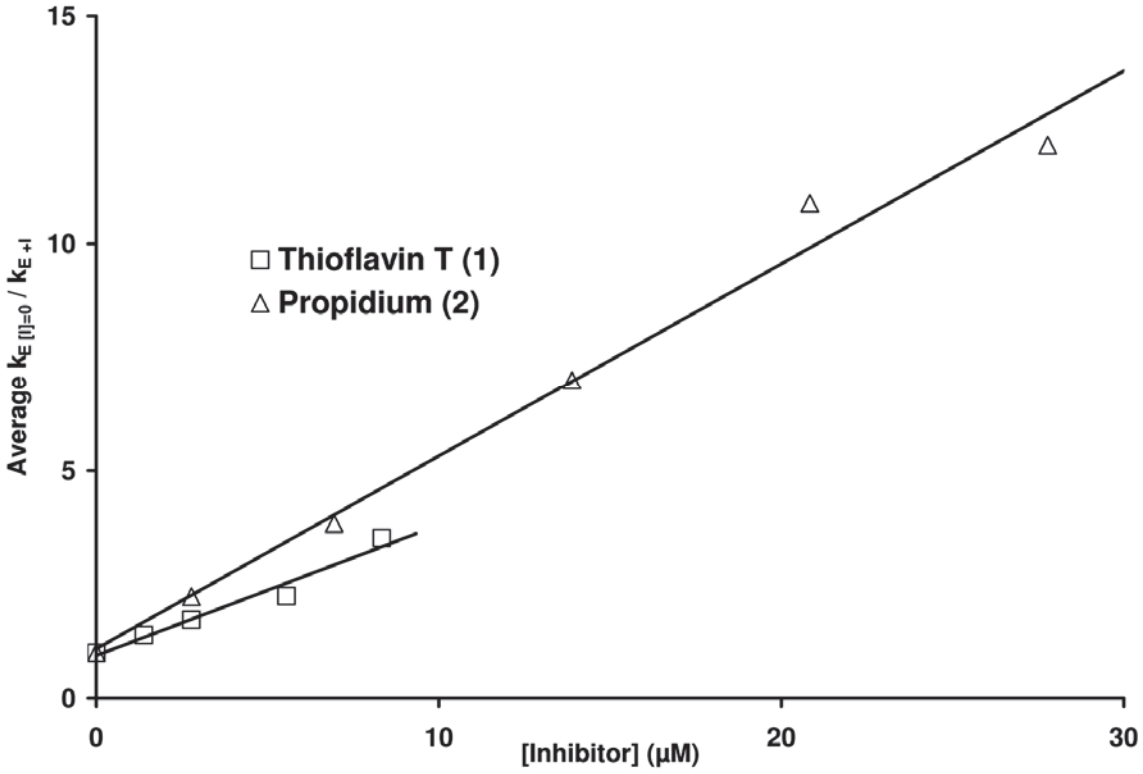

Figure 5.3. Plots of average second-order substrate hydrolysis ratios by BuChE in the absence ($k_{E[I]=0}$) and presence (k_{E+I}) of thioflavin T (**1**) or propidium (**2**). These plots show a linear relationship between second-order hydrolysis rate and inhibitor concentration.

inhibitor of BuChE (Table 5.1) but did not inhibit AChE under the same conditions. Evidence was presented earlier (Darvesh et al., 2007; Darvesh et al., 2010c) that phenothiazines interact with residues such as Y332 near the periphery of the BuChE active site gorge. It may be significant that such aryl residues are part of a polypeptide segment (E-helix, Figure 5.1) that also contains the glutamate (E325) of the catalytic triad and thus, may influence the catalytic activity of the enzyme. No X-ray crystallographic analyses are yet available to establish the peripheral binding sites of inhibitors to BuChE. However, indirect kinetic evidence, as with the phenothiazine derivatives cited above and propidium, (Masson et al., 1996; Saxena et al., 1997) provide some reference for determining binding site locations from inhibitor competition studies.

Thioflavin T (**1**) was chosen as the reference inhibitor for competition studies because of its known binding to the P-site of AChE and because it also inhibits BuChE with comparable potency (K_I, Table 5.1). The other inhibitors (compounds **2-5**, Figure 5.2) were chosen to test for inhibitor competition with thioflavin T (**1**) because of their varied putative sites of interaction with BuChE.

5.4.2 Inhibition Competition Studies

The results of competition studies between thioflavin T (**1**) and compounds **2-5** are summarized in Table 5.1 and related plots presented in Figure 5.4. Competition between thioflavin T (**1**) and propidium (**2**) with AChE confirmed the earlier observation that these two compounds bind to the same site of this enzyme (Auletta et al., 2010). In contrast, the lack of competition between thioflavin T (**1**) and propidium (**2**) with BuChE indicates that these inhibitors bind at different sites on this enzyme. Propidium has been

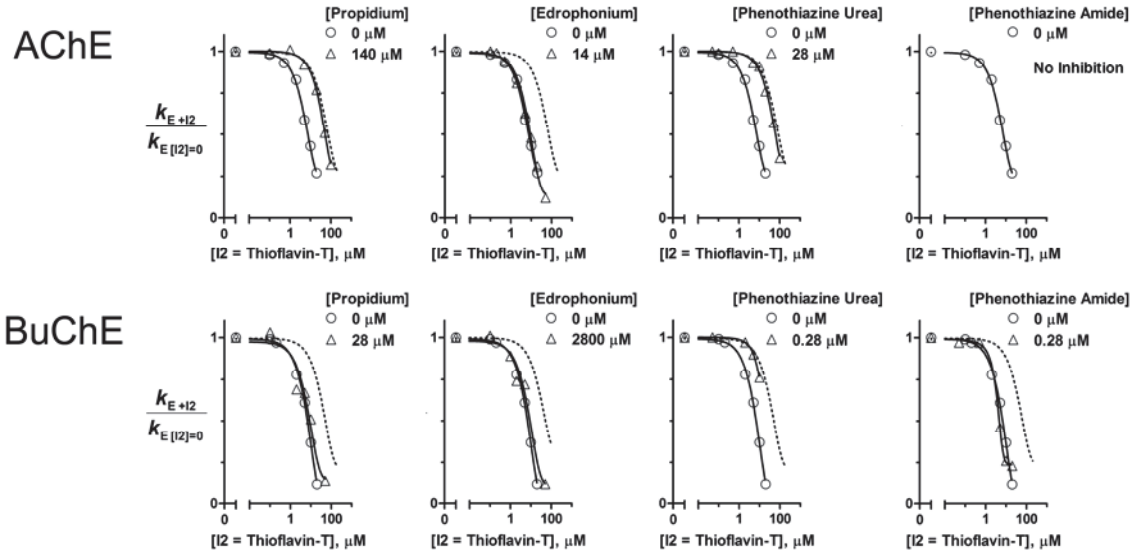

Figure 5.4. Plots of second-order substrate hydrolysis rates by BuChE or AChE with thioflavin T and in the presence (triangle) or absence (circle) of another inhibitor with lines fitted or calculated according to eq 4. Dotted lines represent the theoretical plot that denotes complete competition between the inhibitor and thioflavin T for that enzyme. For example, for BuChE, propidium and thioflavin T do not compete as exemplified by overlap in the plots with and without propidium. In contrast, for AChE, propidium competes with thioflavin T as indicated by absence of overlap in the plots with and without propidium, and overlap between the presence of propidium and complete competition plots.

suggested to bind closer to the catalytic triad in the BuChE active site (Saxena et al., 1997), implying that thioflavin T (**1**) may bind to a more peripheral region of the enzyme active site gorge. Consistent with a previous observation (Auletta et al., 2010), competition studies between thioflavin T (**1**) and edrophonium (**3**) with AChE (Table 5.1, Figure 5.4) indicated different binding sites for these inhibitors. Both observations are in keeping with earlier conclusions that edrophonium (**3**) binds at the A-site of AChE (Taylor and Lappi, 1975; Harel et al., 1993) while thioflavin T (**1**) binds at the P-site (De Ferrari et al., 2001). With BuChE, competition studies between thioflavin T (**1**) and edrophonium (**3**) (Table 5.1, Figure 5.4) suggest that these two inhibitors bind at different sites on this enzyme as well. Similar experiments using thioflavin T (**1**) and the cationic phenothiazine urea derivative (**4**), which is thought to interact with the E-helix and D70 (Darvesh et al., 2010c), demonstrate overlapping binding sites. In contrast, lack of competition between thioflavin T and the neutral phenothiazine amide derivative (**5**) with BuChE (Table 5.1, Figure 5.4) suggests that this phenothiazine derivative has a binding site distinct from that of thioflavin T (**1**) on this enzyme.

In these inhibitor studies with BuChE, lack of competition between thioflavin T (**1**) and inhibitors that are thought to bind near the catalytic triad in the active site, such as propidium (**2**) and edrophonium (**3**), suggests that thioflavin T (**1**) binds to a P-site of this enzyme. This conclusion is further supported by the observation that thioflavin T (**1**) competes with inhibitors such as the phenothiazine urea (**4**), which has multiple binding sites on the enzyme, but not with the phenothiazine amide (**5**), that is thought to bind to the E-helix of the active site gorge (Darvesh et al., 2007).

5.4.3 Butyrylcholinesterase Mutant Studies

The extent of inhibition by compounds **1-5** (Figure 5.2) was determined for wild type BuChE and BuChE mutants D70G, A328Y, F329A and Y332A (Figure 5.5). Although some caution is required to interpret the results from mutation studies because of potential complex indirect effects on the conformation of the active site gorge, such studies do provide insights into the importance of a particular amino acid residues in ligand binding (Shafferman et al., 1996; Nachon et al., 1998; Masson et al., 1999a). For thioflavin T (**1**), replacement of the peripheral anionic site residue D70 with the neutral residue glycine in the BuChE D70G mutant reduced inhibition by this compound compared to wild type and other mutants (Figure 5.5). The similar inhibition constants for AChE and BuChE and the attenuated inhibition towards BuChE D70G suggest that thioflavin T (**1**) binds to D70 in the P-site of BuChE to effect inhibition. Although thioflavin T (**1**) inhibition of the corresponding AChE mutants has not been studied, these results are unexpected based on the X-ray crystal structure of the thioflavin T - AChE complex (Harel et al., 2008). This structure shows no direct interaction between thioflavin T (**1**) and D74 and close contacts of this ligand with the residues corresponding to Y337 (A328 in BuChE) and Y341 (Y332 in BuChE). The P-site localization of thioflavin T (**1**) in BuChE thus may differ somewhat from that of thioflavin T (**1**) in AChE.

Propidium (**2**) had reduced inhibition potency for all BuChE mutants D70G, A328Y, F329A and Y332A compared to wild type (Figure 5.5). This indicates that propidium (**2**) interacts with D70 and its inhibitory action is influenced by aryl residues on the E-helix, F329 and Y332, in BuChE. Thus, even though this inhibitor may

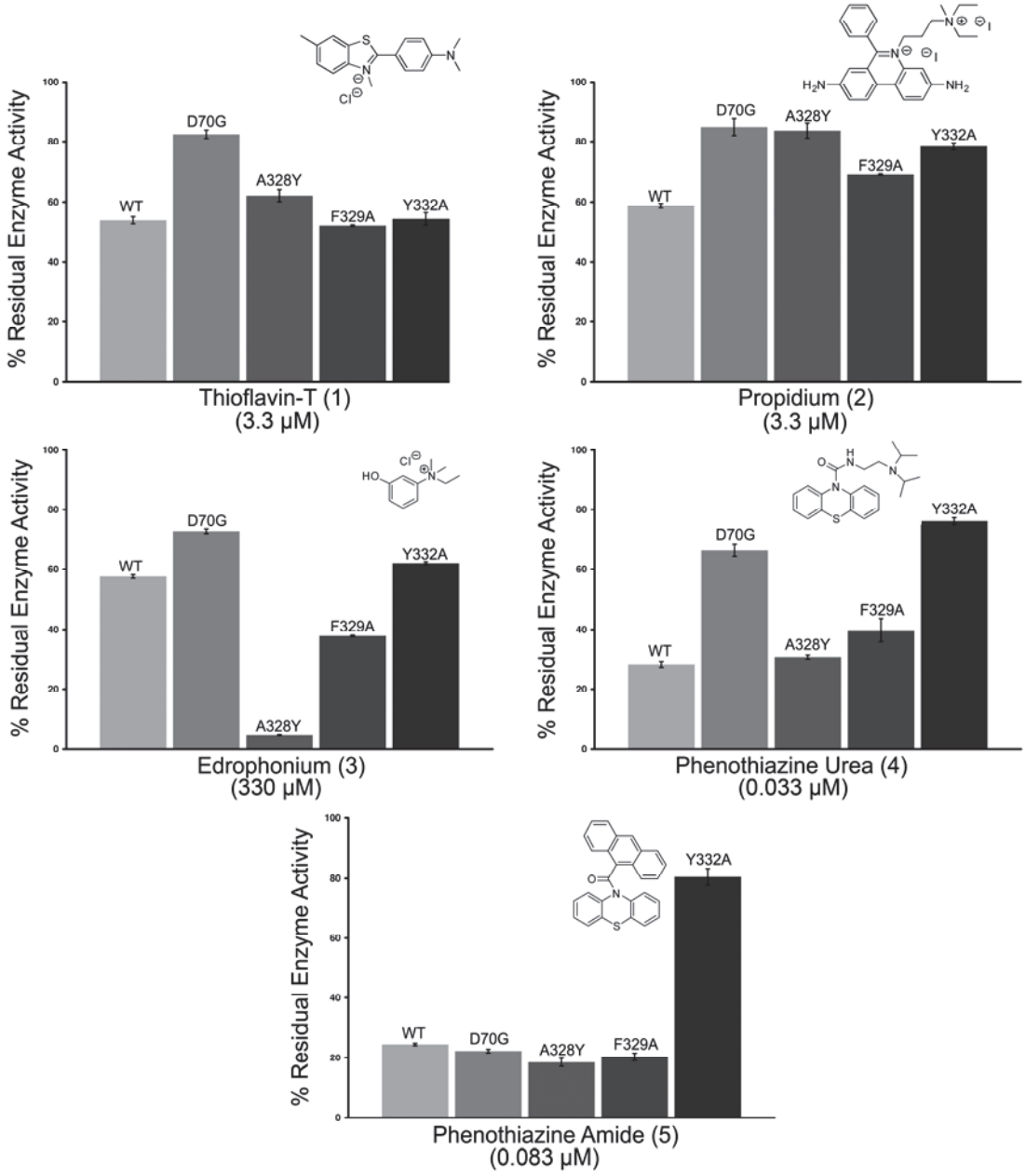

Figure 5.5. Enzyme activity of wild type BuChE and its mutants in the absence and presence of compounds **1**−**5**. The % residual enzyme activity indicates the activity in the presence of inhibitor relative to the activity in the absence of inhibitor for each mutant. Note that D70 mediates, in part, inhibition by all cationic inhibitors (compounds **1**−**4**). In addition, residues of the E-helix, F329 and Y332, are involved in ligand binding (compounds **2**−**5**). Thus, D70, Y332, and F329 are components of the P-site of BuChE.

compete with substrate at the active site (Masson et al., 1996), residues located above the catalytic triad towards the periphery of the active site gorge (D70, F329 and Y332) influence the inhibitory mechanism, perhaps through multi-pronged electrostatic and π-π interactions in the active site gorge. The apparent disruption of the propidium (**2**) inhibition by the AChE-like mutation A328Y (Figure 5.5), also supports the notion of propidium (**2**) interaction with the E-helix.

Edrophonium (**3**) is a potent inhibitor of AChE compared to its effect on BuChE (Table 5.1) (Saxena et al., 1997). This has been attributed to the ability of the compound to interact with Y337 in AChE, which is an alanine residue (A328) in BuChE. This was confirmed here (Figure 5.5) by the greatly increased inhibition of BuChE mutant A328Y over wild type BuChE and by the lack of competition between edrophonium (**3**) and thioflavin T (**1**) for both AChE and BuChE (Table 5.1). Similar to propidium (**2**), the D70G BuChE mutant is more resistant to edrophonium (**3**) inhibition compared to wild type (Figure 5.5). This signifies that, for cationic ligands, binding to D70 partially mediates inhibition potency. Also, replacing F329 with alanine increases inhibition for this mutant over wild type BuChE, suggesting that this aryl residue normally interferes with edrophonium binding to some other residue, such as W82, that now becomes available.

N-[2-(*N*′,*N*′–Diisopropylamino)ethyl]-10H-phenothiazine-10-carboxamide (**4**) inhibition was decreased with the D70G, F329 and Y332A BuChE mutants compared to wild type BuChE, as previously reported (Darvesh et al., 2010c). It has been suggested that the cationic nitrogen of this compound, present at pH 8.0, spans the gorge between

BuChE E-helix residues and D70 and contributes to the high potency of this compound to disrupt substrate hydrolysis (Darvesh et al., 2010c).

Anthracen-9-yl(10H-phenothiazine-10-yl) methanone (**5**) inhibition was significantly decreased only by the Y332A BuChE mutant. This neutral phenothiazine derivative, unlike the cationic amino urea (**4**), would not be expected to bind to the anionic D70. Thus, both these phenothiazine derivatives (**4** and **5**) associate with the E-helix, contributing to their inhibitor potency.

5.5 Conclusions

Determination of inhibition constants, binding site competition values and mutant studies suggest that D70, F329 and Y332 are amino acid residues important for binding inhibitors at the P-site of BuChE.

CHAPTER 6 PET IMAGING OF AD ANIMAL MODELS

6.1 PREFACE

Small animal *in vivo* imaging studies of cholinesterase imaging agents will be crucial for their advancement to clinical trial. In this respect, Chapters 2-4 demonstrated the progression of cholinesterase imaging agent development which culminated in the identification of a promising candidate, ^{123}I-PIP. However, a suitable animal model and *in vivo* imaging protocol must be established before the evaluation of compounds such as ^{123}I-PIP can be performed. This Chapter describes the relationship of glucose metabolism, assessed using small animal imaging, with brain Aβ plaque burden and neuroinflammation in an animal model of AD. This study investigates whether human AD phenotypes, such as altered glucose metabolism in the brain, are recapitulated in an AD mouse model and establishes a neuroimaging approach that can be used to evaluate potential cholinesterase imaging agents.

6.2 INTRODUCTION

Alzheimer's disease (AD) is a neurodegenerative disorder and a significant barrier to healthy aging. AD is characterized by specific memory and behavioural symptoms as well as abnormalities identified through brain imaging. One measure of brain function is glucose metabolism determined with positron emission tomography (PET) scanning using 2-deoxy-2-(^{18}F)fluoro-D-glucose (FDG). In AD, abnormalities in glucose uptake in brain regions such as hippocampus, posterior cingulate, inferior parietal and frontal cortices (Li et al., 2008b), indicate dysfunction or death of neurons in these areas. As AD progresses, the prominence of glucose metabolic disturbances are associated with clinical

severity (Silverman et al., 2001). Importantly, evidence has pointed towards changes in brain glucose metabolism promptly in the disease process suggesting this as a potential early marker for AD (Bateman et al., 2012).

Several pathological hallmarks have been realized for AD and these include β-amyloid (Aβ) plaques, tau neurofibrillary tangles and cerebral amyloid angiopathy. Despite significant advances in our understanding of these structures, in particular, Aβ plaques, disease modifying interventions have yet to emerge for the management of AD. Under the amyloid cascade hypothesis (Hardy and Selkoe, 2002), the presence and aggregation of specific molecular forms of Aβ lead to events that result in neurotoxicity and neurodegeneration characteristic of AD. Thus, a prominent current therapeutic research focus involves interference with this potential cascade process. In light of the putative central role of Aβ in AD, animal mouse models of brain amyloidosis have emerged based on familial AD (FAD) mutations, which result in increased Aβ production and/or aggregation. These FAD models have accelerated the development of therapeutics targeting Aβ; however, aspects of AD animal models common to the human disease, including brain glucose metabolism, have not been fully elucidated.

FAD results from mutations in the amyloid precursor protein (APP) or proteins involved in its processing such as presenilin 1 (PS1). Cleavage of APP can liberate Aβ leading to characteristic plaque deposits in the AD brain. The 5XFAD mouse model of AD overexpresses human APP(695) with the Swedish (K670N, M671L), Florida (I716V), and London (V717I) FAD mutations and human PS1 harbouring two FAD mutations, M146L and L286V (Oakley et al., 2006). This animal model of brain amyloidosis has an aggressive course of Aβ aggregation due to its high number of

familial mutations. Thus, this model has a condensed disease course with initial plaque onset beginning at ~2 months. Additionally, several similarities between this animal model and AD have been documented, including loss of synaptic markers and cognitive impairment (Oakley et al., 2006).

Investigations of differing AD animal models have begun to chronicle the patterns in brain glucose metabolism associated with amyloidosis. However, there is widespread variability among these AD models. The PDAPP (APP_{V717F}), PSAPP ($APP_{K670N/M671L}$ and $PS1_{M146L}$), and 3xTG ($APP_{K670N, M671L}$, $PS1_{M146V}$, and Tau_{P301L}) models demonstrated hypometabolism in regions such as the cingulate cortex (Reiman et al., 2000; Valla et al., 2006; Valla et al., 2008; Nicholson et al., 2010). In contrast, studies in the Tg2576 ($APP_{K670N/M671L}$) mouse found that young animals exhibited hypermetabolism but at older ages there was no detectable difference when compared to control animals (Kuntner et al., 2009; Luo et al., 2012). Finally, some animal models such as APP/PS1 ($APP_{K670N/M671L, V717I)}$ and $PS1_{M146L}$) and $PLB1_{triple}$ ($APP_{K670N/M671L, V717I}$, $PS1_{A246E}$, $Tau_{P301L/R406W}$) exhibit both hyper- and hypometabolism in different brain regions (Dubois et al., 2010; Platt et al., 2011; Poisnel et al., 2012). Thus, there is no clear correlation between amyloidosis and glucose metabolism from these studies of AD animal models.

In addition to neuronal activity, other cell types can contribute to brain glucose metabolism, in particular neuroinflammatory cells. Microglia reactivity is known to accompany Aβ deposition in animal models of AD (Hillmann et al., 2012). Therefore, a neuroinflammatory response may substantially alter glucose metabolism in AD animal models due to active microglia metabolism.

The current work was undertaken to evaluate changes in glucose metabolism in an aggressive model of amyloidosis, the 5XFAD mouse, with respect to Aβ burden and microglial activation.

6.3 Materials and Methods

6.3.1 Animals

Male B6SJL wild-type (WT) mice and male 5XFAD (B6SJL-Tg(APPSwFlLon,PSEN1*M146L*L286V)6799Vas/Mmjax) mice, obtained from Jackson Laboratory (Bar Harbor, ME), were housed with food and water ad libitum in an environment with 12 h light/dark cycles. Animals were cared for according to the guidelines set by the Canadian Council on Animal Care. Formal approval to conduct the experiments was obtained from the Dalhousie University Committee on Laboratory Animals. 5XFAD mice and age-matched WT counterparts at 2 (AD:7; WT:7), 5 (AD:7; WT:4), 8 (AD:2; WT:2) and 13 (AD:12; WT:5) months of age comprised the imaging groups for this study.

6.3.2 PET-CT Imaging

Restrained 5XFAD mice and age matched WT controls were injected via tail vein with ^{18}F-FDG (573-757 μCi, in 140-160 μL saline). Uptake occurred in conscious mice over 30 min under a heat lamp in the presence of a stimulating object (Hurry Scurry Mouse, Toysmith), to facilitate FDG uptake in the brain. Mice were then anaesthetized with 3% isoflurane (in 100% oxygen) in an induction chamber and secured in prone position in a custom, MR compatible animal tray with integrated nosecone and bite bar.

Mice were wrapped in a blanket on a heated bed and maintained under a continuous stream of isoflurane gas anesthetic (1.5-2%), while respiration rate was monitored for the duration of the scan (SA Instruments Inc. Stony Brook, NY). The head region of the mouse was centered on a 37 mm axial field of view (FOV) and PET coincidence events were acquired in list mode over a 30 min scan interval, with a LabPET4 pre-clinical PET scanner (Gamma Medica Ideas, CA).

Immediately following PET scanning, for anatomical reference, a computed tomography (CT) image was performed in fly mode with a 70 kVp x-ray beam energy (160 μA beam current), 512 projections, 4 summed frames/projection, with 2×2 binning and a magnification of 2.26X, providing complete whole brain coverage in 56 mm FOV. CT scan duration was approximately 8.5 min. Once completed, the animal was then immediately transported in the MR compatible bed to the MR imaging scanner.

6.3.3 MR IMAGING

All MRI scans were performed at 3.0 T using a superconducting Magnex Scientific clinical MR "head only" scanner (Oxford, UK) retrofitted for small animal imaging (Magnex Scientific gradient coil, ID of 21 cm; maximum gradient strength of 400 mT/m) and interfaced with a Direct Drive spectrometer (Varian Inc., Palo Alto, CA). A 30 mm ID "Litzcage" quadrature RF coil (Doty Scientific, Columbia, SC), tuned to 128.8 MHz, was used as a transmit/receive volume coil for imaging. *In vivo* anatomical images were obtained using a 3D balanced steady-state free precession, (b-SSFP) imaging sequence (T2/T1-weighting) acquired in a sagittal readout. Repetition time (T_R), echo time (T_E), flip angle and bandwidth (BW) were optimized for best brain image

quality. The sequence consisted of T_R/T_E = 9/4.5 ms, flip angle = 30°, 4 frequencies, 4 signal averages and BW = 40.3 kHz. A FOV of 22.1 × 22.1 × 22.1 with matrix dimensions 156 × 156 × 156 was used to acquire $(142\ \mu m)^3$ isotropic resolution images with full brain coverage (~61 min/scan). Respiratory rate and internal body temperature of the mice were monitored using an MRI compatible physiological monitoring and gating system (SA Instruments Inc., Stony Brook, NY). The temperature of the mouse was maintained at 37±1 °C via temperature control feedback loop controlling an air heating system. After MR imaging the animals were sacrificed and brains removed for histological processing.

6.3.4 B-Amyloid Immunohistochemistry

After a 24 h period to allow decay of radioactivity, mice were sacrificed by somnitol injection, perfused transcardially with saline (25 mL, 0.9% NaCl, 0.1% $NaNO_3$) and 50 mL of 4% paraformaldehyde in 0.1 M phosphate buffer (PB, pH 7.4), the brains removed and post-fixed for 1 h. Brains were frozen with dry ice and cut in 40 µm serial sections (4 series). The sections were stained, using immunohistochemical methods for Aβ. Briefly, sections were rinsed for 30 min in PB pH 7.4, 5 min in 0.05 M PB, followed by distilled water (dH_2O), and then gently shaken in 90% formic acid for 2 min for antigen retrieval. Sections were rinsed 5 times in dH_2O for 1 min each and 2 times in PB for 15 min. Sections were placed in 0.3% H_2O_2 in PB for 30 min to quench endogenous peroxidase activity and rinsed again for 30 min in PB. Sections were then incubated in PB containing 0.1% Triton X-100, normal goat serum (1:100), and a polyclonal rabbit anti-Aβ antibody (1:400; 71-5800, Invitrogen, Camarillo, CA), specific for the 4- to 5-

kDa amyloid peptide (Jankowsky et al., 2007) for approximately 16 h at room temperature. After rinsing, sections were incubated in PB with 0.1% Triton X-100, biotinylated goat anti-rabbit secondary antibody (1:500), and normal goat serum (1:1000) for 1 h. After another rinse, sections were placed in PB with 0.1% Triton X-100 and Vectastain Elite ABC kit (1:182; PK- 6100, Vector Laboratories, Burlingame, CA), according to the manufacturer's instructions, for 1 h. Sections were rinsed and developed in a solution of PB containing 1.39 mM 3,3'- diaminobenzidine tetrahydrochloride (DAB). After 5 min, 50 µL of 0.3% H_2O_2 in dH_2O was added per mL of DAB solution, and the sections were incubated for 5 min. The reaction was stopped by rinsing the sections in 0.01 M acetate buffer (pH 3.3). In control experiments, no staining was observed when the primary antibody was omitted. Sections were mounted onto glass slides, air-dried, rehydrated in dH_2O, dehydrated in a series of ethanol washes, cleared in xylene, and rinsed in 50% ethanol.

6.3.5 B-Amyloid Immunohistochemical Data Analysis

The stained mouse brain sections were analyzed and photographed using a Zeiss Axioplan 2 motorized microscope with a Zeiss Axiocam HRc digital camera using AxioVision 4.6 software (Carl Zeiss Canada Ltd., Toronto, Ontario, Canada). The photographs were assembled using Adobe Photoshop. The images were color balanced, contrast enhanced, and the brightness was adjusted to match the background from different images. The distribution of Aβ-positive plaques in various areas of the 5XFAD mouse brain was determined and; on average, 7 sections were analyzed for plaque load for each area studied. Plaque loads were quantified using ImageJ (National Institutes of

Health) and recorded as a percentage of the total area, as described elsewhere (Shi et al., 2009). Gray-scale images of sections stained for Aβ were taken throughout the brain. An intensity threshold level was set such that stained plaques, but not background, was selected. The areas of interest were parcellated according to the mouse atlas by Paxinos and Franklin (Paxinos and Franklin, 2001) and measured for the percent area covered by plaque staining. The percentage of Aβ plaque pathology was then averaged for each area and compared.

6.3.6 Iba-1 Immunohistochemistry

Immunohistochemical staining was performed using primary antibodies for ionized calcium binding adaptor molecule 1 (Iba-1; Wako Chemicals) that recognizes microglia. Sections were rinsed in PB for 30 min. Endogenous peroxidase activity was quenched by rinsing the tissue in 0.3% hydrogen peroxide in PB followed by a 30 min rinse in PB. Antigen retrieval was done by heating the tissue to 80°C in 0.1 M citrate buffer (pH 6.0) for 20 min. Sections were allowed to cool to room temperature and then rinsed in PB for 30 min. Sections were incubated in PB containing 0.1% triton X-100, normal goat serum (1:100) and Iba-1 primary antibody (1:2000) for about 16 h at room temperature. After rinsing, sections were incubated in PB with 0.1% Triton X-100, biotinylated goat anti-rabbit secondary antibody (1:500), and normal goat serum (1:1000). After another rinse, sections were placed in PB with 0.1% Triton X-100 and Vectastain® Elite ABC kit (Vector) according to the manufacturer's instructions. After rinsing the section, they were developed in a solution of 0.05 M tris buffered saline (TBS pH 8.0) containing 0.009 mM DAB and 0.6% nickel ammonium sulfate. After 5 min, 50

µl 0.3% H_2O_2 in distilled water was added per mL of DAB staining solution and was incubated for 10 min. The reaction was stopped by rinsing the sections in TBS. Sections were mounted onto glass slides, air-dried, rehydrated in dH_2O, dehydrated in a series of ethanol washes, cleared in xylene and coverslipped.

6.3.7 Iba-1 Immunofluorescence and Thioflavin-S Histochemistry Double labelling

Sections were rinsed in PB for 30 min. Antigen retrieval was done by heating the tissue to 80°C in 0.1 M citrate buffer (pH 6.0) for 20 min. Sections were allowed to cool to room temperature and then rinsed in PB for 30 min. Sections were incubated in PB containing 0.1% triton X-100, normal donkey serum (1:100) and Iba-1 primary antibody (1:2000) for 16 h at room temperature. Sections were rinsed in PB and incubated for 1 h in PB with 0.1% Triton X-100 donkey anti-rabbit Alexa Fluor® 555 (1:350; Molecular probes, A31572) secondary antibody. Sections were rinsed in PB, mounted onto glass slides and air-dried overnight. Slides were rehydrated in dH_2O, dehydrated in a series of ethanol washes, cleared in xylene, and partially rehydrated through a graded series of ethanol washes to 50% ethanol. Slides were immersed in 0.05% thioflavin-S in 50% ethanol for 15 min. Slides were rinsed in 80% ethanol for 20 seconds and dH_2O for 5 min. Slides were then coverslipped using a glycerol/gelatin mounting medium.

Sections were analyzed and photographed on a Zeiss Axioplan 2 motorized microscope with a Zeiss Axiocam HRc digital camera and AxioVision 4.6 software. Image levels were adjusted in Adobe Photoshop CS5 so the background from different images matched.

6.3.8 IMAGE PROCESSING

PET list-mode data were temporally histogrammed as a single timeframe and binned according to their line of response. Coincidence events were rebinned over a maximum span field of 31 oblique planes using a single slice rebinning algorithm. An iterative reconstruction approach was employed via a 2D Maximum-Likelihood Expectation Maximization (MLEM) algorithm, which was performed 100 times and constrained to a 46 mm radial FOV. The resultant PET images yielded an effective in-plane resolution of 1.2 mm. Normalization correction (to account for count-rate variability of sensors) and quantitative calibrations were performed weekly for the duration of the study and these corrections were applied in the reconstruction of the data sets. Recovery coefficient corrections were not applied to the PET data.

CT images were reconstructed with a 512×512×512 image matrix over a 56 mm FOV using the built-in optimum noise reconstruction procedure provided with the Triumph XO CT acquisition software, yielding images with $(102\ um)^3$ isotropic resolution.

Fusion of PET and CT images was achieved using the Vivid^{TM} Image Analysis Platform (Gamma Medica Ideas, CA and Amira 4.1, San Diego, CA), which aligns and overlays the common coordinate frames of each modality. Images were assessed by visual inspection by a single observer to ensure accurate fusion results. PET data was then interpolated to 102 μm (resolution-matched to the CT).

MRI images underwent 3D maximum intensity projection (MIP) processing of 4 phase cycle frequencies, resulting reconstructed images were zero-padded (interpolated to

higher resolution grid to increase the effective resolution and image quality) in ImageJ (NIH, USA).

6.3.9 Whole Brain FDG Uptake Analysis

Whole brain uptake was determined using Amira (Visualization Sciences Group, MA, USA). Briefly, PET/CT fused images were imported into Amira, the borders between the brain/skull interface were manually defined on each CT image which permitted selection of the entire brain volume within the skull. This generated a brain mask that was applied to the co-registered PET data. FDG uptake values are reported as standardized uptake values (SUV).

6.3.10 Regional FDG Uptake Analysis

For voxel-based region of interest (ROI) analysis of regional distributions of FDG uptake in the brain, the use of an MR-based 3D digital mouse atlas (Ma et al., 2005; Ma et al., 2008) was employed and inter-modality registration between PET/CT/MRI was performed. Briefly, a semi-automated skull stripping algorithm using BrainSuite 11 (LONI UCLA) was performed on each mouse-specific MR image to remove all extraneous non-brain data. A linear, 6-parameter model rigid body registration was performed using Automated Image Registration 5.3.0 (Woods et al., 1998) between the reoriented skull stripped MR and the standard brain corresponding to the digital atlas. Subsequently, higher order non-linear spatial transformations (warping) of the standard brain to the mouse-specific MR images acquired in this study were carried out to either the 3^{rd} or 5^{th} order polynomial. This provided the necessary transformations to be applied

to the 3D digital mouse atlas. Visualization of the mouse-specific MR image and corresponding warped atlas mask overlay was carried out in RView (Studholme et al., 1996) to assess the goodness of fit. PET/CT fused data, mouse-specific MR image data and the warped digital atlas were imported into AMIDE (Loening and Gambhir, 2003), and were manually aligned to the CT and PET image. ROI statistics were generated from the PET data for 8 structures defined by the warped atlas mask for each animal, which include amygdala, basal forebrain, basal ganglia, cerebellum, hippocampus, hypothalamus, neocortex and thalamus. FDG uptake values are reported as SUVs.

6.3.11 Statistical Analysis

FDG uptake values are presented as mean activity values for each whole brain or parcellated structure, normalized to the injected dose and body weight of each individual animal (SUV). Statistical comparisons of FDG uptake values in whole brain or each of the aforementioned structures were made via unpaired t-tests of group means (AD vs WT) at each age interval. Differences were concluded at a significance level of 5% ($p<0.05$, *) or 1% ($p<0.01$, **). All data are presented as group means ± standard error of mean.

6.4 Results

6.4.1 Whole Brain Metabolism

CT, PET and MRI data were co-registered to provide uptake of FDG in whole brain and parcellated anatomical regions such as the neocortex and thalamus (Figure 6.1). Uptake of FDG was quantified in whole brain, as SUVs, for each animal in the age

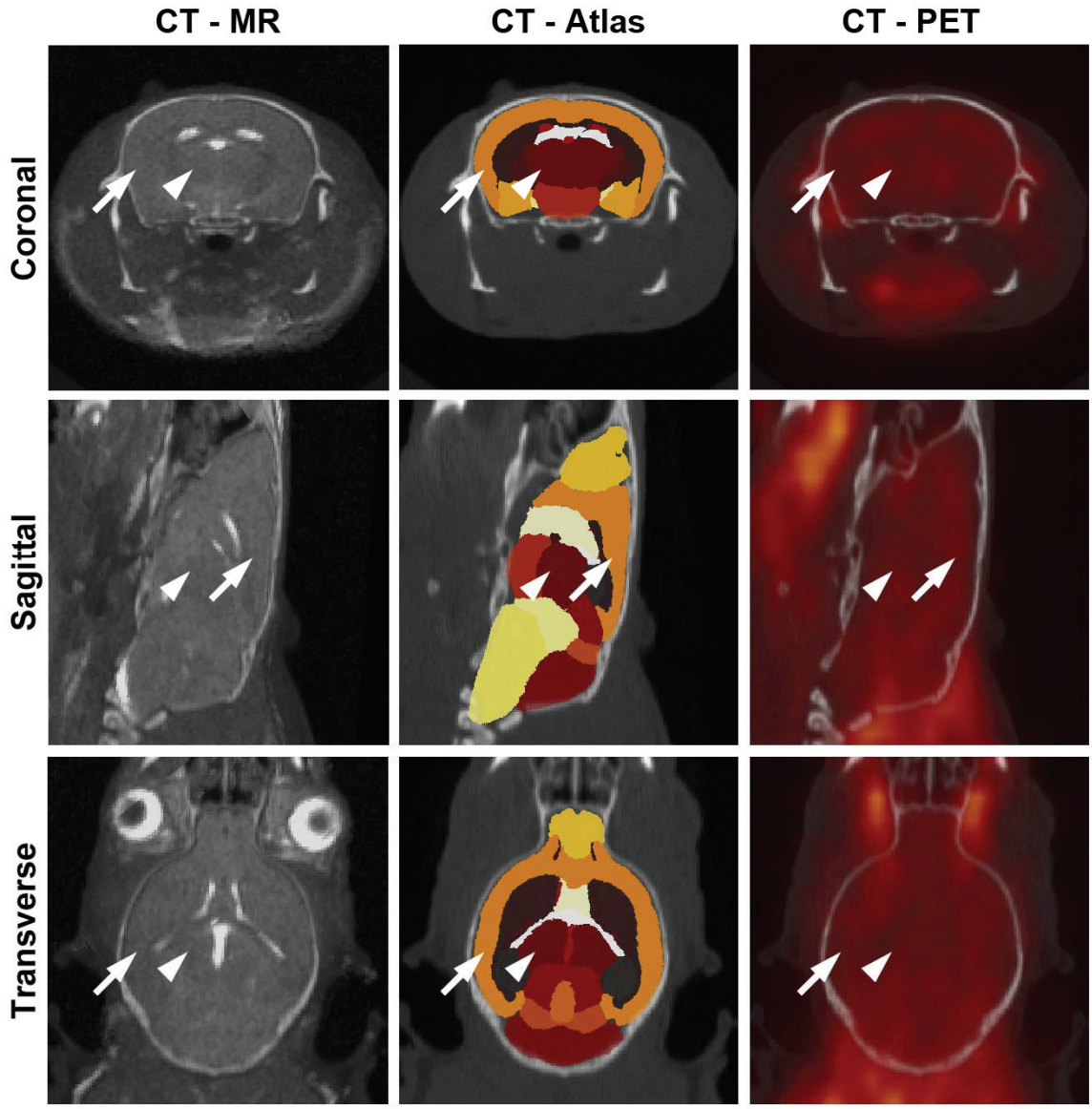

Figure 6.1. Trimodality wild-type and 5XFAD mouse imaging with CT, PET and MR. An example of a 5XFAD animal with overlay of CT with MR (left) demonstrates brain alignment between these modalities. Parcellation of the brain into various regions was accomplished with MR data and aligned with the CT (middle). FDG-PET aligned with the CT (right), was evaluated for whole and regional brain uptake. The neocortex (arrow) and thalamus (arrowhead) are identified as examples of parcellated brain regions.

groups, 2, 5, 8 and 13 months (Figure 6.2). A trend towards lower uptake in the 5XFAD animals compared to WT was observed in the 2 and 5 month animals. The 13 month 5XFAD animals demonstrated significantly lower SUVs compared to WT animals (18.8% decrease, $p < 0.01$).

6.4.2 Regional Brain Metabolism

WT and 5XFAD brains were anatomically parcellated and FDG uptake was evaluated, for eight brain regions (Figure 6.3). These regions were the amygdala, basal forebrain, basal ganglia, cerebellum, hippocampus, hypothalamus, neocortex and thalamus. Generally, there was a trend for reduced FDG uptake in 5XFAD mice compared to WT mice in the various regions examined. 5XFAD animals in the 13 month group demonstrated significantly lower metabolism in the basal ganglia (18.5% decrease, $p < 0.01$), cerebellum (21.1% decrease, $p < 0.01$), hippocampus (19.4% decrease, $p < 0.01$), hypothalamus (17.9% decrease, $p < 0.01$), neocortex (15.9% decrease, $p < 0.01$) and thalamus (24.8% decrease, $p < 0.01$).

In each of the WT and 5XFAD animals, SUVs from parcellated brain regions were normalized to an internal tissue reference within the same animal. Each parcellated brain region was individually used as the reference tissue. Thus, normalized SUVs were calculated for each brain region relative to another and differences in their average identified between WT and AD animals (Figure 6.4). At 2 months of age, 5XFAD animals demonstrated a significantly higher ratio of FDG uptake in the amygdala (14.0% increase, $p < 0.05$), basal forebrain (13.8% increase, $p < 0.01$) and hypothalamus (15.1%

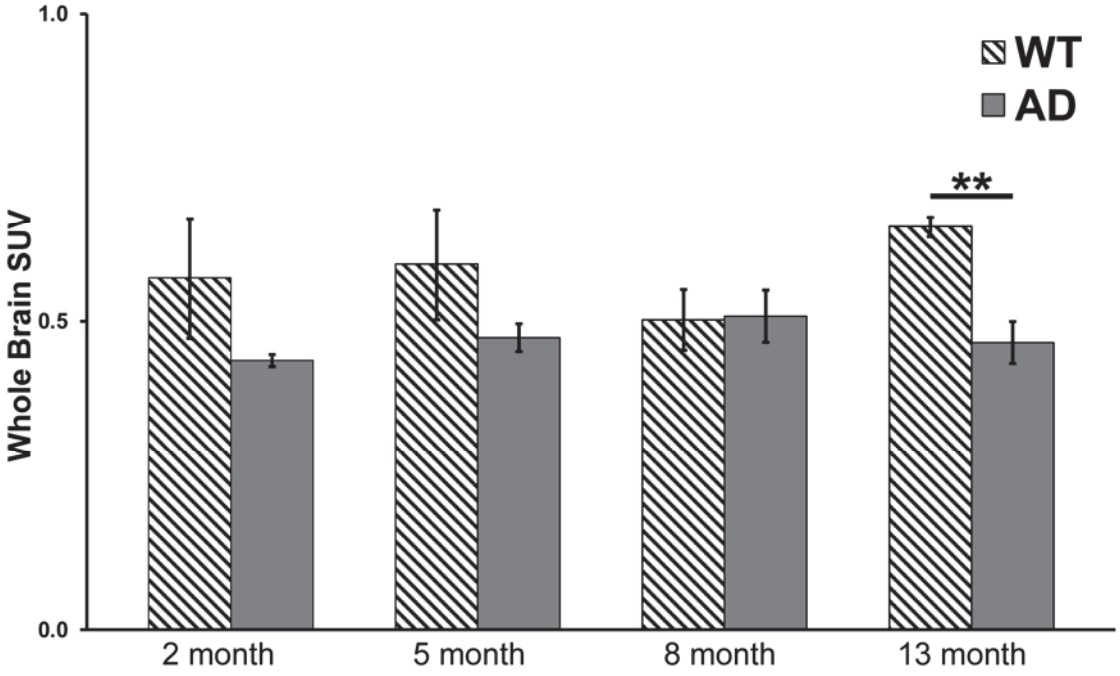

Figure 6.2. FDG-PET whole brain uptake in wild-type (WT) and 5XFAD (AD) animals with respect to age. At 13 months of age 5XFAD animals demonstrated lower uptake of FDG compared to WT (**, $p < 0.01$).

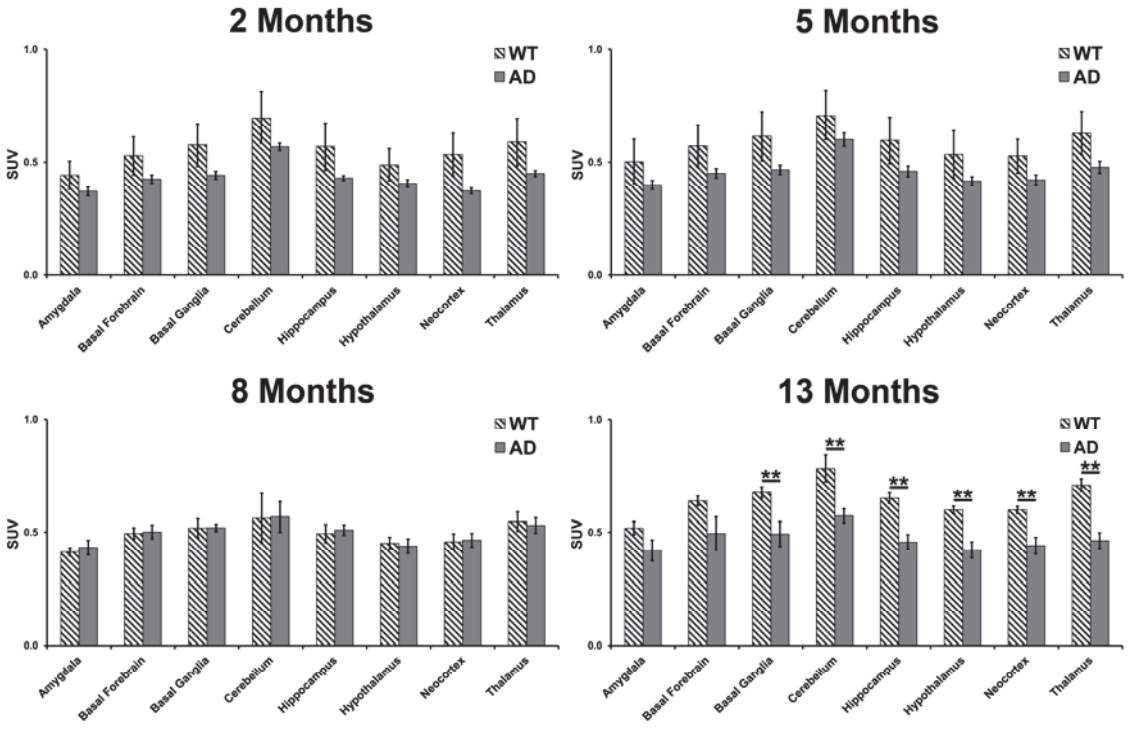

Figure 6.3. FDG-PET uptake in various brain regions in wild-type (WT) and 5XFAD (AD) animals. At 13 months of age 5XFAD animals demonstrated a lower FDG uptake in the basal ganglia, cerebellum, hippocampus, hypothalamus, neocortex and thalamus compared to WT. No other significant differences were observed between 5XFAD and WT animals. (**, $p < 0.01$).

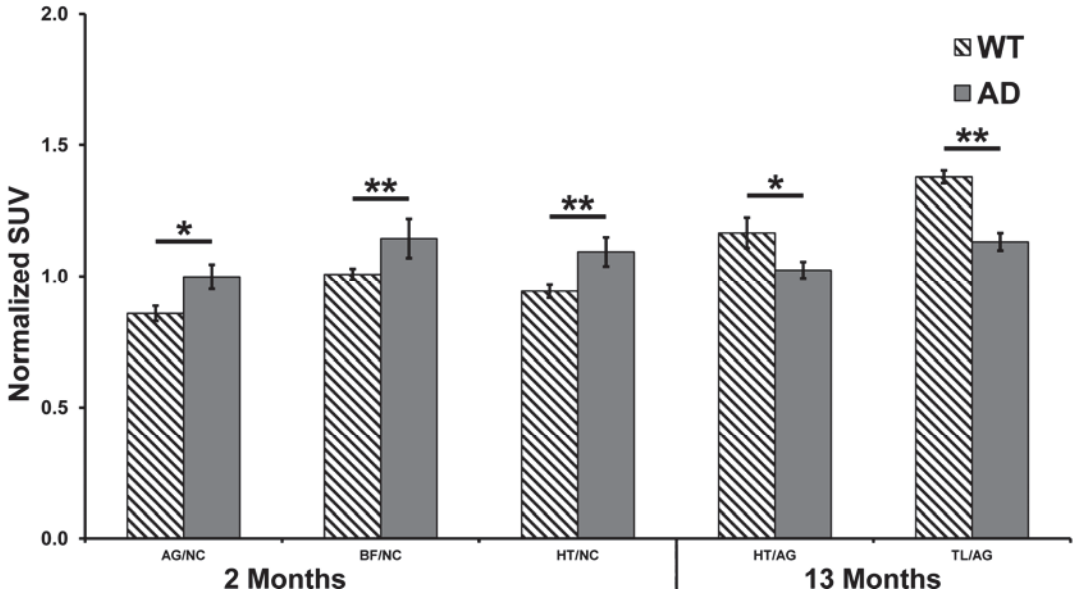

Figure 6.4. Significant differences in FDG-PET uptake in normalized brain regions between wild-type (WT) and 5XFAD (AD) animals. Higher uptake was observed in the 5XFAD 2 month animals in the AG, BF and HT relative to the NC compared with WT. Lower uptake was observed in the 5XFAD 13 month animals in the HT and TL relative to the AG compared with WT. AG, Amygdala; BF, basal forebrain; HT, hypothalamus; NC, neocortex; TL, thalamus. (*, $p < 0.05$; **, $p < 0.01$).

increase, $p < 0.01$) relative to the neocortex when compared to WT animals. At 13 months of age, 5XFAD animals demonstrated a lower ratio of FDG uptake in the hypothalamus (14.4% decrease, $p < 0.05$) and thalamus (24.6% decrease, $p < 0.01$) relative to the amygdala compared with WT animals. Other brain regions, across all the age groups, did not show any significant difference in normalized SUVs between 5XFAD and WT animals.

6.4.3 B-Amyloid Deposition

The degree of Aβ plaque deposition in 5XFAD animals was determined across the age groups in the 8 parcellated brain regions evaluated for FDG uptake (Figure 6.5). Some regions, such as the neocortex, demonstrated relatively high levels of plaque deposition while others, such as the cerebellum, had low plaque levels. All brain regions exhibited a linear increase in the percent area covered with Aβ as the age of the animal increased as exemplified in the neocortex and hippocampus (Figure 6.6). This continued deposition of Aβ in the 5XFAD brain with increasing age is similar to observations made by others (Oakley et al., 2006). The severity of plaque deposition did not correlate with SUV uptake in any of the evaluated brain regions, such as the neocortex and hippocampus (Figure 6.6).

6.4.4 Microglia

Microglia were visualized with Iba-1 immunohistochemistry in WT and 5XFAD animals. The morphology of microglia changed in 5XFAD mice as age increased. In the 5 month age group and older, 5XFAD brains had microglia with larger cell bodies and

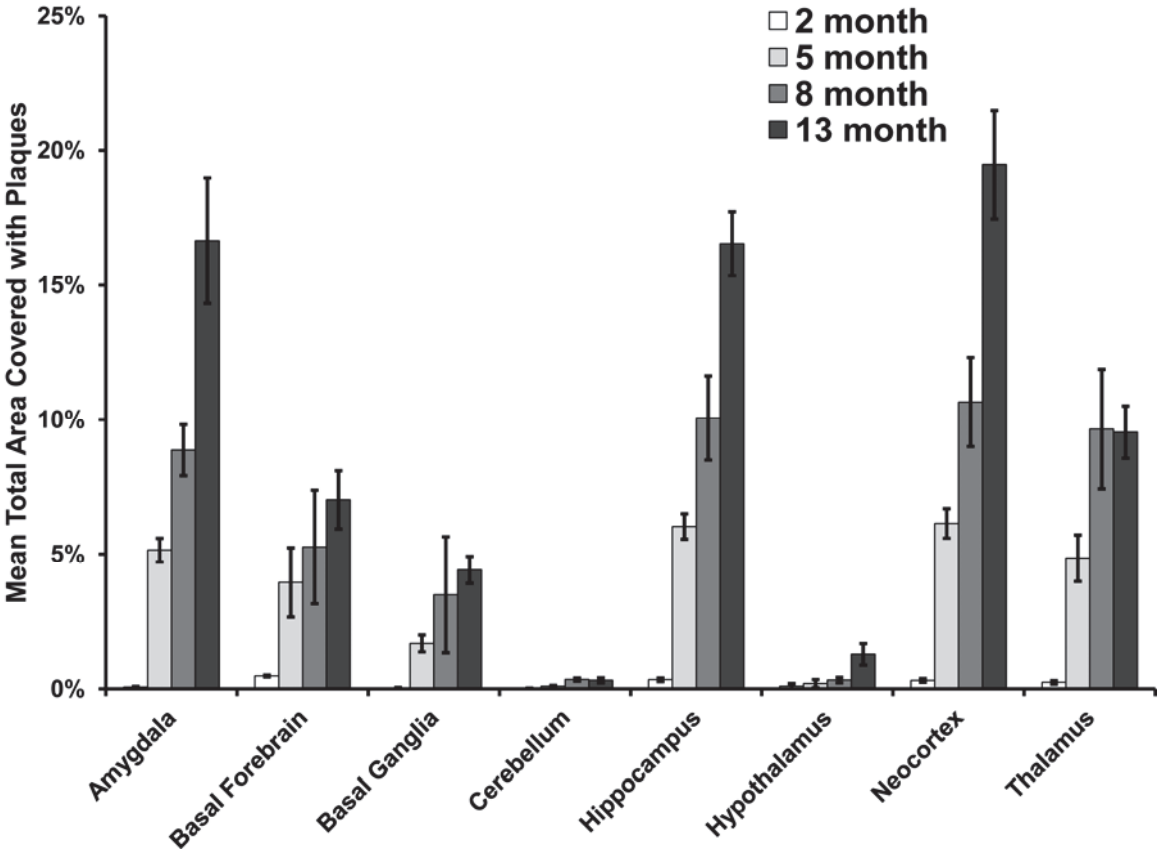

Figure 6.5. Quantification of β-amyloid plaque burden in various 5XFAD brain regions with respect to age. Levels of Aβ deposition varied across brain regions; however, all areas increased in Aβ burden with age.

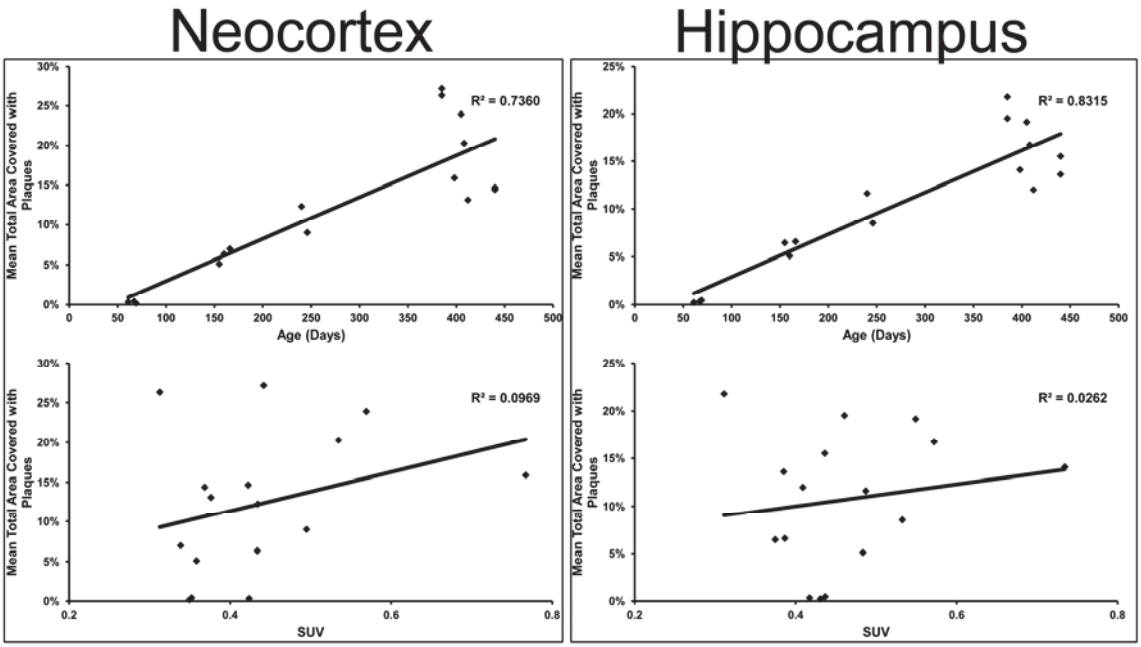

Figure 6.6. Plots of β-amyloid plaque burden with respect to age (top) and FDG-uptake (SUV, bottom) in the neocortex and hippocampus of 5XFAD animals. Aβ deposition was correlated with age in the neocortex ($p < 0.01$) and hippocampus ($p < 0.01$); however, no significant relationship was observed in either region with FDG-uptake.

ramified processes that were more distinct and branched (Figure 6.7A). Double labelling of sections with Iba-1 and thioflavin-S, for visualization of Aβ plaques, demonstrated that many of the microglia with enlarged cell bodies and processes were associated with the perimeters of plaques (Figure 6.7B).

6.5 Discussions

6.5.1 Whole Brain Metabolism

AD is characterized by several pathological hallmarks in the brain, including the emergence of Aβ plaques. In this respect, the 5XFAD mouse is an aggressive model of brain amyloidosis marked by early development of Aβ plaques and cognitive dysfunction (Oakley et al., 2006). It is unknown whether the 5XFAD animal model recapitulates phenotypes of AD such as decreased brain glucose metabolism. Thus, FDG uptake relative to Aβ pathology and neuroinflammation was determined in the 5XFAD animal model at different ages. A recent study has also explored brain metabolic changes in this AD model (Rojas et al., 2013); however both differences and similarities exist between our results and that study.

Measurement of whole brain metabolism herein relied on determining SUVs at each age group, 2, 5, 8 and 13 months (Figure 6.2). In particular, at 2 and 5 months a non-significant trend was observed towards a lower SUV for 5XFAD animals when compared to WT. Furthermore, at 8 months of age, animals exhibited no difference in SUVs between AD and WT animals. The 13 month age group exhibited significantly lower SUVs for the 5XFAD animals compared to WT. This suggests that insult to the brain may accumulate as these animals age, resulting in reduced metabolism late in the

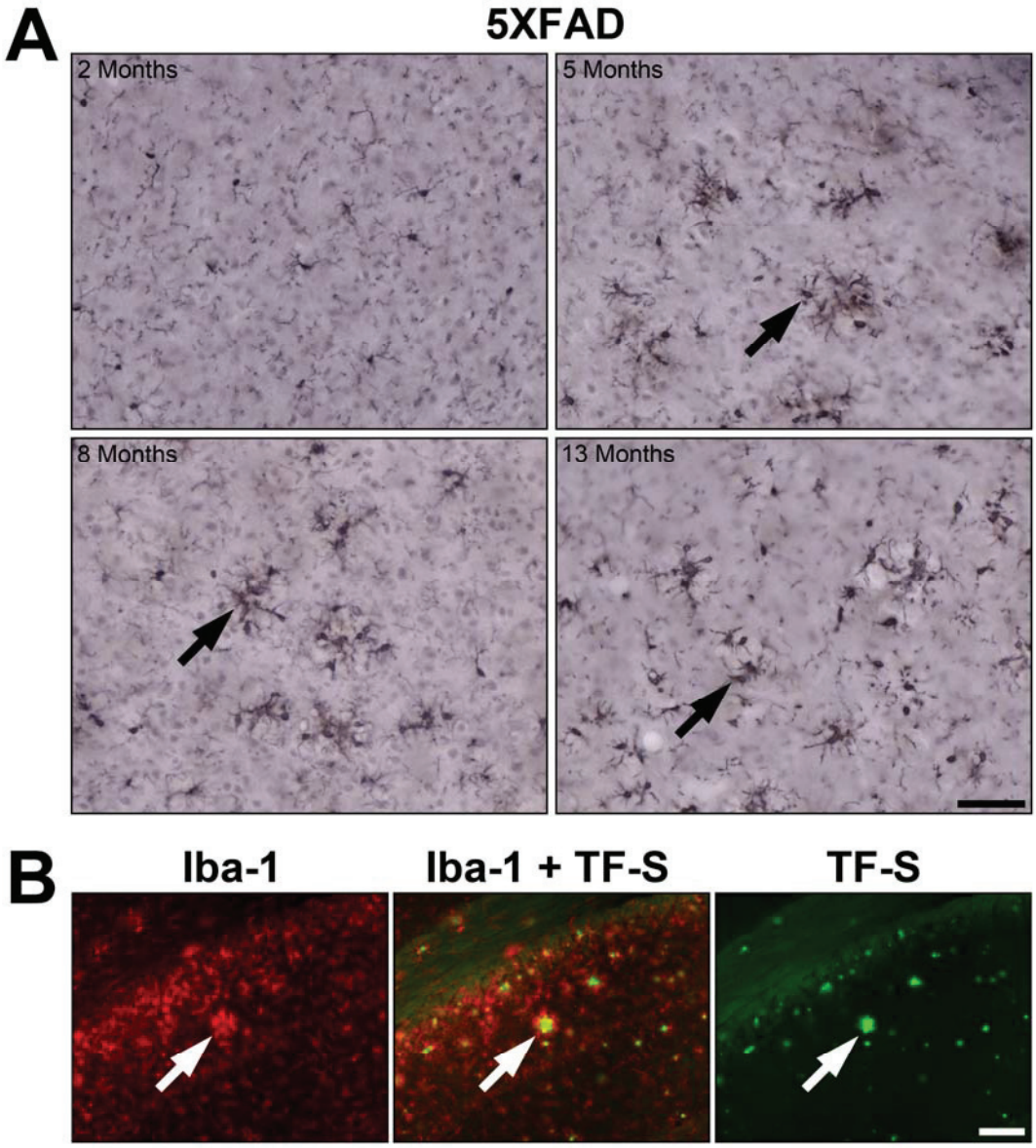

Figure 6.7. Visualization of microglia in the 5XFAD brain. **A.** Iba-1 immunohistochemistry identified reactive microglia (arrows) which increased with age. Microglia in wild-type animals at all ages (not shown) were comparable to the 2 month 5XFAD animals. Scale bar: 50 μm. **B.** Co-localization of Iba-1 immunohistochemistry and thioflavin-S (TF-S) histochemistry, to visualize Aβ deposition, demonstrated the association of reactive microglia around the perimeter of plaques (arrows) in the 5XFAD brain Scale bar: 200 μm.

disease progress. A similar reduction in glucose metabolism has been observed in older 3xTG animals (Nicholson et al., 2010). In contrast, another previous study has reported that, in older 5XFAD animals, the brain has increased uptake of FDG compared to WT animals (Rojas et al., 2013). However, this study used an internal reference tissue, the cerebellum, in contrast to the SUV measurements reported here.

6.5.2 Regional Brain Metabolism

The brains of 5XFAD and WT animals were parcellated into 8 different regions and the SUV for each was determined (Figure 6.3). Reflecting the results for whole brain metabolism, there was no significant difference between 5XFAD and WT SUVs for any of the brain regions for the 2, 5 and 8 month age groups. However, the 2 and 5 month group did indicate a trend towards a lower SUV for the AD animals, again similar to whole brain uptake. The 13 month age group provided significantly lower SUVs for the 5XFAD animals in 6 of the 8 brain regions investigated. These results suggest that the reduced SUV values for the 13 month 5XFAD animals represent a global decrease in metabolic activity across the brain.

Brain regions were also normalized to each of the others in order to provide a measure of glucose uptake relative to an internal reference tissue. An ideal internal reference tissue would demonstrate FDG uptake independent of Aβ deposition and other pathological processes such as neuroinflammation. However, glucose metabolism may be altered in each area of the 5XFAD brain; thus, no single area was identified as an ideal internal reference tissue. Therefore all regions were used individually as the reference tissue. This normalized metabolic activity was compared between WT and 5XFAD

animals and significant differences were determined (Figure 6.4). In 2 months of age animals, the FDG uptake of the amygdala, basal forebrain and hypothalamus, relative to the neocortex, demonstrated an increase in SUV for the 5XFAD animals. This suggests that at an early stage of brain amyloidosis, such as occurs at 2 months, there may be deficits in neocortical function. At 13 months of age, the hypothalamus and thalamus, relative to the amygdala, demonstrated reduced SUVs in 5XFAD compared to WT animals. At this late disease stage, many brain areas demonstrated decreases in glucose metabolism (Figure 6.3). Therefore, these results may signify that the rate of decrease in metabolic function of the amygdala is less than that for the hypothalamus and thalamus. Thus, Aβ deposition may impair function in some parts of the brain, such as the thalamus and hypothalamus, to a greater extent than others, such as the amygdala.

6.5.3 B-Amyloid Deposition

Deposited brain Aβ protein was visualized with immunohistochemistry and quantified as the area covered in each parcellated brain region (Figure 6.5). The amount of Aβ burden varied among different brain regions but was typically high in areas, such as the neocortex and hippocampus, traditionally affected in AD. Mechanisms of Aβ accumulation are unclear but may be influenced by connectivity with other brain regions or inherent susceptibility. In this respect, areas of widespread connectivity, such as the neocortex, display high levels of Aβ deposition. In addition, Aβ burden demonstrated a linear increase with age, signifying a constant brain deposition of the protein that did not reach a plateau by 13 months of age (Figure 6.6). A correlation between Aβ burden and brain SUVs across the age groups was not found. This reflects the disconnection

observed in human AD between Aβ plaque load and brain function (Mortimer, 2012). Much like the human condition, it was not until later in the 5XFAD disease stage, at 13 months, that profound metabolic changes were observed in the brain. These statistically significant changes in 5XFAD SUVs displayed at least a 13% decrease in glucose metabolism compared to WT. Thus, modest changes in metabolic function in young 5XFAD animals, as observed early in human AD (Bateman et al., 2012), may not be detectable in this study.

6.5.4 Microglia

Brain inflammation can lead to increased FDG uptake (Radu et al., 2007) and thus, may contribute to metabolic activity in the AD brain. Increasing levels of activated microglia were observed with increasing age of the 5XFAD animals (Figure 6.7A). In contrast, age-matched WT animals did not show any differences in microglia populations with age. Activated microglia in the 5XFAD animals were observed around the perimeter of Aβ deposits (Figure 6.7B), as noted previously (Hillmann et al., 2012), suggesting that these immune cells may contribute to deficits, such as disrupted synapse integrity, in these animals as has been noted in human AD (Meda et al., 1995; Parachikova et al., 2007). Furthermore, their presence may increase brain FDG uptake in 5XFAD animals, as suggested also by others (Rojas et al., 2013), and thus, may mask potential changes in metabolism, in particular at early ages. This may account for the observations in this study that significant decreases in FDG uptake were not observed at 2, 5 and 8 months of age, despite increasing Aβ burden in the brain. This potential masking effect of FDG uptake by microglia may only be overcome at late stages of

disease where brain function is severely impaired in the 5XFAD animal, such as at 13 months. This would result in the observed decreased glucose metabolism in the 13 month 5XFAD animals.

6.6 Conclusions

The 5XFAD mouse develops aggressive brain amyloidosis early in life. Similar to human AD, altered brain metabolism was observed in late disease stages in this mouse model compared to age matched controls. However, metabolic function did not correlate to Aβ plaque burden in this animal model. FDG uptake by reactive microglia, associated with Aβ plaques in 5XFAD animals, may contribute to this discrepancy. This mouse model recapitulated aspects of human AD such as Aβ deposition, microglia activation and decreases in glucose metabolism. Thus, the 5XFAD mouse model may be a powerful tool for assessing efficacy of diagnostic and therapeutic agents being developed for AD.

CHAPTER 7 CONCLUSIONS

7.1 PREFACE

In the following section, conclusions will be drawn from each Chapter within the context of the development of cholinesterase imaging agents for use in neurological disease. In addition, the relevance of this thesis work to the field of cholinesterase imaging agents will be discussed and future endeavors towards the goal of a clinical cholinesterase radiopharmaceutical will be explored.

7.2 GENERAL CHAPTER CONCLUSIONS

Chapter 1 described the clinical characteristics and putative pathogenesis of Alzheimer's disease (AD) and multiple sclerosis (MS). The management of both of these disorders suffers from the lack of a specific method for definitive diagnosis and monitoring of pathological progression. Neuroimaging, in this respect, could greatly assist clinical diagnosis and accelerate evaluation of novel therapeutics, in particular for AD, in which discovery of disease-modifying therapies has remained elusive. Due to their association with the characteristic pathology of AD and MS, acetylcholinesterase (AChE) and butyrylcholinesterase (BuChE) are potential neuroimaging targets for these disorders. Several cholinesterase imaging agents have been previously developed and tested in neurological diseases. However, none of these agents have visualized cholinesterase activity associated with the pathology of AD and MS. Thus, the principal objective of this thesis was the development and evaluation of imaging agents that recapitulate the association of cholinesterases with AD and MS disease pathology.

Chapters 2-4 described the synthesis and evaluation of several classes of imaging agents towards AChE and BuChE. Ester derivatives, based on the structure of acetylcholine, were the initial agents evaluated as described in Chapter 2. These were successful in recapitulating the distribution of BuChE in the rodent brain *in vivo* (Macdonald et al., 2011). Derivatization of the ester group to thioester functionality permitted the evaluation of a variety of compounds as cholinesterase imaging agents in Chapter 3. This approach allowed for rapid assessment of enzyme kinetics as well as histochemical distribution of compounds, relative to cholinesterase activity, in tissues of interest (Macdonald et al., 2013). This methodology can be employed to rapidly screen appropriate libraries of compounds for the optimization of cholinesterase imaging agents. Chapter 4 presented the synthesis and evaluation of a cholinesterase inhibitor possessing a carbamate functional group as an imaging agent (Darvesh et al., 2012a). This compound, ^{123}I-PIP, successfully visualized cholinesterases associated with AD pathology in both a mouse model of AD and human brain tissues. Furthermore, in contrast to Aβ imaging agents, such as ^{123}I-IMPY, ^{123}I-PIP was able to distinguish AD brain tissues from those of cognitively normal with Aβ plaques. This proof of principle is a critical first step towards the neuroimaging of cholinesterases for the definitive diagnosis of AD.

The synthesis and evaluation of compounds in Chapters 2-4 identified ^{123}I-PIP as a promising cholinesterase imaging agent for use in neurological disease. Optimization of this agent demands an intimate knowledge of amino acid residue binding sites within the active site gorges of AChE and BuChE. Crystal structures of AChE bound to a variety of inhibitors have identified residues important for these enzyme-inhibitor

interactions within the active site gorge. However, parallel x-ray crystallography studies investigating the BuChE active site gorge remain limited. In this respect, Chapter 5 presented a kinetic approach to the identification of inhibitor and ligand binding sites for BuChE (Macdonald et al., 2012). This study identified residues contributing to the P-site of the enzyme that are shown to greatly influence binding characteristics of inhibitors and substrates and, consequently, function of the enzyme. Targeting regions of the active site gorge, such as the P-site, may afford optimized ligands that have great promise as cholinesterase imaging agents.

In order to advance cholinesterase imaging agents into clinical trials, robust pre-clinical testing is required. As a harbinger for *in vivo* small animal evaluation of cholinesterase imaging agents, an initial neuroimaging study of an animal model of AD, the 5XFAD mouse, is described in Chapter 6. Glucose metabolism, using FDG, was assessed with respect to brain amyloidosis and inflammation in this model. This work identified that in late stages of brain amyloidosis in the 5XFAD mouse, a profound decrease in brain metabolism was observed. This is a similar phenotype as human AD. Thus, this combined neuroimaging and pathological analysis method in the 5XFAD mouse is a promising approach for the assessment of cholinesterase imaging agents for the visualization of Aβ plaque pathology.

7.3 Comments on the Future of Cholinesterase Imaging in Neurological Disorders

A significant achievement of this thesis work has been the development of cholinesterase imaging agents that recapitulate the association of AChE and BuChE with the pathology of neurological diseases such as AD. Nevertheless, prominent elements

remain to be addressed before the goal of clinical application of cholinesterase imaging in neurological disease is realized.

Of principal importance is the nature of the association of AChE and BuChE with the pathology of AD. To date, only subjective evidence of the role of these enzymes in AD pathogenesis has been provided in the literature. In particular, a robust investigation into the specificity of cholinesterase-associated plaques and tangles for distinguishing AD relative to cognitively normal brains is required. It is probable that this relationship is a spectrum and therefore, a distinct boundary between diseased and cognitively normal brain with respect to cholinesterase-associated pathology does not exist. Post-mortem brain studies linking detailed clinical history with cholinesterase-associated pathology levels may provide valuable insight in this regard.

In a similar approach to that outlined for AD, the role of cholinesterases, in particular BuChE, in MS requires further investigation. It is unknown whether differences exist between BuChE activity associated with lesions of progressive and relapsing disease courses. Furthermore, characterizing the association of BuChE with cortical MS lesions, an area with high activity of this enzyme in AD, may yield valuable insights into its role in MS. These studies may further establish BuChE as a promising imaging target for the diagnosis and treatment of MS. Work presented in this thesis described the visualization of cholinesterase activity associated with AD pathology using ^{123}I-PIP. Similar autoradiographic studies in post mortem human MS brain tissue and animal models of MS may be a promising start towards cholinesterase imaging for the diagnosis and pathology monitoring of this disease.

In order to optimize the cholinesterase imaging agents described in this thesis, structure-activity-relationships, in particular based on PIP, will be essential. Although the first leaving group of cholinesterase catalyzed hydrolysis of PIP is presumed to be the phenolic moiety, definitive evidence is currently lacking. Furthermore, derivatization of PIP may change the chemical properties of the leaving group, between either the phenolic or anilinic moieties, in the first step of enzymatic catalysis. Elucidation of the mechanism of cholinesterase mediated hydrolysis for PIP and its derivatives will aid in determining the optimal location of a radioisotope on these molecules. Furthermore, synthesis and evaluation of PIP derivatives with a variety of steric and electronic properties may identify potent cholinesterase ligands that are promising candidates as imaging agents. In addition, these structure activity relationships will potentially define ideal kinetic parameters for cholinesterase imaging agents possessing carbamate functionality. In particular, the rate of deactivation (k_a value) and subsequent reactivation ($k_{a'}$) of AChE and BuChE by these compounds may be cardinal for predicting their ability as imaging agents. In addition, evaluation of thiocarbamates using a similar approach as described for thioesters in Chapter 3, may facilitate the kinetic characterization of carabamate derivatives towards AChE and BuChE.

A multitude of ligand binding sites in the AChE and BuChE active site gorges have been identified previously in the literature. Chapter 5 has extended this work for BuChE, in particular characterizing the P-site of this enzyme. Further active site gorge characterizations of the cholinesterases using kinetic and mutant enzyme approaches, as well as x-ray crystallography, may further define residues pivotal for potent binding to

these enzymes. Targeting the binding sites that may result from these studies will serve to accelerate the development of compounds as imaging agents for AChE and BuChE.

Small animal imaging of neurological disease models will aid in the optimization of imaging agents and expedite clinical adoption of radiopharmaceuticals. Assessment of imaging AD pathology and related processes in transgenic animals, such as the 5XFAD model described in Chapter 6, is one approach to validate imaging agents in an *in vivo* system. Cholinesterase imaging of AD and MS mouse models, in conjunction with histological evidence, will accelerate the development of these agents. In this respect, small animal *in vivo* imaging studies have largely been lacking for cholinesterase imaging agents. However, with the increased availability of dedicated small animal scanners, advances in imaging methodology and histologically characterized animal models this approach is poised to be a major contributor to the development of imaging agents for neurodegenerative disorders.

Neurological diseases, such as AD and MS, have plagued humankind for many years without respite. Scientific achievement has brought us to the precipice of effectively treating these disorders and restoring health to those afflicted. Imaging of the living brain has, and will increasingly, accelerate the discovery of pathognomic processes and guide therapeutic interventions. In this respect, cholinesterase imaging may be a decisive contributor towards the diagnosis and pathological monitoring of neurological diseases, such as AD and MS. Continued strides towards a clinical cholinesterase imaging agent has the potential to aid in development of disease modifying therapies, ameliorate patient management and, ultimately, propitiously impact the lives of those suffering the bane of neurological disease.

BIBLIOGRAPHY

Aamodt EJ, Williams RC, Jr. (1984) Microtubule-associated proteins connect microtubules and neurofilaments in vitro. Biochemistry 23:6023-6031.

Adams JC (1977) Technical considerations on the use of horseradish peroxidase as a neuronal marker. Neuroscience 2:141-145.

Agdeppa ED, Kepe V, Liu J, Flores-Torres S, Satyamurthy N, Petric A, Cole GM, Small GW, Huang SC, Barrio JR (2001) Binding characteristics of radiofluorinated 6-dialkylamino-2-naphthylethylidene derivatives as positron emission tomography imaging probes for beta-amyloid plaques in Alzheimer's disease. J Neurosci 21:RC189.

Albert MS, DeKosky ST, Dickson D, Dubois B, Feldman HH, Fox NC, Gamst A, Holtzman DM, Jagust WJ, Petersen RC, Snyder PJ, Carrillo MC, Thies B, Phelps CH (2011) The diagnosis of mild cognitive impairment due to Alzheimer's disease: recommendations from the National Institute on Aging-Alzheimer's Association workgroups on diagnostic guidelines for Alzheimer's disease. Alzheimers Dement 7:270-279.

Alles G, Hawes R (1940) Cholinesterases in the blood of man. J Biol Chem 133:375-390.

Allison RS, Millar JH (1954) Prevalence of disseminated sclerosis in Northern Ireland. Ulster Med J 23:1-27.

Alter M, Okihiro M (1971) When is multiple sclerosis acquired? Neurology 21:1030-1036.

Alter M, Allison RS, Talbert OR, Kurland LT (1960) Geographic distribution of multiple sclerosis - a comparison of prevalence in Charleston County, South Carolina, USA, and Halifax County, Nova Scotia, Canada. World Neurology 1:55-68.

Alter M, Halpern L, Kurland LT, Bornstein B, Leibowitz U, Silberstein J (1962) Multiple sclerosis in Israel. Prevalence among immigrants and native inhabitants. Arch Neurol 7:253-263.

Alzheimer A (1906) Über einen eigenartigen schweren Erkrankungsprozeß der Hirnrinde. Neurologisches Centralblatt 23:1129–1136.

Alzheimer A (1907) Über eine eigenartige Erkrankung der Hirnrinde. Allgemeine Zeitschrift für Psychiatrie und Psychisch-Gerichtliche Medizin 64:146–148.

Andreadis A, Brown WM, Kosik KS (1992) Structure and novel exons of the human tau gene. Biochemistry 31:10626-10633.

Andreadis A, Broderick JA, Kosik KS (1995) Relative exon affinities and suboptimal splice site signals lead to non-equivalence of two cassette exons. Nucleic Acids Res 23:3585-3593.

Arendt T, Bigl V (1986) Alzheimer plaques and cortical cholinergic innervation. Neuroscience 17:277-279.

Arendt T, Bigl V, Arendt A, Tennstedt A (1983) Loss of neurons in the nucleus basalis of Meynert in Alzheimer's disease, paralysis agitans and Korsakoff's Disease. Acta Neuropathol 61:101-108.

Arendt T, Bigl V, Tennstedt A, Arendt A (1985) Neuronal loss in different parts of the nucleus basalis is related to neuritic plaque formation in cortical target areas in Alzheimer's disease. Neuroscience 14:1-14.

Arendt T, Bruckner MK, Lange M, Bigl V (1992) Changes in acetylcholinesterase and butyrylcholinesterase in Alzheimer's disease resemble embryonic development--a study of molecular forms. Neurochem Int 21:381-396.

Arispe N, Pollard HB, Rojas E (1993) Giant Multilevel Cation Channels Formed by Alzheimer-Disease Amyloid Beta-Protein [a-Beta-P-(1-40)] in Bilayer-Membranes. Proceedings of the National Academy of Sciences of the United States of America 90:10573-10577.

Arpagaus M, Kott M, Vatsis KP, Bartels CF, La Du BN, Lockridge O (1990) Structure of the gene for human butyrylcholinesterase. Evidence for a single copy. Biochemistry 29:124-131.

Asanuma C (1997) Distribution of neuromodulatory inputs in the reticular and dorsal thalamic nuclei. In: Thalamus. II. Experimental and Clinical Aspects (Steriade M, Jones EG, McCormick DA, eds). Amsterdam: Elsevier.

Assadi M, Salimipour H, Seyedabadi M, Saberifard J, Javadi H, Nabipour I, Nemati R (2010) Brain single photon emission computed tomography with Tc-99m MIBI or Tc-99m ECD in comparison to MRI in multiple sclerosis. Clin Nucl Med 35:682-686.

Atack JR, Perry EK, Bonham JR, Candy JM, Perry RH (1986) Molecular forms of acetylcholinesterase and butyrylcholinesterase in the aged human central nervous system. J Neurochem 47:263-277.

Atack JR, Perry EK, Bonham JR, Candy JM, Perry RH (1987) Molecular forms of butyrylcholinesterase in the human neocortex during development and degeneration of the cortical cholinergic system. J Neurochem 48:1687-1692.

Auletta JT, Johnson JL, Rosenberry TL (2010) Molecular basis of inhibition of substrate hydrolysis by a ligand bound to the peripheral site of acetylcholinesterase. Chem Biol Interact 187:135-141.

Auriel E, Greenberg SM (2012) The pathophysiology and clinical presentation of cerebral amyloid angiopathy. Curr Atheroscler Rep 14:343-350.

Avila J, Lucas JJ, Perez M, Hernandez F (2004) Role of tau protein in both physiological and pathological conditions. Physiol Rev 84:361-384.

Babbe H, Roers A, Waisman A, Lassmann H, Goebels N, Hohlfeld R, Friese M, Schroder R, Deckert M, Schmidt S, Ravid R, Rajewsky K (2000) Clonal expansions of CD8(+) T cells dominate the T cell infiltrate in active multiple sclerosis lesions as shown by micromanipulation and single cell polymerase chain reaction. J Exp Med 192:393-404.

Bacskai BJ, Hickey GA, Skoch J, Kajdasz ST, Wang Y, Huang GF, Mathis CA, Klunk WE, Hyman BT (2003) Four-dimensional multiphoton imaging of brain entry, amyloid binding, and clearance of an amyloid-beta ligand in transgenic mice. Proc Natl Acad Sci U S A 100:12462-12467.

Baek SH, Ohgi KA, Rose DW, Koo EH, Glass CK, Rosenfeld MG (2002) Exchange of N-CoR corepressor and Tip60 coactivator complexes links gene expression by NF-kappaB and beta-amyloid precursor protein. Cell 110:55-67.

Banati RB, Newcombe J, Gunn RN, Cagnin A, Turkheimer F, Heppner F, Price G, Wegner F, Giovannoni G, Miller DH, Perkin GD, Smith T, Hewson AK, Bydder G, Kreutzberg GW, Jones T, Cuzner ML, Myers R (2000) The peripheral benzodiazepine binding site in the brain in multiple sclerosis: quantitative in vivo imaging of microglia as a measure of disease activity. Brain 123 (Pt 11):2321-2337.

Barak D, Kronman C, Ordentlich A, Ariel N, Bromberg A, Marcus D, Lazar A, Velan B, Shafferman A (1994) Acetylcholinesterase peripheral anionic site degeneracy conferred by amino acid arrays sharing a common core. J Biol Chem 269:6296-6305.

Barbelivien A, Bertrand N, Besret L, Beley A, MacKenzie ET, Dauphin F (1999) Neurochemical stimulation of the rat substantia innominata increases cerebral blood flow (but not glucose use) through the parallel activation of cholinergic and non-cholinergic pathways. Brain Res 840:115-124.

Barkhof F (2002) The clinico-radiological paradox in multiple sclerosis revisited. Curr Opin Neurol 15:239-245.

Barnes J, Bartlett JW, van de Pol LA, Loy CT, Scahill RI, Frost C, Thompson P, Fox NC (2009) A meta-analysis of hippocampal atrophy rates in Alzheimer's disease. Neurobiol Aging 30:1711-1723.

Barrera H, Lyle R (1962) Piperidine Derivatives with a Sulfur-Containing Function in the 4-Position. J Org Chem 27:641-643.

Bartels CF, Jensen FS, Lockridge O, van der Spek AF, Rubinstein HM, Lubrano T, La Du BN (1992) DNA mutation associated with the human butyrylcholinesterase K-variant and its linkage to the atypical variant mutation and other polymorphic sites. Am J Hum Genet 50:1086-1103.

Bartus RT (2000) On neurodegenerative diseases, models, and treatment strategies: lessons learned and lessons forgotten a generation following the cholinergic hypothesis. Exp Neurol 163:495-529.

Bartus RT, Dean RL, 3rd, Beer B, Lippa AS (1982) The cholinergic hypothesis of geriatric memory dysfunction. Science 217:408-414.

Bateman RJ et al. (2012) Clinical and biomarker changes in dominantly inherited Alzheimer's disease. N Engl J Med 367:795-804.

Bellier JP, Kimura H (2011) Peripheral type of choline acetyltransferase: biological and evolutionary implications for novel mechanisms in cholinergic system. J Chem Neuroanat 42:225-235.

Bencherif B, Endres CJ, Musachio JL, Villalobos A, Hilton J, Scheffel U, Dannals RF, Williams S, Frost JJ (2002) PET imaging of brain acetylcholinesterase using [11C]CP-126,998, a brain selective enzyme inhibitor. Synapse 45:1-9.

Benedek S, McGovern V (1949) A case of Alzheimer's disease with amyloidosis of the vessels of the cerebral cortex. Med J Aust 2:429, pl.

Benilova I, Karran E, De Strooper B (2012) The toxic Abeta oligomer and Alzheimer's disease: an emperor in need of clothes. Nat Neurosci 15:349-357.

Bennett BD, Babu-Khan S, Loeloff R, Louis JC, Curran E, Citron M, Vassar R (2000) Expression analysis of BACE2 in brain and peripheral tissues. J Biol Chem 275:20647-20651.

Berman HM, Westbrook J, Feng Z, Gilliland G, Bhat TN, Weissig H, Shindyalov IN, Bourne PE (2000) The Protein Data Bank. Nucleic Acids Res 28:235.

Bertram L, McQueen MB, Mullin K, Blacker D, Tanzi RE (2007) Systematic meta-analyses of Alzheimer disease genetic association studies: the AlzGene database. Nat Genet 39:17-23.

Bickford ME, Gunluk AE, Van Horn SC, Sherman SM (1994) GABAergic projection from the basal forebrain to the visual sector of the thalamic reticular nucleus in the cat. J Comp Neurol 348:481-510.

Bierer LM, Haroutunian V, Gabriel S, Knott PJ, Carlin LS, Purohit DP, Perl DP, Schmeidler J, Kanof P, Davis KL (1995) Neurochemical correlates of dementia severity in Alzheimer's disease: relative importance of the cholinergic deficits. J Neurochem 64:749-760.

Biesold D, Inanami O, Sato A, Sato Y (1989) Stimulation of the nucleus basalis of Meynert increases cerebral cortical blood flow in rats. Neurosci Lett 98:39-44.

Bigl V, Schliebs R (1998) Simulation of cortical cholinergic deficits--a novel experimental approach to study pathogenetic aspects of Alzheimer's disease. J Neural Transm Suppl 54:237-247.

Billo EJ (2011) Excel for Chemists, Third Edition Edition. Hoboken, New Jersey: John Wiley and Sons.

Binder LI, Frankfurter A, Rebhun LI (1985) The distribution of tau in the mammalian central nervous system. J Cell Biol 101:1371-1378.

Birks J (2006) Cholinesterase inhibitors for Alzheimer's disease. Cochrane Database Syst Rev:CD005593.

Bjartmar C, Kinkel RP, Kidd G, Rudick RA, Trapp BD (2001) Axonal loss in normal-appearing white matter in a patient with acute MS. Neurology 57:1248-1252.

Blennow K, de Leon MJ, Zetterberg H (2006) Alzheimer's disease. Lancet 368:387-403.

Blomqvist G, Tavitian B, Pappata S, Crouzel C, Jobert A, Doignon I, Di Giamberardino L (2001) Quantitative measurement of cerebral acetylcholinesterase using [11C]physostigmine and positron emission tomography. J Cereb Blood Flow Metab 21:114-131.

Bo L, Mork S, Kong PA, Nyland H, Pardo CA, Trapp BD (1994a) Detection of MHC class II-antigens on macrophages and microglia, but not on astrocytes and endothelia in active multiple sclerosis lesions. J Neuroimmunol 51:135-146.

Bo L, Dawson TM, Wesselingh S, Mork S, Choi S, Kong PA, Hanley D, Trapp BD (1994b) Induction of nitric oxide synthase in demyelinating regions of multiple sclerosis brains. Ann Neurol 36:778-786.

Bohnen NI, Kaufer DI, Hendrickson R, Ivanco LS, Lopresti BJ, Koeppe RA, Meltzer CC, Constantine G, Davis JG, Mathis CA, Dekosky ST, Moore RY (2005) Degree of inhibition of cortical acetylcholinesterase activity and cognitive effects by donepezil treatment in Alzheimer's disease. J Neurol Neurosurg Psychiatry 76:315-319.

Bolcaen J, Acou M, Mertens K, Hallaert G, Van den Broecke C, Achten E, Goethals I (2012) Structural and Metabolic Features of Two Different Variants of Multiple Sclerosis: A PET/MRI Study. J Neuroimaging.

Boller F, Forbes MM (1998) History of dementia and dementia in history: an overview. J Neurol Sci 158:125-133.

Bondi MW, Houston WS, Eyler LT, Brown GG (2005) fMRI evidence of compensatory mechanisms in older adults at genetic risk for Alzheimer disease. Neurology 64:501-508.

Bonnot-Lours S, Crouzel C, Prenant C, Hinnen F (1993) Carbon-11 labelling of an inhibitor of acetylcholinesterase: [11C]physostigmine. J Labelled Comp Radiopharm 33:277–284.

Bookheimer SY, Strojwas MH, Cohen MS, Saunders AM, Pericak-Vance MA, Mazziotta JC, Small GW (2000) Patterns of brain activation in people at risk for Alzheimer's disease. N Engl J Med 343:450-456.

Boopathy R, Layer PG (2004) Aryl acylamidase activity on acetylcholinesterase is high during early chicken brain development. Protein J 23:325-333.

Borghesani PR, Johnson LC, Shelton AL, Peskind ER, Aylward EH, Schellenberg GD, Cherrier MM (2008) Altered medial temporal lobe responses during visuospatial encoding in healthy APOE*4 carriers. Neurobiol Aging 29:981-991.

Bormans G, Sherman P, Snyder SE, Kilbourn MR (1996) Synthesis of carbon-11- and fluorine-18-labeled 1-methyl-4-piperidyl-4'-fluorobenzoate and their biodistribution in mice. Nucl Med Biol 23:513-517.

Bot JC, Barkhof F (2009) Spinal-cord MRI in multiple sclerosis: conventional and nonconventional MR techniques. Neuroimaging Clin N Am 19:81-99.

Bourne Y, Radic Z, Sulzenbacher G, Kim E, Taylor P, Marchot P (2006) Substrate and product trafficking through the active center gorge of acetylcholinesterase analyzed by crystallography and equilibrium binding. J Biol Chem 281:29256-29267.

Bowen DM, Sims NR, Benton JS, Curzon G, Davison AN, Neary D, Thomas DJ (1981) Treatment of Alzheimer's disease: a cautionary note. N Engl J Med 305:1016.

Bozzali M, Cercignani M, Sormani MP, Comi G, Filippi M (2002) Quantification of brain gray matter damage in different MS phenotypes by use of diffusion tensor MR imaging. AJNR Am J Neuroradiol 23:985-988.

Braak E, Braak H, Mandelkow EM (1994) A sequence of cytoskeleton changes related to the formation of neurofibrillary tangles and neuropil threads. Acta Neuropathol 87:554-567.

Braak H, Braak E (1991) Neuropathological stageing of Alzheimer-related changes. Acta Neuropathol 82:239-259.

Braak H, Braak E (1995) Staging of Alzheimer's disease-related neurofibrillary changes. Neurobiol Aging 16:271-278; discussion 278-284.

Brandt R, Leger J, Lee G (1995) Interaction of tau with the neural plasma membrane mediated by tau's amino-terminal projection domain. J Cell Biol 131:1327-1340.

Briard E, Orain D, Beerli C, Billich A, Streiff M, Bigaud M, Auberson YP (2011) BZM055, an iodinated radiotracer candidate for PET and SPECT imaging of myelin and FTY720 brain distribution. ChemMedChem 6:667-677.

Brown GC, Borutaite V (2002) Nitric oxide inhibition of mitochondrial respiration and its role in cell death. Free Radic Biol Med 33:1440-1450.

Buck D, Forschler A, Lapa C, Schuster T, Vollmar P, Korn T, Nessler S, Stadelmann C, Drzezga A, Buck AK, Wester HJ, Zimmer C, Krause BJ, Hemmer B (2012) 18F-FDG PET detects inflammatory infiltrates in spinal cord experimental autoimmune encephalomyelitis lesions. J Nucl Med 53:1269-1276.

Buee L, Bussiere T, Buee-Scherrer V, Delacourte A, Hof PR (2000) Tau protein isoforms, phosphorylation and role in neurodegenerative disorders. Brain Res Brain Res Rev 33:95-130.

Burns A, Byrne EJ, Maurer K (2002) Alzheimer's disease. Lancet 360:163-165.

Bytyqi AH, Lockridge O, Duysen E, Wang Y, Wolfrum U, Layer PG (2004) Impaired formation of the inner retina in an AChE knockout mouse results in degeneration of all photoreceptors. Eur J Neurosci 20:2953-2962.

Cader S, Cifelli A, Abu-Omar Y, Palace J, Matthews PM (2006) Reduced brain functional reserve and altered functional connectivity in patients with multiple sclerosis. Brain 129:527-537.

Cai XD, Golde TE, Younkin SG (1993) Release of excess amyloid beta protein from a mutant amyloid beta protein precursor. Science 259:514-516.

Calabrese M, Rocca MA, Atzori M, Mattisi I, Favaretto A, Perini P, Gallo P, Filippi M (2010) A 3-year magnetic resonance imaging study of cortical lesions in relapse-onset multiple sclerosis. Ann Neurol 67:376-383.

Calabrese M, Romualdi C, Poretto V, Favaretto A, Morra A, Rinaldi F, Perini P, Gallo P (2013) The changing clinical course of multiple sclerosis: A matter of grey matter. Ann Neurol.

Calabrese M, Agosta F, Rinaldi F, Mattisi I, Grossi P, Favaretto A, Atzori M, Bernardi V, Barachino L, Rinaldi L, Perini P, Gallo P, Filippi M (2009) Cortical lesions and atrophy associated with cognitive impairment in relapsing-remitting multiple sclerosis. Arch Neurol 66:1144-1150.

Cantore WA (1996) Optic neuritis. Pa Med 99 Suppl:96-98.

Cao X, Sudhof TC (2001) A transcriptionally [correction of transcriptively] active complex of APP with Fe65 and histone acetyltransferase Tip60. Science 293:115-120.

Cao X, Sudhof TC (2004) Dissection of amyloid-beta precursor protein-dependent transcriptional transactivation. J Biol Chem 279:24601-24611.

Carlier MF, Simon C, Cassoly R, Pradel LA (1984) Interaction between microtubule-associated protein tau and spectrin. Biochimie 66:305-311.

Carson KA, Geula C, Mesulam MM (1991) Electron microscopic localization of cholinesterase activity in Alzheimer brain tissue. Brain Res 540:204-208.

Castano EM, Prelli F, Soto C, Beavis R, Matsubara E, Shoji M, Frangione B (1996) The length of amyloid-beta in hereditary cerebral hemorrhage with amyloidosis, Dutch type. Implications for the role of amyloid-beta 1-42 in Alzheimer's disease. J Biol Chem 271:32185-32191.

Castellano JM, Kim J, Stewart FR, Jiang H, DeMattos RB, Patterson BW, Fagan AM, Morris JC, Mawuenyega KG, Cruchaga C, Goate AM, Bales KR, Paul SM, Bateman RJ, Holtzman DM (2011) Human apoE isoforms differentially regulate brain amyloid-beta peptide clearance. Sci Transl Med 3:89ra57.

Caulfield MP, Birdsall NJ (1998) International Union of Pharmacology. XVII. Classification of muscarinic acetylcholine receptors. Pharmacol Rev 50:279-290.

Cavallucci V, D'Amelio M, Cecconi F (2012) Abeta toxicity in Alzheimer's disease. Mol Neurobiol 45:366-378.

Cerf E, Gustot A, Goormaghtigh E, Ruysschaert JM, Raussens V (2011) High ability of apolipoprotein E4 to stabilize amyloid-beta peptide oligomers, the pathological entities responsible for Alzheimer's disease. FASEB J 25:1585-1595.

Chandran S, Hunt D, Joannides A, Zhao C, Compston A, Franklin RJ (2008) Myelin repair: the role of stem and precursor cells in multiple sclerosis. Philos Trans R Soc Lond B Biol Sci 363:171-183.

Charcot JM (1877) Lectures on the Disease of the Nervous System. London: The Sydenham Society.

Chatonnet A, Lockridge O (1989) Comparison of butyrylcholinesterase and acetylcholinesterase. Biochem J 260:625-634.

Chauveau F, Boutin H, Van Camp N, Dolle F, Tavitian B (2008) Nuclear imaging of neuroinflammation: a comprehensive review of [11C]PK11195 challengers. Eur J Nucl Med Mol Imaging 35:2304-2319.

Chen TC, Cense B, Pierce MC, Nassif N, Park BH, Yun SH, White BR, Bouma BE, Tearney GJ, de Boer JF (2005) Spectral domain optical coherence tomography: ultra-high speed, ultra-high resolution ophthalmic imaging. Arch Ophthalmol 123:1715-1720.

Cheng CY, Brochmann-Hanssen E, Waters JA (1982) Quantitative structure-activity relationships of aromatic esters of 1-methyl-4-piperidinol as analgesics. J Med Chem 25:145-152.

Choi SR, Golding G, Zhuang Z, Zhang W, Lim N, Hefti F, Benedum TE, Kilbourn MR, Skovronsky D, Kung HF (2009) Preclinical properties of 18F-AV-45: a PET agent for Abeta plaques in the brain. J Nucl Med 50:1887-1894.

Choo IH, Lee DY, Youn JC, Jhoo JH, Kim KW, Lee DS, Lee JS, Woo JI (2007) Topographic patterns of brain functional impairment progression according to clinical severity staging in 116 Alzheimer disease patients: FDG-PET study. Alzheimer Dis Assoc Disord 21:77-84.

Citron M, Oltersdorf T, Haass C, McConlogue L, Hung AY, Seubert P, Vigo-Pelfrey C, Lieberburg I, Selkoe DJ (1992) Mutation of the beta-amyloid precursor protein in familial Alzheimer's disease increases beta-protein production. Nature 360:672-674.

Citron M et al. (1997) Mutant presenilins of Alzheimer's disease increase production of 42-residue amyloid beta-protein in both transfected cells and transgenic mice. Nat Med 3:67-72.

Clark CM, Pontecorvo MJ, Beach TG, Bedell BJ, Coleman RE, Doraiswamy PM, Fleisher AS, Reiman EM, Sabbagh MN, Sadowsky CH, Schneider JA, Arora A, Carpenter AP, Flitter ML, Joshi AD, Krautkramer MJ, Lu M, Mintun MA, Skovronsky DM (2012) Cerebral PET with florbetapir compared with neuropathology at autopsy for detection of neuritic amyloid-beta plaques: a prospective cohort study. Lancet Neurol 11:669-678.

Compston DA, Batchelor JR, McDonald WI (1976) B-lymphocyte alloantigens associated with multiple sclerosis. Lancet 2:1261-1265.

Corder EH, Saunders AM, Strittmatter WJ, Schmechel DE, Gaskell PC, Small GW, Roses AD, Haines JL, Pericak-Vance MA (1993) Gene dose of apolipoprotein E type 4 allele and the risk of Alzheimer's disease in late onset families. Science 261:921-923.

Corder EH, Saunders AM, Risch NJ, Strittmatter WJ, Schmechel DE, Gaskell PC, Jr., Rimmler JB, Locke PA, Conneally PM, Schmader KE, et al. (1994) Protective effect of apolipoprotein E type 2 allele for late onset Alzheimer disease. Nat Genet 7:180-184.

Correas I, Padilla R, Avila J (1990) The tubulin-binding sequence of brain microtubule-associated proteins, tau and MAP-2, is also involved in actin binding. Biochem J 269:61-64.

Coyle JT, Price DL, DeLong MR (1983) Alzheimer's disease: a disorder of cortical cholinergic innervation. Science 219:1184-1190.

Craft S, Teri L, Edland SD, Kukull WA, Schellenberg G, McCormick WC, Bowen JD, Larson EB (1998) Accelerated decline in apolipoprotein E-epsilon4 homozygotes with Alzheimer's disease. Neurology 51:149-153.

Cserr HF, Harling-Berg CJ, Knopf PM (1992) Drainage of brain extracellular fluid into blood and deep cervical lymph and its immunological significance. Brain Pathol 2:269-276.

Cummings JL (2000) The role of cholinergic agents in the management of behavioural disturbances in Alzheimer's disease. Int J Neuropsychopharmacol 3:21-29.

Dale HH, Feldberg W, Vogt M (1936) Release of acetylcholine at voluntary motor nerve endings. J Physiol 86:353-380.

Danysz W, Parsons CG (2012) Alzheimer's disease, beta-amyloid, glutamate, NMDA receptors and memantine--searching for the connections. Br J Pharmacol 167:324-352.

Darreh-Shori T, Hellstrom-Lindahl E, Flores-Flores C, Guan ZZ, Soreq H, Nordberg A (2004) Long-lasting acetylcholinesterase splice variations in anticholinesterase-treated Alzheimer's disease patients. J Neurochem 88:1102-1113.

Darreh-Shori T, Modiri N, Blennow K, Baza S, Kamil C, Ahmed H, Andreasen N, Nordberg A (2011a) The apolipoprotein E epsilon4 allele plays pathological roles in AD through high protein expression and interaction with butyrylcholinesterase. Neurobiol Aging 32:1236-1248.

Darreh-Shori T, Forsberg A, Modiri N, Andreasen N, Blennow K, Kamil C, Ahmed H, Almkvist O, Langstrom B, Nordberg A (2011b) Differential levels of apolipoprotein E and butyrylcholinesterase show strong association with pathological signs of Alzheimer's disease in the brain in vivo. Neurobiol Aging 32:2320 e2315-2332.

Darvesh S (2013) Butyrylcholinesterase radioligands to image Alzheimer's disease brain. Chem Biol Interact 203:354-357.

Darvesh S, Hopkins DA (2003) Differential distribution of butyrylcholinesterase and acetylcholinesterase in the human thalamus. J Comp Neurol 463:25-43.

Darvesh S, Smereczynsky A, Hopkins D (1992) Distribution of butyrylcholinesterase in the rat brain. In: Neurosci Abstr, p 1505.

Darvesh S, Grantham DL, Hopkins DA (1998) Distribution of butyrylcholinesterase in the human amygdala and hippocampal formation. J Comp Neurol 393:374-390.

Darvesh S, Hopkins DA, Geula C (2003a) Neurobiology of butyrylcholinesterase. Nat Rev Neurosci 4:131-138.

Darvesh S, Reid AG, Martin E (2010a) Biochemical and Histochemical Comparison of Cholinesterases in Normal and Alzheimer Brain Tissues. Curr Alzheimer Res 7:386-400.

Darvesh S, Macdonald IR, Martin E, Pottie IR (2012a) Carbamate compounds and methods of use in diseases of the nervous system. In: (Office USPaT, ed). United States of America: Treventis.

Darvesh S, Kumar R, Roberts S, Walsh R, Martin E (2001) Butyrylcholinesterase-Mediated enhancement of the enzymatic activity of trypsin. Cell Mol Neurobiol 21:285-296.

Darvesh S, Cash MK, Reid GA, Martin E, Mitnitski A, Geula C (2012b) Butyrylcholinesterase is associated with beta-amyloid plaques in the transgenic APPSWE/PSEN1dE9 mouse model of Alzheimer disease. J Neuropathol Exp Neurol 71:2-14.

Darvesh S, Leblanc AM, Macdonald IR, Reid GA, Bhan V, Macaulay RJ, Fisk JD (2010b) Butyrylcholinesterase activity in multiple sclerosis neuropathology. Chem Biol Interact 187:425-431.

Darvesh S, Walsh R, Kumar R, Caines A, Roberts S, Magee D, Rockwood K, Martin E (2003b) Inhibition of human cholinesterases by drugs used to treat Alzheimer disease. Alzheimer Dis Assoc Disord 17:117-126.

Darvesh S, McDonald RS, Darvesh KV, Mataija D, Conrad S, Gomez G, Walsh R, Martin E (2007) Selective reversible inhibition of human butyrylcholinesterase by aryl amide derivatives of phenothiazine. Bioorg Med Chem 15:6367-6378.

Darvesh S, Darvesh KV, McDonald RS, Mataija D, Walsh R, Mothana S, Lockridge O, Martin E (2008) Carbamates with differential mechanism of inhibition toward acetylcholinesterase and butyrylcholinesterase. J Med Chem 51:4200-4212.

Darvesh S, Pottie IR, Darvesh KV, McDonald RS, Walsh R, Conrad S, Penwell A, Mataija D, Martin E (2010c) Differential binding of phenothiazine urea derivatives to wild-type human cholinesterases and butyrylcholinesterase mutants. Bioorg Med Chem 18:2232-2244.

Darvesh S, McDonald RS, Penwell A, Conrad S, Darvesh KV, Mataija D, Gomez G, Caines A, Walsh R, Martin E (2005) Structure-activity relationships for inhibition of human cholinesterases by alkyl amide phenothiazine derivatives. Bioorg Med Chem 13:211-222.

Darvesh S, McDonald RS, Darvesh KV, Mataija D, Mothana S, Cook H, Carneiro KM, Richard N, Walsh R, Martin E (2006) On the active site for hydrolysis of aryl amides and choline esters by human cholinesterases. Bioorg Med Chem 14:4586-4599.

Davies P, Maloney AJ (1976) Selective loss of central cholinergic neurons in Alzheimer's disease. Lancet 2:1403.

Davis KL, Mohs RC, Marin D, Purohit DP, Perl DP, Lantz M, Austin G, Haroutunian V (1999) Cholinergic markers in elderly patients with early signs of Alzheimer disease. JAMA 281:1401-1406.

De Ferrari GV, Mallender WD, Inestrosa NC, Rosenberry TL (2001) Thioflavin T is a fluorescent probe of the acetylcholinesterase peripheral site that reveals conformational interactions between the peripheral and acylation sites. J Biol Chem 276:23282-23287.

De Strooper B (2010) Proteases and proteolysis in Alzheimer disease: a multifactorial view on the disease process. Physiol Rev 90:465-494.

De Strooper B, Saftig P, Craessaerts K, Vanderstichele H, Guhde G, Annaert W, Von Figura K, Van Leuven F (1998) Deficiency of presenilin-1 inhibits the normal cleavage of amyloid precursor protein. Nature 391:387-390.

De Vos F, Santens P, Vermeirsch H, Dewolf I, Dumont F, Slegers G, Dierckx RA, De Reuck J (2000) Pharmacological evaluation of [11C]donepezil as a tracer for visualization of acetylcholinesterase by PET. Nucl Med Biol 27:745-747.

Debruyne JC, Versijpt J, Van Laere KJ, De Vos F, Keppens J, Strijckmans K, Achten E, Slegers G, Dierckx RA, Korf J, De Reuck JL (2003) PET visualization of microglia in multiple sclerosis patients using [11C]PK11195. Eur J Neurol 10:257-264.

DeLano WL (2002) The PyMOL Molecular Graphics System. In. SanCarlos, CA, USA: DeLano Scientific.

Detari L, Rasmusson DD, Semba K (1999) The role of basal forebrain neurons in tonic and phasic activation of the cerebral cortex. Prog Neurobiol 58:249-277.

Devous MD, Sr. (2002) Functional brain imaging in the dementias: role in early detection, differential diagnosis, and longitudinal studies. Eur J Nucl Med Mol Imaging 29:1685-1696.

Diamant S, Podoly E, Friedler A, Ligumsky H, Livnah O, Soreq H (2006) Butyrylcholinesterase attenuates amyloid fibril formation in vitro. Proc Natl Acad Sci U S A 103:8628-8633.

Drachman DA (1977) Memory and cognitive function in man: does the cholinergic system have a specific role? Neurology 27:783-790.

Drachman DA, Leavitt J (1974) Human memory and the cholinergic system. A relationship to aging? Arch Neurol 30:113-121.

Drexler W, Morgner U, Ghanta RK, Kartner FX, Schuman JS, Fujimoto JG (2001) Ultrahigh-resolution ophthalmic optical coherence tomography. Nat Med 7:502-507.

Driscoll I, Troncoso JC, Rudow G, Sojkova J, Pletnikova O, Zhou Y, Kraut MA, Ferrucci L, Mathis CA, Klunk WE, O'Brien RJ, Davatzikos C, Wong DF, Resnick SM (2012) Correspondence between in vivo (11)C-PiB-PET amyloid imaging and postmortem, region-matched assessment of plaques. Acta Neuropathol 124:823-831.

Dubois A, Herard AS, Delatour B, Hantraye P, Bonvento G, Dhenain M, Delzescaux T (2010) Detection by voxel-wise statistical analysis of significant changes in regional cerebral glucose uptake in an APP/PS1 transgenic mouse model of Alzheimer's disease. Neuroimage 51:586-598.

Dubois B, Feldman HH, Jacova C, Dekosky ST, Barberger-Gateau P, Cummings J, Delacourte A, Galasko D, Gauthier S, Jicha G, Meguro K, O'Brien J, Pasquier F, Robert P, Rossor M, Salloway S, Stern Y, Visser PJ, Scheltens P (2007) Research criteria for the diagnosis of Alzheimer's disease: revising the NINCDS-ADRDA criteria. Lancet Neurol 6:734-746.

Dubovy P, Haninec P (1990) Non-specific cholinesterase activity of the developing peripheral nerves and its possible function in cells in intimate contact with growing axons of chick embryo. Int J Dev Neurosci 8:589-602.

Durcan N, Costello RW, McLean WG, Blusztajn J, Madziar B, Fenech AG, Hall IP, Gleich GJ, McGarvey L, Walsh MT (2006) Eosinophil-mediated cholinergic nerve remodeling. Am J Respir Cell Mol Biol 34:775-786.

Dutta-Choudhury TA, Rosenberry TL (1984) Human erythrocyte acetylcholinesterase is an amphipathic protein whose short membrane-binding domain is removed by papain digestion. J Biol Chem 259:5653-5660.

Duysen EG, Li B, Lockridge O (2009) The butyrylcholinesterase knockout mouse a research tool in the study of drug sensitivity, bio-distribution, obesity and Alzheimer's disease. Expert Opin Drug Metab Toxicol 5:523-528.

Eastman J, Wilson EJ, Cervenansky C, Rosenberry TL (1995) Fasciculin 2 binds to the peripheral site on acetylcholinesterase and inhibits substrate hydrolysis by slowing a step involving proton transfer during enzyme acylation. J Biol Chem 270:19694-19701.

Eckenstein F, Sofroniew MV (1983) Identification of central cholinergic neurons containing both choline acetyltransferase and acetylcholinesterase and of central neurons containing only acetylcholinesterase. J Neurosci 3:2286-2291.

Edbauer D, Winkler E, Regula JT, Pesold B, Steiner H, Haass C (2003) Reconstitution of gamma-secretase activity. Nat Cell Biol 5:486-488.

Eglen RM (2006) Muscarinic receptor subtypes in neuronal and non-neuronal cholinergic function. Auton Autacoid Pharmacol 26:219-233.

Eisele YS, Obermuller U, Heilbronner G, Baumann F, Kaeser SA, Wolburg H, Walker LC, Staufenbiel M, Heikenwalder M, Jucker M (2010) Peripherally applied Abeta-containing inoculates induce cerebral beta-amyloidosis. Science 330:980-982.

Ellman GL, Courtney KD, Andres V, Jr., Feather-Stone RM (1961) A new and rapid colorimetric determination of acetylcholinesterase activity. Biochem Pharmacol 7:88-95.

Engler H, Forsberg A, Almkvist O, Blomquist G, Larsson E, Savitcheva I, Wall A, Ringheim A, Langstrom B, Nordberg A (2006) Two-year follow-up of amyloid deposition in patients with Alzheimer's disease. Brain 129:2856-2866.

Esch FS, Keim PS, Beattie EC, Blacher RW, Culwell AR, Oltersdorf T, McClure D, Ward PJ (1990) Cleavage of amyloid beta peptide during constitutive processing of its precursor. Science 248:1122-1124.

Evans C, Beland SG, Kulaga S, Wolfson C, Kingwell E, Marriott J, Koch M, Makhani N, Morrow S, Fisk J, Dykeman J, Jette N, Pringsheim T, Marrie RA (2013) Incidence and Prevalence of Multiple Sclerosis in the Americas: A Systematic Review. Neuroepidemiology 40:195-210.

Falugi C, Aluigi MG (2012) Early appearance and possible functions of non-neuromuscular cholinesterase activities. Front Mol Neurosci 5:54.

Farzan M, Schnitzler CE, Vasilieva N, Leung D, Choe H (2000) BACE2, a beta - secretase homolog, cleaves at the beta site and within the amyloid-beta region of the amyloid-beta precursor protein. Proc Natl Acad Sci U S A 97:9712-9717.

Feng G, Krejci E, Molgo J, Cunningham JM, Massoulie J, Sanes JR (1999) Genetic analysis of collagen Q: roles in acetylcholinesterase and butyrylcholinesterase assembly and in synaptic structure and function. J Cell Biol 144:1349-1360.

Ferguson B, Matyszak MK, Esiri MM, Perry VH (1997) Axonal damage in acute multiple sclerosis lesions. Brain 120 (Pt 3):393-399.

Filippi M, Rocca MA, Horsfield MA, Hametner S, Geurts JJ, Comi G, Lassmann H (2013) Imaging Cortical Damage and Dysfunction in Multiple Sclerosis. JAMA Neurol:1-9.

Filippini N, MacIntosh BJ, Hough MG, Goodwin GM, Frisoni GB, Smith SM, Matthews PM, Beckmann CF, Mackay CE (2009) Distinct patterns of brain activity in young carriers of the APOE-epsilon4 allele. Proc Natl Acad Sci U S A 106:7209-7214.

Finkelstein Y, Wolff M, Biegon A (1988) Brain acetylcholinesterase after acute parathion poisoning: a comparative quantitative histochemical analysis post mortem. Ann Neurol 24:252-257.

Fisher RS, Buchwald NA, Hull CD, Levine MS (1988) GABAergic basal forebrain neurons project to the neocortex: the localization of glutamic acid decarboxylase and choline acetyltransferase in feline corticopetal neurons. J Comp Neurol 272:489-502.

Foldes FF, Zsigmond EK, Foldes VM, Erdos EG (1962) The distribution of acetylcholinesterase and butyrylcholinesterase in the human brain. journal of Neurochemistry 9:559-572.

Fookes CJ, Pham TQ, Mattner F, Greguric I, Loc'h C, Liu X, Berghofer P, Shepherd R, Gregoire MC, Katsifis A (2008) Synthesis and biological evaluation of substituted [18F]imidazo[1,2-a]pyridines and [18F]pyrazolo[1,5-a]pyrimidines for the study of the peripheral benzodiazepine receptor using positron emission tomography. J Med Chem 51:3700-3712.

Friede RL (1965) Enzyme histochemical studies of senile plaques. J Neuropathol Exp Neurol 24:477-491.

Friede RL (1967) A comparative histochemical mapping of the distribution of butyryl cholinesterase in the brains of four species of mammals, including man. Acta Anat (Basel) 66:161-177.

Fryer JD, Taylor JW, DeMattos RB, Bales KR, Paul SM, Parsadanian M, Holtzman DM (2003) Apolipoprotein E markedly facilitates age-dependent cerebral amyloid angiopathy and spontaneous hemorrhage in amyloid precursor protein transgenic mice. J Neurosci 23:7889-7896.

Fujii T, Tsuchiya T, Yamada S, Fujimoto K, Suzuki T, Kasahara T, Kawashima K (1996) Localization and synthesis of acetylcholine in human leukemic T cell lines. J Neurosci Res 44:66-72.

Fukuchi K, Ho L, Younkin SG, Kunkel DD, Ogburn CE, LeBoeuf RC, Furlong CE, Deeb SS, Nochlin D, Wegiel J, Wisniewski HM, Martin GM (1996) High levels of circulating beta-amyloid peptide do not cause cerebral beta-amyloidosis in transgenic mice. Am J Pathol 149:219-227.

Funaki Y, Kato M, Iwata R, Sakurai E, Tashiro M, Ido T, Yanai K (2003) Evaluation of the binding characteristics of [5-(11)C-methoxy]Donepezil in the rat brain for in vivo visualization of acetylcholinesterase. J Pharmacol Sci 91:105-112.

Furukawa K, Sopher BL, Rydel RE, Begley JG, Pham DG, Martin GM, Fox M, Mattson MP (1996) Increased activity-regulating and neuroprotective efficacy of alpha-secretase-derived secreted amyloid precursor protein conferred by a C-terminal heparin-binding domain. J Neurochem 67:1882-1896.

Gamblin TC, King ME, Kuret J, Berry RW, Binder LI (2000) Oxidative regulation of fatty acid-induced tau polymerization. Biochemistry 39:14203-14210.

Ganter P, Prince C, Esiri MM (1999) Spinal cord axonal loss in multiple sclerosis: a post-mortem study. Neuropathol Appl Neurobiol 25:459-467.

Getman DK, Eubanks JH, Camp S, Evans GA, Taylor P (1992) The human gene encoding acetylcholinesterase is located on the long arm of chromosome 7. Am J Hum Genet 51:170-177.

Geula C, Mesulam M (1989) Special properties of cholinesterases in the cerebral cortex of Alzheimer's disease. Brain Res 498:185-189.

Geula C, Mesulam MM (1995) Cholinesterases and the pathology of Alzheimer disease. Alzheimer Dis Assoc Disord 9 Suppl 2:23-28.

Geurts JJ, Barkhof F (2008) Grey matter pathology in multiple sclerosis. Lancet Neurol 7:841-851.

Ghebremedhin E, Thal DR, Schultz C, Braak H, Deller T (2007) Homozygosity for the K variant of BCHE gene increases the risk for development of neurofibrillary pathology but not amyloid deposits at young ages. Acta Neuropathol 114:359-363.

Ghersi-Egea JF, Gorevic PD, Ghiso J, Frangione B, Patlak CS, Fenstermacher JD (1996) Fate of cerebrospinal fluid-borne amyloid beta-peptide: rapid clearance into blood and appreciable accumulation by cerebral arteries. J Neurochem 67:880-883.

Giacobini E (2000) Cholinesterases and Cholinesterase Inhibitors. London: Martin Dunitz Ltd.

Giacobini E (2003) Butyrylcholinesterase: Its functions and inhibitors. London and New York: Martin Dunitz.

Glenner GG, Wong CW (1984a) Alzheimer's disease: initial report of the purification and characterization of a novel cerebrovascular amyloid protein. Biochem Biophys Res Commun 120:885-890.

Glenner GG, Wong CW (1984b) Alzheimer's disease and Down's syndrome: sharing of a unique cerebrovascular amyloid fibril protein. Biochem Biophys Res Commun 122:1131-1135.

Gnatt A, Prody CA, Zamir R, Lieman-Hurwitz J, Zakut H, Soreq H (1990) Expression of alternatively terminated unusual human butyrylcholinesterase messenger RNA transcripts, mapping to chromosome 3q26-ter, in nervous system tumors. Cancer Res 50:1983-1987.

Goate A, Chartier-Harlin MC, Mullan M, Brown J, Crawford F, Fidani L, Giuffra L, Haynes A, Irving N, James L, et al. (1991) Segregation of a missense mutation in the amyloid precursor protein gene with familial Alzheimer's disease. Nature 349:704-706.

Goedert M, Jakes R (1990) Expression of separate isoforms of human tau protein: correlation with the tau pattern in brain and effects on tubulin polymerization. EMBO J 9:4225-4230.

Goedert M, Spillantini MG, Cairns NJ, Crowther RA (1992) Tau proteins of Alzheimer paired helical filaments: abnormal phosphorylation of all six brain isoforms. Neuron 8:159-168.

Goedert M, Spillantini MG, Potier MC, Ulrich J, Crowther RA (1989a) Cloning and sequencing of the cDNA encoding an isoform of microtubule-associated protein tau containing four tandem repeats: differential expression of tau protein mRNAs in human brain. EMBO J 8:393-399.

Goedert M, Spillantini MG, Jakes R, Rutherford D, Crowther RA (1989b) Multiple isoforms of human microtubule-associated protein tau: sequences and localization in neurofibrillary tangles of Alzheimer's disease. Neuron 3:519-526.

Goedert M, Jakes R, Spillantini MG, Hasegawa M, Smith MJ, Crowther RA (1996) Assembly of microtubule-associated protein tau into Alzheimer-like filaments induced by sulphated glycosaminoglycans. Nature 383:550-553.

Goldberg P (1974) Multiple sclerosis: vitamin D and calcium as environmental determinants of prevalence. Intern J Environmental Studies 6:19-27.

Goldgaber D, Lerman MI, McBride OW, Saffiotti U, Gajdusek DC (1987) Characterization and chromosomal localization of a cDNA encoding brain amyloid of Alzheimer's disease. Science 235:877-880.

Gomez-Ramos P, Bouras C, Moran MA (1994) Ultrastructural localization of butyrylcholinesterase on neurofibrillary degeneration sites in the brains of aged and Alzheimer's disease patients. Brain Res 640:17-24.

Gomori G (1948) Histochemical demonstration of sites of choline esterase activity. Proc Soc Exp Biol Med 68:354-358.

Gong CX, Liu F, Grundke-Iqbal I, Iqbal K (2005) Post-translational modifications of tau protein in Alzheimer's disease. J Neural Transm 112:813-838.

Grando SA (1997) Biological functions of keratinocyte cholinergic receptors. J Investig Dermatol Symp Proc 2:41-48.

Grando SA, Horton RM (1997) The keratinocyte cholinergic system with acetylcholine as an epidermal cytotransmitter. Curr Opin Dermatol 4:262-268.

Greenberg BD, Carrillo MC, Ryan JM, Gold M, Gallagher K, Grundman M, Berman RM, Ashwood T, Siemers ER (2013) Improving Alzheimer's disease phase II clinical trials. Alzheimers Dement 9:39-49.

Greenberg BM, Frohman E (2010) Optical coherence tomography as a potential readout in clinical trials. Ther Adv Neurol Disord 3:153-160.

Gregoire SM, Charidimou A, Gadapa N, Dolan E, Antoun N, Peeters A, Vandermeeren Y, Laloux P, Baron JC, Jager HR, Werring DJ (2011) Acute ischaemic brain lesions in intracerebral haemorrhage: multicentre cross-sectional magnetic resonance imaging study. Brain 134:2376-2386.

Grehan S, Tse E, Taylor JM (2001) Two distal downstream enhancers direct expression of the human apolipoprotein E gene to astrocytes in the brain. J Neurosci 21:812-822.

Greicius MD, Srivastava G, Reiss AL, Menon V (2004) Default-mode network activity distinguishes Alzheimer's disease from healthy aging: evidence from functional MRI. Proc Natl Acad Sci U S A 101:4637-4642.

Greig NH, Utsuki T, Ingram DK, Wang Y, Pepeu G, Scali C, Yu QS, Mamczarz J, Holloway HW, Giordano T, Chen D, Furukawa K, Sambamurti K, Brossi A, Lahiri DK (2005) Selective butyrylcholinesterase inhibition elevates brain acetylcholine, augments learning and lowers Alzheimer beta-amyloid peptide in rodent. Proc Natl Acad Sci U S A 102:17213-17218.

Griffith LM, Pollard TD (1982) The interaction of actin filaments with microtubules and microtubule-associated proteins. J Biol Chem 257:9143-9151.

Gritti I, Mainville L, Jones BE (1993) Codistribution of GABA- with acetylcholine-synthesizing neurons in the basal forebrain of the rat. J Comp Neurol 329:438-457.

Gritti I, Mainville L, Mancia M, Jones BE (1997) GABAergic and other noncholinergic basal forebrain neurons, together with cholinergic neurons, project to the mesocortex and isocortex in the rat. J Comp Neurol 383:163-177.

Grossman RI, Gonzalez-Scarano F, Atlas SW, Galetta S, Silberberg DH (1986) Multiple sclerosis: gadolinium enhancement in MR imaging. Radiology 161:721-725.

Grundke-Iqbal I, Iqbal K, Quinlan M, Tung YC, Zaidi MS, Wisniewski HM (1986a) Microtubule-associated protein tau. A component of Alzheimer paired helical filaments. J Biol Chem 261:6084-6089.

Grundke-Iqbal I, Iqbal K, Tung YC, Quinlan M, Wisniewski HM, Binder LI (1986b) Abnormal phosphorylation of the microtubule-associated protein tau (tau) in Alzheimer cytoskeletal pathology. Proc Natl Acad Sci U S A 83:4913-4917.

Gsell W, Jungkunz G, Riederer P (2004) Functional neurochemistry of Alzheimer's disease. Curr Pharm Des 10:265-293.

Guillozet AL, Smiley JF, Mash DC, Mesulam MM (1997) Butyrylcholinesterase in the life cycle of amyloid plaques. Ann Neurol 42:909-918.

Haass C, Hung AY, Schlossmacher MG, Teplow DB, Selkoe DJ (1993) beta-Amyloid peptide and a 3-kDa fragment are derived by distinct cellular mechanisms. J Biol Chem 268:3021-3024.

Haass C, Schlossmacher MG, Hung AY, Vigo-Pelfrey C, Mellon A, Ostaszewski BL, Lieberburg I, Koo EH, Schenk D, Teplow DB, et al. (1992) Amyloid beta-peptide is produced by cultured cells during normal metabolism. Nature 359:322-325.

Haense C, Kalbe E, Herholz K, Hohmann C, Neumaier B, Krais R, Heiss WD (2012) Cholinergic system function and cognition in mild cognitive impairment. Neurobiol Aging 33:867-877.

Hagforsen E, Einarsson A, Aronsson F, Nordlind K, Michaelsson G (2000) The distribution of choline acetyltransferase- and acetylcholinesterase-like immunoreactivity in the palmar skin of patients with palmoplantar pustulosis. Br J Dermatol 142:234-242.

Halliday AC, Greenfield SA (2012) From protein to peptides: a spectrum of non-hydrolytic functions of acetylcholinesterase. Protein Pept Lett 19:165-172.

Hardy J, Selkoe DJ (2002) The amyloid hypothesis of Alzheimer's disease: progress and problems on the road to therapeutics. Science 297:353-356.

Hardy JA, Higgins GA (1992) Alzheimer's disease: the amyloid cascade hypothesis. Science 256:184-185.

Harel M, Quinn DM, Nair HK, Silman I, Sussman JL (1996) The X-ray structure of a transition state analog complex reveals the molecular origins of the catalytic power and substrate specificity of acetylcholinesterase. Journal of the American Chemical Society 118:2340-2346.

Harel M, Sonoda LK, Silman I, Sussman JL, Rosenberry TL (2008) Crystal structure of thioflavin T bound to the peripheral site of Torpedo californica acetylcholinesterase reveals how thioflavin T acts as a sensitive fluorescent reporter of ligand binding to the acylation site. J Am Chem Soc 130:7856-7861.

Harel M, Sussman JL, Krejci E, Bon S, Chanal P, Massoulie J, Silman I (1992) Conversion of acetylcholinesterase to butyrylcholinesterase: modeling and mutagenesis. Proc Natl Acad Sci U S A 89:10827-10831.

Harel M, Schalk I, Ehret-Sabatier L, Bouet F, Goeldner M, Hirth C, Axelsen PH, Silman I, Sussman JL (1993) Quaternary ligand binding to aromatic residues in the active-site gorge of acetylcholinesterase. Proc Natl Acad Sci U S A 90:9031-9035.

Harper JD, Wong SS, Lieber CM, Lansbury PT (1997) Observation of metastable Abeta amyloid protofibrils by atomic force microscopy. Chem Biol 4:119-125.

Hasegawa M, Smith MJ, Goedert M (1998) Tau proteins with FTDP-17 mutations have a reduced ability to promote microtubule assembly. FEBS Lett 437:207-210.

Hasegawa M, Morishima-Kawashima M, Takio K, Suzuki M, Titani K, Ihara Y (1992) Protein sequence and mass spectrometric analyses of tau in the Alzheimer's disease brain. J Biol Chem 267:17047-17054.

Hawkins CP, Munro PM, MacKenzie F, Kesselring J, Tofts PS, du Boulay EP, Landon DN, McDonald WI (1990) Duration and selectivity of blood-brain barrier breakdown in chronic relapsing experimental allergic encephalomyelitis studied by gadolinium-DTPA and protein markers. Brain 113 (Pt 2):365-378.

Hebert LE, Beckett LA, Scherr PA, Evans DA (2001) Annual incidence of Alzheimer disease in the United States projected to the years 2000 through 2050. Alzheimer Dis Assoc Disord 15:169-173.

Hecker A, Lips KS, Pfeil U, Kummer W, Padberg W, Grau V (2006) Peripheral choline acetyltransferase is expressed by monocytes and upregulated during renal allograft rejection in rats. J Mol Neurosci 30:23-24.

Hendriks L, van Duijn CM, Cras P, Cruts M, Van Hul W, van Harskamp F, Warren A, McInnis MG, Antonarakis SE, Martin JJ, et al. (1992) Presenile dementia and cerebral haemorrhage linked to a mutation at codon 692 of the beta-amyloid precursor protein gene. Nat Genet 1:218-221.

Henriquez JP, Cross D, Vial C, Maccioni RB (1995) Subpopulations of tau interact with microtubules and actin filaments in various cell types. Cell Biochem Funct 13:239-250.

Herholz K (2003) PET studies in dementia. Ann Nucl Med 17:79-89.

Herholz K (2008) Acetylcholine esterase activity in mild cognitive impairment and Alzheimer's disease. Eur J Nucl Med Mol Imaging 35 Suppl 1:S25-29.

Herms J, Anliker B, Heber S, Ring S, Fuhrmann M, Kretzschmar H, Sisodia S, Muller U (2004) Cortical dysplasia resembling human type 2 lissencephaly in mice lacking all three APP family members. EMBO J 23:4106-4115.

Herzig MC, Van Nostrand WE, Jucker M (2006) Mechanism of cerebral beta-amyloid angiopathy: murine and cellular models. Brain Pathol 16:40-54.

Herzig MC, Winkler DT, Burgermeister P, Pfeifer M, Kohler E, Schmidt SD, Danner S, Abramowski D, Sturchler-Pierrat C, Burki K, van Duinen SG, Maat-Schieman ML, Staufenbiel M, Mathews PM, Jucker M (2004) Abeta is targeted to the vasculature in a mouse model of hereditary cerebral hemorrhage with amyloidosis. Nat Neurosci 7:954-960.

Hillmann A, Hahn S, Schilling S, Hoffmann T, Demuth HU, Bulic B, Schneider-Axmann T, Bayer TA, Weggen S, Wirths O (2012) No improvement after chronic ibuprofen treatment in the 5XFAD mouse model of Alzheimer's disease. Neurobiol Aging 33:833 e839-850.

Himmler A, Drechsel D, Kirschner MW, Martin DW, Jr. (1989) Tau consists of a set of proteins with repeated C-terminal microtubule-binding domains and variable N-terminal domains. Mol Cell Biol 9:1381-1388.

Hiraoka K, Okamura N, Funaki Y, Watanuki S, Tashiro M, Kato M, Hayashi A, Hosokai Y, Yamasaki H, Fujii T, Mori E, Yanai K, Watabe H (2009) Quantitative analysis of donepezil binding to acetylcholinesterase using positron emission tomography and [5-(11)C-methoxy]donepezil. Neuroimage 46:616-623.

Hohlfeld R (1997) Biotechnological agents for the immunotherapy of multiple sclerosis. Principles, problems and perspectives. Brain 120 (Pt 5):865-916.

Holland CM, Charil A, Csapo I, Liptak Z, Ichise M, Khoury SJ, Bakshi R, Weiner HL, Guttmann CR (2011) The relationship between normal cerebral perfusion patterns and white matter lesion distribution in 1,249 patients with multiple sclerosis. J Neuroimaging 22:129-136.

Holman BL, Johnson KA, Gerada B, Carvalho PA, Satlin A (1992) The scintigraphic appearance of Alzheimer's disease: a prospective study using technetium-99m-HMPAO SPECT. J Nucl Med 33:181-185.

Holmes C, Ballard C, Lehmann D, David Smith A, Beaumont H, Day IN, Nadeem Khan M, Lovestone S, McCulley M, Morris CM, Munoz DG, O'Brien K, Russ C, Del Ser T, Warden D (2005) Rate of progression of cognitive decline in Alzheimer's disease: effect of butyrylcholinesterase K gene variation. J Neurol Neurosurg Psychiatry 76:640-643.

Hong M, Zhukareva V, Vogelsberg-Ragaglia V, Wszolek Z, Reed L, Miller BI, Geschwind DH, Bird TD, McKeel D, Goate A, Morris JC, Wilhelmsen KC, Schellenberg GD, Trojanowski JQ, Lee VM (1998) Mutation-specific functional impairments in distinct tau isoforms of hereditary FTDP-17. Science 282:1914-1917.

Horiuchi Y, Kimura R, Kato N, Fujii T, Seki M, Endo T, Kato T, Kawashima K (2003) Evolutional study on acetylcholine expression. Life Sci 72:1745-1756.

Hosey MM (1992) Diversity of structure, signaling and regulation within the family of muscarinic cholinergic receptors. FASEB J 6:845-852.

Howell BW, Hawkes R, Soriano P, Cooper JA (1997) Neuronal position in the developing brain is regulated by mouse disabled-1. Nature 389:733-737.

Huang D, Swanson EA, Lin CP, Schuman JS, Stinson WG, Chang W, Hee MR, Flotte T, Gregory K, Puliafito CA, et al. (1991) Optical coherence tomography. Science 254:1178-1181.

Huse JT, Pijak DS, Leslie GJ, Lee VM, Doms RW (2000) Maturation and endosomal targeting of beta-site amyloid precursor protein-cleaving enzyme. The Alzheimer's disease beta-secretase. J Biol Chem 275:33729-33737.

Huse JT, Liu K, Pijak DS, Carlin D, Lee VM, Doms RW (2002) Beta-secretase processing in the trans-Golgi network preferentially generates truncated amyloid species that accumulate in Alzheimer's disease brain. J Biol Chem 277:16278-16284.

Hutton M et al. (1998) Association of missense and 5'-splice-site mutations in tau with the inherited dementia FTDP-17. Nature 393:702-705.

Hyman BT, Trojanowski JQ (1997) Consensus recommendations for the postmortem diagnosis of Alzheimer disease from the National Institute on Aging and the Reagan Institute Working Group on diagnostic criteria for the neuropathological assessment of Alzheimer disease. J Neuropathol Exp Neurol 56:1095-1097.

Iannotti F (1992) Functional imaging of blood brain barrier permeability by single photon emission computerised tomography and positron emission tomography. Adv Tech Stand Neurosurg 19:103-119.

Ihara Y, Nukina N, Miura R, Ogawara M (1986) Phosphorylated tau protein is integrated into paired helical filaments in Alzheimer's disease. J Biochem 99:1807-1810.

Ikram MA, Vrooman HA, Vernooij MW, den Heijer T, Hofman A, Niessen WJ, van der Lugt A, Koudstaal PJ, Breteler MM (2010) Brain tissue volumes in relation to cognitive function and risk of dementia. Neurobiol Aging 31:378-386.

Inestrosa NC, Alvarez A, Perez CA, Moreno RD, Vicente M, Linker C, Casanueva OI, Soto C, Garrido J (1996) Acetylcholinesterase accelerates assembly of amyloid-beta-peptides into Alzheimer's fibrils: possible role of the peripheral site of the enzyme. Neuron 16:881-891.

Iqbal K, Grundke-Iqbal I, Smith AJ, George L, Tung YC, Zaidi T (1989) Identification and localization of a tau peptide to paired helical filaments of Alzheimer disease. Proc Natl Acad Sci U S A 86:5646-5650.

Irie T, Fukushi K, Akimoto Y, Tamagami H, Nozaki T (1994) Design and evaluation of radioactive acetylcholine analogs for mapping brain acetylcholinesterase (AchE) in vivo. Nucl Med Biol 21:801-808.

Irie T, Fukushi K, Namba H, Iyo M, Tamagami H, Nagatsuka S, Ikota N (1996) Brain acetylcholinesterase activity: validation of a PET tracer in a rat model of Alzheimer's disease. J Nucl Med 37:649-655.

Iwatsubo T, Odaka A, Suzuki N, Mizusawa H, Nukina N, Ihara Y (1994) Visualization of A beta 42(43) and A beta 40 in senile plaques with end-specific A beta monoclonals: evidence that an initially deposited species is A beta 42(43). Neuron 13:45-53.

Iyo M, Namba H, Fukushi K, Shinotoh H, Nagatsuka S, Suhara T, Sudo Y, Suzuki K, Irie T (1997) Measurement of acetylcholinesterase by positron emission tomography in the brains of healthy controls and patients with Alzheimer's disease. Lancet 349:1805-1809.

Jack CR, Jr., Petersen RC, Xu YC, Waring SC, O'Brien PC, Tangalos EG, Smith GE, Ivnik RJ, Kokmen E (1997) Medial temporal atrophy on MRI in normal aging and very mild Alzheimer's disease. Neurology 49:786-794.

Jack CR, Jr., Dickson DW, Parisi JE, Xu YC, Cha RH, O'Brien PC, Edland SD, Smith GE, Boeve BF, Tangalos EG, Kokmen E, Petersen RC (2002) Antemortem MRI findings correlate with hippocampal neuropathology in typical aging and dementia. Neurology 58:750-757.

Jagust W, Thisted R, Devous MD, Sr., Van Heertum R, Mayberg H, Jobst K, Smith AD, Borys N (2001) SPECT perfusion imaging in the diagnosis of Alzheimer's disease: a clinical-pathologic study. Neurology 56:950-956.

Jankowsky JL, Younkin LH, Gonzales V, Fadale DJ, Slunt HH, Lester HA, Younkin SG, Borchelt DR (2007) Rodent A beta modulates the solubility and distribution of amyloid deposits in transgenic mice. J Biol Chem 282:22707-22720.

Jarrett JT, Berger EP, Lansbury PT, Jr. (1993) The carboxy terminus of the beta amyloid protein is critical for the seeding of amyloid formation: implications for the pathogenesis of Alzheimer's disease. Biochemistry 32:4693-4697.

Ji Y, Permanne B, Sigurdsson EM, Holtzman DM, Wisniewski T (2001) Amyloid beta40/42 clearance across the blood-brain barrier following intra-ventricular injections in wild-type, apoE knock-out and human apoE3 or E4 expressing transgenic mice. J Alzheimers Dis 3:23-30.

Joachim CL, Duffy LK, Morris JH, Selkoe DJ (1988) Protein chemical and immunocytochemical studies of meningovascular beta-amyloid protein in Alzheimer's disease and normal aging. Brain Res 474:100-111.

Johnson JL, Cusack B, Davies MP, Fauq A, Rosenberry TL (2003) Unmasking tandem site interaction in human acetylcholinesterase. Substrate activation with a cationic acetanilide substrate. Biochemistry 42:5438-5452.

Johnson KA, Minoshima S, Bohnen NI, Donohoe KJ, Foster NL, Herscovitch P, Karlawish JH, Rowe CC, Carrillo MC, Hartley DM, Hedrick S, Pappas V, Thies WH (2013a) Appropriate Use Criteria for Amyloid PET: A Report of the Amyloid Imaging Task Force, the Society of Nuclear Medicine and Molecular Imaging, and the Alzheimer's Association. J Nucl Med 54:476-490.

Johnson KA, Minoshima S, Bohnen NI, Donohoe KJ, Foster NL, Herscovitch P, Karlawish JH, Rowe CC, Carrillo MC, Hartley DM, Hedrick S, Pappas V, Thies WH (2013b) Appropriate use criteria for amyloid PET: a report of the Amyloid Imaging Task Force, the Society of Nuclear Medicine and Molecular Imaging, and the Alzheimer's Association. Alzheimers Dement 9:e-1-16.

Jones BE, Muhlethaler M (1998) Cholinergic and GABAergic neurons of the basal forebrain: Role in cortical activation. In: The Handbook of Behavioral State Control: Cellular and Molecular Mechanisms (Lydic R, Baghdoyan HA, eds). Boca Raton: CRC Press.

Jonsson T et al. (2012) A mutation in APP protects against Alzheimer's disease and age-related cognitive decline. Nature 488:96-99.

Kaasinen V, Nagren K, Jarvenpaa T, Roivainen A, Yu M, Oikonen V, Kurki T, Rinne JO (2002) Regional effects of donepezil and rivastigmine on cortical acetylcholinesterase activity in Alzheimer's disease. J Clin Psychopharmacol 22:615-620.

Kamal A, Stokin GB, Yang Z, Xia CH, Goldstein LS (2000) Axonal transport of amyloid precursor protein is mediated by direct binding to the kinesin light chain subunit of kinesin-I. Neuron 28:449-459.

Kamal A, Almenar-Queralt A, LeBlanc JF, Roberts EA, Goldstein LS (2001) Kinesin-mediated axonal transport of a membrane compartment containing beta-secretase and presenilin-1 requires APP. Nature 414:643-648.

Kampers T, Friedhoff P, Biernat J, Mandelkow EM, Mandelkow E (1996) RNA stimulates aggregation of microtubule-associated protein tau into Alzheimer-like paired helical filaments. FEBS Lett 399:344-349.

Kang J, Lemaire HG, Unterbeck A, Salbaum JM, Masters CL, Grzeschik KH, Multhaup G, Beyreuther K, Muller-Hill B (1987) The precursor of Alzheimer's disease amyloid A4 protein resembles a cell-surface receptor. Nature 325:733-736.

Karnovsky MJ, Roots L (1964) A "Direct-Coloring" Thiocholine Method for Cholinesterases. J Histochem Cytochem 12:219-221.

Kasuya M, Meguro K, Okamura N, Funaki Y, Ishikawa H, Tanaka N, Iwata R, Yanai K (2012) Greater responsiveness to donepezil in Alzheimer patients with higher levels of acetylcholinesterase based on attention task scores and a donepezil PET study. Alzheimer Dis Assoc Disord 26:113-118.

Kawashima K, Fujii T (2004) Expression of non-neuronal acetylcholine in lymphocytes and its contribution to the regulation of immune function. Front Biosci 9:2063-2085.

Kawashima K, Fujii T, Watanabe Y, Misawa H (1998) Acetylcholine synthesis and muscarinic receptor subtype mRNA expression in T-lymphocytes. Life Sci 62:1701-1705.

Kawashima K, Fujii T, Moriwaki Y, Misawa H (2012) Critical roles of acetylcholine and the muscarinic and nicotinic acetylcholine receptors in the regulation of immune function. Life Sci 91:1027-1032.

Kawashima K, Yoshikawa K, Fujii YX, Moriwaki Y, Misawa H (2007) Expression and function of genes encoding cholinergic components in murine immune cells. Life Sci 80:2314-2319.

Kenessey A, Yen SH (1993) The extent of phosphorylation of fetal tau is comparable to that of PHF-tau from Alzheimer paired helical filaments. Brain Res 629:40-46.

Kermode AG, Thompson AJ, Tofts P, MacManus DG, Kendall BE, Kingsley DP, Moseley IF, Rudge P, McDonald WI (1990) Breakdown of the blood-brain barrier precedes symptoms and other MRI signs of new lesions in multiple sclerosis. Pathogenetic and clinical implications. Brain 113 (Pt 5):1477-1489.

Kikuchi T, Okamura T, Zhang MR, Fukushi K, Irie T (2010) In vivo evaluation of N-[18F]fluoroethylpiperidin-4ylmethyl acetate in rats compared with MP4A as a probe for measuring cerebral acetylcholinesterase activity. Synapse 64:209-215.

Kikuchi T, Zhang MR, Ikota N, Fukushi K, Okamura T, Suzuki K, Arano Y, Irie T (2004) N-[18F]fluoroethylpiperidin-4-ylmethyl butyrate: a novel radiotracer for quantifying brain butyrylcholinesterase activity by positron emission tomography. Bioorg Med Chem Lett 14:1927-1930.

Kikuchi T, Zhang MR, Ikota N, Fukushi K, Okamura T, Suzuki K, Arano Y, Irie T (2005) N-[18F] fluoroethylpiperidin-4ylmethyl acetate, a novel lipophilic acetylcholine analogue for PET measurement of brain acetylcholinesterase activity. J Med Chem 48:2577-2583.

Kikuchi T, Okamura T, Fukushi K, Takahashi K, Toyohara J, Okada M, Zhang MR, Irie T (2007) Cerebral acetylcholinesterase imaging: development of the radioprobes. Curr Top Med Chem 7:1790-1799.

Kikuchi T, Fukushi, K., Ikota, N., Ueda, T., Nagatsuka, S., Arano, Y., Irie, T. (2001) Synthesis of piperidinyl and pyrrolidinyl butyrates for potential In Vivo measurement of cerebral butyrylcholinesterase activity. Journal of Labelled Compounds and Radiopharmaceuticals 44:31-41.

Kilbourn MR, Snyder SE, Sherman PS, Kuhl DE (1996) In vivo studies of acetylcholinesterase activity using a labeled substrate, N-[11C]methylpiperdin-4-yl propionate ([11C]PMP). Synapse 22:123-131.

Kilbourn MR, Nguyen TB, Snyder SE, Sherman P (1998) N-[11C]methylpiperidine esters as acetylcholinesterase substrates: an in vivo structure-reactivity study. Nucl Med Biol 25:755-760.

Kim AR, Rylett RJ, Shilton BH (2006) Substrate binding and catalytic mechanism of human choline acetyltransferase. Biochemistry 45:14621-14631.

Kim DH, Choe YS, Choi JY, Lee KH, Kim BT (2011) Binding of 2-[18F]fluoro-CP-118,954 to mouse acetylcholinesterase: microPET and ex vivo Cerenkov luminescence imaging studies. Nucl Med Biol 38:541-547.

Kim HS, Kim EM, Lee JP, Park CH, Kim S, Seo JH, Chang KA, Yu E, Jeong SJ, Chong YH, Suh YH (2003) C-terminal fragments of amyloid precursor protein exert neurotoxicity by inducing glycogen synthase kinase-3beta expression. FASEB J 17:1951-1953.

Kim ST, Weaver DF (2000) Theoretical studies on Alzheimer's disease: structures of beta-amyloid aggregates. Journal of Molecular Structure-Theochem 527:127-138.

Kimberly WT, Zheng JB, Guenette SY, Selkoe DJ (2001) The intracellular domain of the beta-amyloid precursor protein is stabilized by Fe65 and translocates to the nucleus in a notch-like manner. J Biol Chem 276:40288-40292.

Kimberly WT, LaVoie MJ, Ostaszewski BL, Ye W, Wolfe MS, Selkoe DJ (2003) Gamma-secretase is a membrane protein complex comprised of presenilin, nicastrin, Aph-1, and Pen-2. Proc Natl Acad Sci U S A 100:6382-6387.

Kimberly WT, Gilson A, Rost NS, Rosand J, Viswanathan A, Smith EE, Greenberg SM (2009) Silent ischemic infarcts are associated with hemorrhage burden in cerebral amyloid angiopathy. Neurology 72:1230-1235.

Kimura H, McGeer PL, Peng F, McGeer EG (1980) Choline acetyltransferase-containing neurons in rodent brain demonstrated by immunohistochemistry. Science 208:1057-1059.

Kitaguchi N, Takahashi Y, Tokushima Y, Shiojiri S, Ito H (1988) Novel precursor of Alzheimer's disease amyloid protein shows protease inhibitory activity. Nature 331:530-532.

Kitamoto T, Ogomori K, Tateishi J, Prusiner SB (1987) Formic acid pretreatment enhances immunostaining of cerebral and systemic amyloids. Lab Invest 57:230-236.

Klunk WE, Wang Y, Huang GF, Debnath ML, Holt DP, Mathis CA (2001) Uncharged thioflavin-T derivatives bind to amyloid-beta protein with high affinity and readily enter the brain. Life Sci 69:1471-1484.

Klunk WE, Lopresti BJ, Ikonomovic MD, Lefterov IM, Koldamova RP, Abrahamson EE, Debnath ML, Holt DP, Huang GF, Shao L, DeKosky ST, Price JC, Mathis CA (2005) Binding of the positron emission tomography tracer Pittsburgh compound-B reflects the amount of amyloid-beta in Alzheimer's disease brain but not in transgenic mouse brain. J Neurosci 25:10598-10606.

Klunk WE et al. (2004) Imaging brain amyloid in Alzheimer's disease with Pittsburgh Compound-B. Ann Neurol 55:306-319.

Koehnke J, Jin X, Budreck EC, Posy S, Scheiffele P, Honig B, Shapiro L (2008) Crystal structure of the extracellular cholinesterase-like domain from neuroligin-2. Proc Natl Acad Sci U S A 105:1873-1878.

Koelle GB (1954) The histochemical localization of cholinesterases in the central nervous system of the rat. J Comp Neurol 100:211-235.

Koo EH (2002) The beta-amyloid precursor protein (APP) and Alzheimer's disease: does the tail wag the dog? Traffic 3:763-770.

Koo EH, Sisodia SS, Archer DR, Martin LJ, Weidemann A, Beyreuther K, Fischer P, Masters CL, Price DL (1990) Precursor of amyloid protein in Alzheimer disease undergoes fast anterograde axonal transport. Proc Natl Acad Sci U S A 87:1561-1565.

Kopke E, Tung YC, Shaikh S, Alonso AC, Iqbal K, Grundke-Iqbal I (1993) Microtubule-associated protein tau. Abnormal phosphorylation of a non-paired helical filament pool in Alzheimer disease. J Biol Chem 268:24374-24384.

Kornek B, Lassmann H (1999) Axonal pathology in multiple sclerosis. A historical note. Brain Pathol 9:651-656.

Kosik KS, Joachim CL, Selkoe DJ (1986) Microtubule-associated protein tau (tau) is a major antigenic component of paired helical filaments in Alzheimer disease. Proc Natl Acad Sci U S A 83:4044-4048.

Kosik KS, Kowall NW, McKee A (1989a) Along the way to a neurofibrillary tangle: a look at the structure of tau. Ann Med 21:109-112.

Kosik KS, Orecchio LD, Bakalis S, Neve RL (1989b) Developmentally regulated expression of specific tau sequences. Neuron 2:1389-1397.

Kostovic I, Goldman-Rakic PS (1983) Transient cholinesterase staining in the mediodorsal nucleus of the thalamus and its connections in the developing human and monkey brain. J Comp Neurol 219:431-447.

Kraepelin E (1910) Psychiatrie: Ein Lehrbuch für Studierende und Ärzte. Leipzig: Barth.

Krejci E, Legay C, Thomine S, Sketelj J, Massoulie J (1999) Differences in expression of acetylcholinesterase and collagen Q control the distribution and oligomerization of the collagen-tailed forms in fast and slow muscles. J Neurosci 19:10672-10679.

Krejci E, Thomine S, Boschetti N, Legay C, Sketelj J, Massoulie J (1997) The mammalian gene of acetylcholinesterase-associated collagen. J Biol Chem 272:22840-22847.

Kryger G, Harel M, Giles K, Toker L, Velan B, Lazar A, Kronman C, Barak D, Ariel N, Shafferman A, Silman I, Sussman JL (2000) Structures of recombinant native and E202Q mutant human acetylcholinesterase complexed with the snake-venom toxin fasciculin-II. Acta Crystallogr D Biol Crystallogr 56:1385-1394.

Ksiezak-Reding H, Liu WK, Yen SH (1992) Phosphate analysis and dephosphorylation of modified tau associated with paired helical filaments. Brain Res 597:209-219.

Kuhl DE, Minoshima S, Frey KA, Foster NL, Kilbourn MR, Koeppe RA (2000) Limited donepezil inhibition of acetylcholinesterase measured with positron emission tomography in living Alzheimer cerebral cortex. Ann Neurol 48:391-395.

Kuhl DE, Koeppe RA, Snyder SE, Minoshima S, Frey KA, Kilbourn MR (2006) In vivo butyrylcholinesterase activity is not increased in Alzheimer's disease synapses. Ann Neurol 59:13-20.

Kung MP, Hou C, Zhuang ZP, Cross AJ, Maier DL, Kung HF (2004) Characterization of IMPY as a potential imaging agent for beta-amyloid plaques in double transgenic PSAPP mice. Eur J Nucl Med Mol Imaging 31:1136-1145.

Kuntner C, Kesner AL, Bauer M, Kremslehner R, Wanek T, Mandler M, Karch R, Stanek J, Wolf T, Muller M, Langer O (2009) Limitations of small animal PET imaging with [18F]FDDNP and FDG for quantitative studies in a transgenic mouse model of Alzheimer's disease. Mol Imaging Biol 11:236-240.

Kutzelnigg A, Lucchinetti CF, Stadelmann C, Bruck W, Rauschka H, Bergmann M, Schmidbauer M, Parisi JE, Lassmann H (2005) Cortical demyelination and diffuse white matter injury in multiple sclerosis. Brain 128:2705-2712.

La Du BN, Bartels CF, Nogueira CP, Hajra A, Lightstone H, Van der Spek A, Lockridge O (1990) Phenotypic and molecular biological analysis of human butyrylcholinesterase variants. Clin Biochem 23:423-431.

Landau SM, Breault C, Joshi AD, Pontecorvo M, Mathis CA, Jagust WJ, Mintun MA (2013) Amyloid-beta imaging with Pittsburgh compound B and florbetapir: comparing radiotracers and quantification methods. J Nucl Med 54:70-77.

Landgraf D, Barth M, Layer PG, Sperling LE (2010) Acetylcholine as a possible signaling molecule in embryonic stem cells: studies on survival, proliferation and death. Chem Biol Interact 187:115-119.

Lane R, Feldman HH, Meyer J, He Y, Ferris SH, Nordberg A, Darreh-Shori T, Soininen H, Pirttila T, Farlow MR, Sfikas N, Ballard C, Greig NH (2008) Synergistic effect of apolipoprotein E epsilon4 and butyrylcholinesterase K-variant on progression from mild cognitive impairment to Alzheimer's disease. Pharmacogenet Genomics 18:289-298.

Langbaum JB, Chen K, Lee W, Reschke C, Bandy D, Fleisher AS, Alexander GE, Foster NL, Weiner MW, Koeppe RA, Jagust WJ, Reiman EM (2009) Categorical and correlational analyses of baseline fluorodeoxyglucose positron emission tomography images from the Alzheimer's Disease Neuroimaging Initiative (ADNI). Neuroimage 45:1107-1116.

Langrish CL, Chen Y, Blumenschein WM, Mattson J, Basham B, Sedgwick JD, McClanahan T, Kastelein RA, Cua DJ (2005) IL-23 drives a pathogenic T cell population that induces autoimmune inflammation. J Exp Med 201:233-240.

Lau LF, Schachter JB, Seymour PA, Sanner MA (2002) Tau protein phosphorylation as a therapeutic target in Alzheimer's disease. Curr Top Med Chem 2:395-415.

Layer PG (1990) Cholinesterases preceding major tracts in vertebrate neurogenesis. Bioessays 12:415-420.

Layer PG (1991) Cholinesterases during development of the avian nervous system. Cell Mol Neurobiol 11:7-33.

Lee I, Choe YS, Ryu EK, Choi BW, Choi JY, Choi Y, Lee KH, Kim BT (2007) Synthesis and evaluation of radioiodine-labelled CP-118,954 for the in-vivo imaging of acetylcholinesterase. Nucl Med Commun 28:561-566.

Lee MG, Hassani OK, Alonso A, Jones BE (2005) Cholinergic basal forebrain neurons burst with theta during waking and paradoxical sleep. J Neurosci 25:4365-4369.

Lee SY, Choe YS, Sugimoto H, Kim SE, Hwang SH, Lee K, Choi Y, Lee J, Kim B (2000) Synthesis and biological evaluation of 1-(4-[18F]fluorobenzyl)-4-[(5,6-dimethoxy-1-oxoindan-2-yl)methyl]piperidine for in vivo studies of acetylcholinesterase. Nucl Med Biol 27:741-744.

Lee SY, Choe YS, Kim YR, Paik JY, Choi BW, Kim SE, Lee KH, Choi Y, Kim BT (2004) Synthesis and evaluation of 5,7-dihydro-3-[2-[1-(4-[18F]-fluorobenzyl)-4-piperidinyl]ethyl]-6H-pyrrolo[3,2-f] -1,2-benzisoxazol-6-one for in vivo mapping of acetylcholinesterase. Nucl Med Commun 25:591-596.

Lee VM, Balin BJ, Otvos L, Jr., Trojanowski JQ (1991) A68: a major subunit of paired helical filaments and derivatized forms of normal Tau. Science 251:675-678.

Legay C, Bon S, Massoulie J (1993) Expression of a cDNA encoding the glycolipid-anchored form of rat acetylcholinesterase. FEBS Lett 315:163-166.

Lehmann DJ, Johnston C, Smith AD (1997) Synergy between the genes for butyrylcholinesterase K variant and apolipoprotein E4 in late-onset confirmed Alzheimer's disease. Hum Mol Genet 6:1933-1936.

Lehmann DJ, Williams J, McBroom J, Smith AD (2001) Using meta-analysis to explain the diversity of results in genetic studies of late-onset Alzheimer's disease and to identify high-risk subgroups. Neuroscience 108:541-554.

Lehmann DJ, Nagy Z, Litchfield S, Borja MC, Smith AD (2000) Association of butyrylcholinesterase K variant with cholinesterase-positive neuritic plaques in the temporal cortex in late-onset Alzheimer's disease. Hum Genet 106:447-452.

Leone P, Comoletti D, Taylor P, Bourne Y, Marchot P (2010) Structure-function relationships of the alpha/beta-hydrolase fold domain of neuroligin: a comparison with acetylcholinesterase. Chem Biol Interact 187:49-55.

Leterrier JF, Liem RK, Shelanski ML (1982) Interactions between neurofilaments and microtubule-associated proteins: a possible mechanism for intraorganellar bridging. J Cell Biol 95:982-986.

Levin N, Orlov T, Dotan S, Zohary E (2006) Normal and abnormal fMRI activation patterns in the visual cortex after recovery from optic neuritis. Neuroimage 33:1161-1168.

Levy-Lahad E, Wasco W, Poorkaj P, Romano DM, Oshima J, Pettingell WH, Yu CE, Jondro PD, Schmidt SD, Wang K, et al. (1995) Candidate gene for the chromosome 1 familial Alzheimer's disease locus. Science 269:973-977.

Levy E, Carman MD, Fernandez-Madrid IJ, Power MD, Lieberburg I, van Duinen SG, Bots GT, Luyendijk W, Frangione B (1990) Mutation of the Alzheimer's disease amyloid gene in hereditary cerebral hemorrhage, Dutch type. Science 248:1124-1126.

Li B, Duysen EG, Saunders TL, Lockridge O (2006) Production of the butyrylcholinesterase knockout mouse. J Mol Neurosci 30:193-195.

Li B, Duysen EG, Carlson M, Lockridge O (2008a) The butyrylcholinesterase knockout mouse as a model for human butyrylcholinesterase deficiency. J Pharmacol Exp Ther 324:1146-1154.

Li B, Stribley JA, Ticu A, Xie W, Schopfer LM, Hammond P, Brimijoin S, Hinrichs SH, Lockridge O (2000) Abundant tissue butyrylcholinesterase and its possible function in the acetylcholinesterase knockout mouse. J Neurochem 75:1320-1331.

Li S, Stys PK (2000) Mechanisms of ionotropic glutamate receptor-mediated excitotoxicity in isolated spinal cord white matter. J Neurosci 20:1190-1198.

Li TQ, Wahlund LO (2011) The search for neuroimaging biomarkers of Alzheimer's disease with advanced MRI techniques. Acta Radiol 52:211-222.

Li Y, Camp S, Taylor P (1993) Tissue-specific expression and alternative mRNA processing of the mammalian acetylcholinesterase gene. J Biol Chem 268:5790-5797.

Li Y, Camp S, Rachinsky TL, Getman D, Taylor P (1991) Gene structure of mammalian acetylcholinesterase. Alternative exons dictate tissue-specific expression. J Biol Chem 266:23083-23090.

Li Y, Rinne JO, Mosconi L, Pirraglia E, Rusinek H, DeSanti S, Kemppainen N, Nagren K, Kim BC, Tsui W, de Leon MJ (2008b) Regional analysis of FDG and PIB-PET images in normal aging, mild cognitive impairment, and Alzheimer's disease. Eur J Nucl Med Mol Imaging 35:2169-2181.

Liddell J, Lehmann H, Silk E (1962) A 'silent' pseudo-cholinesterase gene. Nature 193:561-562.

Lin H, Bhatia R, Lal R (2001) Amyloid beta protein forms ion channels: implications for Alzheimer's disease pathophysiology. FASEB J 15:2433-2444.

Lister-James J, Pontecorvo MJ, Clark C, Joshi AD, Mintun MA, Zhang W, Lim N, Zhuang Z, Golding G, Choi SR, Benedum TE, Kennedy P, Hefti F, Carpenter AP, Kung HF, Skovronsky DM (2011) Florbetapir f-18: a histopathologically validated Beta-amyloid positron emission tomography imaging agent. Semin Nucl Med 41:300-304.

Liu JS, Zhao ML, Brosnan CF, Lee SC (2001) Expression of inducible nitric oxide synthase and nitrotyrosine in multiple sclerosis lesions. Am J Pathol 158:2057-2066.

Liu Q, Zerbinatti CV, Zhang J, Hoe HS, Wang B, Cole SL, Herz J, Muglia L, Bu G (2007) Amyloid precursor protein regulates brain apolipoprotein E and cholesterol metabolism through lipoprotein receptor LRP1. Neuron 56:66-78.

Liu Y, Mitchell PJ, Kilpatrick TJ, Stein MS, Harrison LC, Baker J, Ditchfield M, Li K, Egan GF, Butzkueven H, Kolbe SC (2012) Diffusion tensor imaging of acute inflammatory lesion evolution in multiple sclerosis. J Clin Neurosci 19:1689-1694.

Lo RY, Jagust WJ (2013) Effect of Cognitive Reserve Markers on Alzheimer Pathologic Progression. Alzheimer Dis Assoc Disord.

Lockridge O, Bartels CF, Vaughan TA, Wong CK, Norton SE, Johnson LL (1987) Complete amino acid sequence of human serum cholinesterase. J Biol Chem 262:549-557.

Loening AM, Gambhir SS (2003) AMIDE: a free software tool for multimodality medical image analysis. Mol Imaging 2:131-137.

Loewi O (1921) Uber humorale ubertragbarkeit der Herznervenwirkung I. Pflugers Archiv 189:239–242.

Loewi O, Navratil E (1926) Uber humorale Ubertragbarkeit tier Herznervenwirkung. Pflugers Arch 214:678-688.

Loitfelder M, Fazekas F, Petrovic K, Fuchs S, Ropele S, Wallner-Blazek M, Jehna M, Aspeck E, Khalil M, Schmidt R, Neuper C, Enzinger C (2011) Reorganization in cognitive networks with progression of multiple sclerosis: insights from fMRI. Neurology 76:526-533.

Lovas G, Szilagyi N, Majtenyi K, Palkovits M, Komoly S (2000) Axonal changes in chronic demyelinated cervical spinal cord plaques. Brain 123 (Pt 2):308-317.

Lovestone S, Reynolds CH (1997) The phosphorylation of tau: a critical stage in neurodevelopment and neurodegenerative processes. Neuroscience 78:309-324.

Lucas-Meunier E, Fossier P, Baux G, Amar M (2003) Cholinergic modulation of the cortical neuronal network. Pflugers Arch 446:17-29.

Luhrs T, Ritter C, Adrian M, Riek-Loher D, Bohrmann B, Dobeli H, Schubert D, Riek R (2005) 3D structure of Alzheimer's amyloid-beta(1-42) fibrils. Proc Natl Acad Sci U S A 102:17342-17347.

Luiten PG, Gaykema RP, Traber J, Spencer DG, Jr. (1987) Cortical projection patterns of magnocellular basal nucleus subdivisions as revealed by anterogradely transported Phaseolus vulgaris leucoagglutinin. Brain Res 413:229-250.

Luo F, Rustay NR, Ebert U, Hradil VP, Cole TB, Llano DA, Mudd SR, Zhang Y, Fox GB, Day M (2012) Characterization of 7- and 19-month-old Tg2576 mice using multimodal in vivo imaging: limitations as a translatable model of Alzheimer's disease. Neurobiol Aging 33:933-944.

Lycke J, Wikkelso C, Bergh AC, Jacobsson L, Andersen O (1993) Regional cerebral blood flow in multiple sclerosis measured by single photon emission tomography with technetium-99m hexamethylpropyleneamine oxime. Eur Neurol 33:163-167.

Ma Y, Hof PR, Grant SC, Blackband SJ, Bennett R, Slatest L, McGuigan MD, Benveniste H (2005) A three-dimensional digital atlas database of the adult C57BL/6J mouse brain by magnetic resonance microscopy. Neuroscience 135:1203-1215.

Ma Y, Smith D, Hof PR, Foerster B, Hamilton S, Blackband SJ, Yu M, Benveniste H (2008) In Vivo 3D Digital Atlas Database of the Adult C57BL/6J Mouse Brain by Magnetic Resonance Microscopy. Front Neuroanat 2:1.

Macdonald IR, Martin E, Rosenberry TL, Darvesh S (2012) Probing the peripheral site of human butyrylcholinesterase. Biochemistry 51:7046-7053.

Macdonald IR, Jollymore CT, Reid GA, Pottie IR, Martin E, Darvesh S (2013) Thioesters for the in vitro evaluation of agents to image brain cholinesterases. J Enzyme Inhib Med Chem 28:447-455.

Macdonald IR, Reid GA, Joy EE, Pottie IR, Matte G, Burrell S, Mawko G, Martin E, Darvesh S (2011) Synthesis and preliminary evaluation of piperidinyl and pyrrolidinyl iodobenzoates as imaging agents for butyrylcholinesterase. Mol Imaging Biol 13:1250-1261.

Machulda MM, Ward HA, Borowski B, Gunter JL, Cha RH, O'Brien PC, Petersen RC, Boeve BF, Knopman D, Tang-Wai DF, Ivnik RJ, Smith GE, Tangalos EG, Jack CR, Jr. (2003) Comparison of memory fMRI response among normal, MCI, and Alzheimer's patients. Neurology 61:500-506.

Mainero C, Pantano P, Caramia F, Pozzilli C (2006) Brain reorganization during attention and memory tasks in multiple sclerosis: insights from functional MRI studies. J Neurol Sci 245:93-98.

Mallender WD, Szegletes T, Rosenberry TL (2000) Acetylthiocholine binds to asp74 at the peripheral site of human acetylcholinesterase as the first step in the catalytic pathway. Biochemistry 39:7753-7763.

Malthe-Sorenssen D (1976) Choline acetyltransferase--evidence for acetyl transfer by a histidine residue. J Neurochem 27:873-881.

Mandybur TI (1986) Cerebral amyloid angiopathy: the vascular pathology and complications. J Neuropathol Exp Neurol 45:79-90.

Marcone A, Garibotto V, Moresco RM, Florea I, Panzacchi A, Carpinelli A, Virta JR, Tettamanti M, Borroni B, Padovani A, Bertoldo A, Herholz K, Rinne JO, Cappa SF, Perani D (2012) [(11)C]-MP4A PET cholinergic measurements in amnestic mild cognitive impairment, probable Alzheimer's disease, and dementia with Lewy bodies: a Bayesian method and voxel-based analysis. J Alzheimers Dis 31:387-399.

Margolis G (1959) Senile cerebral disease: a critical survey of traditional concepts based upon observations with newer technics. Lab Invest 8:335-370.

Martinez-Murillo R, Rodrigo J (1995) The localization of cholinergic neurons andmarkers in the CNS. In: CNS Neurotransmitters and neuromodulators: Acetylcholine (Stone T, ed), pp 1–38. Boca Raton: CRC Press.

Masson P, Froment MT, Bartels CF, Lockridge O (1996) Asp7O in the peripheral anionic site of human butyrylcholinesterase. Eur J Biochem 235:36-48.

Masson P, Legrand P, Bartels CF, Froment MT, Schopfer LM, Lockridge O (1997) Role of aspartate 70 and tryptophan 82 in binding of succinyldithiocholine to human butyrylcholinesterase. Biochemistry 36:2266-2277.

Masson P, Clery C, Guerra P, Redslob A, Albaret C, Fortier PL (1999a) Hydration change during the aging of phosphorylated human butyrylcholinesterase: importance of residues aspartate-70 and glutamate-197 in the water network as probed by hydrostatic and osmotic pressures. Biochem J 343 Pt 2:361-369.

Masson P, Froment MT, Gillon E, Nachon F, Lockridge O, Schopfer LM (2007) Hydrolysis of oxo- and thio-esters by human butyrylcholinesterase. Biochim Biophys Acta 1774:16-34.

Masson P, Xie W, Froment MT, Levitsky V, Fortier PL, Albaret C, Lockridge O (1999b) Interaction between the peripheral site residues of human butyrylcholinesterase, D70 and Y332, in binding and hydrolysis of substrates. Biochim Biophys Acta 1433:281-293.

Massoulie J (2002) The origin of the molecular diversity and functional anchoring of cholinesterases. Neurosignals 11:130-143.

Massoulie J, Pezzementi L, Bon S, Krejci E, Vallette FM (1993) Molecular and cellular biology of cholinesterases. Prog Neurobiol 41:31-91.

Massoulie J, Anselmet A, Bon S, Krejci E, Legay C, Morel N, Simon S (1998) Acetylcholinesterase: C-terminal domains, molecular forms and functional localization. J Physiol Paris 92:183-190.

Masters CL, Simms G, Weinman NA, Multhaup G, McDonald BL, Beyreuther K (1985) Amyloid plaque core protein in Alzheimer disease and Down syndrome. Proc Natl Acad Sci U S A 82:4245-4249.

Masuda J, Tanaka K, Ueda K, Omae T (1988) Autopsy study of incidence and distribution of cerebral amyloid angiopathy in Hisayama, Japan. Stroke 19:205-210.

Mathis CA, Wang Y, Holt DP, Huang GF, Debnath ML, Klunk WE (2003) Synthesis and evaluation of 11C-labeled 6-substituted 2-arylbenzothiazoles as amyloid imaging agents. J Med Chem 46:2740-2754.

Mathis CA, Bacskai BJ, Kajdasz ST, McLellan ME, Frosch MP, Hyman BT, Holt DP, Wang Y, Huang GF, Debnath ML, Klunk WE (2002) A lipophilic thioflavin-T derivative for positron emission tomography (PET) imaging of amyloid in brain. Bioorg Med Chem Lett 12:295-298.

Matsuda H (2007) Role of neuroimaging in Alzheimer's disease, with emphasis on brain perfusion SPECT. J Nucl Med 48:1289-1300.

Matsumura S et al. (2011) Two distinct amyloid beta-protein (Abeta) assembly pathways leading to oligomers and fibrils identified by combined fluorescence correlation spectroscopy, morphology, and toxicity analyses. J Biol Chem 286:11555-11562.

Mattner F, Katsifis A, Staykova M, Ballantyne P, Willenborg DO (2005) Evaluation of a radiolabelled peripheral benzodiazepine receptor ligand in the central nervous system inflammation of experimental autoimmune encephalomyelitis: a possible probe for imaging multiple sclerosis. Eur J Nucl Med Mol Imaging 32:557-563.

Mattson MP (1997) Cellular actions of beta-amyloid precursor protein and its soluble and fibrillogenic derivatives. Physiol Rev 77:1081-1132.

Matus A (1994) Stiff microtubules and neuronal morphology. Trends Neurosci 17:19-22.

Maurer K, Volk S, Gerbaldo H (1997) Auguste D and Alzheimer's disease. Lancet 349:1546-1549.

McDonald WI, Compston A, Edan G, Goodkin D, Hartung HP, Lublin FD, McFarland HF, Paty DW, Polman CH, Reingold SC, Sandberg-Wollheim M, Sibley W, Thompson A, van den Noort S, Weinshenker BY, Wolinsky JS (2001) Recommended diagnostic criteria for multiple sclerosis: guidelines from the International Panel on the diagnosis of multiple sclerosis. Ann Neurol 50:121-127.

McGuire MC, Nogueira CP, Bartels CF, Lightstone H, Hajra A, Van der Spek AF, Lockridge O, La Du BN (1989) Identification of the structural mutation responsible for the dibucaine-resistant (atypical) variant form of human serum cholinesterase. Proc Natl Acad Sci U S A 86:953-957.

McKhann G, Drachman D, Folstein M, Katzman R, Price D, Stadlan EM (1984) Clinical diagnosis of Alzheimer's disease: report of the NINCDS-ADRDA Work Group under the auspices of Department of Health and Human Services Task Force on Alzheimer's Disease. Neurology 34:939-944.

McKhann GM, Knopman DS, Chertkow H, Hyman BT, Jack CR, Jr., Kawas CH, Klunk WE, Koroshetz WJ, Manly JJ, Mayeux R, Mohs RC, Morris JC, Rossor MN, Scheltens P, Carrillo MC, Thies B, Weintraub S, Phelps CH (2011) The diagnosis of dementia due to Alzheimer's disease: recommendations from the National Institute on Aging-Alzheimer's Association workgroups on diagnostic guidelines for Alzheimer's disease. Alzheimers Dement 7:263-269.

Meanwell NA, Hewawasam P, Thomas JA, Wright JJ, Russell JW, Gamberdella M, Goldenberg HJ, Seiler SM, Zavoico GB (1993) Inhibitors of blood platelet cAMP phosphodiesterase. 4. Structural variation of the side-chain terminus of water-soluble 1,3-dihydro-2H-imidazo[4,5-b]quinolin-2-one derivatives. J Med Chem 36:3251-3264.

Meda L, Cassatella MA, Szendrei GI, Otvos L, Jr., Baron P, Villalba M, Ferrari D, Rossi F (1995) Activation of microglial cells by beta-amyloid protein and interferon-gamma. Nature 374:647-650.

Mejri N, Said NM, Guizani S, Essouissi I, Saidi M (2013) Preliminary studies of acetylcholinesterase activity in the rat brain using N-phenylferrocenecarboxamide labelled by the technetium-99m. Nucl Med Biol.

Mejri N, Barhoumi C, Trabelsi M, Mekni A, Said NM, Saidi M (2010) A 1-methyl-4-piperidinyl cytectrene carboxylate labeled by the technetium 99m, a radiotracer for rat brain acetylcholinesterase activity. Nucl Med Biol 37:143-148.

Mendel B, Rudney H (1943) On the Type of Cholinesterase Present in Brain Tissue. Science 98:201-202.

Mesulam MM (1986) Alzheimer plaques and cortical cholinergic innervation. Neuroscience 17:275-276.

Mesulam MM, Asuncion Moran M (1987) Cholinesterases within neurofibrillary tangles related to age and Alzheimer's disease. Ann Neurol 22:223-228.

Mesulam MM, Geula C (1991) Acetylcholinesterase-rich neurons of the human cerebral cortex: cytoarchitectonic and ontogenetic patterns of distribution. J Comp Neurol 306:193-220.

Mesulam MM, Geula C (1994) Butyrylcholinesterase reactivity differentiates the amyloid plaques of aging from those of dementia. Ann Neurol 36:722-727.

Mesulam MM, Geula C, Moran MA (1987) Anatomy of cholinesterase inhibition in Alzheimer's disease: effect of physostigmine and tetrahydroaminoacridine on plaques and tangles. Ann Neurol 22:683-691.

Mesulam MM, Guillozet A, Shaw P, Levey A, Duysen EG, Lockridge O (2002) Acetylcholinesterase knockouts establish central cholinergic pathways and can use butyrylcholinesterase to hydrolyze acetylcholine. Neuroscience 110:627-639.

Miao J, Xu F, Davis J, Otte-Holler I, Verbeek MM, Van Nostrand WE (2005) Cerebral microvascular amyloid beta protein deposition induces vascular degeneration and neuroinflammation in transgenic mice expressing human vasculotropic mutant amyloid beta precursor protein. Am J Pathol 167:505-515.

Micu I, Jiang Q, Coderre E, Ridsdale A, Zhang L, Woulfe J, Yin X, Trapp BD, McRory JE, Rehak R, Zamponi GW, Wang W, Stys PK (2006) NMDA receptors mediate calcium accumulation in myelin during chemical ischaemia. Nature 439:988-992.

Millard CB, Broomfield CA (1992) A computer model of glycosylated human butyrylcholinesterase. Biochem Biophys Res Commun 189:1280-1286.

Miller DH, Barkhof F, Frank JA, Parker GJ, Thompson AJ (2002) Measurement of atrophy in multiple sclerosis: pathological basis, methodological aspects and clinical relevance. Brain 125:1676-1695.

Miller DL, Papayannopoulos IA, Styles J, Bobin SA, Lin YY, Biemann K, Iqbal K (1993) Peptide compositions of the cerebrovascular and senile plaque core amyloid deposits of Alzheimer's disease. Arch Biochem Biophys 301:41-52.

Miners JS, Baig S, Tayler H, Kehoe PG, Love S (2009) Neprilysin and insulin-degrading enzyme levels are increased in Alzheimer disease in relation to disease severity. J Neuropathol Exp Neurol 68:902-914.

Mintun MA, Larossa GN, Sheline YI, Dence CS, Lee SY, Mach RH, Klunk WE, Mathis CA, DeKosky ST, Morris JC (2006) [11C]PIB in a nondemented population: potential antecedent marker of Alzheimer disease. Neurology 67:446-452.

Mirzabekov T, Lin MC, Yuan WL, Marshall PJ, Carman M, Tomaselli K, Lieberburg I, Kagan BL (1994) Channel formation in planar lipid bilayers by a neurotoxic fragment of the beta-amyloid peptide. Biochem Biophys Res Commun 202:1142-1148.

Miyata Y, Hoshi M, Nishida E, Minami Y, Sakai H (1986) Binding of microtubule-associated protein 2 and tau to the intermediate filament reassembled from neurofilament 70-kDa subunit protein. Its regulation by calmodulin. J Biol Chem 261:13026-13030.

Molchan SE, Martinez RA, Hill JL, Weingartner HJ, Thompson K, Vitiello B, Sunderland T (1992) Increased cognitive sensitivity to scopolamine with age and a perspective on the scopolamine model. Brain Res Brain Res Rev 17:215-226.

Moran MA, Mufson EJ, Gomez-Ramos P (1993) Colocalization of cholinesterases with beta amyloid protein in aged and Alzheimer's brains. Acta Neuropathol 85:362-369.

Morishima-Kawashima M, Hasegawa M, Takio K, Suzuki M, Yoshida H, Titani K, Ihara Y (1995) Proline-directed and non-proline-directed phosphorylation of PHF-tau. J Biol Chem 270:823-829.

Mortimer JA (2012) The Nun Study: risk factors for pathology and clinical-pathologic correlations. Curr Alzheimer Res 9:621-627.

Muhlau M, Buck D, Forschler A, Boucard CC, Arsic M, Schmidt P, Gaser C, Berthele A, Hoshi M, Jochim A, Kronsbein H, Zimmer C, Hemmer B, Ilg R (2013) White-matter lesions drive deep gray-matter atrophy in early multiple sclerosis: support from structural MRI. Mult Scler.

Mullan M, Crawford F, Axelman K, Houlden H, Lilius L, Winblad B, Lannfelt L (1992) A pathogenic mutation for probable Alzheimer's disease in the APP gene at the N-terminus of beta-amyloid. Nat Genet 1:345-347.

Murphy MP, Hickman LJ, Eckman CB, Uljon SN, Wang R, Golde TE (1999) gamma-Secretase, evidence for multiple proteolytic activities and influence of membrane positioning of substrate on generation of amyloid beta peptides of varying length. J Biol Chem 274:11914-11923.

Musachio JL, Flesher JE, Scheffel UA, Rauseo P, Hilton J, Mathews WB, Ravert HT, Dannals RF, Frost JJ (2002) Radiosynthesis and mouse brain distribution studies of [11C] CP-126,998: a PET ligand for in vivo study of acetylcholinesterase. Nucl Med Biol 29:547-552.

Nachmansohn D, Machado AL (1943) The formation of acetylcholine. A new enzyme choline acetylase. J Neurophysiol 6:397–403.

Nachmansohn D, Wilson IB (1951) The enzymic hydrolysis and synthesis of acetylcholine. Adv Enzymol Relat Subj Biochem 12:259-339.

Nachon F, Ehret-Sabatier L, Loew D, Colas C, van Dorsselaer A, Goeldner M (1998) Trp82 and Tyr332 are involved in two quaternary ammonium binding domains of human butyrylcholinesterase as revealed by photoaffinity labeling with [3H]DDF. Biochemistry 37:10507-10513.

Nachon F, Nicolet Y, Viguie N, Masson P, Fontecilla-Camps JC, Lockridge O (2002) Engineering of a monomeric and low-glycosylated form of human butyrylcholinesterase: expression, purification, characterization and crystallization. Eur J Biochem 269:630-637.

Namba H, Irie T, Fukushi K, Iyo M (1994) In vivo measurement of acetylcholinesterase activity in the brain with a radioactive acetylcholine analog. Brain Res 667:278-282.

Namba H, Iyo M, Shinotoh H, Nagatsuka S, Fukushi K, Irie T (1998) Preserved acetylcholinesterase activity in aged cerebral cortex. Lancet 351:881-882.

Namba H, Iyo M, Fukushi K, Shinotoh H, Nagatsuka S, Suhara T, Sudo Y, Suzuki K, Irie T (1999) Human cerebral acetylcholinesterase activity measured with positron emission tomography: procedure, normal values and effect of age. Eur J Nucl Med 26:135-143.

Namba Y, Tomonaga M, Kawasaki H, Otomo E, Ikeda K (1991) Apolipoprotein E immunoreactivity in cerebral amyloid deposits and neurofibrillary tangles in Alzheimer's disease and kuru plaque amyloid in Creutzfeldt-Jakob disease. Brain Res 541:163-166.

Nechushtan H, Soreq H, Kuperstein V, Tshori S, Razin E (1996) Murine and human mast cell express acetylcholinesterase. FEBS Lett 379:1-6.

Neumann MA (1960) Combined amyloid vascular changes and argyrophilic plaques in the central nervous system. J Neuropathol Exp Neurol 19:370-382.

Neumann S, Razen M, Habermehl P, Meyer CU, Zepp F, Kirkpatrick CJ, Wessler I (2007) The non-neuronal cholinergic system in peripheral blood cells: effects of nicotinic and muscarinic receptor antagonists on phagocytosis, respiratory burst and migration. Life Sci 80:2361-2364.

Neuropathology Group Medical Research Council Cognitive Function and Aging Study (2001) Pathological correlates of late-onset dementia in a multicentre, community-based population in England and Wales. Neuropathology Group of the Medical Research Council Cognitive Function and Ageing Study (MRC CFAS). Lancet 357:169-175.

Neville LF, Gnatt A, Loewenstein Y, Seidman S, Ehrlich G, Soreq H (1992) Intramolecular relationships in cholinesterases revealed by oocyte expression of site-directed and natural variants of human BCHE. EMBO J 11:1641-1649.

Nicholson RM, Kusne Y, Nowak LA, LaFerla FM, Reiman EM, Valla J (2010) Regional cerebral glucose uptake in the 3xTG model of Alzheimer's disease highlights common regional vulnerability across AD mouse models. Brain Res 1347:179-185.

Nicolet Y, Lockridge O, Masson P, Fontecilla-Camps JC, Nachon F (2003) Crystal structure of human butyrylcholinesterase and of its complexes with substrate and products. J Biol Chem 278:41141-41147.

Nicoll JA, Yamada M, Frackowiak J, Mazur-Kolecka B, Weller RO (2004) Cerebral amyloid angiopathy plays a direct role in the pathogenesis of Alzheimer's disease. Pro-CAA position statement. Neurobiol Aging 25:589-597; discussion 603-584.

Niedowicz DM, Beckett TL, Matveev S, Weidner AM, Baig I, Kryscio RJ, Mendiondo MS, LeVine H, 3rd, Keller JN, Murphy MP (2012) Pittsburgh compound B and the postmortem diagnosis of Alzheimer disease. Ann Neurol 72:564-570.

Nizri E, Hamra-Amitay Y, Sicsic C, Lavon I, Brenner T (2006) Anti-inflammatory properties of cholinergic up-regulation: A new role for acetylcholinesterase inhibitors. Neuropharmacology 50:540-547.

Nizri E, Irony-Tur-Sinai M, Faranesh N, Lavon I, Lavi E, Weinstock M, Brenner T (2008) Suppression of neuroinflammation and immunomodulation by the acetylcholinesterase inhibitor rivastigmine. J Neuroimmunol 203:12-22.

Noble W, Olm V, Takata K, Casey E, Mary O, Meyerson J, Gaynor K, LaFrancois J, Wang L, Kondo T, Davies P, Burns M, Veeranna, Nixon R, Dickson D, Matsuoka Y, Ahlijanian M, Lau LF, Duff K (2003) Cdk5 is a key factor in tau aggregation and tangle formation in vivo. Neuron 38:555-565.

Noguchi A et al. (2009) Isolation and characterization of patient-derived, toxic, high mass amyloid beta-protein (Abeta) assembly from Alzheimer disease brains. J Biol Chem 284:32895-32905.

Noseworthy JH, Lucchinetti C, Rodriguez M, Weinshenker BG (2000) Multiple sclerosis. N Engl J Med 343:938-952.

O'Nuallain B, Freir DB, Nicoll AJ, Risse E, Ferguson N, Herron CE, Collinge J, Walsh DM (2010) Amyloid beta-protein dimers rapidly form stable synaptotoxic protofibrils. J Neurosci 30:14411-14419.

Oakley H, Cole SL, Logan S, Maus E, Shao P, Craft J, Guillozet-Bongaarts A, Ohno M, Disterhoft J, Van Eldik L, Berry R, Vassar R (2006) Intraneuronal beta-amyloid aggregates, neurodegeneration, and neuron loss in transgenic mice with five familial Alzheimer's disease mutations: potential factors in amyloid plaque formation. J Neurosci 26:10129-10140.

Oh J, Saidha S, Chen M, Smith SA, Prince J, Jones C, Diener-West M, van Zijl PC, Reich DS, Calabresi PA (2013) Spinal cord quantitative MRI discriminates between disability levels in multiple sclerosis. Neurology 80:540-547.

Okamura N, Funaki Y, Tashiro M, Kato M, Ishikawa Y, Maruyama M, Ishikawa H, Meguro K, Iwata R, Yanai K (2008) In vivo visualization of donepezil binding in the brain of patients with Alzheimer's disease. Br J Clin Pharmacol 65:472-479.

Okazaki H, Reagan TJ, Campbell RJ (1979) Clinicopathologic studies of primary cerebral amyloid angiopathy. Mayo Clin Proc 54:22-31.

Oki T, Takagi Y, Inagaki S, Taketo MM, Manabe T, Matsui M, Yamada S (2005) Quantitative analysis of binding parameters of [3H]N-methylscopolamine in central nervous system of muscarinic acetylcholine receptor knockout mice. Brain Res Mol Brain Res 133:6-11.

Okinaka S, Yoshikawa M, Uono M, Muro T, Mozai T, Igata A, Tanabe H, Ueda S, Tomonaga M (1961) Distribution of cholinesterase activity in the human cerebral cortex. Am J Phys Med 40:135-145.

Ollis DL, Cheah E, Cygler M, Dijkstra B, Frolow F, Franken SM, Harel M, Remington SJ, Silman I, Schrag J, et al. (1992) The alpha/beta hydrolase fold. Protein Eng 5:197-211.

Ormerod IE, Miller DH, McDonald WI, du Boulay EP, Rudge P, Kendall BE, Moseley IF, Johnson G, Tofts PS, Halliday AM, et al. (1987) The role of NMR imaging in the assessment of multiple sclerosis and isolated neurological lesions. A quantitative study. Brain 110 (Pt 6):1579-1616.

Ossenkoppele R, Tolboom N, Foster-Dingley JC, Adriaanse SF, Boellaard R, Yaqub M, Windhorst AD, Barkhof F, Lammertsma AA, Scheltens P, van der Flier WM, van Berckel BN (2012) Longitudinal imaging of Alzheimer pathology using [11C]PIB, [18F]FDDNP and [18F]FDG PET. Eur J Nucl Med Mol Imaging 39:990-1000.

Oster-Granite ML, McPhie DL, Greenan J, Neve RL (1996) Age-dependent neuronal and synaptic degeneration in mice transgenic for the C terminus of the amyloid precursor protein. J Neurosci 16:6732-6741.

Palmer JC, Baig S, Kehoe PG, Love S (2009) Endothelin-converting enzyme-2 is increased in Alzheimer's disease and up-regulated by Abeta. Am J Pathol 175:262-270.

Papasozomenos SC, Binder LI (1987) Phosphorylation determines two distinct species of Tau in the central nervous system. Cell Motil Cytoskeleton 8:210-226.

Pappata S, Tavitian B, Traykov L, Jobert A, Dalger A, Mangin JF, Crouzel C, DiGiamberardino L (1996) In vivo imaging of human cerebral acetylcholinesterase. J Neurochem 67:876-879.

Parachikova A, Agadjanyan MG, Cribbs DH, Blurton-Jones M, Perreau V, Rogers J, Beach TG, Cotman CW (2007) Inflammatory changes parallel the early stages of Alzheimer disease. Neurobiol Aging 28:1821-1833.

Paraoanu LE, Layer PG (2008) Acetylcholinesterase in cell adhesion, neurite growth and network formation. FEBS J 275:618-624.

Paraoanu LE, Steinert G, Koehler A, Wessler I, Layer PG (2007) Expression and possible functions of the cholinergic system in a murine embryonic stem cell line. Life Sci 80:2375-2379.

Paraoanu LE, Steinert G, Klaczinski J, Becker-Rock M, Bytyqi A, Layer PG (2006) On functions of cholinesterases during embryonic development. J Mol Neurosci 30:201-204.

Pardossi-Piquard R, Petit A, Kawarai T, Sunyach C, Alves da Costa C, Vincent B, Ring S, D'Adamio L, Shen J, Muller U, St George Hyslop P, Checler F (2005) Presenilin-dependent transcriptional control of the Abeta-degrading enzyme neprilysin by intracellular domains of betaAPP and APLP. Neuron 46:541-554.

Patrikios P, Stadelmann C, Kutzelnigg A, Rauschka H, Schmidbauer M, Laursen H, Sorensen PS, Bruck W, Lucchinetti C, Lassmann H (2006) Remyelination is extensive in a subset of multiple sclerosis patients. Brain 129:3165-3172.

Patrucco L, Rojas JI, Cristiano E (2012) Assessing the value of spinal cord lesions in predicting development of multiple sclerosis in patients with clinically isolated syndromes. J Neurol 259:1317-1320.

Paudel HK, Li W (1999) Heparin-induced conformational change in microtubule-associated protein Tau as detected by chemical cross-linking and phosphopeptide mapping. J Biol Chem 274:8029-8038.

Paxinos G, Franklin K (2001) The Mouse Brain in Stereotaxic Coordinates, 2nd Edition. San Diego, CA: Academic Press.

Perrier AL, Massoulie J, Krejci E (2002) PRiMA: the membrane anchor of acetylcholinesterase in the brain. Neuron 33:275-285.

Perry EK, Perry RH, Blessed G, Tomlinson BE (1977) Necropsy evidence of central cholinergic deficits in senile dementia. Lancet 1:189.

Perry EK, Perry RH, Blessed G, Tomlinson BE (1978) Changes in brain cholinesterases in senile dementia of Alzheimer type. Neuropathol Appl Neurobiol 4:273-277.

Perry RH, Blessed G, Perry EK, Tomlinson BE (1980) Histochemical observations on cholinesterase activities in the brains of elderly normal and demented (Alzheimer-type) patients. Age Ageing 9:9-16.

Pfeifer LA, White LR, Ross GW, Petrovitch H, Launer LJ (2002) Cerebral amyloid angiopathy and cognitive function: the HAAS autopsy study. Neurology 58:1629-1634.

Pitas RE, Boyles JK, Lee SH, Hui D, Weisgraber KH (1987) Lipoproteins and their receptors in the central nervous system. Characterization of the lipoproteins in cerebrospinal fluid and identification of apolipoprotein B,E(LDL) receptors in the brain. J Biol Chem 262:14352-14360.

Planas AM, Crouzel C, Hinnen F, Jobert A, Ne F, DiGiamberardino L, Tavitian B (1994) Rat brain acetylcholinesterase visualized with [11C]physostigmine. Neuroimage 1:173-180.

Platt B, Drever B, Koss D, Stoppelkamp S, Jyoti A, Plano A, Utan A, Merrick G, Ryan D, Melis V, Wan H, Mingarelli M, Porcu E, Scrocchi L, Welch A, Riedel G (2011) Abnormal cognition, sleep, EEG and brain metabolism in a novel knock-in Alzheimer mouse, PLB1. PLoS One 6:e27068.

Podlisny MB, Ostaszewski BL, Squazzo SL, Koo EH, Rydell RE, Teplow DB, Selkoe DJ (1995) Aggregation of secreted amyloid beta-protein into sodium dodecyl sulfate-stable oligomers in cell culture. J Biol Chem 270:9564-9570.

Podoly E, Shalev DE, Shenhar-Tsarfaty S, Bennett ER, Ben Assayag E, Wilgus H, Livnah O, Soreq H (2009) The butyrylcholinesterase K variant confers structurally derived risks for Alzheimer pathology. J Biol Chem 284:17170-17179.

Poisnel G, Herard AS, El Tannir El Tayara N, Bourrin E, Volk A, Kober F, Delatour B, Delzescaux T, Debeir T, Rooney T, Benavides J, Hantraye P, Dhenain M (2012) Increased regional cerebral glucose uptake in an APP/PS1 model of Alzheimer's disease. Neurobiol Aging 33:1995-2005.

Politis M, Giannetti P, Su P, Turkheimer F, Keihaninejad S, Wu K, Waldman A, Malik O, Matthews PM, Reynolds R, Nicholas R, Piccini P (2012) Increased PK11195 PET binding in the cortex of patients with MS correlates with disability. Neurology 79:523-530.

Polman CH, Reingold SC, Edan G, Filippi M, Hartung HP, Kappos L, Lublin FD, Metz LM, McFarland HF, O'Connor PW, Sandberg-Wollheim M, Thompson AJ, Weinshenker BG, Wolinsky JS (2005) Diagnostic criteria for multiple sclerosis: 2005 revisions to the "McDonald Criteria". Ann Neurol 58:840-846.

Polman CH, Reingold SC, Banwell B, Clanet M, Cohen JA, Filippi M, Fujihara K, Havrdova E, Hutchinson M, Kappos L, Lublin FD, Montalban X, O'Connor P, Sandberg-Wollheim M, Thompson AJ, Waubant E, Weinshenker B, Wolinsky JS (2011) Diagnostic criteria for multiple sclerosis: 2010 revisions to the McDonald criteria. Ann Neurol 69:292-302.

Ponte P, Gonzalez-DeWhitt P, Schilling J, Miller J, Hsu D, Greenberg B, Davis K, Wallace W, Lieberburg I, Fuller F (1988) A new A4 amyloid mRNA contains a domain homologous to serine proteinase inhibitors. Nature 331:525-527.

Poorkaj P, Bird TD, Wijsman E, Nemens E, Garruto RM, Anderson L, Andreadis A, Wiederholt WC, Raskind M, Schellenberg GD (1998) Tau is a candidate gene for chromosome 17 frontotemporal dementia. Ann Neurol 43:815-825.

Poser CM, Brinar VV (2004) Diagnostic criteria for multiple sclerosis: an historical review. Clin Neurol Neurosurg 106:147-158.

Pottie IR, Higgins EA, Blackman RA, Macdonald IR, Martin E, Darvesh S (2011) Cysteine Thioesters as Myelin Proteolipid Protein Analogues to Examine the Role of Butyrylcholinesterase in Myelin Decompaction. ACS Chem Neurosci 2:151-159.

Pozzilli C, Pantano P, Bozzao L, Bernardi S, Carolei A, Fieschi C (1987) Sequential computed tomography and 123I-HIPDM scans in multiple sclerosis with large plaque. A case report. Eur Neurol 27:88-91.

Pozzilli C, Passafiume D, Bernardi S, Pantano P, Incoccia C, Bastianello S, Bozzao L, Lenzi GL, Fieschi C (1991) SPECT, MRI and cognitive functions in multiple sclerosis. J Neurol Neurosurg Psychiatry 54:110-115.

Prabhakaran S, Gupta R, Ouyang B, John S, Temes RE, Mohammad Y, Lee VH, Bleck TP (2010) Acute brain infarcts after spontaneous intracerebral hemorrhage: a diffusion-weighted imaging study. Stroke 41:89-94.

Prelli F, Castano E, Glenner GG, Frangione B (1988) Differences between vascular and plaque core amyloid in Alzheimer's disease. J Neurochem 51:648-651.

Prenant C, Crouzel C (1990) Synthesis of [11C]-sarin. J Labelled Comp Radiopharm 28:645-651.

Preston SD, Steart PV, Wilkinson A, Nicoll JA, Weller RO (2003) Capillary and arterial cerebral amyloid angiopathy in Alzheimer's disease: defining the perivascular route for the elimination of amyloid beta from the human brain. Neuropathol Appl Neurobiol 29:106-117.

Primo-Parmo SL, Bartels CF, Wiersema B, van der Spek AF, Innis JW, La Du BN (1996) Characterization of 12 silent alleles of the human butyrylcholinesterase (BCHE) gene. Am J Hum Genet 58:52-64.

Pruessner JC, Li LM, Serles W, Pruessner M, Collins DL, Kabani N, Lupien S, Evans AC (2000) Volumetry of hippocampus and amygdala with high-resolution MRI and three-dimensional analysis software: minimizing the discrepancies between laboratories. Cereb Cortex 10:433-442.

Querbes O, Aubry F, Pariente J, Lotterie JA, Demonet JF, Duret V, Puel M, Berry I, Fort JC, Celsis P (2009) Early diagnosis of Alzheimer's disease using cortical thickness: impact of cognitive reserve. Brain 132:2036-2047.

Quinn DM (1987) Acetylcholinesterase - Enzyme Structure, Reaction Dynamics, and Virtual Transition-States. Chemical Reviews 87:955-979.

Radic Z, Pickering NA, Vellom DC, Camp S, Taylor P (1993) Three distinct domains in the cholinesterase molecule confer selectivity for acetyl- and butyrylcholinesterase inhibitors. Biochemistry 32:12074-12084.

Radu CG, Shu CJ, Shelly SM, Phelps ME, Witte ON (2007) Positron emission tomography with computed tomography imaging of neuroinflammation in experimental autoimmune encephalomyelitis. Proc Natl Acad Sci U S A 104:1937-1942.

Raichle ME, MacLeod AM, Snyder AZ, Powers WJ, Gusnard DA, Shulman GL (2001) A default mode of brain function. Proc Natl Acad Sci U S A 98:676-682.

Raine CS (1994) The Dale E. McFarlin Memorial Lecture: the immunology of the multiple sclerosis lesion. Ann Neurol 36 Suppl:S61-72.

Ramanan VK, Risacher SL, Nho K, Kim S, Swaminathan S, Shen L, Foroud TM, Hakonarson H, Huentelman MJ, Aisen PS, Petersen RC, Green RC, Jack CR, Koeppe RA, Jagust WJ, Weiner MW, Saykin AJ (2013) APOE and BCHE as modulators of cerebral amyloid deposition: a florbetapir PET genome-wide association study. Mol Psychiatry.

Reddy PH, Manczak M, Mao P, Calkins MJ, Reddy AP, Shirendeb U (2010) Amyloid-beta and mitochondria in aging and Alzheimer's disease: implications for synaptic damage and cognitive decline. J Alzheimers Dis 20 Suppl 2:S499-512.

Reiman EM, Uecker A, Gonzalez-Lima F, Minear D, Chen K, Callaway NL, Berndt JD, Games D (2000) Tracking Alzheimer's disease in transgenic mice using fluorodeoxyglucose autoradiography. Neuroreport 11:987-991.

Rendon A, Jung D, Jancsik V (1990) Interaction of microtubules and microtubule-associated proteins (MAPs) with rat brain mitochondria. Biochem J 269:555-556.

Riley KP, Snowdon DA, Markesbery WR (2002) Alzheimer's neurofibrillary pathology and the spectrum of cognitive function: findings from the Nun Study. Ann Neurol 51:567-577.

Ring S, Weyer SW, Kilian SB, Waldron E, Pietrzik CU, Filippov MA, Herms J, Buchholz C, Eckman CB, Korte M, Wolfer DP, Muller UC (2007) The secreted beta-amyloid precursor protein ectodomain APPs alpha is sufficient to rescue the anatomical, behavioral, and electrophysiological abnormalities of APP-deficient mice. J Neurosci 27:7817-7826.

Rinne JO, Kaasinen V, Jarvenpaa T, Nagren K, Roivainen A, Yu M, Oikonen V, Kurki T (2003) Brain acetylcholinesterase activity in mild cognitive impairment and early Alzheimer's disease. J Neurol Neurosurg Psychiatry 74:113-115.

Robakis NK, Ramakrishna N, Wolfe G, Wisniewski HM (1987) Molecular cloning and characterization of a cDNA encoding the cerebrovascular and the neuritic plaque amyloid peptides. Proc Natl Acad Sci U S A 84:4190-4194.

Roberts SB, Ripellino JA, Ingalls KM, Robakis NK, Felsenstein KM (1994) Non-amyloidogenic cleavage of the beta-amyloid precursor protein by an integral membrane metalloendopeptidase. J Biol Chem 269:3111-3116.

Roby J, Voyer N (1997) Protection of a protecting Group: Preparation of stable N-silylated t-butyl carbamates. Tetrahedron Letters 38:191-194.

Rocca MA, Valsasina P, Martinelli V, Misci P, Falini A, Comi G, Filippi M (2012) Large-scale neuronal network dysfunction in relapsing-remitting multiple sclerosis. Neurology 79:1449-1457.

Rocca MA, Colombo B, Falini A, Ghezzi A, Martinelli V, Scotti G, Comi G, Filippi M (2005) Cortical adaptation in patients with MS: a cross-sectional functional MRI study of disease phenotypes. Lancet Neurol 4:618-626.

Rogaev EI, Sherrington R, Rogaeva EA, Levesque G, Ikeda M, Liang Y, Chi H, Lin C, Holman K, Tsuda T, et al. (1995) Familial Alzheimer's disease in kindreds with missense mutations in a gene on chromosome 1 related to the Alzheimer's disease type 3 gene. Nature 376:775-778.

Roivainen A, Rinne J, Virta J, Jarvenpaa T, Salomaki S, Yu M, Nagren K (2004) Biodistribution and blood metabolism of 1-11C-methyl-4-piperidinyl n-butyrate in humans: an imaging agent for in vivo assessment of butyrylcholinesterase activity with PET. J Nucl Med 45:2032-2039.

Rojas S, Herance JR, Gispert JD, Abad S, Torrent E, Jimenez X, Pareto D, Perpina U, Sarroca S, Rodriguez E, Ortega-Aznar A, Sanfeliu C (2013) In vivo evaluation of amyloid deposition and brain glucose metabolism of 5XFAD mice using positron emission tomography. Neurobiol Aging 34:1790-1798.

Rubinstein HM, Dietz AA, Lubrano T (1978) E1k, another quantitative variant at cholinesterase locus 1. J Med Genet 15:27-29.

Rudick RA, Goodman A, Herndon RM, Panitch HS (1999a) Selecting relapsing remitting multiple sclerosis patients for treatment: the case for early treatment. J Neuroimmunol 98:22-28.

Rudick RA, Fisher E, Lee JC, Simon J, Jacobs L (1999b) Use of the brain parenchymal fraction to measure whole brain atrophy in relapsing-remitting MS. Multiple Sclerosis Collaborative Research Group. Neurology 53:1698-1704.

Ryu EK, Choe YS, Park EY, Paik JY, Kim YR, Lee KH, Choi Y, Kim SE, Kim BT (2005) Synthesis and evaluation of 2-[18F]fluoro-CP-118,954 for the in vivo mapping of acetylcholinesterase. Nucl Med Biol 32:185-191.

Saez-Valero J, Sberna G, McLean CA, Small DH (1999) Molecular isoform distribution and glycosylation of acetylcholinesterase are altered in brain and cerebrospinal fluid of patients with Alzheimer's disease. J Neurochem 72:1600-1608.

Samuraki M, Matsunari I, Chen WP, Yajima K, Yanase D, Fujikawa A, Takeda N, Nishimura S, Matsuda H, Yamada M (2007) Partial volume effect-corrected FDG PET and grey matter volume loss in patients with mild Alzheimer's disease. Eur J Nucl Med Mol Imaging 34:1658-1669.

Saper CB (1984) Organization of cerebral cortical afferent systems in the rat. II. Magnocellular basal nucleus. J Comp Neurol 222:313-342.

Sato A, Sato Y, Uchida S (2004) Activation of the intracerebral cholinergic nerve fibers originating in the basal forebrain increases regional cerebral blood flow in the rat's cortex and hippocampus. Neurosci Lett 361:90-93.

Saunders AM, Strittmatter WJ, Schmechel D, George-Hyslop PH, Pericak-Vance MA, Joo SH, Rosi BL, Gusella JF, Crapper-MacLachlan DR, Alberts MJ, et al. (1993) Association of apolipoprotein E allele epsilon 4 with late-onset familial and sporadic Alzheimer's disease. Neurology 43:1467-1472.

Saxena A, Redman AM, Jiang X, Lockridge O, Doctor BP (1997) Differences in active site gorge dimensions of cholinesterases revealed by binding of inhibitors to human butyrylcholinesterase. Biochemistry 36:14642-14651.

Saxena A, Redman AM, Jiang X, Lockridge O, Doctor BP (1999) Differences in active-site gorge dimensions of cholinesterases revealed by binding of inhibitors to human butyrylcholinesterase. Chem Biol Interact 119-120:61-69.

Scheltens P, Leys D, Barkhof F, Huglo D, Weinstein HC, Vermersch P, Kuiper M, Steinling M, Wolters EC, Valk J (1992) Atrophy of medial temporal lobes on MRI in "probable" Alzheimer's disease and normal ageing: diagnostic value and neuropsychological correlates. J Neurol Neurosurg Psychiatry 55:967-972.

Scheuner D et al. (1996) Secreted amyloid beta-protein similar to that in the senile plaques of Alzheimer's disease is increased in vivo by the presenilin 1 and 2 and APP mutations linked to familial Alzheimer's disease. Nat Med 2:864-870.

Schliebs R, Arendt T (2006) The significance of the cholinergic system in the brain during aging and in Alzheimer's disease. J Neural Transm 113:1625-1644.

Schliebs R, Rossner S, Bigl V (1996) Immunolesion by 192IgG-saporin of rat basal forebrain cholinergic system: a useful tool to produce cortical cholinergic dysfunction. Prog Brain Res 109:253-264.

Schumacker GA, Beebe G, Kibler RF, Kurland LT, Kurtzke JF, McDowell F, Nagler B, Sibley WA, Tourtellotte WW, Willmon TL (1965) Problems of Experimental Trials of Therapy in Multiple Sclerosis: Report by the Panel on the Evaluation of Experimental Trials of Therapy in Multiple Sclerosis. Ann N Y Acad Sci 122:552-568.

Schwartz P, Kurucz J, Kurucz A (1965) Fluorescence Microscopy Demonstration of Cerebrovascular and Pancreatic Insular Amyloid in Presenile and Senile States. J Am Geriatr Soc 13:199-205.

Scolding N, Franklin R, Stevens S, Heldin CH, Compston A, Newcombe J (1998) Oligodendrocyte progenitors are present in the normal adult human CNS and in the lesions of multiple sclerosis. Brain 121 (Pt 12):2221-2228.

Seewann A, Kooi EJ, Roosendaal SD, Pouwels PJ, Wattjes MP, van der Valk P, Barkhof F, Polman CH, Geurts JJ (2012) Postmortem verification of MS cortical lesion detection with 3D DIR. Neurology 78:302-308.

Selden SC, Pollard TD (1983) Phosphorylation of microtubule-associated proteins regulates their interaction with actin filaments. J Biol Chem 258:7064-7071.

Selkoe DJ (1991) The molecular pathology of Alzheimer's disease. Neuron 6:487-498.

Selkoe DJ, Abraham CR, Podlisny MB, Duffy LK (1986) Isolation of low-molecular-weight proteins from amyloid plaque fibers in Alzheimer's disease. J Neurochem 46:1820-1834.

Selkoe DJ, Podlisny MB, Joachim CL, Vickers EA, Lee G, Fritz LC, Oltersdorf T (1988) Beta-amyloid precursor protein of Alzheimer disease occurs as 110- to 135-kilodalton membrane-associated proteins in neural and nonneural tissues. Proc Natl Acad Sci U S A 85:7341-7345.

Semba K, Fibiger HC (1989) Organization of central cholinergic systems. Prog Brain Res 79:37-63.

Semba K, Reiner PB, McGeer EG, Fibiger HC (1989) Brainstem projecting neurons in the rat basal forebrain: neurochemical, topographical, and physiological distinctions from cortically projecting cholinergic neurons. Brain Res Bull 22:501-509.

Serbecic N, Aboul-Enein F, Beutelspacher SC, Graf M, Kircher K, Geitzenauer W, Brannath W, Lang P, Kristoferitsch W, Lassmann H, Reitner A, Schmidt-Erfurth U (2010) Heterogeneous pattern of retinal nerve fiber layer in multiple sclerosis. High resolution optical coherence tomography: potential and limitations. PLoS One 5:e13877.

Sergott RC, Frohman E, Glanzman R, Al-Sabbagh A (2007) The role of optical coherence tomography in multiple sclerosis: expert panel consensus. J Neurol Sci 263:3-14.

Seshadri S, Beiser A, Kelly-Hayes M, Kase CS, Au R, Kannel WB, Wolf PA (2006) The lifetime risk of stroke: estimates from the Framingham Study. Stroke 37:345-350.

Shafferman A, Ordentlich A, Barak D, Stein D, Ariel N, Velan B (1996) Aging of phosphylated human acetylcholinesterase: catalytic processes mediated by aromatic and polar residues of the active centre. Biochem J 318 (Pt 3):833-840.

Shafferman A, Kronman C, Flashner Y, Leitner M, Grosfeld H, Ordentlich A, Gozes Y, Cohen S, Ariel N, Barak D, et al. (1992) Mutagenesis of human acetylcholinesterase. Identification of residues involved in catalytic activity and in polypeptide folding. J Biol Chem 267:17640-17648.

Shankar GM, Li S, Mehta TH, Garcia-Munoz A, Shepardson NE, Smith I, Brett FM, Farrell MA, Rowan MJ, Lemere CA, Regan CM, Walsh DM, Sabatini BL, Selkoe DJ (2008) Amyloid-beta protein dimers isolated directly from Alzheimer's brains impair synaptic plasticity and memory. Nat Med 14:837-842.

Shao X, Butch ER, Kilbourn MR, Snyder SE (2003) N-[(18)F]Fluoroethylpiperidinyl, N-[(18)F]fluoroethylpiperidinemethyl and N-[(18)F]fluoroethylpyrrolidinyl esters as radiotracers for acetylcholinesterase. Nucl Med Biol 30:491-500.

Shao X, Koeppe RA, Butch ER, Kilbourn MR, Snyder SE (2005) Evaluation of 18F-labeled acetylcholinesterase substrates as PET radiotracers. Bioorg Med Chem 13:869-875.

Sherrington R et al. (1995) Cloning of a gene bearing missense mutations in early-onset familial Alzheimer's disease. Nature 375:754-760.

Shi Q, Prior M, He W, Tang X, Hu X, Yan R (2009) Reduced amyloid deposition in mice overexpressing RTN3 is adversely affected by preformed dystrophic neurites. J Neurosci 29:9163-9173.

Shi Y, Feng Y, Kang J, Liu C, Li Z, Li D, Cao W, Qiu J, Guo Z, Bi E, Zang L, Lu C, Zhang JZ, Pei G (2007) Critical regulation of CD4+ T cell survival and autoimmunity by beta-arrestin 1. Nat Immunol 8:817-824.

Shibata M, Yamada S, Kumar SR, Calero M, Bading J, Frangione B, Holtzman DM, Miller CA, Strickland DK, Ghiso J, Zlokovic BV (2000) Clearance of Alzheimer's amyloid-B(1-40) peptide from brain by LDL receptor-related protein-1 at the blood-brain barrier. J Clin Invest 106:1489-1499.

Shinotoh H, Namba H, Fukushi K, Nagatsuka S, Tanaka N, Aotsuka A, Tanada S, Irie T (2000) Brain acetylcholinesterase activity in Alzheimer disease measured by positron emission tomography. Alzheimer Dis Assoc Disord 14 Suppl 1:S114-118.

Shoghi-Jadid K, Small GW, Agdeppa ED, Kepe V, Ercoli LM, Siddarth P, Read S, Satyamurthy N, Petric A, Huang SC, Barrio JR (2002) Localization of neurofibrillary tangles and beta-amyloid plaques in the brains of living patients with Alzheimer disease. Am J Geriatr Psychiatry 10:24-35.

Signoret J, Hauw J (2001) Maladie d’Alzheimer et autres demences.

Silver A (1974) The Biology of Cholinesterases. Amsterdam: Elsevier.

Silverman DH et al. (2001) Positron emission tomography in evaluation of dementia: Regional brain metabolism and long-term outcome. JAMA 286:2120-2127.

Simon JH, Jacobs LD, Campion MK, Rudick RA, Cookfair DL, Herndon RM, Richert JR, Salazar AM, Fischer JS, Goodkin DE, Simonian N, Lajaunie M, Miller DE, Wende K, Martens-Davidson A, Kinkel RP, Munschauer FE, 3rd, Brownscheidle CM (1999) A longitudinal study of brain atrophy in relapsing multiple sclerosis. The Multiple Sclerosis Collaborative Research Group (MSCRG). Neurology 53:139-148.

Sims NR, Bowen DM, Smith CC, Flack RH, Davison AN, Snowden JS, Neary D (1980) Glucose metabolism and acetylcholine synthesis in relation to neuronal activity in Alzheimer's disease. Lancet 1:333-336.

Singh S, Basmadjian GP, Avor KS, Pouw B, Seale TW (1997) Synthesis and ligand binding studies of 4'-iodobenzoyl esters of tropanes and piperidines at the dopamine transporter. J Med Chem 40:2474-2481.

Sinha S et al. (1999) Purification and cloning of amyloid precursor protein beta-secretase from human brain. Nature 402:537-540.

Sinko G, Kovarik Z, Reiner E, Simeon-Rudolf V, Stojan J (2011) Mechanism of stereoselective interaction between butyrylcholinesterase and ethopropazine enantiomers. Biochimie 93:1797-1807.

Sisodia SS (1992) Beta-amyloid precursor protein cleavage by a membrane-bound protease. Proc Natl Acad Sci U S A 89:6075-6079.

Small GW, Kepe V, Siddarth P, Ercoli LM, Merrill DA, Donoghue N, Bookheimer SY, Martinez J, Omalu B, Bailes J, Barrio JR (2013) PET Scanning of Brain Tau in Retired National Football League Players: Preliminary Findings. Am J Geriatr Psychiatry 21:138-144.

Smallman BN, Maneckjee A (1981) The synthesis of acetylcholine by plants. Biochem J 194:361-364.

Smetanin P, Kobak P, Briante C, Stiff D, Sherman G, Ahmad S (2009) Rising Tide: The Impact of Dementia in Canada 2008 to 2038. In: RiskAnalytica.

Smith KJ, Lassmann H (2002) The role of nitric oxide in multiple sclerosis. Lancet Neurol 1:232-241.

Snitz BE, Weissfeld LA, Lopez OL, Kuller LH, Saxton J, Singhabahu DM, Klunk WE, Mathis CA, Price JC, Ives DG, Cohen AD, McDade E, Dekosky ST (2013) Cognitive trajectories associated with beta-amyloid deposition in the oldest-old without dementia. Neurology.

Snowdon DA (1997) Aging and Alzheimer's disease: lessons from the Nun Study. Gerontologist 37:150-156.

Snowdon DA (2003) Healthy aging and dementia: findings from the Nun Study. Ann Intern Med 139:450-454.

Snyder SE, Tluczek L, Jewett DM, Nguyen TB, Kuhl DE, Kilbourn MR (1998) Synthesis of 1-[11C]methylpiperidin-4-yl propionate ([11C]PMP) for in vivo measurements of acetylcholinesterase activity. Nucl Med Biol 25:751-754.

Snyder SE, Gunupudi N, Sherman PS, Butch ER, Skaddan MB, Kilbourn MR, Koeppe RA, Kuhl DE (2001) Radiolabeled cholinesterase substrates: in vitro methods for determining structure-activity relationships and identification of a positron emission tomography radiopharmaceutical for in vivo measurement of butyrylcholinesterase activity. J Cereb Blood Flow Metab 21:132-143.

Song W, Nadeau P, Yuan M, Yang X, Shen J, Yankner BA (1999) Proteolytic release and nuclear translocation of Notch-1 are induced by presenilin-1 and impaired by pathogenic presenilin-1 mutations. Proc Natl Acad Sci U S A 96:6959-6963.

Sorensen TL, Frederiksen JL, Bronnum-Hansen H, Petersen HC (1999) Optic neuritis as onset manifestation of multiple sclerosis: a nationwide, long-term survey. Neurology 53:473-478.

Soreq H, Seidman S (2001) Acetylcholinesterase--new roles for an old actor. Nat Rev Neurosci 2:294-302.

Sorg C, Riedl V, Muhlau M, Calhoun VD, Eichele T, Laer L, Drzezga A, Forstl H, Kurz A, Zimmer C, Wohlschlager AM (2007) Selective changes of resting-state networks in individuals at risk for Alzheimer's disease. Proc Natl Acad Sci U S A 104:18760-18765.

Sparkes RS, Field LL, Sparkes MC, Crist M, Spence MA, James K, Garry PJ (1984) Genetic linkage studies of transferrin, pseudocholinesterase, and chromosome 1 loci. Hum Hered 34:96-100.

Spillantini MG, Murrell JR, Goedert M, Farlow MR, Klug A, Ghetti B (1998) Mutation in the tau gene in familial multiple system tauopathy with presenile dementia. Proc Natl Acad Sci U S A 95:7737-7741.

Srinivasan R, Sailasuta N, Hurd R, Nelson S, Pelletier D (2005) Evidence of elevated glutamate in multiple sclerosis using magnetic resonance spectroscopy at 3 T. Brain 128:1016-1025.

St George-Hyslop PH, Tanzi RE, Polinsky RJ, Haines JL, Nee L, Watkins PC, Myers RH, Feldman RG, Pollen D, Drachman D, et al. (1987) The genetic defect causing familial Alzheimer's disease maps on chromosome 21. Science 235:885-890.

Staff RT, Murray AD, Ahearn T, Salarirad S, Mowat D, Starr JM, Deary IJ, Lemmon H, Whalley LJ (2010) Brain volume and survival from age 78 to 85: the contribution of Alzheimer-type magnetic resonance imaging findings. J Am Geriatr Soc 58:688-695.

Stankoff B, Freeman L, Aigrot MS, Chardain A, Dolle F, Williams A, Galanaud D, Armand L, Lehericy S, Lubetzki C, Zalc B, Bottlaender M (2011) Imaging central nervous system myelin by positron emission tomography in multiple sclerosis using [methyl-(1)(1)C]-2-(4'-methylaminophenyl)- 6-hydroxybenzothiazole. Ann Neurol 69:673-680.

State FA, El-Eishi HI, Hamed MS (1977) Myelination and cholinesterase activity of chick embryo spinal cord. Acta Anat (Basel) 99:469-476.

Stedman E, Easson LH (1932) Choline-esterase. An enzyme present in the blood-serum of the horse. Biochem J 26:2056-2066.

Stephenson M, Rowatt E (1947) The production of acetylcholine by a strain of Lactobacillus plantarum. J Gen Microbiol 1:279-298.

Sternfeld M, Shoham S, Klein O, Flores-Flores C, Evron T, Idelson GH, Kitsberg D, Patrick JW, Soreq H (2000) Excess "read-through" acetylcholinesterase attenuates but the "synaptic" variant intensifies neurodeterioration correlates. Proc Natl Acad Sci U S A 97:8647-8652.

Strittmatter WJ, Saunders AM, Schmechel D, Pericak-Vance M, Enghild J, Salvesen GS, Roses AD (1993) Apolipoprotein E: high-avidity binding to beta-amyloid and increased frequency of type 4 allele in late-onset familial Alzheimer disease. Proc Natl Acad Sci U S A 90:1977-1981.

Studholme C, Hill DL, Hawkes DJ (1996) Automated 3-D registration of MR and CT images of the head. Med Image Anal 1:163-175.

Sussman JL, Harel M, Silman I (1993) Three-dimensional structure of acetylcholinesterase and of its complexes with anticholinesterase drugs. Chem Biol Interact 87:187-197.

Sussman JL, Harel M, Frolow F, Oefner C, Goldman A, Toker L, Silman I (1991) Atomic structure of acetylcholinesterase from Torpedo californica: a prototypic acetylcholine-binding protein. Science 253:872-879.

Suzuki N, Cheung TT, Cai XD, Odaka A, Otvos L, Jr., Eckman C, Golde TE, Younkin SG (1994) An increased percentage of long amyloid beta protein secreted by familial amyloid beta protein precursor (beta APP717) mutants. Science 264:1336-1340.

Szegletes T, Mallender WD, Rosenberry TL (1998) Nonequilibrium analysis alters the mechanistic interpretation of inhibition of acetylcholinesterase by peripheral site ligands. Biochemistry 37:4206-4216.

Tago H, Maeda T, McGeer PL, Kimura H (1992) Butyrylcholinesterase-rich neurons in rat brain demonstrated by a sensitive histochemical method. J Comp Neurol 325:301-312.

Takashima A, Murayama M, Murayama O, Kohno T, Honda T, Yasutake K, Nihonmatsu N, Mercken M, Yamaguchi H, Sugihara S, Wolozin B (1998) Presenilin 1 associates with glycogen synthase kinase-3beta and its substrate tau. Proc Natl Acad Sci U S A 95:9637-9641.

Takasugi N, Tomita T, Hayashi I, Tsuruoka M, Niimura M, Takahashi Y, Thinakaran G, Iwatsubo T (2003) The role of presenilin cofactors in the gamma-secretase complex. Nature 422:438-441.

Tanzi RE, McClatchey AI, Lamperti ED, Villa-Komaroff L, Gusella JF, Neve RL (1988) Protease inhibitor domain encoded by an amyloid protein precursor mRNA associated with Alzheimer's disease. Nature 331:528-530.

Tanzi RE, Gusella JF, Watkins PC, Bruns GA, St George-Hyslop P, Van Keuren ML, Patterson D, Pagan S, Kurnit DM, Neve RL (1987) Amyloid beta protein gene: cDNA, mRNA distribution, and genetic linkage near the Alzheimer locus. Science 235:880-884.

Tas MW, Barkhol F, van Walderveen MA, Polman CH, Hommes OR, Valk J (1995) The effect of gadolinium on the sensitivity and specificity of MR in the initial diagnosis of multiple sclerosis. AJNR Am J Neuroradiol 16:259-264.

Tavitian B, Pappata S, Bonnot-Lours S, Prenant C, Jobert A, Crouzel C, Di Giamberardino L (1993) Positron emission tomography study of [11C]methyl-tetrahydroaminoacridine (methyl-tacrine) in baboon brain. Eur J Pharmacol 236:229-238.

Tayebati SK, El-Assouad D, Ricci A, Amenta F (2002) Immunochemical and immunocytochemical characterization of cholinergic markers in human peripheral blood lymphocytes. J Neuroimmunol 132:147-155.

Taylor P, Lappi S (1975) Interaction of fluorescence probes with acetylcholinesterase. The site and specificity of propidium binding. Biochemistry 14:1989-1997.

Tekkok SB, Goldberg MP (2001) Ampa/kainate receptor activation mediates hypoxic oligodendrocyte death and axonal injury in cerebral white matter. J Neurosci 21:4237-4248.

Terasaki PI, Park MS, Opelz G, Ting A (1976) Multiple sclerosis and high incidence of a B lymphocyte antigen. Science 193:1245-1247.

Terry AV, Jr., Buccafusco JJ (2003) The cholinergic hypothesis of age and Alzheimer's disease-related cognitive deficits: recent challenges and their implications for novel drug development. J Pharmacol Exp Ther 306:821-827.

Tetko I, Tanchuk V, Villa A (2001) Prediction of n-octanol/water partition coefficients from PHYSPROP database using artificial neural networks and E-state indices. J Chem Inf Comput Sci 41:1407–1421.

Tewari JP, Sehgal SS, Malhotra SK (1982) Microanalysis of the reaction product in Karnovsky and Roots histochemical localization of acetylcholinesterase. J Histochem Cytochem 30:436-440.

Thal DR, Rub U, Orantes M, Braak H (2002) Phases of A beta-deposition in the human brain and its relevance for the development of AD. Neurology 58:1791-1800.

Thinakaran G, Borchelt DR, Lee MK, Slunt HH, Spitzer L, Kim G, Ratovitsky T, Davenport F, Nordstedt C, Seeger M, Hardy J, Levey AI, Gandy SE, Jenkins NA, Copeland NG, Price DL, Sisodia SS (1996) Endoproteolysis of presenilin 1 and accumulation of processed derivatives in vivo. Neuron 17:181-190.

Tolboom N, van der Flier WM, Yaqub M, Koene T, Boellaard R, Windhorst AD, Scheltens P, Lammertsma AA, van Berckel BN (2009a) Differential association of [11C]PIB and [18F]FDDNP binding with cognitive impairment. Neurology 73:2079-2085.

Tolboom N, Yaqub M, van der Flier WM, Boellaard R, Luurtsema G, Windhorst AD, Barkhof F, Scheltens P, Lammertsma AA, van Berckel BN (2009b) Detection of Alzheimer pathology in vivo using both 11C-PIB and 18F-FDDNP PET. J Nucl Med 50:191-197.

Torack R (1983) The early history of senile dementia. In: Alzheimer’s Disease: The Standard Reference (Reisberg B, ed), pp 23–28. New York: The Free Press.

Tormos JR, Wiley KL, Seravalli J, Nachon F, Masson P, Nicolet Y, Quinn DM (2005) The reactant state for substrate-activated turnover of acetylthiocholine by butyrylcholinesterase is a tetrahedral intermediate. J Am Chem Soc 127:14538-14539.

Trapp BD, Peterson J, Ransohoff RM, Rudick R, Mork S, Bo L (1998) Axonal transection in the lesions of multiple sclerosis. N Engl J Med 338:278-285.

Traykov L, Tavitian B, Jobert A, Boller F, Forette F, Crouzel C, Di Giamberardino L, Pappata S (1999) In vivo PET study of cerebral [11C] methyl-tetrahydroaminoacridine distribution and kinetics in healthy human subjects. Eur J Neurol 6:273-278.

Trivedi MA, Schmitz TW, Ries ML, Torgerson BM, Sager MA, Hermann BP, Asthana S, Johnson SC (2006) Reduced hippocampal activation during episodic encoding in middle-aged individuals at genetic risk of Alzheimer's disease: a cross-sectional study. BMC Med 4:1.

Tsigelny I, Shindyalov IN, Bourne PE, Sudhof TC, Taylor P (2000) Common EF-hand motifs in cholinesterases and neuroligins suggest a role for Ca2+ binding in cell surface associations. Protein Sci 9:180-185.

Valla J, Schneider L, Reiman EM (2006) Age- and transgene-related changes in regional cerebral metabolism in PSAPP mice. Brain Res 1116:194-200.

Valla J, Gonzalez-Lima F, Reiman EM (2008) FDG autoradiography reveals developmental and pathological effects of mutant amyloid in PDAPP transgenic mice. Int J Dev Neurosci 26:253-258.

van der Valk P, De Groot CJ (2000) Staging of multiple sclerosis (MS) lesions: pathology of the time frame of MS. Neuropathol Appl Neurobiol 26:2-10.

Van Dorpe J, Smeijers L, Dewachter I, Nuyens D, Spittaels K, Van Den Haute C, Mercken M, Moechars D, Laenen I, Kuiperi C, Bruynseels K, Tesseur I, Loos R, Vanderstichele H, Checler F, Sciot R, Van Leuven F (2000) Prominent cerebral amyloid angiopathy in transgenic mice overexpressing the london mutant of human APP in neurons. Am J Pathol 157:1283-1298.

Van Gassen G, Annaert W, Van Broeckhoven C (2000) Binding partners of Alzheimer's disease proteins: are they physiologically relevant? Neurobiol Dis 7:135-151.

Vassar R, Kovacs DM, Yan R, Wong PC (2009) The beta-secretase enzyme BACE in health and Alzheimer's disease: regulation, cell biology, function, and therapeutic potential. J Neurosci 29:12787-12794.

Vassar R et al. (1999) Beta-secretase cleavage of Alzheimer's amyloid precursor protein by the transmembrane aspartic protease BACE. Science 286:735-741.

Vaucher E, Borredon J, Seylaz J, Lacombe P (1995) Autoradiographic distribution of cerebral blood flow increases elicited by stimulation of the nucleus basalis magnocellularis in the unanesthetized rat. Brain Res 691:57-68.

Vellom DC, Radic Z, Li Y, Pickering NA, Camp S, Taylor P (1993) Amino acid residues controlling acetylcholinesterase and butyrylcholinesterase specificity. Biochemistry 32:12-17.

Verbout NG, Jacoby DB (2012) Muscarinic receptor agonists and antagonists: effects on inflammation and immunity. Handb Exp Pharmacol:403-427.

Verghese PB, Castellano JM, Holtzman DM (2011) Apolipoprotein E in Alzheimer's disease and other neurological disorders. Lancet Neurol 10:241-252.

Villain N, Chetelat G, Grassiot B, Bourgeat P, Jones G, Ellis KA, Ames D, Martins RN, Eustache F, Salvado O, Masters CL, Rowe CC, Villemagne VL (2012) Regional dynamics of amyloid-beta deposition in healthy elderly, mild cognitive impairment and Alzheimer's disease: a voxelwise PiB-PET longitudinal study. Brain 135:2126-2139.

Villalobos A, Butler TW, Chapin DS, Chen YL, DeMattos SB, Ives JL, Jones SB, Liston DR, Nagel AA, Nason DM, et al. (1995) 5,7-dihydro-3-[2-[1-(phenylmethyl)-4-piperidinyl]ethyl]-6H- pyrrolo[3,2-f]-1,2-benzisoxazol-6-one: a potent and centrally-selective inhibitor of acetylcholinesterase with an improved margin of safety. J Med Chem 38:2802-2808.

Villemagne VL, Burnham S, Bourgeat P, Brown B, Ellis KA, Salvado O, Szoeke C, Macaulay SL, Martins R, Maruff P, Ames D, Rowe CC, Masters CL (2013) Amyloid beta deposition, neurodegeneration, and cognitive decline in sporadic Alzheimer's disease: a prospective cohort study. Lancet Neurol 12:357-367.

Vinters HV (1987) Cerebral amyloid angiopathy. A critical review. Stroke 18:311-324.

Vinters HV, Gilbert JJ (1983) Cerebral amyloid angiopathy: incidence and complications in the aging brain. II. The distribution of amyloid vascular changes. Stroke 14:924-928.

Virta JR, Tolvanen T, Nagren K, Bruck A, Roivainen A, Rinne JO (2008) 1-11C-methyl-4-piperidinyl-N-butyrate radiation dosimetry in humans by dynamic organ-specific evaluation. J Nucl Med 49:347-353.

Virta JR, Laatu S, Parkkola R, Oikonen V, Rinne JO, Ruutiainen J (2011) Cerebral acetylcholinesterase activity is not decreased in MS patients with cognitive impairment. Mult Scler 17:931-938.

Vogel-Hopker A, Sperling LE, Layer PG (2012) Co-opting functions of cholinesterases in neural, limb and stem cell development. Protein Pept Lett 19:155-164.

von Rotz RC, Kohli BM, Bosset J, Meier M, Suzuki T, Nitsch RM, Konietzko U (2004) The APP intracellular domain forms nuclear multiprotein complexes and regulates the transcription of its own precursor. J Cell Sci 117:4435-4448.

Wagner S, Breyholz HJ, Faust A, Holtke C, Levkau B, Schober O, Schafers M, Kopka K (2006) Molecular imaging of matrix metalloproteinases in vivo using small molecule inhibitors for SPECT and PET. Curr Med Chem 13:2819-2838.

Wahl M, Hubers A, Lauterbach-Soon B, Hattingen E, Jung P, Cohen LG, Ziemann U (2011) Motor callosal disconnection in early relapsing-remitting multiple sclerosis. Hum Brain Mapp 32:846-855.

Walker LC, Koliatsos VE, Kitt CA, Richardson RT, Rokaeus A, Price DL (1989) Peptidergic neurons in the basal forebrain magnocellular complex of the rhesus monkey. J Comp Neurol 280:272-282.

Walsh DM, Lomakin A, Benedek GB, Condron MM, Teplow DB (1997) Amyloid beta-protein fibrillogenesis. Detection of a protofibrillar intermediate. J Biol Chem 272:22364-22372.

Walsh DM, Tseng BP, Rydel RE, Podlisny MB, Selkoe DJ (2000) The oligomerization of amyloid beta-protein begins intracellularly in cells derived from human brain. Biochemistry 39:10831-10839.

Walsh DM, Hartley DM, Kusumoto Y, Fezoui Y, Condron MM, Lomakin A, Benedek GB, Selkoe DJ, Teplow DB (1999) Amyloid beta-protein fibrillogenesis. Structure and biological activity of protofibrillar intermediates. J Biol Chem 274:25945-25952.

Walter J, Fluhrer R, Hartung B, Willem M, Kaether C, Capell A, Lammich S, Multhaup G, Haass C (2001) Phosphorylation regulates intracellular trafficking of beta-secretase. J Biol Chem 276:14634-14641.

Wang H, Liao H, Ochani M, Justiniani M, Lin X, Yang L, Al-Abed Y, Metz C, Miller EJ, Tracey KJ, Ulloa L (2004) Cholinergic agonists inhibit HMGB1 release and improve survival in experimental sepsis. Nat Med 10:1216-1221.

Wang H, Yu M, Ochani M, Amella CA, Tanovic M, Susarla S, Li JH, Yang H, Ulloa L, Al-Abed Y, Czura CJ, Tracey KJ (2003) Nicotinic acetylcholine receptor alpha7 subunit is an essential regulator of inflammation. Nature 421:384-388.

Wang HY, Lee DH, D'Andrea MR, Peterson PA, Shank RP, Reitz AB (2000) beta-Amyloid(1-42) binds to alpha7 nicotinic acetylcholine receptor with high affinity. Implications for Alzheimer's disease pathology. J Biol Chem 275:5626-5632.

Wang K, Liang M, Wang L, Tian L, Zhang X, Li K, Jiang T (2007) Altered functional connectivity in early Alzheimer's disease: a resting-state fMRI study. Hum Brain Mapp 28:967-978.

Wang M, Wang JQ, Gao M, Zheng QH (2008) Facile synthesis of new carbon-11 labeled conformationally restricted rivastigmine analogues as potential PET agents for imaging AChE and BChE enzymes. Appl Radiat Isot 66:506-512.

Wang Y, Wu C, Caprariello AV, Somoza E, Zhu W, Wang C, Miller RH (2009) In vivo quantification of myelin changes in the vertebrate nervous system. J Neurosci 29:14663-14669.

Waters JA, Hollingsworth EB, Daly JW, Lewandowski G, Creveling CR (1986) Anticonvulsant activity of piperidinol and (dialkylamino)alkanol esters. J Med Chem 29:1512-1516.

Wavefunction (2006) Spartan. In, 1.1.0 Edition. Irvine CA: Wavefunction Incorporated.

Weidemann A, Konig G, Bunke D, Fischer P, Salbaum JM, Masters CL, Beyreuther K (1989) Identification, biogenesis, and localization of precursors of Alzheimer's disease A4 amyloid protein. Cell 57:115-126.

Weingarten MD, Lockwood AH, Hwo SY, Kirschner MW (1975) A protein factor essential for microtubule assembly. Proc Natl Acad Sci U S A 72:1858-1862.

Weller RO, Massey A, Kuo YM, Roher AE (2000) Cerebral amyloid angiopathy: accumulation of A beta in interstitial fluid drainage pathways in Alzheimer's disease. Ann N Y Acad Sci 903:110-117.

Weller RO, Massey A, Newman TA, Hutchings M, Kuo YM, Roher AE (1998) Cerebral amyloid angiopathy: amyloid beta accumulates in putative interstitial fluid drainage pathways in Alzheimer's disease. Am J Pathol 153:725-733.

Wessler I, Kirkpatrick CJ, Racke K (1998) Non-neuronal acetylcholine, a locally acting molecule, widely distributed in biological systems: expression and function in humans. Pharmacol Ther 77:59-79.

Wessler I, Kirkpatrick CJ, Racke K (1999) The cholinergic 'pitfall': acetylcholine, a universal cell molecule in biological systems, including humans. Clin Exp Pharmacol Physiol 26:198-205.

Wessler I, Roth E, Deutsch C, Brockerhoff P, Bittinger F, Kirkpatrick CJ, Kilbinger H (2001) Release of non-neuronal acetylcholine from the isolated human placenta is mediated by organic cation transporters. Br J Pharmacol 134:951-956.

Wessler I, Reinheimer T, Kilbinger H, Bittinger F, Kirkpatrick CJ, Saloga J, Knop J (2003) Increased acetylcholine levels in skin biopsies of patients with atopic dermatitis. Life Sci 72:2169-2172.

Wessler IK, Kirkpatrick CJ (2001) The Non-neuronal cholinergic system: an emerging drug target in the airways. Pulm Pharmacol Ther 14:423-434.

West HL, Rebeck GW, Hyman BT (1994) Frequency of the apolipoprotein E epsilon 2 allele is diminished in sporadic Alzheimer disease. Neurosci Lett 175:46-48.

Wevers A (2011) Localisation of pre- and postsynaptic cholinergic markers in the human brain. Behav Brain Res 221:341-355.

Wevers A, Monteggia L, Nowacki S, Bloch W, Schutz U, Lindstrom J, Pereira EF, Eisenberg H, Giacobini E, de Vos RA, Steur EN, Maelicke A, Albuquerque EX, Schroder H (1999) Expression of nicotinic acetylcholine receptor subunits in the cerebral cortex in Alzheimer's disease: histotopographical correlation with amyloid plaques and hyperphosphorylated-tau protein. Eur J Neurosci 11:2551-2565.

Whitehouse PJ, Price DL, Struble RG, Clark AW, Coyle JT, Delon MR (1982) Alzheimer's disease and senile dementia: loss of neurons in the basal forebrain. Science 215:1237-1239.

Whittaker V (1963) Identification of acetylcholine and related esters of biological origin. In: Handbuch Der Experimentellen Pharmakologie (Eichler O, Farah A, Koelle G, eds). Berlin: Springer-Verlag.

Williams A, Piaton G, Aigrot MS, Belhadi A, Theaudin M, Petermann F, Thomas JL, Zalc B, Lubetzki C (2007) Semaphorin 3A and 3F: key players in myelin repair in multiple sclerosis? Brain 130:2554-2565.

Winkler DT, Bondolfi L, Herzig MC, Jann L, Calhoun ME, Wiederhold KH, Tolnay M, Staufenbiel M, Jucker M (2001) Spontaneous hemorrhagic stroke in a mouse model of cerebral amyloid angiopathy. J Neurosci 21:1619-1627.

Wischik CM, Novak M, Thogersen HC, Edwards PC, Runswick MJ, Jakes R, Walker JE, Milstein C, Roth M, Klug A (1988) Isolation of a fragment of tau derived from the core of the paired helical filament of Alzheimer disease. Proc Natl Acad Sci U S A 85:4506-4510.

Wogulis M, Wright S, Cunningham D, Chilcote T, Powell K, Rydel RE (2005) Nucleation-dependent polymerization is an essential component of amyloid-mediated neuronal cell death. J Neurosci 25:1071-1080.

Wolk DA, Zhang Z, Boudhar S, Clark CM, Pontecorvo MJ, Arnold SE (2012a) Amyloid imaging in Alzheimer's disease: comparison of florbetapir and Pittsburgh compound-B positron emission tomography. J Neurol Neurosurg Psychiatry 83:923-926.

Wolk DA, Price JC, Madeira C, Saxton JA, Snitz BE, Lopez OL, Mathis CA, Klunk WE, DeKosky ST (2012b) Amyloid imaging in dementias with atypical presentation. Alzheimers Dement 8:389-398.

Woods RP, Grafton ST, Holmes CJ, Cherry SR, Mazziotta JC (1998) Automated image registration: I. General methods and intrasubject, intramodality validation. J Comput Assist Tomogr 22:139-152.

Woolf NJ, Eckenstein F, Butcher LL (1983) Cholinergic projections from the basal forebrain to the frontal cortex: a combined fluorescent tracer and immunohistochemical analysis in the rat. Neurosci Lett 40:93-98.

World Health Organization and Alzheimer’s Disease International (2012) Dementia: a public health priority.

Wright CI, Guela C, Mesulam MM (1993a) Protease inhibitors and indoleamines selectively inhibit cholinesterases in the histopathologic structures of Alzheimer disease. Proc Natl Acad Sci U S A 90:683-686.

Wright CI, Geula C, Mesulam MM (1993b) Neurological cholinesterases in the normal brain and in Alzheimer's disease: relationship to plaques, tangles, and patterns of selective vulnerability. Ann Neurol 34:373-384.

Xie W, Stribley JA, Chatonnet A, Wilder PJ, Rizzino A, McComb RD, Taylor P, Hinrichs SH, Lockridge O (2000) Postnatal developmental delay and supersensitivity to organophosphate in gene-targeted mice lacking acetylcholinesterase. J Pharmacol Exp Ther 293:896-902.

Xu PT, Schmechel D, Qiu HL, Herbstreith M, Rothrock-Christian T, Eyster M, Roses AD, Gilbert JR (1999) Sialylated human apolipoprotein E (apoEs) is preferentially associated with neuron-enriched cultures from APOE transgenic mice. Neurobiol Dis 6:63-75.

Xu PT, Schmechel D, Rothrock-Christian T, Burkhart DS, Qiu HL, Popko B, Sullivan P, Maeda N, Saunders AM, Roses AD, Gilbert JR (1996) Human apolipoprotein E2, E3, and E4 isoform-specific transgenic mice: human-like pattern of glial and neuronal immunoreactivity in central nervous system not observed in wild-type mice. Neurobiol Dis 3:229-245.

Yan R, Bienkowski MJ, Shuck ME, Miao H, Tory MC, Pauley AM, Brashier JR, Stratman NC, Mathews WR, Buhl AE, Carter DB, Tomasselli AG, Parodi LA, Heinrikson RL, Gurney ME (1999) Membrane-anchored aspartyl protease with Alzheimer's disease beta-secretase activity. Nature 402:533-537.

Yang F, Lum JB, McGill JR, Moore CM, Naylor SL, van Bragt PH, Baldwin WD, Bowman BH (1984) Human transferrin: cDNA characterization and chromosomal localization. Proc Natl Acad Sci U S A 81:2752-2756.

Yang L, Rieves D, Ganley C (2012) Brain amyloid imaging--FDA approval of florbetapir F18 injection. N Engl J Med 367:885-887.

Yankner BA, Dawes LR, Fisher S, Villa-Komaroff L, Oster-Granite ML, Neve RL (1989) Neurotoxicity of a fragment of the amyloid precursor associated with Alzheimer's disease. Science 245:417-420.

Zaborszky L, Cullinan WE, Braun A (1991) Afferents to basal forebrain cholinergic projection neurons: an update. In: The Basal Forebrain (Napier TC, Kalivas PW, Hanin I, eds). New York: Plenum.

Zajicek JP, Wing M, Scolding NJ, Compston DA (1992) Interactions between oligodendrocytes and microglia. A major role for complement and tumour necrosis factor in oligodendrocyte adherence and killing. Brain 115 (Pt 6):1611-1631.

Zeis T, Graumann U, Reynolds R, Schaeren-Wiemers N (2008) Normal-appearing white matter in multiple sclerosis is in a subtle balance between inflammation and neuroprotection. Brain 131:288-303.

Zhang MR, Tsuchiyama A, Haradahira T, Furutsuka K, Yoshida Y, Kida T, Noguchi J, Irie T, Suzuki K (2002) Synthesis and preliminary evaluation of [18F]FEtP4A, a promising PET tracer for mapping acetylcholinesterase in vivo. Nucl Med Biol 29:463-468.

Zhang W, Kung MP, Oya S, Hou C, Kung HF (2007a) 18F-labeled styrylpyridines as PET agents for amyloid plaque imaging. Nucl Med Biol 34:89-97.

Zhang W, Oya S, Kung MP, Hou C, Maier DL, Kung HF (2005) F-18 Polyethyleneglycol stilbenes as PET imaging agents targeting Abeta aggregates in the brain. Nucl Med Biol 32:799-809.

Zhang YW, Wang R, Liu Q, Zhang H, Liao FF, Xu H (2007b) Presenilin/gamma-secretase-dependent processing of beta-amyloid precursor protein regulates EGF receptor expression. Proc Natl Acad Sci U S A 104:10613-10618.

Zhuang ZP, Kung MP, Wilson A, Lee CW, Plossl K, Hou C, Holtzman DM, Kung HF (2003) Structure-activity relationship of imidazo[1,2-a]pyridines as ligands for detecting beta-amyloid plaques in the brain. J Med Chem 46:237-243.

APPENDIX A COPYRIGHT PERMISSION LETTERS

SPRINGER LICENSE
TERMS AND CONDITIONS

Apr 16, 2013

This is a License Agreement between Ian R Macdonald ("You") and Springer ("Springer") provided by Copyright Clearance Center ("CCC"). The license consists of your order details, the terms and conditions provided by Springer, and the payment terms and conditions.

All payments must be made in full to CCC. For payment instructions, please see information listed at the bottom of this form.

License Number	3131070417541
License date	Apr 16, 2013
Licensed content publisher	Springer
Licensed content publication	Molecular Imaging and Biology
Licensed content title	Synthesis and Preliminary Evaluation of Piperidinyl and Pyrrolidinyl Iodobenzoates as Imaging Agents for Butyrylcholinesterase
Licensed content author	Ian R. Macdonald
Licensed content date	Jan 1, 2010
Volume number	13
Issue number	6
Type of Use	Thesis/Dissertation
Portion	Full text
Number of copies	5
Author of this Springer article	Yes and you are the sole author of the new work
Order reference number	
Title of your thesis / dissertation	DEVELOPMENT OF BUTYRYLCHOLINESTERASE LIGANDS FOR THE IMAGING OF NEUROLOGICAL DISORDERS
Expected completion date	Jun 2013
Estimated size(pages)	500
Total	0.00 CAD
Terms and Conditions	

Introduction

The publisher for this copyrighted material is Springer Science + Business Media. By clicking "accept" in connection with completing this licensing transaction, you agree that the following terms and conditions apply to this transaction (along with the Billing and Payment terms and conditions established by Copyright Clearance Center, Inc. ("CCC"), at the time that you opened your Rightslink account and that are available at any time at http://myaccount.copyright.com).

Limited License

With reference to your request to reprint in your thesis material on which Springer Science and Business Media control the copyright, permission is granted, free of charge, for the use indicated in your enquiry.

Licenses are for one-time use only with a maximum distribution equal to the number that you identified in the licensing process.

This License includes use in an electronic form, provided its password protected or on the university's intranet or repository, including UMI (according to the definition at the Sherpa website: http://www.sherpa.ac.uk/romeo/). For any other electronic use, please contact Springer at (permissions.dordrecht@springer.com or permissions.heidelberg@springer.com).

The material can only be used for the purpose of defending your thesis, and with a maximum of 100 extra copies in paper.

Although Springer holds copyright to the material and is entitled to negotiate on rights, this license is only valid, subject to a courtesy information to the author (address is given with the article/chapter) and provided it concerns original material which does not carry references to other sources (if material in question appears with credit to another source, authorization from that source is required as well).

Permission free of charge on this occasion does not prejudice any rights we might have to charge for reproduction of our copyrighted material in the future.

Altering/Modifying Material: Not Permitted

You may not alter or modify the material in any manner. Abbreviations, additions, deletions and/or any other alterations shall be made only with prior written authorization of the author(s) and/or Springer Science + Business Media. (Please contact Springer at (permissions.dordrecht@springer.com or permissions.heidelberg@springer.com)

Reservation of Rights

Springer Science + Business Media reserves all rights not specifically granted in the combination of (i) the license details provided by you and accepted in the course of this licensing transaction, (ii) these terms and conditions and (iii) CCC's Billing and Payment terms and conditions.

Copyright Notice:Disclaimer

You must include the following copyright and permission notice in connection with any reproduction of the licensed material: "Springer and the original publisher /journal title, volume, year of publication, page, chapter/article title, name(s) of author(s), figure number(s), original copyright notice) is given to the publication in which the material was originally published, by adding; with kind permission from Springer Science and Business Media"

Warranties: None

Example 1: Springer Science + Business Media makes no representations or warranties with respect to the licensed material.

Example 2: Springer Science + Business Media makes no representations or warranties with respect to the licensed material and adopts on its own behalf the limitations and disclaimers established by CCC on its behalf in its Billing and Payment terms and conditions for this licensing transaction.

Indemnity
You hereby indemnify and agree to hold harmless Springer Science + Business Media and CCC, and their respective officers, directors, employees and agents, from and against any and all claims arising out of your use of the licensed material other than as specifically authorized pursuant to this license.

No Transfer of License
This license is personal to you and may not be sublicensed, assigned, or transferred by you to any other person without Springer Science + Business Media's written permission.

No Amendment Except in Writing
This license may not be amended except in a writing signed by both parties (or, in the case of Springer Science + Business Media, by CCC on Springer Science + Business Media's behalf).

Objection to Contrary Terms
Springer Science + Business Media hereby objects to any terms contained in any purchase order, acknowledgment, check endorsement or other writing prepared by you, which terms are inconsistent with these terms and conditions or CCC's Billing and Payment terms and conditions. These terms and conditions, together with CCC's Billing and Payment terms and conditions (which are incorporated herein), comprise the entire agreement between you and Springer Science + Business Media (and CCC) concerning this licensing transaction. In the event of any conflict between your obligations established by these terms and conditions and those established by CCC's Billing and Payment terms and conditions, these terms and conditions shall control.

Jurisdiction
All disputes that may arise in connection with this present License, or the breach thereof, shall be settled exclusively by arbitration, to be held in The Netherlands, in accordance with Dutch law, and to be conducted under the Rules of the 'Netherlands Arbitrage Instituut' (Netherlands Institute of Arbitration).***OR:***

All disputes that may arise in connection with this present License, or the breach thereof, shall be settled exclusively by arbitration, to be held in the Federal Republic of Germany, in accordance with German law.

Other terms and conditions:

v1.3

If you would like to pay for this license now, please remit this license along with your payment made payable to "COPYRIGHT CLEARANCE CENTER" otherwise you will be invoiced within 48 hours of the license date. Payment should be in the form of a check or money order referencing your account number and this invoice number RLNK501001393. Once you receive your invoice for this order, you may pay your invoice by credit card.

Please follow instructions provided at that time.

Make Payment To:
Copyright Clearance Center
Dept 001
P.O. Box 843006
Boston, MA 02284-3006

For suggestions or comments regarding this order, contact RightsLink Customer Support: customercare@copyright.com or +1-877-622-5543 (toll free in the US) or +1-978-646-2777.

Gratis licenses (referencing $0 in the Total field) are free. Please retain this printable license for your reference. No payment is required.

Title:	Thioesters for the in vitro evaluation of agents to image brain cholinesterases
Author:	Ian R. Macdonald, Courtney T. Jollymore, G. Andrew Reid et al.
Publication:	Journal of Enzyme Inhibition and Medicinal Chemistry
Publisher:	Informa Healthcare
Date:	Jun 1, 2013

Order Completed

Thank you very much for your order.

This is a License Agreement between Ian R Macdonald ("You") and Informa Healthcare ("Informa Healthcare") The license consists of your order details, the terms and conditions provided by Informa Healthcare, and the payment terms and conditions.

License number	Reference confirmation email for license number
License date	Apr 16, 2013
Licensed content publisher	Informa Healthcare
Licensed content publication	Journal of Enzyme Inhibition and Medicinal Chemistry
Licensed content title	Thioesters for the in vitro evaluation of agents to image brain cholinesterases
Licensed content author	Ian R. Macdonald, Courtney T. Jollymore, G. Andrew Reid et al.
Licensed content date	Jun 1, 2013
Type of Use	Dissertation/Thesis
Volume number	28
Issue number	3
Start page	447
End page	455
Requestor type	Author
Format	print and electronic
Portion	Full article
Will you be translating?	no
Number of copies	50
Order reference number	
Title of your thesis / dissertation	DEVELOPMENT OF BUTYRYLCHOLINESTERASE LIGANDS FOR THE IMAGING OF NEUROLOGICAL DISORDERS
Expected completion date	Jun 2013
Estimated Size (pages)	500
Billing Type	Invoice
Billing address	Rm 12D, 5850 College Street Halifax, NS B3H4R2

	Canada
Total	0.00 USD

CLOSE WINDOW

APPENDIX B SYNTHETIC CHEMICAL CHARACTERIZATION DATA

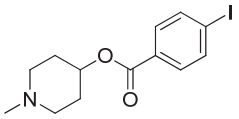

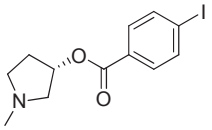

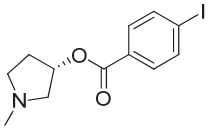

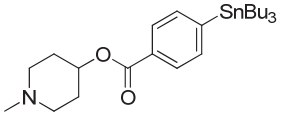

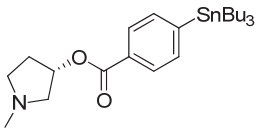

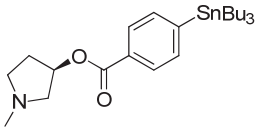

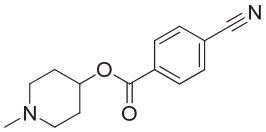

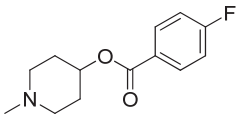

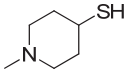

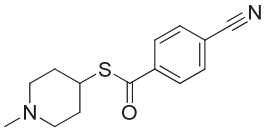

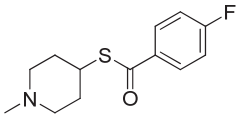

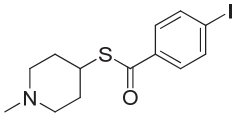

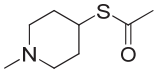

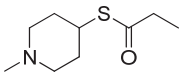

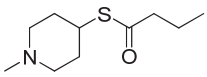

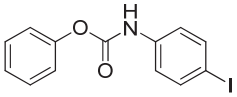

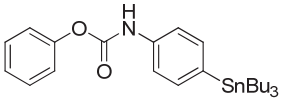

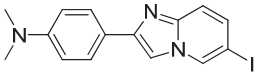

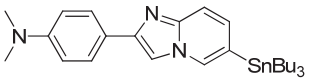

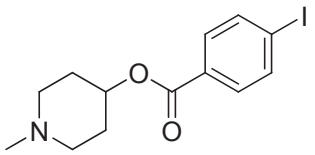

1-methylpiperidin-4-yl 4-iodobenzoate (**1**)

^{1}H NMR

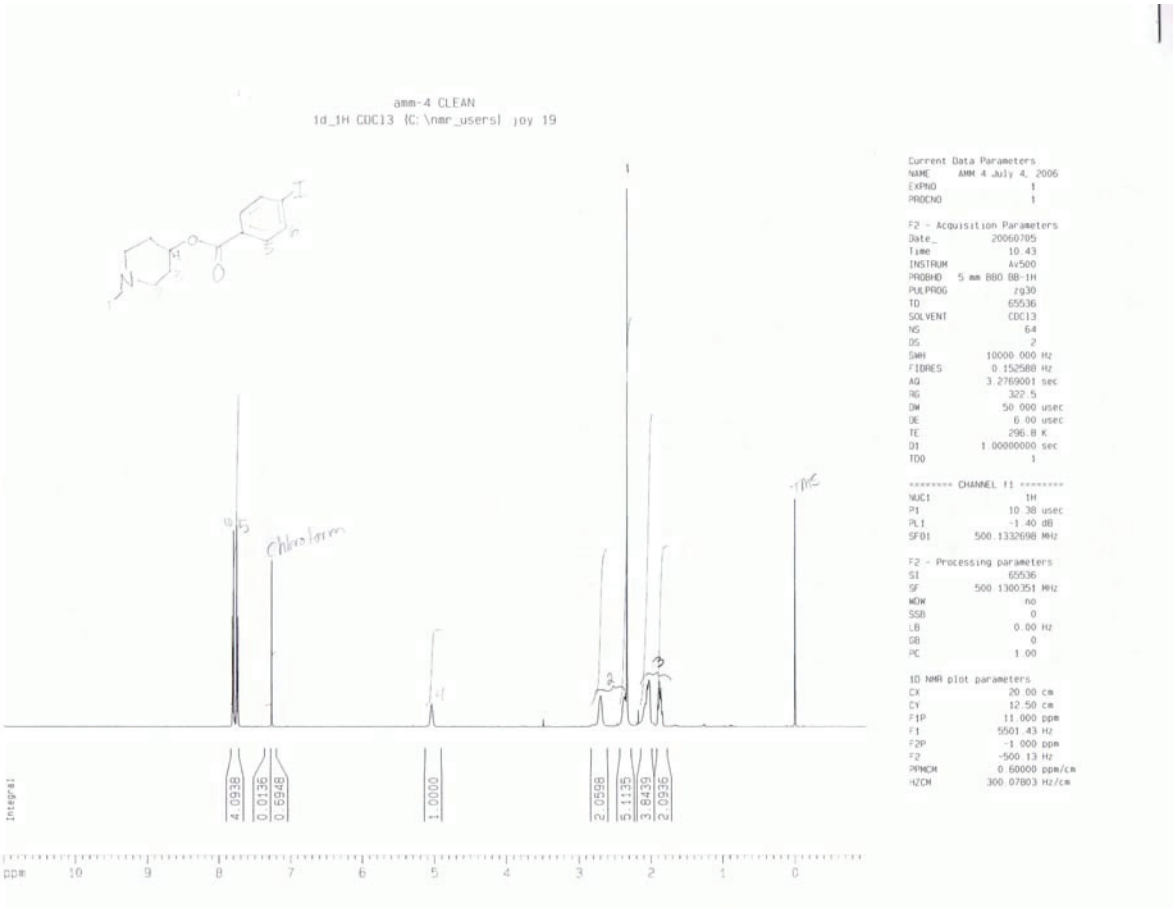

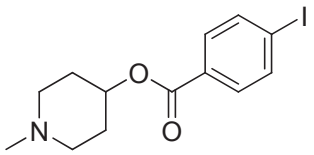

1-methylpiperidin-4-yl 4-iodobenzoate (**1**)

^{13}C NMR

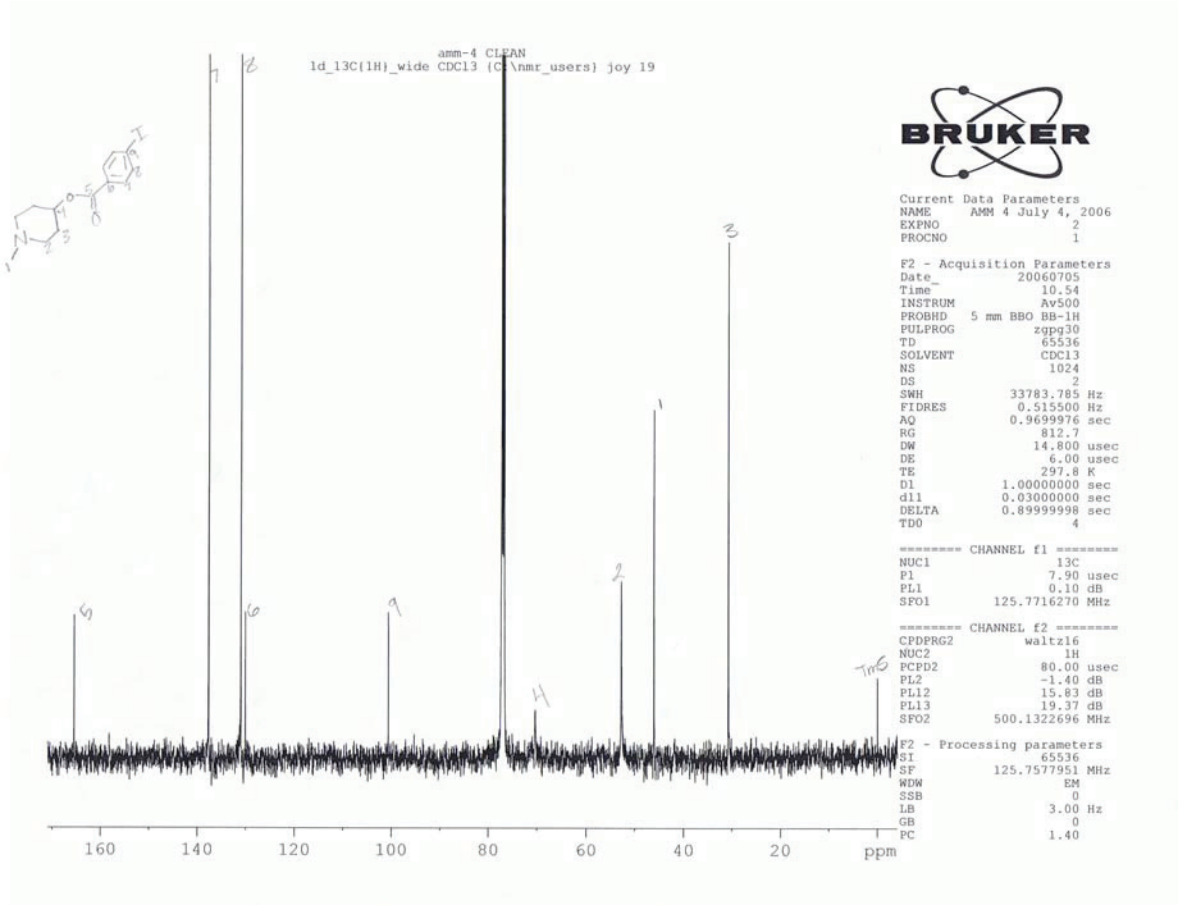

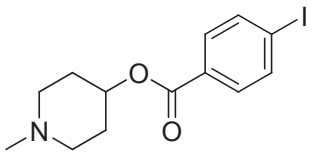

1-methylpiperidin-4-yl 4-iodobenzoate (**1**)

IR

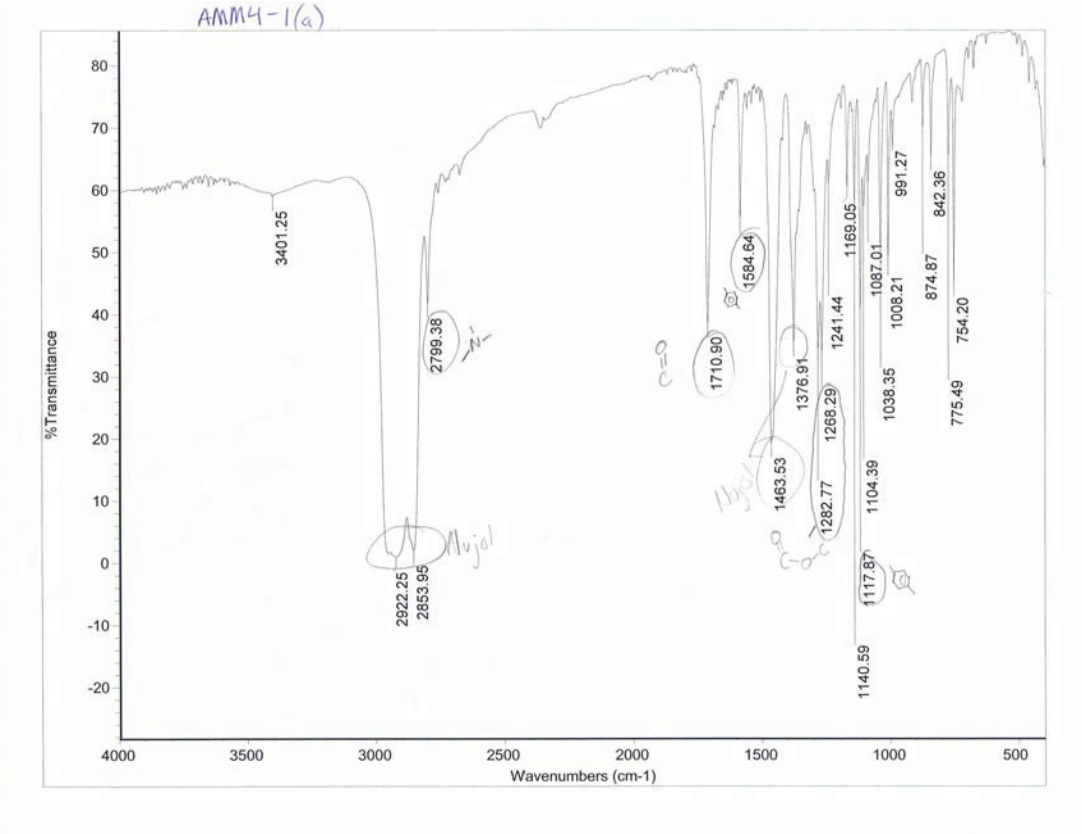

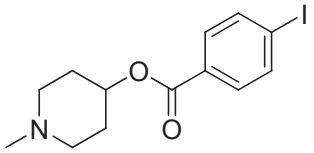

1-methylpiperidin-4-yl 4-iodobenzoate (**1**)

LRMS

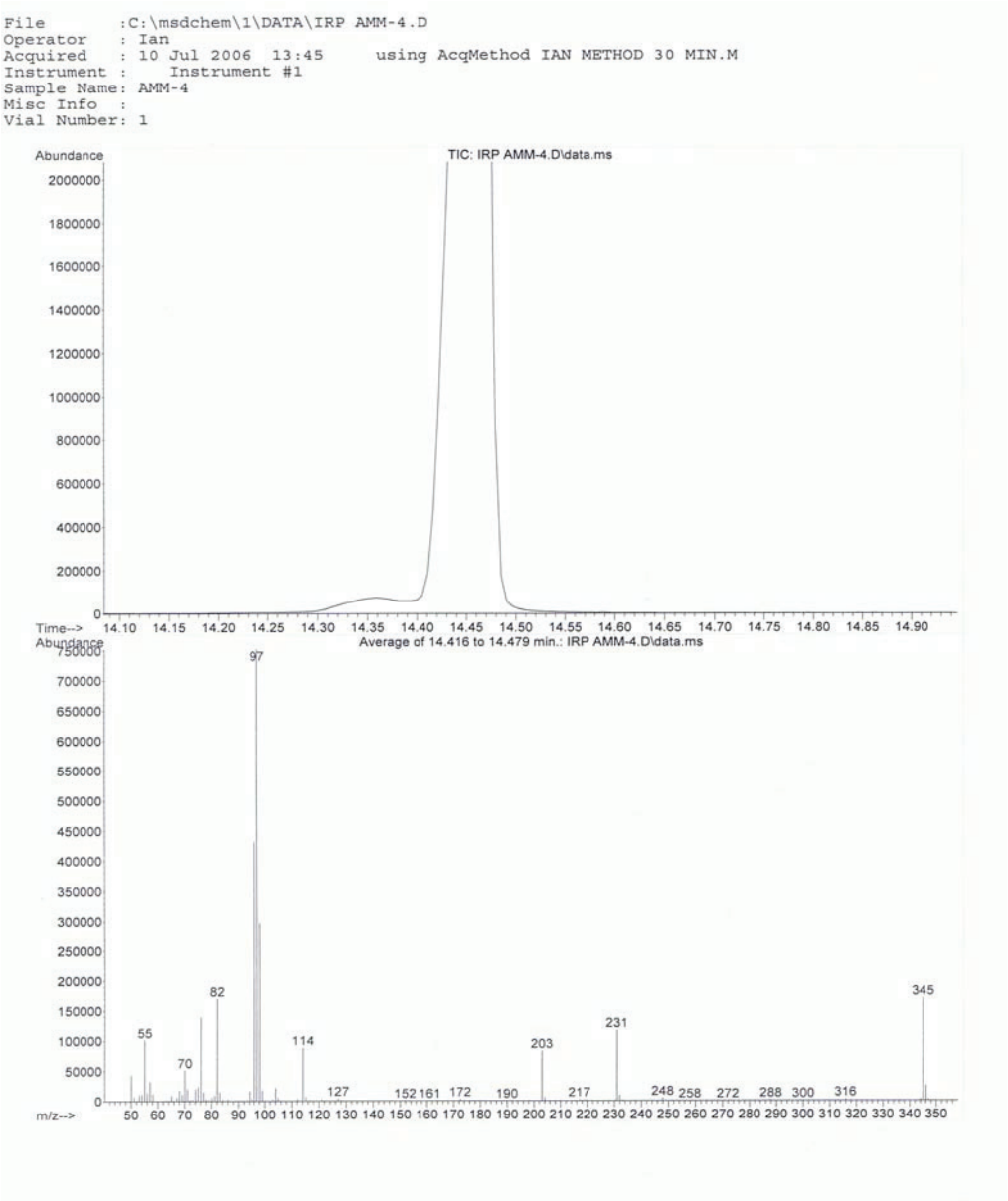

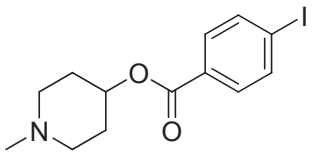

1-methylpiperidin-4-yl 4-iodobenzoate (**1**)

HRMS

DALHOUSIE CHEMISTRY DEPARTMENT MASS SPECTRAL DATA

ACCURATE MASS MEASUREMENT - CEC 21-110B

Name: ERIC

Date: 2006.7.26

Sample identifier: AMM4

Probe temperature: ~~-384.5~~ 92°C °C

Source temperature: 170°C

Ionization voltage: 70.0 eV

Sample ion formula proposed by the user: C13H16INO2

Actual mass of this sample ion: 345.0226 amu.

Formula of the ion chosen as reference: C8F13

Reference mass: 342.9792 amu.

The resolution setting of the 21-110B for accurate mass determination is usually between 5000 and 10,000.
The standard deviation of mass measurement is +/-0.0008 amu, which is an average of 3.6 ppm over the mass range 100 to 300 amu.

The measured sample ion mass is 345.0233 +/-0.0008 amu.

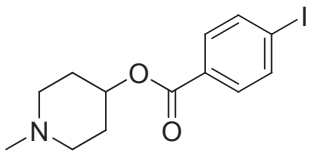

1-methylpiperidin-4-yl 4-iodobenzoate (**1**)

HPLC

```
Data File C:\CHEM32\1\DATA\I MACDONALD\IRM07072010E 2010-07-07 16-18-43\022-0201.D
Sample Name: AMM-4

=====================================================================
Acq. Operator   : Ian                          Seq. Line :   2
Acq. Instrument : Instrument 1                  Location : Vial 22
Injection Date  : 7/7/2010 4:35:26 PM                Inj :   1
                                              Inj Volume : 100 µl
Acq. Method     : C:\Chem32\1\DATA\I MACDONALD\IRM07072010E 2010-07-07 16-18-43\
                  MACDONLAD NORMAL PHASE 20UL.M
Last changed    : 7/7/2010 4:18:41 PM by Ian
Analysis Method : C:\CHEM32\1\DATA\I MACDONALD\IRM07072010E 2010-07-07 16-18-43\022-
                  0201.D\DA.M (MACDONLAD NORMAL PHASE 20UL.M)
Last changed    : 7/28/2010 9:41:20 AM by Ian
                  (modified after loading)
Method Info     : Reverse Phase Methanol
```

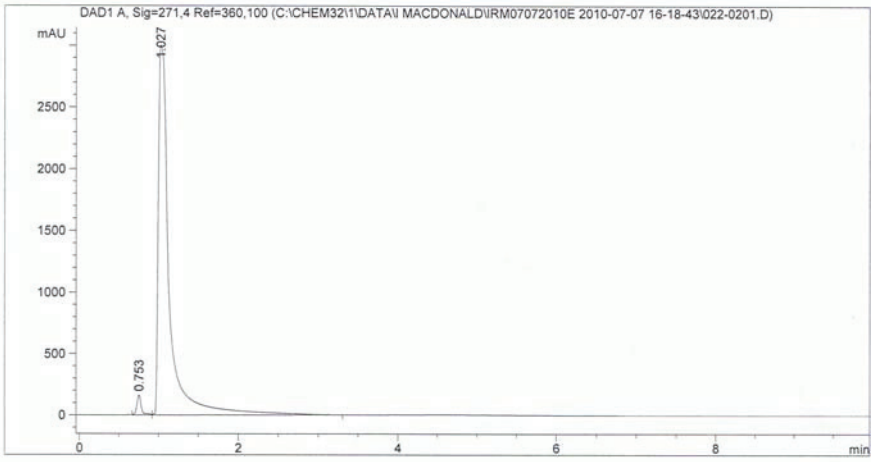


```
=====================================================================
                        Area Percent Report
=====================================================================

Sorted By             :      Signal
Multiplier            :      1.0000
Dilution              :      1.0000
Use Multiplier & Dilution Factor with ISTDs


Signal 1: DAD1 A, Sig=271,4 Ref=360,100

Peak RetTime Type  Width     Area      Height     Area
  #   [min]       [min]   [mAU*s]     [mAU]       %
----|-------|----|-------|----------|----------|--------|
   1   0.753 VV    0.0566  625.11566  163.37341   2.0891
   2   1.027 VB    0.1437 2.92977e4  3005.00415  97.9109

Totals :                  2.99228e4  3168.37756

Instrument 1 7/28/2010 9:41:30 AM Ian                          Page   1 of 2
```

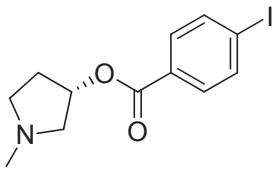

(S)-1-methylpyrrolidin-3-yl 4-iodobenzoate (**2**)

^{1}H NMR

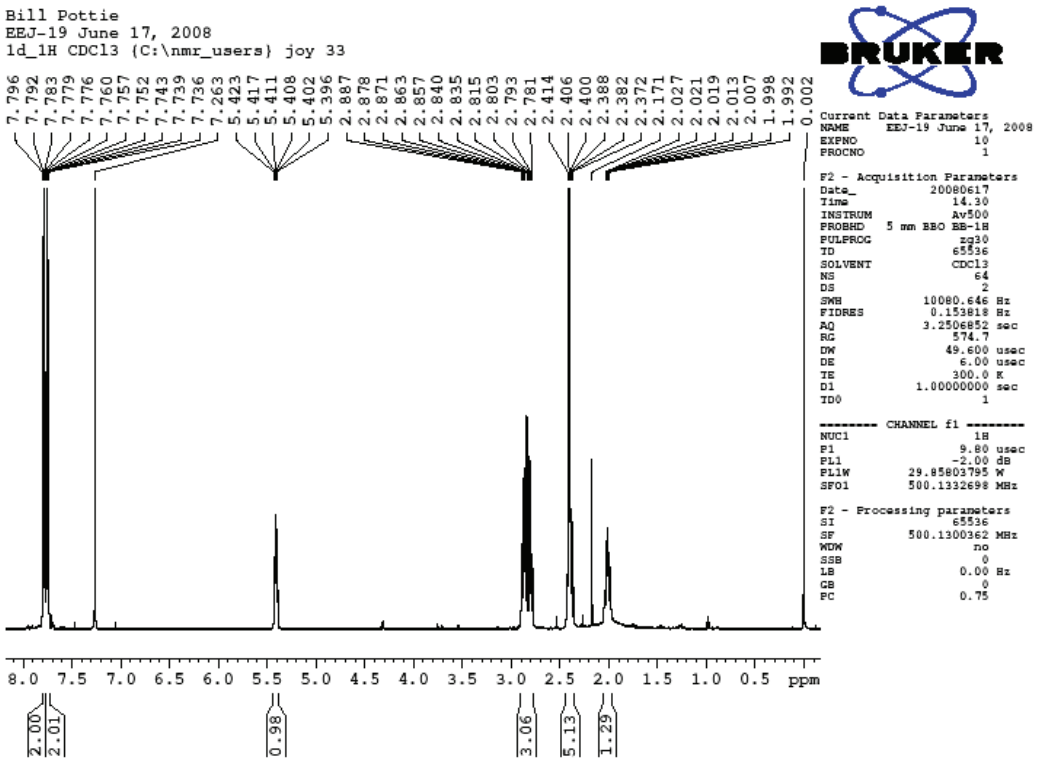

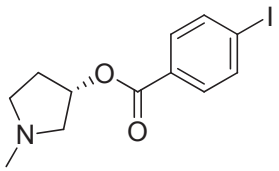

(S)-1-methylpyrrolidin-3-yl 4-iodobenzoate (**2**)
^{13}C NMR

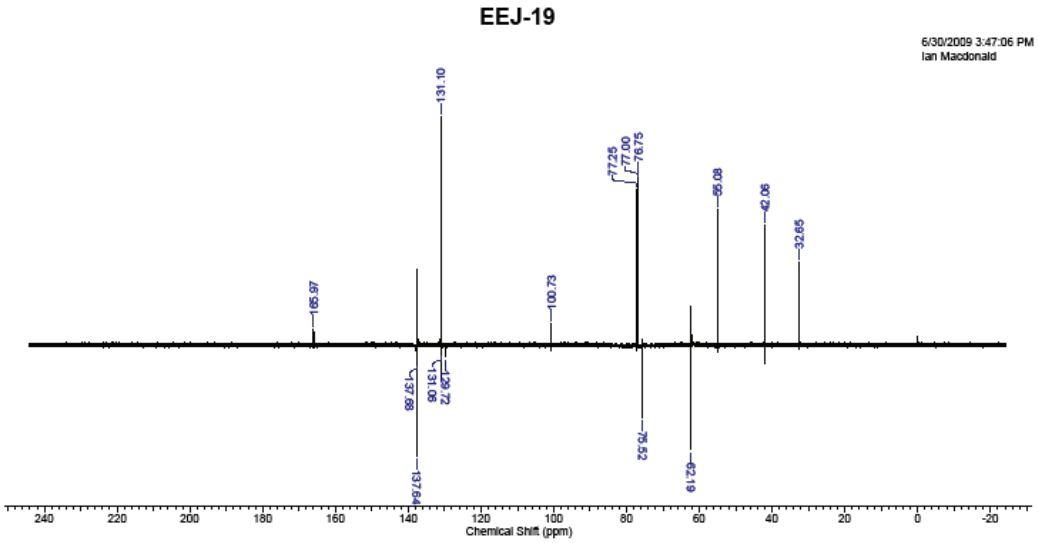

No.	(ppm)	(Hz)	Height
1	32.65	4105.6	0.3625
2	42.06	5289.2	0.5223
3	55.08	6926.5	0.5900
4	62.19	7821.4	-0.4591
5	75.52	9497.6	-0.3204
6	76.75	9651.4	0.7433
7	77.00	9683.3	0.7234
8	77.25	9715.3	0.6823
9	100.73	12667.1	0.0951
10	129.72	16312.7	-0.0525
11	131.06	16481.8	-0.0399
12	131.10	16486.9	1.0000
13	131.13	16490.0	0.0624

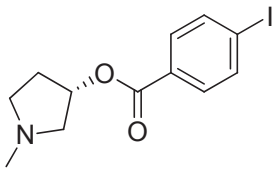

(S)-1-methylpyrrolidin-3-yl 4-iodobenzoate (**2**)
IR

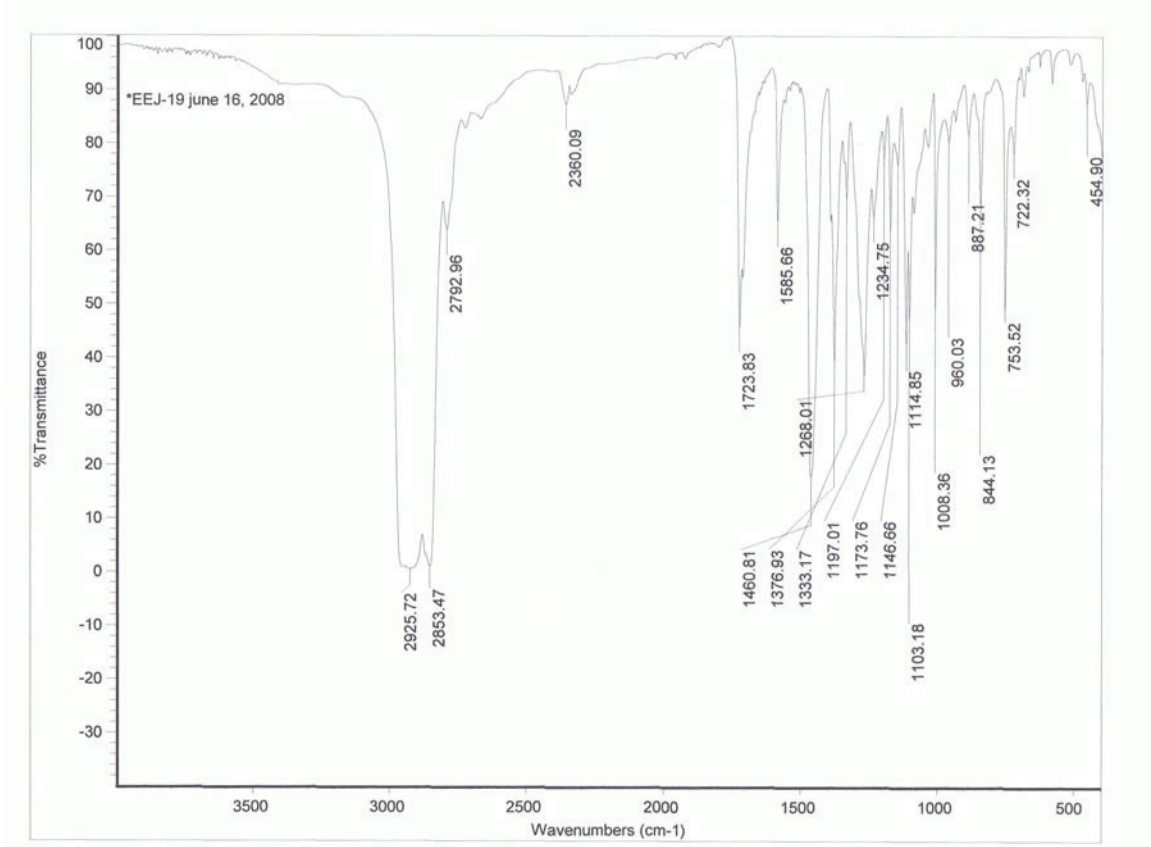

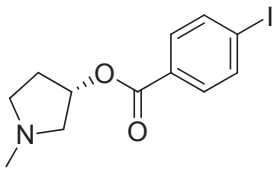

(S)-1-methylpyrrolidin-3-yl 4-iodobenzoate (**2**)
LRMS

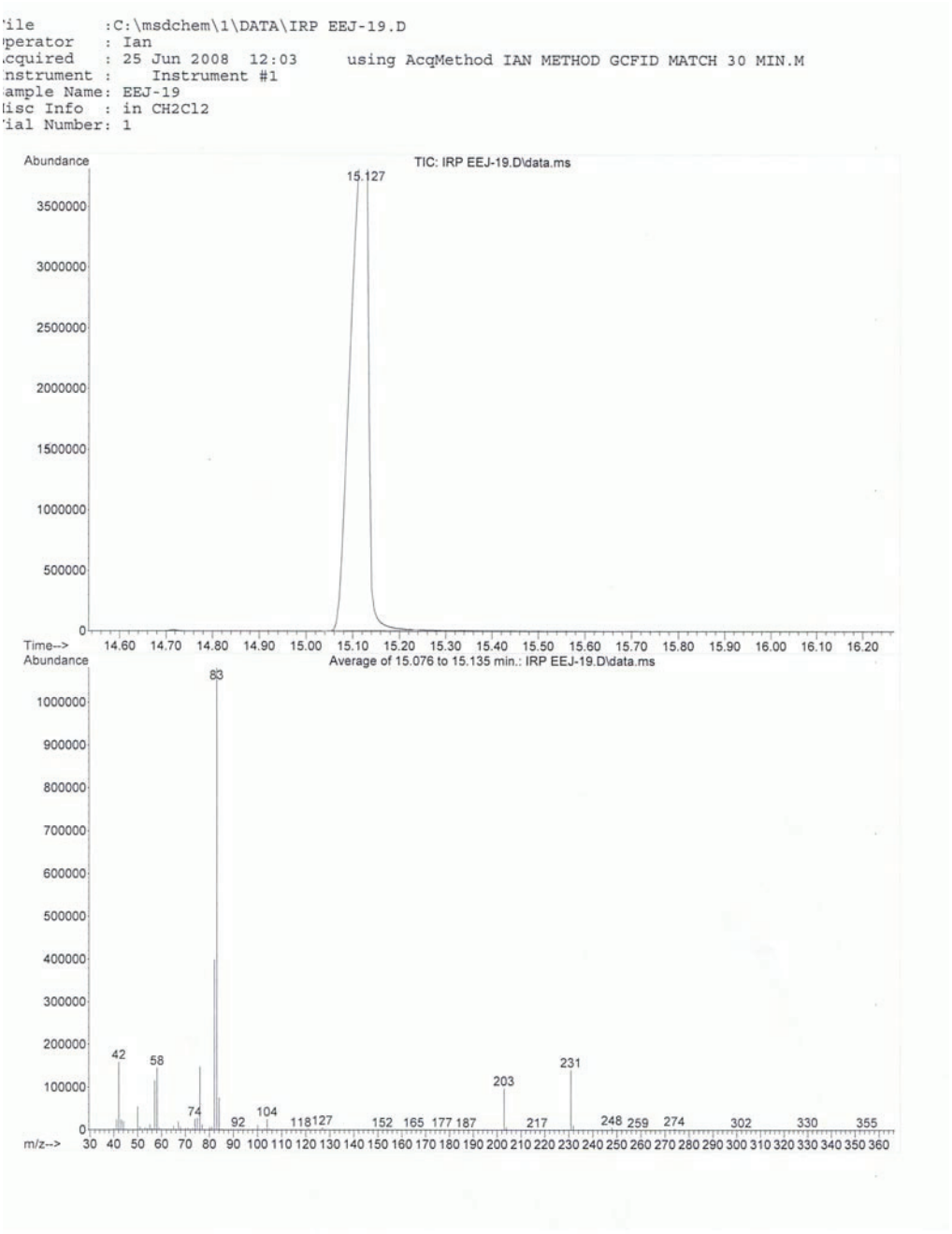

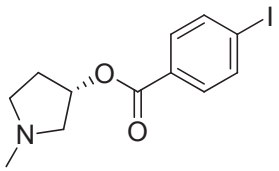

(S)-1-methylpyrrolidin-3-yl 4-iodobenzoate (**2**)
HRMS

Mass Spectrum Molecular Formula Report

Analysis Info

Analysis Name	D:\Data\Xiao\Aug 14 09000008.d	Acquisition Date	8/14/2009 11:48:37 AM
Method	xiaofengpos.m	Operator	Administrator
Sample Name	EEJ-19	Instrument	micrOTOF 57
Comment			

Acquisition Parameter

Source Type	ESI	Ion Polarity	Positive	Set Corrector Fill	52 V
Scan Range	n/a	Capillary Exit	150.0 V	Set Pulsar Pull	398 V
Scan Begin	50 m/z	Hexapole RF	130.0 V	Set Pulsar Push	398 V
Scan End	1500 m/z	Skimmer 1	55.0 V	Set Reflector	1300 V
		Hexapole 1	26.0 V	Set Flight Tube	9000 V
				Set Detector TOF	1960 V

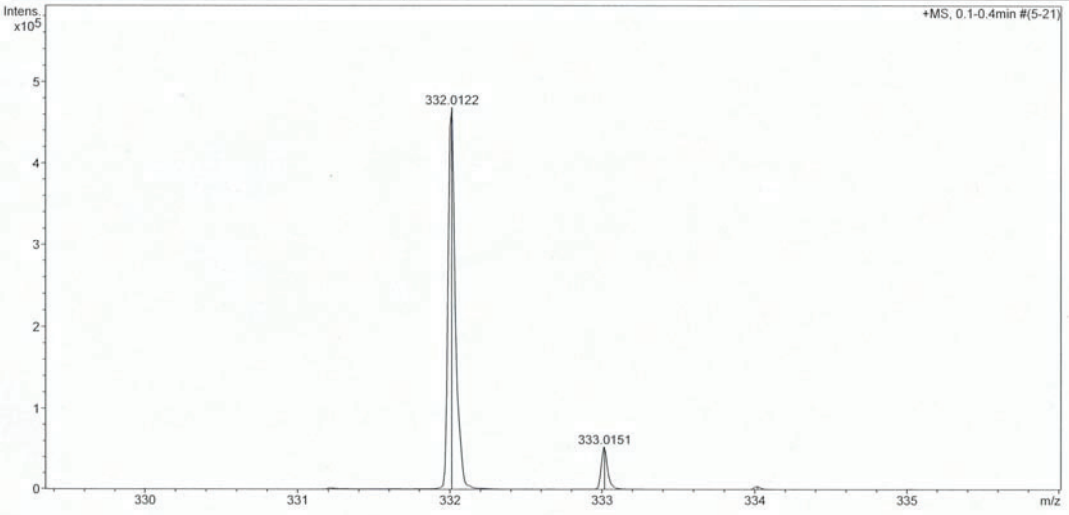

Bruker Daltonics DataAnalysis 3.3 printed: 8/14/2009 11:53:22 AM Page 1 of 2

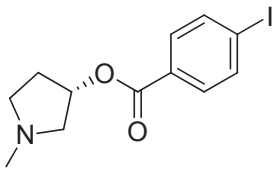

(S)-1-methylpyrrolidin-3-yl 4-iodobenzoate (**2**)
HPLC

```
Data File C:\CHEM32\1\DATA\I MACDONALD\IRM07072010E 2010-07-07 16-18-43\023-0301.D
Sample Name: EEJ-19

    ======================================================================
    Acq. Operator   : Ian                          Seq. Line :   3
    Acq. Instrument : Instrument 1                  Location : Vial 23
    Injection Date  : 7/7/2010 4:49:07 PM              Inj :   1
                                                   Inj Volume : 100 µl
    Acq. Method     : C:\Chem32\1\DATA\I MACDONALD\IRM07072010E 2010-07-07 16-18-43\
                      MACDONLAD NORMAL PHASE 20UL.M
    Last changed    : 7/7/2010 4:18:41 PM by Ian
    Analysis Method : C:\CHEM32\1\DATA\I MACDONALD\IRM07072010E 2010-07-07 16-18-43\023-
                      0301.D\DA.M (MACDONLAD NORMAL PHASE 20UL.M)
    Last changed    : 7/28/2010 9:43:24 AM by Ian
                      (modified after loading)
    Method Info     : Reverse Phase Methanol
```

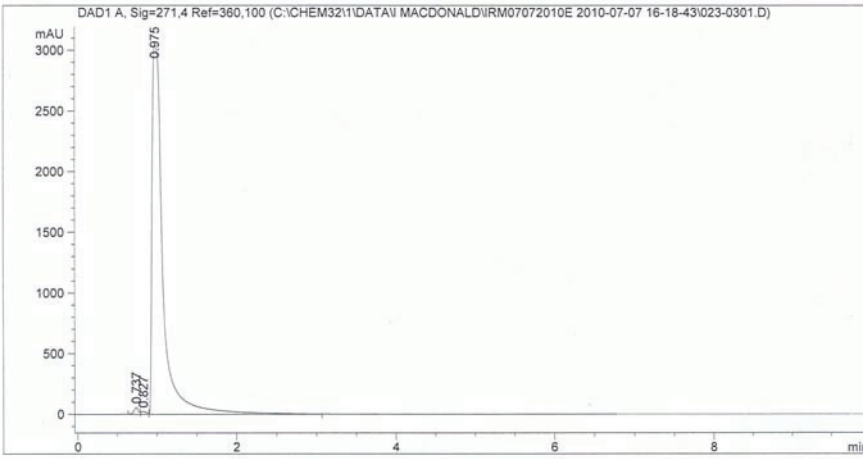


```
    ======================================================================
                              Area Percent Report
    ======================================================================

    Sorted By             :      Signal
    Multiplier            :      1.0000
    Dilution              :      1.0000
    Use Multiplier & Dilution Factor with ISTDs


    Signal 1: DAD1 A, Sig=271,4 Ref=360,100

    Peak RetTime Type  Width     Area      Height     Area
      #   [min]       [min]   [mAU*s]     [mAU]       %
    ----|-------|----|-------|----------|----------|--------|
       1   0.737 VV    0.0579  229.82965   58.38594   0.7766
       2   0.827 VV    0.0718  118.63393   24.79618   0.4009
       3   0.975 VB    0.1461 2.92459e4  3043.49756  98.8225

    Totals :                   2.95944e4  3126.67968

Instrument 1 7/28/2010 9:43:27 AM Ian                              Page   1 of 2
```

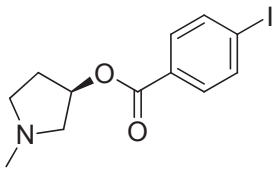

(R)-1-methylpyrrolidin-3-yl 4-iodobenzoate (**3**)
^{1}H NMR

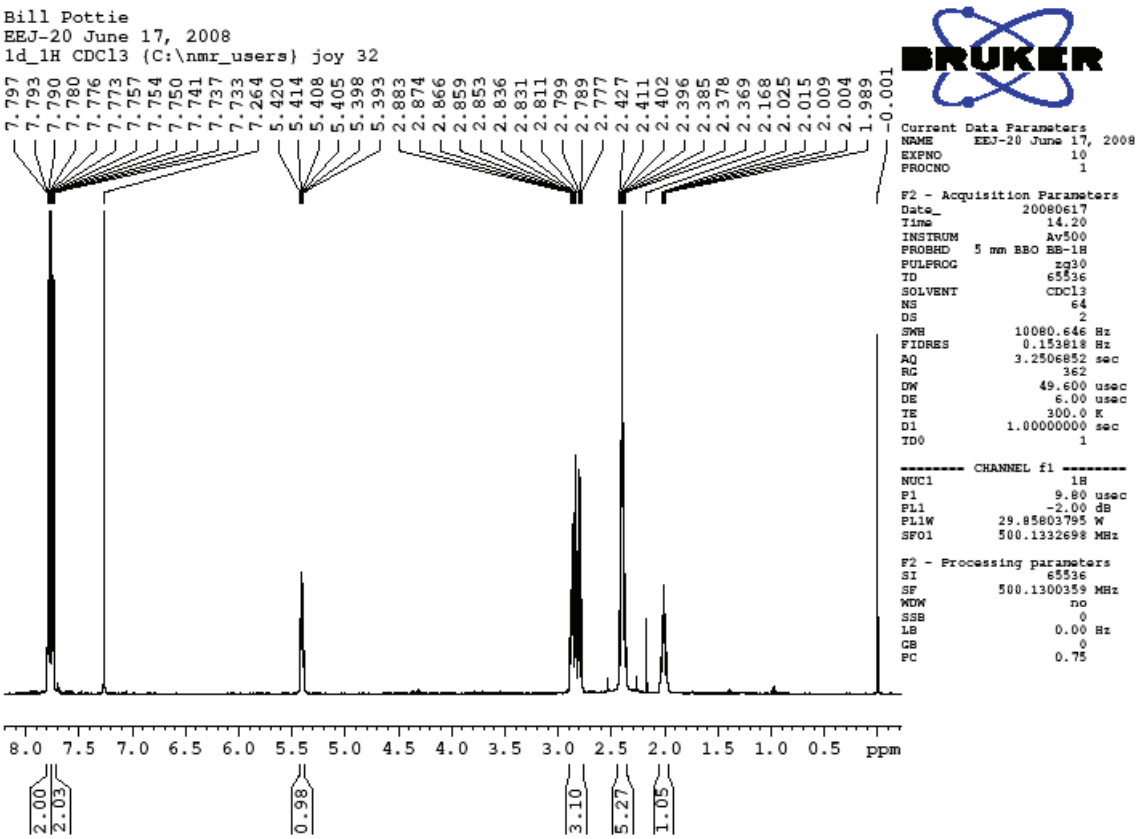

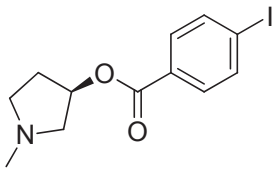

(R)-1-methylpyrrolidin-3-yl 4-iodobenzoate (**3**)
^{13}C NMR

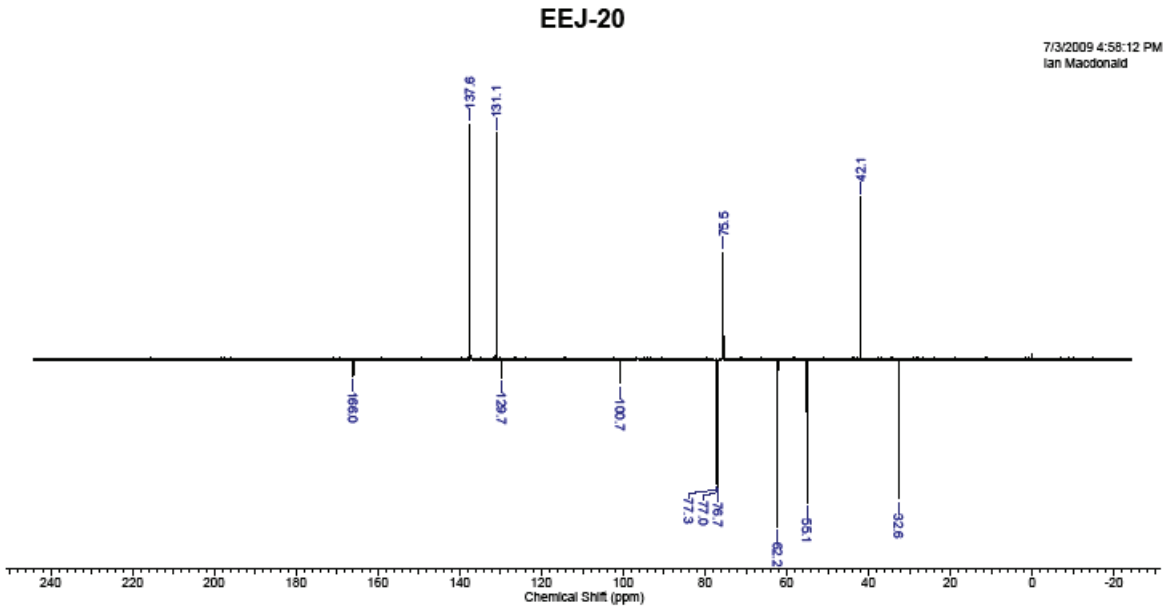

No.	(ppm)	(Hz)	Height
1	32.65	4105.6	-0.5936
2	42.05	5288.2	0.6917
3	55.07	6925.4	-0.6142
4	62.19	7820.3	-0.7115
5	75.52	9496.7	0.4558
6	76.75	9651.4	-0.5439
7	77.00	9683.3	-0.5367
8	77.25	9715.3	-0.5264
9	100.73	12667.1	-0.1028
10	129.71	16311.6	-0.0764
11	131.09	16485.9	0.9631
12	137.63	17307.6	1.0000
13	165.95	20869.7	-0.0729

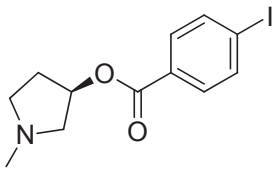

(R)-1-methylpyrrolidin-3-yl 4-iodobenzoate (**3**)
IR

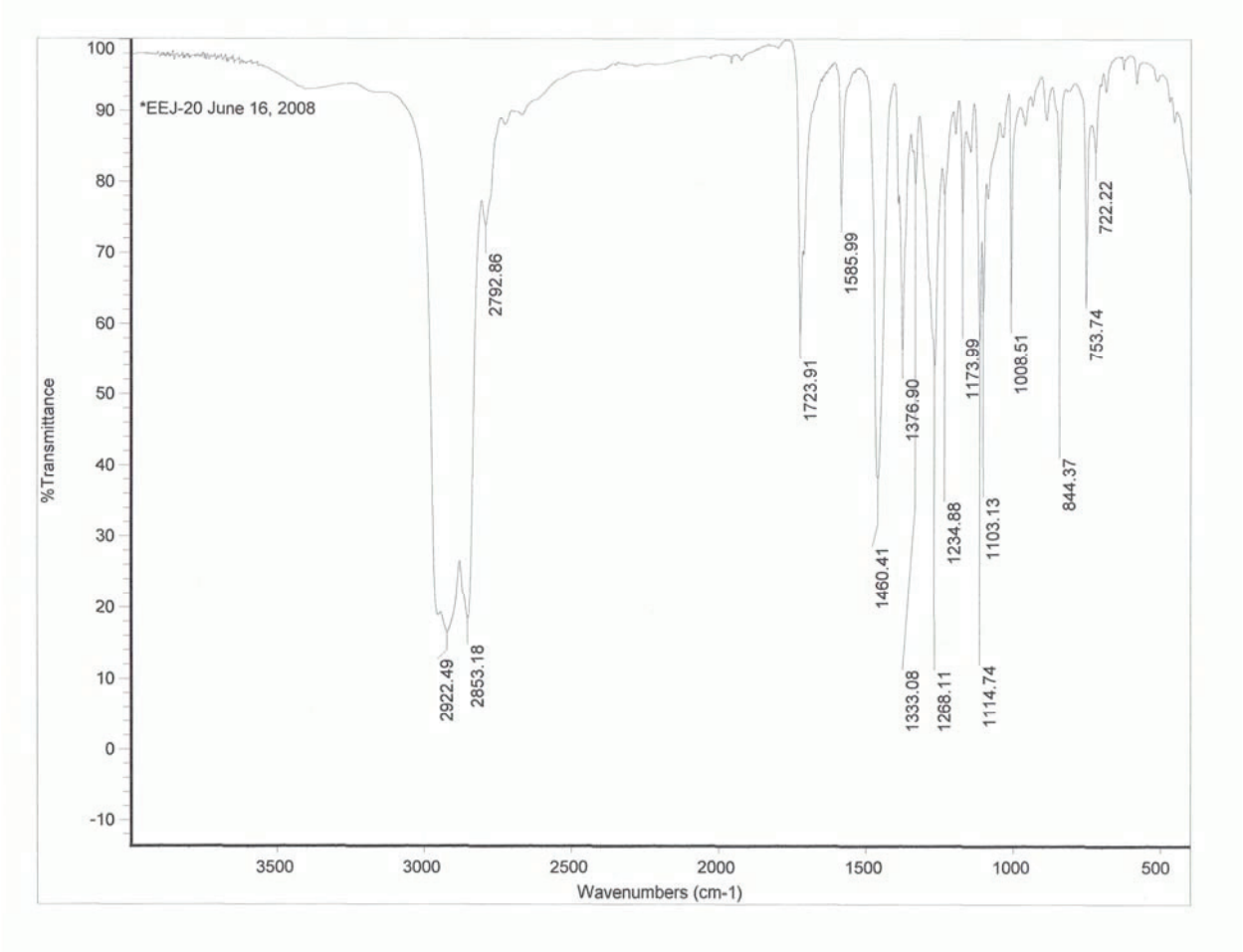

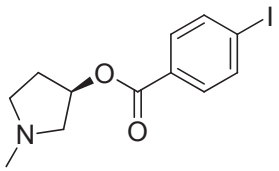

(R)-1-methylpyrrolidin-3-yl 4-iodobenzoate (**3**)
LRMS

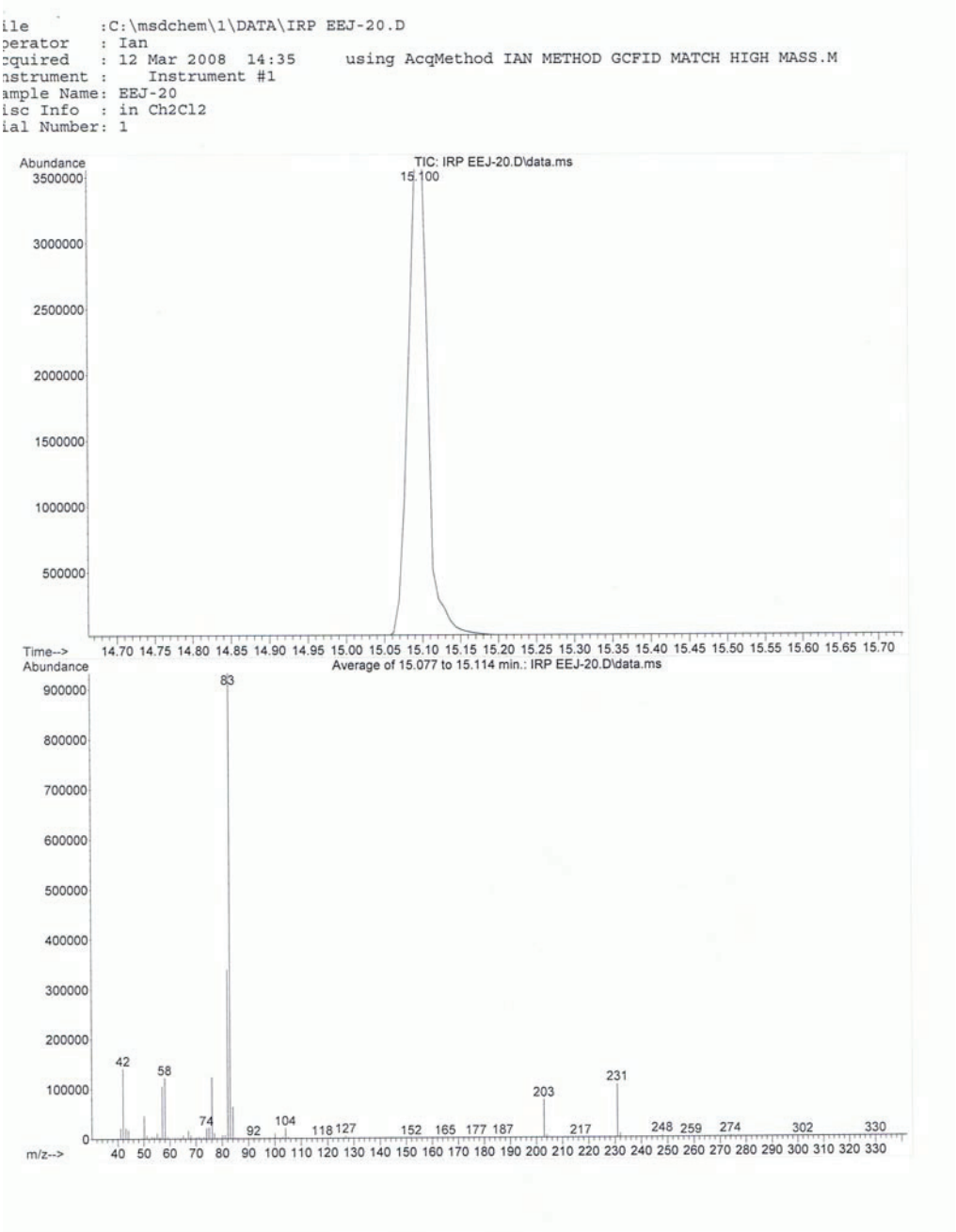

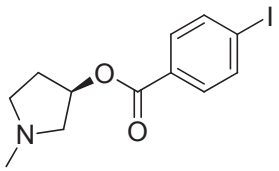

(R)-1-methylpyrrolidin-3-yl 4-iodobenzoate (**3**)
HRMS

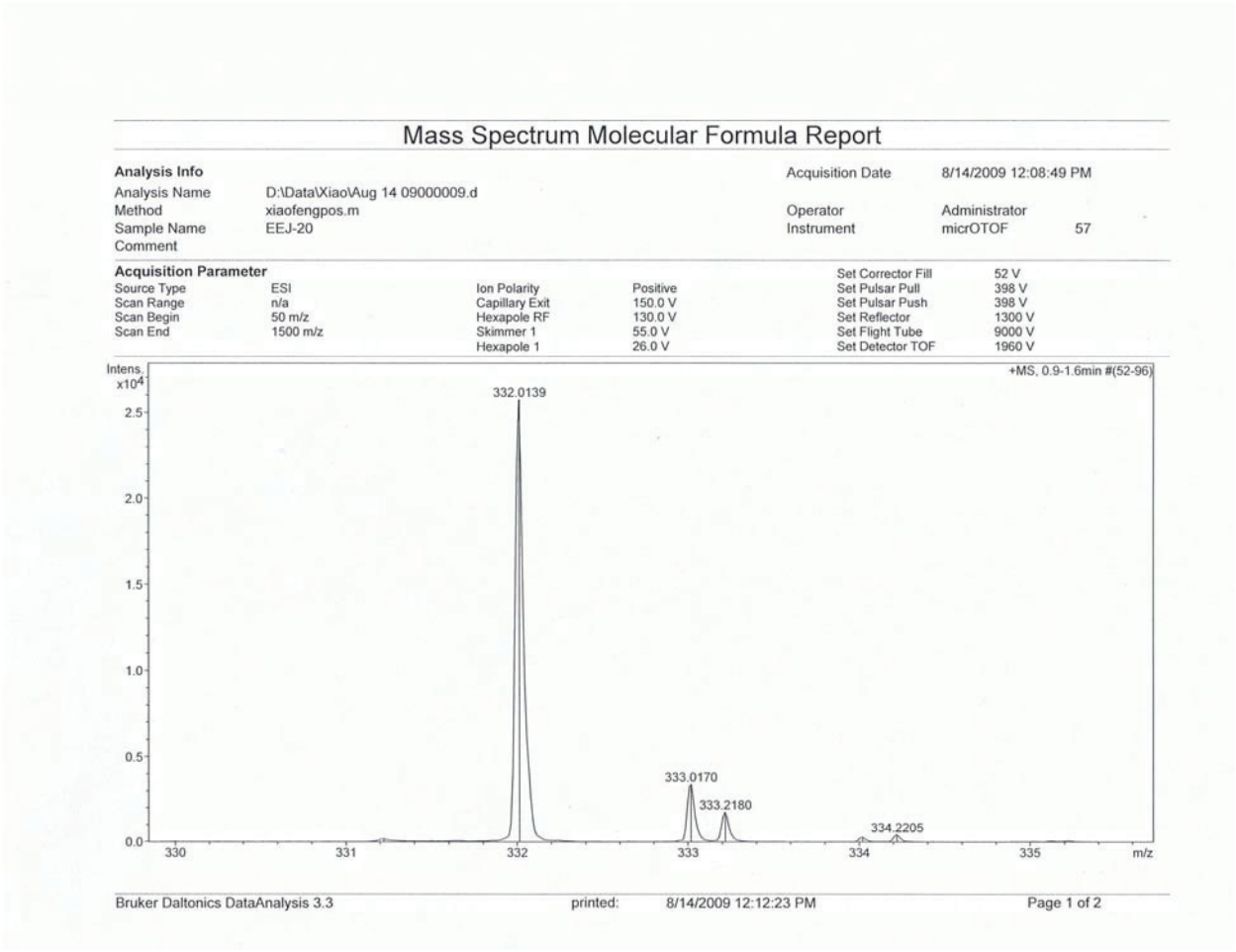

Mass Spectrum Molecular Formula Report

Analysis Info

Analysis Name	D:\Data\Xiao\Aug 14 09000009.d	Acquisition Date	8/14/2009 12:08:49 PM
Method	xiaofengpos.m		
Sample Name	EEJ-20	Operator	Administrator
Comment		Instrument	micrOTOF 57

Acquisition Parameter

Source Type	ESI	Ion Polarity	Positive	Set Corrector Fill	52 V
Scan Range	n/a	Capillary Exit	150.0 V	Set Pulsar Pull	398 V
Scan Begin	50 m/z	Hexapole RF	130.0 V	Set Pulsar Push	398 V
Scan End	1500 m/z	Skimmer 1	55.0 V	Set Reflector	1300 V
		Hexapole 1	26.0 V	Set Flight Tube	9000 V
				Set Detector TOF	1960 V

Bruker Daltonics DataAnalysis 3.3 printed: 8/14/2009 12:12:23 PM Page 1 of 2

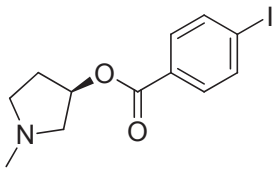

(R)-1-methylpyrrolidin-3-yl 4-iodobenzoate (**3**)
HPLC

```
Data File C:\Chem32\1\DATA\UREAS\DAR26062009C 2009-06-26 14-59-32\051-0101.D
Sample Name: EEEJ-20

    ======================================================================
    Acq. Operator   : Ian                              Seq. Line :   1
    Acq. Instrument : Instrument 1                     Location : Vial 51
    Injection Date  : 6/26/2009 3:00:49 PM                 Inj :   1
                                                     Inj Volume : 10 µl
    Sequence File   : C:\Chem32\1\DATA\UREAS\DAR26062009C 2009-06-26 14-59-32\DAR26062009C.S
    Method          : C:\Chem32\1\DATA\UREAS\DAR26062009C 2009-06-26 14-59-32\REV PHASE METHANOL
                      10UL.M
    Last changed    : 6/26/2009 2:59:29 PM by Ian
    Method Info     : Reverse Phase Methanol
```

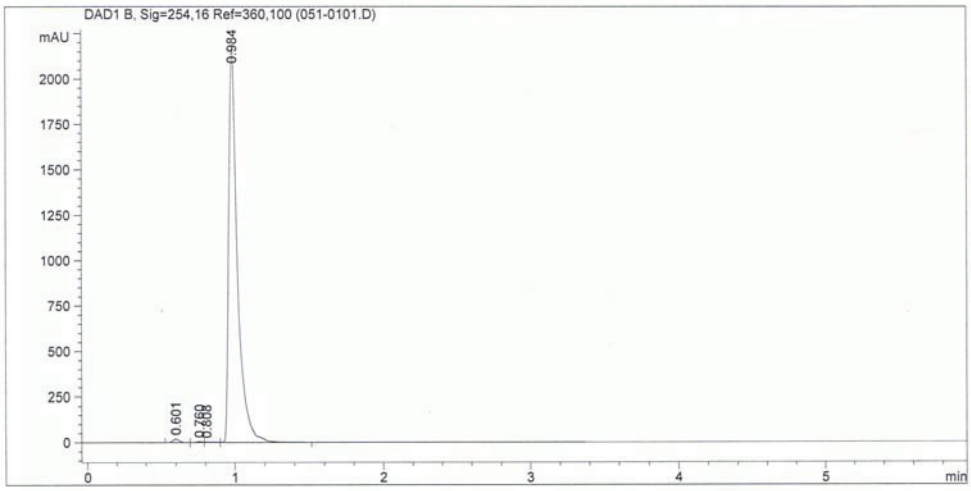


```
    ======================================================================
                              Area Percent Report
    ======================================================================

    Sorted By             :      Signal
    Multiplier            :      1.0000
    Dilution              :      1.0000
    Use Multiplier & Dilution Factor with ISTDs


    Signal 1: DAD1 B, Sig=254,16 Ref=360,100

    Peak RetTime Type  Width     Area      Height     Area
      #   [min]        [min]   [mAU*s]     [mAU]       %
    ----|-------|----|-------|----------|----------|--------|
       1   0.601 BV    0.0490   57.85556   19.27723   0.6439
       2   0.760 VV    0.0493   14.70636    4.60321   0.1637
       3   0.808 VV    0.0650   14.72179    3.01563   0.1639
       4   0.984 VB    0.0614 8897.45410 2187.77734  99.0285

    Totals :                   8984.73781 2214.67342


Instrument 1 6/26/2009 3:07:13 PM Ian                          Page   1 of 2
```

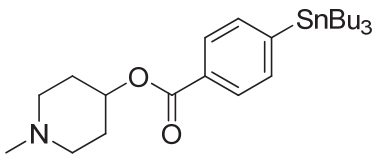

1-methylpiperidin-4-yl 4-(tributylstannyl)benzoate (**4**)

^{1}H NMR

EEJ-10

Ian Macdonald

Acquisition Time (sec)	3.2768	*Comment*	EEJ-10-r May 08-07 1d 1H CDCl3 {C:\nmr users} macdonald 9			*Date*	09 May 2007 20:04:32
Date Stamp	09 May 2007 20:04:32			*File Name*	C:\nmrdata\data\eric joy\nmr\EEJ-10-r May 08-07\10\PDATA\1\1r		
Frequency (MHz)	500.13	*Nucleus*	1H	*Number of Transients*	16	*Origin*	Av500
Original Points Count	32768	*Owner*	queue	*Points Count*	65536	*Pulse Sequence*	zg30
Receiver Gain	362.00	*SW(cyclical) (Hz)*	10000.00	*Solvent*	CHLOROFORM-d		
Spectrum Offset (Hz)	3231.5828	*Spectrum Type*	STANDARD	*Sweep Width (Hz)*	9999.85	*Temperature (degree C)*	27.000

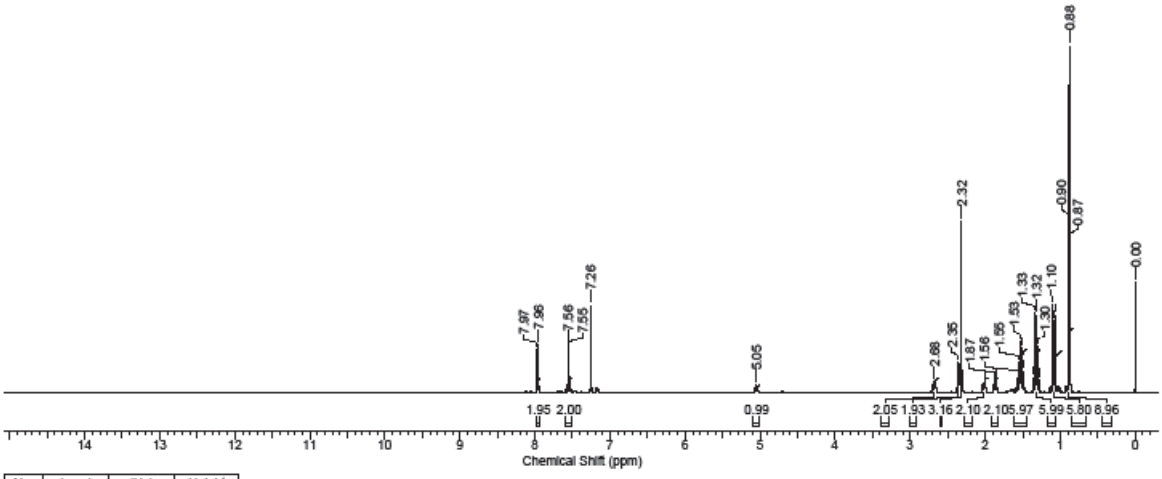

No.	(ppm)	(Hz)	Height
1	0.00	0.0	0.3178
2	0.87	434.0	0.4394
3	0.88	441.3	1.0000
4	0.90	448.6	0.4966
5	1.06	531.6	0.2240
6	1.08	538.0	0.1349
7	1.08	539.6	0.2058
8	1.08	542.3	0.0970
9	1.10	547.9	0.2525
10	1.29	644.1	0.0377
11	1.30	651.4	0.1333

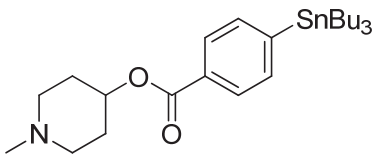

1-methylpiperidin-4-yl 4-(tributylstannyl)benzoate (**4**)
^{13}C NMR

EEJ-10

Ian Macdonald

Acquisition Time (sec)	0.7499	*Comment*	EEJ-10 June 14, 2007 1d 13C DEPTQ135 n CDCl3 (C:\nmr users) joy 26				
Date	16 Jun 2007 20:21:36			*Date Stamp*	16 Jun 2007 20:21:36		
File Name	C:\nmrdata\dataveric joy\nmr\EEJ-10 June 14, 2007\11\PDATA\1\1r			*Frequency (MHz)*	125.76	*Nucleus*	13C
Number of Transients	2048	*Origin*	Av500	*Original Points Count*	25335	*Owner*	armrc
Points Count	65536	*Pulse Sequence*	deptqsp.dmo	*Receiver Gain*	10321.30	*SW(cyclical) (Hz)*	33783.79
Solvent	CHLOROFORM-d	*Spectrum Offset (Hz)*	13834.2939	*Sweep Width (Hz)*	33783.27	*Temperature (degree C)*	27.448

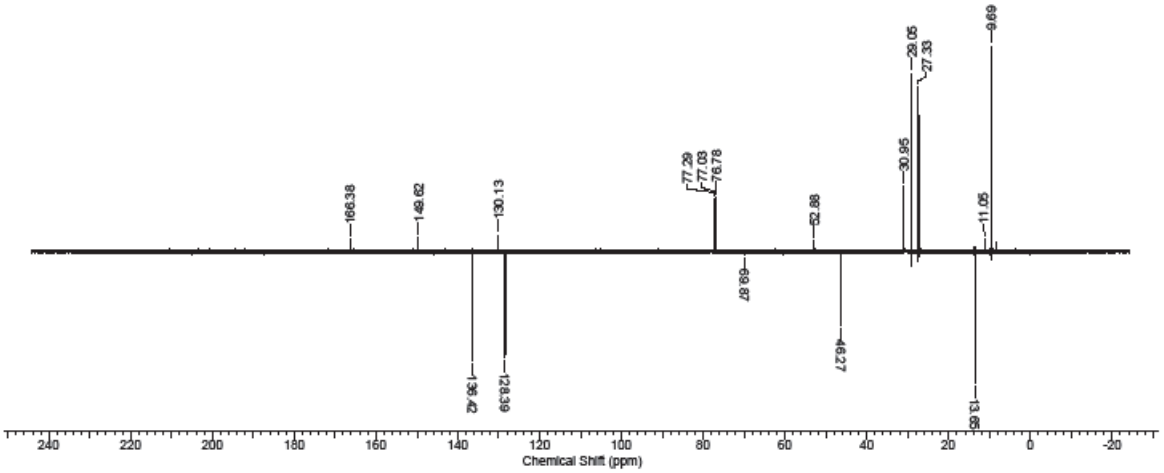

No.	(ppm)	(Hz)	Height
1	9.67	1216.7	0.0676
2	9.69	1218.2	1.0000
3	11.05	1389.4	0.0588
4	13.65	1717.2	-0.6375
5	27.32	3435.9	0.0726
6	27.33	3437.4	0.7984
7	28.97	3643.1	0.0639
8	29.05	3653.4	0.8676
9	29.06	3655.0	0.0734
10	30.95	3892.6	0.3184
11	46.27	5818.5	-0.3556

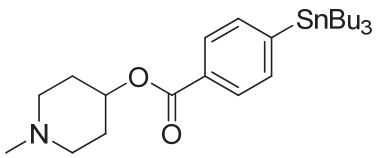

1-methylpiperidin-4-yl 4-(tributylstannyl)benzoate (**4**)

IR

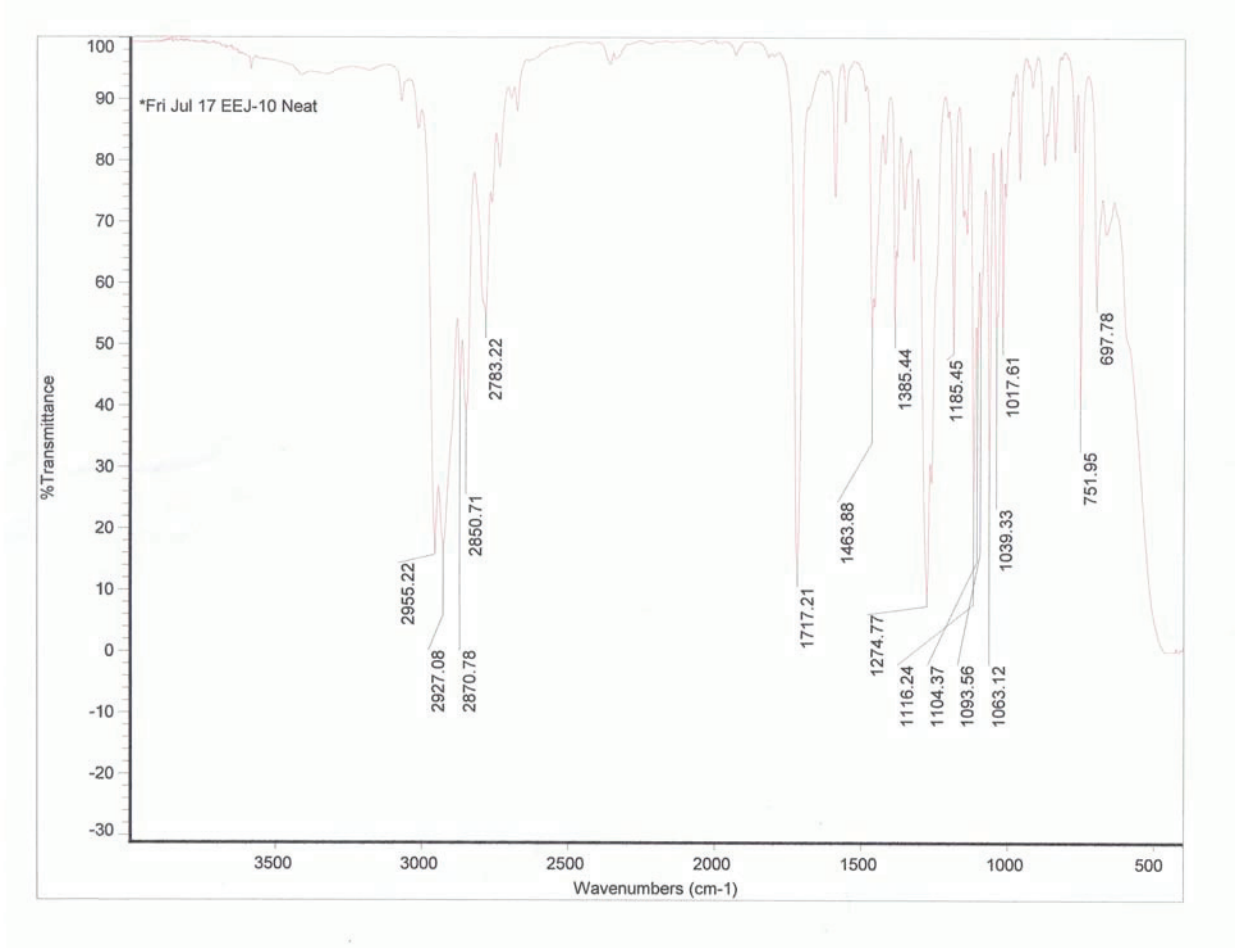

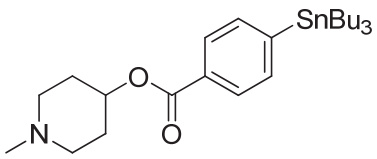

1-methylpiperidin-4-yl 4-(tributylstannyl)benzoate (**4**)

LRMS

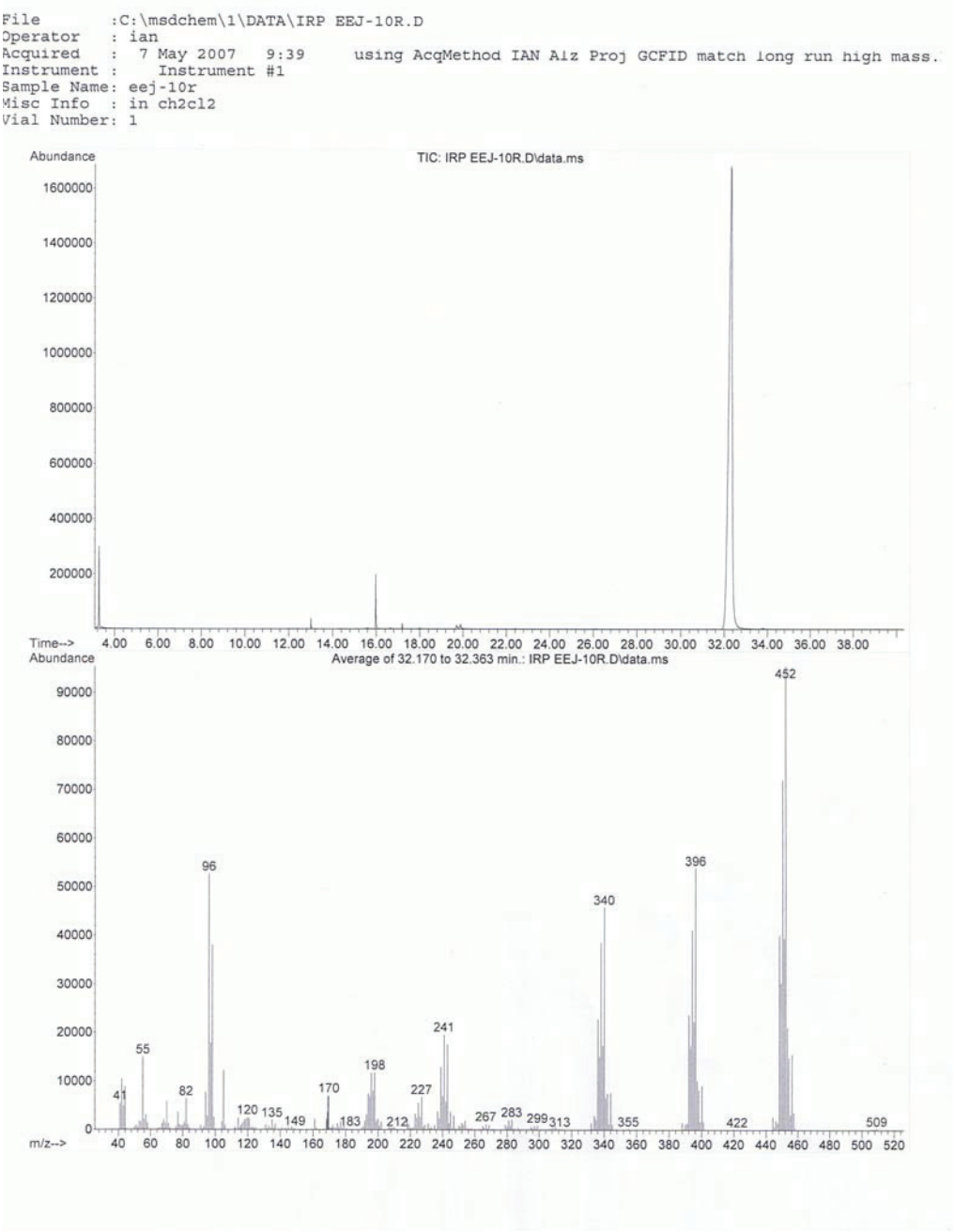

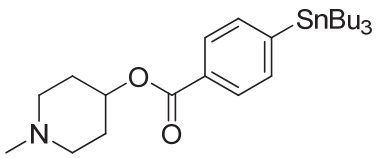

1-methylpiperidin-4-yl 4-(tributylstannyl)benzoate (**4**)

HRMS

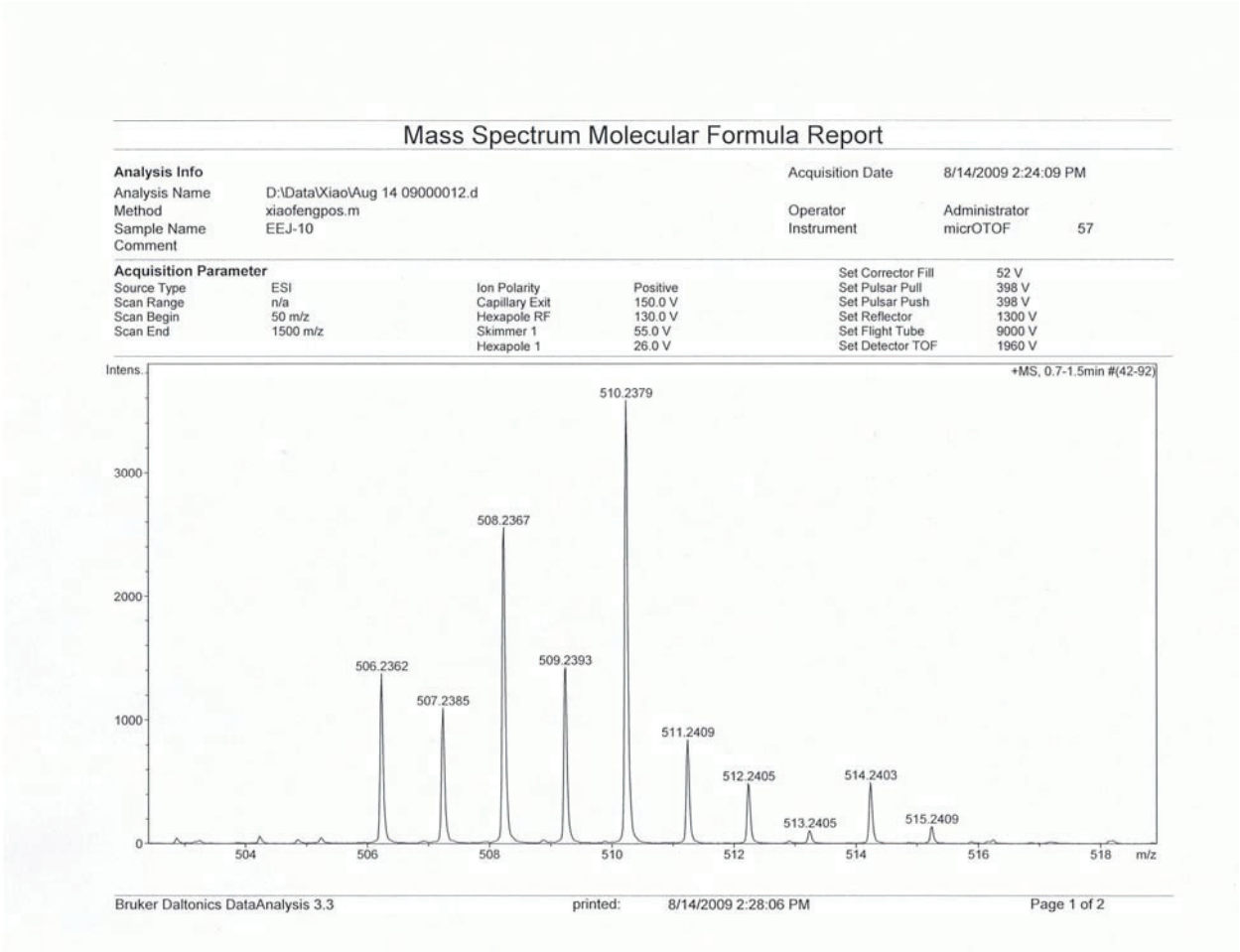

Mass Spectrum Molecular Formula Report

Analysis Info

Analysis Name	D:\Data\Xiao\Aug 14 09000012.d	Acquisition Date	8/14/2009 2:24:09 PM
Method	xiaofengpos.m		
Sample Name	EEJ-10	Operator	Administrator
Comment		Instrument	micrOTOF 57

Acquisition Parameter

Source Type	ESI	Ion Polarity	Positive	Set Corrector Fill	52 V
Scan Range	n/a	Capillary Exit	150.0 V	Set Pulsar Pull	398 V
Scan Begin	50 m/z	Hexapole RF	130.0 V	Set Pulsar Push	398 V
Scan End	1500 m/z	Skimmer 1	55.0 V	Set Reflector	1300 V
		Hexapole 1	26.0 V	Set Flight Tube	9000 V
				Set Detector TOF	1960 V

Bruker Daltonics DataAnalysis 3.3 printed: 8/14/2009 2:28:06 PM Page 1 of 2

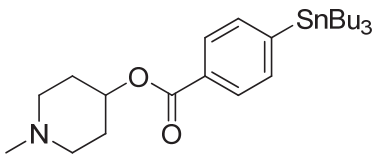

1-methylpiperidin-4-yl 4-(tributylstannyl)benzoate (**4**)

HPLC

```
Data File C:\CHEM32\1\DATA\I MACDONALD\IRM07072010E 2010-07-07 16-18-43\024-0401.D
Sample Name: EEJ-10

======================================================================
Acq. Operator   : Ian                          Seq. Line :   4
Acq. Instrument : Instrument 1                 Location : Vial 24
Injection Date  : 7/7/2010 5:02:51 PM             Inj :   1
                                               Inj Volume : 100 µl
Acq. Method     : C:\Chem32\1\DATA\I MACDONALD\IRM07072010E 2010-07-07 16-18-43\
                  MACDONLAD NORMAL PHASE 20UL.M
Last changed    : 7/7/2010 4:18:41 PM by Ian
Analysis Method : C:\CHEM32\1\DATA\I MACDONALD\IRM07072010E 2010-07-07 16-18-43\024-
                  0401.D\DA.M (MACDONLAD NORMAL PHASE 20UL.M)
Last changed    : 7/28/2010 9:46:58 AM by Ian
                  (modified after loading)
Method Info     : Reverse Phase Methanol
```

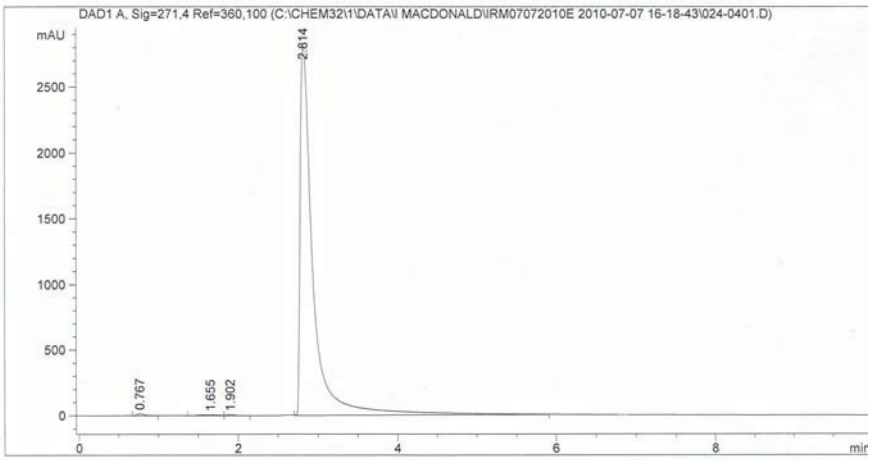


```
======================================================================
                          Area Percent Report
======================================================================

Sorted By             :      Signal
Multiplier            :      1.0000
Dilution              :      1.0000
Use Multiplier & Dilution Factor with ISTDs


Signal 1: DAD1 A, Sig=271,4 Ref=360,100

Peak RetTime Type  Width     Area      Height     Area
  #   [min]       [min]   [mAU*s]     [mAU]       %
----|-------|----|-------|----------|----------|--------|
   1   0.767 VV    0.1068  118.90839   15.98234   0.3716
   2   1.655 VV    0.2225  134.09378    7.80183   0.4191
   3   1.902 VB    0.1030   61.04632    8.58030   0.1908
   4   2.814 VB    0.1616 3.16829e4  2808.55176  99.0185


Instrument 1 7/28/2010 9:47:01 AM Ian                          Page   1 of 2
```

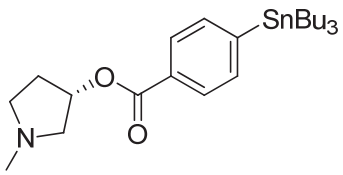

(S)-1-methylpyrrolidin-3-yl 4-(tributylstannyl)benzoate (**5**)
^{1}H NMR

IRM-116 July 21, 2009

7/21/2009 2:28:38 PM
Ian Macdonald

Acquisition Time (sec)	3.2768	*Comment*	Bill Pottle 1d 1H DMSO {C:\nmr users} pilgrim 6			*Date*	21 Jul 2009 12:55:44
Date Stamp	21 Jul 2009 12:55:44			*File Name*	C:\nmrdata\data\Ian Macdonald\NMR\IRM-116 Jul 21, 2009\10\fid		
Frequency (MHz)	500.13	*Nucleus*	1H	*Number of Transients*	64	*Origin*	spect
Original Points Count	32768	*Owner*	nmr	*Points Count*	32768	*Pulse Sequence*	zg30
Receiver Gain	362.00	*SW(cyclical) (Hz)*	10000.00	*Solvent*	DMSO-d6	*Spectrum Offset (Hz)*	3228.9324
Spectrum Type	STANDARD	*Sweep Width (Hz)*	9999.70	*Temperature (degree C)*	21.967		

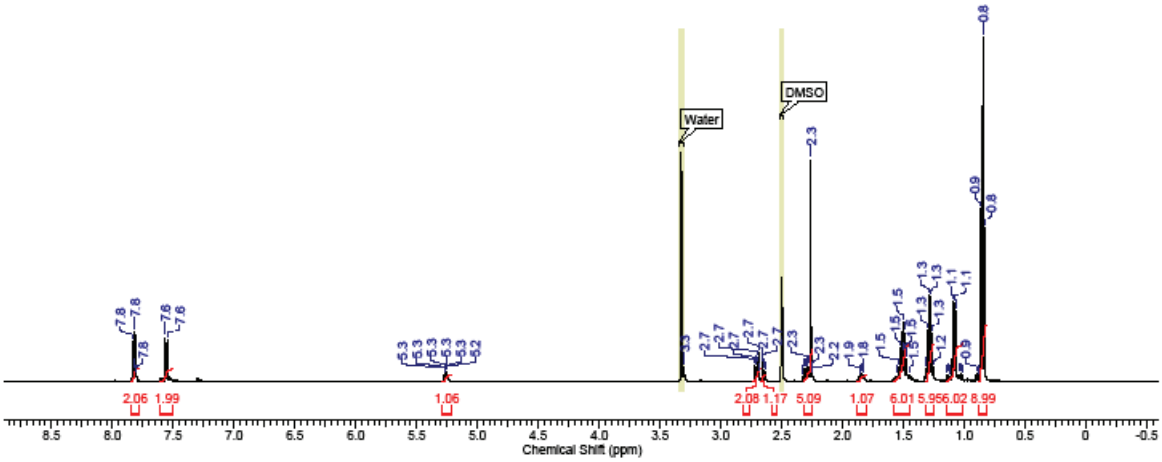

No.	(ppm)	(Hz)	Height	No.	(ppm)	(Hz)	Height	No.	(ppm)	(Hz)	Height	No.	(ppm)	(Hz)	Height
1	0.83	417.2	0.4481	12	1.10	548.7	0.2318	23	1.47	737.6	0.0667	34	1.85	922.9	0.0223
2	0.85	424.5	1.0000	13	1.12	556.2	0.0150	24	1.49	743.4	0.0858	35	1.86	928.1	0.0199
3	0.86	431.8	0.5015	14	1.13	565.8	0.0206	25	1.49	745.6	0.1414	36	1.86	930.2	0.0156
4	0.88	440.4	0.0176	15	1.15	574.4	0.0173	26	1.50	750.4	0.0812	37	1.86	932.0	0.0155
5	0.89	442.8	0.0145	16	1.25	624.4	0.0404	27	1.51	752.9	0.1743	38	2.25	1123.1	0.0194
6	0.90	450.2	0.0249	17	1.26	631.4	0.1403	28	1.52	761.1	0.0959	39	2.25	1125.5	0.0354
7	1.01	506.6	0.0172	18	1.28	638.8	0.2453	29	1.54	768.1	0.0439	40	2.26	1131.0	0.6448
8	1.03	514.2	0.0226	19	1.29	646.1	0.2518	30	1.56	779.7	0.0169	41	2.28	1138.6	0.0446
9	1.05	522.8	0.0208	20	1.31	653.4	0.1496	31	1.83	913.1	0.0161	42	2.29	1143.2	0.0372
10	1.06	532.6	0.2053	21	1.32	660.7	0.0392	32	1.83	915.2	0.0194	43	2.29	1146.9	0.0545
11	1.08	540.5	0.2287	22	1.45	726.6	0.0178	33	1.84	920.1	0.0218	44	2.30	1151.1	0.0359

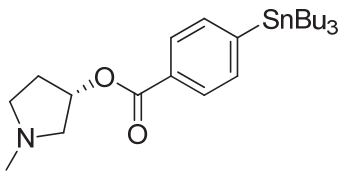

(S)-1-methylpyrrolidin-3-yl 4-(tributylstannyl)benzoate (**5**)
^{13}C NMR

IRM-116

Ian Macdonald

Acquisition Time (sec)	0.7499				
Comment	Bill Pottle 1d_13C_DEPTQ135_n DMSO {C:\nmr_users} pilgrim 6 Best S/N after 128 scans was 23.5 Best S/N after 256 scans was 30.6 Best S/N after 384 scans was 35.4 Best S/N after 512 scans was 37.7 Best S/N after 640 scans was 42.7 Best S/N after 768 sca				
Date	22 Jul 2009 22:27:28	*Date Stamp*	22 Jul 2009 22:27:28		
File Name	C:\nmrdata\data\Ian Macdonald\NMR\IRM-116 Jul 21, 2009\11\PDATA\1\1r			*Frequency (MHz)*	125.76
Nucleus	13C	*Number of Transients*	2000	*Origin*	spect
Original Points Count	25335	*Owner*	nmr	*Points Count*	65536
Pulse Sequence	deptqsp.dmo	*Receiver Gain*	9195.20	*SW(cyclical) (Hz)*	33783.79
Solvent	DMSO-d6	*Spectrum Offset (Hz)*	13754.0957	*Sweep Width (Hz)*	33783.27
Temperature (degree C)	21.987				

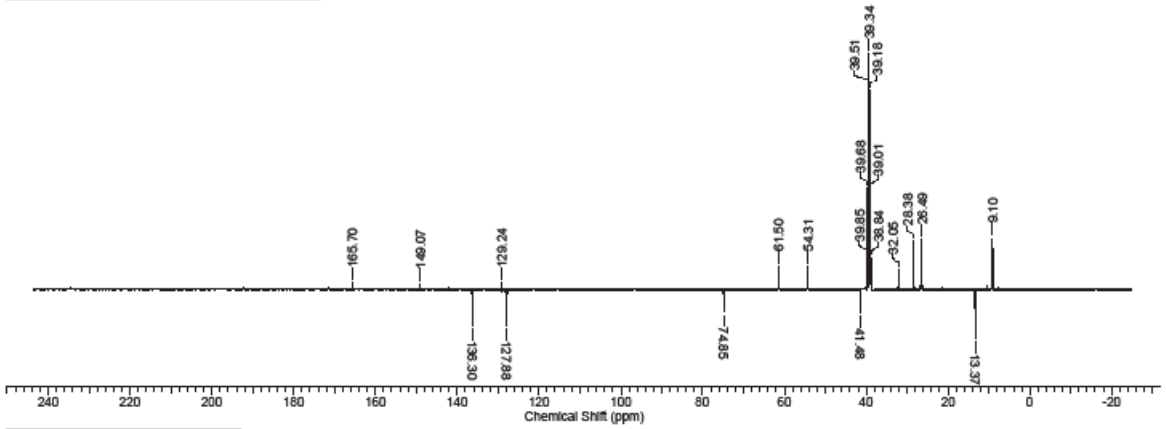

No.	(ppm)	(Hz)	Height
1	9.10	1144.2	0.2154
2	13.37	1681.9	-0.2087
3	26.49	3331.0	0.2106
4	28.38	3568.6	0.2052
5	28.46	3578.9	0.0236
6	32.05	4030.0	0.0846
7	38.84	4884.7	0.1343
8	39.01	4905.8	0.4182
9	39.18	4926.9	0.8451
10	39.34	4947.6	1.0000

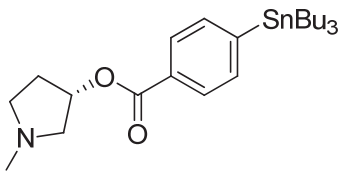

(S)-1-methylpyrrolidin-3-yl 4-(tributylstannyl)benzoate (**5**)
IR

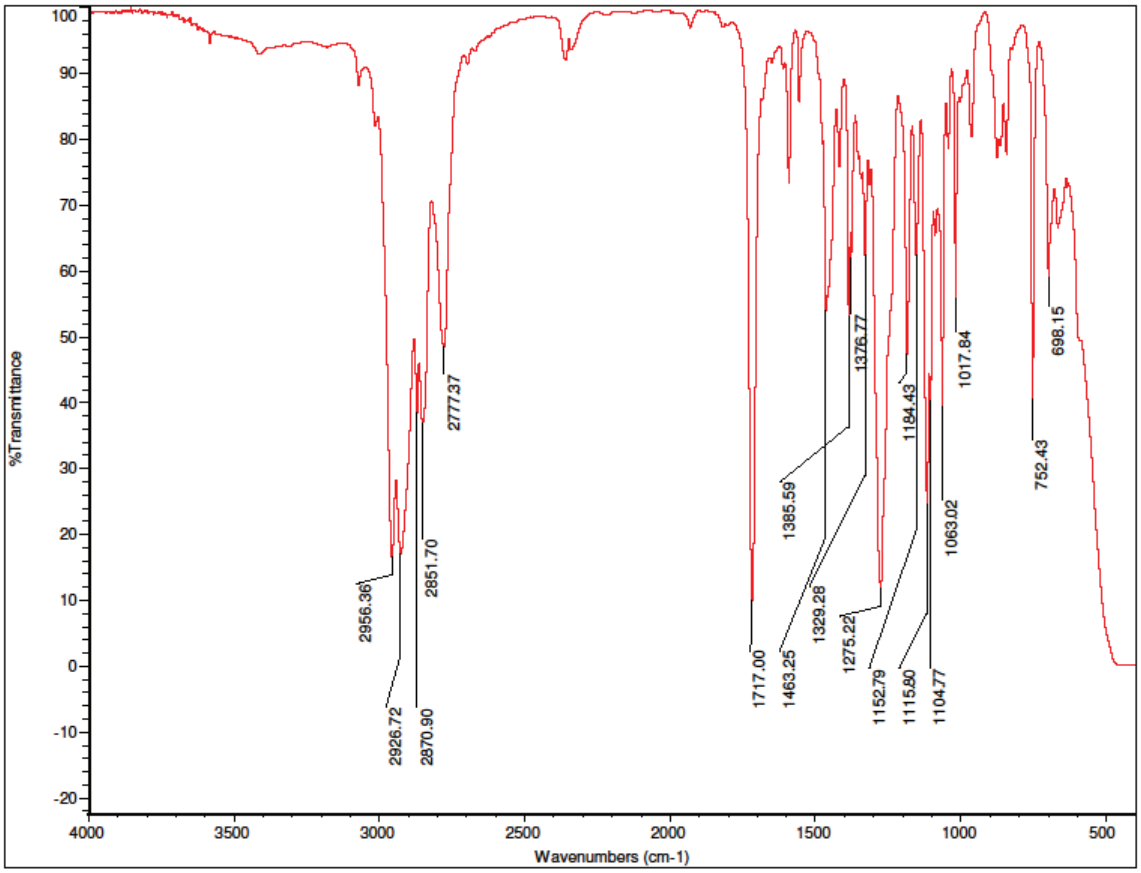

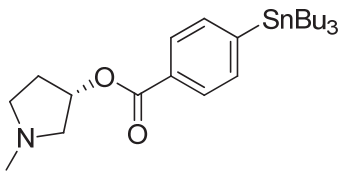

(S)-1-methylpyrrolidin-3-yl 4-(tributylstannyl)benzoate (**5**)
LRMS

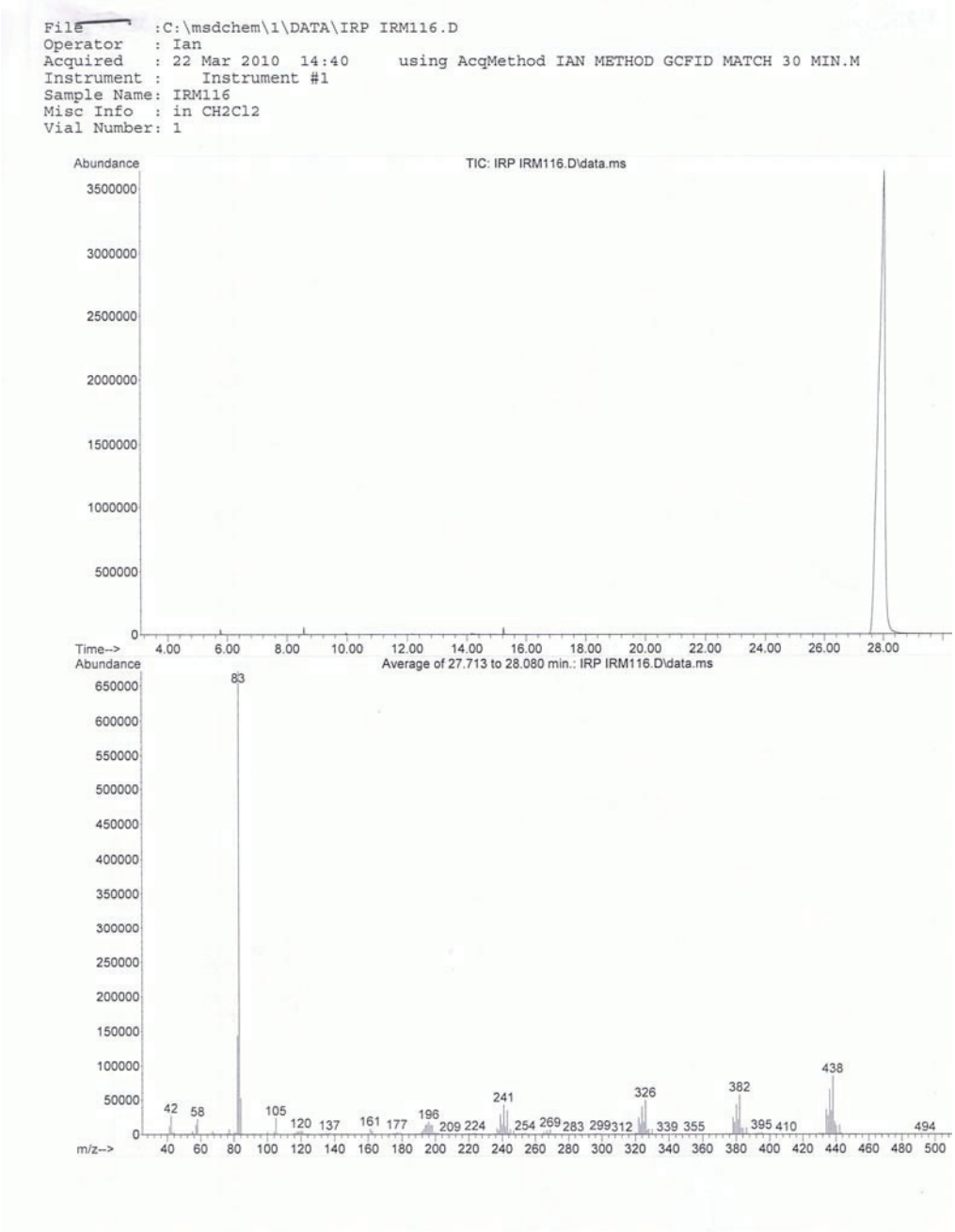

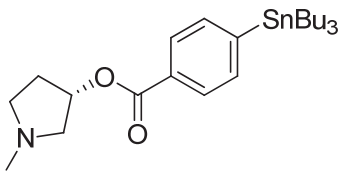

(S)-1-methylpyrrolidin-3-yl 4-(tributylstannyl)benzoate (**5**)
HRMS

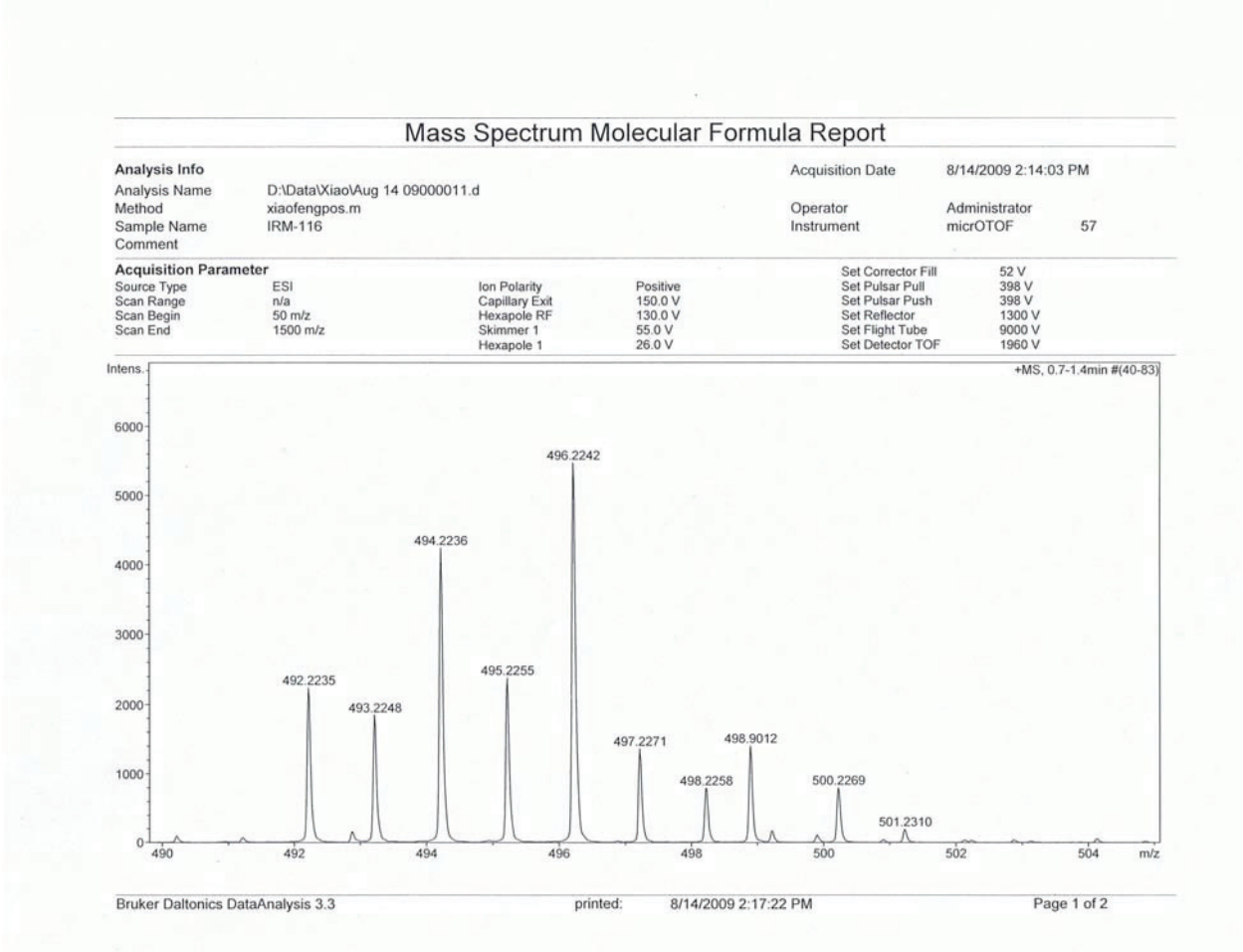

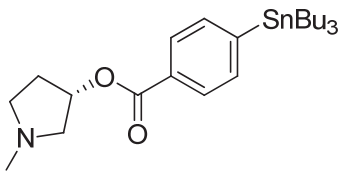

(S)-1-methylpyrrolidin-3-yl 4-(tributylstannyl)benzoate (**5**)
HPLC

```
Data File C:\CHEM32\1\DATA\IAN MACDONALD\IRM07282010B 2010-07-28 15-54-38\034-0401.D
Sample Name: IRM-116

=====================================================================
Acq. Operator   : Ian                          Seq. Line :   4
Acq. Instrument : Instrument 1                  Location : Vial 34
Injection Date  : 7/28/2010 4:40:00 PM               Inj :   1
                                               Inj Volume : 100 µl
Acq. Method     : C:\Chem32\1\DATA\IAN MACDONALD\IRM07282010B 2010-07-28 15-54-38\
                  MACDONLAD NORMAL PHASE 20UL.M
Last changed    : 7/7/2010 4:18:41 PM by Ian
Analysis Method : C:\CHEM32\1\DATA\IAN MACDONALD\IRM07282010B 2010-07-28 15-54-38\034-
                  0401.D\DA.M (MACDONLAD NORMAL PHASE 20UL.M)
Last changed    : 7/29/2010 10:22:47 AM by Ian
                  (modified after loading)
Method Info     : Reverse Phase Methanol
```

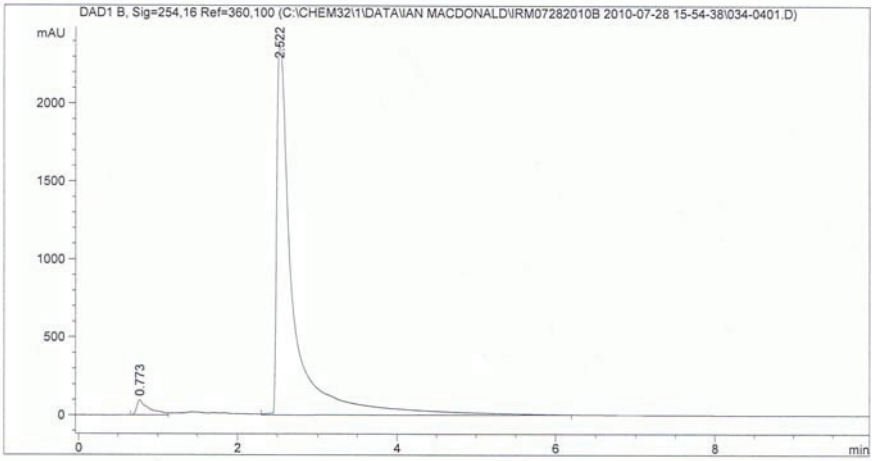


```
=====================================================================
                        Area Percent Report
=====================================================================

Sorted By             :      Signal
Multiplier            :      1.0000
Dilution              :      1.0000
Use Multiplier & Dilution Factor with ISTDs


Signal 1: DAD1 B, Sig=254,16 Ref=360,100

Peak RetTime Type  Width     Area      Height     Area
  #   [min]        [min]   [mAU*s]     [mAU]       %
----|-------|----|-------|----------|----------|--------|
   1   0.773 VV    0.1433 1047.39624   97.55672   2.9982
   2   2.522 VB    0.1983 3.38869e4  2376.76367  97.0018

Totals :                  3.49343e4  2474.32039

Instrument 1 7/29/2010 10:22:52 AM Ian                    Page   1 of 2
```

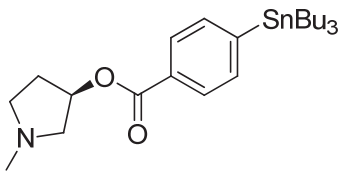

(R)-1-methylpyrrolidin-3-yl 4-(tributylstannyl)benzoate (**6**)
^{1}H NMR

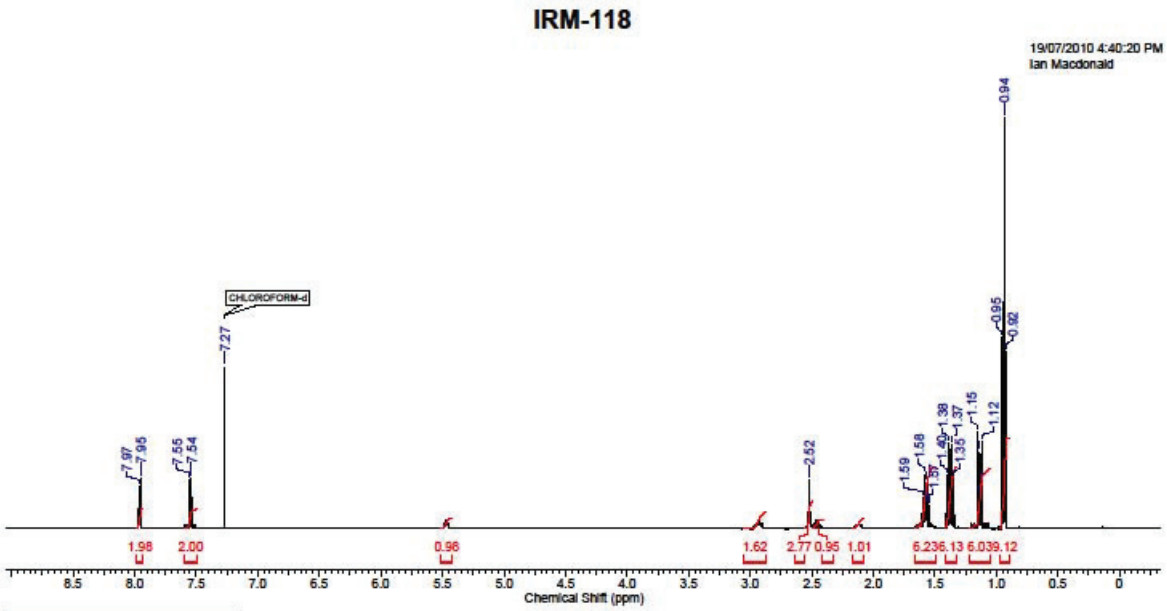

No.	(ppm)	(Hz)	Height
1	0.92	461.5	0.4316
2	0.94	468.8	1.0000
3	0.95	476.2	0.4651
4	1.12	558.6	0.2105
5	1.13	565.0	0.1132
6	1.13	566.5	0.1865
7	1.14	568.0	0.0839
8	1.14	569.2	0.0820
9	1.15	574.7	0.2357
10	1.35	676.0	0.1206
11	1.37	683.4	0.2048
12	1.38	690.7	0.2081
13	1.40	698.0	0.1294

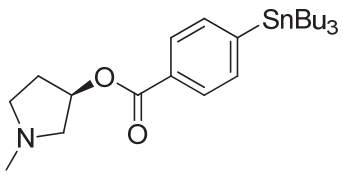

(R)-1-methylpyrrolidin-3-yl 4-(tributylstannyl)benzoate (**6**)
^{13}C NMR

IRM-118

22/07/2010 10:54:09 AM
Ian Macdonald

Acquisition Time (sec)	0.7499				
Comment	Bill Pottle 1d_13C_DEPTQ135_n CDCl3 {C:\nmr_users} lmacdonald 35 Best S/N after 128 scans was 8.5 Best S/N after 256 scans was 13.8 Best S/N after 384 scans was 17.9 Best S/N after 512 scans was 20.6 Best S/N after 640 scans was 22.0 Best S/N after 768				
Date	07 Jul 2010 18:28:32	*Date Stamp*	07 Jul 2010 18:28:32		
File Name	\\APPS2\USER\SHARED\Organic Chemistry Research\Ian Macdonald\NMR Data\Ian Macdonald\NMR\IRM-118 July 12, 2010\11\PDATA\1\1r				
Frequency (MHz)	125.76	*Nucleus*	13C	*Number of Transients*	1024
Origin	spect	*Original Points Count*	25335	*Owner*	nmr
Points Count	65536	*Pulse Sequence*	deptqsp.dmo	*Receiver Gain*	9195.20
SW(cyclical) (Hz)	33783.79	*Solvent*	CHLOROFORM-d	*Spectrum Offset (Hz)*	13868.8486
Sweep Width (Hz)	33783.27	*Temperature (degree C)*	21.967		

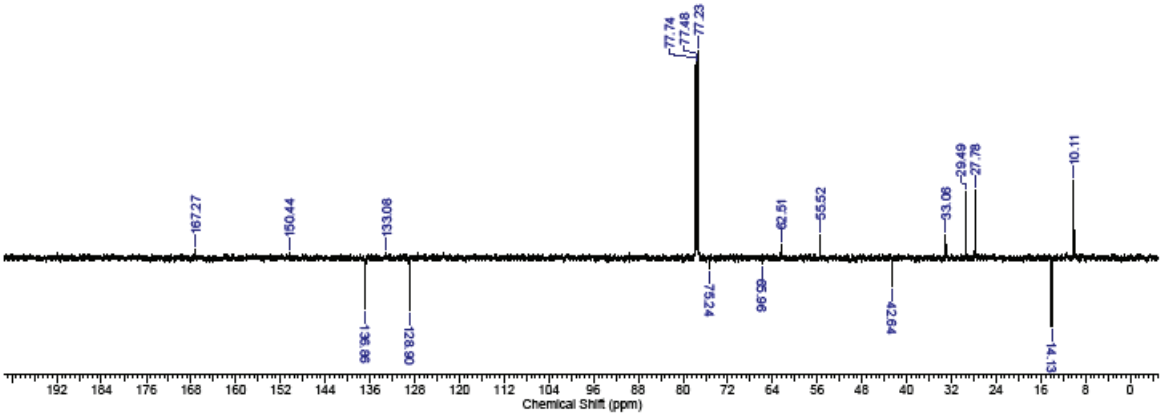

No.	(ppm)	(Hz)	Height
1	10.11	1271.7	0.3717
2	14.13	1777.4	-0.3304
3	27.78	3494.1	0.3253
4	29.49	3708.5	0.3216
5	33.06	4157.5	0.1127
6	42.64	5361.7	-0.1407
7	55.52	6982.4	0.1101
8	62.51	7861.4	0.0609
9	65.96	8294.9	-0.0311
10	75.24	9462.5	-0.0546

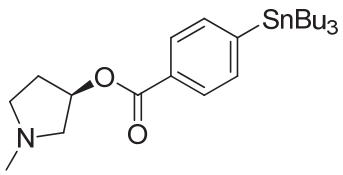

(R)-1-methylpyrrolidin-3-yl 4-(tributylstannyl)benzoate (**6**)
IR

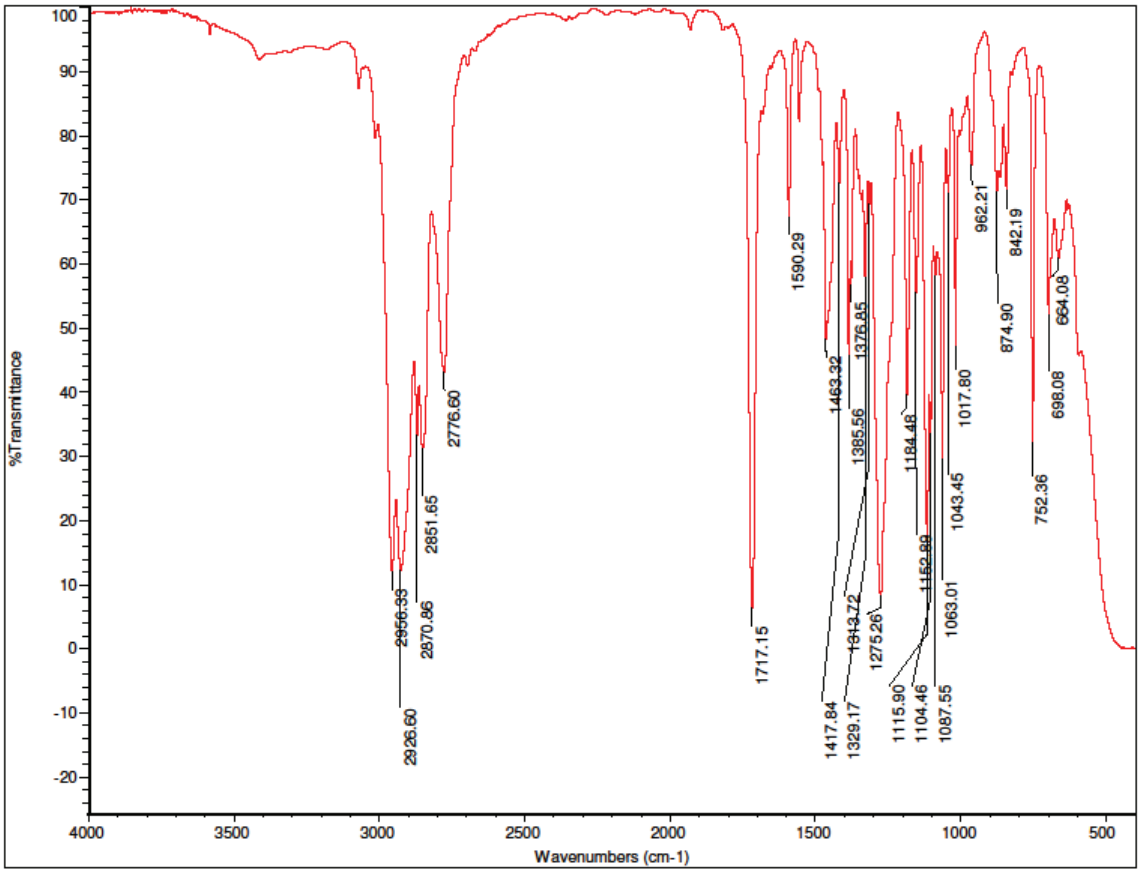

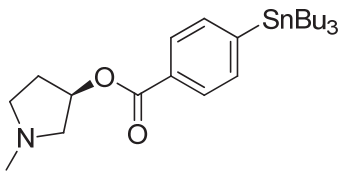

(R)-1-methylpyrrolidin-3-yl 4-(tributylstannyl)benzoate (**6**)
LRMS

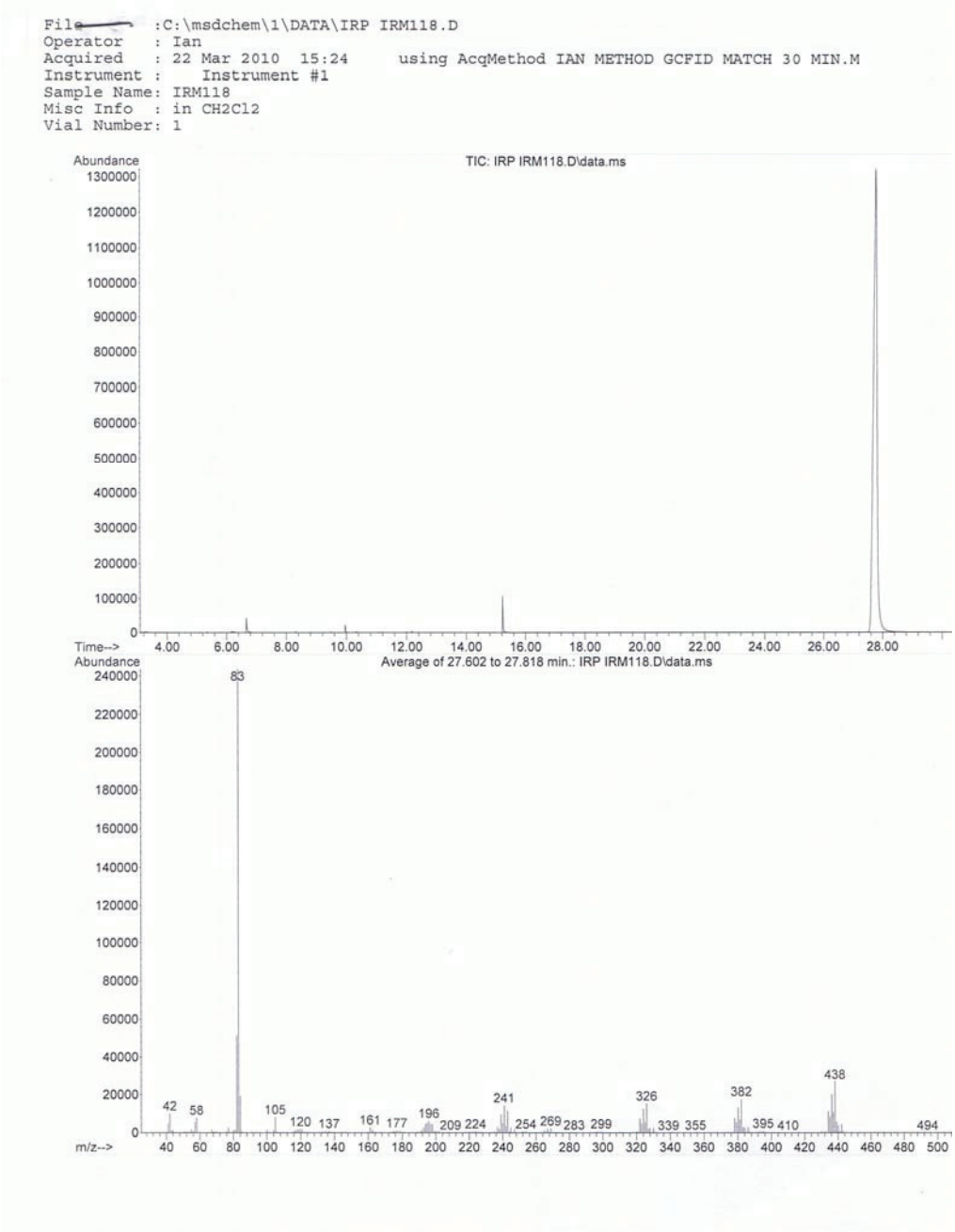

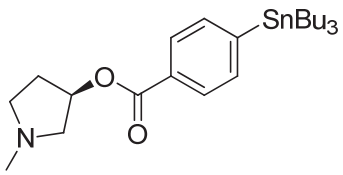

(R)-1-methylpyrrolidin-3-yl 4-(tributylstannyl)benzoate (**6**)
HRMS

Mass Spectrum Molecular Formula Report

Analysis Info

Analysis Name	D:\Data\Xiao\Aug 14 09000010.d	Acquisition Date	8/14/2009 2:01:03 PM
Method	xiaofengpos.m	Operator	Administrator
Sample Name	IRM-118	Instrument	micrOTOF 57
Comment			

Acquisition Parameter

Source Type	ESI	Ion Polarity	Positive	Set Corrector Fill	52 V
Scan Range	n/a	Capillary Exit	150.0 V	Set Pulsar Pull	398 V
Scan Begin	50 m/z	Hexapole RF	130.0 V	Set Pulsar Push	398 V
Scan End	1500 m/z	Skimmer 1	55.0 V	Set Reflector	1300 V
		Hexapole 1	26.0 V	Set Flight Tube	9000 V
				Set Detector TOF	1960 V

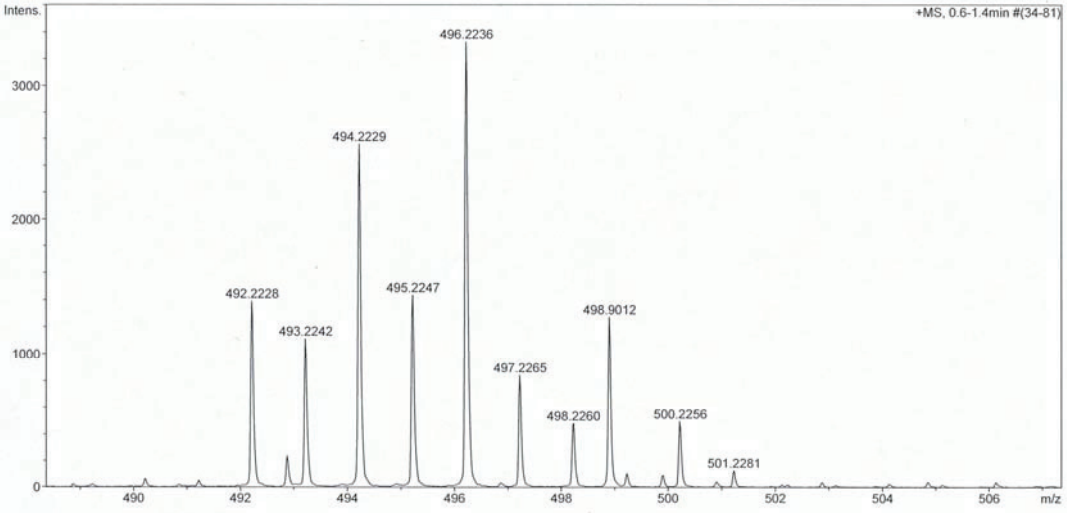

Bruker Daltonics DataAnalysis 3.3 printed: 8/14/2009 2:04:54 PM Page 1 of 2

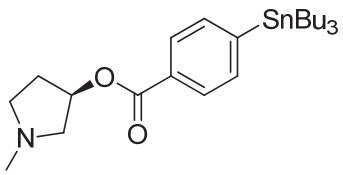

(R)-1-methylpyrrolidin-3-yl 4-(tributylstannyl)benzoate (**6**)
HPLC

```
Data File C:\CHEM32\1\DATA\I MACDONALD\IRM07072010E 2010-07-07 16-18-43\026-0601.D
Sample Name: IRM-118

=====================================================================
Acq. Operator   : Ian                          Seq. Line :   6
Acq. Instrument : Instrument 1                  Location : Vial 26
Injection Date  : 7/7/2010 5:30:14 PM              Inj :   1
                                               Inj Volume : 100 µl
Acq. Method     : C:\Chem32\1\DATA\I MACDONALD\IRM07072010E 2010-07-07 16-18-43\
                  MACDONLAD NORMAL PHASE 20UL.M
Last changed    : 7/7/2010 4:18:41 PM by Ian
Analysis Method : C:\CHEM32\1\DATA\I MACDONALD\IRM07072010E 2010-07-07 16-18-43\026-
                  0601.D\DA.M (MACDONLAD NORMAL PHASE 20UL.M)
Last changed    : 7/28/2010 9:47:52 AM by Ian
                  (modified after loading)
Method Info     : Reverse Phase Methanol
```

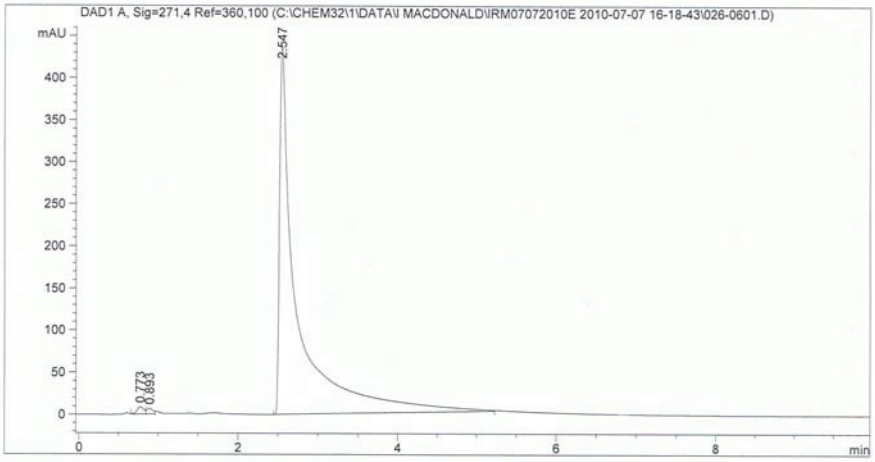


```
=====================================================================
                        Area Percent Report
=====================================================================

Sorted By             :      Signal
Multiplier            :      1.0000
Dilution              :      1.0000
Use Multiplier & Dilution Factor with ISTDs


Signal 1: DAD1 A, Sig=271,4 Ref=360,100

Peak RetTime Type  Width     Area      Height     Area
  #   [min]        [min]   [mAU*s]     [mAU]       %
----|-------|----|-------|----------|----------|--------|
   1   0.773 VV    0.0851   49.92460    8.67594   0.7306
   2   0.893 VV    0.0741   33.51238    6.73509   0.4904
   3   2.547 BB    0.1975 6750.02441  438.80695  98.7790

Totals :                  6833.46140  454.21798

Instrument 1 7/28/2010 9:47:56 AM Ian                    Page   1 of 2
```

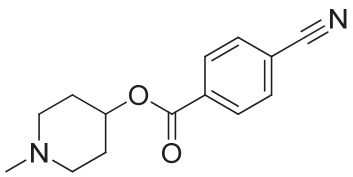

N-methylpiperidin-4-yl 4-cyanobenzoate (**7**)

^{1}H NMR

Courtney Jollymore

Acquisition Time (sec)	3.2768	***Comment***	Bill Pottie 1d_1H CDCl3 {C:\nmr_users} jollymore 8			***Date***	27 May 2010 09:20:16
Date Stamp	27 May 2010 09:20:16						
File Name	\\APPS2\USER\SHARED\Organic Chemistry Research\Courtney Jollymore\Summer 2010\CTJ-3\10\fid					***Frequency (MHz)***	500.13
Nucleus	1H	***Number of Transients***	16	***Origin***	spect	***Original Points Count***	32768
Owner	nmr	***Points Count***	65536	***Pulse Sequence***	zg30	***Receiver Gain***	322.50
SW(cyclical) (Hz)	10000.00	***Solvent***	CHLOROFORM-d	***Spectrum Offset (Hz)***	3239.7507	***Sweep Width (Hz)***	9999.85
Temperature (degree C)	21.987						

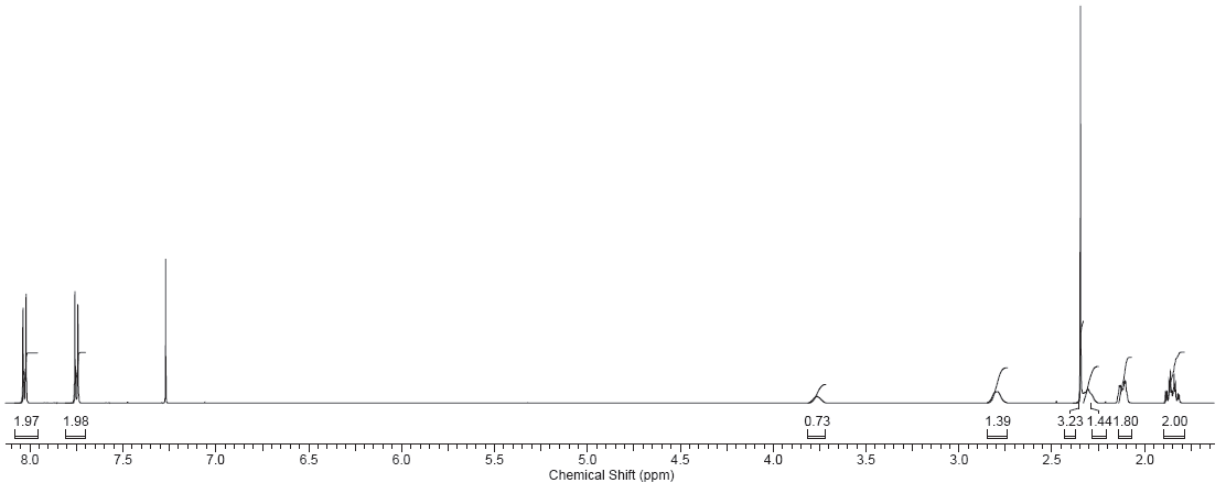

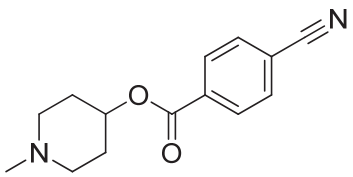

N-methylpiperidin-4-yl 4-cyanobenzoate (**7**)
^{13}C NMR

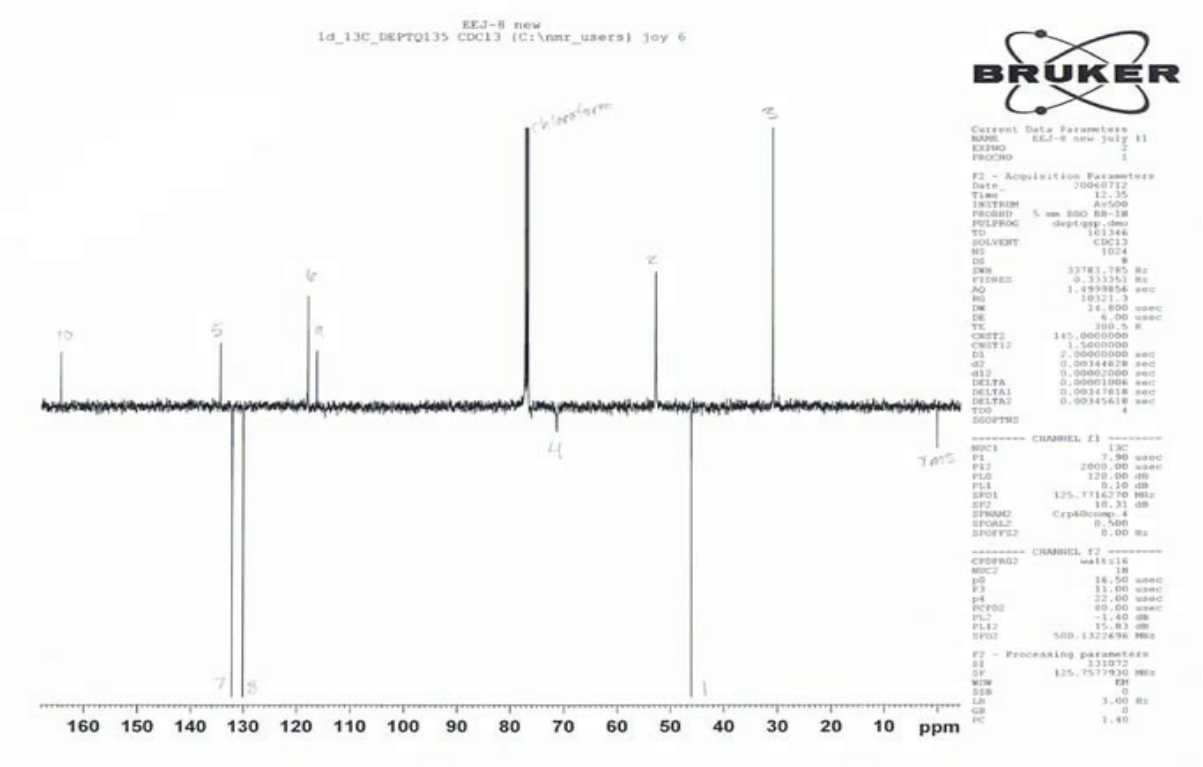

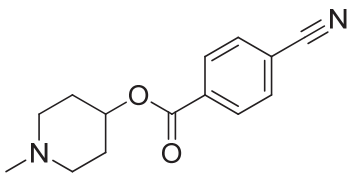

N-methylpiperidin-4-yl 4-cyanobenzoate (**7**)
IR

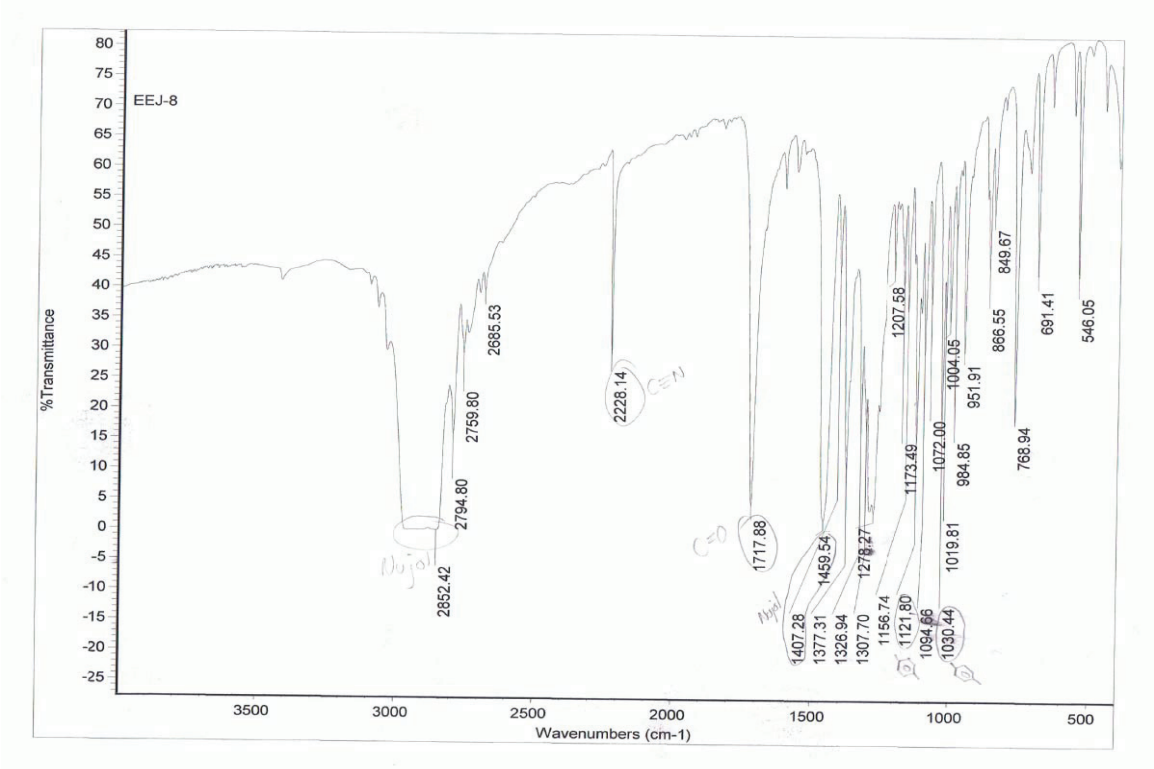

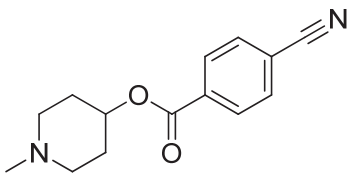

N-methylpiperidin-4-yl 4-cyanobenzoate (**7**)
LRMS

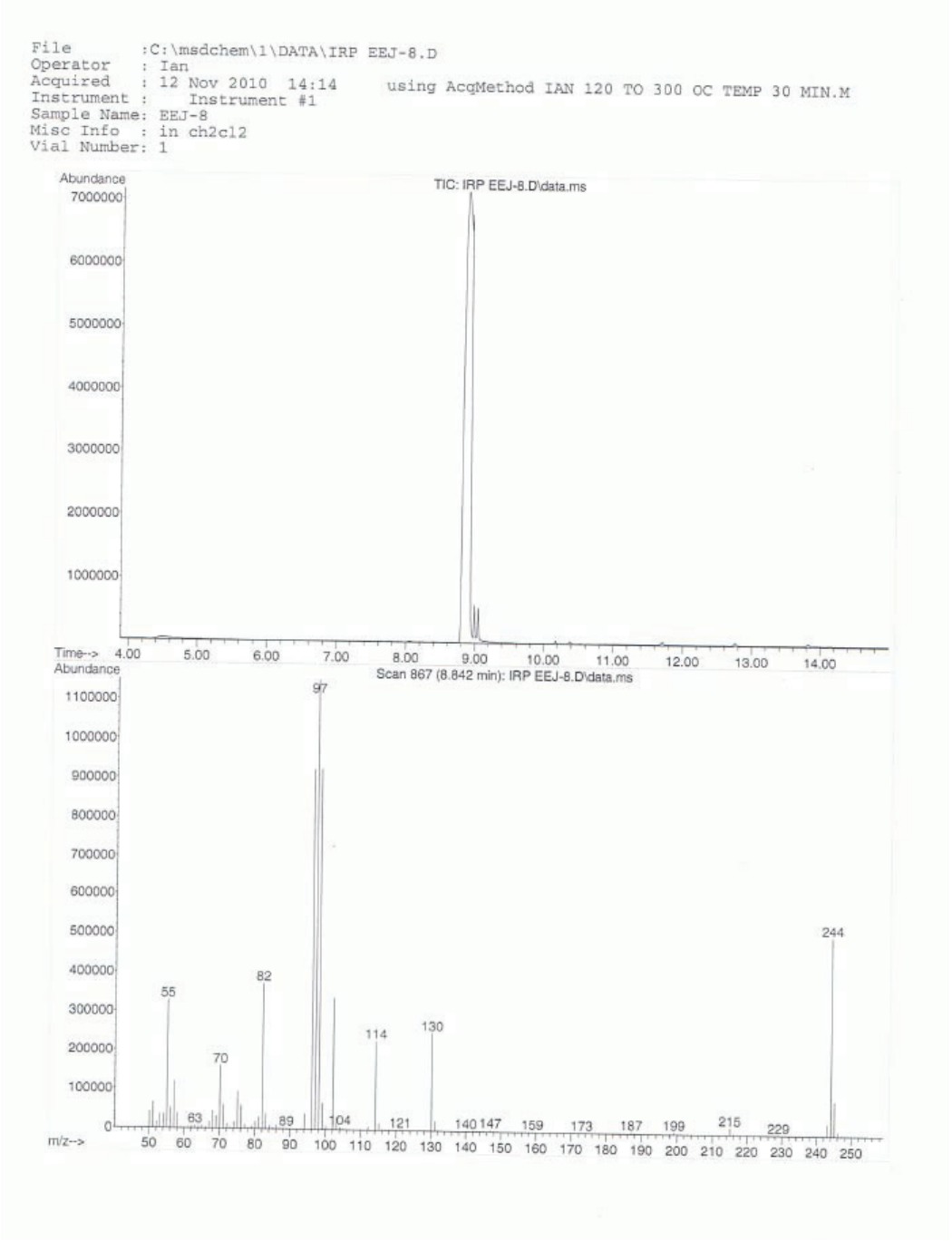

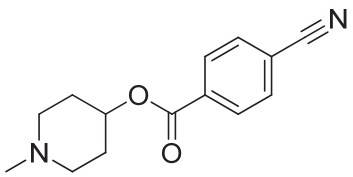

N-methylpiperidin-4-yl 4-cyanobenzoate (**7**)
HRMS

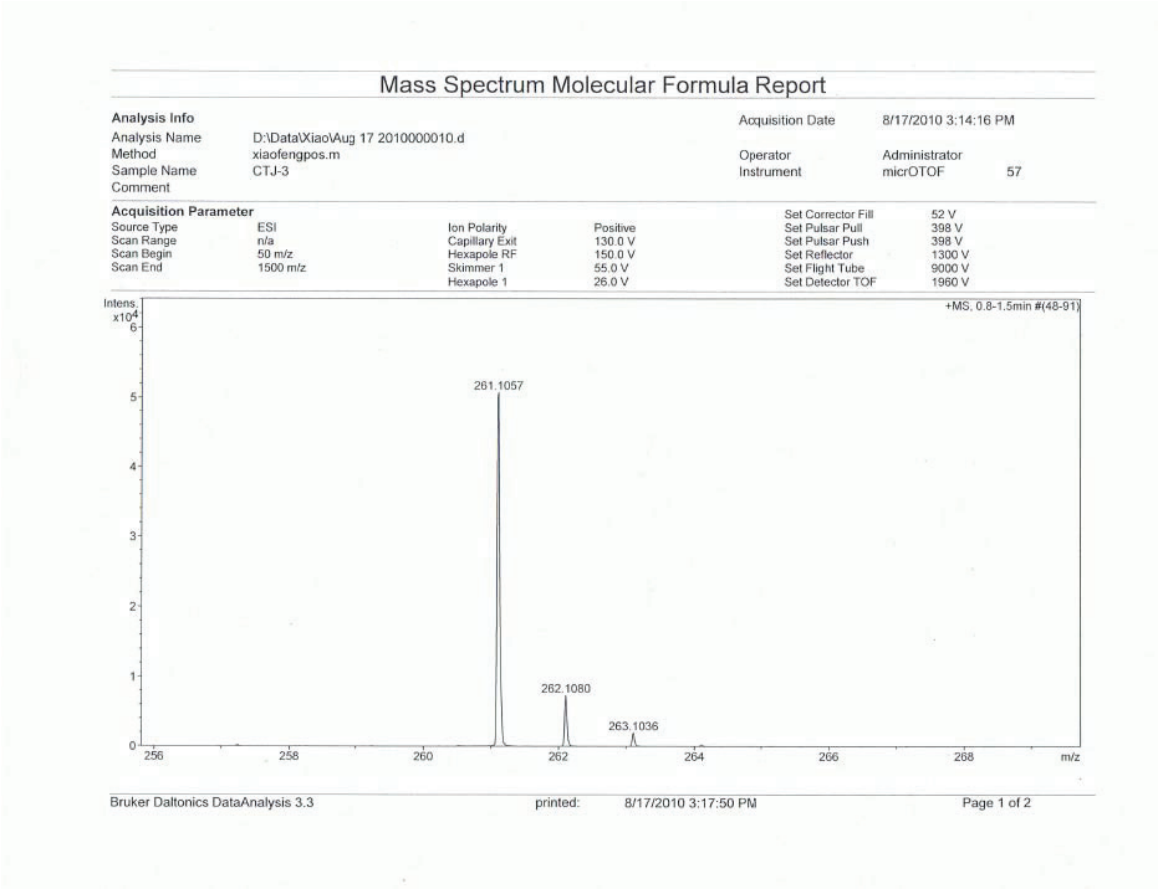

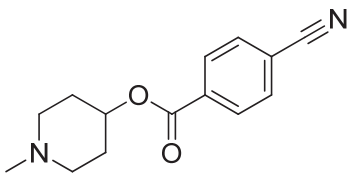

N-methylpiperidin-4-yl 4-cyanobenzoate (**7**)
HPLC

Data File C:\CHEM32\1\DATA\COURTNEY JOLLYMORE\CTJ08102010A 2010-10-08 12-27-11\024-0401.D
Sample Name: EEJ8

Acq. Operator	: Courtney	Seq. Line	: 4
Acq. Instrument	: Instrument 1	Location	: Vial 24
Injection Date	: 10/8/2010 12:49:02 PM	Inj	: 1
		Inj Volume	: 20 µl
Acq. Method	: C:\Chem32\1\DATA\COURTNEY JOLLYMORE\CTJ08102010A 2010-10-08 12-27-11\ REV PHASE METHANOL 20UL.M		
Last changed	: 9/21/2010 11:17:40 AM by Courtney		
Analysis Method	: C:\CHEM32\1\DATA\COURTNEY JOLLYMORE\CTJ08102010A 2010-10-08 12-27-11\ 024-0401.D\DA.M (REV PHASE METHANOL 20UL.M)		
Last changed	: 10/8/2010 12:59:16 PM by Courtney (modified after loading)		
Method Info	: Alzheimer project - ShutDown		

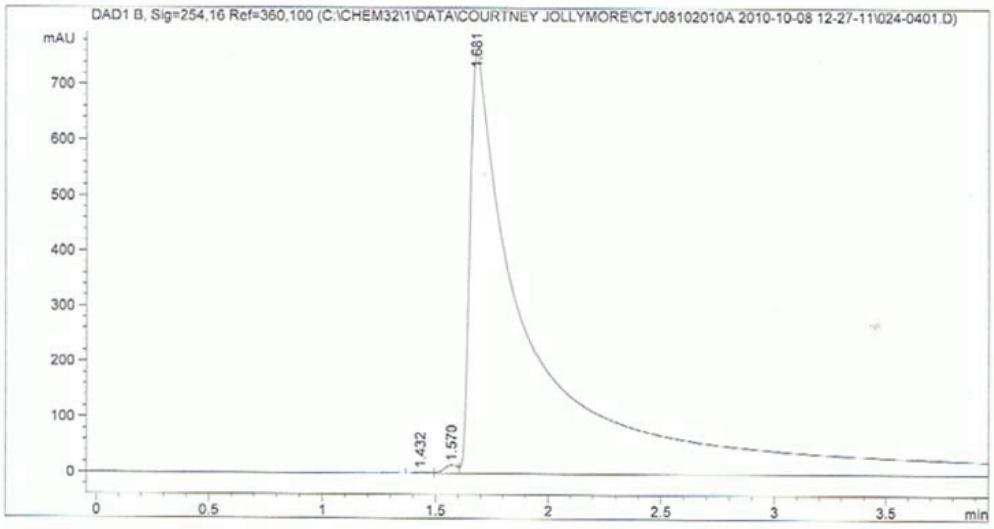

Area Percent Report

Sorted By : Signal
Multiplier : 1.0000
Dilution : 1.0000
Use Multiplier & Dilution Factor with ISTDs

Signal 1: DAD1 B, Sig=254,16 Ref=360,100

Peak #	RetTime [min]	Type	Width [min]	Area [mAU*s]	Height [mAU]	Area %
1	1.432	VV	0.0682	9.72626	2.01968	0.0621
2	1.570	VV	0.0626	62.71712	15.04676	0.4004
3	1.681	VBA	0.2592	1.55895e4	760.23511	99.5375
Totals :				1.56620e4	777.30155	

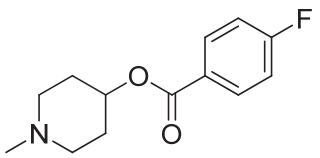

N-methylpiperidin-4-yl 4-fluorobenzoate (**8**)

^{1}H NMR

12/05/2011 2:33:01 PM
Courtney Jollymore

Acquisition Time (sec)	3.2506	***Comment***	Bill Pottie 1d_1H CDCl3 {C:\nmr_users} jollymore 59			***Date***	04 Aug 2010 16:16:16
Date Stamp	04 Aug 2010 16:16:16						
File Name	\\APPS2\USER\SHARED\Organic Chemistry Research\Courtney Jollymore\Summer 2010\NMRs\EEJ-5 Aug 4\10\fid					***Frequency (MHz)***	500.13
Nucleus	1H	***Number of Transients***	16	***Origin***	spect	***Original Points Count***	32768
Owner	nmr	***Points Count***	65536	***Pulse Sequence***	zg30	***Receiver Gain***	128.00
SW(cyclical) (Hz)	10080.65	***Solvent***	CHLOROFORM-d	***Spectrum Offset (Hz)***	3236.5791	***Sweep Width (Hz)***	10080.49
Temperature (degree C)	21.987						

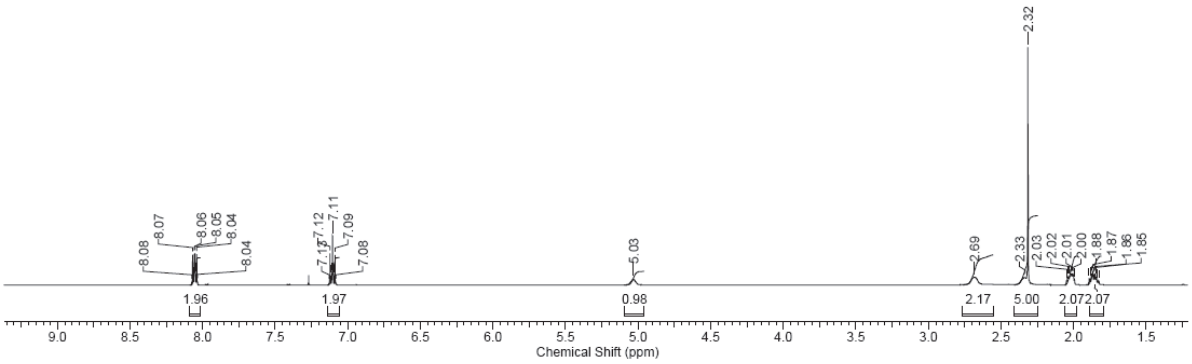

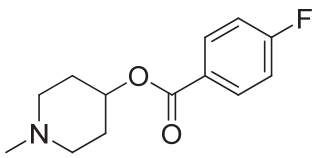

N-methylpiperidin-4-yl 4-fluorobenzoate (**8**)
^{13}C NMR

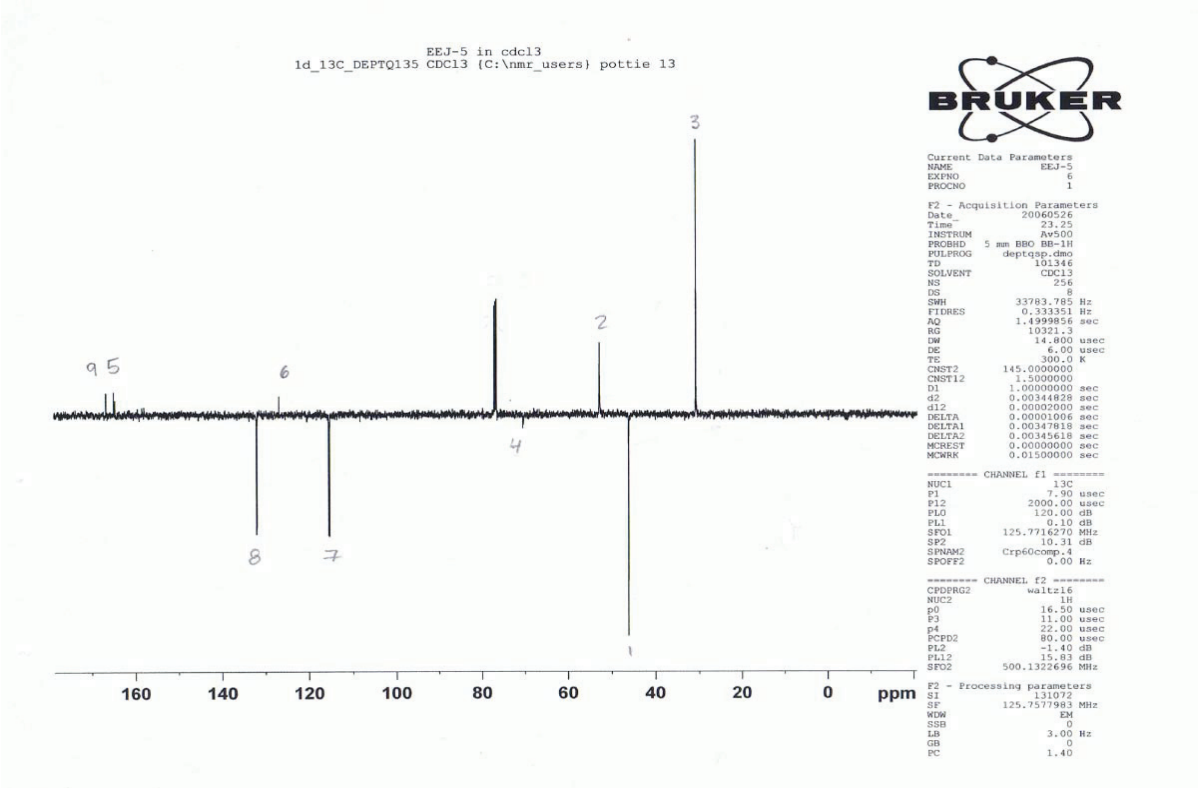

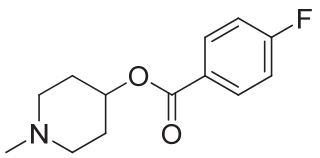

N-methylpiperidin-4-yl 4-fluorobenzoate (**8**)

IR

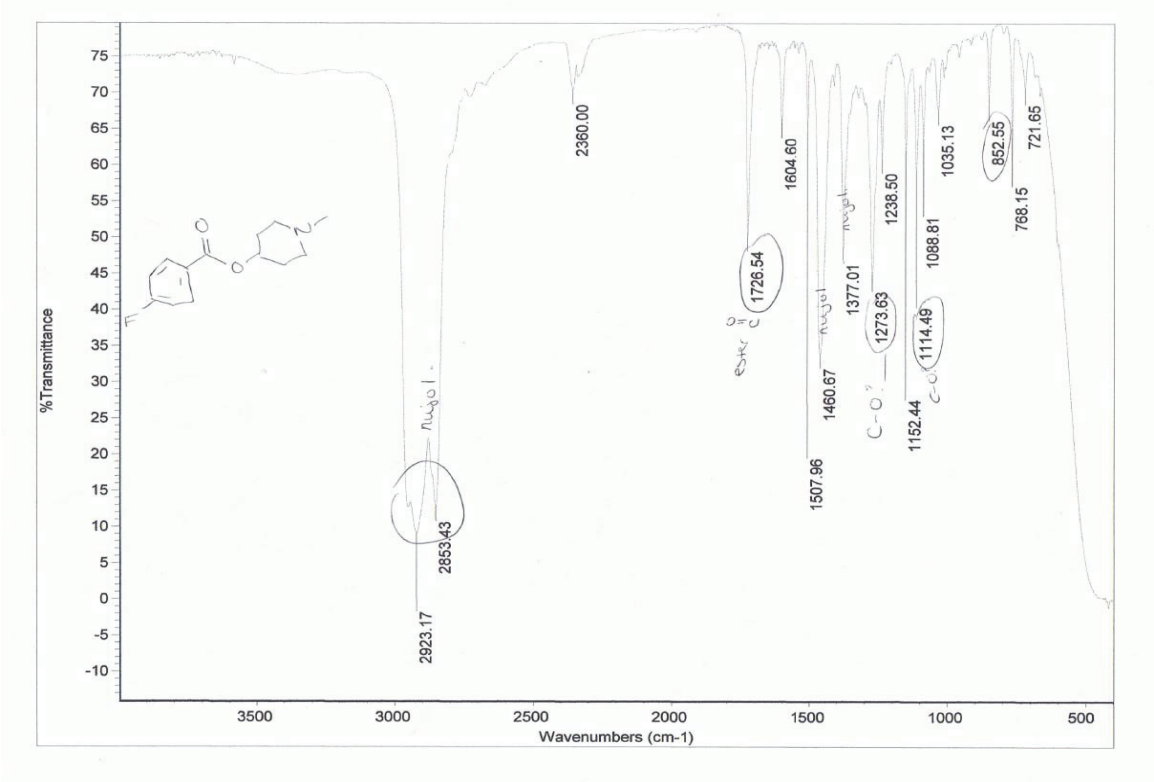

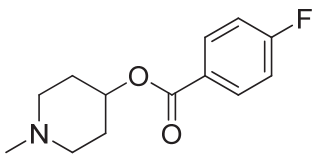

N-methylpiperidin-4-yl 4-fluorobenzoate (**8**)
LRMS

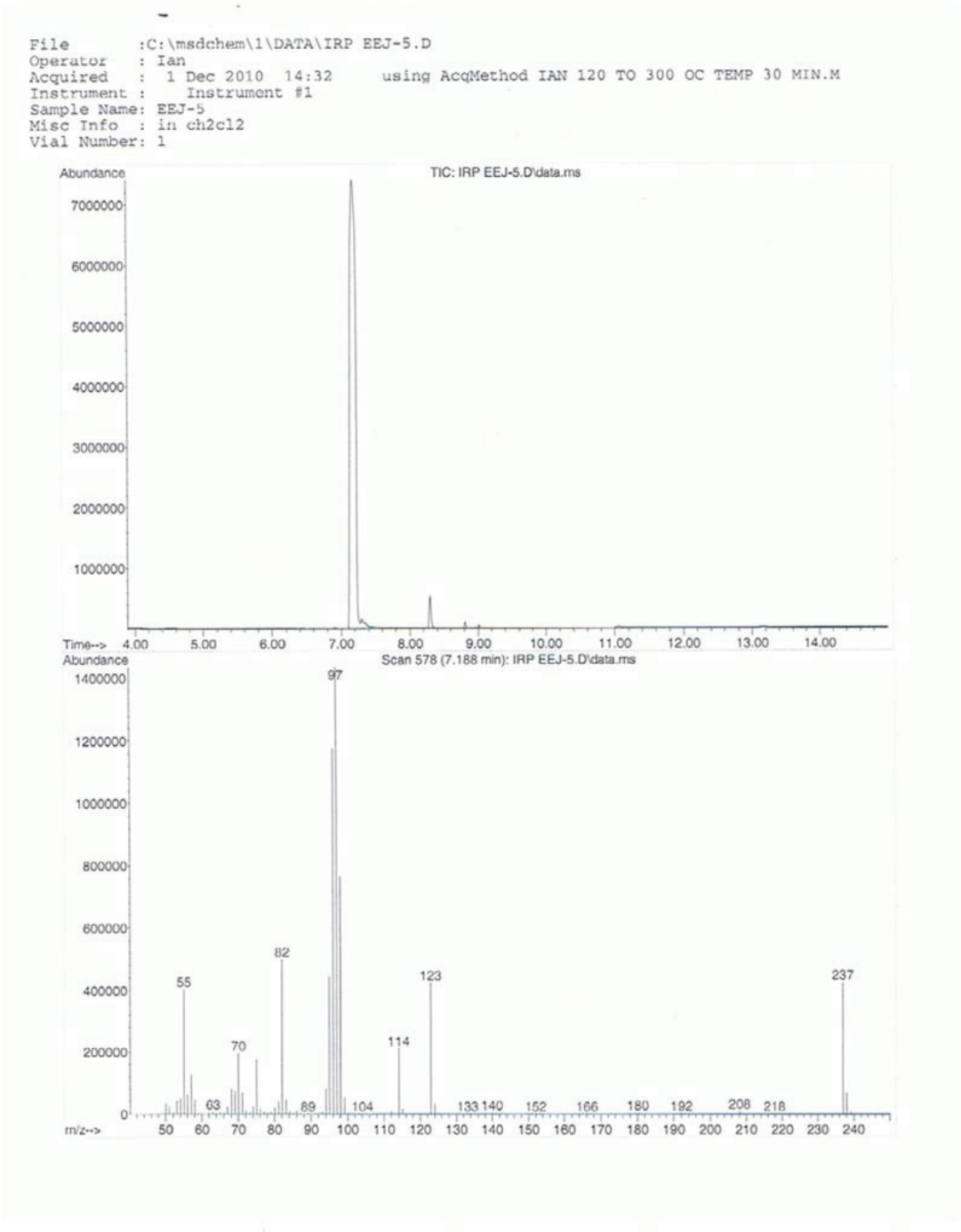

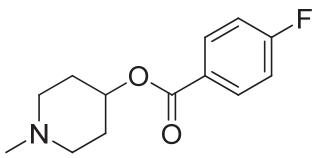

N-methylpiperidin-4-yl 4-fluorobenzoate (**8**)
HRMS

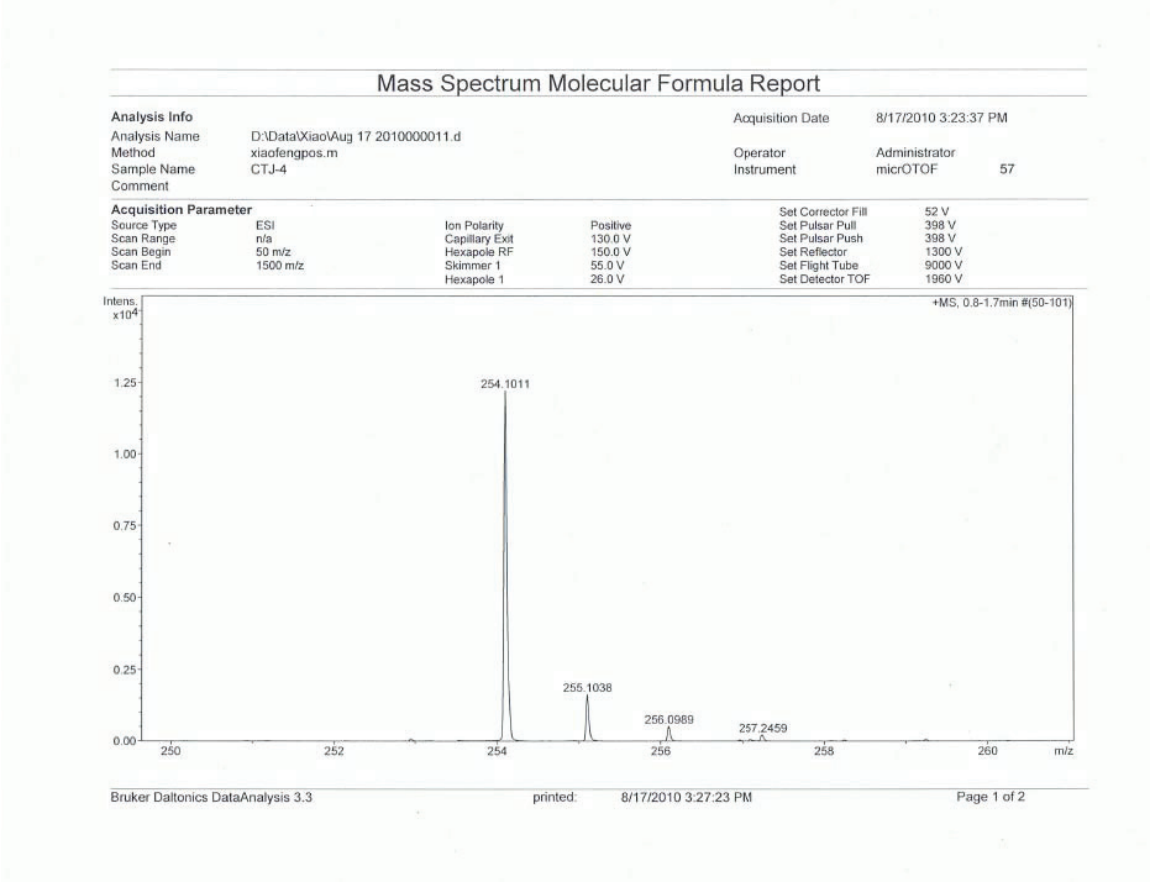

Mass Spectrum Molecular Formula Report

Analysis Info

Analysis Name	D:\Data\Xiao\Aug 17 2010000011.d	Acquisition Date	8/17/2010 3:23:37 PM
Method	xiaofengpos.m	Operator	Administrator
Sample Name	CTJ-4	Instrument	micrOTOF 57
Comment			

Acquisition Parameter

Source Type	ESI	Ion Polarity	Positive	Set Corrector Fill	52 V
Scan Range	n/a	Capillary Exit	130.0 V	Set Pulsar Pull	398 V
Scan Begin	50 m/z	Hexapole RF	150.0 V	Set Pulsar Push	398 V
Scan End	1500 m/z	Skimmer 1	55.0 V	Set Reflector	1300 V
		Hexapole 1	26.0 V	Set Flight Tube	9000 V
				Set Detector TOF	1960 V

Bruker Daltonics DataAnalysis 3.3 printed: 8/17/2010 3:27:23 PM Page 1 of 2

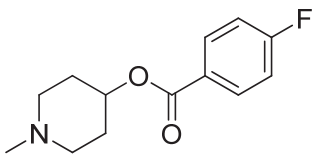

N-methylpiperidin-4-yl 4-fluorobenzoate (**8**)
HPLC

Data File C:\Chem32\1\DATA\COURTNEY JOLLYMORE\CTJ21092010B 2010-09-21 16-15-48\021-0201.D
Sample Name: EEJ-5

Acq. Operator	: Courtney	Seq. Line	: 2
Acq. Instrument	: Instrument 1	Location	: Vial 21
Injection Date	: 9/21/2010 4:24:10 PM	Inj	: 1
		Inj Volume	: 20 µl
Sequence File	: C:\Chem32\1\DATA\COURTNEY JOLLYMORE\CTJ21092010B 2010-09-21 16-15-48\CTJ21092010B.S		
Method	: C:\Chem32\1\DATA\COURTNEY JOLLYMORE\CTJ21092010B 2010-09-21 16-15-48\REV PHASE METHANOL 20UL.M		
Last changed	: 9/21/2010 11:17:40 AM by Courtney		
Method Info	: Reverse Phase Methanol		

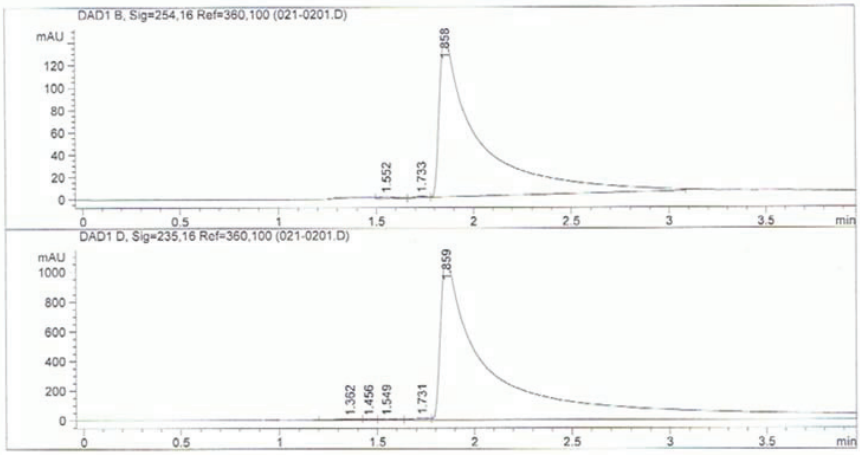

Fraction Information

Fraction collection off

No Fractions found.

Area Percent Report

Sorted By	:	Signal
Multiplier	:	1.0000
Dilution	:	1.0000

Use Multiplier & Dilution Factor with ISTDs

Instrument 1 9/21/2010 4:29:24 PM Courtney Page 1 of 2

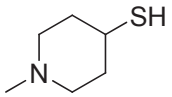

N-methyl-4-piperidinethiol (**9**)
^{1}H NMR

Acquisition Time (sec)	3.2768	***Comment***	Bill Pottie 1d_1H CDCl3 (C:\nmr_users) imacdonald 29			***Date***	26 Nov 2010 04:12:48
Date Stamp	26 Nov 2010 04:12:48						
File Name	\\APPS2\USER\SHARED\Organic Chemistry Research\Ian Macdonald\NMR Data\Ian Macdonald\NMR\IRM-135 Nov25, 2010\10\fid						
Frequency (MHz)	500.13	***Nucleus***	1H	***Number of Transients***	64	***Origin***	spect
Original Points Count	32768	***Owner***	nmr	***Points Count***	32768	***Pulse Sequence***	zg30
Receiver Gain	362.00	***SW(cyclical) (Hz)***	10000.00	***Solvent***	CHLOROFORM-d	***Spectrum Offset (Hz)***	3238.7588
Spectrum Type	STANDARD	***Sweep Width (Hz)***	9999.70	***Temperature (degree C)***	21.987		

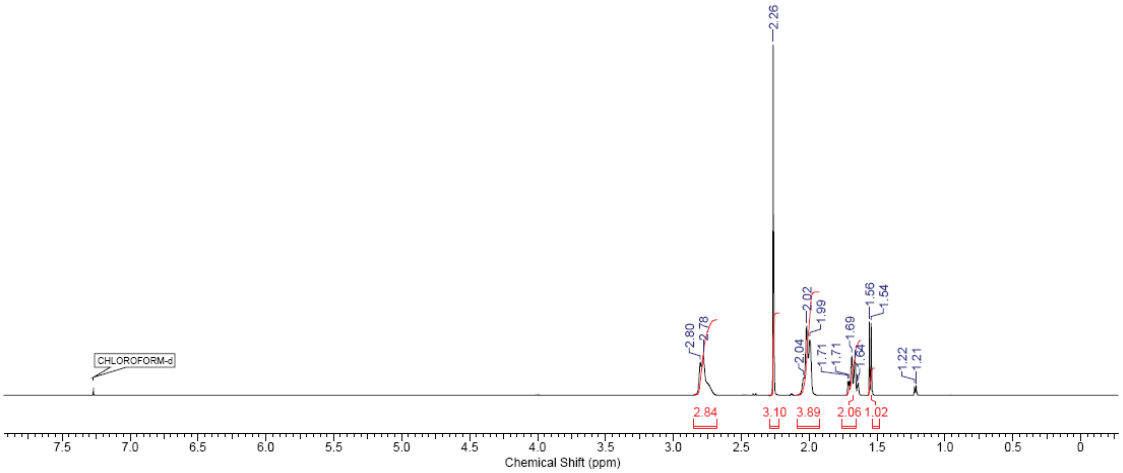

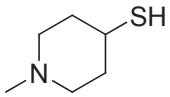

N-methyl-4-piperidinethiol (**9**)
^{13}C NMR

01/12/2010 1:49:31 PM

Acquisition Time (sec)	0.7600				
Comment	Bill Pottie 1d_13C_DEPTQ135_n CDCl3 {C:\nmr_users} imacdonald 26 Best S/N after 128 scans was 51.8 Best S/N after 256 scans was 81.6 Best S/N after 384 scans was 97.3 Best S/N after 512 scans was 115.5 Best S/N after 640 scans was 133.6 Best S/N after				
Date	30 Nov 2010 19:17:20	***Date Stamp***	30 Nov 2010 19:17:20		
File Name	\\APPS2\USER\SHARED\Organic Chemistry Research\Ian Macdonald\NMR Data\Ian Macdonald\NMR\IRM-135 Nov 29, 2010\11\PDATA\1\1r				
Frequency (MHz)	125.76	***Nucleus***	13C	***Number of Transients***	896
Origin	spect	***Original Points Count***	25335	***Owner***	nmr
Points Count	65536	***Pulse Sequence***	deptqsp.dmo	***Receiver Gain***	9195.20
SW(cyclical) (Hz)	33333.33	***Solvent***	CHLOROFORM-d	***Spectrum Offset (Hz)***	13815.9336
Sweep Width (Hz)	33332.82	***Temperature (degree C)***	21.987		

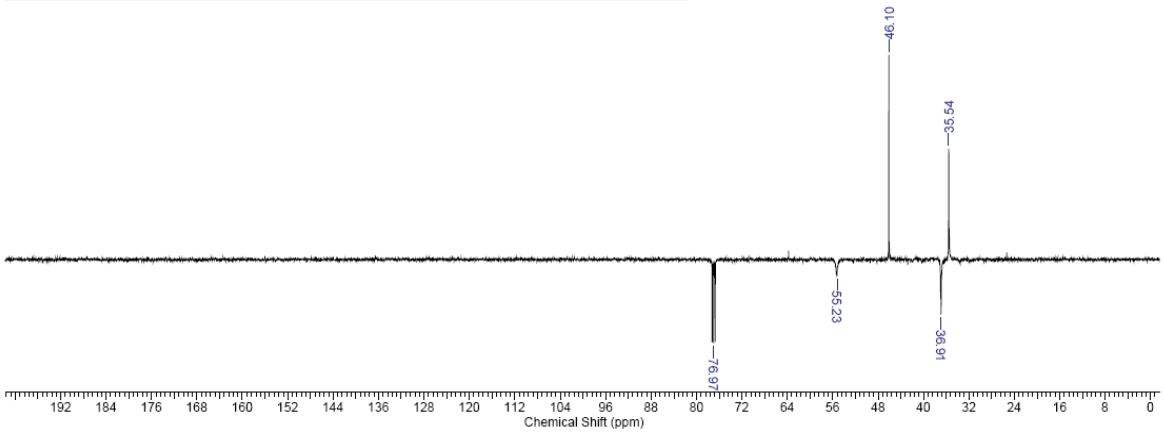

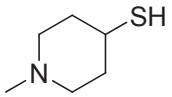

N-methyl-4-piperidinethiol (**9**)
IR

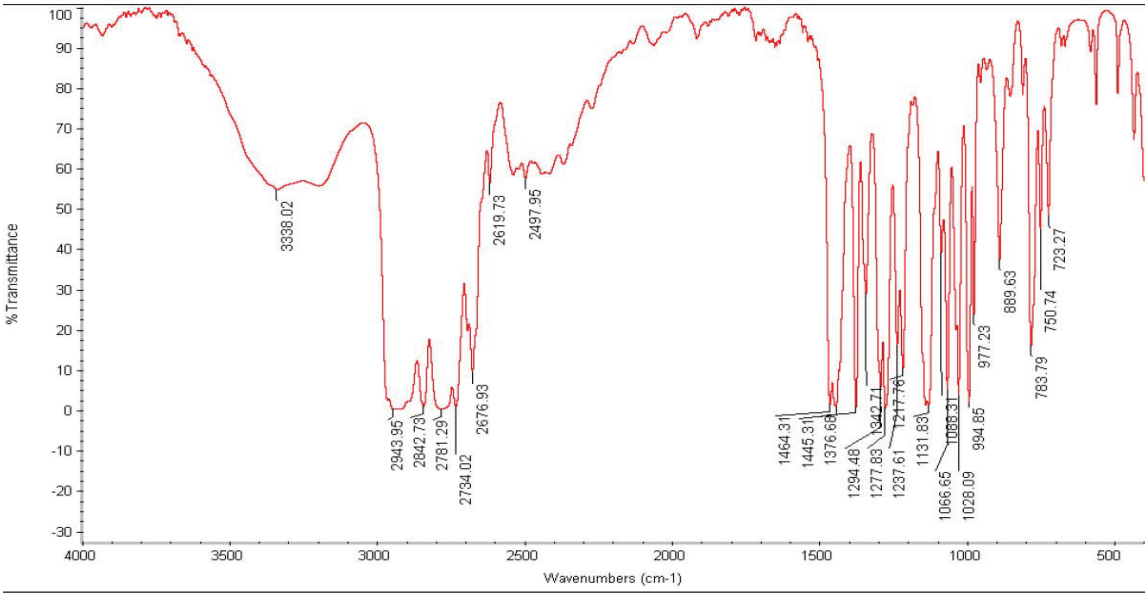

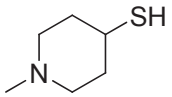

N-methyl-4-piperidinethiol (**9**)
LRMS

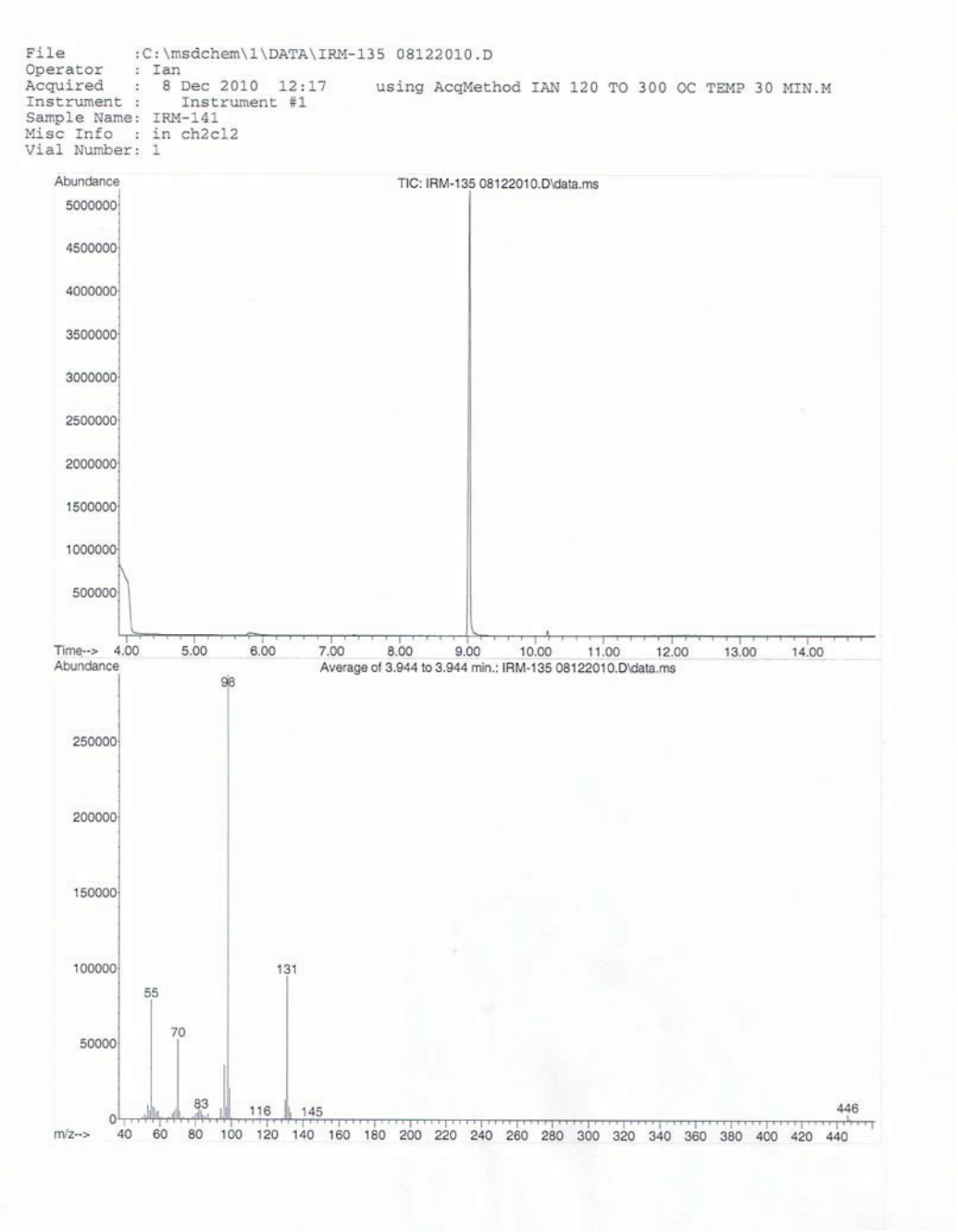

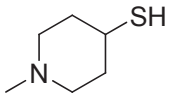

N-methyl-4-piperidinethiol (**9**)
HRMS

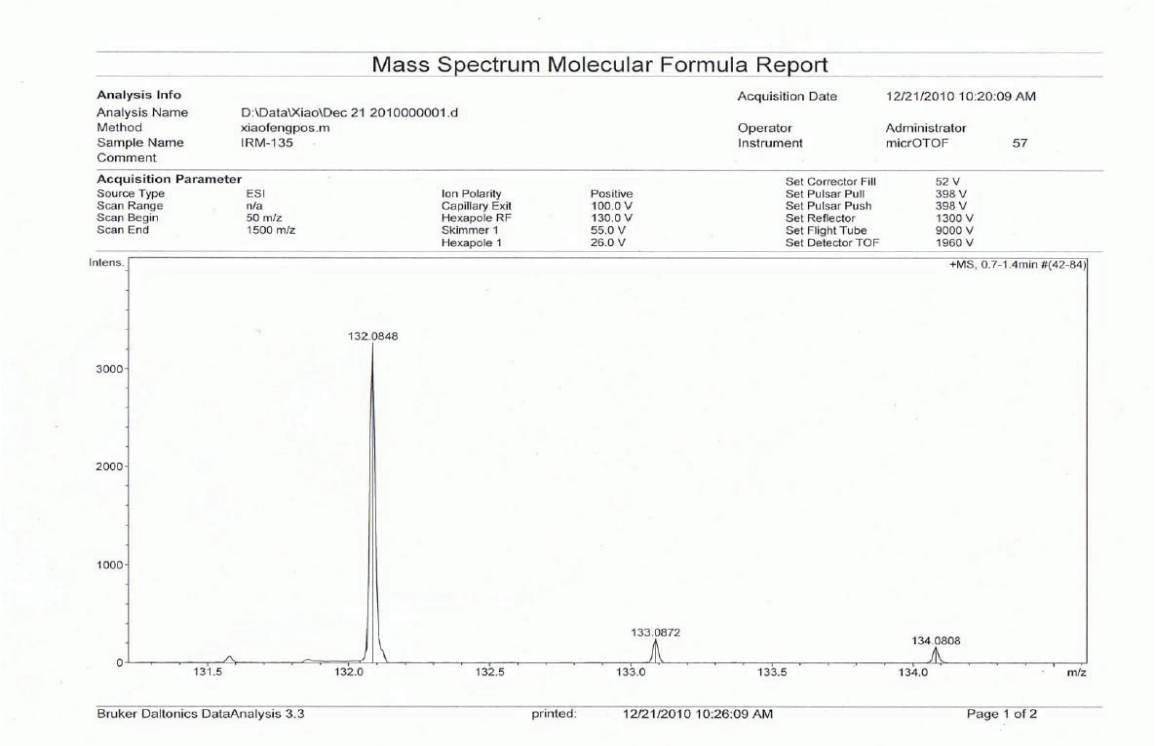

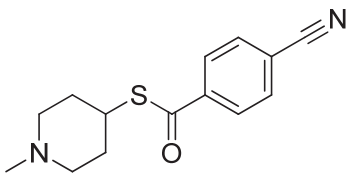

(N-methylpiperidin-4-yl) 4-cyanobenzenecarbothioate (**10**)
^{1}H NMR

10/05/2011 4:36:04 PM
Courtney Jollymore

Acquisition Time (sec)	3.2768	*Comment*	Bill Pottie 1d 1H CDCl3 {C:\nmr_users} jollymore 8			*Date*	27 May 2010 09:20:16
Date Stamp	27 May 2010 09:20:16						
File Name	\\APPS2\USER\SHARED\Organic Chemistry Research\Courtney Jollymore\Summer 2010\CTJ-3\10\fid					*Frequency (MHz)*	500.13
Nucleus	1H	*Number of Transients*	16	*Origin*	spect	*Original Points Count*	32768
Owner	nmr	*Points Count*	65536	*Pulse Sequence*	zg30	*Receiver Gain*	322.50
SW(cyclical) (Hz)	10000.00	*Solvent*	CHLOROFORM-d	*Spectrum Offset (Hz)*	3239.7507	*Sweep Width (Hz)*	9999.85
Temperature (degree C)	21.987						

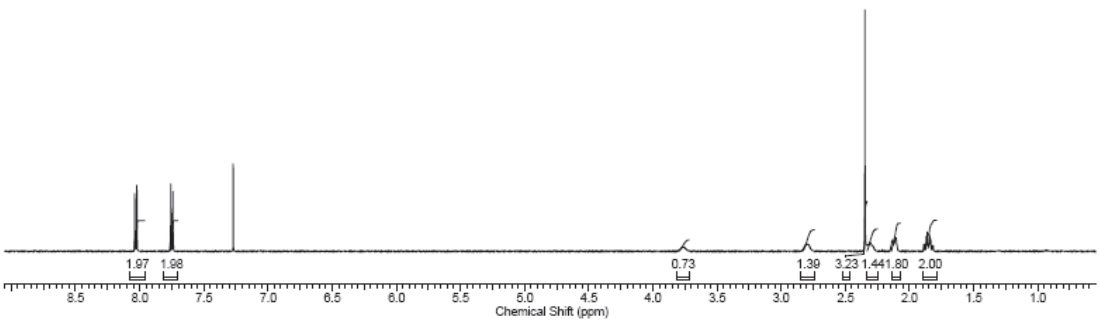

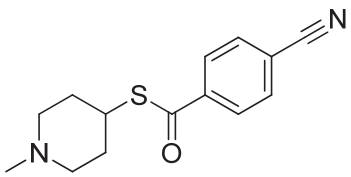

(N-methylpiperidin-4-yl) 4-cyanobenzenecarbothioate (**10**)

^{13}C NMR

Acquisition Time (sec)	0.7499				
Comment	Bill Pottie 1d_13C_DEPTQ135_n CDCl3 {C:\nmr_users} jollymore 8 Best S/N after 128 scans was 41.7 Best S/N after 256 scans was 61.2 Best S/N after 384 scans was 78.1 Best S/N after 512 scans was 83.7				
Date	27 May 2010 20:21:36	***Date Stamp***	27 May 2010 20:21:36		
File Name	\\APPS2\USER\SHARED\Organic Chemistry Research\Courtney Jollymore\Summer 2010\CTJ-3\11\PDATA\1\1r				
Frequency (MHz)	125.76	***Nucleus***	13C	***Number of Transients***	512
Origin	spect	***Original Points Count***	25335	***Owner***	nmr
Points Count	65536	***Pulse Sequence***	deptqsp.dmo	***Receiver Gain***	9195.20
SW(cyclical) (Hz)	33783.79	***Solvent***	CHLOROFORM-d	***Spectrum Offset (Hz)***	13827.1895
Sweep Width (Hz)	33783.27	***Temperature (degree C)***	21.987		

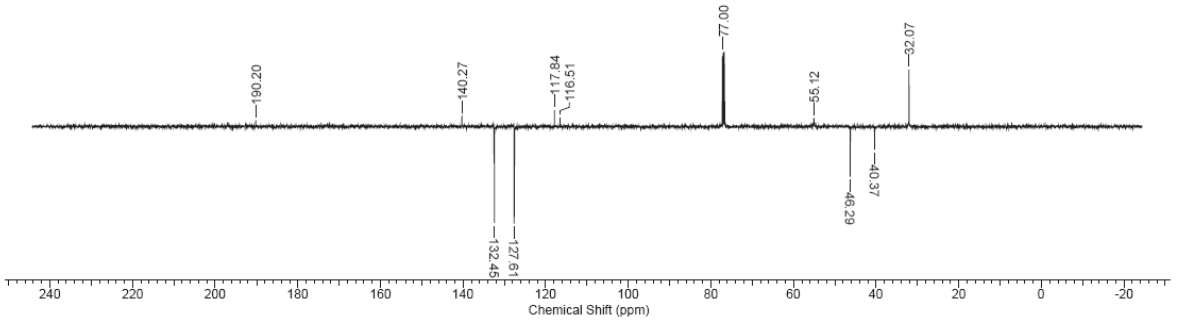

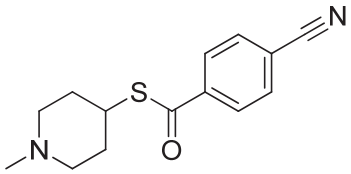

(N-methylpiperidin-4-yl) 4-cyanobenzenecarbothioate (**10**)

IR

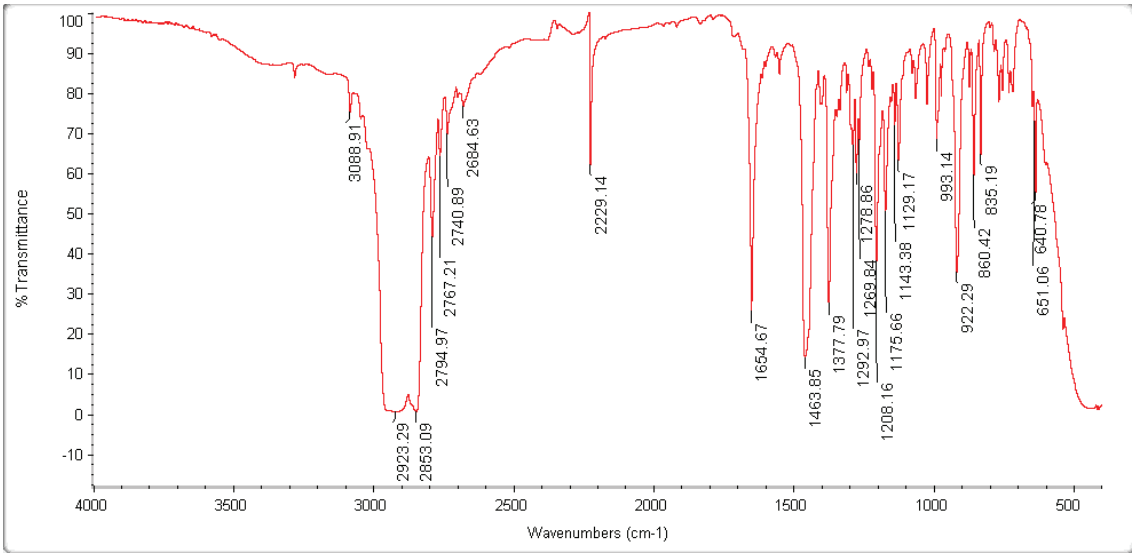

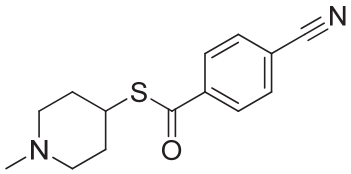

(N-methylpiperidin-4-yl) 4-cyanobenzenecarbothioate (**10**)
LRMS

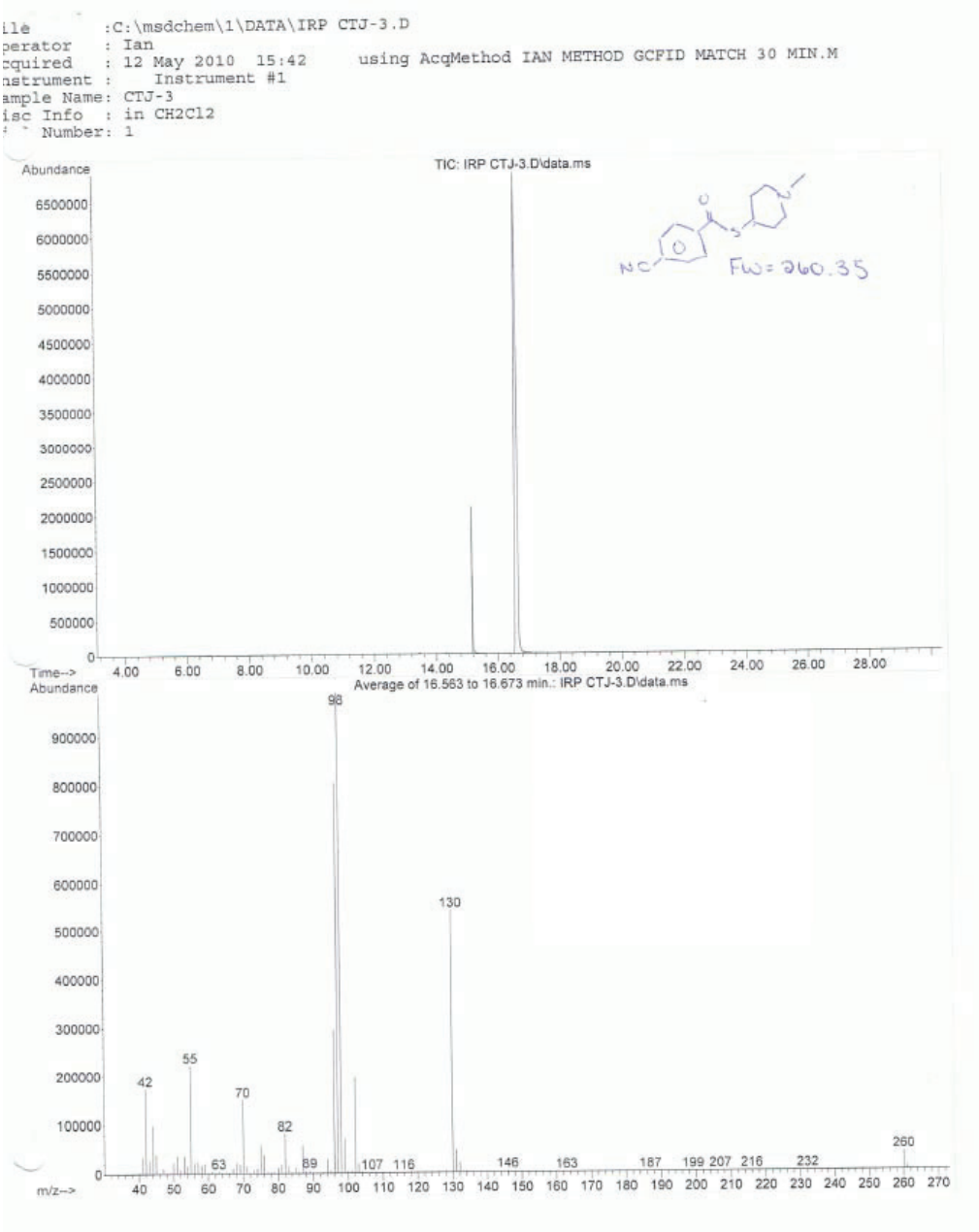

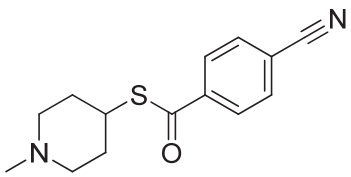

(N-methylpiperidin-4-yl) 4-cyanobenzenecarbothioate (**10**)
HRMS

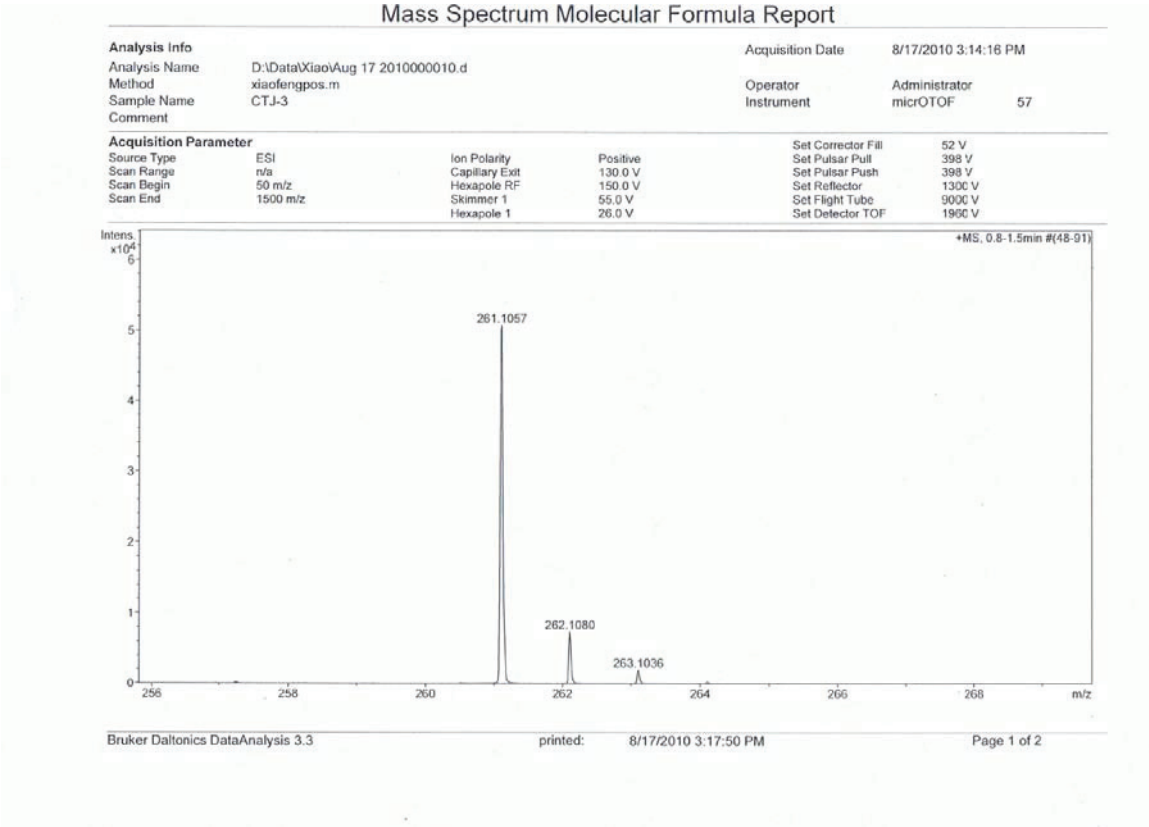

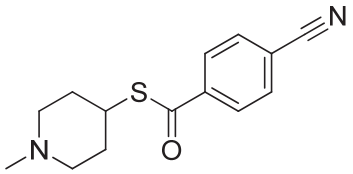

(N-methylpiperidin-4-yl) 4-cyanobenzenecarbothioate (**10**)
HPLC

Data File C:\Chem32\1\DATA\JEREMY\JER091008CFRACS 2008-10-09 15-09-59\POTTIE\IRP27052010B 2010-05-
Sample Name: CTJ-3

Acq. Operator	: Ian	Seq. Line	: 4
Acq. Instrument	: Instrument 1	Location	: Vial 14
Injection Date	: 5/27/2010 12:35:06 PM	Inj	: 1
		Inj Volume	: 20 µl
Sequence File	: C:\Chem32\1\DATA\JEREMY\JER091008CFRACS 2008-10-09 15-09-59\POTTIE\IRP27052010B 2010-05-27 12-13-18\IRP27052010B.S		
Method	: C:\Chem32\1\DATA\JEREMY\JER091008CFRACS 2008-10-09 15-09-59\POTTIE\IRP27052010B 2010-05-27 12-13-18\REV PHASE METHANOL 20UL.M		
Last changed	: 5/27/2010 12:09:38 PM by Ian		
Method Info	: Reverse Phase Methanol		

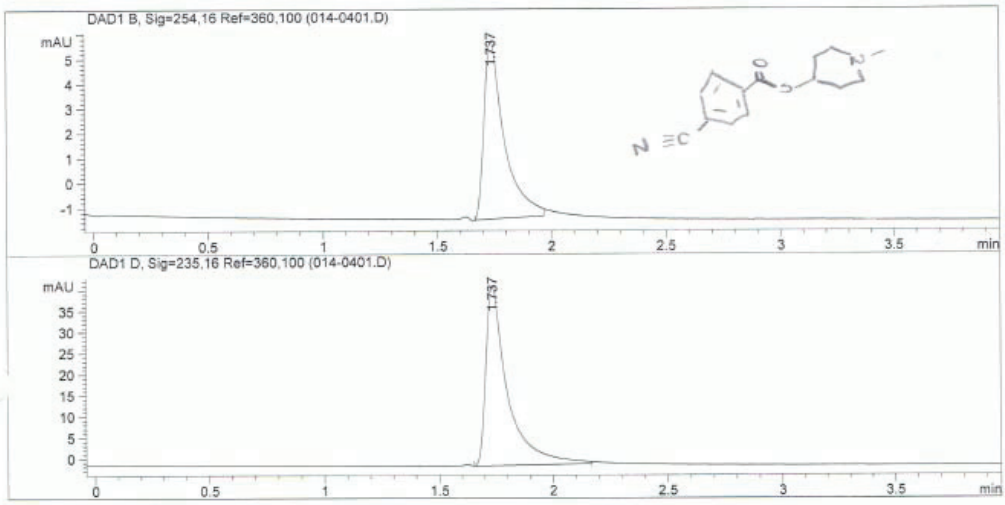

Fraction Information

Fraction collection off

No Fractions found.

Area Percent Report

Sorted By	:	Signal
Multiplier	:	1.0000
Dilution	:	1.0000

Use Multiplier & Dilution Factor with ISTDs

Instrument 1 5/27/2010 12:40:25 PM Ian Page 1 of 2

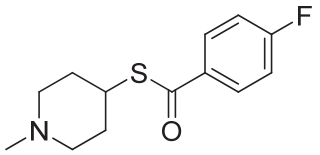

(N-methylpiperidin-4-yl) 4-fluorobenzenecarbothioate (**11**)

^{1}H NMR

Acquisition Time (sec)	3.2768	***Comment***	Bill Pottie 1d_1H CDCl3 {C:\nmr_users} jollymore 52			***Date***	14 Jul 2010 01:01:04
Date Stamp	14 Jul 2010 01:01:04						
File Name	\\APPS2\USER\SHARED\Organic Chemistry Research\Courtney Jollymore\Summer 2010\NMRs\CTJ 4(2)\10\fid					***Frequency (MHz)***	500.13
Nucleus	1H	***Number of Transients***	16	***Origin***	spect	***Original Points Count***	32768
Owner	nmr	***Points Count***	65536	***Pulse Sequence***	zg30	***Receiver Gain***	362.00
SW(cyclical) (Hz)	10000.00	***Solvent***	CHLOROFORM-d	***Spectrum Offset (Hz)***	3239.9033	***Spectrum Type***	STANDARD
Sweep Width (Hz)	9999.85	***Temperature (degree C)***	21.987				

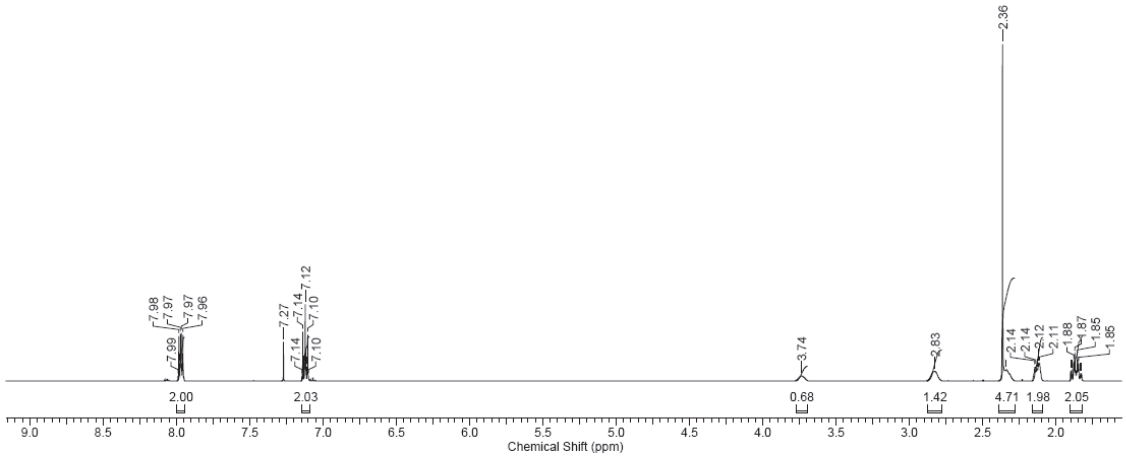

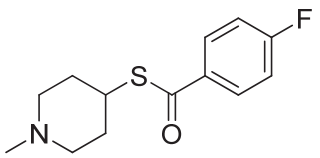

(N-methylpiperidin-4-yl) 4-fluorobenzenecarbothioate (**11**)

^{13}C NMR

20/12/2010 5:54:13 PM
Courtney Jollymore

Acquisition Time (sec)	0.7600				
Comment	Bill Pottie 1d_13C_DEPTQ135_n CDCl3 {C:\nmr_users} pilgrim 27 Best S/N after 128 scans was 14.8 Best S/N after 256 scans was 20.7 Best S/N after 384 scans was 24.0 Best S/N after 512 scans was 28.5				
Date	15 Jul 2010 17:18:08	*Date Stamp*	15 Jul 2010 17:18:08		
File Name	\\STUDENT1\DATA1\USERS\JMSV0502\CTJ-4(2)\10\PDATA\1\1r			*Frequency (MHz)*	125.76
Nucleus	13C	*Number of Transients*	512	*Origin*	spect
Original Points Count	25335	*Owner*	nmr	*Points Count*	65536
Pulse Sequence	deptqsp.dmo	*Receiver Gain*	9195.20	*SW(cyclical) (Hz)*	33333.33
Solvent	CHLOROFORM-d	*Spectrum Offset (Hz)*	13887.9482	*Sweep Width (Hz)*	33332.82
Temperature (degree C)	21.987				

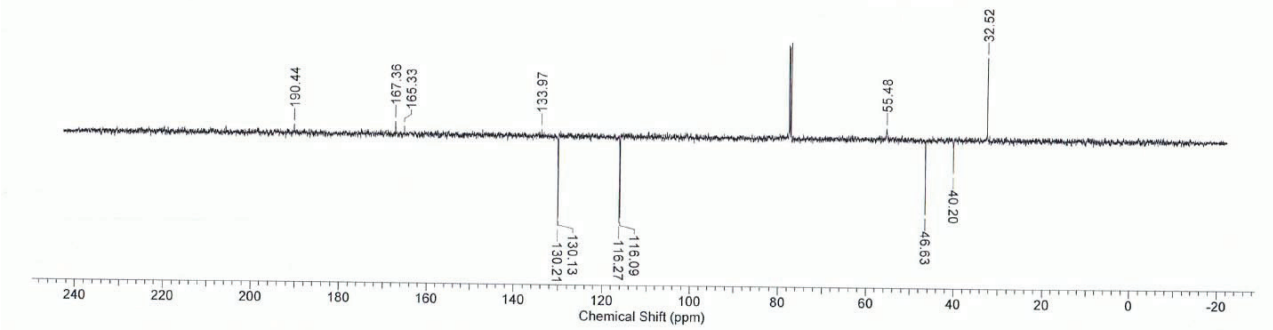

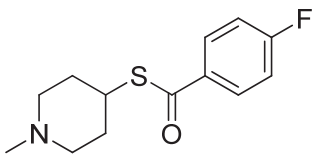

(N-methylpiperidin-4-yl) 4-fluorobenzenecarbothioate (**11**)

IR

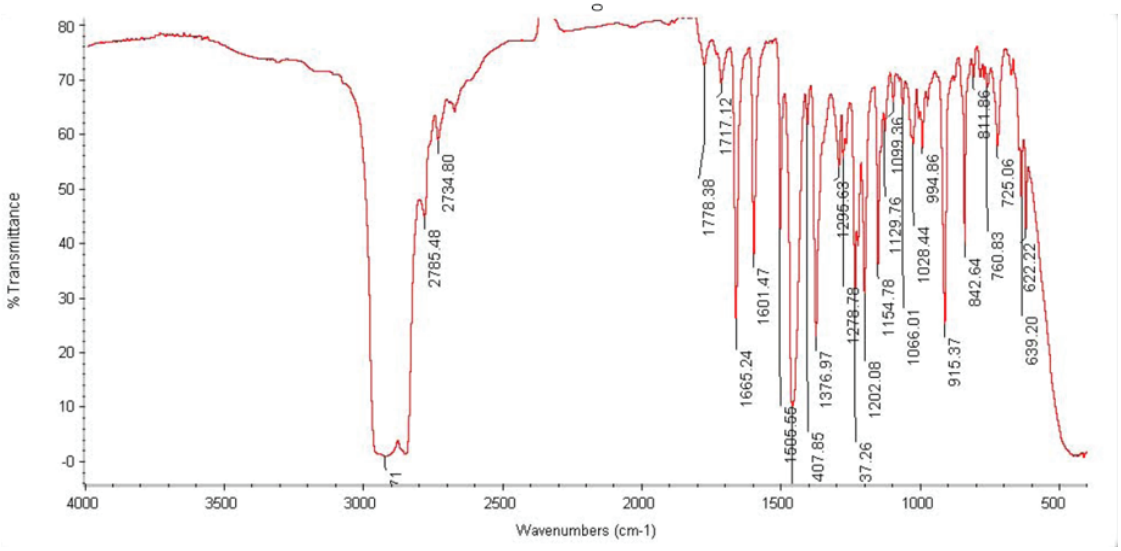

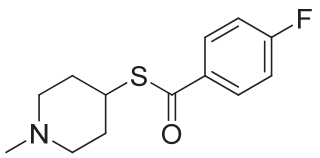

(N-methylpiperidin-4-yl) 4-fluorobenzenecarbothioate (**11**)
LRMS

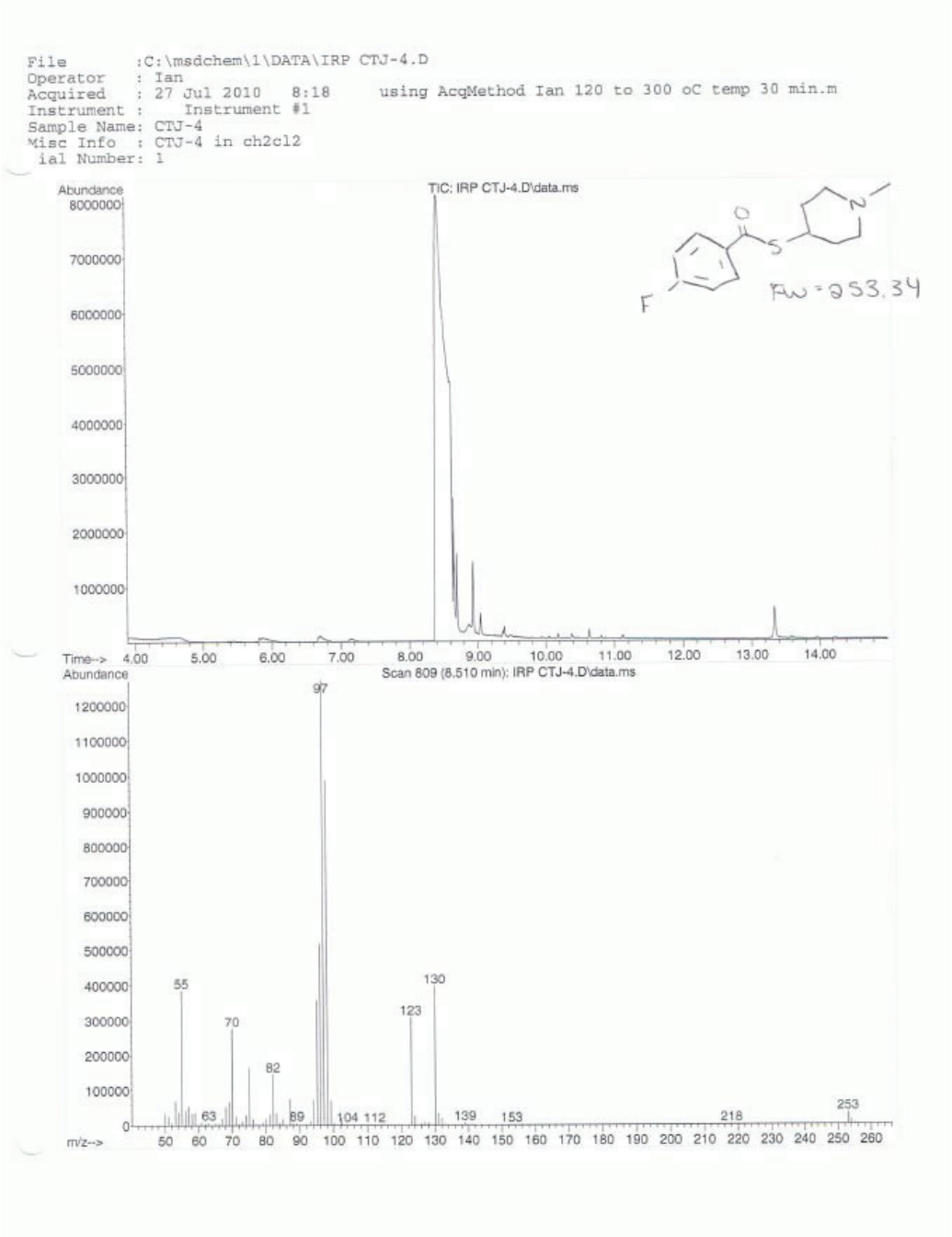

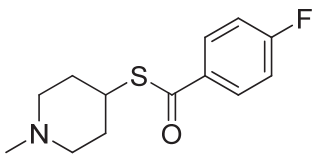

(N-methylpiperidin-4-yl) 4-fluorobenzenecarbothioate (**11**)
HRMS

Mass Spectrum Molecular Formula Report

Analysis Info

Analysis Name	D:\Data\Xiao\Aug 17 2010000011.d	Acquisition Date	8/17/2010 3:23:37 PM
Method	xiaofengpos.m		
Sample Name	CTJ-4	Operator	Administrator
Comment		Instrument	micrOTOF 57

Acquisition Parameter

Source Type	ESI	Ion Polarity	Positive	Set Corrector Fill	52 V
Scan Range	n/a	Capillary Exit	130.0 V	Set Pulsar Pull	398 V
Scan Begin	50 m/z	Hexapole RF	150.0 V	Set Pulsar Push	398 V
Scan End	1500 m/z	Skimmer 1	55.0 V	Set Reflector	1300 V
		Hexapole 1	26.0 V	Set Flight Tube	9000 V
				Set Detector TOF	1960 V

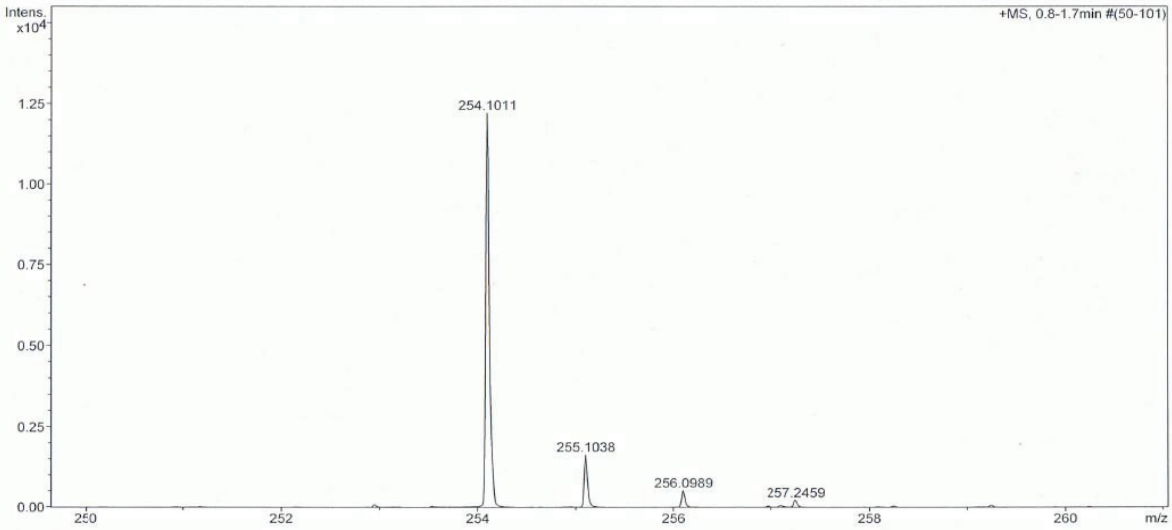

Bruker Daltonics DataAnalysis 3.3 printed: 8/17/2010 3:27:23 PM Page 1 of 2

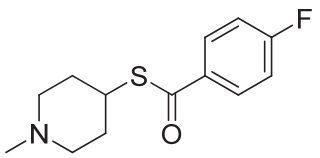

(N-methylpiperidin-4-yl) 4-fluorobenzenecarbothioate (**11**)
HPLC

Data File C:\Chem32\1\DATA\COURTNEY JOLLYMORE\CTJ22072010E 2010-07-23 11-09-38\031-0201.D
Sample Name: CTJ-4

Acq. Operator	: Ian	Seq. Line	: 2
Acq. Instrument	: Instrument 1	Location	: Vial 31
Injection Date	: 7/23/2010 11:20:52 AM	Inj	: 1
		Inj Volume	: 50 µl
Sequence File	: C:\Chem32\1\DATA\COURTNEY JOLLYMORE\CTJ22072010E 2010-07-23 11-09-38\CTJ22072010E.S		
Method	: C:\Chem32\1\DATA\COURTNEY JOLLYMORE\CTJ22072010E 2010-07-23 11-09-38\REV PHASE METHANOL 20UL.M		
Last changed	: 7/23/2010 11:02:17 AM by Ian		
Method Info	: Reverse Phase Methanol		

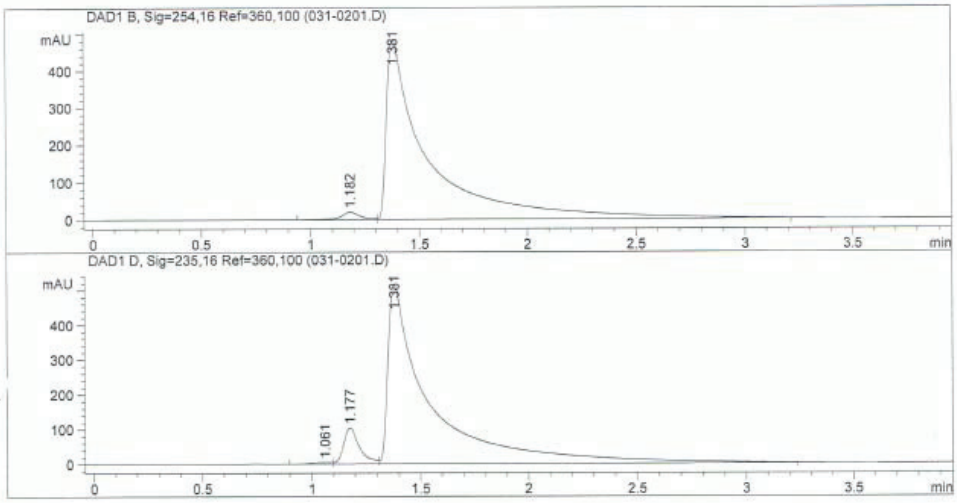

Fraction Information

Fraction collection off

No Fractions found.

Area Percent Report

Sorted By	:	Signal
Multiplier	:	1.0000
Dilution	:	1.0000

Use Multiplier & Dilution Factor with ISTDs

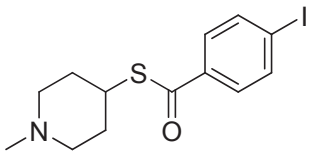

(N-methylpiperidin-4-yl) 4-iodobenzenecarbothioate (**12**)

^{1}H NMR

12/05/2011 1:27:16 PM
Courtney Jollymore

Acquisition Time (sec)	3.2768	***Comment***	Bill Pottie 1d_1H CDCl3 {C:\nmr_users} jollymore 34			***Date***	16 Jun 2010 13:21:20
Date Stamp	16 Jun 2010 13:21:20						
File Name	\\APPS2\USER\SHARED\Organic Chemistry Research\Courtney Jollymore\Summer 2010\NMRs\CTJ-2_3\10\fid					***Frequency (MHz)***	500.13
Nucleus	1H	***Number of Transients***	16	***Origin***	spect	***Original Points Count***	32768
Owner	nmr	***Points Count***	65536	***Pulse Sequence***	zg30	***Receiver Gain***	362.00
SW(cyclical) (Hz)	10000.00	***Solvent***	CHLOROFORM-d	***Spectrum Offset (Hz)***	3239.9033	***Spectrum Type***	STANDARD
Sweep Width (Hz)	9999.85	***Temperature (degree C)***	21.987				

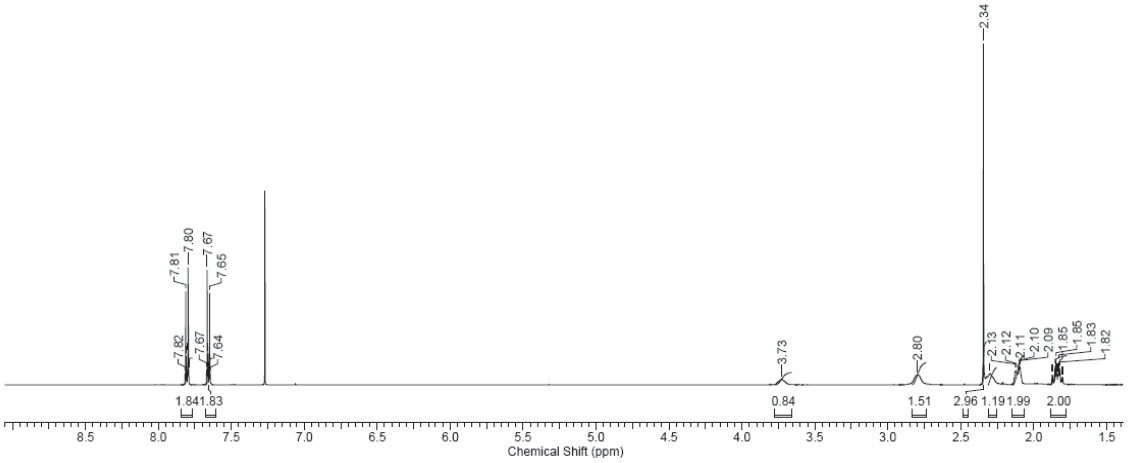

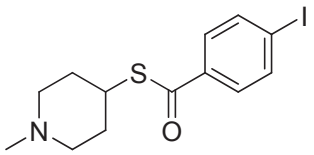

(N-methylpiperidin-4-yl) 4-iodobenzenecarbothioate (**12**)

^{13}C NMR

Acquisition Time (sec)	0.7499				
Comment	Bill Pottie 1d_13C_DEPTQ135_n CDCl3 {C:\nmr_users} jollymore 34 Best S/N after 128 scans was 29.0 Best S/N after 256 scans was 40.1 Best S/N after 384 scans was 50.1 Best S/N after 512 scans was 57.0				
Date	17 Jun 2010 21:42:40	***Date Stamp***	17 Jun 2010 21:42:40		
File Name	\\APPS2\USER\SHARED\Organic Chemistry Research\Courtney Jollymore\Summer 2010\NMRs\CTJ-2_3\11\PDATA\1\1r				
Frequency (MHz)	125.76	***Nucleus***	13C	***Number of Transients***	512
Origin	spect	***Original Points Count***	25335	***Owner***	nmr
Points Count	65536	***Pulse Sequence***	deptqsp.dmo	***Receiver Gain***	9195.20
SW(cyclical) (Hz)	33783.79	***Solvent***	CHLOROFORM-d	***Spectrum Offset (Hz)***	13795.7441
Sweep Width (Hz)	33783.27	***Temperature (degree C)***	21.987		

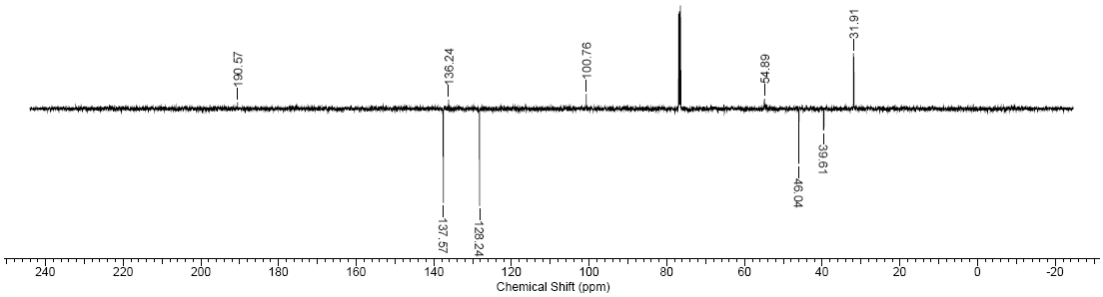

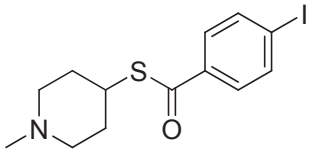

(N-methylpiperidin-4-yl) 4-iodobenzenecarbothioate (**12**)

IR

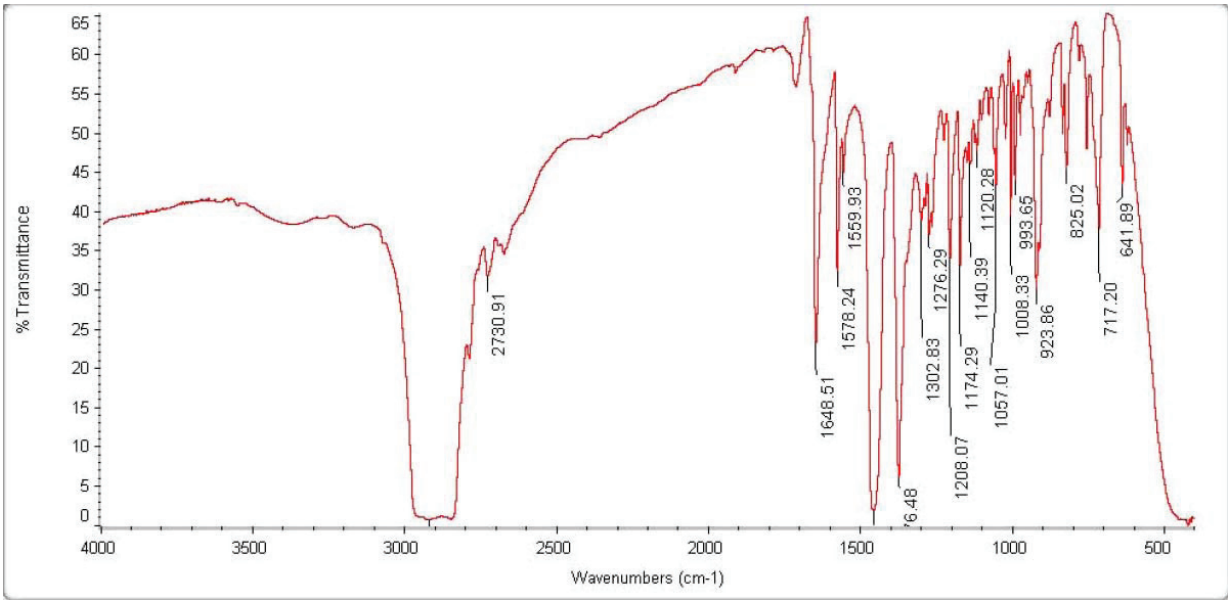

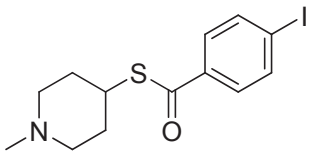

(N-methylpiperidin-4-yl) 4-iodobenzenecarbothioate (**12**)
LRMS

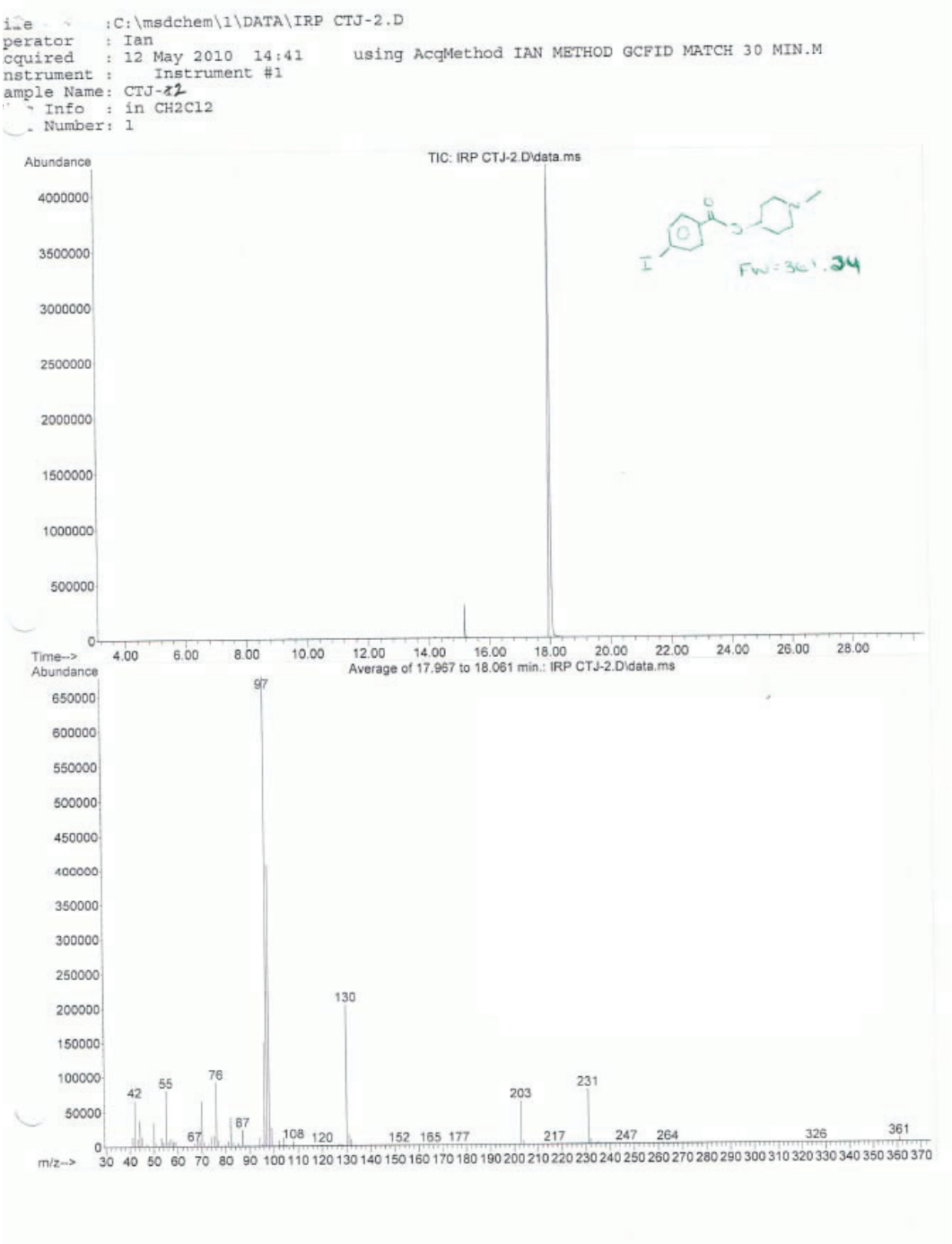

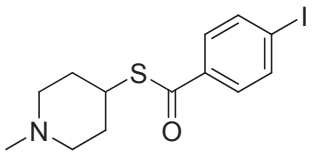

(N-methylpiperidin-4-yl) 4-iodobenzenecarbothioate (**12**)
HRMS

Mass Spectrum Molecular Formula Report

Analysis Info

Analysis Name	D:\Data\Xiao\Aug 17 2010000009.d	Acquisition Date	8/17/2010 2:59:35 PM
Method	xiaofengpos.m	Operator	Administrator
Sample Name	CTJ-2	Instrument	micrOTOF 57
Comment			

Acquisition Parameter

Source Type	ESI	Ion Polarity	Positive	Set Corrector Fill	52 V
Scan Range	n/a	Capillary Exit	130.0 V	Set Pulsar Pull	398 V
Scan Begin	50 m/z	Hexapole RF	150.0 V	Set Pulsar Push	398 V
Scan End	1500 m/z	Skimmer 1	55.0 V	Set Reflector	1300 V
		Hexapole 1	26.0 V	Set Flight Tube	9000 V
				Set Detector TOF	1960 V

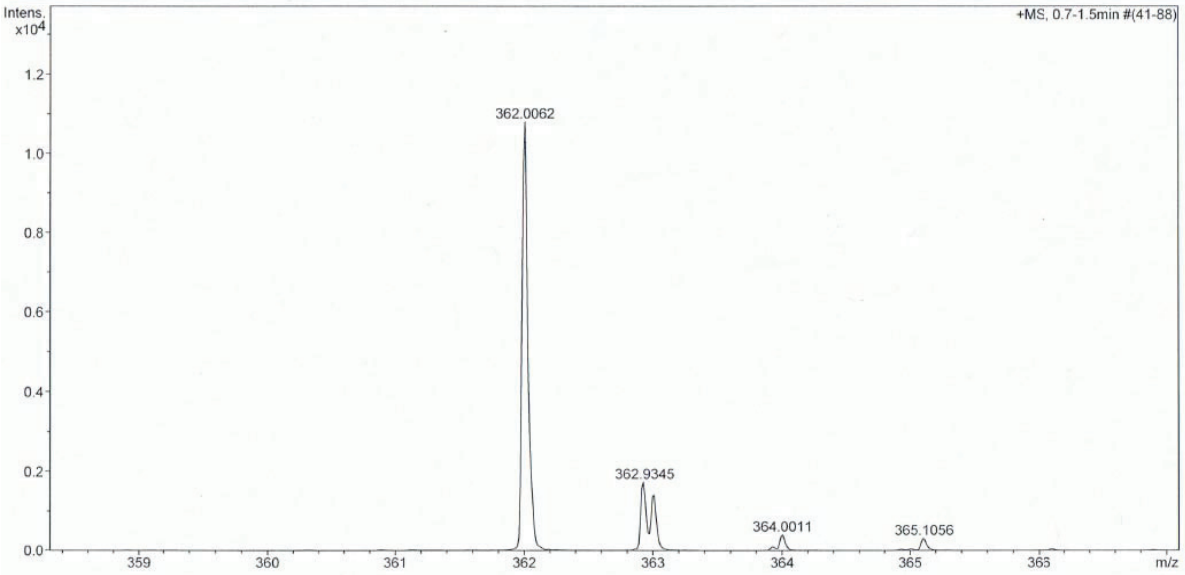

Bruker Daltonics DataAnalysis 3.3 printed: 8/17/2010 3:08:01 PM Page 1 of 2

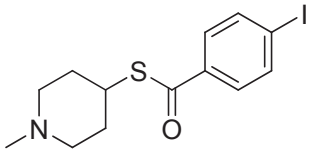

(N-methylpiperidin-4-yl) 4-iodobenzenecarbothioate (**12**)
HPLC

Data File C:\Chem32\1\DATA\JEREMY\JER091008CFRACS 2008-10-09 15-09-59\EAH31052010B 2010-05-31 13-3
Sample Name: CTJ-2

Acq. Operator	: Ian	Seq. Line	: 2
Acq. Instrument	: Instrument 1	Location	: Vial 22
Injection Date	: 5/31/2010 1:39:41 PM	Inj	: 1
		Inj Volume	: 20 µl
Sequence File	: C:\Chem32\1\DATA\JEREMY\JER091008CFRACS 2008-10-09 15-09-59\EAH31052010B 2010-05-31 13-31-15\EAH31052010B.S		
Method	: C:\Chem32\1\DATA\JEREMY\JER091008CFRACS 2008-10-09 15-09-59\EAH31052010B 2010-05-31 13-31-15\REV PHASE METHANOL 20UL.M		
Last changed	: 5/31/2010 1:28:28 PM by Ian		
Method Info	: Reverse Phase Methanol		

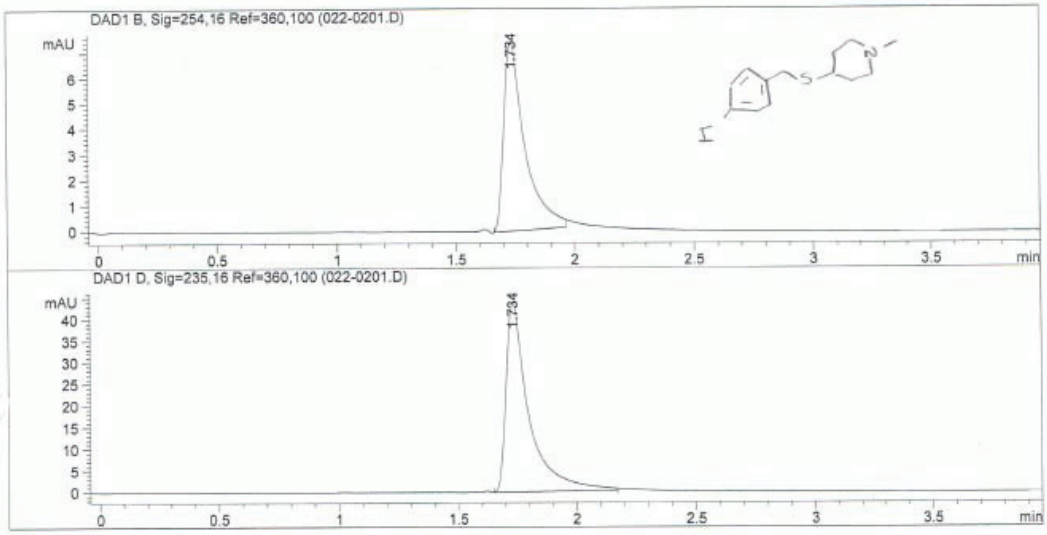

Fraction Information

Fraction collection off

No Fractions found.

Area Percent Report

Sorted By : Signal
Multiplier : 1.0000
Dilution : 1.0000
Use Multiplier & Dilution Factor with ISTDs

Instrument 1 5/31/2010 1:45:06 PM Ian Page 1 of 2

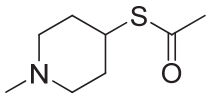

(N-methylpiperidin-4-yl) ethanethioate (**13**)

^{1}H NMR

Courtney Jollymore

Acquisition Time (sec)	3.2506	***Comment***	Bill Pottie 1d_1H CDCl3 {C:\nmr_users} pilgrim 13			***Date***	12 Jul 2010 11:53:52
Date Stamp	12 Jul 2010 11:53:52						
File Name	\\APPS2\USER\SHARED\Organic Chemistry Research\Courtney Jollymore\Summer 2010\NMRs\CTJ-6\10\fid					***Frequency (MHz)***	500.13
Nucleus	1H	***Number of Transients***	16	***Origin***	spect	***Original Points Count***	32768
Owner	nmr	***Points Count***	65536	***Pulse Sequence***	zg30	***Receiver Gain***	64.00
SW(cyclical) (Hz)	10080.65	***Solvent***	CHLOROFORM-d	***Spectrum Offset (Hz)***	3236.4253	***Sweep Width (Hz)***	10080.49
Temperature (degree C)	21.987						

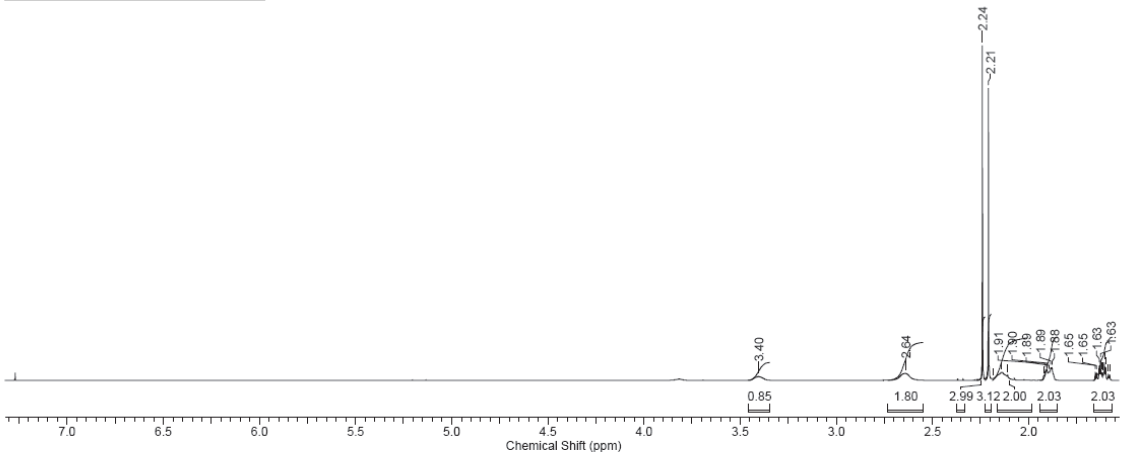

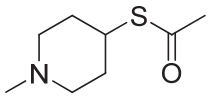

(N-methylpiperidin-4-yl) ethanethioate (**13**)

^{13}C NMR

Coutrney Jollymore

Acquisition Time (sec)	0.7499				
Comment	Bill Pottie 1d_13C_DEPTQ135_n CDCl3 {C:\nmr_users} pilgrim 13 Signal to noise predictions indicate that you submitted more scans than required For future samples at this concentration, a value for NS of about 128 appears to be adequate				
Date	12 Jul 2010 17:33:04	***Date Stamp***	12 Jul 2010 17:33:04		
File Name	\\APPS2\USER\SHARED\Organic Chemistry Research\Courtney Jollymore\Summer 2010\NMRs\CTJ-6\11\PDATA\1\1r				
Frequency (MHz)	125.76	***Nucleus***	13C	***Number of Transients***	128
Origin	spect	***Original Points Count***	25335	***Owner***	nmr
Points Count	65536	***Pulse Sequence***	deptqsp.dmo	***Receiver Gain***	7298.20
SW(cyclical) (Hz)	33783.79	***Solvent***	CHLOROFORM-d	***Spectrum Offset (Hz)***	13813.3486
Sweep Width (Hz)	33783.27	***Temperature (degree C)***	21.987		

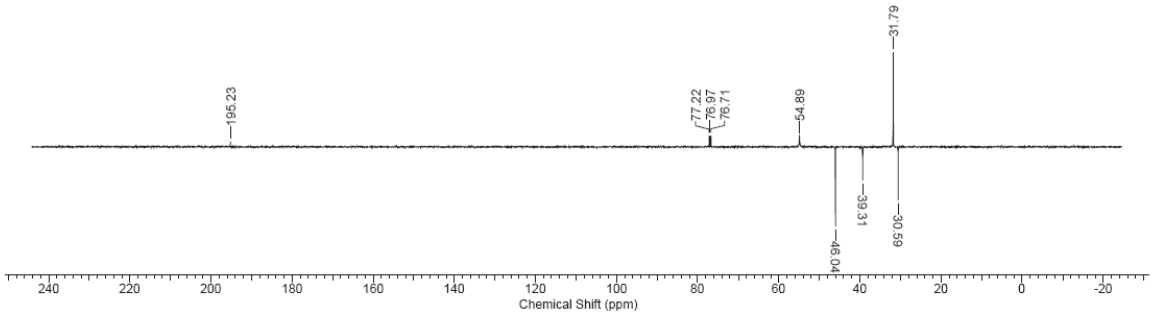

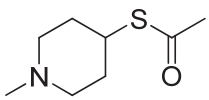

(N-methylpiperidin-4-yl) ethanethioate (**13**)

IR

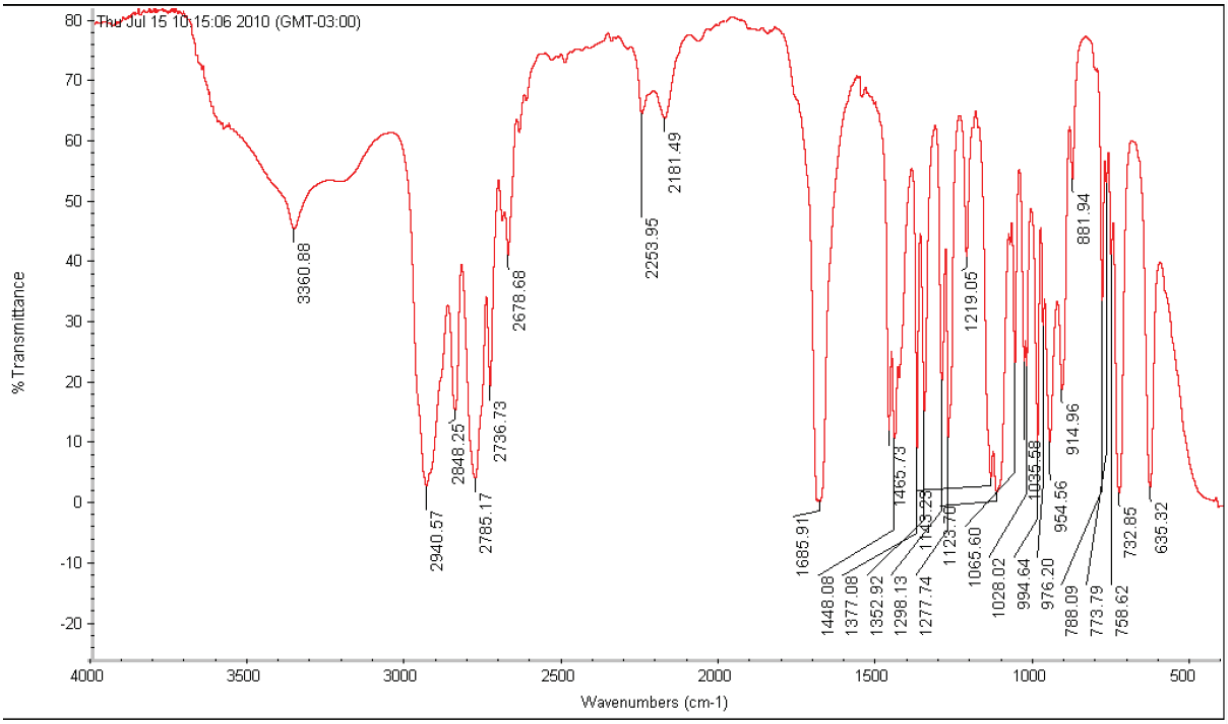

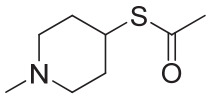

(N-methylpiperidin-4-yl) ethanethioate (**13**)
LRMS

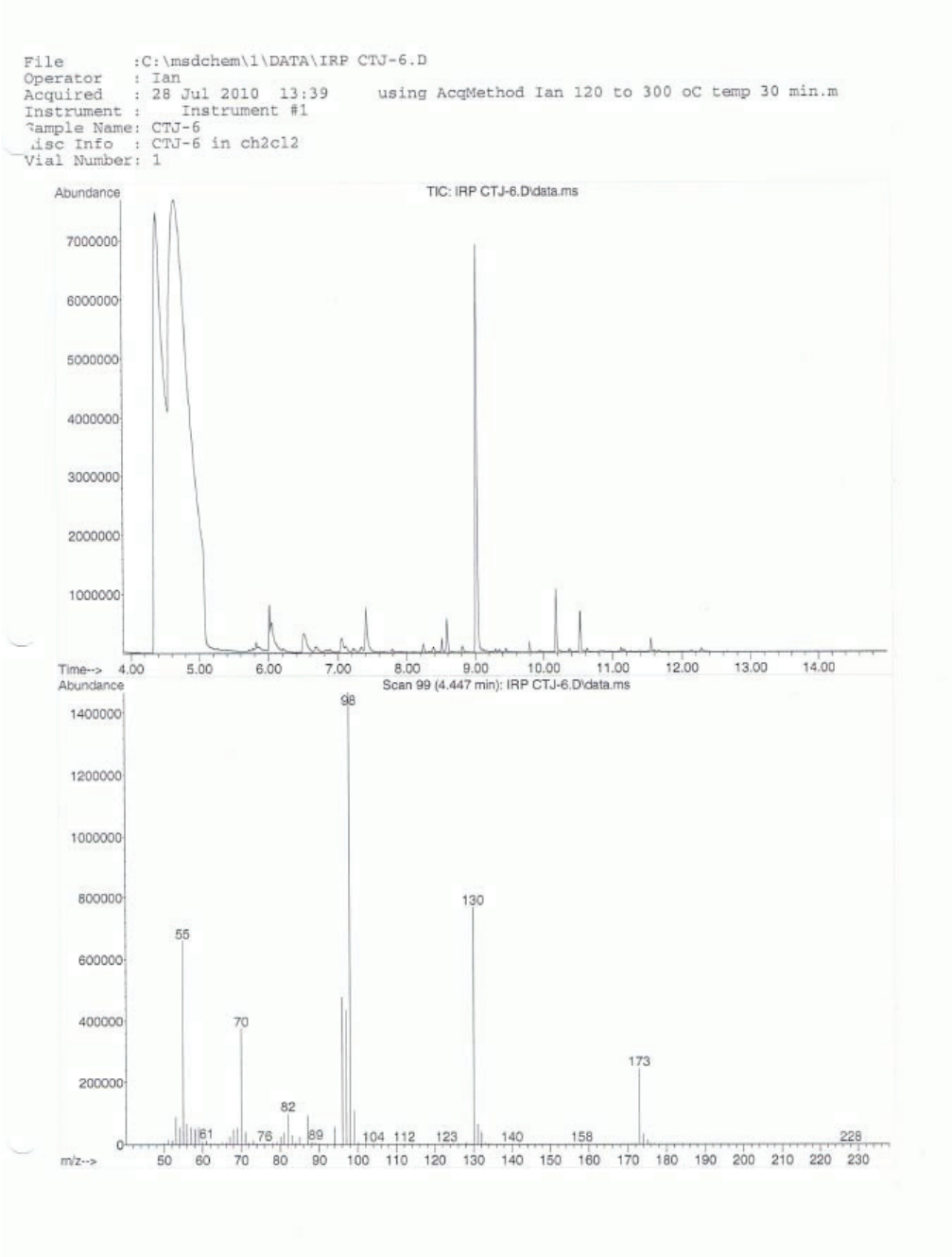

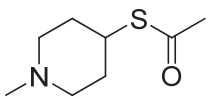

(N-methylpiperidin-4-yl) ethanethioate (**13**)
HRMS

Mass Spectrum Molecular Formula Report

Analysis Info

Analysis Name	D:\Data\Xiao\Dec 21 2010000002.d	Acquisition Date	12/21/2010 10:37:20 AM
Method	xiaofengpos.m	Operator	Administrator
Sample Name	IRM-137	Instrument	micrOTOF 57
Comment			

Acquisition Parameter

Source Type	ESI	Ion Polarity	Positive	Set Corrector Fill	52 V
Scan Range	n/a	Capillary Exit	90.0 V	Set Pulsar Pull	398 V
Scan Begin	50 m/z	Hexapole RF	130.0 V	Set Pulsar Push	398 V
Scan End	1500 m/z	Skimmer 1	55.0 V	Set Reflector	1300 V
		Hexapole 1	26.0 V	Set Flight Tube	9000 V
				Set Detector TOF	1960 V

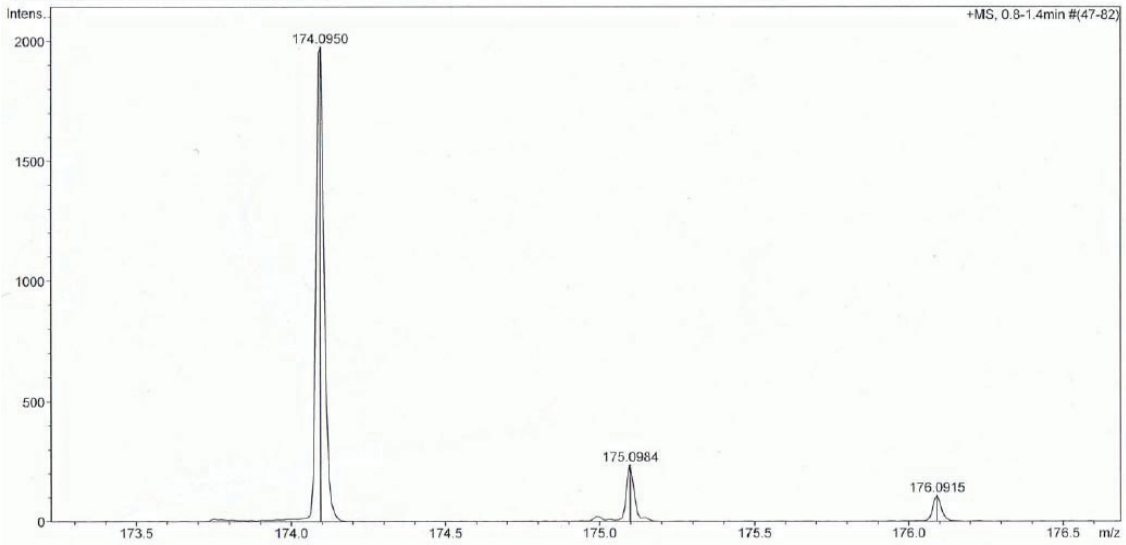

Bruker Daltonics DataAnalysis 3.3 printed: 12/21/2010 10:43:11 AM Page 1 of 2

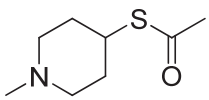

(N-methylpiperidin-4-yl) ethanethioate (**13**)
HPLC

Data File C:\CHEM32\1\DATA\JEREMY\JER091008CFRACS 2008-10-09 15-09-59\CTJ22072010A 2010-07-22 10-1
Sample Name: CTJ-6

Acq. Operator	: Ian	Seq. Line	: 2
Acq. Instrument	: Instrument 1	Location	: Vial 32
Injection Date	: 7/22/2010 10:27:39 AM	Inj	: 1
		Inj Volume	: 50 µl
Acq. Method	: C:\Chem32\1\DATA\JEREMY\JER091008CFRACS 2008-10-09 15-09-59\ CTJ22072010A 2010-07-22 10-18-27\REV PHASE METHANOL 20UL.M		
Last changed	: 6/2/2010 2:56:03 PM by Ian		
Analysis Method	: C:\CHEM32\1\DATA\JEREMY\JER091008CFRACS 2008-10-09 15-09-59\ CTJ22072010A 2010-07-22 10-18-27\032-0201.D\DA.M (REV PHASE METHANOL 20UL.M)		
Last changed	: 6/2/2010 2:56:03 PM by Ian		
Method Info	: Reverse Phase Methanol		

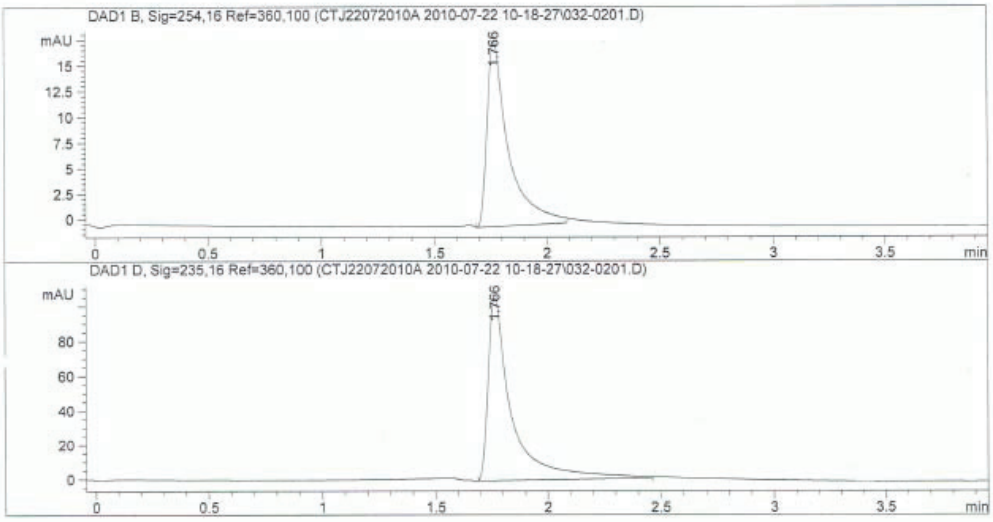

Fraction Information

Fraction collection off

No Fractions found.

Area Percent Report

Sorted By	:	Signal
Multiplier	:	1.0000
Dilution	:	1.0000

Use Multiplier & Dilution Factor with ISTDs

Instrument 1 7/28/2010 4:01:09 PM Ian Page 1 of 2

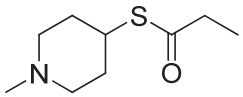

(N-methylpiperidin-4-yl) propanethioate (**14**)

^{1}H NMR

07/12/2010 12:26:37 PM

Acquisition Time (sec)	3.2768	***Comment***	Bill Pottie 1d_1H CDCl3 {C:\nmr_users} imacdonald 13			***Date***	06 Dec 2010 22:27:12
Date Stamp	06 Dec 2010 22:27:12						
File Name	\\APPS2\USER\SHARED\Organic Chemistry Research\Ian Macdonald\NMR Data\Ian Macdonald\NMR\IRM-138 Dec 6, 2010\10\fid						
Frequency (MHz)	500.13	***Nucleus***	1H	***Number of Transients***	64	***Origin***	spect
Original Points Count	32768	***Owner***	nmr	***Points Count***	32768	***Pulse Sequence***	zg30
Receiver Gain	114.00	***SW(cyclical) (Hz)***	10000.00	***Solvent***	CHLOROFORM-d	***Spectrum Offset (Hz)***	3239.6743
Spectrum Type	STANDARD	***Sweep Width (Hz)***	9999.70	***Temperature (degree C)***	21.987		

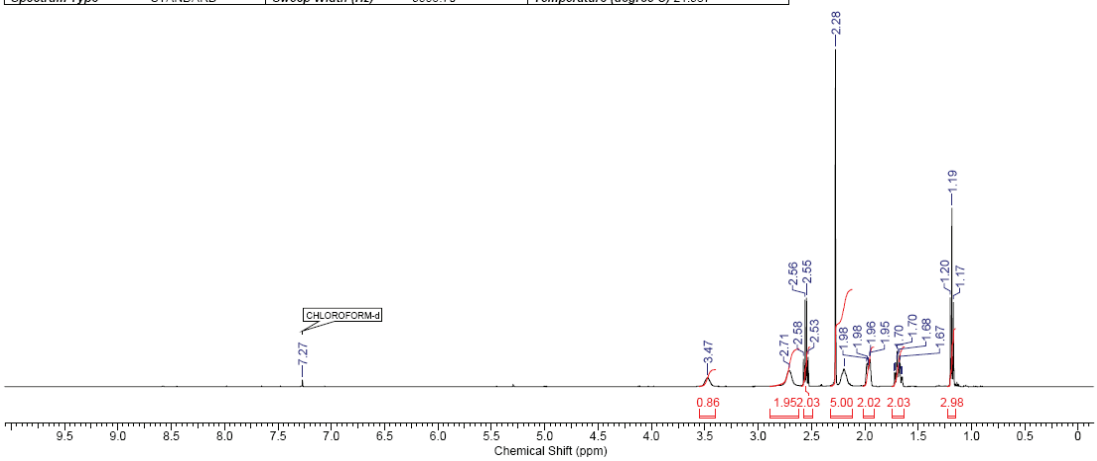

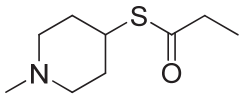

(N-methylpiperidin-4-yl) propanethioate (**14**)

^{13}C NMR

07/12/2010 12:31:13 PM

Acquisition Time (sec)	0.7600				
Comment	Bill Pottie 1d_13C_DEPTQ135_n CDCl3 (C:\nmr_users) imacdonald 13 Best S/N after 128 scans was 43.7 Best S/N after 256 scans was 65.4 Best S/N after 384 scans was 76.5 Best S/N after 512 scans was 91.5 Best S/N after 640 scans was 100.5 Best S/N after 7				
Date	06 Dec 2010 22:35:44	***Date Stamp***	06 Dec 2010 22:35:44		
File Name	\\APPS2\USER\SHARED\Organic Chemistry Research\Ian Macdonald\NMR Data\Ian Macdonald\NMR\IRM-138 Dec 6, 2010\11\PDATA\1\1r				
Frequency (MHz)	125.76	***Nucleus***	13C	***Number of Transients***	1024
Origin	spect	***Original Points Count***	25335	***Owner***	nmr
Points Count	65536	***Pulse Sequence***	deptqsp.dmo	***Receiver Gain***	9195.20
SW(cyclical) (Hz)	33333.33	***Solvent***	CHLOROFORM-d	***Spectrum Offset (Hz)***	13823.3145
Sweep Width (Hz)	33332.82	***Temperature (degree C)***	21.987		

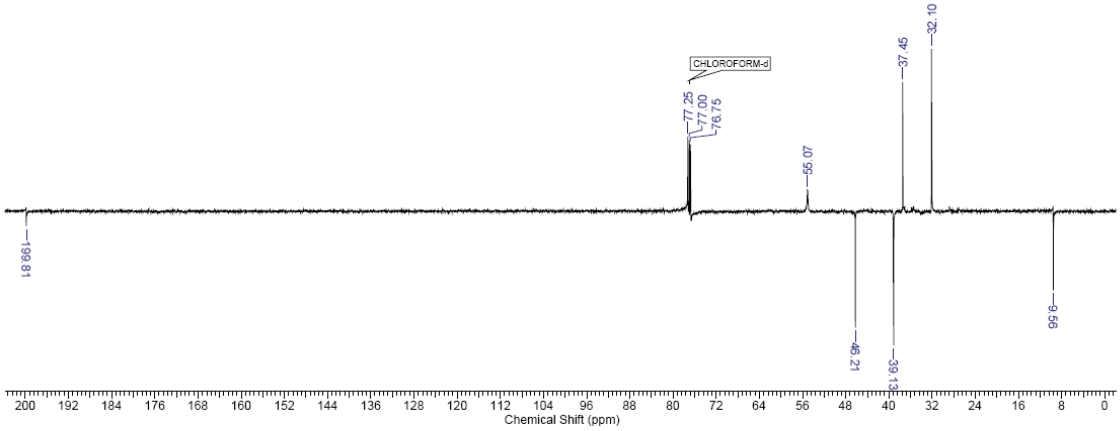

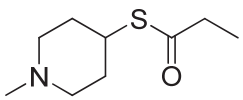

(N-methylpiperidin-4-yl) propanethioate (**14**)

IR

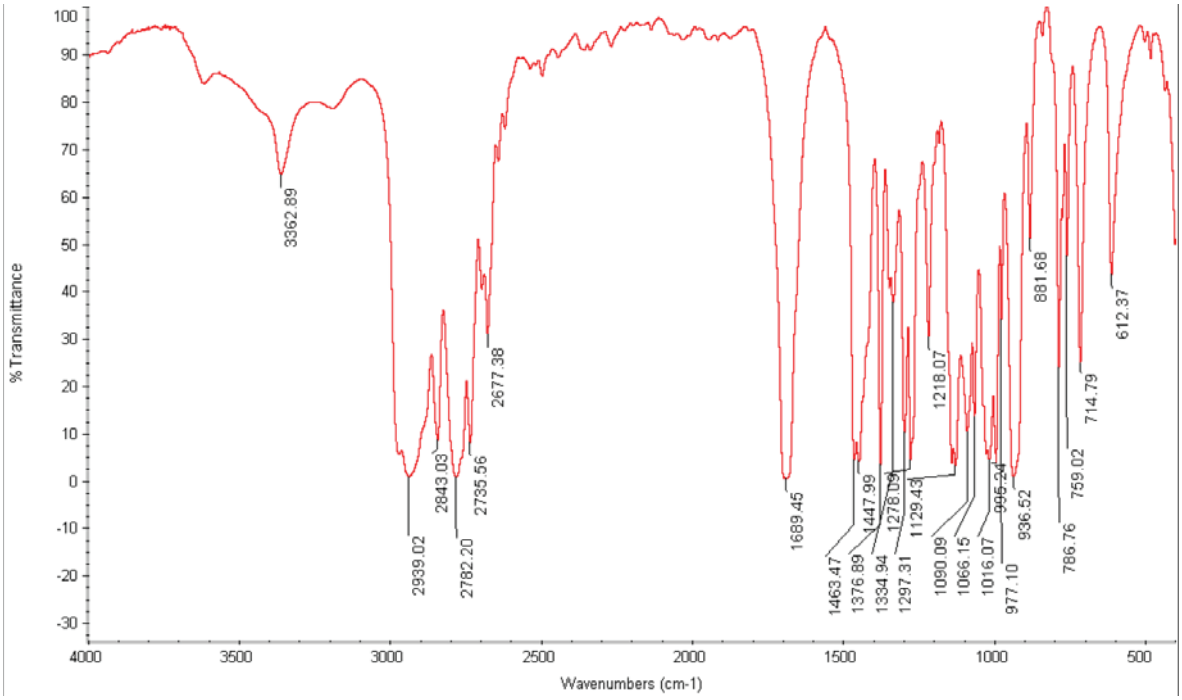

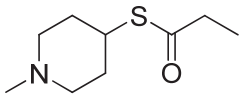

(N-methylpiperidin-4-yl) propanethioate (**14**)
LRMS

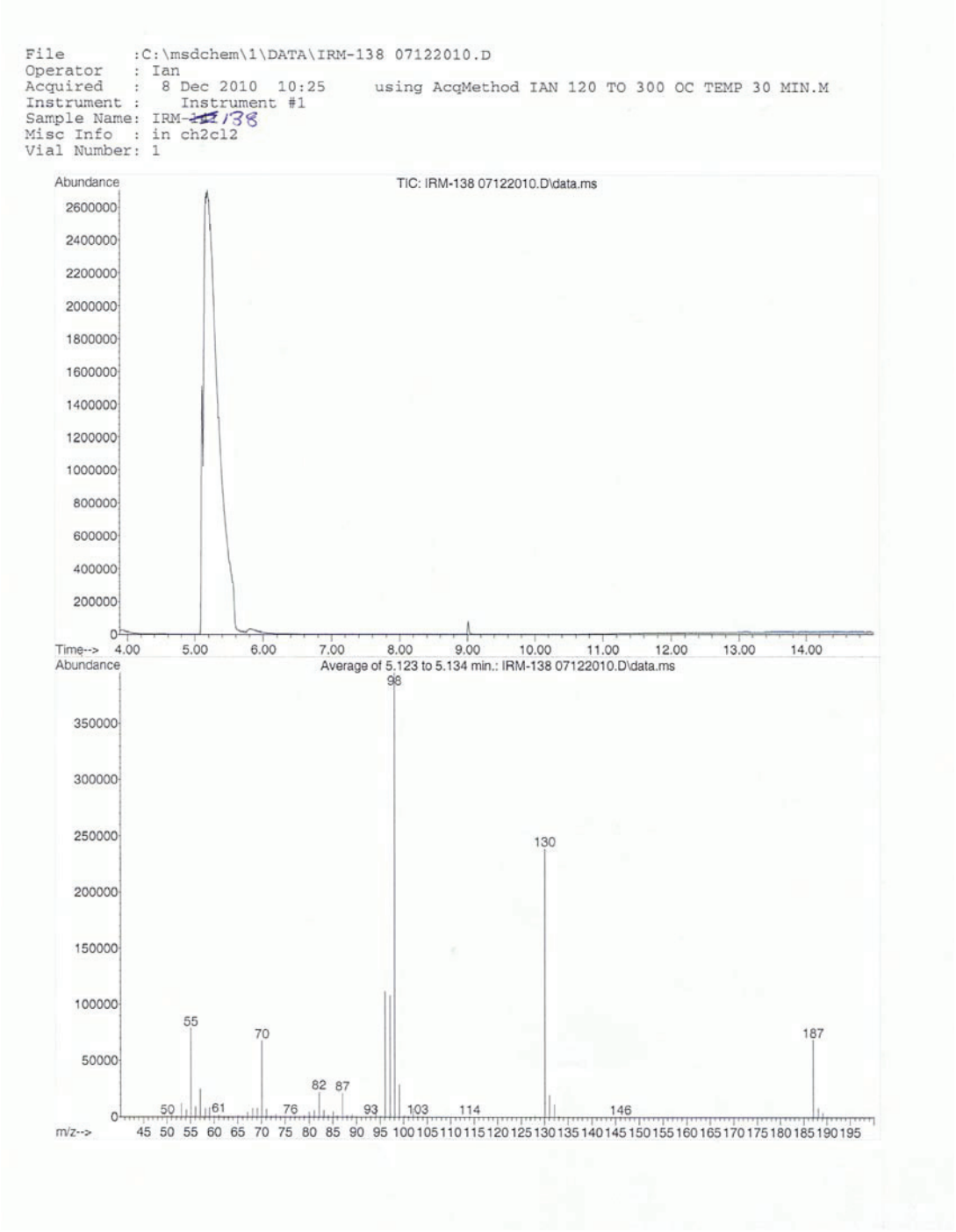

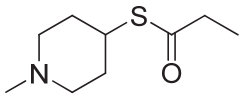

(N-methylpiperidin-4-yl) propanethioate (**14**)
HRMS

Mass Spectrum Molecular Formula Report

Analysis Info

Analysis Name	D:\Data\Xiao\Dec 21 2010000003.d	Acquisition Date	12/21/2010 10:48:41 AM
Method	xiaofengpos.m	Operator	Administrator
Sample Name	IRM-138	Instrument	micrOTOF 57
Comment			

Acquisition Parameter

Source Type	ESI	Ion Polarity	Positive	Set Corrector Fill	52 V
Scan Range	n/a	Capillary Exit	90.0 V	Set Pulsar Pull	398 V
Scan Begin	50 m/z	Hexapole RF	130.0 V	Set Pulsar Push	398 V
Scan End	1500 m/z	Skimmer 1	55.0 V	Set Reflector	1300 V
		Hexapole 1	26.0 V	Set Flight Tube	9000 V
				Set Detector TOF	1960 V

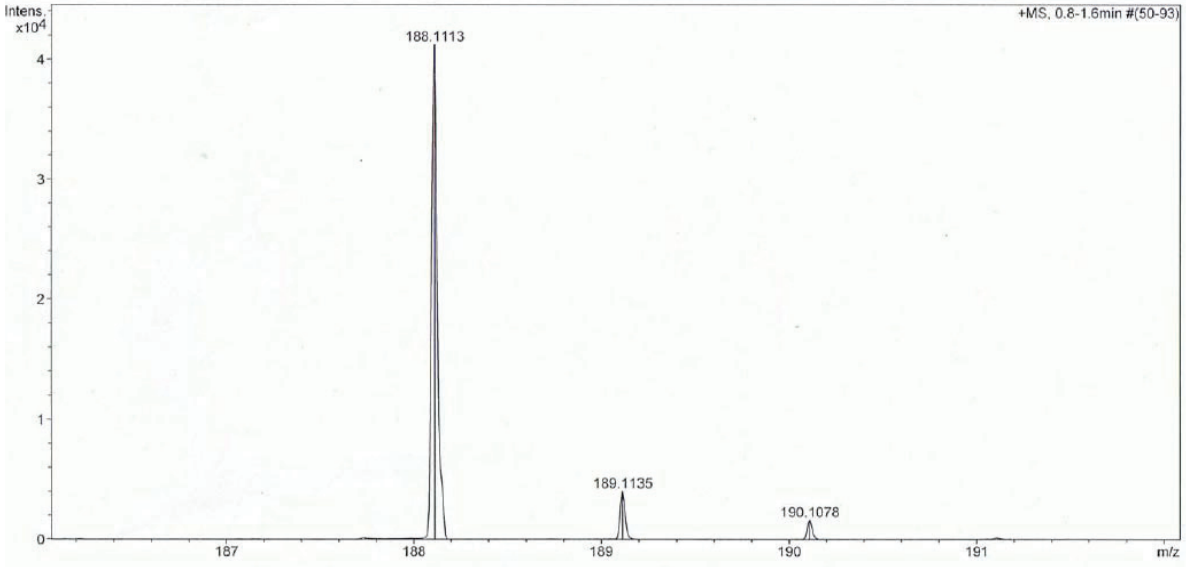

Bruker Daltonics DataAnalysis 3.3 printed: 12/21/2010 10:53:14 AM Page 1 of 2

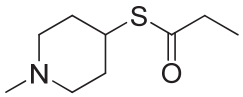

(N-methylpiperidin-4-yl) propanethioate (**14**)
HPLC

Data File C:\CHEM32\1\DATA\IAN MACDONALD\IRM09122010A 2010-12-09 16-41-09\021-0101.D
Sample Name: IRM-138

Acq. Operator	: Ian Macdonald	Seq. Line	: 1
Acq. Instrument	: Instrument 1	Location	: Vial 21
Injection Date	: 12/9/2010 4:44:12 PM	Inj	: 1
		Inj Volume	: 100 µl
Acq. Method	: C:\Chem32\1\DATA\IAN MACDONALD\IRM09122010A 2010-12-09 16-41-09\ MACDONLAD REVERSE PHASE 20UL.M		
Last changed	: 12/8/2010 10:24:23 AM by Ian Macdonald		
Analysis Method	: C:\CHEM32\1\DATA\IAN MACDONALD\IRM09122010A 2010-12-09 16-41-09\021-0101.D\DA.M (MACDONLAD REVERSE PHASE 20UL.M)		
Last changed	: 12/8/2010 10:24:23 AM by Ian Macdonald		
Method Info	: Ian Shutdown		

Fraction Information

Fraction collection off

No Fractions found.

Area Percent Report

Sorted By	:	Signal
Multiplier	:	1.0000
Dilution	:	1.0000

Use Multiplier & Dilution Factor with ISTDs

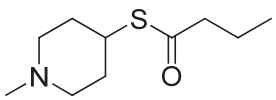

(N-methylpiperidin-4-yl) butanethioate (**15**)

^{1}H NMR

07/12/2010 12:54:07 PM

Acquisition Time (sec)	3.2768	*Comment*	Bill Pottie 1d_1H CDCl3 {C:\nmr_users} imacdonald 15			*Date*	06 Dec 2010 23:52:32
Date Stamp	06 Dec 2010 23:52:32						
File Name	\\APPS2\USER\SHARED\Organic Chemistry Research\Ian Macdonald\NMR Data\Ian Macdonald\NMR\IRM-141 Dec 6, 2010\10\fid						
Frequency (MHz)	500.13	*Nucleus*	1H	*Number of Transients*	64	*Origin*	spect
Original Points Count	32768	*Owner*	nmr	*Points Count*	32768	*Pulse Sequence*	zg30
Receiver Gain	64.00	*SW(cyclical) (Hz)*	10000.00	*Solvent*	CHLOROFORM-d	*Spectrum Offset (Hz)*	3239.3694
Spectrum Type	STANDARD	*Sweep Width (Hz)*	9999.70	*Temperature (degree C)*	21.987		

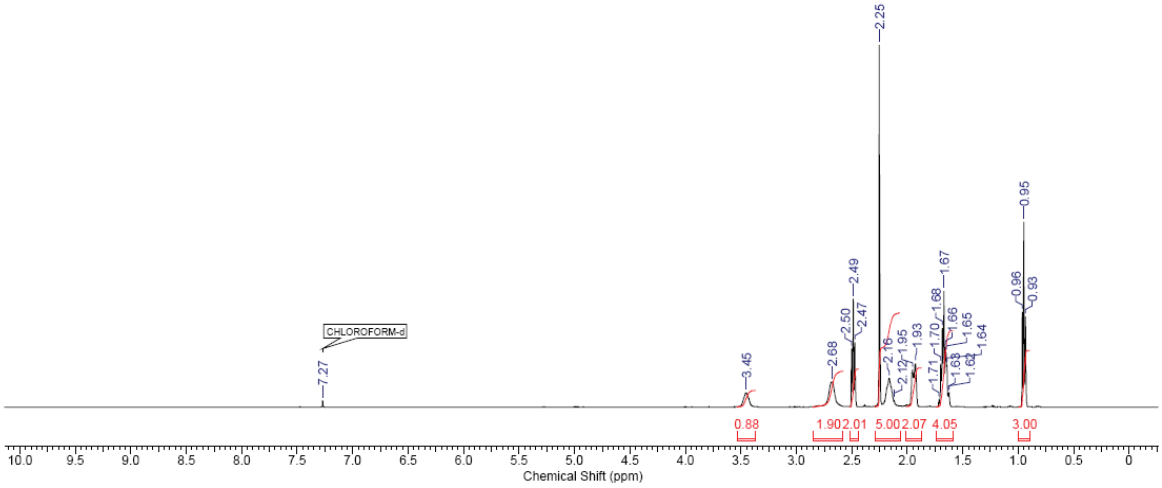

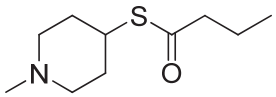

(N-methylpiperidin-4-yl) butanethioate (**15**)

^{13}C NMR

13/12/2010 2:03:49 PM

Acquisition Time (sec)	0.7600				
Comment	Bill Pottie 1d_13C_DEPTQ135_n CDCl3 {C:\nmr_users} imacdonald 16 Best S/N after 128 scans was 103.9 Signal to noise predictions indicate that you submitted more scans than required For future samples at this concentration, a value for NS of about 256				
Date	09 Dec 2010 22:52:48	***Date Stamp***	09 Dec 2010 22:52:48		
File Name	\\APPS2\USER\SHARED\Organic Chemistry Research\Ian Macdonald\NMR Data\Ian Macdonald\NMR\IRM-141 Dec 9, 2010\11\PDATA\1\1r				
Frequency (MHz)	125.76	***Nucleus***	13C	***Number of Transients***	256
Origin	spect	***Original Points Count***	25335	***Owner***	nmr
Points Count	65536	***Pulse Sequence***	deptqsp.dmo	***Receiver Gain***	9195.20
SW(cyclical) (Hz)	33333.33	***Solvent***	CHLOROFORM-d	***Spectrum Offset (Hz)***	13816.5742
Sweep Width (Hz)	33332.82	***Temperature (degree C)***	21.987		

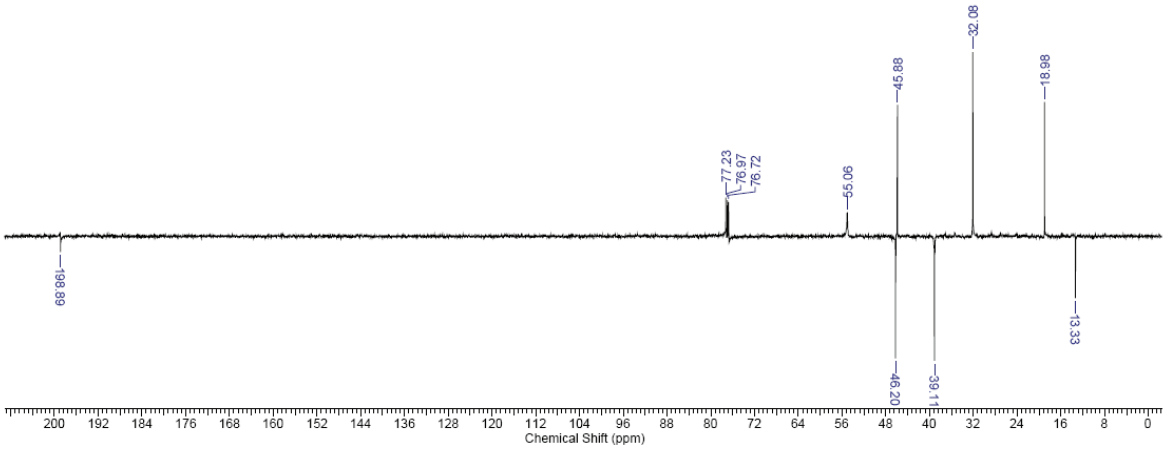

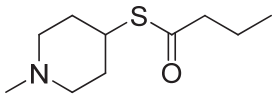

(N-methylpiperidin-4-yl) butanethioate (**15**)

IR

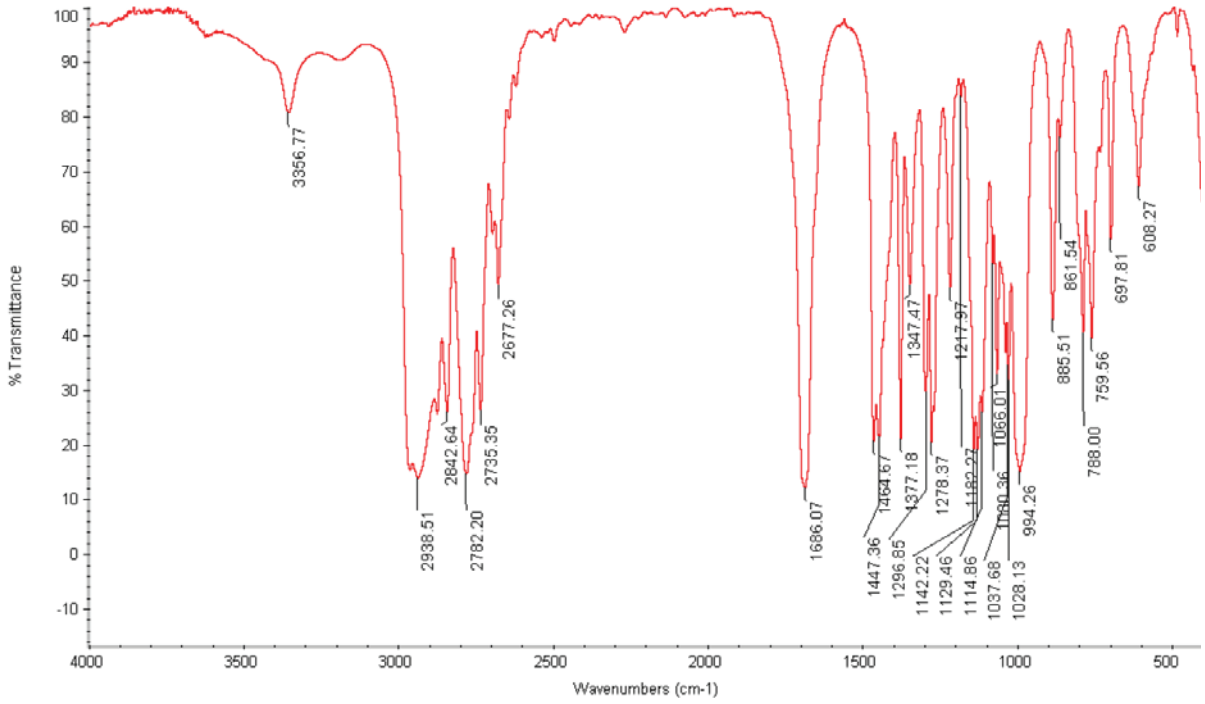

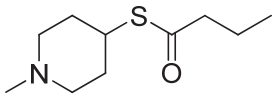

(N-methylpiperidin-4-yl) butanethioate (**15**)
LRMS

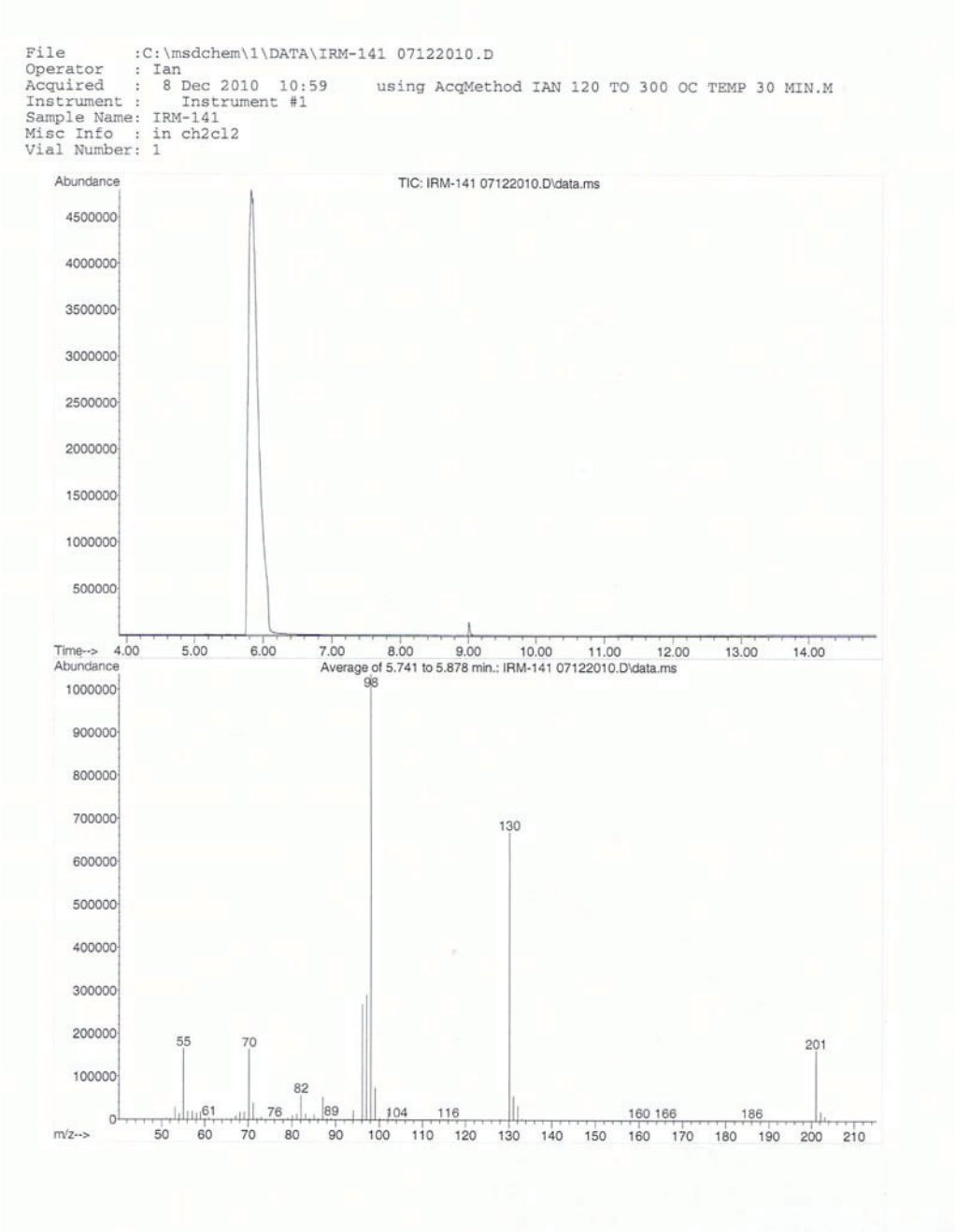

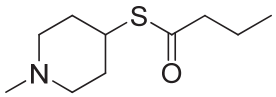

(N-methylpiperidin-4-yl) butanethioate (**15**)
HRMS

Mass Spectrum Molecular Formula Report

Analysis Info

Analysis Name	D:\Data\Xiao\Dec 21 2010000004.d	Acquisition Date	12/21/2010 11:01:42 AM
Method	xiaofengpos.m	Operator	Administrator
Sample Name	IRM-141	Instrument	micrOTOF 57
Comment			

Acquisition Parameter

Source Type	ESI	Ion Polarity	Positive	Set Corrector Fill	52 V
Scan Range	n/a	Capillary Exit	90.0 V	Set Pulsar Pull	398 V
Scan Begin	50 m/z	Hexapole RF	130.0 V	Set Pulsar Push	398 V
Scan End	1500 m/z	Skimmer 1	55.0 V	Set Reflector	1300 V
		Hexapole 1	26.0 V	Set Flight Tube	9000 V
				Set Detector TOF	1950 V

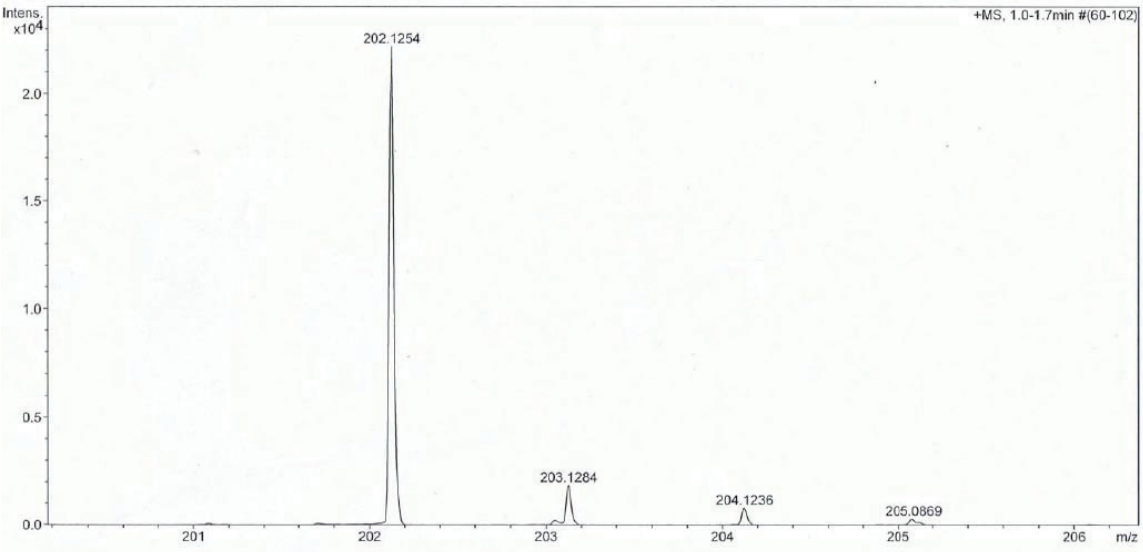

Bruker Daltonics DataAnalysis 3.3 printed: 12/21/2010 11:05:23 AM Page 1 of 2

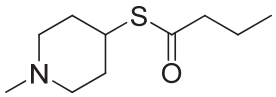

(N-methylpiperidin-4-yl) butanethioate (**15**)
HPLC

Data File C:\CHEM32\1\DATA\IAN MACDONALD\IRM09122010A 2010-12-09 16-41-09\022-0201.D
Sample Name: IRM-141

Acq. Operator	: Ian Macdonald	Seq. Line	: 2
Acq. Instrument	: Instrument 1	Location	: Vial 22
Injection Date	: 12/9/2010 4:57:52 PM	Inj	: 1
		Inj Volume	: 100 µl
Acq. Method	: C:\Chem32\1\DATA\IAN MACDONALD\IRM09122010A 2010-12-09 16-41-09\ MACDONLAD REVERSE PHASE 20UL.M		
Last changed	: 12/8/2010 10:24:23 AM by Ian Macdonald		
Analysis Method	: C:\CHEM32\1\DATA\IAN MACDONALD\IRM09122010A 2010-12-09 16-41-09\022-0201.D\DA.M (MACDONLAD REVERSE PHASE 20UL.M)		
Last changed	: 12/9/2010 5:28:13 PM by Ian Macdonald (modified after loading)		
Method Info	: Ian Shutdown		

Fraction Information

Fraction collection off

No Fractions found.

Area Percent Report

Sorted By	:	Signal
Multiplier	:	1.0000
Dilution	:	1.0000

Use Multiplier & Dilution Factor with ISTDs

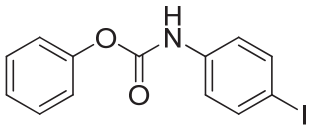

Phenyl-4-phenylcarbamate (**16**)
^{1}H NMR

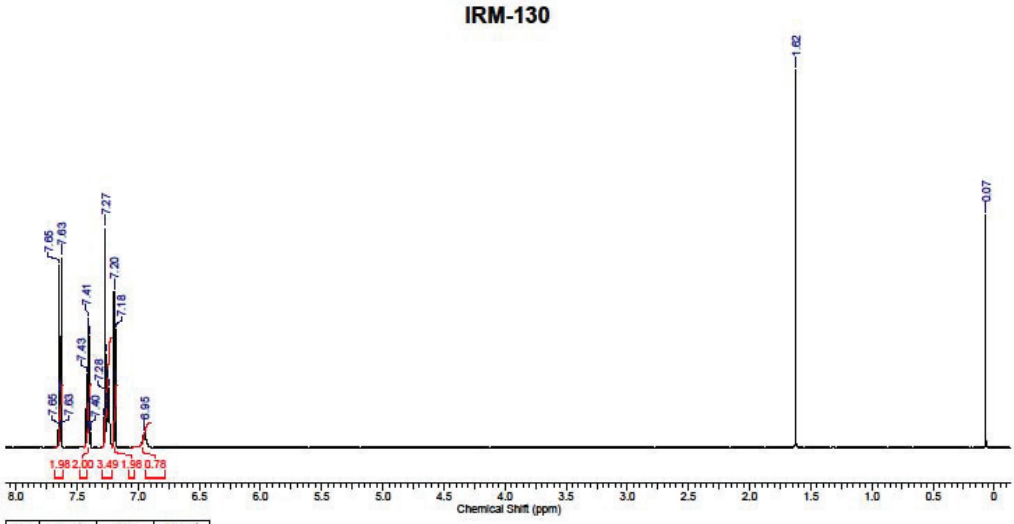

No.	(ppm)	(Hz)	Height
1	0.07	34.6	0.6146
2	1.62	811.8	1.0000
3	6.95	3475.7	0.0408
4	7.18	3592.0	0.2711
5	7.18	3593.2	0.3108
6	7.19	3594.1	0.1799
7	7.19	3595.1	0.1044
8	7.19	3598.4	0.0961
9	7.20	3600.5	0.4124
10	7.20	3601.8	0.3404
11	7.20	3603.0	0.0644
12	7.21	3603.6	0.0605
13	7.24	3619.2	0.1579
14	7.25	3623.7	0.1096

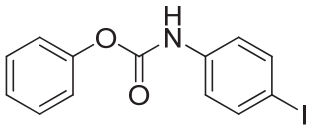

Phenyl-4-phenylcarbamate (**16**)
^{13}C NMR

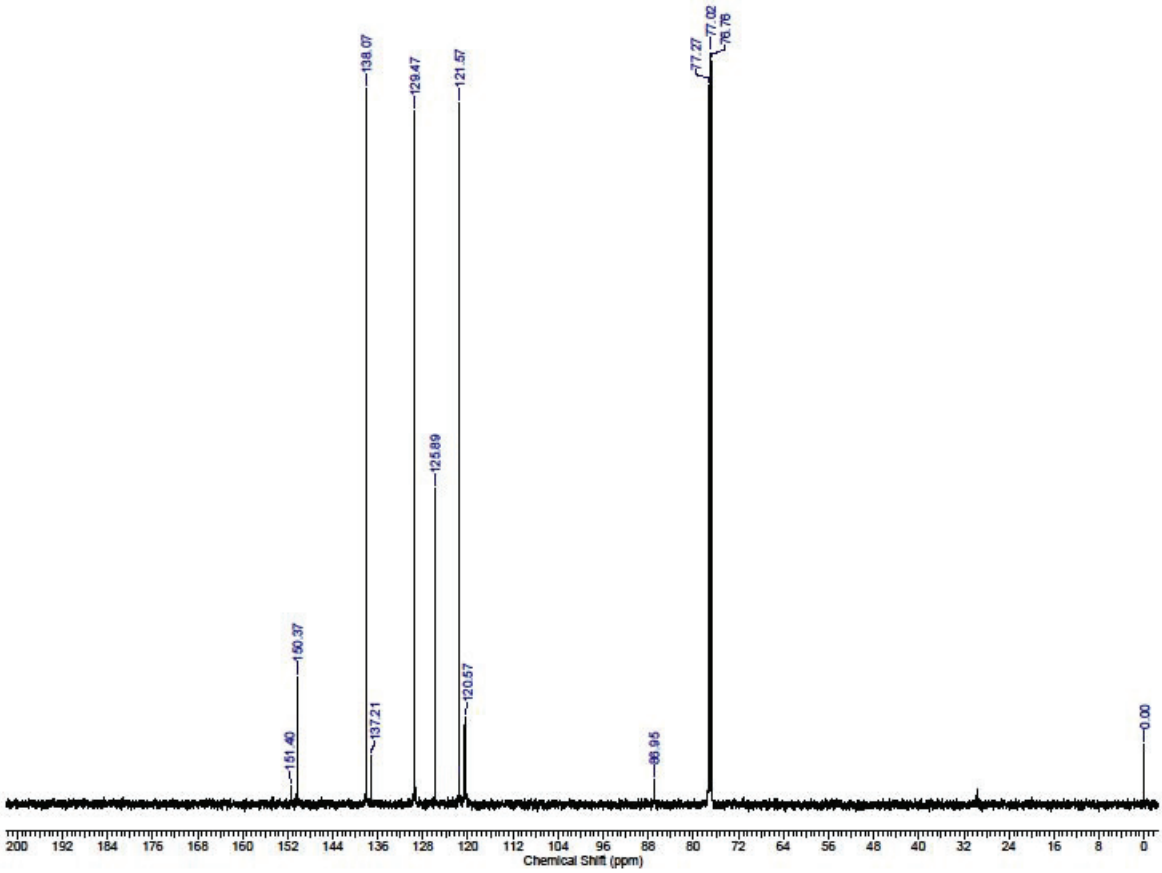

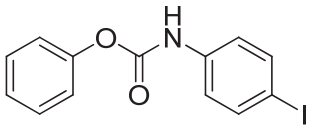

Phenyl-4-phenylcarbamate (**16**)
IR

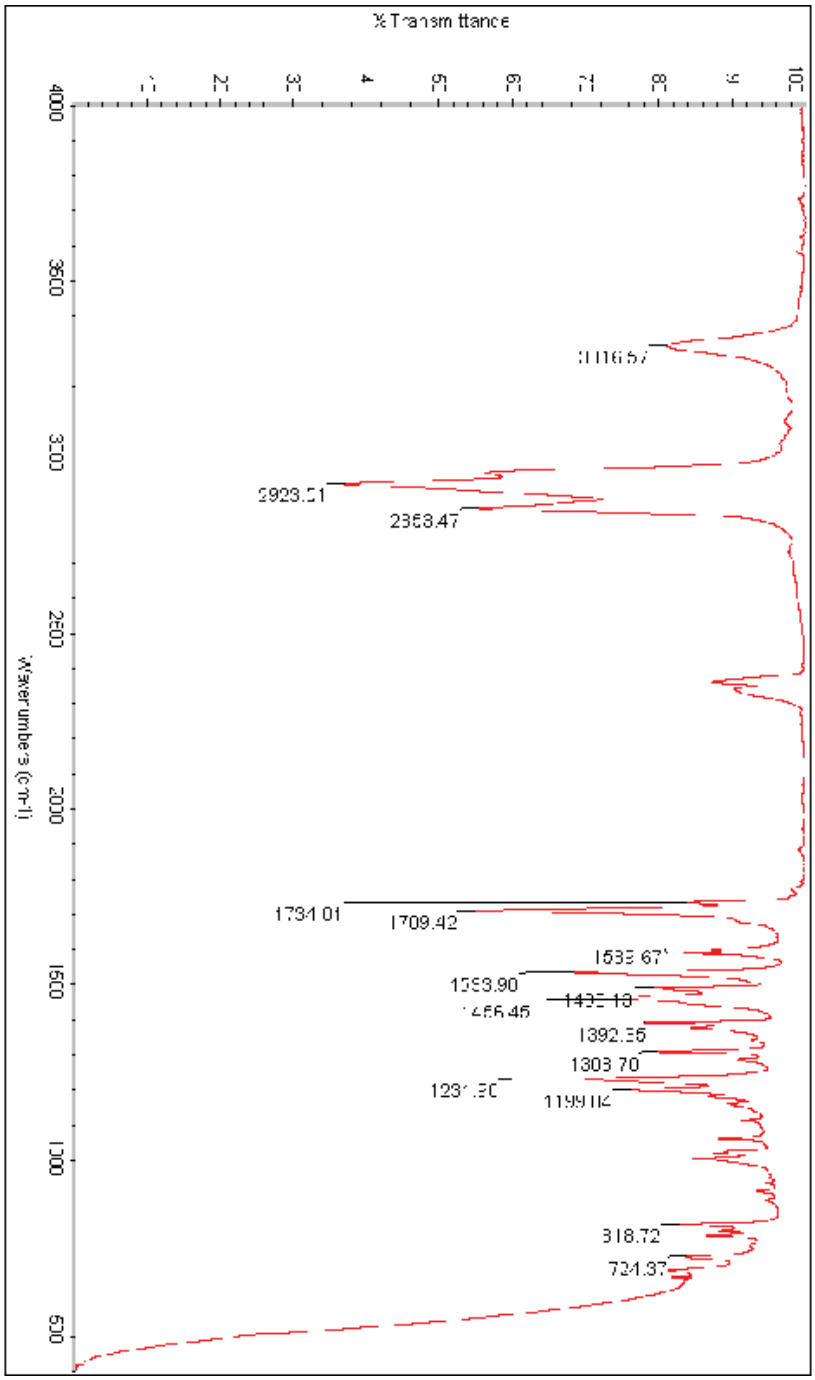

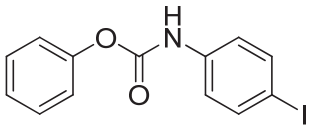

Phenyl-4-phenylcarbamate (**16**)
LRMS

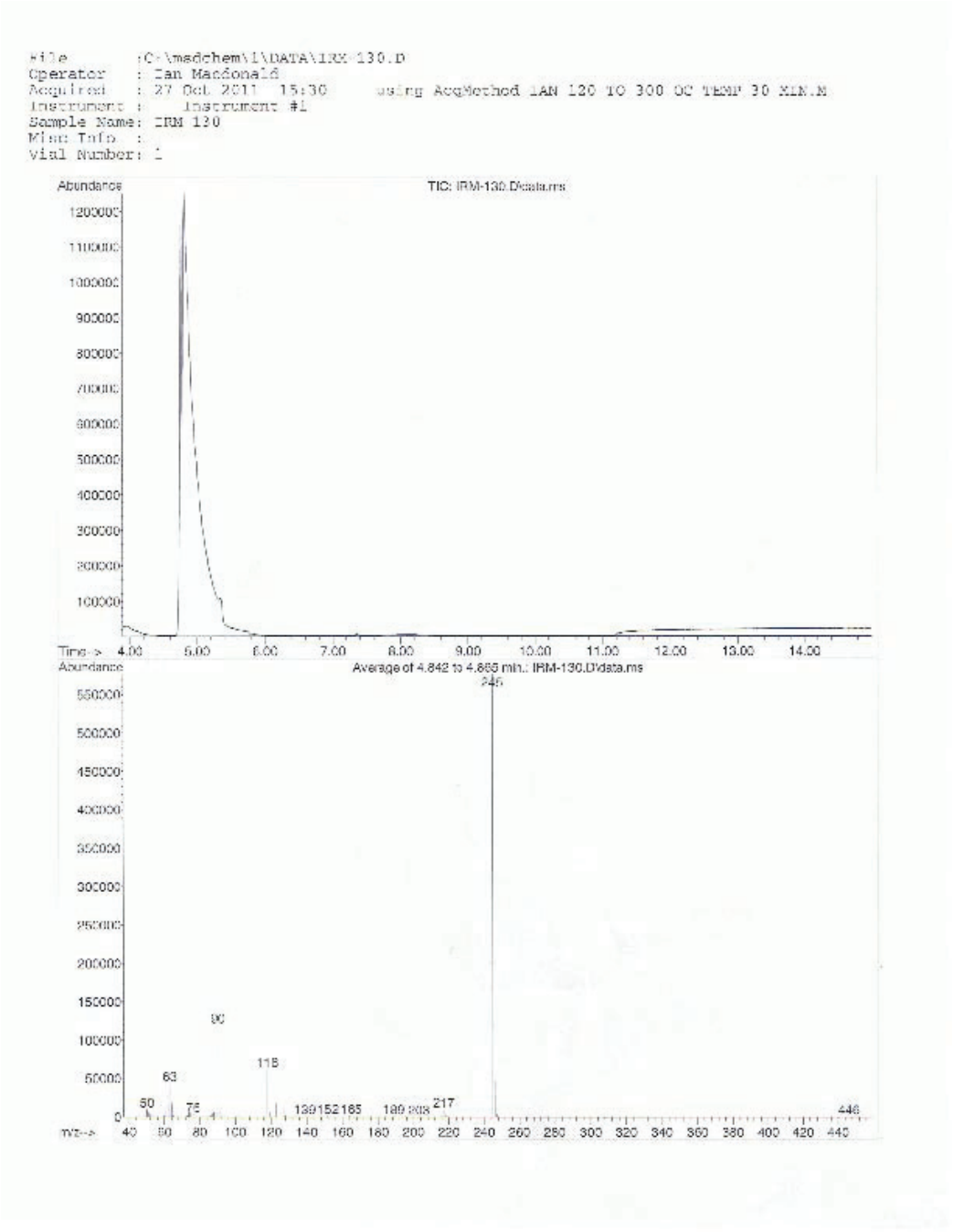

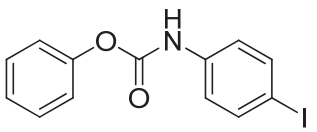

Phenyl-4-phenylcarbamate (**16**)
HRMS

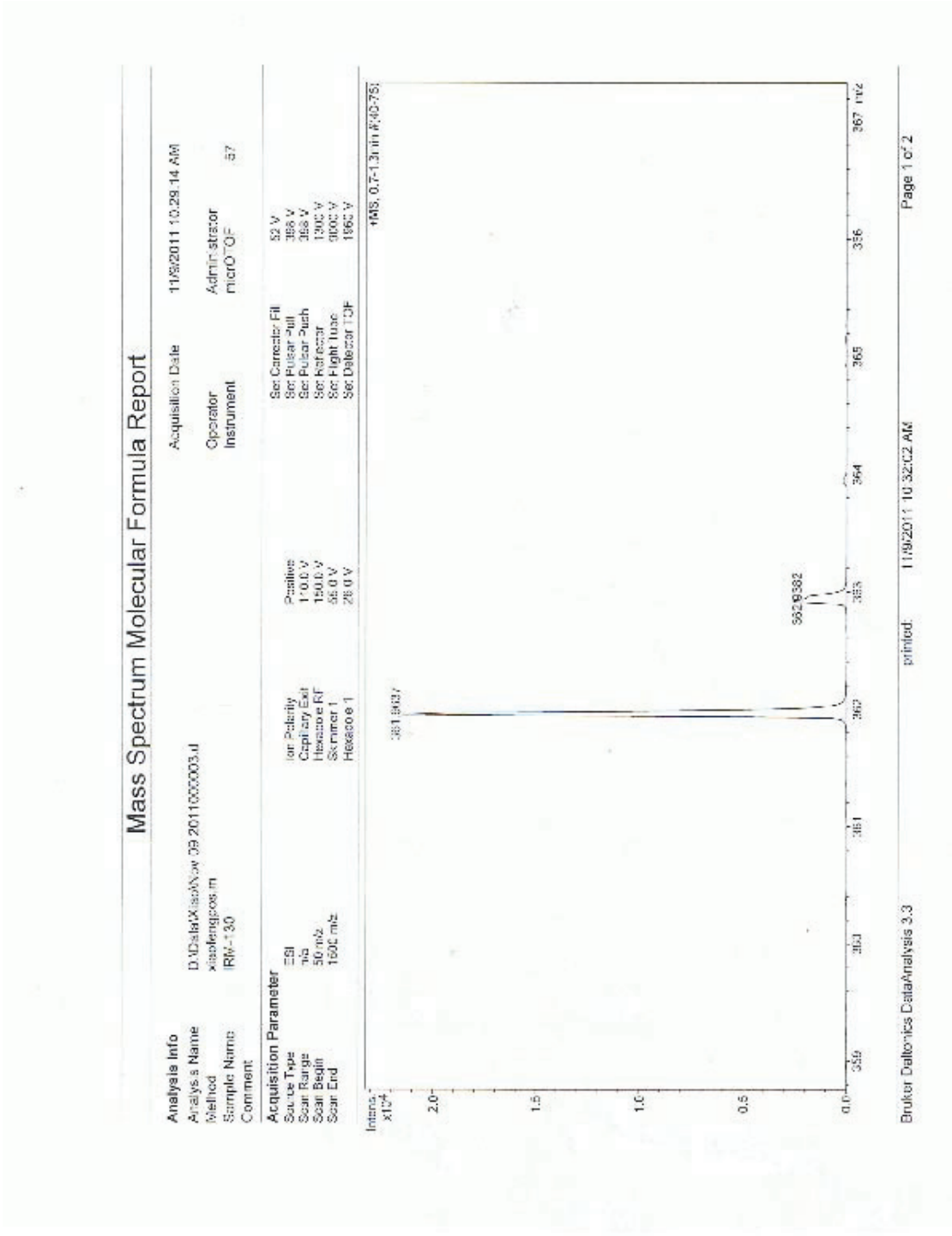

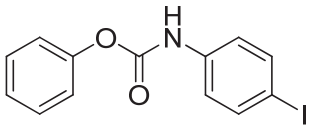

Phenyl-4-phenylcarbamate (**16**)
HPLC

```
Data File C:\CHEM32\1\DATA\IMACDONALD\IMACDONALD00049.D
Sample Name: IRM-160
    ======================================================================
    Acq. Operator   : Ian Macdonald
    Acq. Instrument : Instrument 1                  Location : Vial 1
    Injection Date  : 19/09/2011 5:34:22 PM
                                                    Inj Volume : Manually
    Acq. Method     : C:\CHEM32\1\METHODS\IRMSTABILITYTEST.M
    Last changed    : 19/09/2011 5:29:40 PM by Ian Macdonald
    Analysis Method : C:\CHEM32\1\METHODS\IRMSTABILITYTEST.M
    Last changed    : 19/09/2011 5:42:25 PM by Ian Macdonald
    Sample Info     : IRM-160, 80% MeOH / 20% Water (1 mL/min), MeOH 200 min,
                      Sept 19, 2011

    ======================================================================
```

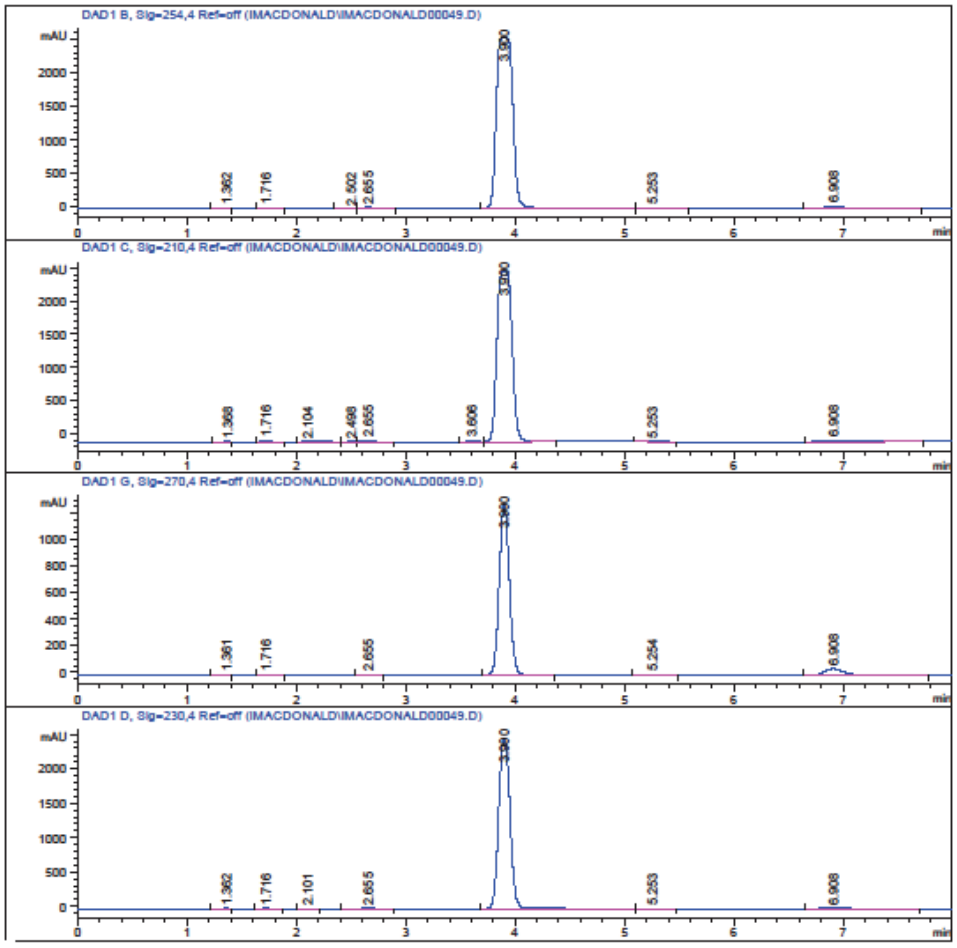


```
Instrument 1 19/09/2011 5:42:26 PM Ian Macdonald                Page   3 of 5
```

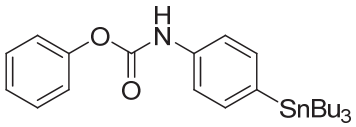

Phenyl 4-(tributylstannyl)phenylcarbamate (**17**)
^{1}H NMR

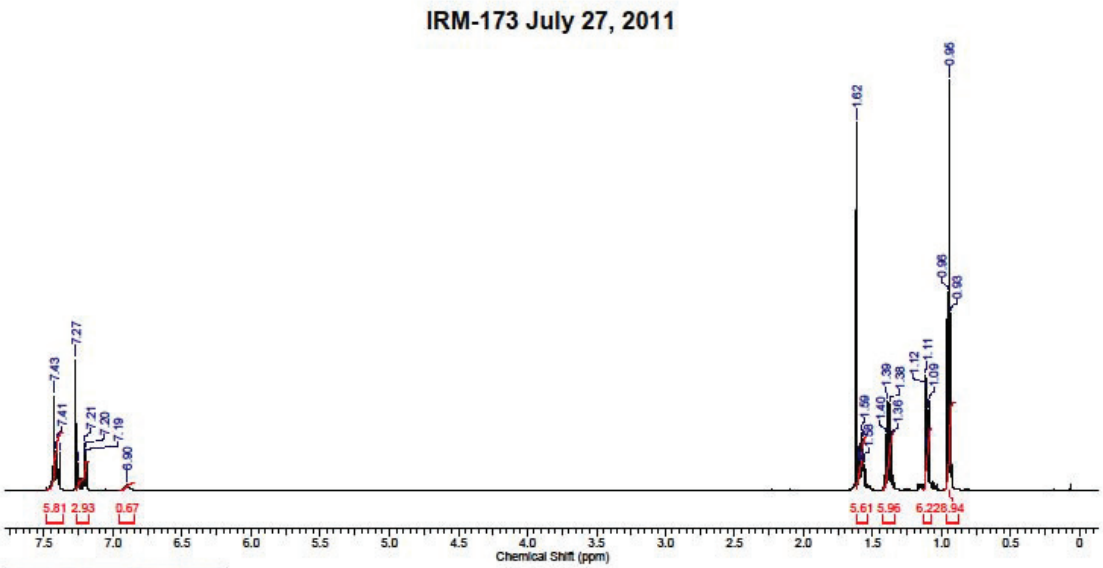

No.	(ppm)	(Hz)	Height
1	0.93	465.5	0.4313
2	0.95	472.8	1.0000
3	0.96	480.1	0.4833
4	1.09	543.0	0.2159
5	1.10	549.4	0.1264
6	1.10	550.9	0.1949
7	1.11	553.7	0.0992
8	1.11	556.7	0.2792
9	1.12	559.2	0.2476
10	1.36	680.6	0.1267
11	1.38	687.9	0.2106
12	1.39	695.3	0.2177
13	1.40	702.6	0.1338
14	1.55	777.4	0.0615

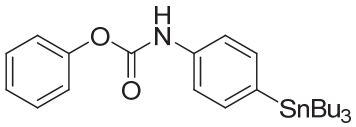

Phenyl 4-(tributylstannyl)phenylcarbamate (**17**)
^{13}C NMR

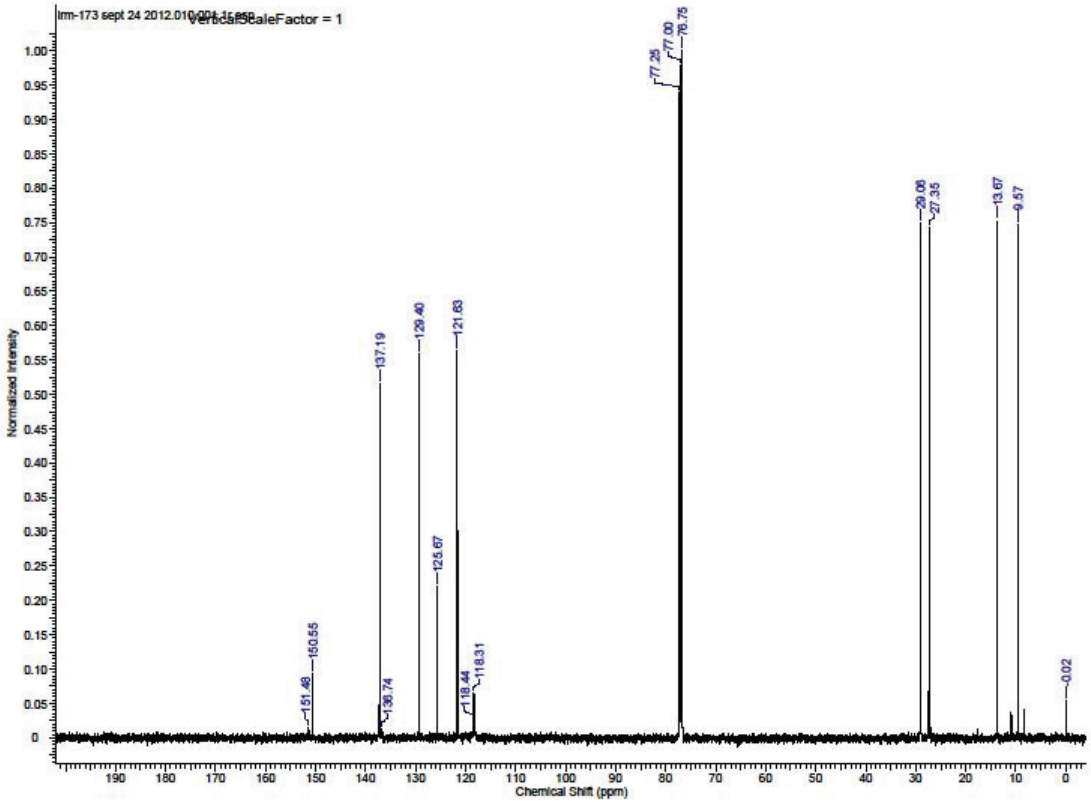

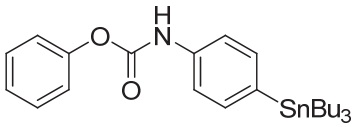

Phenyl 4-(tributylstannyl)phenylcarbamate (**17**)

IR

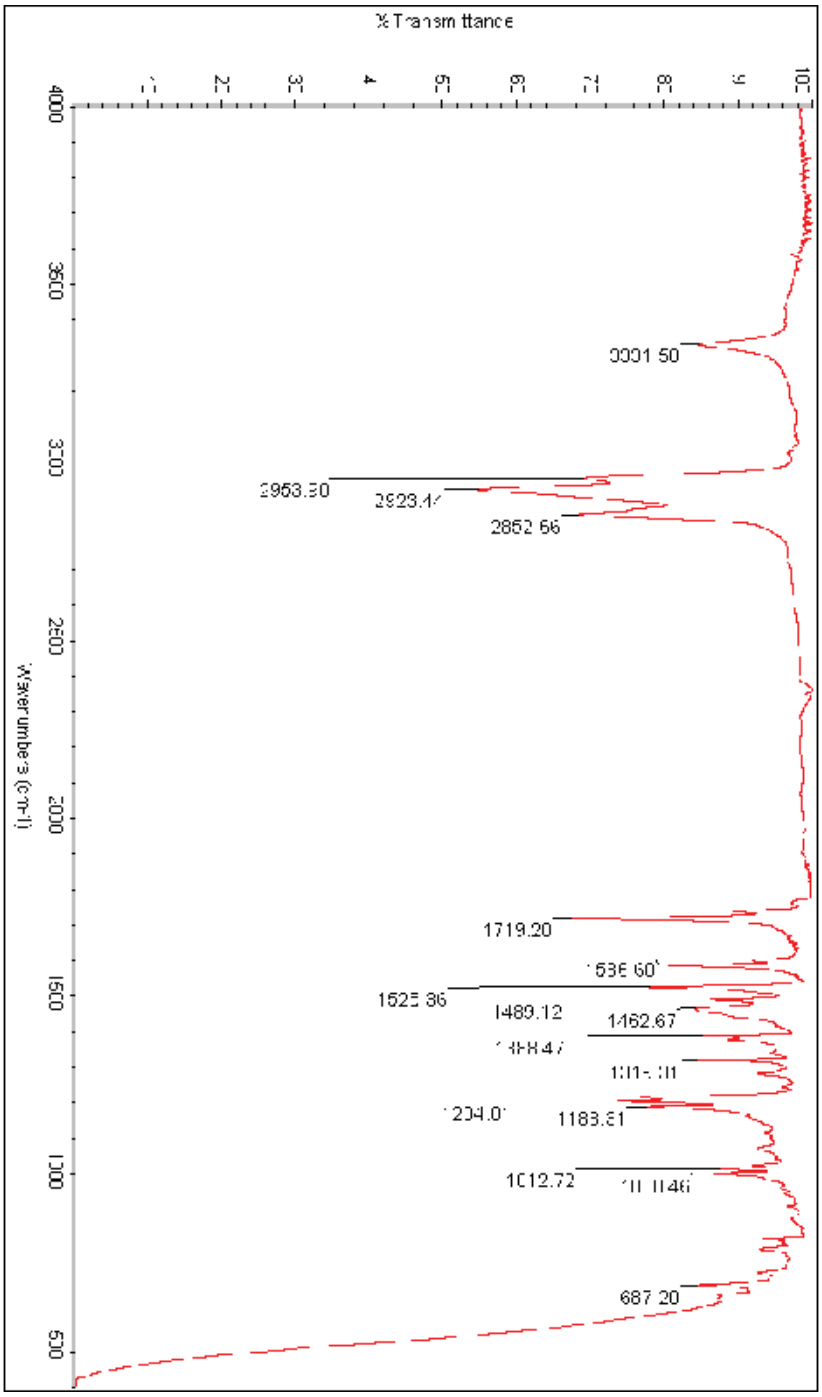

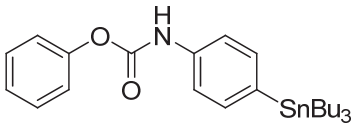

Phenyl 4-(tributylstannyl)phenylcarbamate (**17**)
LRMS

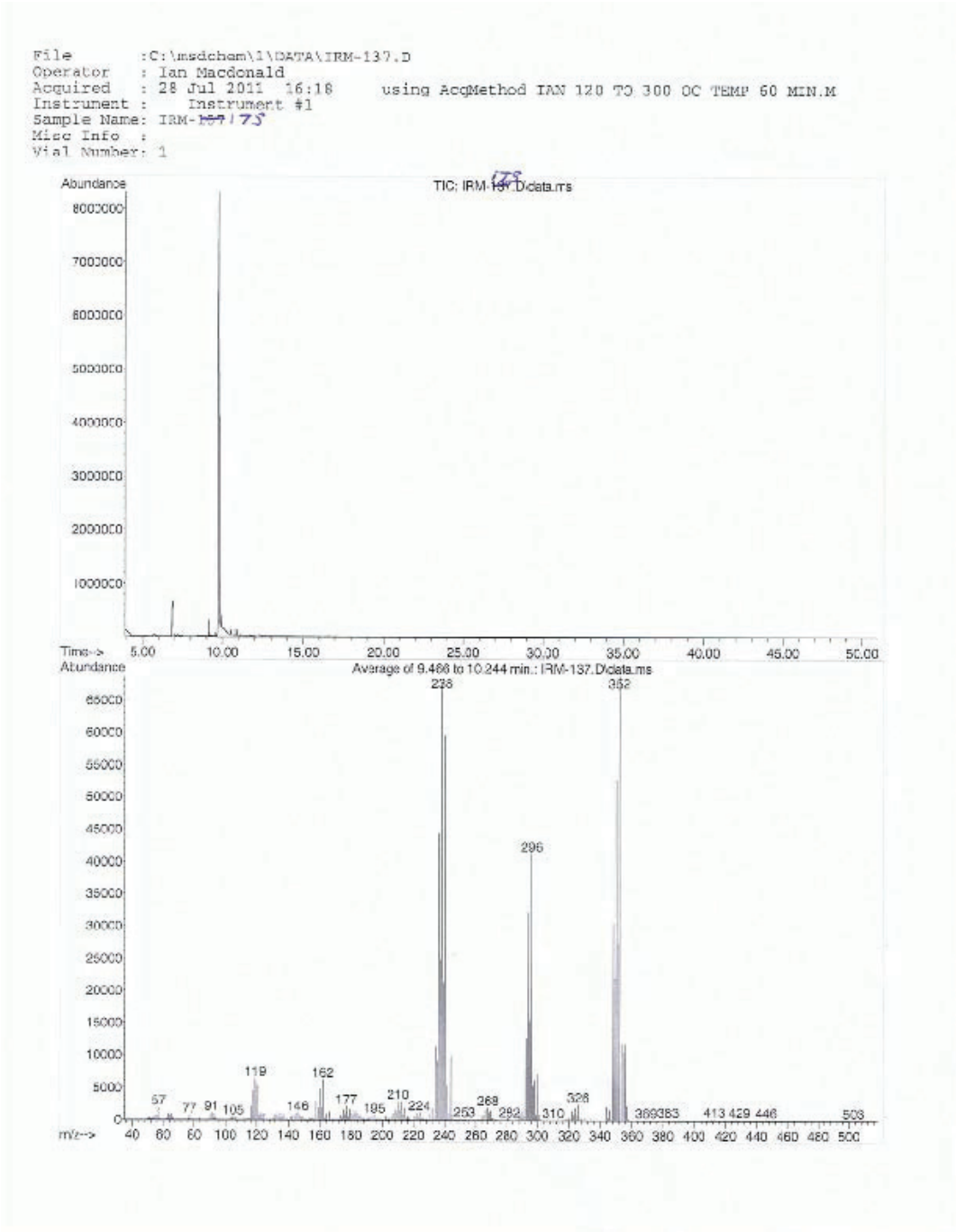

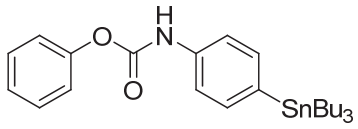

Phenyl 4-(tributylstannyl)phenylcarbamate (**17**)
HRMS

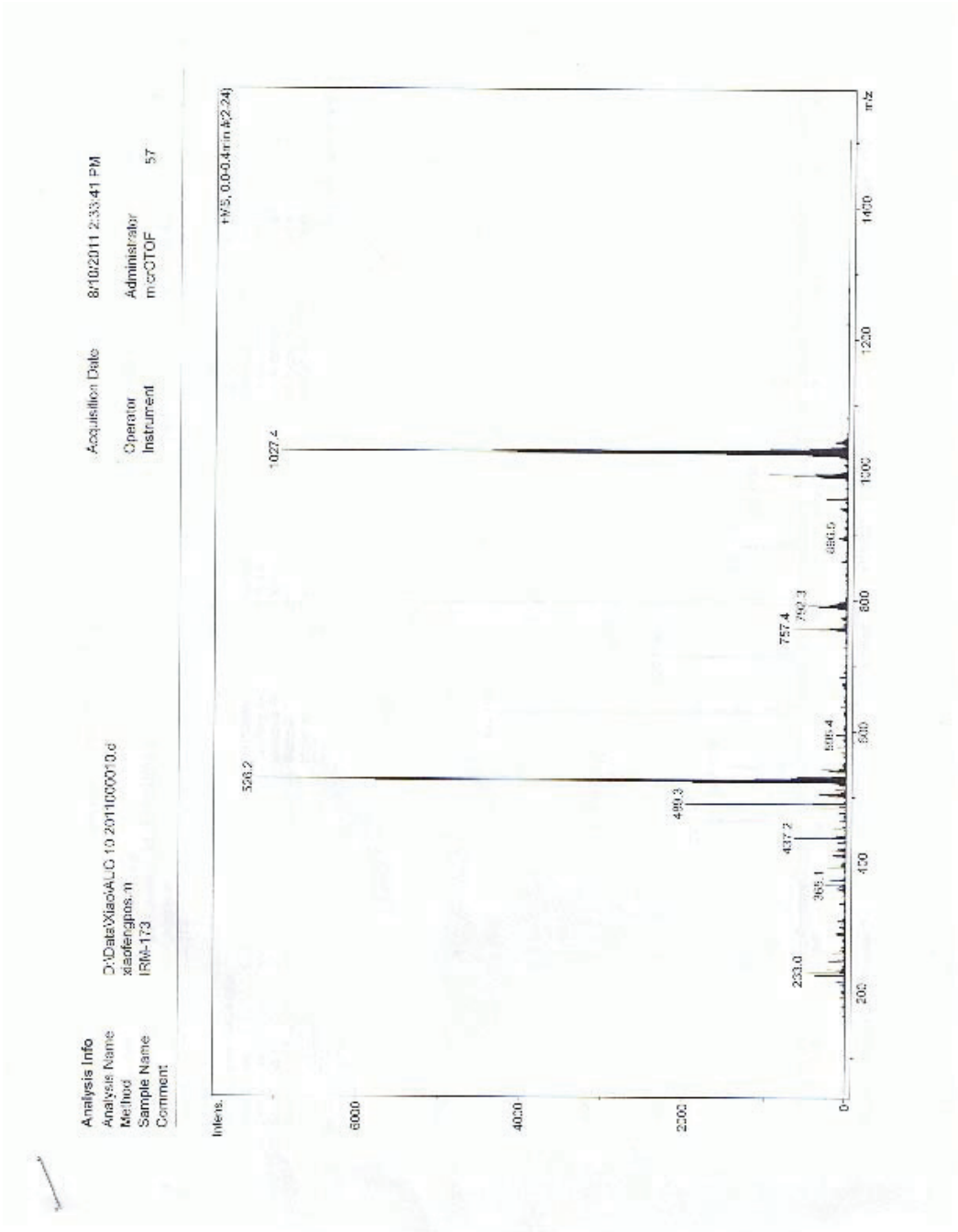

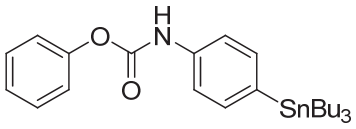

Phenyl 4-(tributylstannyl)phenylcarbamate (**17**)
HPLC

```
Data File C:\CHEM32\1\DATA\IMACDONALD\SIG10016.D
Sample Name: IRM-173
    ======================================================================
    Acq. Operator   : Ian Macdonald
    Acq. Instrument : Instrument 1                    Location : Vial 1
    Injection Date  : 01/08/2011 3:35:34 PM
                                                    Inj Volume : Manually
    Acq. Method     : C:\CHEM32\1\METHODS\IRM.M
    Last changed    : 01/08/2011 3:34:16 PM by Ian Macdonald
                      (modified after loading)
    Analysis Method : C:\CHEM32\1\METHODS\IRM.M
    Last changed    : 01/08/2011 4:05:38 PM by Ian Macdonald
                      (modified after loading)
    Sample Info     : IRM-173 1:100, 100% MeOH, 20 uL, 1mL/min,  Aug 1, 2011


    ======================================================================
```

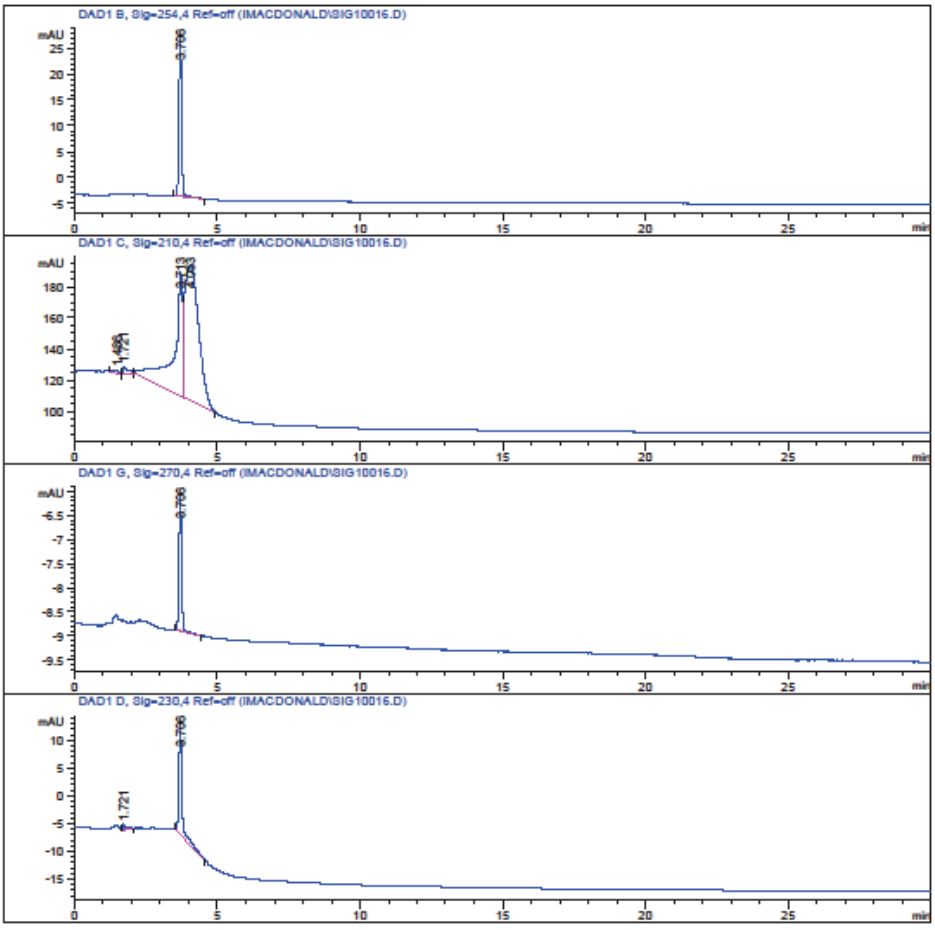


```
Instrument 1 01/08/2011 4:05:38 PM Ian Macdonald                Page   3 of 5
```

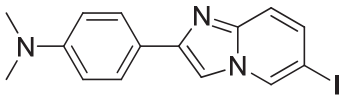

2-(4'-Dimethylaminophenyl)-6-iodoimidazol[1,2-a]pyridine (**18**)
^{1}H NMR

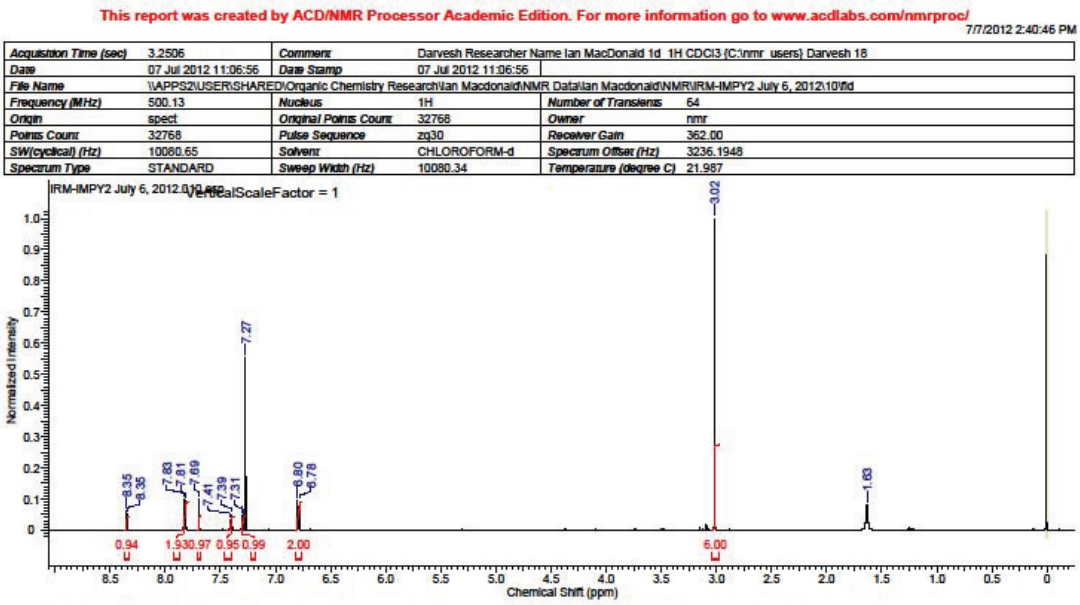

No.	(ppm)	(Hz)	Height
1	1.63	817.4	0.0796
2	3.02	1509.3	1.0000
3	6.78	3392.6	0.0919
4	6.80	3401.5	0.0964
5	7.27	3636.0	0.5520

No.	(ppm)	(Hz)	Height
6	7.29	3644.0	0.0339
7	7.31	3653.5	0.0470
8	7.31	3655.0	0.0496
9	7.39	3698.4	0.0492
10	7.41	3708.0	0.0329

No.	(ppm)	(Hz)	Height
11	7.69	3847.3	0.1003
12	7.69	3847.9	0.1010
13	7.81	3907.0	0.0967
14	7.83	3916.2	0.0991
15	8.35	4175.9	0.0504

No.	(ppm)	(Hz)	Height
16	8.35	4176.8	0.0599
17	8.35	4177.7	0.0551
18	8.35	4178.3	0.0488

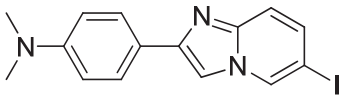

2-(4'-Dimethylaminophenyl)-6-iodoimidazol[1,2-a]pyridine (**18**)
^{13}C NMR

Acquisition Time (sec)	0.7600				
Comment	Darvesh Researcher Name Ian MacDonald 1d_13C_DEPTQ135_n CDCl3 {C:\nmr_users} Darvesh 10 Best S/N after 128 scans was 19.2 Best S/N after 256 scans was 21.9 Best S/N after 384 scans was 29.2 Best S/N after 512 scans was 34.8 Best S/N after 640 scans was				
Date	24 Jul 2012 03:15:28	*Date Stamp*	24 Jul 2012 03:15:28		
File Name	\\APPS2\USER\SHARED\Organic Chemistry Research\Ian Macdonald\NMR Data\Ian Macdonald\NMR\IRM-IMPY2 July 23, 2012\11\PDATA\1\1r				
Frequency (MHz)	125.76	*Nucleus*	13C	*Number of Transients*	940
Origin	spect	*Original Points Count*	25335	*Owner*	nmr
Points Count	65536	*Pulse Sequence*	deptqsp.dmo	*Receiver Gain*	9195.20
SW(cyclical) (Hz)	33333.33	*Solvent*	CHLOROFORM-d	*Spectrum Offset (Hz)*	13826.8701
Sweep Width (Hz)	33332.82	*Temperature (degree C)*	21.851		

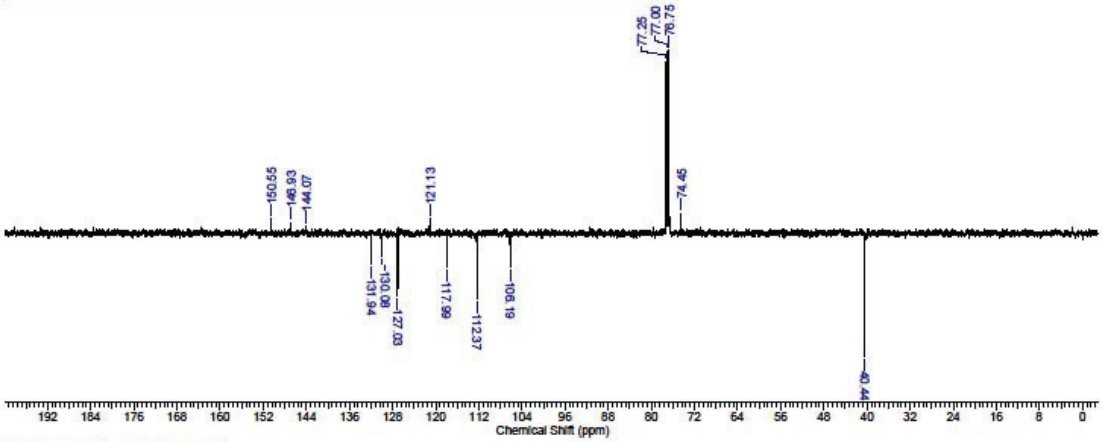

No.	(ppm)	(Hz)	Height
1	40.44	5085.4	-0.6729
2	74.45	9362.4	0.1091
3	76.75	9651.3	1.0000
4	77.00	9683.3	0.9961
5	77.25	9715.4	0.9378
6	106.19	13354.1	-0.1851
7	112.37	14131.3	-0.3583
8	117.99	14837.8	-0.1865
9	121.13	15233.5	0.0789
10	127.03	15975.6	-0.3383
11	130.08	16358.1	-0.1281

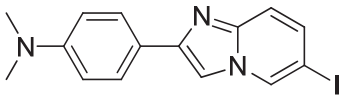

2-(4'-Dimethylaminophenyl)-6-iodoimidazol[1,2-a]pyridine (**18**)
IR

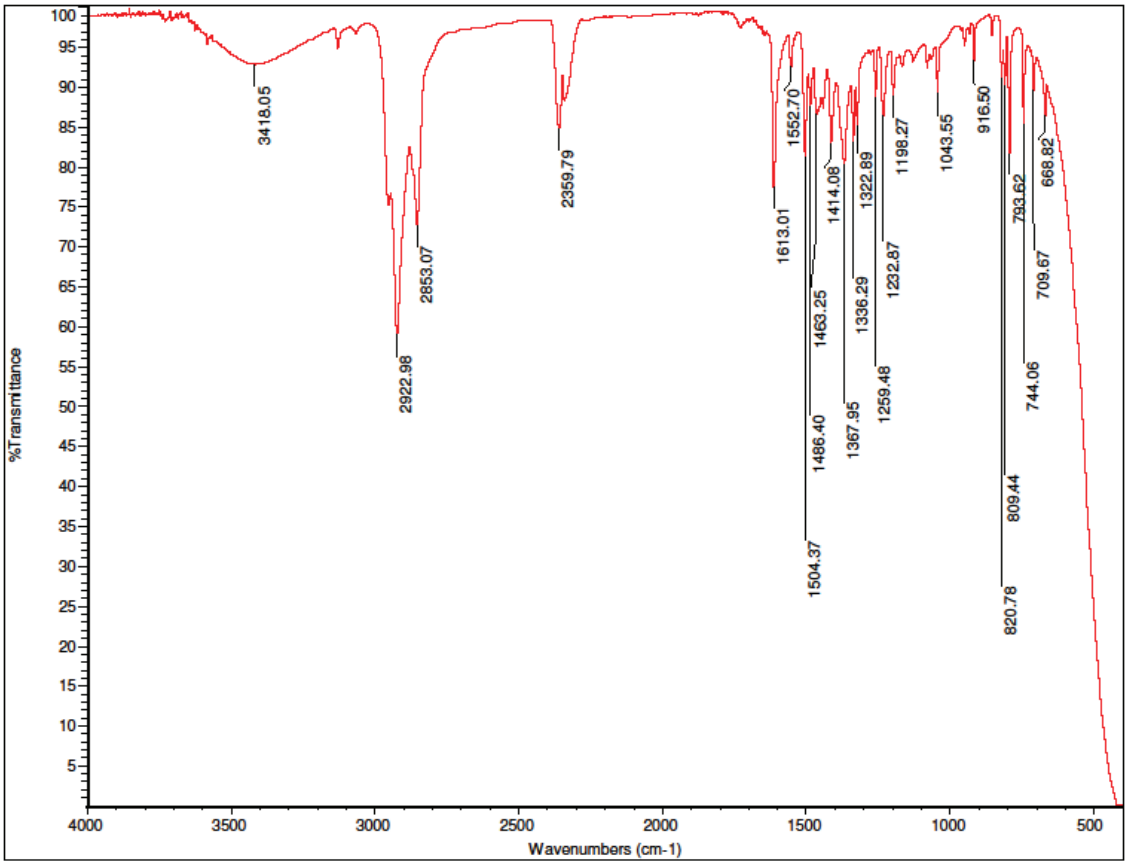

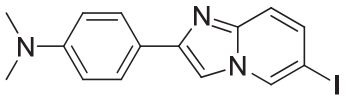

2-(4'-Dimethylaminophenyl)-6-iodoimidazol[1,2-a]pyridine (**18**)
LRMS

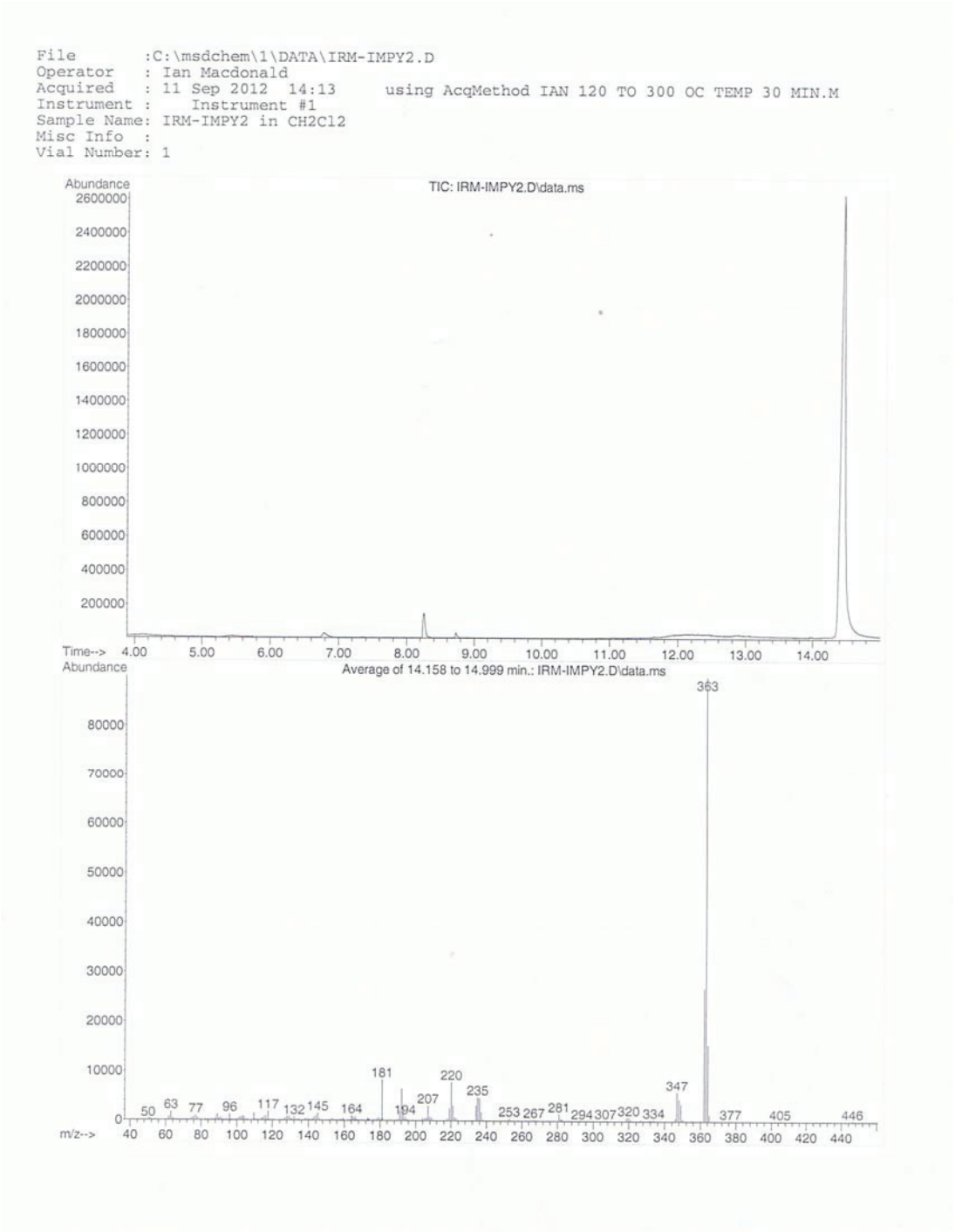

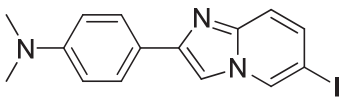

2-(4'-Dimethylaminophenyl)-6-iodoimidazol[1,2-a]pyridine (**18**)
HRMS

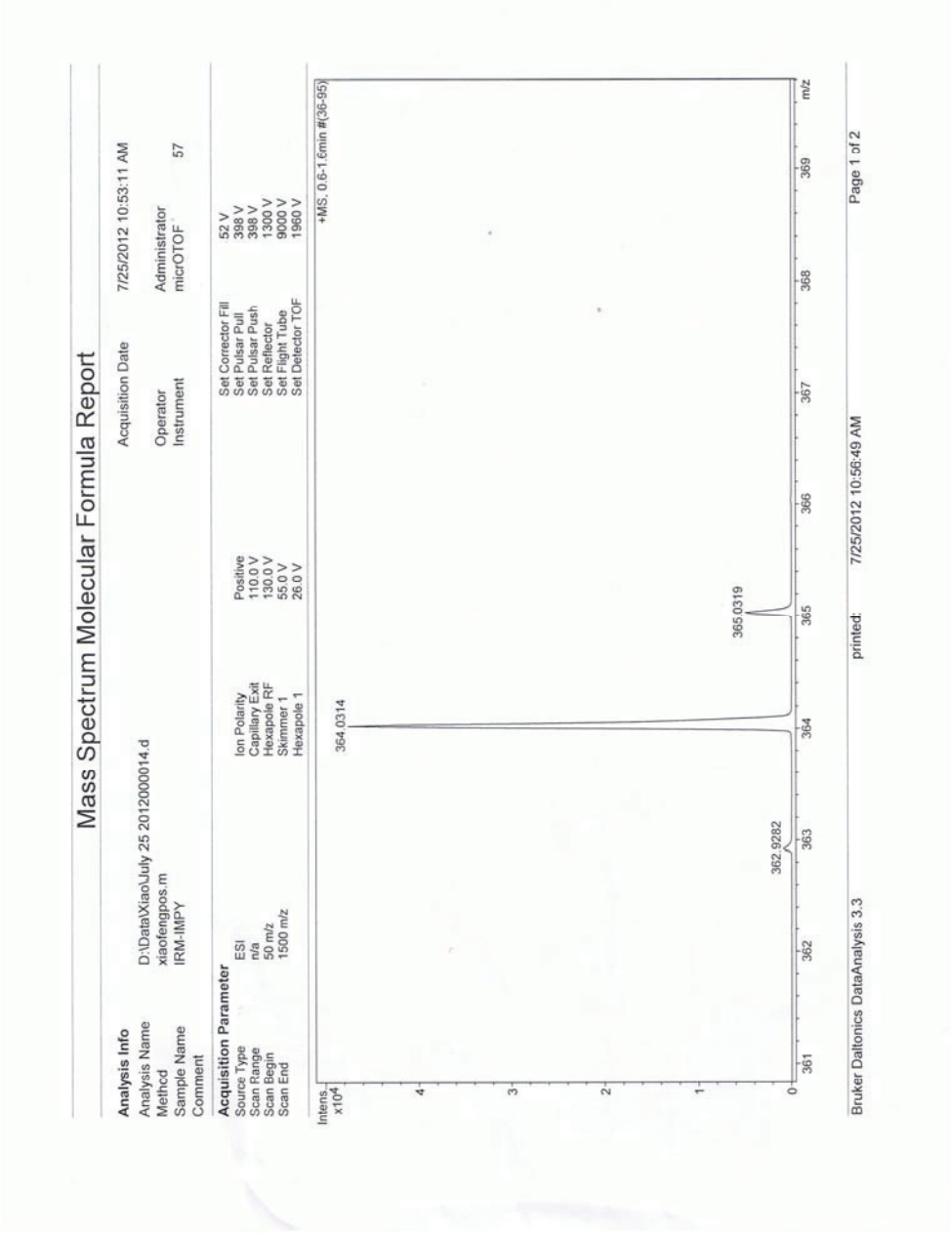

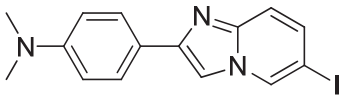

2-(4'-Dimethylaminophenyl)-6-iodoimidazol[1,2-a]pyridine (**18**)
HPLC

```
Data File C:\CHEM32\1\DATA\IMACDONALD\IMACDONALD00150.D
Sample Name: IRM-IMPY2
    ========================================================================
    Acq. Operator   : Ian Macdonald
    Acq. Instrument : Instrument 1                    Location : Vial 1
    Injection Date  : 24/10/2012 12:44:54 PM
                                                    Inj Volume : Manually
    Acq. Method     : C:\CHEM32\1\METHODS\IRM.M
    Last changed    : 24/10/2012 12:30:06 PM by Ian Macdonald
    Analysis Method : C:\CHEM32\1\METHODS\SHUTDOWN.M
    Last changed    : 31/10/2012 2:52:20 PM by Ian Macdonald
                      (modified after loading)
    Sample Info     : 2012-10-24 IRM-IMPY2
                      80% MeOH 20% H20 for 15 min, 100% MeOH for 10 min


    Additional Info : Peak(s) manually integrated
    ========================================================================
```

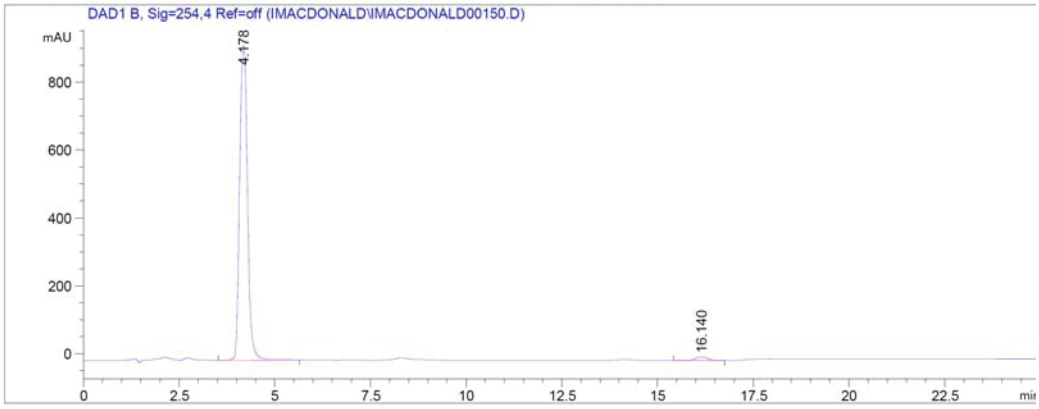


```
    ========================================================================
                              Area Percent Report
    ========================================================================

    Sorted By             :      Signal
    Multiplier:                   :      1.0000
    Dilution:                     :      1.0000
    Use Multiplier & Dilution Factor with ISTDs


    Signal 1: DAD1 B, Sig=254,4 Ref=off

    Peak RetTime Type  Width     Area      Height     Area
      #   [min]        [min]   [mAU*s]     [mAU]       %
    ----|-------|----|-------|----------|----------|--------|
       1   4.178 BB    0.2316 1.32537e4   922.41736  98.1848
       2  16.140 BB    0.3751  245.03178   10.54317   1.8152

    Totals :                  1.34988e4   932.96053


    ========================================================================

Instrument 1 31/10/2012 2:53:48 PM Ian Macdonald                Page   3 of 3
```

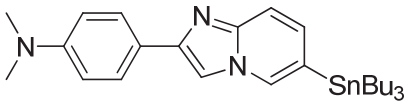

2-(4'-Dimethylaminophenyl)-6-tributylstannylimidazol[1,2-a]pyridine (**19**)
^{1}H NMR

Acquisition Time (sec)	3.2768	*Comment*	Darvesh Researcher Name Ian MacDonald 1d 1H CDCl3 (C:\nmr users) Darvesh 11				
Date	23 Jul 2012 15:52:48	*Date Stamp*	23 Jul 2012 15:52:48				
File Name	\\APPS2\USER\SHARED\Organic Chemistry Research\Ian Macdonald\NMR Data\Ian Macdonald\NMR\IRM-180 July 23, 2012\10\fid						
Frequency (MHz)	500.13	*Nucleus*	1H	*Number of Transients*	64	*Origin*	spect
Original Points Count	32768	*Owner*	nmr	*Points Count*	32768	*Pulse Sequence*	zg30
Receiver Gain	90.50	*SW(cyclical) (Hz)*	10000.00	*Solvent*	CHLOROFORM-d	*Spectrum Offset (Hz)*	3239.3694
Spectrum Type	STANDARD	*Sweep Width (Hz)*	9999.70	*Temperature (degree C)*	20.767		

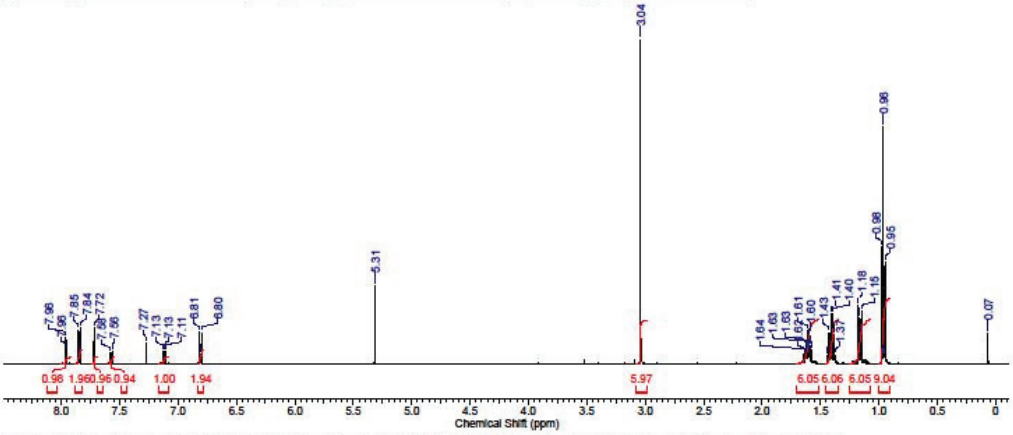

No.	(ppm)	(Hz)	Height	No.	(ppm)	(Hz)	Height	No.	(ppm)	(Hz)	Height	No.	(ppm)	(Hz)	Height
1	0.07	33.7	0.0961	13	1.37	684.3	0.0280	25	1.62	807.9	0.0453	37	7.11	3556.3	0.0411
2	0.95	474.0	0.3159	14	1.38	691.6	0.0929	26	1.62	810.3	0.0297	38	7.13	3563.9	0.0413
3	0.95	476.8	0.0250	15	1.40	698.6	0.1542	27	1.63	813.4	0.0576	39	7.13	3564.8	0.0423
4	0.96	481.3	0.7325	16	1.41	706.3	0.1566	28	1.63	814.6	0.0528	40	7.27	3635.9	0.0656
5	0.97	486.2	0.0293	17	1.43	713.6	0.0974	29	1.64	820.7	0.0297	41	7.56	3783.0	0.0389
6	0.98	488.7	0.3620	18	1.44	720.9	0.0260	30	3.04	1520.5	1.0000	42	7.58	3791.6	0.0351
7	1.15	573.8	0.1636	19	1.58	789.9	0.0440	31	5.31	2658.2	0.2431	43	7.72	3859.9	0.1110
8	1.16	580.2	0.0910	20	1.59	795.4	0.0571	32	6.80	3399.4	0.0973	44	7.84	3919.5	0.1111
9	1.16	581.7	0.1443	21	1.60	798.1	0.0879	33	6.80	3401.6	0.0298	45	7.84	3921.6	0.0323
10	1.17	583.3	0.0682	22	1.60	799.9	0.0370	34	6.81	3406.5	0.0319	46	7.85	3926.2	0.0319
11	1.17	584.5	0.0661	23	1.60	802.4	0.0505	35	6.81	3408.3	0.0990	47	7.85	3928.3	0.1058
12	1.18	590.0	0.1817	24	1.61	805.4	0.1030	36	7.11	3555.4	0.0410	48	7.96	3979.0	0.0439

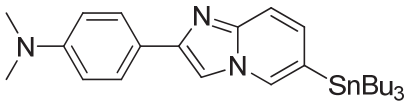

2-(4'-Dimethylaminophenyl)-6-tributylstannylimidazol[1,2-a]pyridine (**19**)
^{13}C NMR

7/24/2012 2:03:57 PM

Acquisition Time (sec)	0.7600				
Comment	Darvesh Researcher Name Ian MacDonald 1d_13C_DEPTQ135_n CDCl3 {C:\nmr_users} Darvesh 25 Best S/N after 128 scans was 38.4 Best S/N after 256 scans was 53.1 Best S/N after 384 scans was 62.5 Best S/N after 512 scans was 70.9 Best S/N after 640 scans was				
Date	24 Jul 2012 12:19:28	*Date Stamp*	24 Jul 2012 12:19:28		
File Name	\\APPS2\USER\SHARED\Organic Chemistry Research\Ian Macdonald\NMR Data\Ian Macdonald\NMR\IRM-180 July 24, 2012\10\fid				
Frequency (MHz)	125.76	*Nucleus*	13C	*Number of Transients*	936
Origin	spect	*Original Points Count*	25335	*Owner*	nmr
Points Count	32768	*Pulse Sequence*	deptqsp.dmo	*Receiver Gain*	9195.20
SW(cyclical) (Hz)	33333.33	*Solvent*	CHLOROFORM-d	*Spectrum Offset (Hz)*	13824.0771
Sweep Width (Hz)	33332.32	*Temperature (degree C)*	21.716		

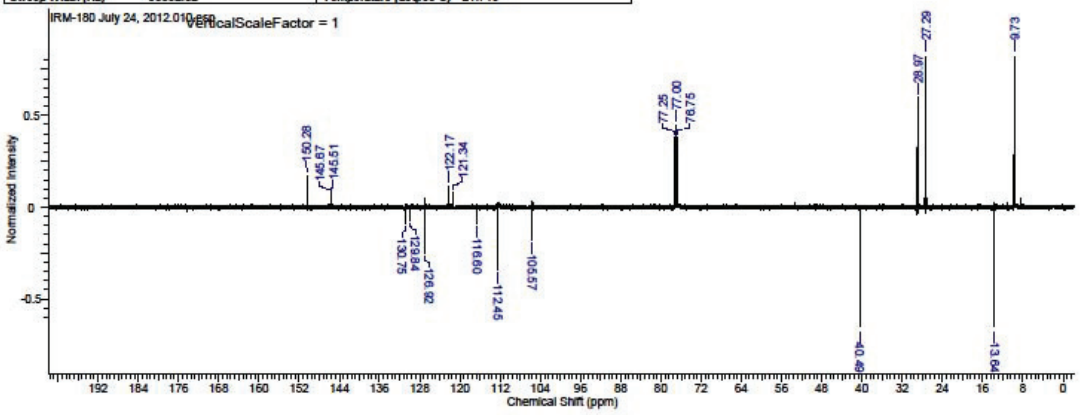

No.	(ppm)	(Hz)	Height
1	9.73	1223.9	0.8542
2	13.64	1715.2	-0.9398
3	27.29	3431.3	0.8785
4	28.97	3642.9	0.5965
5	40.49	5092.5	-1.0000

No.	(ppm)	(Hz)	Height
6	76.75	9651.8	0.3810
7	77.00	9683.4	0.4492
8	77.25	9714.9	0.3793
9	105.57	13276.3	-0.1789
10	112.45	14142.0	-0.3396

No.	(ppm)	(Hz)	Height
11	116.60	14662.8	-0.0889
12	121.34	15258.9	0.0837
13	122.17	15363.7	0.1166
14	126.92	15960.8	-0.2535
15	129.84	16328.0	-0.0713

No.	(ppm)	(Hz)	Height
16	130.75	16443.0	-0.0912
17	145.51	18298.5	0.0698
18	145.67	18318.8	0.0601
19	150.28	18898.6	0.1723

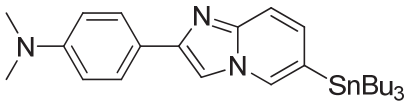

2-(4'-Dimethylaminophenyl)-6-tributylstannylimidazol[1,2-a]pyridine (**19**)
IR

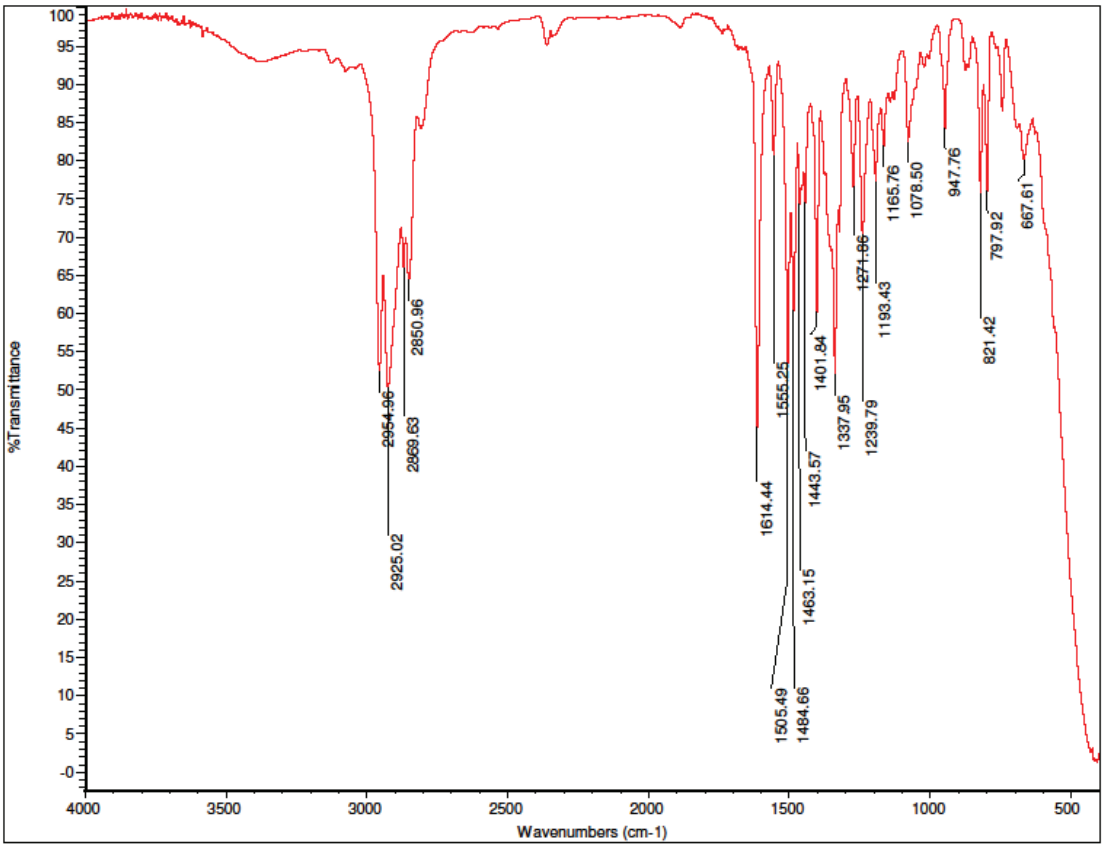

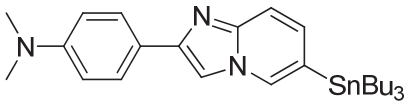

2-(4'-Dimethylaminophenyl)-6-tributylstannylimidazol[1,2-a]pyridine (**19**)
LRMS

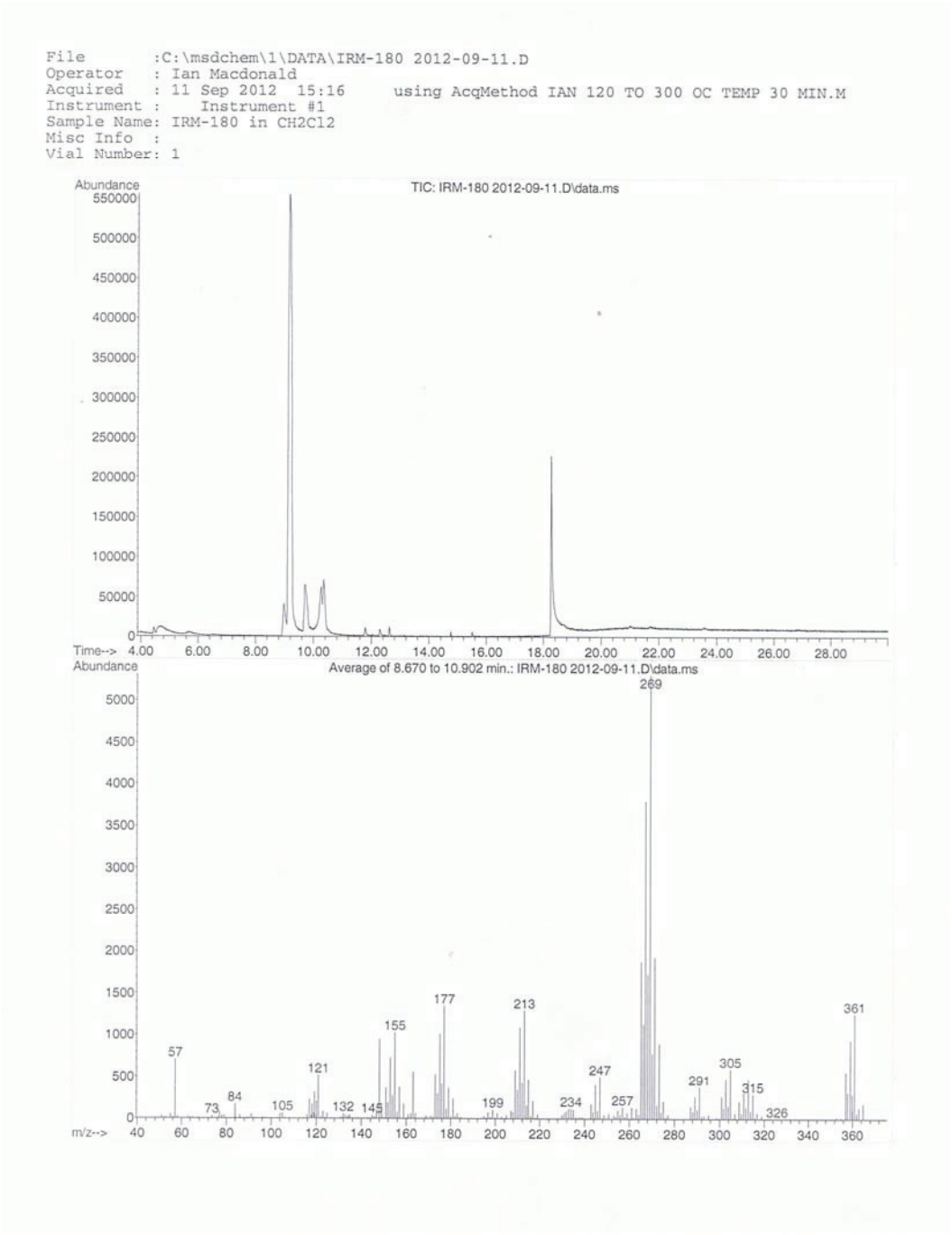

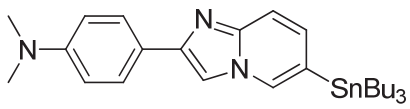

2-(4'-Dimethylaminophenyl)-6-tributylstannylimidazol[1,2-a]pyridine (**19**)
HRMS

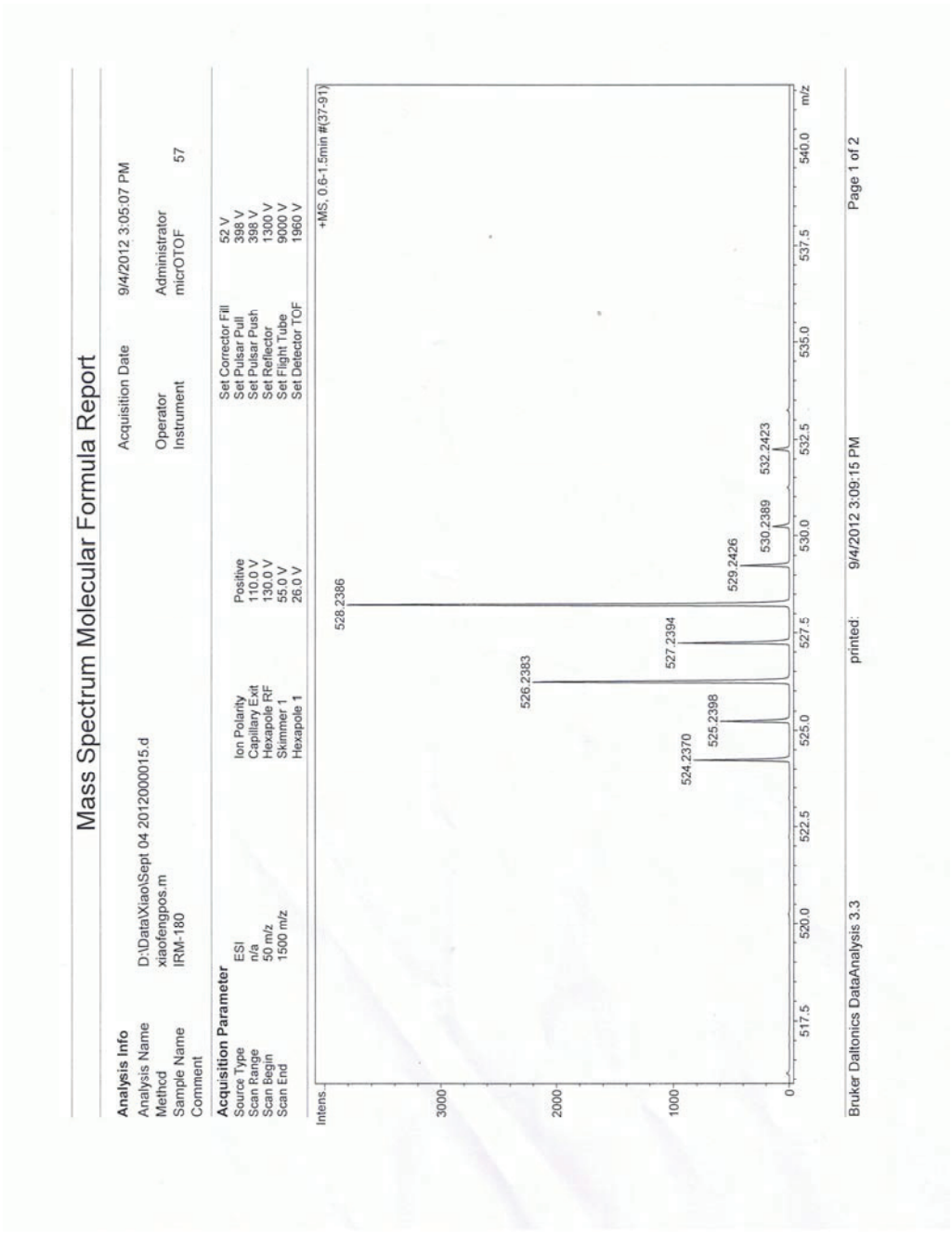

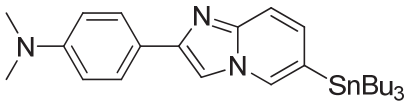

2-(4'-Dimethylaminophenyl)-6-tributylstannylimidazol[1,2-a]pyridine (**19**)
HPLC

```
Data File C:\CHEM32\1\DATA\IMACDONALD\IMACDONALD00144.D
Sample Name: IRM-183
    ========================================================================
    Acq. Operator   : Ian Macdonald
    Acq. Instrument : Instrument 1                    Location : Vial 1
    Injection Date  : 23/10/2012 12:04:00 PM
                                                     Inj Volume : Manually
    Acq. Method     : C:\CHEM32\1\METHODS\IRM.M
    Last changed    : 10/08/2011 2:53:08 PM by Ian Macdonald
    Analysis Method : C:\CHEM32\1\METHODS\SHUTDOWN.M
    Last changed    : 31/10/2012 3:08:35 PM by Ian Macdonald
                      (modified after loading)
    Sample Info     : 2012-10-23 IRM-183
                      80% MeOH 20% H20 for 15 min, 100% MeoH for 10 min


    ========================================================================
```

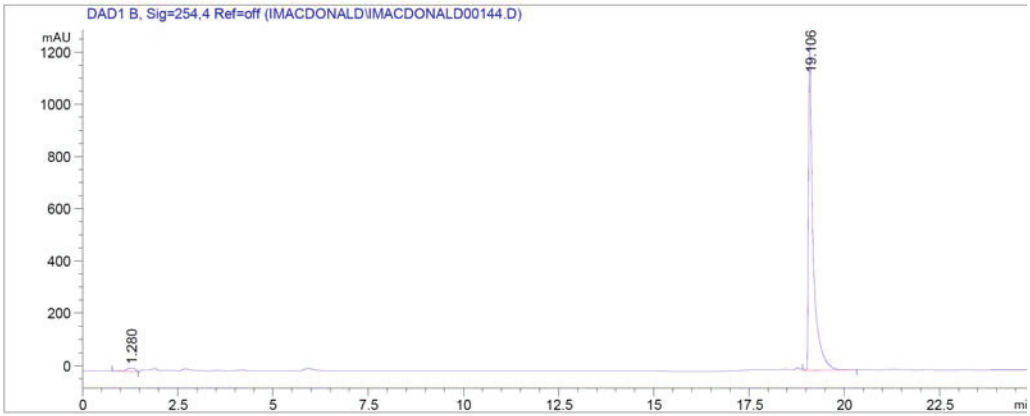


```
    ========================================================================
                            Area Percent Report
    ========================================================================

    Sorted By             :      Signal
    Multiplier:                   :      1.0000
    Dilution:                     :      1.0000
    Use Multiplier & Dilution Factor with ISTDs


    Signal 1: DAD1 B, Sig=254,4 Ref=off

    Peak RetTime Type  Width     Area      Height     Area
      #   [min]        [min]   [mAU*s]     [mAU]       %
    ----|-------|----|-------|----------|----------|--------|
       1   1.280 BB    0.2730  204.59424   11.87529   1.9326
       2  19.106 VB    0.1468 1.03821e4  1134.56726  98.0674

    Totals :                  1.05867e4  1146.44255

    ========================================================================
                            *** End of Report ***

Instrument 1 31/10/2012 3:09:02 PM Ian Macdonald                Page   3 of 3
```